

**Decomposition,
quantitative and qualitative evaluation
of TiO₂ thin film Raman spectra**

Der Fakultät für Physik der Universität Duisburg-Essen vorgelegte

Dissertation

zur Erlangung des akademischen Grades eines Doktors der Naturwissenschaften

Dr. rer. nat.

Von

Sebastian Schipporeit

Geboren am 24.07.1982

in Krefeld

Tag der Einreichung: 15.05.2020

Tag der Disputation: 14.09.2020

Prüfungsvorsitzender: Prof. Dr. Dr. h.c. Volker Buck

Erster Gutachter: Prof. Dr. Dieter Mergel

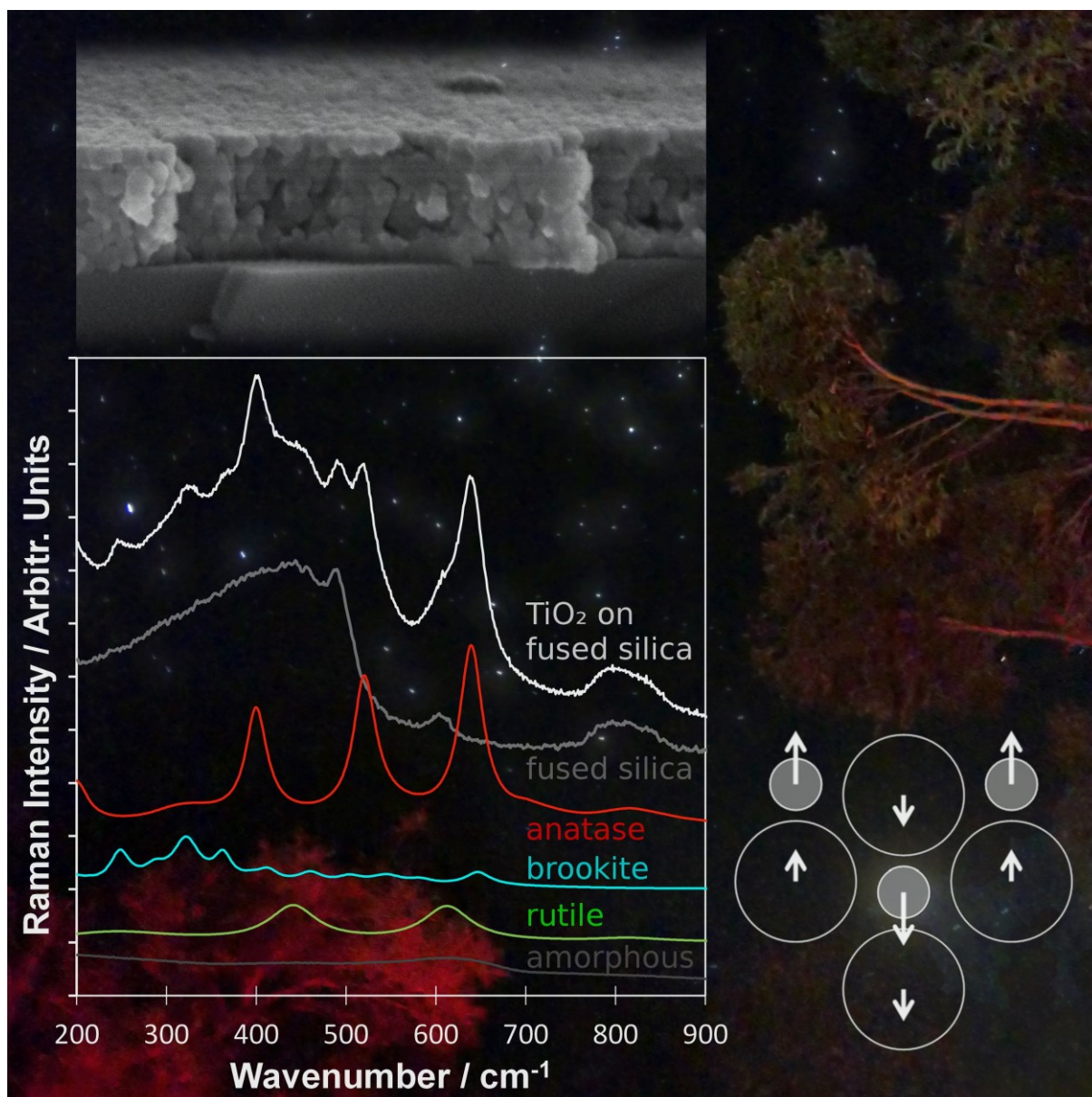
Zweiter Gutachter: Prof. Dr. Matthias Wuttig



This work is licensed under a Creative Commons Attribution 4.0 International License (CC BY 4.0). <https://creativecommons.org/licenses/by/4.0/>

The CC BY 4.0 licence does not account for the chapters 2.2.1.1, 3.1, and 4.1.3. These chapters sum up to the full text of the publication *Spectral decomposition of Raman spectra of mixed-phase TiO₂ thin films on Si and silicate substrates* published by Sebastian Schipporeit and Dieter Mergel in the Journal of Raman spectroscopy.¹ Copyright © 2018 John Wiley & Sons, Ltd.

Furthermore, the CC BY 4.0 licence does not account for the cover image. An altered version of the cover image has been published as cover image of the Journal of Raman Spectroscopy.² Copyright © 2018 John Wiley & Sons, Ltd.



An altered version of this cover image has been published as a cover image of the *Journal of Raman Spectroscopy*. Copyright © 2018 John Wiley & Sons, Ltd.²

Die Suche nach neuen Fragestellungen
ist spannender als die Beantwortung bereits gestellter Fragen.

Contents

Abstract	6
Zusammenfassung	7
Introduction	8
List of abbreviations	13
1 Fundamentals	14
1.1 Thin film vapor deposition	14
1.1.1 Evaporation.....	15
1.1.2 Sputtering	16
1.1.2.1 Diode sputtering.....	18
1.1.2.2 Magnetron sputtering	19
1.1.3 Radio-frequency sputtering	19
1.2 Thin film growth.....	21
1.3 TiO ₂	23
1.3.1 TiO ₂ anatase	24
1.3.2 TiO ₂ rutile	24
1.3.3 TiO ₂ brookite.....	24
1.4 Raman scattering	25
1.4.1 Raman spectroscopy	25
1.4.2 Fundamentals of Raman scattering	25
1.4.2.1 Raman effect	25
1.4.2.2 Classic representation of Raman scattering	28
1.4.2.3 The Raman tensor	30
1.4.2.4 Raman intensity invariants	31
1.4.2.5 Raman intensity.....	32
1.4.3 Raman spectra of TiO ₂	34
1.4.3.1 Raman spectrum of anatase TiO ₂	34
1.4.3.2 Raman spectrum of brookite TiO ₂	35
1.4.3.3 Raman spectrum of rutile TiO ₂	36
1.4.3.4 Raman spectra of nanostructured anatase TiO ₂	37
1.4.4 Raman scattering of amorphous materials	40
1.4.5 Raman bands of Si and of silica glass substrates.....	41
1.4.5.1 Raman spectrum of Si.....	41
1.4.5.2 Raman bands of silica glasses	42
1.5 X-ray diffraction	43
2 Experiments	46
2.1 Thin film preparation	46
2.1.1 Deposition of rf-diode sputtered TiO ₂ films	46

2.1.2	Deposition and annealing of reactive e-beam evaporated TiO ₂ films.....	48
2.1.3	Deposition of plasma-emission controlled rf-magnetron sputtered TiO ₂ films	51
2.2	Analytics	54
2.2.1	Raman spectroscopy	54
2.2.1.1	Measurement and preprocessing of the spectra	54
2.2.1.2	Noise filter	56
2.2.2	Raman maps	57
2.2.2.1	Raman phonon maps.....	60
2.2.2.2	Raman TiO ₂ phase maps.....	63
2.2.3	X-ray diffraction	64
2.2.4	Surface topology	68
2.2.5	Chemical Composition	68
2.2.6	Film thickness, mass, and mass density	68
2.2.7	Electrical properties	69
3	Concepts and models for the decomposition of Raman spectra and X-ray diffractograms	70
3.1	Decomposition of Raman spectra of mixed-phase TiO ₂ thin films on Si and silicate substrates	70
3.1.1	Summary.....	70
3.1.2	Introduction	71
3.1.3	Concept of the Raman fitting model.....	72
3.1.4	Models for TiO ₂ spectra	74
3.1.4.1	Amorphous phase	74
3.1.4.2	Crystalline phases.....	75
3.1.4.3	First-order scattering models	76
3.1.4.3.1	<i>Simplified models for first-order scattering</i>	<i>77</i>
3.1.4.4	Models for phase background spectra	78
3.1.4.4.1	<i>Decomposition of reference phase background spectra.....</i>	<i>78</i>
3.1.4.4.2	<i>Adjustable spectral bands for phase backgrounds</i>	<i>81</i>
3.1.4.4.3	<i>Simplified models for phase backgrounds</i>	<i>82</i>
3.1.5	Models for substrate spectra	82
3.1.5.1	Substrates with strong and sharp Raman peaks.....	83
3.1.5.2	Models for luminescent substrates	85
3.1.5.2.1	<i>Simple model for luminescent substrates</i>	<i>88</i>
3.1.5.2.2	<i>Individual-band model for luminescent substrates.....</i>	<i>88</i>
3.1.6	Conclusions	90
3.2	Models for the simulation of Raman spectra.....	92
3.2.1	Main concept of the thin film Raman fitting model.....	92
3.2.2	Raman models for TiO ₂ thin films	93
3.2.2.1	Amorphous TiO ₂ model	93
3.2.2.2	Models for crystalline phases.....	93
3.2.2.3	First-order scattering models	94
3.2.2.3.1	<i>First-order scattering model of anatase</i>	<i>95</i>

3.2.2.3.2	<i>First-order scattering model of rutile</i>	95
3.2.2.3.3	<i>First-order scattering model of brookite</i>	97
3.2.2.4	Models for phase background spectra	98
3.2.2.4.1	<i>Crystalline background of anatase</i>	99
3.2.2.4.2	<i>Crystalline background of brookite</i>	102
3.2.2.4.3	<i>Crystalline background of rutile</i>	103
3.2.3	Raman models for substrate spectra	104
3.2.3.1	Si substrate model.....	105
3.2.3.2	Models for luminescent substrates	106
3.3	Models for the simulation of X-ray diffractograms.....	107
3.3.1	Main concept of the thin film XRD fitting model	107
3.3.2	XRD model for the amorphous TiO ₂ phase	109
3.3.3	XRD models of crystalline phases.....	110
3.3.3.1	XRD model for single-phase anatase	111
3.3.3.2	XRD models for multi-phase anatase and rutile.....	111
3.3.3.3	XRD models for minor-phase brookite	112
3.3.4	XRD models for substrates and background	113
4	Decomposed X-ray diffractograms and Raman spectra	116
4.1	Decomposed X-ray diffractograms and Raman spectra of rf-diode sputtered multi-phase TiO ₂ films.....	116
4.1.1	Decomposed multi-phase TiO ₂ X-ray diffractograms.....	117
4.1.2	Decomposed multi-phase TiO ₂ 633 nm and 532 nm Raman spectra	120
4.1.3	Decomposed TiO ₂ spectra on Si, crown glass, and fused silica	123
4.2	Decomposed X-ray diffractograms and Raman spectra of e-beam evaporated anatase TiO ₂ films	128
4.2.1	Decomposed undoped and Nb-doped anatase TiO ₂ X-ray diffractograms	129
4.2.2	Decomposed undoped and Nb-doped anatase TiO ₂ Raman spectra	134
5	Quantitative evaluation of decomposed Raman spectra and X-ray diffractograms	142
5.1	Quantification of Raman spectra and X-ray diffractograms	142
5.2	Quantitative comparison of Raman with XRD on diode sputtered multi-phase TiO ₂ films	145
5.2.1	Phase quantification with XRD and Raman.....	145
5.2.2	Influence of laser wavelength on the intensity of TiO ₂ phases in Raman spectra	148
5.2.3	Correlation between total XRD and Raman intensities.....	150
5.2.4	Correlation between relative XRD and Raman intensities	155
5.2.5	Conclusions	156
5.2.6	Suggested further studies	158
5.3	Influence of the substrate on the phase composition of multi-phase TiO ₂ films.....	160
5.4	Quantitative comparison of Raman with XRD on e-beam evaporated TiO ₂ anatase films	163
5.4.1	Phase quantification with XRD and Raman.....	163
5.4.2	Correlation between total XRD and Raman intensities.....	167
5.4.3	Correlation between relative XRD and Raman intensities	169

5.4.4	Conclusions	170
5.5	Comparison of the quantitative studies on rf-sputtered and evaporated TiO ₂ films.....	172
6	TiO₂ studies including decomposed TiO₂ Raman spectra	176
6.1	Studies including first-order spectra from decomposed TiO ₂ Raman spectra	176
6.1.1	Structural effects of the deposition temperature on diode-sputtered multi-phase TiO ₂ films.....	176
6.1.1.1	X-ray diffractograms.....	177
6.1.1.2	Raman spectra.....	180
6.1.1.3	Crystallite size and defect density	182
6.1.1.4	Q-vector relaxation models	184
6.1.1.5	Application of the QVRM.....	186
6.1.1.6	Defect density.....	191
6.1.1.7	Diode Sputtered films – connection between quantitative and qualitative Raman and XRD studies	193
6.1.1.8	Conclusions.....	193
6.1.2	Structural, electrical, and optical properties of Nb doped e-beam evaporated TiO ₂ films	196
6.1.2.1	Stoichiometry	196
6.1.2.2	Film thickness	196
6.1.2.3	XRD.....	196
6.1.2.3.1	<i>Lattice parameters and unit cell volume</i>	199
6.1.2.3.2	<i>Texture</i>	200
6.1.2.3.3	<i>Crystallite size and strain</i>	201
6.1.2.4	Raman spectra.....	204
6.1.2.4.1	<i>Raman peak intensities</i>	209
6.1.2.4.2	<i>Raman peak positions and widths</i>	212
6.1.2.4.3	<i>Causes of Raman peak shifts</i>	214
6.1.2.4.4	<i>Raman peak asymmetry</i>	215
6.1.2.4.5	<i>Polarized Raman spectra</i>	217
6.1.2.5	Optical measurements	221
6.1.2.5.1	<i>Optical band gap</i>	223
6.1.2.5.2	<i>SCOUT fits</i>	225
6.1.2.5.3	<i>Refractive index</i>	226
6.1.2.6	DC conductivity.....	226
6.1.2.7	Conclusions.....	228
6.1.3	Nb-doped TiO ₂ films sputtered with plasma emission control	231
6.1.3.1	Structural and electrical properties of PEM sputtered Nb-doped TiO ₂ films	231
6.1.3.2	2D representations of film parameters	232
6.1.3.3	Electrical and Raman properties of PEM sputtered Nb-doped TiO ₂ films	234
6.1.3.4	Variation of film thickness	239
6.1.3.5	Conclusions.....	241
6.2	Phase background spectra of undoped and Nb-doped TiO ₂ anatase films.....	243
6.2.1	Phase background spectra of e-beam evaporated undoped TiO ₂ films.....	243
6.2.2	Phase background spectra of e-beam evaporated Nb-doped TiO ₂ films	246

6.2.3	Conclusions	247
6.3	Raman spectrum and XRD of amorphous TiO ₂	249
6.3.1	Decomposition of an amorphous TiO ₂ Raman spectrum into nominal crystalline Raman spectra.....	250
6.3.2	Interpretation of the fit parameters as disordered nanoparticles	253
6.3.3	Disorder-band at 850 cm ⁻¹	254
6.3.4	Conclusions	255
7	Analysis of microstructure including Raman maps	257
7.1	Raman maps of diode sputtered multi-phase TiO ₂ films	258
7.2	Raman maps of reactive e-beam evaporated TiO ₂ anatase films	261
7.2.1	TiO ₂ phase composition maps.....	261
7.2.2	Anatase phonon maps: variation of Nb content and annealing temperature	265
7.2.3	Topographical analysis using SEM & EDX.....	268
7.2.4	Crystallization process of Ti _{0.92} O _{2.25} Nb _{0.08} films.....	276
7.2.5	Crystallization of films with stoichiometric oxygen content	278
7.2.6	Conclusions	279
7.3	Plasma-emission controlled rf-magnetron sputtered Nb-doped TiO ₂ films.....	281
7.3.1	Anatase Raman phonon maps of PEM sputtered Nb-doped TiO ₂ films	281
7.3.2	Variation of the sample position and film thickness	287
7.3.3	Conclusions	288
8	Complementary findings of chapters 4, 5, 6, and 7	290
8.1	Correlations in the studies of the rf-diode sputtered films.....	290
8.2	Correlations in the studies of the reactive e-beam coated films	290
8.3	Correlation between the Raman spectra of amorphous and crystalline TiO ₂ phases.....	291
8.4	Correlations in the studies of the PEM controlled rf-magnetron sputtered films	291
	Appendices	292
	References	321
	List of Figures	330
	List of Tables	342
	Acknowledgements.....	343

Abstract

We developed a method to decompose Raman spectra of mixed-phase TiO₂ thin films on silicon wafers, fused silica, and crown glass substrates using adjustable model spectra of the different components of the substrate and the thin film. The modeled spectra were successfully fit to measured spectra.

We split the TiO₂ thin film spectrum into one spectrum for the amorphous phase and spectra for each crystalline phase (anatase, rutile, and brookite). The spectrum of each crystalline phase is divided into first-order scattering spectra and a phase background (including second-order scattering). The substrate spectrum is split into luminescence and Raman spectra in case the substrate is luminescent.

This approach is integral, thus each contribution to the Raman spectra is fitted by models and there is no arbitrary background that has to be subtracted from the spectrum. All spectra are fitted simultaneously to the measured spectra whereas the fitting parameters of each spectrum are restricted to a reasonable degree. For example, while for single phase anatase spectra, the parameters of each first-order Raman peak is fitted individually, the background of minor-phase brookite is fitted by only one fit parameter. We explain the main strategies that we used to prepare the models so that they should be applicable to other materials.

We took the spectra as Raman maps of $30\ \mu\text{m} \times 30\ \mu\text{m}$ at 121×121 measurement points on undoped or Nb-doped TiO₂ films that were prepared by reactive e-beam evaporation, rf-magnetron sputtering, or rf-diode sputtering. We evaluated the individual resulting Raman spectra quantitatively and qualitatively.

We used similar models to decompose X-ray diffractograms and quantified the number of counts that each of the TiO₂ phases contribute to measured Raman spectra as well as to X-ray diffractograms. In strongly crystallized samples, we estimate the intensity ratio of Raman spectra vs. X-ray diffractograms of the TiO₂ phases to the Raman spectra as *brookite : anatase : amorphous : rutile* = 10 : 5 : 3 : 1. This means for example that for a given amount, the ratio of anatase Raman intensity vs. anatase X-ray intensity is *five* times higher as compared to rutile.

For a film that contains crystalline anatase islands that are surrounded by amorphous TiO₂, the Raman to X-ray intensity ratio is *twice* as high than in fully crystallized films in which the crystallites are separated from one another by grain boundaries.

Nb-doped thin films consist of micro domains that contain nanocrystallites with equal orientation. The electrical conductivity of the films increases strongly with the micrograin size.

Zusammenfassung

Wir haben eine Methode entwickelt, mit der man Raman-Spektren von Mischphasen-TiO₂-Dünnschichten auf Silizium-, Quarzglas- und Kronglas-Substraten unter Verwendung verstellbarer Modellspektren in ihre Komponenten (aus Dünnschicht und Substrat) zerlegen kann. Dabei haben wir die Modellspektren erfolgreich an gemessene Spektren angepasst.

Wir zerlegen das TiO₂-Dünnschichtspektrum in Komponenten für die amorphe Phase und die kristallinen Phasen (Anatas, Rutil und Brookit). Das Spektrum der kristallinen Phasen unterteilen wir in Ramanspektren 1. Ordnung und einen Phasenhintergrund (einschließlich Ramanstreuung 2. Ordnung). Das Substratspektrum wird in Lumineszenz- und Raman-Spektren aufgeteilt, falls das Substrat lumineszierend ist.

Dieser Ansatz ist ganzheitlich, daher wird jeder Beitrag zu den Raman-Spektren durch die Modelle angepasst, und es gibt keinen beliebigen Hintergrund, der vom Spektrum abgezogen werden muss. Alle Spektren werden gleichzeitig an die gemessenen Spektren angepasst, während die Anpassungsparameter jedes Spektrums auf angemessene Weise beschränkt sind. Während beispielsweise für reine Anatas-Schichten die Parameter für jeden Raman-Peak erster Ordnung einzeln angepasst werden, wird der Phasenhintergrund von in Spuren vorkommendem Brookit nur durch einen Anpassungsparameter (Intensität) manipuliert.

Wir haben die Spektren in Form von $30\ \mu\text{m} \times 30\ \mu\text{m}$ Raman-Karten mit 121×121 Messpunkten auf undotierten oder Nb-dotierten TiO₂-Schichten aufgenommen, welche durch reaktive Elektronenstrahlverdampfung, HF-Magnetron-Sputtern bzw. HF-Dioden-Sputtern hergestellt wurden. Wir haben die einzelnen resultierenden Raman-Spektren quantitativ und qualitativ ausgewertet.

Die Beiträge der TiO₂-Phasen zu den gemessenen Raman-Spektren wurden mit denen von Röntgendiffraktogrammen (XRD) verglichen. In stark kristallisierten Proben schätzen wir das *Intensitätsverhältnis Raman/XRD* der TiO₂-Phasen als *Brookit : Anatas : amorph : Rutil = 10 : 5 : 3 : 1*. Das bedeutet z.B., dass das Verhältnis der Anatas-Raman-Intensität zur Anatas-Röntgenintensität im Vergleich zu Rutil *fünffmal* höher ist.

Bei einer Schicht, die kristalline Anatas-Inseln enthält, die von amorphem TiO₂ umgeben sind, ist das Intensitätsverhältnis von Raman zu XRD *doppelt* so hoch wie bei vollständig kristallisierten Proben, bei denen die Kristallite durch Korngrenzen voneinander getrennt sind.

Die untersuchten Nb-dotierten Schichten bestehen aus homogenen Mikro-Domänen, welche Nanokristallite mit gleichen Orientierungen enthalten. Die elektrische Leitfähigkeit korreliert stark mit der Größe der Mikro-Domäne.

Introduction

Since Fujishima and Honda discovered that TiO_2 (anatase) can be used as a photoanode in a photoelectrochemical cell to split water into H_2 and O_2 ,³ TiO_2 materials have become the most studied photocatalytic semiconductor, because they are highly efficient, chemically and biologically stable, and (low- or) non-toxic at low cost.⁴ For these applications, the materials are often synthesized as thin film or other nanomaterial.

The main polymorphs of TiO_2 that occur in nature are anatase, rutile, and, rarely, brookite. Anatase and rutile have been extensively studied.⁵ Brookite has a more complex structure,⁶ and it is considered difficult to synthesize.^{5,7-10} That is why it was studied experimentally only seldom until 2012. It is an efficient photocatalyst and interest has grown to produce, study, and utilize brookite in recent years after several attempts to produce brookite were successful.^{4,11-16}

As compared to single-phase TiO_2 , mixed-phase TiO_2 (consisting of two or more TiO_2 phases) is more flexible for various photocatalytic applications.^{5,17,18} Therefore, interest is growing in mixed-phase TiO_2 .

This makes it necessary to quantify the phase composition and to study each phase independently. X-ray diffraction (XRD) and Raman have high potential for such analysis because they are non-invasive. For multi-phase materials, the contributions of the individual phases to the spectra or diffractograms have to be separated from each other. Furthermore, the substrate spectrum is often more intense than the thin film spectrum.

XRD is commonly used for phase quantification, but it has to meet shortcomings such as a decreasing sensitivity to small nanocrystallites. Raman spectroscopy is still often considered a non-quantitative method, although Raman instrumentation has improved in the last decades and its usage for quantification of materials is increasing.¹⁹

Shortcomings of quantification by Raman spectroscopy are for example that luminescence can occur and might superimpose the measured spectra and that structural properties can change the intensity of certain Raman peaks. Furthermore, the peak intensity ratios of a certain material depend on the alignment of the crystals. Yet, the effect of alignment is not crucial in nanostructured material because the orientation of the crystallites has a certain distribution.

In Raman spectra, crystalline phases contain a background additionally to the commonly analyzed first-order Raman spectra. Especially, nanostructured thin film Raman spectra contain high intensities from sources other than the first-order Raman spectra. The background consists for example of second-order scattering and disorder-induced scattering.

The main focus of this work is on the decomposition as well as quantitative and qualitative interpretation of TiO₂ thin film Raman spectra. For our studies, we (the author, Dipl.-Phys.Ing. Martin Jerman, Dr. rer. nat. Sanat Kumar Mukherjee, M.Sc. Jingy Shi, and M.Sc. Shixun Cui) have produced different sets of TiO₂ films. The coating methods are rf-diode sputtering, reactive e-beam evaporation, and rf-magnetron sputtering with controlled oxidation of the Ti target.

The rf-diode sputtered films were produced at varying deposition temperatures. The e-beam films contain varying amount of Nb (mostly *0 at.%, 8 at.%, and 16 at.%*) and were post-heated at varying temperatures. The rf-magnetron sputtered films were deposited with four different oxidation states of the Ti target and were placed at three different positions inside a sputter coater in which a Nb wire was put onto the sputter grave.

We describe the film preparation and the parameters of the most important analytics in chapter 2. We provide the corresponding fundamentals in chapter 1.

In literature, analysis of thin film Raman spectra is often limited to the evaluation of only the strongest Raman peak(s), because of the strong background arising from the substrate.^{20,21} For this reason, quantitative evaluation of thin film Raman spectra is barely undertaken. The same accounts if luminescence occurs in the spectra. Several approaches are applied to reduce such noise, for example shifted excitation Raman difference spectroscopy, or computational background removal.^{22–24} Cordero et al. give an overview of these approaches.²⁵

Backgrounds are often subtracted from spectra arbitrarily by a straight line or a polynomial function by common Raman evaluation software.²⁶ Yet, this procedure fails for thin films, where the background signals are in the same order of magnitude than the Raman spectra of the films.

In this work, we developed an approach to separate the thin film and the substrate spectra that contribute to measured Raman spectra of TiO₂ thin films. We built adjustable model spectra which we use to decompose a measured spectrum into its components. For that it is necessary that the models cover all sources that contribute to a measured spectrum.

We built models to simulate the Raman spectra of the TiO₂ phases, anatase, brookite, rutile, and amorphous TiO₂, and the Raman spectra of three different substrates (silicon wafers, fused silica, and B270 crown glass).

We attempt to demonstrate that a separation of the substrate spectra and thin film spectra can be achieved to a reasonable degree if all spectra are modeled simultaneously and if adequate simplifications are made. We thereby adapt the flexibility of the models have to the complexity

of the spectra to be fitted. The models are described and discussed in chapter 3. We prepared each model for a 633 nm as well as for a 532 nm laser, additionally.

Several issues have to be met to cover *all* signals from the substrate or the thin film that contribute to the measured signal. Each of the crystalline Raman spectra contains an individual phase background. This is considered only seldom in literature.^{27–30} We meet this problem by simulating *two* spectra for each crystalline phase – one for the first-order Raman scattering signal and one for the phase background.

In literature, it is stated that one cannot decompose TiO_2 Raman spectra into amorphous and crystalline content.^{27–30} Yet the measurement range in those studies was limited. Therefore, we use a wider measurement range in order to distinguish between crystalline and amorphous spectra (chapter 3.1.4).

The spectra of both kinds of substrates (crystalline and glassy) have individual problems when they have to be separated from a thin film spectrum (chapter 3.1.5). In the measured spectra of the crystalline Si wafer, there is an intense peak at 520.7 cm^{-1} , which is orders of magnitudes more intense than the TiO_2 thin film spectrum. Additionally, there are further strong and sharp characteristics of the Si spectrum that overlap with the thin film spectra and lead to artefacts when fitted (see chapter 4.1.3). We built models that distinguish well between the contributions of Si wafers and the TiO_2 thin films to measured Raman spectra, but three areas are being excluded from the fit.

The two glassy substrate materials are luminescent. Thus, the substrate is simulated by two spectra – one for the material's Raman footprint and one for the luminescence background. The models for both kinds of substrates contain instrument background or further experimental background.

In chapter 4, we demonstrate decomposed Raman spectra and X-ray diffractograms of (undoped or Nb-doped) TiO_2 thin films that we coated onto Si wafers, fused silica, or B270 glass by rf-diode sputtering, reactive e-beam evaporation, and rf-magnetron sputtering.

We have published the preprocessing of the spectra (chapter 2.2.1.1), the concepts of the models used for the decomposition of the Raman spectra (chapter 3.1), and a selection of the decomposed spectra (chapter 4.1.3) in the Journal of Raman spectroscopy [*Volume 49, Issue 7, 1217-1229 (2018)*],¹ where a figure that represents our work was used as the back cover of the issue.²

The decomposition of the Raman spectra into their components provide the possibility to further evaluate the resulting spectra, which we do quantitatively in chapter 5 and qualitatively in chapter 6.

In the quantitative part of this work, we evaluate the contributions of the various TiO₂ phases to the measured Raman spectra. We do not estimate the atomic or weight percentage of the phases in the samples. A correlation between Raman intensity and actual atomic percentage should be carried out in future work. At first, we take Raman spectra of a set of rf-diode sputtered multi-phase TiO₂ films with a 633 nm and with a 532 nm laser, and we quantify and compare the intensities of the TiO₂ phases that we find in those spectra (chapter 5.2.2). Afterwards, we quantify the (relative and total) contributions of the TiO₂ phases to the Raman spectra and their contributions to the corresponding X-ray diffractograms. This is done for samples coated at varying deposition temperatures (chapter 5.2) and also for samples coated onto three different substrates (5.3). We then repeat the procedure with undoped and Nb-doped TiO₂ thin films prepared by reactive e-beam evaporation (5.4). We interpret the resulting Raman/XRD intensity ratios of the different TiO₂ phases as a conservative estimate of the corresponding Raman and X-ray scattering cross sections (chapter 5.5).

In the qualitative part of this work (chapter 6), we evaluate the Raman spectra with further analysis such as X-ray diffractograms, scanning electron microscopy, UV-VIS-NIR transmittance and reflectance measurements, four-point-probe measurements, Rutherford backscattering.

We use the Raman spectra of the diode sputtered films together with X-ray diffractograms in order to estimate the defect density in the films with the q -vector relaxation model and compare our interpretation of the model to literature. We suggest to extend the model by adding a parameter for the average number of defects inside a crystal (chapter 6.1.1).

The production of Nb-doped anatase TiO₂ thin films by reactive e-beam evaporation is a new approach developed by Dipl.-Phys.Ing. Martin Jerman and Prof. Dr. Dieter Mergel. We characterize the electrical, structural, and optical properties of these films together with undoped films that we prepared likewise (evaporated by Dipl.-Phys.Ing. Martin Jerman, post-heated by the author). As part of the characterization, we use the decomposed Raman spectra, and X-ray diffractograms to interpret the conductivities of the films (chapter 6.1.2).

In chapter 6.1.3, we analyze electrical and structural properties of rf-magnetron sputtered Nb-doped TiO₂ films.

Furthermore, we discuss the anatase phase backgrounds that we found in the Raman spectra of the e-beam evaporated films (chapter 6.2). Also, we simulate the Raman spectrum of amorphous TiO₂ by broad Raman features that resemble those of the crystalline TiO₂ phases (chapter 6.3).

We obtained all spectra by measuring Raman maps and taking the average spectrum of each map. The maps have a size of $30\ \mu\text{m} \times 30\ \mu\text{m}$ with 121×121 measurement points. We present and interpret these maps in chapter 7. They provide information on film growth, topography, and Raman domain size.

In parts, the quantitative, qualitative, and mapping evaluation provide complementary information, which are summed up in chapter 8. The main chapters begin with short overviews that tell the reader what is done in the sub-chapters, and they provide information on how the chapters relate to the other chapters of the work. There will be individual conclusions at the end of each chapter.

List of abbreviations

e-beam:	electron-beam
%-ox.t.	assumed oxidation of a sputter target surface
Å	Ångström. $1 \text{ Å} = 100 \text{ pm} = 0.1 \text{ nm}$.
at.%	atomic percent; <i>8 at.%</i> or <i>16 at.%</i> of Nb refers to $Nb/(Ti+Nb)$, thus, relative to Ti. This is common praxis in literature. ^{31–33}
blueshift	In Raman spectroscopy, blueshift is an increase of the wavenumber of a Raman peak. In this work it does not refer to relativistic Doppler, cosmological, or gravitational effects.
CVD	chemical vapor deposition
dc	direct current
e-beam	electron beam
EDX	energy dispersive X-ray spectroscopy
kcps	kilo counts per second (one thousand collected phonons per second)
Nb0:	undoped e-beam evaporated TiO ₂ film
Nb1:	Nb-doped e-beam evaporated titanium-oxide film with a stoichiometry of Ti _{0.92} O _{2.25} Nb _{0.08}
Nb2:	Nb-doped e-beam evaporated titanium-oxide film with a stoichiometry of Ti _{0.84} O _{2.25} Nb _{0.16}
PEM	Plasma emission monitoring: sputter coating with controlled oxidation state of the target by monitoring the intensity of a certain plasma line.
PVD	physical vapor deposition
RBS	Rutherford backscattering spectrometry
redshift	In Raman spectroscopy, redshift is a decrease of the wavenumber of a Raman peak. In this work it does not refer to relativistic Doppler, cosmological, or gravitational effects.
rf	radio frequency
RT	room temperature
SEM	scanning electron microscope
TCO	transparent conductive oxide
UV-VIS-NIR	ultraviolet, visual, and near-infrared range of electromagnetic radiation
XPS	X-ray photoelectron spectroscopy
XRD	X-ray diffraction / X-ray diffractometry

1 Fundamentals

1.1 Thin film vapor deposition

Vapor deposition is a technique to deposit films of materials which are in the gas phase (or plasma) during the deposition. There are several methods to deposit thin films using vapor deposition. These methods have in common that coating takes place in a vacuum chamber, which is equipped with vacuum pumps, an evaporation source, and substrates to be coated.

A vacuum is characterized by the mean free path λ , which is the mean distance the residual gas particles fly before they collide with another gas particle. For Ar, O₂, N and air, the mean free path λ is commonly estimated by³⁴:

$$\lambda = \frac{6.3 \cdot 10^{-3} m}{p [Pa]} = \frac{6.3 \cdot 10^{-3} cm}{p [mbar]}, \quad (1)$$

where p is the pressure. The non-SI unit *mbar* ($1 \text{ mbar} = 100 \text{ Pa}$) is commonly used in vacuum science and vapor deposition techniques because typical distances of source material and substrates to be coated are in ranges of a few *cm*.

Vapor deposition techniques are categorized into physical vapor deposition (PVD) and chemical vapor deposition (CVD). PVD is based on purely physical processes, in which a material vapor condenses on the substrate surface. In general, in PVD processes a material goes from solid form to a vapor phase and then condenses back to a solid thin film. The most common PVD techniques are evaporation and sputter deposition.

Most evaporation techniques can be operated in low as well as ultrahigh vacuum. Common evaporation methods are thermal evaporation, electron-beam (e-beam) physical vapor deposition (often called e-beam evaporation), arc deposition (cathodic or anodic arc evaporation), and pulsed laser ablation. In plasma deposition, the charged particles can be accelerated by bias voltages.

CVD is characterized by a gas phase reaction (usually at the substrate surface or close to it). CVD processes are classified by the deposition pressure (atmospheric pressure, low-pressure, ultrahigh vacuum), physical characteristics of the vapor (for example liquid injection or aerosol-assisted), and the reactor design (cold wall or hot wall). If the technique uses a plasma, also the plasma methods are classified (for example plasma-enhanced CVD, microwave plasma-enhanced CVD).

CVD cannot always be separated from PVD. PVD processes can become CVD processes for example when reactive gases are let into the deposition chamber. Examples are reactive sputtering and reactive e-beam evaporation.

1.1.1 Evaporation

There are several ways of converting a material to the gas phase by evaporation, depending on the area of application. The simplest type is thermal evaporation (also: vapor deposition). In this process the evaporation source is mostly placed inside a resistance-heated crucible. Electrically conductive materials can also be heated directly, for example by eddy currents (induction evaporator). The coating material can also be heated by a laser, which allows targeted dosing, for example for the precise production of multilayered film. However, the latter process is associated with high costs and a low coating rate.

The evaporation method used in this work is e-beam evaporation. Here, an electron gun bombards the coating material with electrons. This process has a high energy density and offers the possibility to vaporize almost all solids with high purity from water-cooled crucibles and also to achieve high deposition rates. Around 15% – 40% of the e-beam power is dissipated by electron backscattering. Evaporation rate can be controlled by altering the power or the energy density of the electron beam (using electro-optical beam control) in a wide range of 10^{-2} nm/s to 10^3 nm/s. At room temperature the thermal energy of gas particles is $1/40$ eV. The energy of vapor particles is around *ten* times as much ($1/4$ eV).

TiO₂ thin films are produced by reactive e-beam evaporation, for which oxygen gas is added to the coating chamber. The target material can be Ti, TiO, Ti₂O₃, or TiO₂ – each resulting in different thin film properties, for example a variation of the refractive index.³⁴

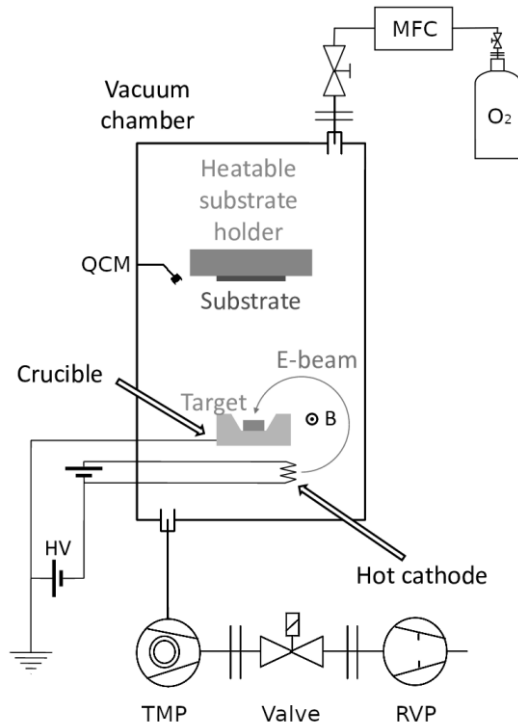


Fig. 1: Schematic diagram of an electron beam chamber (adapted from Mazzi³⁵ and Filipov³⁶) with a mass flow controller (MFC), quartz crystal monitor (QCM), a turbo-molecular pump (TMP), and a rotary vane pump (RVP).

Fig. 1 shows a schematic diagram of a reactive electron beam evaporation chamber. Vacuum is created using a rotary vane pump (RVP) and a turbomolecular pump (TMP). Oxygen gas is let into the chamber using a mass flow controller (MFC). The substrates to be coated are mounted onto a heated substrate holder. The source material (target) to be evaporated is placed inside a water-cooled crucible. A hot cathode emits electrons, which are accelerated by an electric field (not shown). The electron beam is then deflected by a magnetic field B , which guides the electron beam onto the evaporation material. The electron beam heats the material until it becomes so hot that it evaporates (or sublimates).

Deposition rate and film thickness are monitored using a quartz crystal monitor (QCM). The principles of QCM are described by Sauerbrey³⁷, and the operation is described by Kanazawa³⁸ as well as Janshoff and Steinem³⁹.

1.1.2 Sputtering

In the sputtering process, a working gas is led into an evacuated vacuum chamber and a glow discharge is ignited and the plasma ions are accelerated against a target. Usually, noble gases (mostly argon) are used as working gas because they are inert.⁴⁰ Sputtering is the removal of surface-near target atoms through high-energy particle beams through collision cascades.

When high energy particles bombard the surface of a solid, the ion can penetrate into the volume of the material and trigger collision cascades that extend further into the material. Various phenomena result in energy loss of the ions such as atom ejection, ionization, production of phonons, or the collision cascades that follow the first impact.⁴¹ Fig. 2 schematically shows the most important collision events that occur when matter is bombarded with ions.

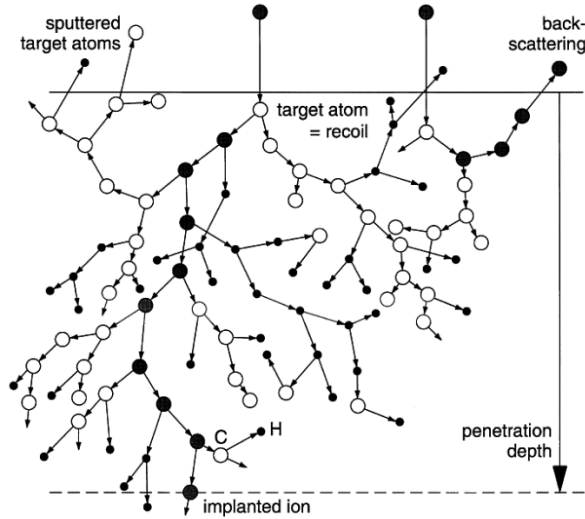


Fig. 2: Schematic representation of the atomistic processes that occur when energetic particles collide with a solid surface. This example shows a collision cascade in hydrocarbon. The incident particles are black, C atoms are white, and H atoms are small black circles.⁴²

The incoming ion (black), which is shown in the middle at the top of Fig. 2, hits several target atoms (white), which in turn collide with other atoms and result in a collision cascade. The collisions can be elastic or inelastic, such as ejection of an electron. The electron can leave the target or ionize further atoms. If a target atom escapes from the target through the cascade, this process is called sputtering. The originally arriving ion can be implanted (bottom of the figure) or back-scattered (as shown at the top right end of the figure).

The sputtering yield Y is the number of sputtered atoms per incident ion. In the range of a few 100 eV , it is estimated by⁴³:

$$Y = \text{const.} \cdot (E_{ion} - E_{min}) = \text{const.} \cdot e \cdot (U_P - U_B - U_{min}), \quad (2)$$

where E_{ion} is the energy of the incident ion, and E_{min} is the threshold energy that is necessary that sputtering of a target atom occurs. For the sputtering of Ti with Ar E_{min} is 20 eV .³⁴ U_P is the plasma potential, U_B is the discharge voltage, U_{min} is the potential that corresponds to the threshold energy, and e is the elementary charge of the electron. The sputtering yield per

Ar^+ ion is 0.2 Ti atoms for Ar ion energies of 200 eV, and 0.6 Ti atoms for Ar ion energies of 600 eV. Typical energies of sputtered particles are 10 eV – 40 eV.³⁴

For the production of TiO_2 films, oxygen gas is added to the deposition chamber (in addition to Ar), which causes two O atoms and one Ti atom to combine to TiO_2 . Such a coating processes is called *reactive sputtering*. Reactions between oxygen atoms and titanium atoms take place at the target surface as well as at the substrate surface (and also to a non-negligible degree in the gas phase if the mean free path is smaller than the target-substrate distance).

In this work, mainly two reactive sputtering deposition techniques were used: rf-diode sputtering and rf-magnetron sputtering. In early experiments, also dc-magnetron sputtering was used. In the following, we describe diode and magnetron sputtering.

1.1.2.1 Diode sputtering

A negative potential is applied to the target (which is the material to be sputtered). The positive ions in the plasma are accelerated by the resulting electric field. Fig. 3 shows a schematic diagram of a direct current (dc) diode sputter coating process.

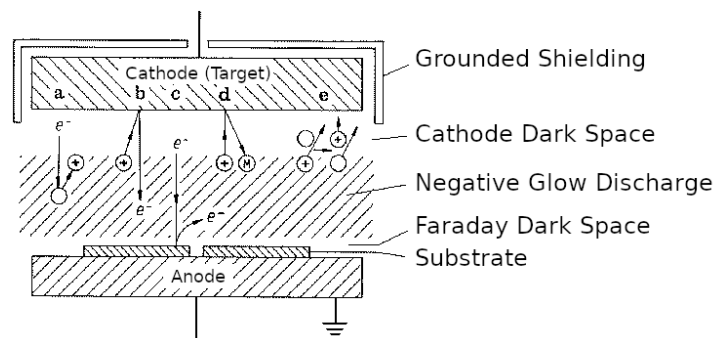


Fig. 3: Schematic diagram of a dc-diode sputter coating process. Atoms are marked as white circles, positive ions as circles with a plus sign, and electrons as e^- ; adapted from Frey and Kienel.³⁴

The area in front of the cathode is the cathode dark space, also known as the Aston dark space, in which the ion density is very low. A grounded shield is attached around the cathode in a distance smaller than the thickness of the dark cathode space, so that the plasma is formed only between the target and the substrate.

The following transport processes are most important: (a) In the cathode dark space, accelerated electrons collide with argon atoms and ionize the argon atoms. (b) The argon ions are accelerated towards the cathode and can emit electrons. (c) If these electrons hit the substrate, further ionization can take place there. (d) Argon ions remove atoms from the target surface through collision cascades, which is the actual "sputtering". (e) Charge reversal processes occur between Ar^+ ions and Ar atoms.⁴⁰

1.1.2.2 Magnetron sputtering

In magnetron sputtering, the electric field is superimposed with a magnetic field. Therefore, permanent magnets (a few hundredths T) are placed behind the water cooled cathode. Fig. 4 compares diode sputtering (left-side), with magnetron sputtering (right-side).

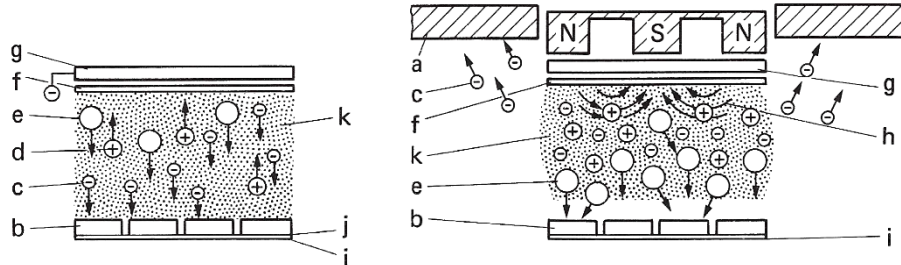


Fig. 4: Schematic diagram of dc-diode sputtering (left) and magnetron sputtering (right). The letters symbolize: (a) recipient wall, (b) substrates, (c) secondary electrons, (d) ions, (e) metal atoms, (f) target, (g) cathode, (h) magnetic field lines, (i) substrate holder, (j) anode, and (k) plasma. Adapted from Frey.³⁴

The magnetic field penetrates the target, and the combination of an electric and magnetic field causes the electrons in the plasma to no longer move along the electric field lines but in cycloid orbits in the plasma. The $E \times B$ drift velocity of the electrons and ions is equal, because it depends on only the electric and magnetic field strength, the particle's charge, independently of their thermal energies. Because of their smaller mass, the gyration radii of the electrons are smaller than those of the ions, and the electrons are concentrated close to the target. This results in a higher number of collisions of electrons with the working gas atoms, and thus in a higher degree of ionization in the plasma. Therefore, a lower discharge voltage or pressure is necessary for the same charge density in the plasma.³⁴

1.1.3 Radio-frequency sputtering

In radio-frequency (rf) sputter processes, an rf-generator (2 MHz , 13.56 MHz , or 27.2 MHz) is connected between the target and the substrate electrode and a capacitor is attached between the generator and the target. The rf-oscillation of the electrons increases their path in the plasma and thus the ion density and ion current increase. Therefore, sputtering can take place at a lower pressure than in the case of dc-sputtering (1 Pa vs. 10 Pa for diode sputtering).

Because of the low mass, electrons have a higher mobility in the plasma as compared to ions. Thus, more electrons than ions hit the target surface, the target becomes negatively charged and the potential of the plasma close to the target is negative as compared to the substrate anode. Thus over time, the plasma potential of the rf-arrangement behaves like a dc-arrangement.

An advantage of the rf-arrangement compared to the dc-arrangement is that insulator and semiconductor materials can also be used as targets. Also, at lower gas pressure the mean free path λ is larger (see equation (1)): for diode sputtering, the mean free path is around $\lambda = 6 \text{ mm}$ at 1 Pa , and around $\lambda = 0,6 \text{ mm}$ at 10 Pa . This results in less thermalization of the sputtered particles at lower pressure during deposition.³⁴

1.2 Thin film growth

The growth of a layer from a flow of free atoms or particles is determined by various factors such as the substrate and particles properties, the kinetic energy of the particles, the collision rate, the angle of incidence, and the chemical properties of the involved materials.

Particle flows in a vacuum carry mass as well as energy and impulse current densities. The energy of the particle consists of kinetic energy as well as potential energy (depending on the particle's temperature and on ignited states).

Fig. 5 shows the process probabilities schematically that take place during the collision between an impact particle and the substrate surface depending on the order of magnitude of the kinetic energy of the particle. The probabilities are estimated on the basis of energetic data, such as adsorption, chemical binding energy, or lattice energy.

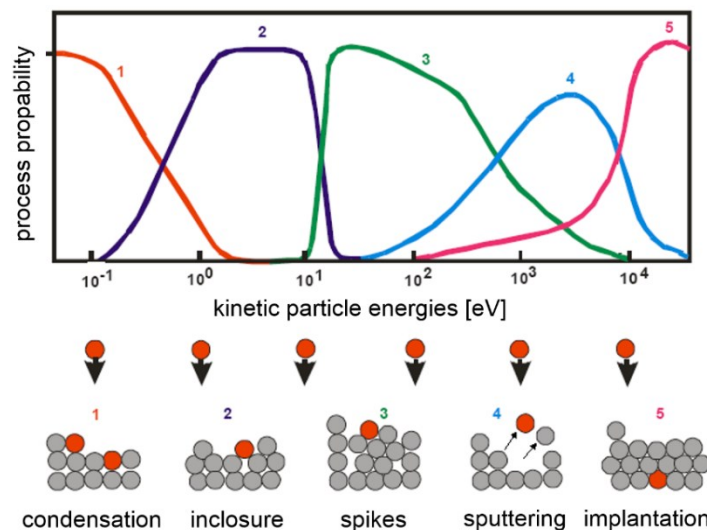


Fig. 5: Process probability vs. kinetic particle energy of impact atoms resulting from collisions with a solid surface. Adapted from Dzur.⁴⁴

(1) At low particle energies (around 0.1 eV), particles condense at the substrate's surface. When no chemical reaction takes place (at prepared surfaces or in reactive atmosphere), the adhesion is very low. (2) Particle energies of $1 \text{ eV} - 10 \text{ eV}$ are in the order of magnitude of chemical bonds. Chemical bonds are broken, and the particles can be chemically bound to surface atoms. (3) At kinetic particle energies of $10 \text{ eV} - 500 \text{ eV}$ strong densification takes place at the surface, which can lead to phase changes. (4) Sputtering takes place most probably at kinetic energies of $500 \text{ eV} - 10000 \text{ eV}$. (5) At 10000 eV implantation of the impact particle becomes the most probable process. These values are coarse and depend on the material's properties.

The deposition parameters influence the structure of the growing films during vapor deposition. These are for example substrate temperature, gas pressure, gas mixture, substrate

bias voltage, deposition rate (particle energy). These parameters influence the energy impact on the growing film and, thus, on the desorption, the reactivity at the film surface, and the adatom surface mobility. Movchan and Demchishin observed the influence of the substrate temperature on the micro-structure of the growing films and categorized the structures into three zones (see Fig. 6 (a)).

In this model, the different zones depend on the ratio of substrate temperature T_s to the melting point of the thin film material T_m . In zone I, at temperatures below $T_s/T_m = 0.3$ the films grow with low surface mobility and have a porous columnar structure with fibers of $1\text{ nm} - 10\text{ nm}$ width depending on the nucleation density. In zone II, at higher temperatures ($0.3 < T_s/T_m < 0.5$), the growth is still columnar, but with higher adatom surface mobility, resulting in broader columns with a higher density. In zone III, at high temperatures ($T_s/T_m > 0.5$) allow bulk diffusion resulting in dense recrystallized grain structures with smooth surfaces.^{34,45}

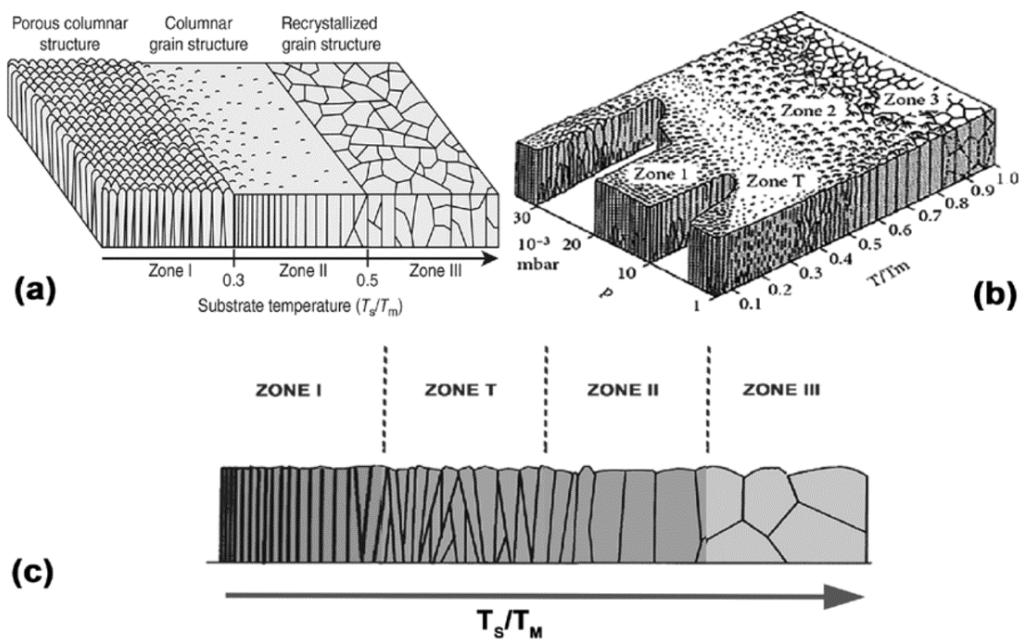


Fig. 6: (a) Structure zone model by Movchan and Demchishin⁴⁵ (b) Modified structure zone model by Thornton⁴⁶, (c) cross-section of the structure zones. Adapted from Zeeshan.⁴⁷

Thornton added a transition zone (or T-zone) for sputter-coated films into the model between zones I and II. The zone depends on the gas pressure during sputter deposition. A high pressure, the sputtered particles undergo an increasing number of collisions with the working gas and lose kinetic energy (thermalization). The self-surface diffusion is high, yet the grain boundary diffusion is limited. The structure of the zone is inhomogeneous along the film thickness with fine crystallites at the substrate surface and columnar structure at the upper part of the film.⁴⁶

1.3 TiO₂

Titanium dioxide (TiO₂) or titania, is the naturally occurring polymorph oxide of titanium. At standard pressure it occurs in nature mainly as the tetragonal phases, rutile and anatase, and rarely as the orthorhombic brookite. Rutile is stable, while anatase and brookite are metastable and convert to rutile at temperatures of 700 °C – 1000 °C.⁴⁸

Additionally, two dense high-pressure TiO₂ polymorphs are found in nature: a monoclinic baddeleyite-like form known as akaogiite, and a scrutinyite-type structure known as TiO₂-II. Both can be found at the Nördlinger Ries meteorite impact crater in Germany.⁴⁹ Several synthetically produced metastable phases also exist.

The vast majority of TiO₂ is used as pigments, for example in paints, paper, plastics, cosmetics or sunscreen. Further uses are thin-film applications, such as solar cells or optical coatings for dielectric mirrors, self-sterilizing coatings in biomedicine, electrolysis, air purification, or water treatment.⁵ In 1972, Fujishima and Honda observed photocatalytic splitting of water on TiO₂ electrodes. UV light that has energy higher than the material's band gap (see Table 1) activates the photocatalysis of TiO₂. By now, TiO₂ has become the most studied photocatalyst. The *three* naturally occurring polymorphs, rutile, anatase, and brookite, have high photocatalytic activity.^{4,18,50,51} Mixed-phase TiO₂ composites are more effective photocatalysts.⁴ Table 1 shows a selection of structural properties of the three TiO₂ allomorphs and amorphous TiO₂.

Table 1: Structural properties of TiO₂ allomorphs

TiO ₂ phase	anatase	brookite	rutile	amorphous
Crystalline structure ⁵¹	tetragonal	rhombohedral	tetragonal	–
Lattice constants ⁵¹ [\AA] (1 \AA = 100 pm)	$a = b = 3.73$ $c = 9.37$	$a = 5.44$ $b = 9.17$ $c = 5.14$	$a = b = 4.58$ $c = 2.95$	–
Unit cell volume [\AA^3]	130.4	256.4	61.9	–
Mass density ^{51,52} [g/cm^3]	3.83	4.17	4.24	2.4 – 3.3
Band gap ^{4,51} [eV]	3.2	3.1 – 3.4	3.0	3.2 – 3.4
Refractive index ^{51,53} [n_g]	2.56	2.81	2.95	2.0 – 2.3

Fig. 7 shows *balls and sticks* schemes of the unit cells of anatase (left), brookite (mid), and rutile (right). Large light spheres represent Ti atoms and small red spheres represent O atoms. We have sized the schemes so that the lengths of the vertically displayed lattice parameters (anatase-*c*, brookite-*a*, rutile-*b*) are in the same scale.

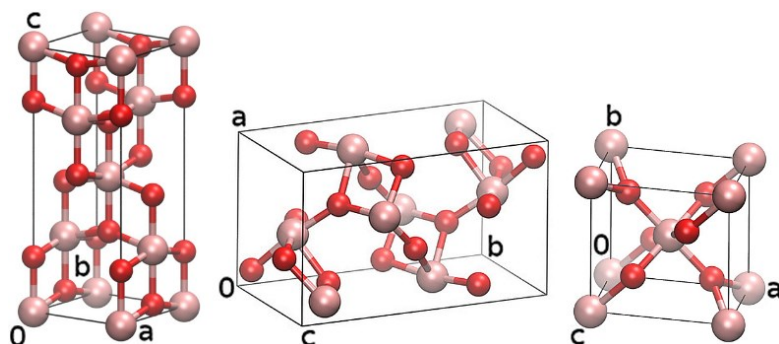


Fig. 7: Unit cell balls and sticks schemes of anatase (left), brookite (mid), rutile (right). Large light spheres represent Ti atoms and small red spheres represent O atoms. Adapted from Moellmann et al.⁵⁴

1.3.1 TiO₂ anatase

Undoped and undistorted anatase is an insulator with a resistivity of $10^{13} \Omega\text{cm}$.⁵⁵ Yet, anatase becomes a semi-conductor when it is doped with other elements, such as Nb^{32,56,57}, Ta⁵⁸, Fe⁵⁹, La⁶⁰. In 2005, Furubayashi et al. discovered that Nb-doped TiO₂ anatase is a transparent conductive oxide (TCO). The discovered material has a carrier density of $1 \cdot 10^{19} \text{ cm}^{-3}$ to $2 \cdot 10^{21} \text{ cm}^{-3}$ and transmittance of 85% – 97 % in the visible range, depending on the Nb content. The transport and optical properties of the low-cost material are comparable to those of conventional TCOs such as Sn-doped In₂O₃ (ITO) or ZnO, of which ITO is the most widely used.^{18,56}

1.3.2 TiO₂ rutile

Rutile is the most common crystal structure of TiO₂. It is stable to a temperature of 1800 K. Due to its high refractive index and effective ultraviolet absorption, it is widely used for pigments, sunscreens and optical coatings. In the last decades, it gained scientific interest in the application as photocatalyst and solar cells.⁶¹

1.3.3 TiO₂ brookite

Scientific and technological interest in brookite has been growing in the last years since around the year 2000, because by then it had been considered difficult to synthesize. Thus it is the least studied TiO₂ photocatalyst. Brookite photocatalysts have been tested for hydrogen formation, Li ion batteries, environmental remediation, and organic syntheses.⁴

The orthorhombic crystalline structure of brookite has a unit cell described by the space group *Pbca*. The structure consists of octahedra, each with a titanium atom at its center. All bond lengths between the titanium and oxygen atoms differ from each other.⁴

1.4 Raman scattering

In the following chapters, we will introduce Raman spectroscopy (1.4.1), provide the fundamentals of Raman scattering (1.4.2), present the characteristics of the Raman spectra of the crystalline TiO₂ phases (1.4.3), of amorphous materials (1.4.4) and of the substrate materials that are coated in this work, Si wafers and silica glasses (1.4.5).

1.4.1 Raman spectroscopy

Raman spectroscopy measures the intensity and wavelength of inelastically scattered light. For this purpose, a sample is irradiated with monochromatic light (usually laser) and the retroreflection is detected.

Raman spectroscopy provides information about vibrational and rotational states of molecules and is based on the Raman effect. The obtained parameters are wavenumber shift, the state of polarization, and the Raman line intensities.⁶² The shift is expressed in cm^{-1} and is the difference of the wavenumbers of the incident exciting light and the Raman lines. The actual frequencies of the corresponding modes of vibration are obtained by multiplying the shift with the velocity of light c .

The photons transfer energy to the molecule (Stokes lines) or absorb energy (Anti-Stokes lines). The energy that is released or absorbed corresponds to the difference between two energy levels of molecular vibrations.

While overtones and combinational vibrations are strong in infrared absorption spectra (if the sample is sufficiently thick), they are weak in Raman spectra and referred to as “second-order scattering” in literature.⁶²

Raman lines are often classically explained by the change of polarizability of symmetrical valence vibrations. In contrast, infrared active vibrations are characterized by a change of the dipole moment of asymmetric valence vibrations. The intensity of Raman lines are explained by quantum mechanics.

1.4.2 Fundamentals of Raman scattering

In chapter 1.4.2.1, we describe the discovery and the main phenomena of the Raman effect. In chapter 1.4.2.2, we present a classic approach of Raman scattering, and in the chapters 1.4.2.3 to 1.4.2.5, we present a quantum mechanical approach of describing Raman scattering.

1.4.2.1 Raman effect

In 1922, C. G. Darwin attempted to reconcile the quantum theory with the wave theory by proposing a quantum theory of dispersion. In his theory, according to laws of probability

molecules can emit secondary spherical waves that match with quantum frequencies of the molecules. Thereby, electromagnetic classical mechanic eigenfrequencies are replaced by a dispersion relation of quantum frequencies.^{63,64}

Yet for a stationary molecule, the dispersion relation violates the energy equilibrium between radiation and matter. In 1923, Adolf Smekal proposed that such an equilibrium should be generally impossible for a stationary atom or molecule – in order to restore the inviolability of energy equilibrium. From this he concluded that there must exist an unknown kind of *translational* quantum transition.⁶⁵

The interaction between light and matter is described by an inelastic collision process. The molecule has a mass m and a quantized energy state E_m , and the incidence light quantum has the energy $h\nu$ and the impulse $h\nu/c$. Before the interaction, the molecule has an arbitrarily oriented translational speed v against the direction of incidence photon. Then, there is a certain probability that the molecule will change to another energy state E_n , changes its velocity and direction to v' , and the scattered photon has the frequency ν_s . From the conservation of energy and momentum follows:

$$\frac{mv^2}{2} + E_m + h\nu_0 = \frac{mv'^2}{2} + E_n + h\nu_s. \quad (3)$$

The energy of phonons with a frequency in the visual range (or close to it), is insignificant as compared to the kinetic energy of the molecule. Thus in equation (3) the impact of the phonon on the kinetic energy of the molecule can be ignored and the equation can be simplified to

$$E_m + h\nu_0 = E_n + h\nu_s. \quad (4)$$

Thus, after the interaction, the scattered photon has another frequency, which is shifted by $\Delta\nu$:

$$\Delta\nu = \nu_0 - \nu_s = \frac{1}{h}(E_n - E_m). \quad (5)$$

Following from this, ν_s can be either equal to, or higher or (symmetrically) lower than ν_0 (or $\Delta\nu$ is either *zero*, or > 0 , or < 0), depending on if E_m is the same, or smaller or larger than E_n . These three kinds of scattering are called Rayleigh radiation ($\Delta\nu = 0$), Stokes ($\Delta\nu < 0$), or Anti-Stokes ($\Delta\nu > 0$) scattering. The corresponding frequencies are shown in Fig. 8.

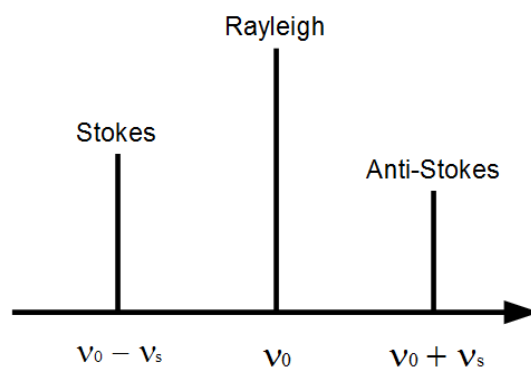


Fig. 8: Schematic representation of Stokes, Rayleigh, and Anti-Stokes frequencies.

These are the lines that are measured by Raman spectroscopy. For convenience ν_0 is usually set to zero and the sign of the frequency shift is reversed so that in measured spectra Stokes lines have a positive sign, because Stokes lines are more intense.

More specifically, the Raman effect arises from phonon-photon interaction which can be represented in a Jabłoński diagram. A phonon is a collective excitation in periodically arranged molecules or atoms in which a lattice of atoms or molecules uniformly oscillates at a single frequency. The Jabłoński diagram in Fig. 9 presents schematic representations of Raman and Rayleigh scattering in comparison to infrared absorption and fluorescence.

Fluorescence requires an excited electronic energy level, which can be a result of UV/visible absorption. Infrared absorption involves only one transition which directly changes the vibrational energy level within an electronic energy level. In contrast, Rayleigh and Raman scattering involve a virtual electronic energy level which corresponds to the energy of the exciting laser photons.⁶²

For Raman scattering to occur, there has to exist a virtual energy mode. Such virtual modes occur when vibrational modes of a molecule produce changes in the induced electric moment of the molecule. This is called polarizability. It occurs for symmetrical molecule oscillations, while anti-symmetrical oscillations are infrared active. This is the selection rule (which is not strict in real crystals). Thus Raman spectra and infrared absorption spectra are complimentary.⁶²

In Raman scattering, the photon is not absorbed but it is scattered. When the photon collides with the molecule it excites the molecule to an imaginary state and after about 10^{-12} s, the molecule has changed to a certain quantized vibrational state. The lifetime of the virtual state follows from Einstein's theory of absorption and emission of light, which also explains the lower propagation speed of light in optically denser media.

In the case of Rayleigh scattering the final state is in the same vibrational energy than the starting state (elastic scattering). In the case of Stokes Raman scattering the final state is in a

higher vibrational energy level, and for Anti-Stokes Raman scattering the final state is in a lower vibrational energy level than the starting state.⁶⁶

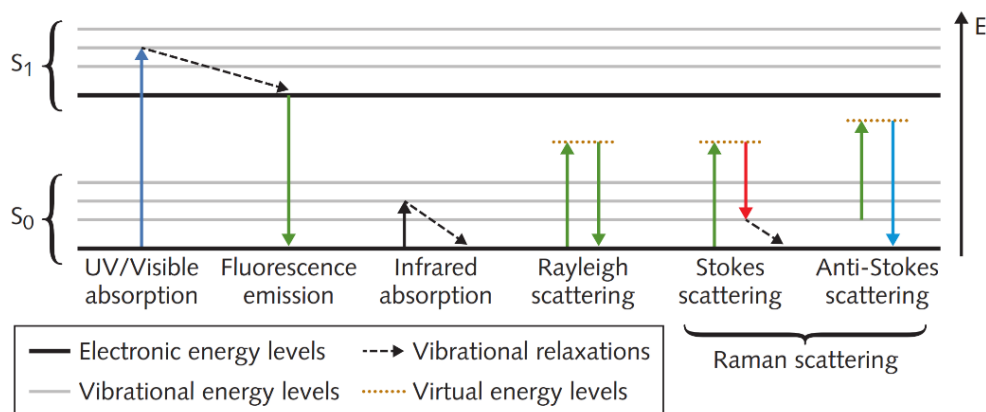


Fig. 9: Schematic representations of ultraviolet/visible absorption, fluorescence, infrared absorption, Rayleigh scattering, Stokes Raman scattering, and Anti-Stokes Raman scattering. Taken from Chimenti.⁶⁶

Smekal assumed that under good experimental conditions the deviation from the classic wave theory should be easily measurable.⁶⁵ In 1928, C. V. Raman discovered these transitions during experiments on light scattering of liquids using spectral lamps, assisted by his student K. S. Krishnan. Independently, G. S. Landsberg and L. J. Mandelstam discovered the same effect for solids in the same year. The underlying effect was named after Raman, and in 1930 he received the Nobel Prize in Physics for the discovery. The invention of the laser by S. P. S. Porto and D. L. Wood in 1960, allowed faster and more producible Raman spectroscopy.

1.4.2.2 Classic representation of Raman scattering

In classical mechanics, we examine the polarization that light generates in an oscillating molecule. Polarization is caused by a displacement of electrons or ions (or a displacement orientation of a permanent dipole moments) from their normal position. An electromagnetic wave induces electrical dipole moments when it passes through a medium. For a given electric field strength, the induced dipole moment becomes larger the more polarizable a medium is. If the electromagnetic field is sufficiently weak, the induced dipole moment p and electric field E are proportional:

$$\overline{p(t)} = \alpha \cdot \overline{E(t)}, \quad (6)$$

with the polarizability of the molecule α . Dipole moment and electric field are vectors, and the orientation of the molecule to the electric field influences the polarizability. Thus, the polarizability is a second order tensor. The tensor is symmetric with $\alpha_{ij} = \alpha_{ji}$. When

monochromatic light with a frequency of $\omega_0 = 2\pi\nu_0$ hits a molecule, the electrons of the shell follow the periodically vibrating electric field and the dipole moment results in:

$$\overline{p(t)} = \alpha \cdot \overline{E_0} \cdot \cos(\omega_0 t), \quad (7)$$

This vibrating dipole emits light with a frequency of ω_0 . This is the classic description for Rayleigh scattering, which occurs when the polarizability is not equal to zero.

Depending on the state of matter, molecules rotate or vibrate, and both can lead to changes in the polarizability. If the distance r between two nuclei changes periodically during a molecular oscillation, the polarizability α also changes with the same frequency. If r_0 be the equilibrium position, a first approximation of Taylor expansion provides for $\alpha(r)$:

$$\alpha(r) \approx \alpha(r_0) + \left. \frac{\partial \alpha}{\partial r} \right|_{r=r_0} \cdot (r - r_0). \quad (8)$$

If we look at the polarizability at the equilibrium position, then be $\alpha_0 = \alpha(r_0)$ and $\alpha' = \left. \frac{\partial \alpha}{\partial r} \right|_{r=r_0}$, and equation (6) simplifies to

$$\alpha(r) = \alpha_0 + \alpha' \cdot (r - r_0) \quad (9)$$

for each component of the tensor α . From this follows that the time dependent polarizability $\alpha(t)$ of molecular vibrations with the frequency ω_s and the amplitude $\alpha_l = \alpha' A$ is

$$\alpha(t) = \alpha_0 + \alpha_1 \cdot \cos(\omega_s t + \phi), \quad (10)$$

with the phase position ϕ . From equations (9) and (10) follows

$$(r - r_0) = A \cdot \cos(\omega_s t + \phi). \quad (11)$$

When we combine equations (7) and (10) and ignore the phase, then we get

$$\overline{p(t)} = (\alpha_0 + \alpha_1 \cos(\omega_s t)) \cdot \overline{E_0} \cos(\omega_0 t). \quad (12)$$

Using the trigonometric relationship

$$\cos(\alpha) \cdot \cos(\beta) = \frac{1}{2} \cos(\alpha + \beta) + \frac{1}{2} \cos(\alpha - \beta), \quad (13)$$

we get (for each component):

$$\overline{p}(\vec{t}) = \underbrace{\alpha_0 \vec{E}_0 \cos(w_0 t)}_{\text{Rayleigh}} + \underbrace{\frac{1}{2} \alpha_1 \vec{E}_0 \cos((w_0 + w_s) t)}_{\text{Anti-Stokes}} + \underbrace{\frac{1}{2} \alpha_1 \vec{E}_0 \cos((w_0 - w_s) t)}_{\text{Stokes}}, \quad (14)$$

which is the sum of Rayleigh, Anti-Stokes, and Stokes dipole moment. In the equations, one can see that Raman scattering occurs only when $a_l \neq 0$, thus only when the polarization tensor is varied. These equations describe vibrations. The polarization of rotations is equivalent, whereas the frequency has to be multiplied with a factor of *two*, because the direction becomes relevant.^{67,68}

In the classical representation, the vibrations should radiate energy. Thus, the stationary, quantum mechanical, virtual energy state is necessary to describe Raman scattering (see chapter 1.4.2.1). Also, in the classical representation, the Anti-Stokes lines should be as intense as the Stokes lines. Yet, in the quantum mechanics representation, the Anti-Stokes lines are transitions from a higher vibrational energy level to a lower level. Thus, energy (for example by temperature) is needed before Anti-Stokes Raman scattering can occur. Thus, the probability of Anti-Stokes scattering is absent at a temperature of 0 K and increases with increasing temperature.⁶⁸

1.4.2.3 The Raman tensor

The cross-section of light absorption at a frequency ν for a resonant transition between the initial vibrational quantum energy state m and the final state n at $T = 0\text{ K}$ can be described by the electric dipole operator $\hat{\mu}$ the energy E_j of the excited molecular state j , and the velocity of light:

$$I(\nu) \propto \left(\frac{\nu}{c}\right) \sum_j \frac{|(m|\hat{\mu}|j)|^2 \Gamma_j}{(E_j - h\nu)^2 + \Gamma_j^2}, \quad (15)$$

where Γ_j is a damping factor associated with the energy state j .⁶⁹ The nature and information of the scattered light is affected by changes in its polarization state. The intensity of light scattering $I(\tilde{e}^{d*}, \tilde{e}^i)$ depends on the polarizability tensor $\tilde{\alpha}_{\alpha\beta}$, the polarization vector of the incident \tilde{e}_β^i and of the scattered radiation \tilde{e}_α^{d*} .⁷⁰

$$I(\tilde{e}^{d*}, \tilde{e}^i) = k \langle |\tilde{e}_\alpha^d \tilde{\alpha}_{\alpha\beta} \tilde{e}_\beta^i|^2 \rangle. \quad (16)$$

The tilde indicates that the quantities are complex numbers and the asterisk superscript indicates complex conjugation. The bra-ket designate an average over all angles of orientation of the molecule. The Greek subscripts α and β imply a summation over the Cartesian directions

x , y , and z . Thus, equation (17) has *nine* terms (for each component pair xx , xy , xz , yx , yy , yz , zx , zy , zz). The constant k is composed of:

$$k = \left(\frac{\omega^2 \mu_0 \tilde{E}^{(0)}}{4\pi R} \right)^2, \quad (17)$$

with the angular frequency of light ω , the magnetic permeability μ_0 , the electric field strength of the incident laser $\tilde{E}^{(0)}$, and the distance of the position of scattering to the detector R . The polarizability tensor $\tilde{\alpha}_{\alpha\beta}$ is given by the summation over all electronic states j of the molecule divided by the reduced Planck constant \hbar , and consists of resonant and nonresonant terms^{69,70}:

$$\tilde{\alpha}_{\alpha\beta} = \frac{1}{\hbar} \sum_{j \neq m, n} \left(\underbrace{\frac{\langle m | \hat{\mu}_\alpha | j \rangle \langle j | \hat{\mu}_\beta | n \rangle}{\omega_{jn} - \omega_0 + i\Gamma_j}}_{\text{resonant term}} + \underbrace{\frac{\langle m | \hat{\mu}_\beta | j \rangle \langle j | \hat{\mu}_\alpha | n \rangle}{\omega_{jm} - \omega_0 + i\Gamma_j}}_{\text{nonresonant term}} \right), \quad (18)$$

where ω_{jn} or ω_{jm} are the differences of the angular frequency of the vibronic state j and the states m or n (before or after the scattering process, respectively). The imaginary terms $i\Gamma_j$ of the damping factor are proportional to the width of the state j and is inversely proportional to its lifetime. In the following the damping will be ignored. $\hat{\mu}_\alpha$ and $\hat{\mu}_\beta$ are electric dipole moment operators. The dipole moment operators are the summation over the products of charge e and position r in the l th direction (with $l = \alpha$ or β) of all particles k in the molecule:

$$\hat{\mu}_l = \sum_k e_k \cdot r_{kl}. \quad (19)$$

For Raman scattering, these particles are only electrons, because the nuclei make no contribution to the polarizability.

The operator $\hat{\mu}_\beta$ describes the interaction between the molecule and the incident radiation, and $\hat{\mu}_\alpha$ describes the interaction between the molecule and the scattered radiation. In a time-ordered sense, the matrix elements can be read from right to left. Thus, the resonant term describes how the molecule interacts with the incidence laser photon and then creates a scattered photon. The nonresonant term reverses the order.⁷⁰

1.4.2.4 Raman intensity invariants

Following from equation (16), Raman intensity is proportional to the square of the quantity of the polarization tensor. This equation is sufficient for single crystals, but for randomly oriented materials such as powder, gases, liquids or polycrystalline films,

orientational averaging has to be carried out. There exist invariant values of linear combinations of polarizability tensors that are independent of the orientation of the molecule. All Raman intensities from spectra of randomly oriented samples can be expressed by only *three* invariants: the isotropic invariant α^2 , the symmetric anisotropy $\beta_s(\alpha)^2$, and the antisymmetric anisotropy $\beta_a(\alpha)^2$. They are given by:

$$\alpha^2 = \frac{1}{9} \text{Re} [(\tilde{\alpha}_{\alpha\alpha})^s (\tilde{\alpha}_{\beta\beta})^{s*}], \quad (20)$$

$$\beta_s(\alpha)^2 = \frac{1}{2} \text{Re} [3(\tilde{\alpha}_{\alpha\beta})^s (\tilde{\alpha}_{\alpha\beta})^{s*} - (\tilde{\alpha}_{\alpha\alpha})^s (\tilde{\alpha}_{\beta\beta})^{s*}], \quad (21)$$

$$\beta_a(\alpha)^2 = \frac{1}{2} \text{Re} [3(\tilde{\alpha}_{\alpha\beta})^a (\tilde{\alpha}_{\alpha\beta})^{a*}], \quad (22)$$

where $(\tilde{\alpha}_{\alpha\beta})^s$ and $(\tilde{\alpha}_{\alpha\beta})^a$ are the symmetric and antisymmetric forms of the polarizability tensor. They are given by:

$$(\tilde{\alpha}_{\alpha\beta})^s = \frac{1}{2} [(\tilde{\alpha}_{\alpha\beta}) + (\tilde{\alpha}_{\beta\alpha})], \quad (23)$$

$$(\tilde{\alpha}_{\alpha\beta})^a = \frac{1}{2} [(\tilde{\alpha}_{\alpha\beta}) - (\tilde{\alpha}_{\beta\alpha})]. \quad (24)$$

Again, the Greek subscripts α and β indicate the summation over *nine* terms (one for each pair) of the Cartesian directions x, y , and z . These three invariants provide the basis for a general theory of Raman scattering that describes the depolarization ratios in Raman experiments.⁷⁰

1.4.2.5 Raman intensity

Placzek showed that the theory of Raman scattering simplifies if certain conditions are satisfied: the ground state of the molecule must be a singlet sigma electronic state ($^1\Sigma$), the Born Oppenheimer approximation (which separates the electronic motion from vibration and rotation of the nuclei)⁷¹ should be valid, and that the exciting frequency ν_0 should be very much less than the lowest allowed excited electronic state of the molecule. This is the case for most molecules and lasers in conventional Raman spectroscopy (as opposed to resonant Raman scattering).⁷²

This limit is also referred to as the far-from-resonance limit. In this case, the interaction between the molecule and the light is approximately the same for the incident and the scattered photon. Thus, the Raman tensor becomes symmetric and the antisymmetric anisotropic invariant vanishes in equations (22) and (24). Thus, we have:

$$\beta(\alpha)^2 = \beta_s(\alpha)^2, \quad (25)$$

$$\beta_\alpha(\alpha)^2 = 0. \quad (26)$$

Thus, only two Raman invariants remain (equations (20) and (21)). They simplify to:

$$\alpha^2 = \frac{1}{9} a_{\alpha\alpha} a_{\beta\beta}, \quad (27)$$

$$\beta(\alpha)^2 = \frac{1}{2} (3a_{\alpha\beta} a_{\beta\alpha} - a_{\alpha\alpha} a_{\beta\beta}), \quad (28)$$

where $a_{\alpha\beta}$ is the far-from-resonance polarizability. For $a_{\alpha\beta}$, the resonant term vanishes in equation (18) and we have:

$$a_{\alpha\beta} = \frac{2}{\hbar} \sum_{j \neq n} \left(\frac{\omega_{jn}}{\omega_{jn}^2 - \omega_0^2} \text{Re}[\langle m | \hat{\mu}_\beta | j \rangle \langle j | \hat{\mu}_\alpha | n \rangle] \right), \quad (29)$$

where only the real part (Re) of the matrix element product is needed in the nonresonant term. In the far-from-resonance approximation, the two invariants (equations (27) and (28)), can be used to express the intensity of Raman scattering for all polarizations and in all scattering geometries.⁷⁰

Polavarapu introduced *ab initio* quantum mechanical methods to calculate vibrational Raman spectra intensities by starting in the zero-frequency limit of the far-from-resonance polarizability, where the final and initial states are equal:

$$a_{\alpha\beta} = \frac{2}{\hbar} \sum_{j \neq n} (\text{Re}[\langle m | \hat{\mu}_\beta | j \rangle \langle j | \hat{\mu}_\alpha | n \rangle]). \quad (30)$$

Raman intensities can be calculated with the electric field perturbation approach, where the tensors are varied with the normal coordinates of vibrational motion. Using *ab initio* calculations, good agreement between theory and experiment have been achieved. Frequently used approaches are based on the density functional theory (DFT).⁷⁰

Van Vleck showed that for a molecule in a vibronic state m that is perturbed by an electromagnetic wave and passes into state n while it scatters light of the frequency $\nu_0 + \nu_{mn}$, the intensity of Raman scattered light is (after averaging over all orientations):

$$I_{mn} = \frac{2^7 \pi^5}{3^2 c^4} I_0 (\nu_0 + \nu_{mn})^4 \sum_{\alpha\beta} \left| (a_{\alpha\beta})_{mn} \right|^2, \quad (31)$$

where c is the speed of light, $\nu_{mn} = \nu_m - \nu_n$, and ν_0 and I_0 are the frequency and the intensity of the incoming light.

1.4.3 Raman spectra of TiO₂

The following chapters provide a brief overview on the general nature of Raman spectra of the crystalline TiO₂ phases anatase (1.4.3.1), brookite (1.4.3.2), and rutile (1.4.3.3). In this work, the crystalline phases are nanostructured. As anatase is the most prominent phase that occurs in this work, we give a brief review (1.4.3.4) on Raman spectra of nanostructured anatase in literature.

1.4.3.1 Raman spectrum of anatase TiO₂

The unit cell of anatase contains two TiO₂ units with 6 atoms, leading to 18 vibrational modes, of which 15 are optical and 3 are acoustic. According to factor group analysis, the optical modes at the Γ point (Γ_{opt}) can be classified as

$$\Gamma_{opt} = A_{1g} + A_{2u} + 2B_{1g} + B_{2u} + 3E_g + 2E_u. \quad (32)$$

Six of these modes, A_{1g} , $2 B_{1g}$, and $3 E_g$ modes, are Raman active, while A_{2u} and $2E_u$ are IR-active, and the B_{2u} mode is silent.⁵⁸ The positions of the Raman peaks are around $E_g(1)$ (143 cm^{-1}), $E_g(2)$ (197 cm^{-1}), B_{1g} (399 cm^{-1}), A_{1g} (515 cm^{-1}), B_{1g} (519 cm^{-1}), and $E_g(3)$ (639 cm^{-1}), and differ by a few cm^{-1} in literature.^{73,74}

Typical anatase Raman spectra measured in this work can be found in Fig. 102 in chapter 6.1.2.4. The 3D vibrational anatase Raman modes are projected to the (200)-plane in Fig. 10 with large white Ti atoms and small gray O atoms, where the arrows mark the exaggerated amplitudes of the eigenvectors based on factor group analysis according to Ohsaka et al.⁷³

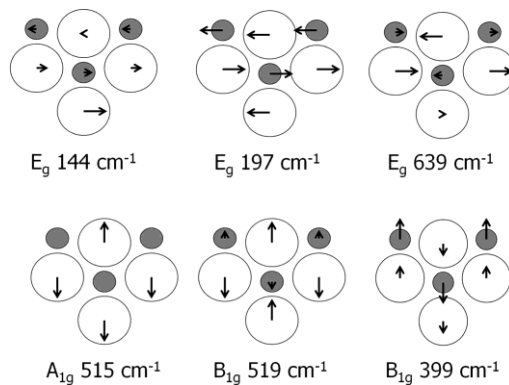


Fig. 10: Anatase vibrational Raman modes of anatase TiO₂ – 3d vibrations projected to the (200)-plane, based on factor group analysis.⁷³

The doubly degenerate E_g modes are (Ti—O—Ti) symmetric stretching vibrations perpendicular to the c -axis. The A_{1g} mode causes (in general O) anti-symmetric bending vibrations parallel to the c -axis, and B_{1g} modes cause (O—Ti—O) symmetric bending vibrations parallel to the c -axis. Depending on the model used for the calculation the amplitudes

may vary. A scheme of Raman active anatase atomic vibrations is given in Fig. 11, where arrows mark exaggerated amplitudes of the eigenvectors according to Frank et al.⁷⁴

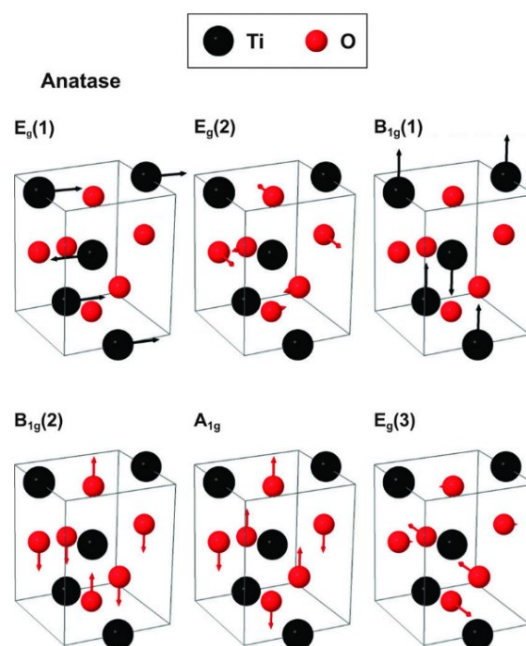


Fig. 11: Scheme of Raman active atomic vibrations in anatase. Ti atoms are large black and O atoms are small red spheres. The arrows indicate the movements of the atoms. Adopted from Frank et al.⁷⁴

1.4.3.2 Raman spectrum of brookite TiO_2

Due to the large unit cell and low symmetry, brookite has a large number of Raman and IR active phonons. From symmetry considerations brookite is expected to have 36 Raman active phonons (9 A_{1g} , 9 B_{1g} , 9 B_{2g} , and 9 B_{3g}), 24 infrared active phonons (8 B_{1u} , 8 B_{2u} , and 8 B_{3u}), 9 silent modes (A_{1u}), and 3 acoustic modes (B_{1u} , B_{2u} , and B_{3u}). Values for all 36 modes were obtained by DFT calculations. All A_{1g} and most B_{1g} and B_{2g} Raman vibrations were experimentally found in literature: A_{1g} (at 125, 152, 194, 246, 324, 412, 492, 545, and 640 $[cm^{-1}]$), B_{1g} (at 169, 212, 283, 327, 381, 449, and 622 $[cm^{-1}]$), B_{2g} (at 160, 254, 325, 366, 391, 460, and 584 $[cm^{-1}]$), B_{3g} (at 132, 212, 318, 416, 500, 460, and 584 $[cm^{-1}]$).⁷⁵

Typical literature brookite Raman spectra can be found in Fig. 49 in chapter 3.2.2.4.2. A schematic depiction of Raman active brookite A_{1g} atomic vibrations is given in Fig. 12, where the arrows mark exaggerated amplitudes of the eigenvectors according to Iliev et al.⁷⁵

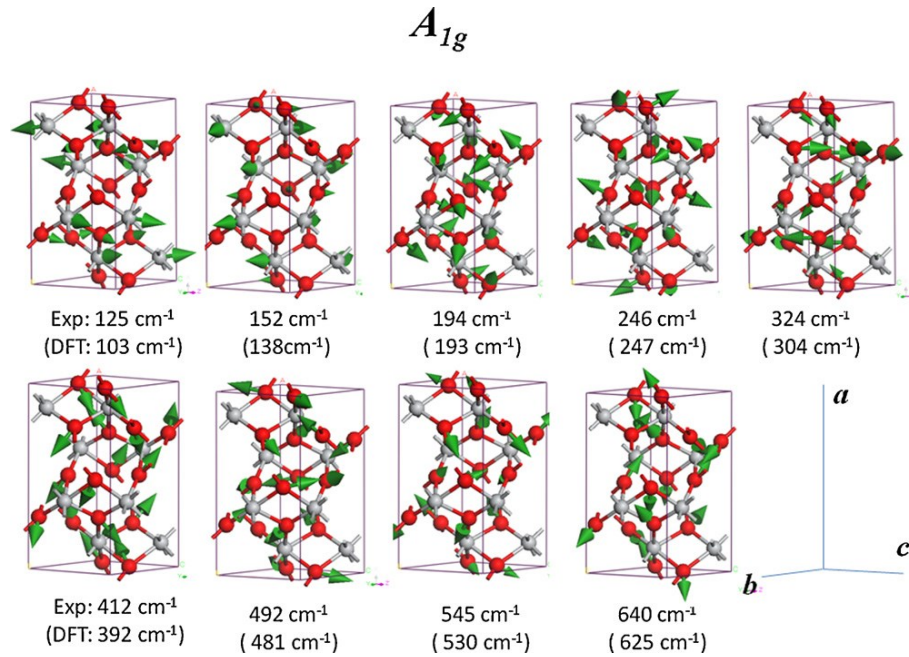


Fig. 12: Scheme of Raman active atomic vibrations in brookite. Ti atoms are light gray and O atoms are red spheres. The green arrows indicate the movements of the atoms. The experimental and DFT values were obtained by Iliev et al.⁷⁵

1.4.3.3 Raman spectrum of rutile TiO_2

Rutile has 15 vibrational modes, of which *four* are infrared active (1 A_{2u} and 3 E_u) and *four* are Raman active modes, which are located around B_{1g} (143 cm^{-1}), E_g (447 cm^{-1}), A_{1g} (612 cm^{-1}), and B_{1g} (826 cm^{-1}).⁷⁶ The values in literature differ depending on the source by a few cm^{-1} . Rutile Raman spectra taken at room temperature contain intense two-phonon bands, especially around 250 cm^{-1} .

A typical rutile literature Raman spectrum can be found in Fig. 50 in chapter 3.2.2.4.3. A scheme of Raman active atomic vibrations of rutile is given in Fig. 13 where the arrows mark exaggerated amplitudes of the eigenvectors according to Frank et al.⁷⁴

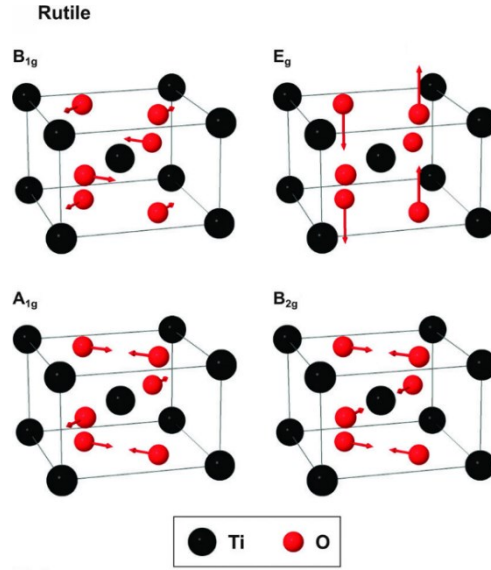


Fig. 13: Scheme of Raman active atomic vibrations in rutile. Ti atoms are large black and O atoms are small red spheres. The arrows indicate the movements of the atoms. Adopted from Frank et al.⁷⁴

1.4.3.4 Raman spectra of nanostructured anatase TiO_2

In order to interpret peak shift and broadening for nanosized structures, one has to consider various factors, including grain size effects such as phonon confinement, and phonon coupling, average or inhomogeneous strain, stoichiometry defects,⁷⁷ and intrinsic anharmonicity.⁷⁸ According to Georgescu et al., Sahoo et al., and Spanier et al., only phonon confinement, inhomogeneous strain and an asymmetric distribution of crystallite sizes can induce asymmetric broadening of Raman peaks.⁷⁷⁻⁷⁹

Grain size effects are described by phonon confinement models, which explain asymmetric peak broadening and peak shifts by phonon dispersion in nanosized particles.⁸⁰ The model expresses the relationship between particle size and phonon position based on the Heisenberg uncertainty principle:

$$\Delta x \Delta p \geq \frac{\hbar^2}{4L}, \quad (33)$$

where Δx is the particle size, Δp the phonon momentum distribution, \hbar the reduced Planck's constant, and L the crystallite size. With decreasing crystal size, the phonon can only propagate within a crystallite and not indefinitely as in a perfect crystal. Thus, the phonon is confined within the crystal, which results in increasing phonon momentum distribution. According to the law of conservation of momentum, this broadening of the phonon momentum leads to a broadening of the scattered phonon momentum.

Most studies focus on the resulting peak shift for only the most prominent Raman modes.⁵⁸ In order to distinguish between effects arising from the crystal size and from other

factors such as stoichiometry and stress, we recommend to also consider the B1g phonon at 399 cm^{-1} . For anatase, phonon confinement leads to asymmetric broadening as well as a blueshift of the Eg(1) peak at 143 cm^{-1} and a redshift of the B1g(1) peak at 399 cm^{-1} with decreasing particle size. The peak width of the Eg(1) and Eg(3) modes at 143 cm^{-1} and 639 cm^{-1} increase stronger at wavenumbers higher than the center of the peak, which results in the peak width on the right side w_r being higher than on the left side w_l : $w_r/w_l > 1$. Peak asymmetry of the B1g mode at 399 cm^{-1} is of opposite nature than that of the Eg modes due to negative dispersion of the B1g phonon dispersion curve. Georgescu et al. consider Raman peak asymmetry as a measure of the phonon confinement effect if the size distribution of the TiO₂ anatase crystallites is symmetric. A more detailed overview and discussion on phonon confinement can be found in chapters 6.1.1.3 to 6.1.1.6.

Yin et al. demonstrated that (unlike the rutile phase) the band gap of anatase can be effectively tuned by applying stress along the soft *c*-direction, using first-principles band structure calculations. According to their calculations, uniaxial compressive/tensile stress of $-10\text{ GPa}/+10\text{ GPa}$ along the *c*-axis increases/lowers the band gap by $\pm 0.3\text{ eV}$. Epitaxial stress shows the opposite behavior, which is not of interest for thin films on amorphous substrates.⁸¹ Average strain arising from changes in lattice parameters with crystallite size can affect the Raman peak position. This effect becomes stronger for small crystallite sizes. Although Ager and Goudadec state that strain has impact only on the position of Raman peaks, and defects only widen them,^{82,83} in experimental studies on TiO₂, under-stoichiometric oxygen content or oxygen vacancies, lead to a blue shift of the most intense Eg(1) peak at 143 cm^{-1} .^{84,85} The same effect was found in diamond Raman spectra by Ager et al., who suggest that the degree of compressive stress may depend on the density of microcrystalline defects.

Strain is positive for compressive strain and leads to a blueshift of phonon wavenumbers in Raman spectra.⁷⁰ According to Georgescu et al., the position of the B1g 399 cm^{-1} band correlates more with the crystal size as compared to the position of the Eg(1) and Eg(3) bands at 143 cm^{-1} and 639 cm^{-1} and they found the best correlation of peak width with crystal size the Eg(3) band. Anyway, in a study of Swamy et al., there is a stronger trend in the blue shift of the Eg(1) and Eg(2) peaks with pressure than for the B1g and A1g + B1g peaks.⁸⁶

Although Raman peak widths are theoretically considered to be independent of temperature,⁸⁷ several researchers observed broadening of anatase Raman peaks with increasing temperature.^{77,78,88,89}

Typically, Raman modes in ionic crystals are softened by increasing temperature, which results in a redshift of the Raman peaks.⁸⁸ However, the behavior of anatase peak positions is not consistent in literature.

Ohsaka noticed various changes in the position of single crystal anatase Raman peaks. The Eg(3) peak shifted to smaller wavenumbers with increasing temperature, as expected, but the Eg(1) and Eg(2) peaks at 143 cm^{-1} and 197 cm^{-1} underwent a blueshift and the position of the B1g peak at 399 cm^{-1} increased to a maximum at 250 K and then decreased with further increasing temperature.⁸⁸

Hearne et al. observed behavior of the Raman peak positions that differed strongly from Ohsaka's results, but which was consistent for commercially bulk TiO₂ anatase and TiO_{1.92} anatase nanoparticles (12 nm), synthesized by lyophilization. There, most of the investigated peaks (Eg(3), B1g, A1g+B1g) exhibited typical softening and an associated decrease of the wavenumber with temperature. The positions of these peaks were similar for nanoparticles and the bulk material. The Eg(1) peak was the only one in which the position grew with temperature for both, nano and bulk material.

Sahoo et al. recorded an increase of local temperature, position and width of the Eg(1) peak at 143 cm^{-1} of nanocrystals with laser power from 5 mW to 200 mW . These effects became more pronounced for smaller crystal sizes in the range of 17 nm to 5.5 nm . For 5.5 nm crystals, the local temperature grew from room temperature to 800 K , the Eg peak shifted by $+4\text{ cm}^{-1}$ and the peak broadened by 17 cm^{-1} when the laser power was increased from 5 mW to 200 mW .

Table 2 sums up the influence of several material properties on Raman peak shape (shift, width, and asymmetry) of the Eg(1) peak at 143 cm^{-1} and the B1g peak at 399 cm^{-1} , and on the optical band gap. The left column names certain conditions. The “+” sign indicates that the condition causes an increase of the respective parameter, “-“ indicates a decrease of a parameter, and “0” indicates that the parameter is not affected by the condition. Numerical values are examples found in literature. The numerical values in the row “Decreasing crystallite size/phonon confinement” refer to the Bersani model⁹⁰ using the parameters of Sahoo et al.⁷⁸ and Georgescu et al.⁷⁷ for 6 nm crystals as compared to bulk TiO₂.

Table 2: Influence of material properties on Raman peak shape and band gap.

condition	Raman Eg(1) peak			Raman B1g peak			band gap
	shift	width	asym.*	shift	width	asym.*	
Decreasing crystallite size / phonon confinement	+8 cm^{-1} for 6 nm. ⁷⁸ +4.5 cm^{-1} for 6 nm. ⁷⁷ + ⁸⁶	+9 cm^{-1} for 6 nm. ^{77,78}	+5 cm^{-1} for 6 nm. ⁷⁸	-3 cm^{-1} for 6 nm. ⁷⁸	+8 cm^{-1} for 6 nm. ⁷⁸ + ⁸⁶	-3 cm^{-1} for 6 nm. ⁷⁸	+ ^{91,92}
phonon coupling		+ ⁷⁷	0 ⁷⁷		+ ⁷⁷	0 ⁷⁷	
under-stoichiometric O content / oxygen vacancies	+11 cm^{-1} (TiO _{1.89}) ⁸⁵ 0 ^{82,83}	+ ^{77,78,83} +22 cm^{-1} (TiO _{1.89}) ⁸⁵	0 ⁷⁷	0 ^{82,83}	+ ^{77,82,83}	0 ⁷⁷	- ⁹³
titanium vacancies	0 ^{82,83}	+ ^{77,82,83}	0 ⁷⁷	0 ^{82,83}	+ ^{77,82,83}	0 ⁷⁷	
compressive (neg.) internal stress/average strain / high pressure	+ ^{82,83,86,94}	0 ^{82,83}	0 ⁷⁷	+ ^{86,94}	0 ^{82,83}	0 ⁷⁷	
tensile (pos.) internal stress/average strain			0 ⁷⁷			0 ⁷⁷	
inhomogeneous strain			+ ⁷⁷			+ ⁷⁷	
uniaxial stress along the <i>c</i> -axis							±0.3 eV for ±10 GPa ⁸¹
Temperature (above room temperature)	+ ^{87,88}	+ ^{77,78,87,88}	0 ⁷⁷	- ⁸⁸	+ ^{77,78,88}	0 ⁷⁷	-0.2 eV at 530 K (vs. RT) ⁸¹

-: decrease, 0: no influence, +: increase; *RT* is room temperature

*) for asymmetry, -/+ means broader at lower/higher wavenumbers

1.4.4 Raman scattering of amorphous materials

The most common models of the Raman scattering of glass and other amorphous materials are based on the structural theory of glass by Goldschmidt and Zachariasen. The two main assumptions are that, firstly, the interatomic bonding forces in amorphous phase are similar to those in crystals because the mechanical properties are of comparable magnitudes. Secondly, there is no long-distance order, since the character of X-ray scattering is diffuse. Both is for example reflected in the Raman spectra of amorphous and crystalline silica (see Fig. 14 b).

In terms of a ‘lattice’, one can consider the distribution of the bonding forces as a disordered elementary cell of infinite size. This can be interpreted as a Brillouin zone that is reduced to zero, which results in a diffuse spectrum that is related to a density of states rather than individual lines. The folding of such a Brillouin zone is depicted in Fig. 14 a.⁷⁰

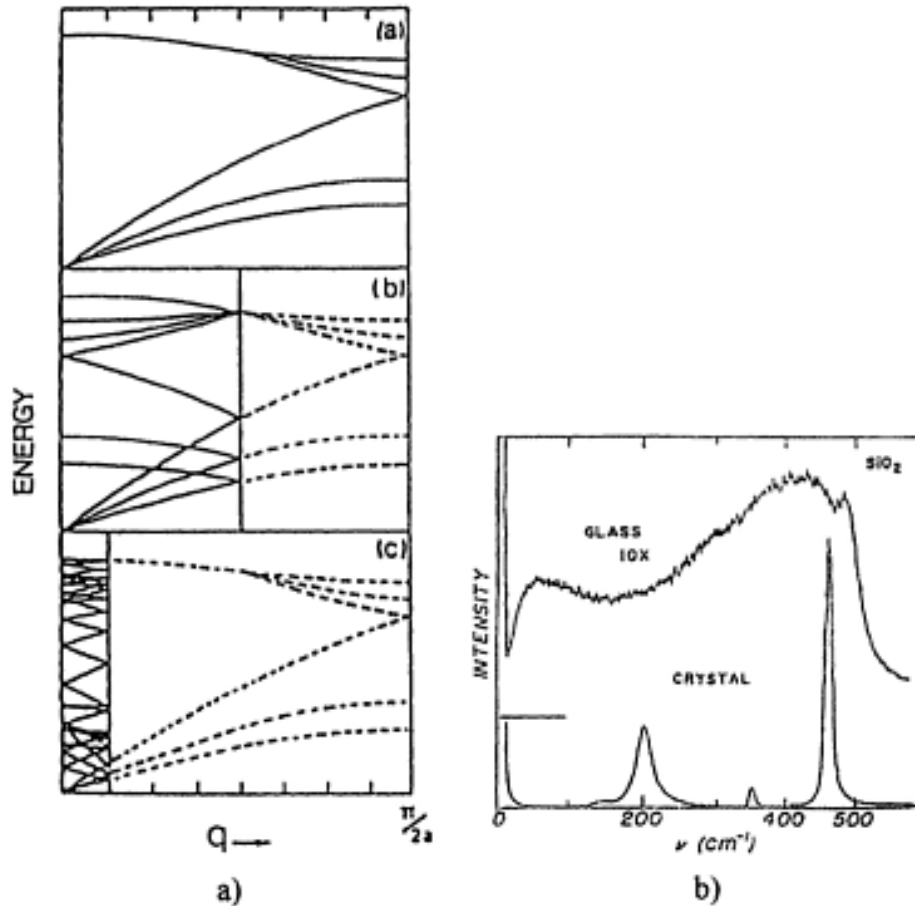


Fig. 14: a) Folding of a silica Brillouin zone towards zero, b) Raman spectra of amorphous (glass) and crystalline silica.⁷⁰

1.4.5 Raman bands of Si and of silica glass substrates

The following chapters give an overview of the main Raman bands of the two kinds of substrates that are coated with TiO₂ films in this work: Si wafers and silica glasses.

1.4.5.1 Raman spectrum of Si

The main one-phonon peak can be found at 520.7 cm^{-1} . Weak structures between 200 cm^{-1} and 520 cm^{-1} arise from the structure in the inverse lifetime of the zone-center optical phonon. Anharmonic coupling between the normal modes in the harmonic approximation determine their lifetime.

The L -point TO phonon causes bands with maxima at around 620 cm^{-1} , 665 cm^{-1} , and 825 cm^{-1} . Its two-phonon overtone occurs as a tale in the two-phonon spectrum, which is

strongest between 600 cm^{-1} and 1045 cm^{-1} and is most intense between 920 cm^{-1} and 1045 cm^{-1} .⁹⁵ Examples of Si Raman spectra and further information is given in chapter 3.1.5.1.

1.4.5.2 Raman bands of silica glasses

The most prominent bands in Raman spectra of glasses which overlap with Raman active vibrations of TiO_2 are around 440 cm^{-1} , 550 cm^{-1} and 800 cm^{-1} . The first two correspond to a three-dimensional lattice of the SiO_4 tetrahedra. The 440 cm^{-1} band emerges from O vacancies in the Si–O–Si bonds between two coupled tetrahedra and decreases with the concentration of silica. The asymmetric band at 550 cm^{-1} is due to deformation modes of decoupled tetrahedra and increases with the concentration of silica. The band around 800 cm^{-1} is attributed to the symmetric vibrations of two neighbor Ti atoms and a bridging O atom and decreases with the bonding angle of Si–O–Si. Further specific bands occur when other elements are present in the glass and can be found in the *Handbook of Raman Spectroscopy*, by I.R. Lewis and Howell Edwards.⁷⁰ Examples of Raman spectra of silica glasses and further information is given in chapter 3.1.5.2.

1.5 X-ray diffraction

X-ray diffraction (XRD) is the diffraction of X-ray waves which are scattered by atom's electrons. X-ray diffractometry is used to investigate the structure of crystals. It provides information on the presence and nature of crystalline phases (such as crystallize size, strain, or texture), and is also used to estimate the crystalline and amorphous fraction in a sample.

Crystalline materials are characterized by a periodic arrangement of atoms, which can be seen as a three-dimensional lattice (cubic, tetragonal, hexagonal, etc.), where the atoms are located in the nodes of the lattice. The lattice forms parallel planes with a distance d characteristic of a certain crystalline structure. The distances are usually in the order of a few \AA ($1 \text{\AA} = 0.1 \text{ nm}$). That is why crystal lattices are often discussed in the non-SI unit \AA .⁹⁶

In 1912, William Lawrence Bragg and his father Sir William Henry Bragg found the condition that must be fulfilled for constructive interference of diffracted rays to occur (which was later called Bragg's law):

$$n \cdot \lambda = 2 \cdot d \cdot \sin \theta, \quad (34)$$

with the order of diffraction n , the wavelength of the radiation λ ($Cu_{K\alpha 1} = 1.54051 \text{\AA}$), the distance between the planes in the atomic lattice d , and the Bragg angle θ .⁹⁷ The Bragg angle θ is the angle between the incident X-ray and the diffracted beam. The theoretical distance d_{hkl} can be calculated by:

$$d_{hkl} = \frac{1}{\sqrt{\left(\frac{h}{a}\right)^2 + \left(\frac{k}{b}\right)^2 + \left(\frac{l}{c}\right)^2}}, \quad (35)$$

with the Miller indices h , k , and l of the corresponding lattice planes, and the lattice constants a , b , and c . For the tetragonal anatase and rutile lattice b is equal to a . The theoretical value assumes perfectly aligned monochromatic X-rays as well as perfect, undistorted crystals, which would lead to sharp diffraction peaks.

In experimental diffractograms, the coherence length is limited by crystallite size, crystal imperfection or defects (such as dislocations, vacancies, interstitials, or grain boundaries), which leads to peak broadening. The Scherrer equation describes the diffraction peak broadening $b_{cryst.}$ caused by a finite coherence length L (often interpreted as crystallite size) from XRD:

$$b_{cryst.} = k \cdot \frac{\lambda}{L \cdot \cos(\theta)}, \quad (36)$$

with the crystallite size L , the width or peak broadening b_{cryst} of the reflex (in radians), and the Scherrer constant k .⁹⁸ k depends on the definition of ‘width’, the crystallite shape, and the crystallite size distribution.⁹⁹ In our case, the width is the half-width at half maximum of a Lorentzian function, the shape is a tetrahedra for anatase as well as for rutile, and the size distribution is not known. According to Langford and Wilson, the Scherrer constant k is 0.7262 for the anatase (101) and the rutile (110) reflection.⁹⁹ We calibrated the width b with after measuring LaB₆ 660 a powder as described in chapter 2.2.3.

The applicability of the Scherrer equation depends on the Bragg angle θ and the material’s absorption coefficient μ_0 and is approximately 12% of the extinction length. Miranda and Sasaki estimated the upper Scherrer limit to be between 100 cm^{-1} and 200 cm^{-1} for most materials.

In addition to crystallite size, peak broadening is associated with lattice strain. In 1923, John M. Cowley described strain induced diffraction peak broadening b_{strain} by:

$$b_{strain} = \epsilon \cdot \tan \theta, \quad (37)$$

with the lattice strain $\epsilon = \Delta d/d$.¹⁰⁰ In 1953, G. K. Williamson and W. H. Hall established a method used to distinguish between diffraction peak broadening caused by crystallite size and by strain.¹⁰¹ Thereby the peak width b_r is considered as the sum of the b_{cryst} and b_{strain} .

$$b_r = b_{cryst} + b_{strain}. \quad (38)$$

When we insert equations (36) and (37) in (38) we get:

$$b_r = k \cdot \frac{\lambda}{L \cdot \cos(\theta)} + \epsilon \cdot \tan(\theta). \quad (39)$$

Multiplying equation (39) by $\cos(\theta)$ results in:

$$b_r \cdot \cos(\theta) = k \cdot \frac{\lambda}{L} + \epsilon \cdot \sin(\theta). \quad (40)$$

In a plot $b_r \cdot \cos(\theta)$ against $\sin(\theta)$, we use a linear fit with slope ϵ and intercept $k \cdot \lambda / L$.¹⁰¹ In such a plot (called Williamson-Hall plot), the slope indicates strain, while the intercept indicates the grain size. A typical Williamson-Hall plot of our measurements is shown in Fig. 15.

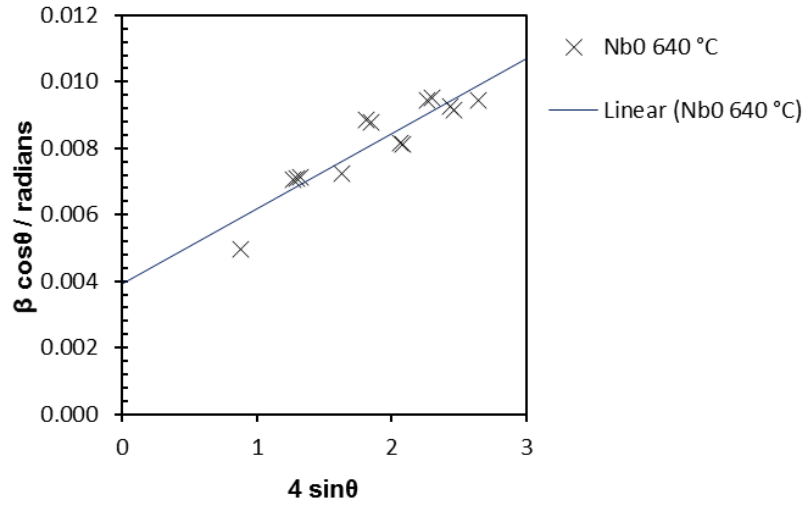


Fig. 15: Williamson-Hall plot of an e-beam evaporated undoped TiO₂ thin film after annealing at 640 °C.

Further evaluation is specified in the chapters 3.3, and in the sub-chapters of chapters 5, and 6, where X-ray diffractograms are analyzed.

2 Experiments

In the following chapters, we describe the methods and the most important parameters that we used to prepare (2.1) and to analyze (2.2) TiO₂ thin films. We produced undoped or Nb-doped TiO₂ thin films using three different deposition techniques: rf-diode sputtering (2.1.1), reactive e-beam evaporation (2.1.2), and rf-magnetron sputtering (2.1.3).

2.1 Thin film preparation

The rf-diode sputtered films prepared in chapter 2.1.1 are undoped multi-phase TiO₂ films that were coated onto B270 glass, fused silica, and Si at varying substrate temperatures and are not post-heated.

The reactive e-beam evaporated films prepared in chapter 2.1.2 are undoped as well as Nb-doped TiO₂ films (with *0 at.%, 8 at.%, or 16 at.%* Nb) coated onto B270 glass, fused silica, and Si at a substrate temperature of *250 °C*, and are post-heated at various temperatures (*350 °C – 750 °C*).

The rf-magnetron sputtered films prepared in chapter 2.1.3 are Nb-doped TiO₂ films with varying Nb content coated onto B270 glass (and Si) at a substrate temperature of *60 °C*. The films are deposited using various controlled oxidation states of the metallic Ti target. They are post-heated at ca. *475 °C* or *530 °C*.

We post-heated the e-beam coated films and the rf-magnetron sputtered films after a base pressure of *10⁻⁴ Pa* is reached in the vacuum chamber that is also used for the rf-magnetron sputter deposition. Sample pre-treatment was similar for each set of samples. Prior to deposition, we cleaned the substrates in an ultrasonic bath in isopropanol for *30 min* at *80 °C*, rinsed them in deionized water, and dried them with a nitrogen pistol.

2.1.1 Deposition of rf-diode sputtered TiO₂ films

TiO₂ thin films were diode-sputtered by M.Sc. Jingyi Shi in her master's thesis¹⁰² and by the author onto B270 Glass substrates at *155 °C* to *415 °C (±20 °C)* using a *Perkin-Elmer PE 2400* sputter coater (Fig. 16) with radio-frequency plasma excitation.



Fig. 16: Perkin-Elmer PE 2400 sputter coater.¹⁰²

The advantage of this method is a large area of homogeneous coating. The Ti target has a diameter of 25 cm and we measured a constant film thickness of $100 \text{ nm} \pm 5 \text{ nm}$ within a circular area with 10 cm diameter. The geometry of the coater and the sputter arrangement are shown in Fig. 17.

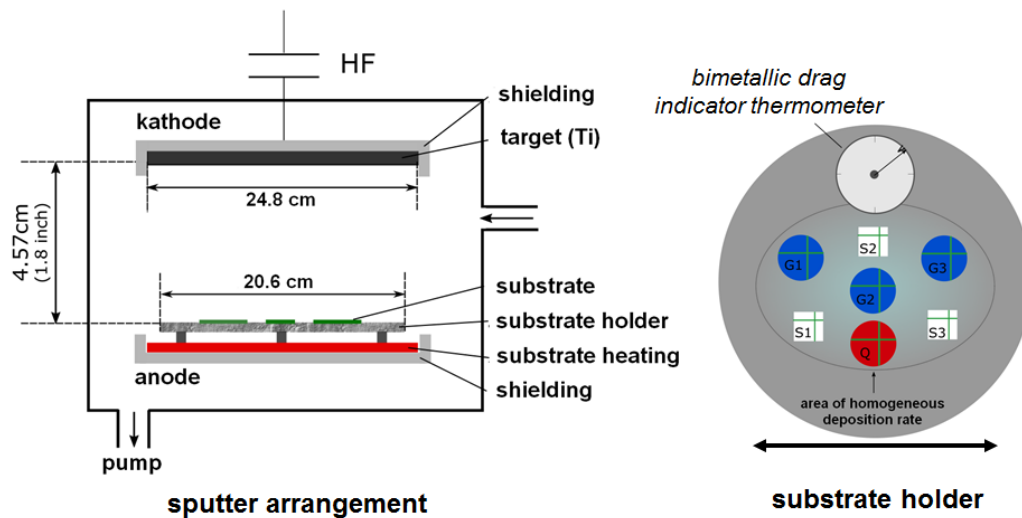


Fig. 17: Geometry of the Perkin-Elmer PE 2400 sputter coater (left), sputter arrangement and area of homogeneous deposition rate (right). Taken from Shi and modified.¹⁰²

The deposition parameters used in this study are given in Table 3.

Table 3: Deposition parameters of rf-diode sputtered films

rf-diode sputtering power	400 W
target	Ti
substrates	B270 glass, quartz glass, Si wafer
distance substrate – target	4.6 cm (1.8 inches)
substrate temperatures	155 °C – 415 °C
gas mixture	Ar (25.5 sccm), O (0.5 sccm)
working pressure	$6 \cdot 10^{-1}$ Pa
deposition time	60 min

2.1.2 Deposition and annealing of reactive e-beam evaporated TiO₂ films

We applied a new technique for depositing Nb-doped TiO₂ films by reactive electron beam evaporation. Nb-doped and undoped TiO₂ thin films were deposited from crucibles filled with self-made pellets made from granular Ti₂O₃ and Nb₂O₅. The films are deposited in a *Balzers Process Systems BAK 640 coating system* high vacuum chamber. Fig. 18 shows the vacuum chamber with two quartz crystals and a rotatable calotte.



Fig. 18: Balzers Process Systems BAK 640 coating system high vacuum chamber, with a calotte and quartz crystals.

For the deposition, the crucibles shown in Fig. 19 are placed below the quartz crystals. For three sets of samples, the pellets were mixed with Ti₂O₃/Nb₂O₅ weight ratios of 20:0, 20:1, or 20:2, which produced films with 0 at.%, 8 at.%, or 16 at.% in relation to the Ti content.

Thus, the films have $Nb/(Ti+Nb)$ ratios of 0, 0.08, and 0.16. We refer to these films as “Nb0”, “Nb1”, and “Nb2” respectively.



Fig. 19: Crucibles to be filled with self-made Ti_2O_3 or Nb_2O_5 pellets.

Three different kinds of substrates with a diameter of 25 mm were coated. The substrates are B270 glass discs (1 mm thick), fused silica discs (2 mm), and Si wafers (0.5 mm). They were mounted on the rotating calotte. A bottom view of the calotte is shown in Fig. 20.



Fig. 20: Rotatable calotte used as a substrate holder.

Prior to deposition, the vacuum chamber was pumped to a base pressure of $3 \cdot 10^{-4}$ Pa by a diffusion pump. The films were deposited in an oxygen atmosphere of $3 \cdot 10^{-2}$ Pa and a substrate temperature of 250 °C with thicknesses between 230 nm and 300 nm at a deposition rate of 0.4 nm/s. The deposition rate was controlled by quartz oscillators shown in Fig. 18.

A further quartz cylinder (hidden behind aluminum foil in Fig. 20) calibrated to a mass density of 3.5 g/cm^3 was used to control the deposition time until an approximate film thickness of 300 nm is reached. The samples coated on B270 glass were individually post-heated at various temperatures ranging from 350 °C to 640 °C for 2 h in vacuum at a pressure of $1 \cdot 10^{-5}$ Pa. Films on fused silica were post-heated at 750 °C. Further films with varying stoichiometry and varying post-heating temperatures were produced additionally. The films were deposited by Dipl.-Phys.Ing. Martin Jerman in the optical workshop of the *University of Duisburg-Essen* and they have been post-heated by the author in this work. The temperatures have uncertainties of about 20 °C.

The used deposition parameters resulted from a publication of Jerman and Mergel.¹⁰³ There, TiO₂ films were produced at various substrate temperatures from 150 °C to 350 °C and post-heated at temperatures from 150 °C to 850 °C. Films that were prepared there at 350 °C were anatase as-deposited and transformed to rutile after post-heating at 850 °C. The films deposited with a substrate temperature of 250 °C were amorphous as deposited and yielded the highest densities in mass and crystalline grains after annealing. Furthermore, the refractive index of the 250 °C films was reproducible. Thus, we expect the best mechanical, optical, and electrical properties for this coating temperature, and chose to post-heat at temperatures below 800 °C in order to avoid a phase transition to rutile.

Fig. 21 shows Raman spectra (633 nm) of the Ti₂O₃ coating material. The spectra were taken as described in chapter 2.2.1 with 100x lenses and a spot size of around 1 μm.

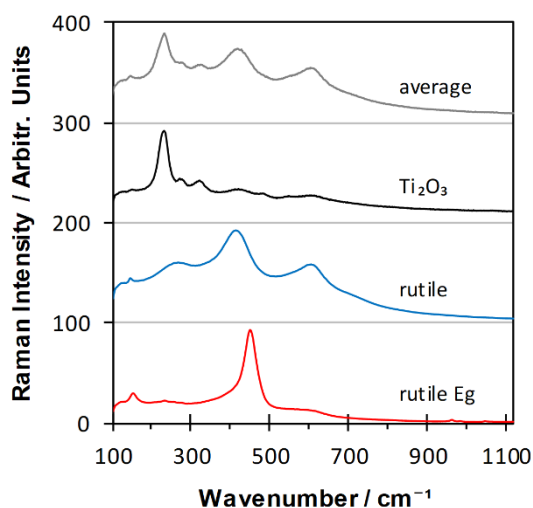


Fig. 21: Raman spectra of the Ti₂O₃ coating material to be evaporated. The gray spectrum (shifted by 300 units) is the average spectrum of 80 measurements taken at distances of 1 μm. The other three spectra are taken at single grains found at the surface of a Ti₂O₃ pellet.

The gray spectrum at the top shows the average spectrum of 80 measurements taken in distances of 1 μm. The black line is a spectrum of pure Ti₂O₃, and the two spectra at the bottom show rutile. The upper one (shifted by 100 intensity units) shows a broad and distorted rutile spectrum that resembles the spectrum of a rutile nanocrystal. The red spectrum at the bottom shows a rutile spectrum with a narrow Eg peak at ca. 445 cm⁻¹, a broad B1g peak at 145 cm⁻¹, and the multi-phonon peak at 245 cm⁻¹. The A1g peak at around 612 cm⁻¹ is extremely weak or not present. The spectra are normalized. Although the pellet consists of mainly Ti₂O₃, the average spectrum contains a high amount of signals arising from rutile. Rutile produces a higher Raman intensity than Ti₂O₃. The measured rutile spectrum (blue) is 30 times more intense than the Ti₂O₃ intensity. This might be caused partly by the high surface roughness of the Ti₂O₃

grains. The laser could be better focused at the surface of the rutile crystal. Raman spectra (633 nm) of the Nb₂O₅ coating material are shown in Fig. 22.

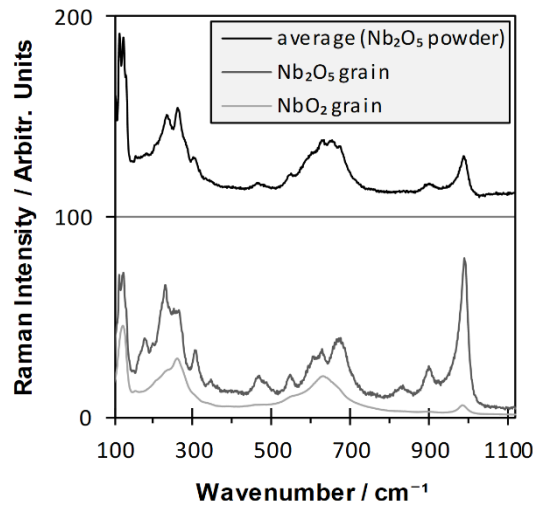


Fig. 22: Raman spectra of the Nb₂O₅ coating material to be evaporated. The black spectrum (shifted by 100 units) is the average spectrum of 80 measurements taken at distances of 1 μm. The other two spectra are taken at single grains found at the surface of the pellet.

The Nb₂O₅ pellet contains Nb₂O₅ (dark gray) as well as NbO₂ (light gray) grains. The spectra of both crystal configurations contribute to the average spectrum (black).

2.1.3 Deposition of plasma-emission controlled rf-magnetron sputtered TiO₂ films

We produced Nb-doped TiO₂ thin films by plasma-emission controlled magnetron-sputtering, as described in Mukherjee et al.¹⁰⁴ In a previous study we had deposited films using the same sputter coater and compared dc- and rf-magnetron sputtered TiO₂ films. The rf-sputtered films had higher densities which were closer to standard anatase.¹⁰⁵ We therefore chose to deposit the Nb-doped films with rf-sputtering.

The samples were produced in the Thin Film group of the University of Duisburg-Essen by Dr. rer. nat. Sanat Kumar Mukherjee¹⁰⁴, M.Sc. Shixun Cui¹⁰⁶, and by the author (for details see below). For the deposition used a *Von Ardenne Anlagentechnik GmbH LS500s* sputter coater equipped with a plasma-emission monitor (PEM) shown in Fig. 23.



Fig. 23: Von Ardenne Anlagentechnik GmbH LS500s sputter coater equipped with a PEM.¹⁰⁶

Fig. 24 displays the sputter geometry. A Von Ardenne Anlagentechnik GmbH PEM 05 plasma-emission monitor is attached to the sputtering coater using an optical fiber and a photo multiplier. It is used to stabilize the oxidation state of the metallic Ti target by controlling the oxygen flow using an RS 232 interface. Therefore, the intensity of the Ti 453 nm plasma line (neutral Ti atom) is measured.¹⁰⁴

In this work, we use the common abbreviation *PEM* (plasma emission monitoring) for a sputter coating process in which the oxidation state of the Ti target is controlled using plasma emission monitoring.

The multiplier voltage is initially set to a value of 90 (“*PEM90*”), which also corresponds to the intensity of an oxygen-free Ti target is normalized to a value of 90 and the intensity is zero for a fully oxidized Ti target. We produced various sets of samples with *PEM30*, *PEM35*, *PEM37.5*, or *PEM40*, of the intensity. We roughly estimate the oxidation state of the target linearly to be 78%, 71%, 68%, and 65%.

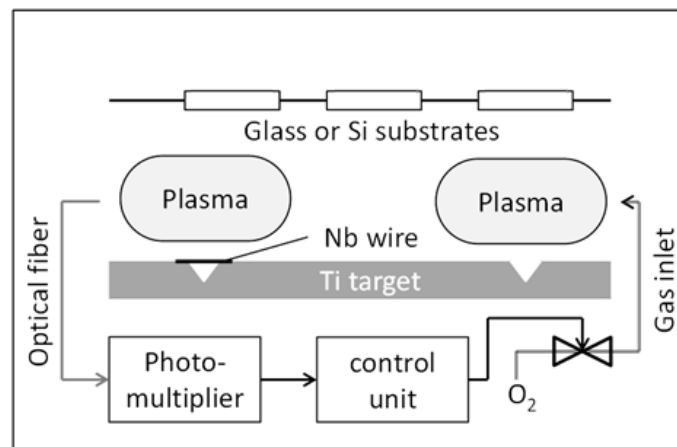


Fig. 24: Sputter geometry including the placement of the Nb wire and the substrates. Taken from Mukherjee et al. and modified.¹⁰⁴

The target has a diameter of ca. *150 mm*. Two Nb wires (*99.99%* purity) with *1 mm* diameter and *20 mm* length, are put onto one side of the sputter track of the target. At each deposition process, *three* substrates are coated simultaneously, and are placed (a) *12.5 mm*, (b) *42.5 mm*, and (c) *72.5 mm* horizontally away from the Nb wires. The substrates are discs of B270 Crown glass or Si wafers with diameters of *25 mm* and thicknesses of *1 mm* or *0.5 mm*, respectively.

Dr. rer. nat. Sanat Kumar Mukherjee produced the first set of samples and post-heated them at around $530\text{ }^{\circ}\text{C}^{104}$ (the publication says $400\text{ }^{\circ}\text{C}$, but we have re-calibrated the heating afterwards). The author of this work repeated the deposition processes using the four mentioned oxidation states (*78%*, *71%*, *68%*, and *65%*) and post-heated the *twelve* samples at $475\text{ }^{\circ}\text{C} \pm 20\text{ }^{\circ}\text{C}$. M.Sc. Shixun Cui produced films using a *71%* oxidized Ti target with varying deposition time.

2.2 Analytics

The main focus of this work is the evaluation of Raman spectra of TiO₂ thin films coated onto various substrates. We therefore describe in detail the Raman measurements in chapter 2.2.1 and the production of Raman maps in chapter 2.2.2. The Raman spectra are (quantitatively and qualitatively) compared to X-ray diffractograms, which were taken and evaluated as described in chapter 2.2.3. In chapters 2.2.4 to 2.2.7 we briefly report experimental parameters of further analysis of surface topology, chemical composition, film thickness, mass, density, and electrical properties.

2.2.1 Raman spectroscopy

We measured Raman spectra of rf-diode sputtered multi-phase TiO₂ thin films, e-beam coated undoped and Nb-doped TiO₂ thin films and rf-magnetron sputtered Nb-doped TiO₂ thin films with a *Renishaw InVia μ Raman* spectrometer at ICAN. We used a red 633 nm HeNe laser and a green 532 nm frequency doubled diode-pumped solid-state laser. The lasers were set to a power of 8 mW and 0.8 mW, respectively, which was measured after the light having passed the beam expander and the pinhole. The beams were then focused through a lens with a magnification of 100 with a spot size < 1 μ m. The power of the green 532 nm laser was chosen lower than that of the 633 nm laser in order to avoid effects in the Raman spectra arising from local heating caused by a smaller spot size. It was checked that the Raman spectra did not change for multiple repetitions of the experiments. The 532 nm Raman spectra were measured as repetitive 1 s scans taken 100 times. The 633 nm Raman spectra were produced as described in chapter 2.2.1.1.

A darkfield spectrum of a measurement with a closed spectrometer and without an incident laser beam is presented in Fig. 165 in the appendices. We estimate the spectral resolution of the spectra that were taken in this work as 1 cm^{-1} , which is the width of sharp spectral signals that is produced by cosmic ray. Before processing, each Raman map that was taken within 8 hours includes roughly 30 or more cosmic rays.

2.2.1.1 Measurement and preprocessing of the spectra

[This chapter is part of a publication in the Journal of Raman Spectroscopy, Volume 49, Issue 7, 1217-1229 (2018).]¹ Copyright © 2018 John Wiley & Sons, Ltd.

Raman maps were created within areas of 30 μ m x 30 μ m in 250 nm steps in snake mode summing up to 14641 spectra. Each position was irradiated for 1 s and measured once. Every 500 measurements, the laser focus was adjusted automatically. This setup minimizes laser

impact on the structure of the samples. The spectra were averaged for each sample after cosmic ray removal. The high amount of measurements allows significant noise removal so that the fitting routine described in this work can be applied to the single spectra of each individual position. We used the software *Wire*TM 4 for the described processing of the spectra.²⁶ A detailed overview about noise reduction and other preprocessing can be found in Pelletier et al. 2003.¹⁹

The measured spectral range has to be wider than the range which contains the most important information of the measurement because Raman spectra generally feature artefacts caused by the experimental setup within the lowest and highest wavenumbers. The most significant signals of the TiO₂ phases are in the range from 100 cm^{-1} to 900 cm^{-1} . Furthermore, we examined the characteristics of the Rayleigh peak around zero shift as an indicator for the quality and reproducibility of a measurement. Taking this into account, we measured our spectra from -144 cm^{-1} to 1118 cm^{-1} . The range below 130 cm^{-1} is excluded from our models to avoid impairment of the Rayleigh filter, which affects the evaluation of the spectra below 130 cm^{-1} and makes fitting impossible below 120 cm^{-1} . Furthermore, rotational modes of the air occur in the range of $100\text{ cm}^{-1} - 140\text{ cm}^{-1}$.¹⁰⁷ The range above 1000 cm^{-1} is fitted with less priority because of artefacts from the spectrometer that occur at the highest energies of any measured spectral range.

Amorphous pure and Nb-doped TiO₂ thin films with a thickness of 250 nm were deposited by electron beam evaporation from Ti₂O₃ and Nb₂O₅ powders in custom made evaporators onto 1 mm thick discs of B270 crown glass substrates with a diameter of 25 mm . These films were used for preparing the amorphous reference spectra. Films that were post-heated at temperatures from 350 °C to 750 °C were used for testing and calibrating the decomposition of the measured Raman spectra into thin film and substrate spectra, for the models for first-order scattering and the background spectrum of anatase as well as for the simplified model for rutile as a minor phase.

Mixed-phase films containing anatase, rutile, brookite, and an amorphous content were deposited by rf-diode sputtering with a thickness of 70 nm at various substrate temperatures ranging from 155 °C to 415 °C onto discs of Si, B270 crown glass, and fused silica with a diameter of 25 mm . The models for mixed-phase modelling were developed using Raman measurements of these samples. Spectra of TiO₂ thin films prepared by magnetron sputtering could also be analyzed with our model but are not reported here explicitly. Raman spectra for six individual samples of each substrate material were measured and prepared with the same procedure as above. Four of each set of spectra were used to build the substrate models to be fitted to the spectra of the fifth and sixth samples.

2.2.1.2 Noise filter

The single spectra of each position within the maps have low signal-to-noise ratios. For the average spectra of the Raman maps, the use of a noise filter is not necessary, because 14641 spectra irradiated each for 1 s provide enough information to minimize shot noise. But when single spectra within the maps are analyzed, the unfiltered spectra are not evaluable, and a noise filter must be used. Also, noise filtering drastically improves visualized Raman maps.

Fig. 25 shows spectra of a Nb doped thin film TiO_2 (sputter deposited with an oxidation state of the target of 65% “Ox-65”) after cosmic rays and the substrate spectrum are removed (sorted by the height of the $\text{Eg}(1)$ peak at around 146 cm^{-1}). The gray spectra are from several positions of a map, each measured for one second. The numbers in brackets are the positions in μm as seen from the center of the Raman map. The green spectrum is the average spectrum of the whole map. The visible noise in the single spectra is as intense as the strong Eg peak at 145 cm^{-1} in the average spectrum and an order of magnitude higher than the intensities of the A1g peak and the A1g/B1g doublet.

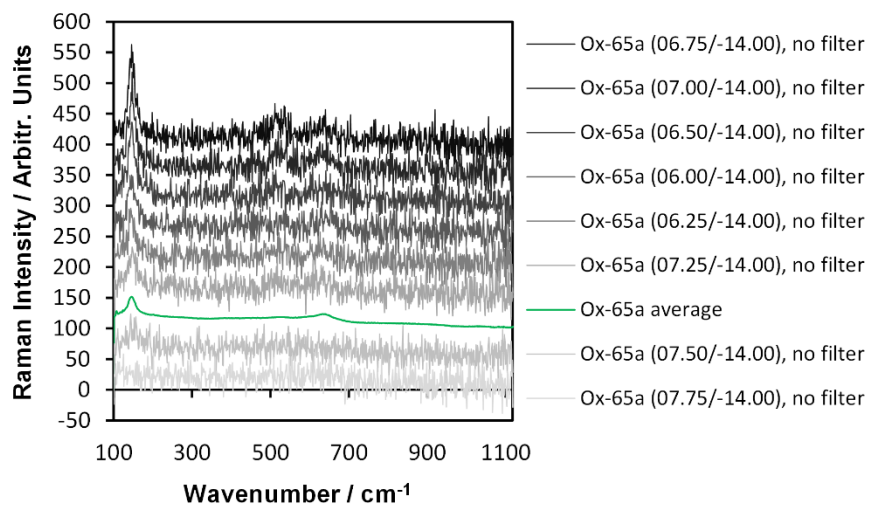


Fig. 25: Raman spectra of a Nb doped TiO_2 (Ox-65) thin film after cosmic ray removal and subtraction of the substrate spectrum. The gray spectra are from several positions measured for one second. The numbers in brackets are the position in μm from the center of the Raman map. The green spectrum is the average spectrum of the whole map.

A noise filter algorithm is implemented into Wire 4.0 software using principal component analysis (PCA). Principal component analysis describes most of the variance in a dataset by a linear combination of a certain amount of correlated parameters. Thereby, the data are transformed to a new coordinate system.¹⁰⁸ In literature, this method is successfully used in the study of superclusters of galaxies. In the noise filter program, the PCAs are ordered by their Eigenvalues and, thus, by the amount of variance covered within the projection of the data. The

idea of using PCA as a noise filter is that, in general, the first few components cover most of the Raman information and the highest components cover more noise than information.

Fig. 26 shows spectra of three positions already shown in Fig. 25 without noise filter (gray), with a noise filter that deleted all components after the first 100 components “c100” (green), and with noise filter keeping only 15 components “c15” (red). The unfiltered signal is extremely noisy, the c100 spectra show visible peaks, the c15 spectra are lacking important spectral information in the two crystalline spectra.

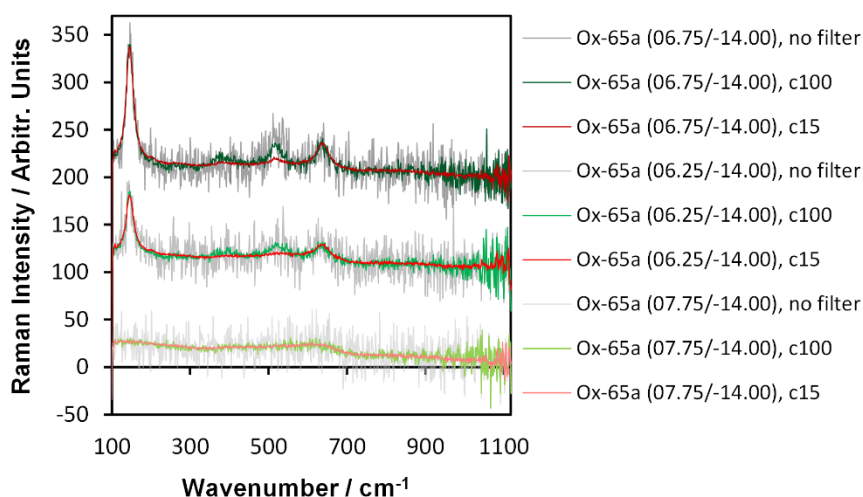


Fig. 26: Three spectra of Fig. 25 without noise filter (gray), with a noise filter that deleted all components after the first 100 components “c100” (green), with noise filter keeping only 15 components “c15” (red).

A screenshot of the Renishaw noise filter program is shown in Fig. 166 in the appendices. The top left window shows the correlation function, the top right figure is the map and the amount of signal (low = green, high = red) that is affected by the PCA component (here, component 100 is shown). The lower window shows the residual signal (at a chosen measurement point in the displayed map) that remains when all higher components are deleted. As one can see in the residual spectrum, artefacts at the peak position of the Eg(1) peak at 146 cm^{-1} are visible.

A correlation function that displays more components is shown in Fig. 167 in the appendices. The function becomes stationary between 100 and 200 components. Thus keeping ca. the first 100 components is a reasonable amount for optimum noise filtering with minimal corruption of spectral information.

2.2.2 Raman maps

The theoretical limit for spatial resolution d_{lim} of the Raman laser that is focused through an optical lens can be quantified by the Rayleigh criterion for an airy disc of light with

$$d_{lim} = 0.61 \cdot \frac{\lambda}{NA}, \quad (41)$$

where λ is the wavelength of the laser, and NA is the numerical aperture of the microscope objective. For a 633 nm laser with a $0.90/100x$ objective this results in a spatial resolution limit of $0.4 \mu\text{m}$. Several sources wrongly use the equation $d'_{lim} = 1.22 \lambda / NA$, which describes the distance between the first two minima of the airy function and not the theoretical diffraction limit.¹⁰⁹ Yet, the “wrong” equation might be suitable for real experiments. The laser spot is not a perfectly airy disc and the samples to be analyzed do scatter the light. Thus, a real laser spot can be larger than the theoretical limit by roughly a factor of *two*.

In order to scan sharp images, one has to oversample the scan. Adar et al. demonstrated that oversampling enhances the spatial resolution of Raman maps. They scanned polystyrene microspheres with diameters of around $5 \mu\text{m}$ and $8 \mu\text{m}$ dispersed on silicon, with a 532 nm laser passing a $100x$ objective with a power of 10 mW . They gained sharp images when the distance between two adjacent measurement points is $0.1 \mu\text{m}$.¹¹⁰

We chose a distance of $0.25 \mu\text{m}$ for our scans using the 633 nm laser, which we estimate to result in an oversampling factor of 3. Which is a compromise between the resulting sharpness and the resulting area ($30 \mu\text{m} \times 30 \mu\text{m}^2$) that can be measured during an 8 h session on the other hand. The resulting maps have a resolution of around $0.6 \mu\text{m}$.

Fig. 27 shows a map that was created for an intensity around 270 cm^{-1} using the signal-to-baseline area in the range from 260 cm^{-1} to 280 cm^{-1} after a noise filter with 150 components was applied. The map shows horizontal wave-like structures parallel to the path of the laser beam with alternating strong and weak intensities. The distance between the maxima is around $10 \mu\text{m}$. It is improbable that these structures are caused by fluctuation of the sample thickness, because these structures occur only perpendicular to the measurement direction. This suggests that this is an artefact caused by the positioning of the sample stage which might affect the laser focus.

Furthermore, several spots with a size of circa $1 \mu\text{m}$ show much higher intensity than the rest of the map. Such spots are also found in AFM and look like burst bubbles (see the AFM images of a glass substrate in Fig. 185 in the appendices).

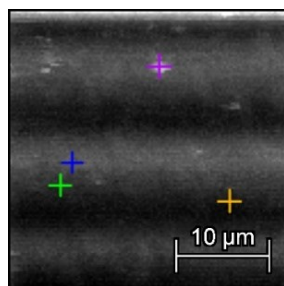


Fig. 27: Map of the Raman intensity from 235 cm^{-1} to 255 cm^{-1} of a B270 glass substrate

Four positions with varying intensities were chosen on the map in Fig. 27 and for each position four neighboring spectra were averaged and are shown in Fig. 28 together with the average spectrum of the whole map in red (for clarity in the figure, a stronger noise filter (c10) was applied).

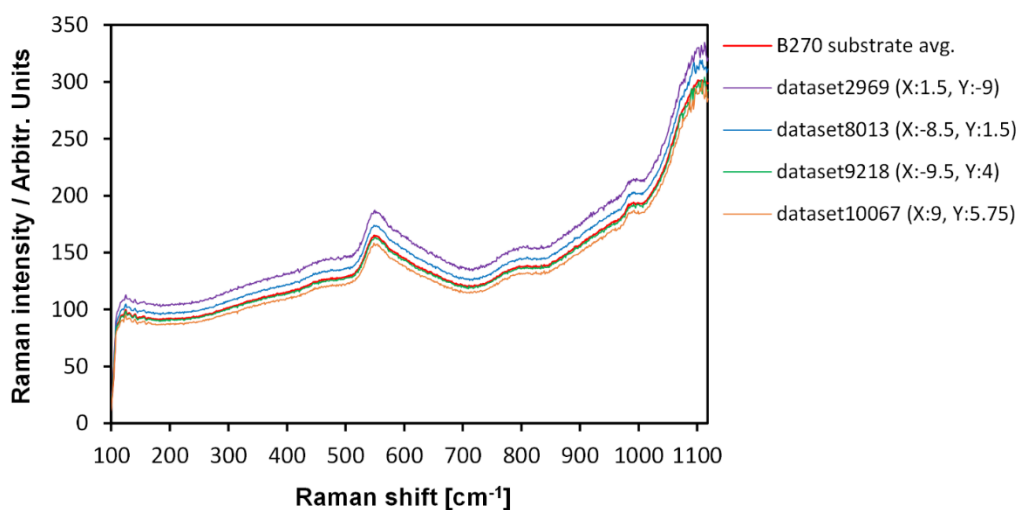


Fig. 28: Spectra of a B270 glass substrate at four different positions marked on the map in Fig. 27. The coordinates in brackets are in μm in relation to the center of the map.

The colors of the spectra in Fig. 28 correspond to the marked positions in Fig. 27. The coordinates in brackets in the legend are values in μm in relation to the center of the map. The trend of the intensities from 235 cm^{-1} to 255 cm^{-1} in Fig. 27 is visible for the four spectra over the whole range of measurement.

A drift in z-direction (height) of the substrate holder of several μm occurs during the measurements of the Raman maps. In order to compensate for the drift and to have the laser in focus during the eight hours of measurements, we programmed a focus track automation that corrects the laser focus after each 500 measurements.

Intensities of a map that was measured using using the focus tracks are presented in Fig. 29. It shows normalized maps of (a) I_{270} , (b) focus track values, (c) I_{1000} , and (d) I_{270}/I_{1000} . The I_{270} map displays the intensities in the range of $270\text{ cm}^{-1} \pm 10\text{ cm}^{-1}$ (i.e. the area between the

Raman signal and the wavenumber axis from 260 cm^{-1} to 280 cm^{-1}) for each measurement point. The I_{1000} map displays the intensities in the range of $1000\text{ cm}^{-1} \pm 10\text{ cm}^{-1}$. The (d) I_{270}/I_{1000} map is explained below the figure.

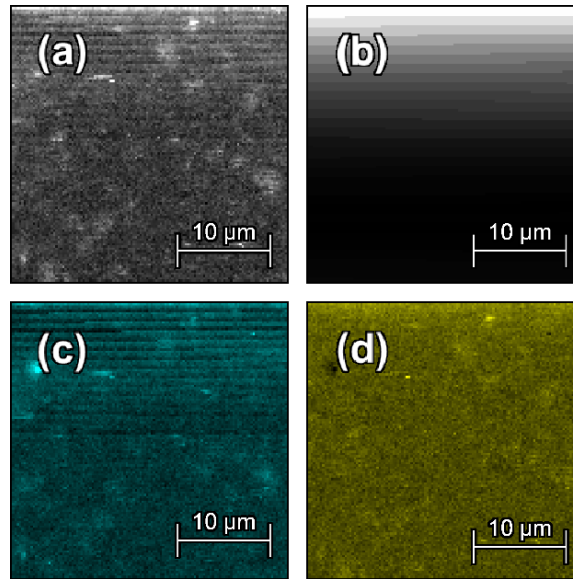


Fig. 29: Raman maps of a B270 glass substrate: (a) Raman intensity I_{270} (signal-to-axis $260\text{ cm}^{-1} - 280\text{ cm}^{-1}$), (b) focus track value, (c) Raman intensity I_{1000} (at $990\text{ cm}^{-1} - 1010\text{ cm}^{-1}$), (d) ratio map I_{270}/I_{1000} (a) vs. (c).

Using the focus track, more details are visible on the surface of the glass substrate (Fig. 29 (a) and (c)) as compared to Fig. 27. Yet, artefacts occur from the focus track: the focus track displayed in Fig. 29 (b) is clearly visible in (a) and (c). A map that is almost free of such artefacts is shown in (d) which is a combination of (a) and (c). It is a normalized ratio map that displays the intensity ratios of map (a) and (c) for each measurement point. In the following, we will name such *ratio maps* as e.g. “ I_{270}/I_{1000} ”.

2.2.2.1 Raman phonon maps

We did the same procedure for all TiO_2 thin film maps, which is presented in Fig. 30 exemplarily for a $\text{Ti}_{9.84}\text{O}_{2.25}\text{Nb}_{0.16}$ film that was prepared by reactive e-beam evaporation and post-heated at $420\text{ }^\circ\text{C}$. Fig. 30 (a) shows an I_{149} map (normalized map of the signal-to-axis values in the range $149\text{ cm}^{-1} \pm 10\text{ cm}^{-1}$), (b) I_{270} , (c) focus track values ($-0.11\text{ }\mu\text{m}$ to $6.14\text{ }\mu\text{m}$), (d) a I_{149}/I_{270} ratio map. 149 cm^{-1} is the center of the $\text{Eg}(1)$ peak of that sample in the average spectrum of this map.

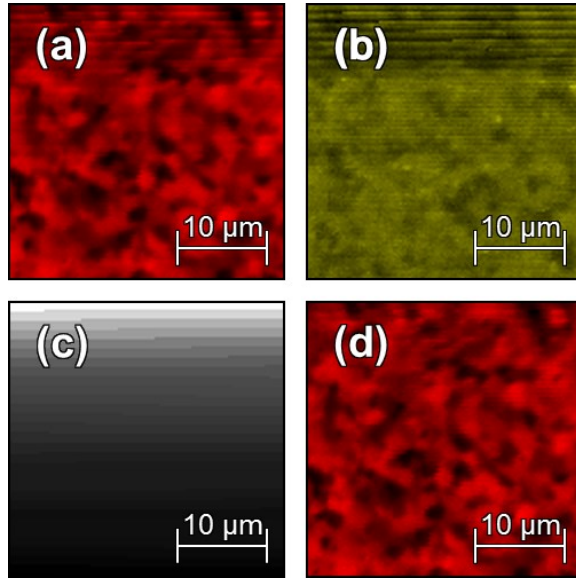


Fig. 30: Normalized maps of $\text{Ti}_{9.84}\text{O}_{2.25}\text{Nb}_{0.16}$ ($420\text{ }^\circ\text{C}$), (a) I_{149} (signal-to-axis $139\text{ }cm^{-1} - 159\text{ }cm^{-1}$), (b) I_{270} (signal-to-axis $260\text{ }cm^{-1} - 280\text{ }cm^{-1}$), (c) focus track value ($-0.11\text{ }\mu\text{m}$ to $6.14\text{ }\mu\text{m}$), (d) ratio map I_{149}/I_{270} ((a) vs. (b)).

We chose the intensity at $270\text{ }cm^{-1} \pm 10\text{ }cm^{-1}$ as the denominator of the *ratio maps*, because here, the superposition with first-order anatase, brookite or rutile Raman peaks is minimal. It is in between the strongest Raman peak (Eg(1) at $143\text{ }cm^{-1}$) and the other first-order Raman peak of anatase (see), which is the main crystalline phase in the analyzed films. The anatase phase background model spectra developed in this work (see chapter 3.1.4.4) are most intense above $300\text{ }cm^{-1}$ in the analyzed Raman spectra of undoped TiO_2 and above $280\text{ }cm^{-1}$ in the Nb doped films. The range includes signals from a rutile (multi-phonon) band and of brookite first-order Raman peaks, but it is a minimum between two brookite peaks (A1g around $247\text{ }cm^{-1}$ and the less intense B3g peak around $287\text{ }cm^{-1}$). See the rutile and brookite Raman spectra in Fig. 76 in chapter 5.2.3 and the valley around $270\text{ }cm^{-1}$ in the multi-phase Raman spectra in Fig. 86 in chapter 6.1.1.2).

For each analyzed sample, we produced such *ratio maps* for the anatase phonons Eg(1) around $143\text{ }cm^{-1}$, B1g around $399\text{ }cm^{-1}$, and the A1g/B1g-doublet around $517\text{ }cm^{-1}$ and name these *ratio maps* as “*phonon maps*”. The *phonon maps* are normalized to the color scale from black (lowest intensity) to full color (highest intensity), thus black does not stand for zero intensity.

Fig. 31 shows the *phonon maps* of (a) Eg(1) (red), (b) AB1g (blue), (c) B1g (green) of a Nb-doped TiO_2 film that was deposited by plasma emission controlled rf-magnetron sputtering with a 68% oxidized Ti target that was post-heated at $475\text{ }^\circ\text{C}$.

Beforehand, the average peak positions had been determined using the Raman fitting models for TiO₂ thin films on a luminescent substrate as described in 3.1. We then superimposed the three *phonon maps* by placing them on top of each other as layers with the *modus lighten only* in the free graphics software *Gimp*. By doing so, the color information adds up in the *combined phonon map* (d).

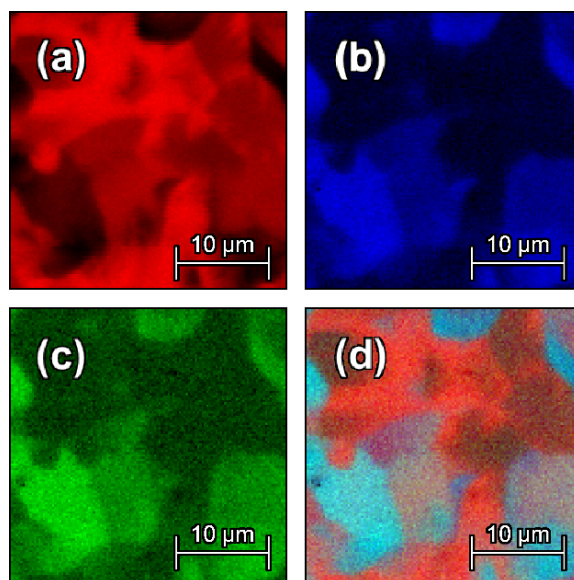


Fig. 31: Phonon maps of maps of a Nb-doped TiO₂ thin film coated onto B270 glass by plasma emission controlled rf-magnetron sputtering with a 68% oxidized Ti target: (a) Eg(1) (red), (b) AB1g (blue), (c) B1g (green), (d) *combined phonon map*.

The colors of the individual three *phonon maps* are red, green, and blue, because in an additive RGB color space any chromaticity can be produced by these three primary colors. This allows us to interpret the intensity of the individual phonons simultaneously in one single image. The RGB space provides us color coding to read the information of the individual parts within the *combined phonon maps* as is listed in Table 4 (‘+’/’-’ is strongest/weakest intensity):

Table 4: Interpretation of colors in the *combined phonon maps* or *TiO₂ phase maps*

color	Eg(1)* <i>anatase**</i>	B1g* <i>amorphous/brookite**</i>	AB1g* <i>rutile**</i>
black	-	-	-
red	+	-	-
green	-	+	-
blue	-	-	+
yellow	+	+	-
magenta	+	-	+

cyan	-	+	+
white	+	+	+

*) Raman phonon maps; **) Raman TiO₂ phase maps

2.2.2.2 Raman TiO₂ phase maps

We produced Raman *TiO₂ phase maps* that illustrate the distribution of TiO₂ phase composition on the samples. The procedure will be explained exemplarily with the Raman maps of a reactive e-beam coated TiO₂ thin film (on B270 glass). In order to prepare the anatase phase maps, beforehand *combined phonon maps* were made for anatase as described in chapter 2.2.2.1. Fig. 32 shows the anatase *phonon maps* of (a) Eg(1), (b) B1g, (c) AB1g, and (d) the *combined phonon map*, which is an overlay figure of (a), (b), and (c).

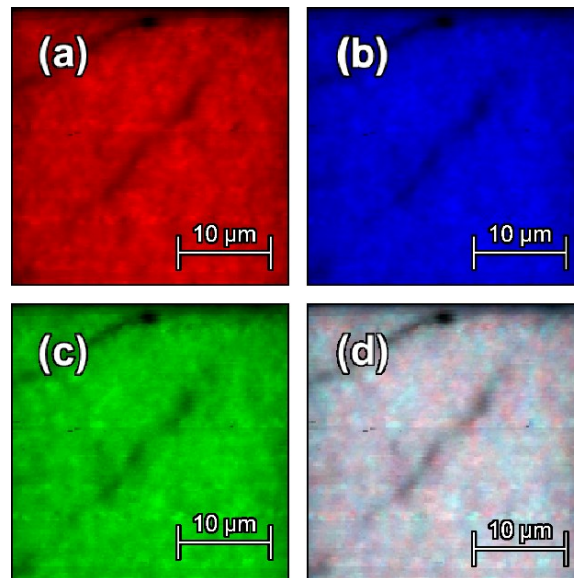


Fig. 32: Phonon maps of a TiO₂ thin film coated onto fused silica by reactive e-beam evaporation post-heated at 750 °C: (a) Eg(1) (red), (b) AB1g (blue), (c) B1g (green), (d) combined phonon map.

We then converted the *combined phonon map* of anatase (Fig. 32 (d)) into grayscale and colored it to red (displayed in Fig. 33 (a)). Fig. 33 (b) shows the corresponding brookite map (green) and (c) shows the rutile map (blue) of the same sample. The brookite (A1g) map was created as a I_{247}/I_{270} *ratio map* which depicts the normalized *ratio map* of the intensity maps I_{247} (signal-to-axis area from 237 cm^{-1} to 257 cm^{-1}) and I_{270} (signal-to-axis area from 260 cm^{-1} to 280 cm^{-1}) for each measurement point. The rutile (Eg) maps are I_{447}/I_{467} *ratio maps*. Fig. 33 (d) shows the *TiO₂ phase map*, which is an overlay image of (a), (b), and (c). Like the *combined phonon maps*, the *TiO₂ phase map* can be interpreted according to Table 4.

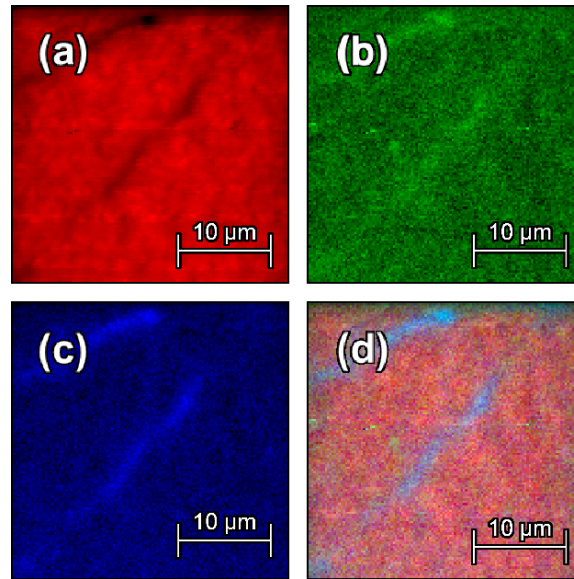


Fig. 33: TiO_2 phase maps of a TiO_2 thin film coated onto fused silica by reactive e-beam evaporation post-heated at $750\text{ }^\circ\text{C}$: (a) anatase, (b) brookite, (c) rutile, (d) combined TiO_2 phase map.

The distribution of the main phase, anatase, is represented by three phonons (see Fig. 32), while brookite is solely represented by the $A1g$ peak at 247 cm^{-1} and rutile is represented solely by the $E1g$ peak at 447 cm^{-1} . This causes inaccuracy, but the other brookite or rutile first-order Raman peaks are too heavily superimposed by signals from anatase. Furthermore, the rutile multi-phonon peak at 245 cm^{-1} might be misinterpreted as brookite. The anatase spectra in the dark areas of Fig. 32 (d) or Fig. 33 (a) are weaker than in the colored areas. In the same areas, the brookite (Fig. 33 (b)) and rutile (Fig. 33 (c)) maps show the highest intensities.

In several maps post-heated at lower temperatures, rutile could not be detected in the single specially resolved spectra, and brookite is homogeneously distributed. There, we found regions with higher amorphous content in the anatase Raman spectra, and we thus created maps for anatase as well as amorphous content. The amorphous content is depicted by I_{270}/I_{1000} maps. The combined maps than are overlay maps of anatase and amorphous TiO_2 maps (examples can be seen in Fig. 139 in chapter 7.2.1).

The amorphous maps leave a lot of room for misinterpretation, because the range of 1000 cm^{-1} depends strongly on the substrate's luminescence and high intensity in the range of 270 cm^{-1} area can also be caused by broadened brookite spectra.

2.2.3 X-ray diffraction

In addition to Raman spectroscopy, we investigated the crystal structure with X-ray diffraction (XRD) using a *Panalytical X'Pert PRO* powder diffractometer in the *Nanopartikel-Prozesstechnik Group (nppt)* at the University of Duisburg-Essen. We used copper K_α radiation and operated the diffractometer with 40 mA at 40 kV . We equipped the *PW3011/20* detector

with a 0.18° parallel plate collimator. We placed a 10 mm mask 122 mm and a $\frac{1}{4}^\circ$ divergence slit 140 mm in front of the sample within a diffracted beam path of 240 mm . Prior to the measurements, we calibrated height and *omega* offsets for each sample. We performed the scan for *four times* in grazing incidence ($2\theta = 7^\circ$) as well as in θ - θ geometry at diffraction angles from 23° to 87° in steps of 0.05° with a step-time of 4 s .

We measured *LaB₆ 660 a* reference powder¹¹¹ using the same experimental parameters (in a range from $2\theta = 10^\circ$ to 100°). We made these reference measurements in order to calibrate the fitting of the peak parameters for the evaluation of the measured TiO_2 diffractograms. We used the reference measurements to correct the peak positions, peak widths (left and right), peak height with polynomials, as described in the following.

We demonstrate the evaluation of the *LaB₆* reference measurements for the grazing incidence ($2\theta = 7^\circ$) measurements exemplarily. We performed the same procedure for the measurements in θ - θ geometry, resulting in different polynomial correction curves (which will not be presented).

Fig. 34 shows the measured diffractogram (black), a fit to the measured signal (dashed red), background signals (blue), literature intensities and peak positions¹¹¹ (green), and the residual signal between the fit and the measured signal (gray). We fitted the peaks with asymmetric Lorentzian peaks. The principles of the fitting routine are described in chapter 3.3.

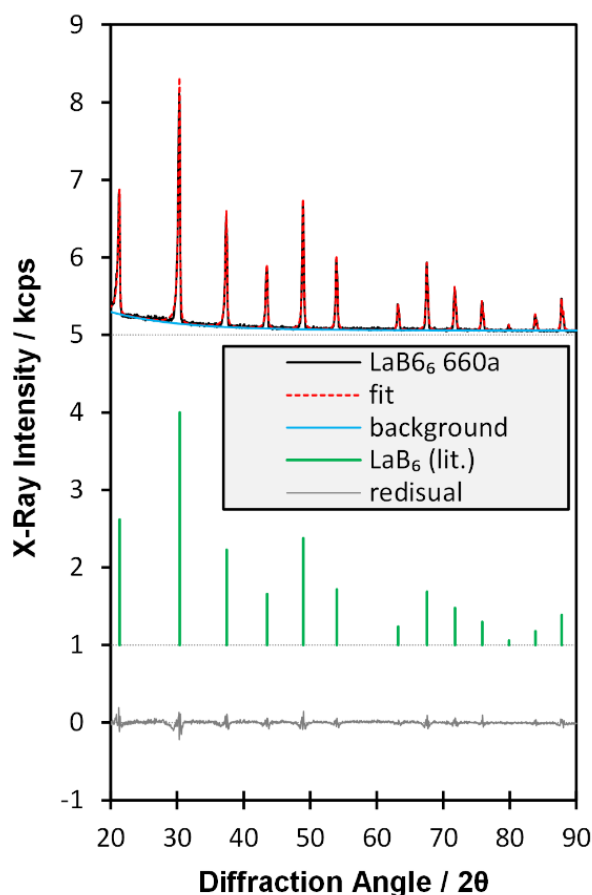


Fig. 34: Measured LaB₆ 660 a diffractogram (black), fit to the measured signal (dashed red), instrument background signals (light blue), LaB₆ 660 a literature intensities and peak positions¹¹¹ (vertical green lines), and the residual signal between the fit and the measured signal (gray).

Fig. 35 shows the range around chosen LaB₆ reflexes: (100) (left), (110) (mid), and (320) (right). The main XRD peaks of anatase (101) and rutile (110) TiO₂ powder diffractograms are between the LaB₆ (100) and (110) peak. As one can see in the figure, the reflexes are asymmetrically broadened. The (100) peak is strongly broadened to the left of the peak center. The positions of the two peaks at the lower diffraction angles are shifted to the left (smaller diffraction angles), while the K α_1 segment of the (320) peak is close to the literature position. In the measured and the fitted diffractograms, the splitting of the K α line into K α_1 and K α_2 radiation is clearly visible for the (320) peak, but not for the two other peaks at smaller diffraction angles.

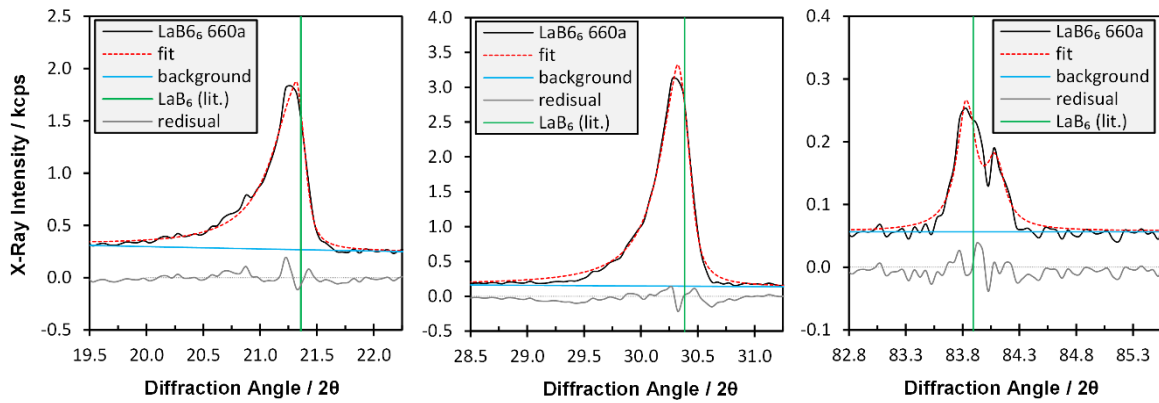


Fig. 35: Details view on ranges of the diffractograms shown in Fig. 34 around the (100) (left), (110) (mid), and (320) reflexes. Colors are as in Fig. 34: measured LaB₆ 660 a diffractogram (black), a fit to the measured signal (dashed red), an instrument background signals (light blue), LaB₆ 660 a literature peak positions¹¹¹ (vertical green lines), and the residual signal between the fit and the measured signal (gray).

Fig. 36 displays the deviations of the fitted peak parameters as compared to standard values. The left graph shows the half-width at half maximum on the left side of the peak center (*h.w.h.m.l*) (gray squares), the half-width at half maximum on the right side of the peak center (*h.w.h.m.r*) (black circles), and the shift of the peak positions. The graph on the right side shows the relative peak height (black triangles) and relative intensity (gray triangles) of the peaks, both divided by the standard values. Therefore, the intensity (or height) of the most intense quotient of the most intense LaB₆ peak, (110), is normalized to one before we formed the quotients. The fitted intensities result from the peak parameters *h.w.h.m.l*, *h.w.h.m.r*, and peak height.

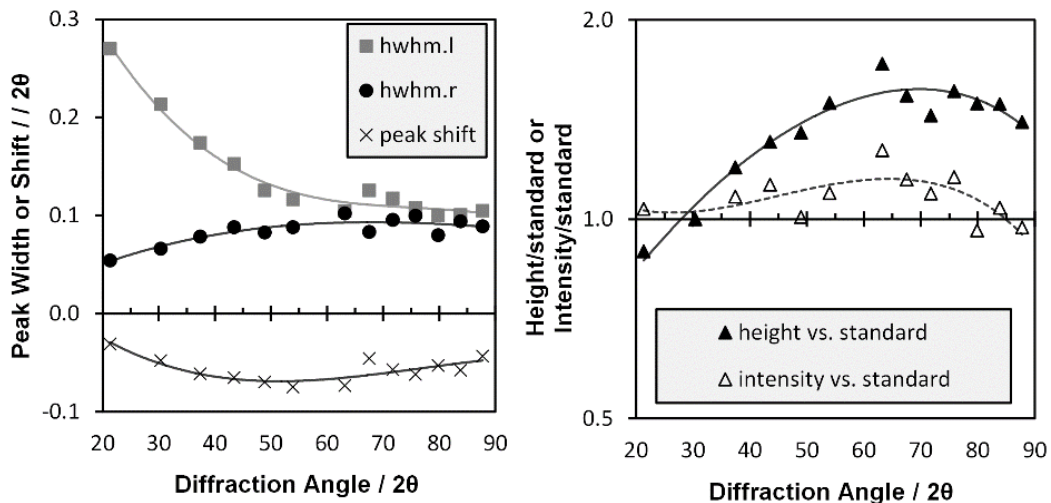


Fig. 36: Left: half-width at half maximum on the left side of the peak center (*h.w.h.m.l*) (gray squares), half-width at half maximum on the right side of the peak center (*h.w.h.m.r*) (black circles), and the shift of the peak positions; right: relative peak height (black triangles) and relative peak intensity (gray triangles) as compared to standard values. Trendlines are added as third-degree polynomials.

Third degree polynomials are added to the figure as trendlines. We use these polynomials for the correction in the fitting routines of the peak parameters in chapter 6.

2.2.4 Surface topology

We produced topographic images of the surfaces and of prepared film edges with the scanning electron microscopes (SEM) *Jeol JSM-7500F* and *ESEM Quanta 400 FEG*. We analyzed the particle sizes using the free software *imagej* or by manually measuring the particles on SEM images at varying magnifications ranging from 4000 to 1000000.

Atomic force microscopy (AFM) images were made by Dr.-Ing. Steffen Franzka using a *Bruker Dimension Icon* at the Interdisciplinary Center for Analytics on the Nanoscale (ICAN). ICAN is located in the NanoEnergieTechnikZentrum (NETZ), which is the central research building of the Center for Nanointegration Duisburg-Essen (CENIDE). It is located at the campus of the University of Duisburg-Essen.

2.2.5 Chemical Composition

We quantified chemical composition by energy dispersive X-ray spectroscopy (EDX), by Rutherford backscattering spectrometry (RBS), and by X-ray photoelectron spectroscopy (XPS).

We made the EDX measurements with a *Bruker Quantax 200* equipped with a 30 mm² SSD crystal, which is attached to the *Jeol JSM-7500F* SEM in the *nppt* group. RBS measurements were performed by Dr. rer. Nat. Hans-Werner Becker using a *Dynamitron Tandem* accelerator in the *Rubion* group at the *Ruhr University Bochum*. Ulrich Hageman carried out the XPS measurements at ICAN using a *Phi 5000 Versaprobe II*.

2.2.6 Film thickness, mass, and mass density

We determined film thicknesses by profilometry, optical ultraviolet/visual/near-infrared (UV/VIS/NIR) spectrometry, ellipsometry, SEM, RBS, or XPS. We used a *Veeco Dektak 6M* profilometer to measure the thickness at prepared film edges at ICAN.

We obtained film thicknesses from UV/VIS/NIR spectra by dielectric simulation of measured optical transmission and reflection spectra using the software *SCOUT*. Dipl.-Phys.Ing. Martin Jerman measured the optical spectra with a *Perkin-Elmer LAMBDA-9* Spectrometer at the optical workshop of the university of Duisburg-Essen. Measurement took place in 1 nm steps from 200 nm – 2500 nm (transmittance) and 5 nm steps from 200 nm – 2000 nm (reflectance). The estimated error of the thicknesses is 3 nm.

Dipl.-Phys.Ing. Klaus Pärshke performed and evaluated the ellipsometry measurements taken with a *HORIBA Jobin Yvon MM-16*. We took SEM images at film edges, which we prepared by breaking the samples in liquid nitrogen.

We determined film masses by weighing the substrates for *five* times before and after the deposition with a *Sartorius C50* mass comparator. The estimated error is $30 \mu\text{g}$. Film densities result from the quotient of the measured masses and thicknesses. The error of film density is around 0.2 g/cm^3 .

2.2.7 Electrical properties

We determined electrical properties, such as refractive index, electrical conductivity or band gap from the UV/VIS/NIR spectra using the software *SCOUT* or by Tauc plots (see chapter 6.1.2.5).

We performed DC conductivity measurements with a *Keithley 4200-SCS* four-point-probe at the department Nanostrukturtechnik (NST) at the University of Duisburg-Essen. Four-point measurements separate the current and the voltage contacts, which avoids additional probe resistances in comparison to a two-point measurement.

The probe is equipped with tungsten carbide probe tips. We took each measurement for 20 times in 2 s intervals at three different positions in the center of each sample. We measured with a current of 10^{-7} A and set the compliance to a voltage 150 V. Thus, both, current and voltage are limited. As a result, values for the films with good conductance are measured at 10^{-7} A and the values for the barely conductive films are measured at 150 V.

3 Concepts and models for the decomposition of Raman spectra and X-ray diffractograms

In this chapter, we introduce concepts and models for the decomposition of Raman spectra and X-ray diffractograms into different components. In chapter 3.1 we present and discuss the concepts of the Raman models that we developed in this work. The chapter is written in a didactical way so that the concepts of building such models should be easily applicable to other materials.

The modeled and measured spectra in chapter 3.1 are exemplarily shown for Raman spectra taken with a *633 nm* laser. The same procedures were also performed with a *532 nm* analogously.

In chapter 3.2 we define the parameters of the models for the simulation of Raman spectra, and in chapter 3.3 we introduce models that we developed for the simulation of X-ray diffractograms and define the parameters used.

3.1 Decomposition of Raman spectra of mixed-phase TiO₂ thin films on Si and silicate substrates

[This chapter is part of a publication in the Journal of Raman Spectroscopy, Volume 49, Issue 7, 1217-1229 (2018).]¹ Copyright © 2018 John Wiley & Sons, Ltd.

3.1.1 Summary

We present a method to fit Raman spectra of TiO₂ thin films on silicon wafers, fused silica, and crown glass with adjustable model spectra of the different components of the substrate and the thin film. With reasonable restrictions of the fitting parameters, the method developed in this work allows a simultaneous fit to the measured spectra. The TiO₂ thin film spectrum is split into one spectrum for the amorphous phase and spectra for each crystalline phase (anatase, rutile, and brookite) that are divided into first-order scattering and a phase background (including second-order scattering). Moreover, if the substrate is luminescent, the substrate spectrum is split into luminescence and Raman spectra. All decisions on parameters are made by the fitting procedure within a simultaneous fit of a series of spectral models to the observed Raman spectrum. The main strategies for preparing such models are pointed out in a way that they should be applicable to other materials.

TiO₂ is a promising and flexible material for photocatalytic applications with rapidly growing interest in mixed-phase TiO₂ as nanostructured material or thin film. For the analysis of such films it is important to differentiate the signals of the various phases and to distinguish

between signals from the substrate and the film. This provides a means to improve the quantitative evaluation of Raman spectra.

3.1.2 Introduction

Mixed-phase TiO₂ is a very flexible group of materials for various photocatalytic applications.^{5,17,18} TiO₂ is a widely used and the most studied photocatalyst – mainly as thin films or nanomaterials – because it is highly efficient, chemically and biologically stable, and non-toxic at low cost.⁴ The polymorphs of TiO₂ that occur at atmospheric pressure at room temperature are anatase, rutile, and brookite. The photocatalytic performance of anatase and rutile has been extensively studied.⁵ The structure of brookite is more complex⁶ and brookite was seldom studied experimentally until 2012 because it is difficult to synthesize.^{5,7-10} Yet, interest has rapidly grown in recent years because of its excellent photocatalytic performance.^{4,11-16} The growing interest in mixed-phase TiO₂ necessitates to quantify the relative amount of the phases and to analyze each phase independently. Raman spectroscopy has high potential for such analysis because it is highly sensitive and non-invasive. Nevertheless, two issues have to be met: The substrate spectrum has to be separated from the thin film spectrum, and the spectra of the phases have to be separated from each other.

Analysis in literature of thin film spectra or materials in luminescent media is often limited because large parts of the spectra to be studied are overshadowed by the background signals. Several computational and experimental approaches like shifted excitation Raman difference spectroscopy are used to remove such noise.²²⁻²⁴ An overview and comparison of these approaches can be found in Cordero et al.²⁵ The Raman activity of substrates is an issue in thin film Raman spectroscopy.^{20,21} Often, arbitrary linear ‘backgrounds’ are subtracted before Raman peaks are fitted, which is inappropriate for cases in which the intensity of the Raman ‘background’ characteristic is in the same order of magnitude or higher than the Raman spectra of the analyte. That is why the evaluation of thin film Raman measurements is often very restricted, and they are discussed mainly qualitatively and often only the most intense peaks are considered. Common evaluation software programs of Raman spectrometers provide the possibility to subtract backgrounds by means of a polynomial function, ignoring the physics behind the spectra.²⁶ For thin films, this approach leads to poor results because substrate signals are inadequately taken into account. In this work, we strive to demonstrate that – with the right choice of simplifications – a separation of the substrates’ and thin films’ spectra can be achieved to a feasible degree, allowing a more elaborate evaluation of the film spectra. Apart from the

distinction between the substrate and the thin film spectrum, quantitative phase separation within the thin film spectrum is necessary in order to analyze each phase independently.

Quantitative evaluation of Raman spectra is known since more than half a century. Yet, Raman spectroscopy is still associated mainly with qualitative rather than quantitative analysis. Nevertheless, Pelletier gives an elaborate introduction to quantitative analysis using Raman spectroscopy. He recognizes growing interest in this topic, caused by improved instrumentation, and lists over 200 published examples, already in 2003. The basis for a quantitative evaluation of Raman spectra is a proportional relationship between Raman scattering intensity and the concentration of the measured material. The extremely low cross-section of Raman scattering (one Raman photon per 10^8 excitation photons) leads to negligible interference between Raman photons allowing to treat Raman spectra with the principle of linear superposition. Several approaches for the quantification of analyte concentration with spectral properties of Raman spectra are described by Pelletier, including the comparison of band heights or band areas, principal component analysis, partial least squares, change in band position, principal components regression, and cross-correlation.¹⁹

Clegg et al., Beuvier et al., and Castrejón-Sánchez et al. demonstrated the quantification of phase content in TiO₂ using Raman spectroscopy in 2001, 2009, and 2014, respectively. The first two compared their results to quantification using X-ray diffractograms, and the latter constructed calibration curves using mixtures of TiO₂ powders with varying anatase/rutile weight ratios.^{112–114} In these studies, the intensity ratios of only single peaks of certain phases were compared to each other. This approach works well for polycrystalline TiO₂ with arbitrarily oriented crystals. Though, the relative intensities of the peaks of a certain phase can differ for oriented or textured samples because of geometric properties of the experimental setup like the orientation of the sample towards the laser or because of structural properties. Furthermore, in the analysis of TiO₂ Raman spectra, second-order scattering of anatase is considered only seldom and solely in qualitative analysis, and a decomposition of measured spectra into amorphous and crystalline content is considered impossible.^{27–30} In our approach, we fit model spectra for the different TiO₂ phases, including the phase backgrounds and amorphous content, as well as model spectra for luminescent and non-luminescent substrates to the measured spectra.

3.1.3 Concept of the Raman fitting model

Spectra from Raman measurements are decomposed into several components. The contributions of the components are represented by model spectra and include Raman scattering

and luminescence. The models were built by analyzing evaporated and sputtered TiO₂ thin films on the substrates silicon wafers, fused silica, and crown glass (B270).

First, we decompose the spectra into their two main components substrate and film. The spectrum of the film is, furthermore, split into an amorphous content and the Raman active modes of the various crystal phases. An example spectrum of a weakly crystallized TiO₂:Nb anatase thin film on a B270 glass substrate is shown in Fig. 37. The light blue line represents the modeled substrate spectrum and the dark red line represents the modeled TiO₂ thin film. The thin film is further decomposed into an amorphous (gray) and an anatase (green) model spectrum. The amorphous, anatase, and substrate spectra sum up to the fit (dashed red line). The light gray residual spectrum is the difference of the measured spectrum and the fit.

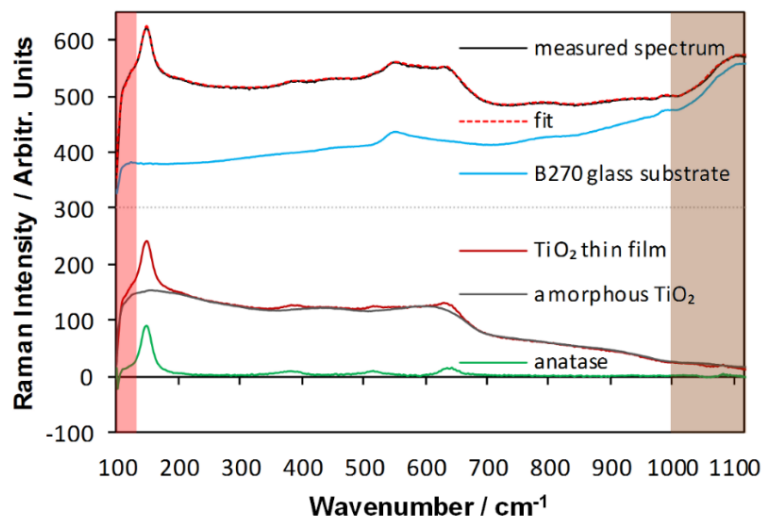


Fig. 37: Measured Raman spectrum (black) of a TiO₂ thin film on a B270 glass substrate and its decomposition into B270 glass substrate (light blue) and thin film (dark red). The thin film is furthermore split into an amorphous phase (dark gray) and a crystalline anatase content (green). The measured spectrum, fit (red dotted line), and substrate spectra are shifted by 300 units on the intensity axis. The excluded range is light red and the low priority range is light brown.

However, this decomposition is too coarse to describe a spectrum adequately. In all circumstances, individual sources of signals in the Raman spectrum from the film and the substrate must be considered: the Raman active modes of each crystalline phase include first-order scattering as well as a background containing second-order scattering and disorder-induced scattering. Furthermore, if the substrate is luminescent, the spectrum of the substrate has to be decomposed into a luminescence background and Raman active modes.

All fitting procedures are performed using a spreadsheet (*Microsoft Excel*), thus access to special Raman evaluation software is not necessary. We need adjustable model spectra for each component to model a total spectrum. The sum of these models is the model we fit against the measured spectrum by the least-squares method. The difference between the fit and the

measured spectrum is squared for each data point and the sum of these values is reduced by the generalized reduced gradient algorithm of *solver*, which is implemented into *Microsoft Excel*. The described decomposition is made possible by processing all fitting procedures simultaneously. This makes our modeling routine more powerful as compared to commercial step-by-step Raman evaluation software, which does not provide the possibility to discriminate between luminescence and Raman spectra of a substrate as well as thin film spectra within one measured spectrum – above all for mixed-phase films.

This algorithm provides locally optimal solutions for non-convex problems.¹¹⁵ Thus, reasonable start values and constraints (upper and lower limits) have to be assigned to the variables. The main issue for building the models for the individual components is to prevent them to interfere with each other. The models and their appropriate fitting parameters are described below – firstly, for the TiO₂ thin films and, secondly, for the different kind of substrates. It must be pointed out that the model allows to simulate a certain phase's relative content of counts within a measured spectrum, but a quantification of the mass fraction necessitates calibration measurements.

3.1.4 Models for TiO₂ spectra

The models for TiO₂ spectra cover the amorphous phase and the crystalline phases, anatase, rutile, and brookite. Each crystalline phase is decomposed into first-order and phase-background spectra. Depending on the complexity of a spectrum, the relative intensity of a phase within the spectrum and the signal-to-noise ratio, different models with various degrees of simplifications are necessary. The models presented here were built for TiO₂ thin films but should be applicable to bulk material also.

3.1.4.1 Amorphous phase

A spectrum for the amorphous TiO₂ phase is added to the total spectrum with a fitting factor. For the model of the amorphous phase, spectra of amorphous undoped and doped TiO₂ thin films with 0 at.%, 8 at.% and, 16 at.% Nb content on B270 crown glass substrates were measured. These films were prepared by e-beam evaporation to avoid the implementation of crystal nuclei. The backsides of each sample were measured as reference and subtracted from the spectrum so that glass features were minimized in the resulting spectra. The spectra are shown in Fig. 38, normalized to a total intensity of 100000 counts. The character of the amorphous spectrum is not suitable to estimate the Nb content because the nature of the spectrum does not change significantly with the Nb content.

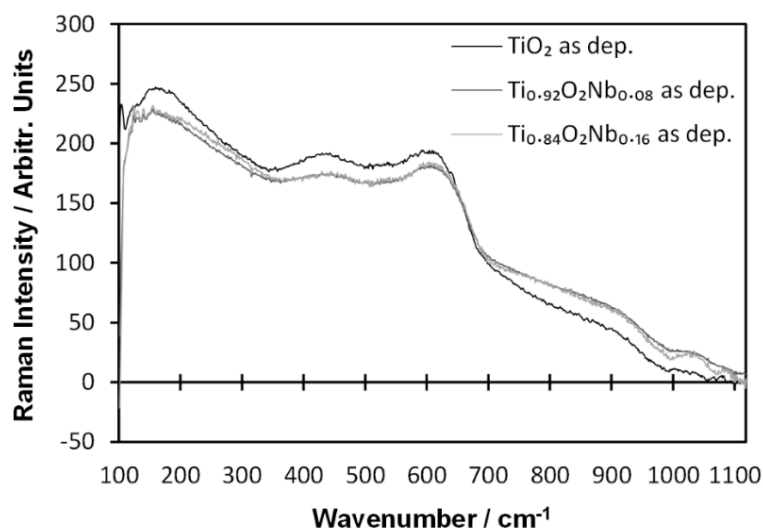


Fig. 38: Raman spectra of amorphous TiO_2 (black), $\text{Ti}_{0.92}\text{O}_2\text{Nb}_{0.08}$ (dark gray), and $\text{Ti}_{0.84}\text{O}_2\text{Nb}_{0.16}$ (light gray), normalized to 100000 counts after the subtraction of the substrate spectra from the measured spectra.

The amorphous phase of TiO_2 has broad bands, which makes fitting difficult. This is the reason why the quantification of amorphous contents in Raman spectra is considered impossible in literature.³⁰ Anyway, measuring over a wide range allows to differentiate the amorphous spectrum from other components in a TiO_2 Raman spectrum. The change of a plateau at low wavenumbers to a rather straight downwards slope around 700 cm^{-1} is the most prominent feature of the amorphous spectrum. In Fig. 37, one can see clearly that the spectra of the amorphous phase and the crystalline phase are distinct.

3.1.4.2 Crystalline phases

In our fitting routine, each crystalline phase is composed of the main *first-order* Raman scattering spectrum and a ‘*phase background*’. The main *first-order* Raman spectra models describe Lorentzian functions of optical first-order Raman scattering (from the center of the Brillouin zone with a phonon wave-vector = 0). The *phase background* models cover second-order scattering and all other additional spectral information of a certain phase that are not described by the *first-order* model. Defects or disorder caused by doping, grain or phase boundaries, or further lattice disorders disturb the translational symmetry, which causes a breakdown of selection rules. Additional modes specific to the dopant atoms and Raman inactive phonons (IR-active or silent ones) can be activated. Dispersion peaks appear if the crystallite size is smaller than the laser wavelength. Furthermore, acoustic phonons (coherent vibrations of adjacent atoms), overtones (twice the wavenumber of the fundamental), and anharmonic coupling of phonons to other phonons occur. Anharmonic coupling can occur by an optical phonon decaying symmetrically into two acoustic phonons with opposite momenta

at the same energy or by decaying asymmetrically into a longitudinal acoustic and a transverse optical phonon.^{78,79,116–121} Acoustic vibrations of anatase are most pronounced below 50 cm^{-1} and, thus, are not relevant to our model.¹²²

The intensity of the phase background spectrum is often considered as a degree of anharmonicity of the vibrations within a crystal caused by defects, in addition to shape width, and the position of first-order scattering peaks.^{28,29,61,73} Thus, thin films, nano-particles or nano-structured materials have strong phase background spectra. Rutile Raman spectra are generally even stronger in second-order scattering than in first-order scattering, which reflects the anharmonic vibrations of phonons in rutile.⁷³ Furthermore, second-order Raman scattering gets resonantly enhanced by interband transitions of a semiconductor.¹²³

Beside an amorphous content, our TiO₂ films consist of either (a) partly crystallized anatase, (b) anatase and rutile, or (c) anatase, rutile, and brookite. Thus, rutile and brookite never occur solely in our films, but only in smaller addition to anatase. They are therefore implemented into the fitting routine as simplified models.

In mixed-phase films, simplifications in the fitting routines become inevitable in order to avoid heavy interference in the modeling of overlapping peaks. Simplifications of first-order scattering and phase background models are described below. Simplifications for first-order scattering models are essential especially if the signal of a phase does not provide enough information for individual peak fitting. In such cases, we recommend different grades of simplifications: *light simplifications* for dominant phases, *strong simplifications* for minor phases, and *strict simplifications* for minor phases with high complexity or of which only traces are visible in the Raman spectrum. In our mixed-phase fitting routine, the intensity ratios of the phase background model spectra depend on the intensity ratios of the first-order scattering model spectra.

3.1.4.3 First-order scattering models

The first-order scattering peaks of Raman active modes are represented by asymmetric Lorentzian functions as described in equation (42):

$$I = \frac{A}{1 + \left(\frac{x-x_0}{\Delta x_l}\right)^2} \text{ for } x \leq x_0 \text{ and } I = \frac{A}{1 + \left(\frac{x-x_0}{\Delta x_r}\right)^2} \text{ for } x > x_0. \quad (42)$$

with intensity I , wavenumber x and the four fitting factors peak position x_0 on the wavenumber axis, peak amplitude A on the intensity axis, half-width on the left-side Δx_l and half-width on the right-side Δx_r , as shown in Fig. 39. In the fitting routine, minimum and

maximum values have to be defined for these four peak parameters. The Raman active modes to be fitted and the start positions for the peaks of each phase are taken from literature.^{8,73,76}

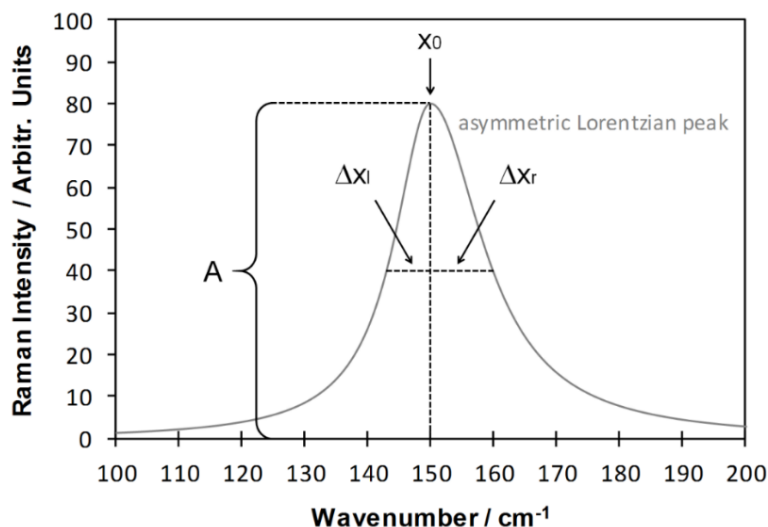


Fig. 39: Asymmetric Lorentzian function and its four fitting factors: position x_0 , height A , half-width at half maximum on the left-side Δx_l and on the right-side Δx_r .

3.1.4.3.1 Simplified models for first-order scattering

As described above, three different grades of model simplifications are necessary for those of our spectra that contain more than one crystalline phase – as a compromise between accuracy and feasibility. We have used *light simplifications* for two different phases. Omitting peak asymmetry works well for anatase and rutile. This simplification is adequate for the main crystal phase in our films (anatase). For a phase with low complexity and less than 20% of the counts in the spectra, which is rutile in our case, linking of parameters, in addition to the use of symmetrical Lorentzian functions, leads to good results. Two kinds of linking were used: the first one is to assign the same peak width to different peaks (the rutile Eg peak around 447 cm^{-1} and the rutile B1g peak around 612 cm^{-1}) and the second one is fixing the ratios of different peaks (such as the ratio of the intensity between the weak rutile A1g peak around 145 cm^{-1} and the Eg or B1g peak).

The *strong* simplification for a complex phase (in our case brookite) is the use of global fit parameters. Therefore, we model a reference spectrum – the ‘processed’ spectrum in Fig. 40 – with Lorentzian functions at fixed peak positions with fixed height ratios and manipulate the spectrum with global fit parameters for height and width for the whole set of all functions. Height ratios and peak positions are fitted manually. A *strict* simplification for phases of which only traces are visible is implemented by adding a reference spectrum of a certain phase with only one fitting factor to the total spectrum.

3.1.4.4 Models for phase background spectra

In the following, we describe the preparation of our phase background models by decomposing reference raw spectra into first- and remaining background spectra. The methods shown in Fig. 40 and Fig. 41 (I) and (II) are not applicable in the main fitting routine when we fit a measured spectrum that is taken from a TiO₂ thin film on a substrate. The models that we obtain by this preparation have to be rigid when they are fitted to measured spectra. They are modeled by the fitting factors discussed in each model, instead.

We suggest working with two different kinds of models for phase background spectra. For adequate fitting, a phase with high intensity and high signal to noise-ratio necessitates a model in which the shape and positions of the individual bands can be adjusted. Minor phases with weak signal or phases with complex Raman spectra, on the other hand, require a simple and robust model to make the modelling of phase backgrounds feasible.

The nature of a phase background spectrum depends strongly on the crystal phase and the excitation wavelength.^{73,124} We have used a 633 nm laser in our experiments, but reference Raman spectra with that wavelength were not available in the literature. Thus, we have built the phase background spectra models for each phase twice for the excitation wavelengths 532 nm and 780 nm, for which literature data of monocrystalline bulk samples exist.^{125–127} A combination of the models for these two wavelengths serves well as a model for the 633 nm laser Raman measurements.

3.1.4.4.1 Decomposition of reference phase background spectra

In order to prepare phase background models, reference spectra have to be decomposed into first-order scattering and the phase background spectrum. Thus, spectra have to be available by measurement or by literature spectra. The RRUFF project – a website containing a database of Raman spectra, X-ray diffraction and chemistry data for minerals – provides reference spectra of numerous minerals as ASCII files.¹²⁸ Most spectra are available as ‘raw’ files as well as ‘processed’ files. The raw files contain the spectra as measured while the ‘processed’ files contain the first-order scattering modes only.

If such raw and processed data are available, first-order and phase background spectra are already separated. Thus, reference phase background spectra of a certain phase can be easily deduced, as we will demonstrate for the brookite phase. We have subtracted the processed spectra from the raw spectra and smoothed the resulting spectra. We interpret these difference spectra as the phase background of the brookite phase. Fig. 40 shows the decomposition of a brookite TiO₂ Raman spectrum from RRUFF database produced with a 780 nm laser.¹²⁵ The

dark red line is the raw spectrum as measured and the red line is the 'processed' spectrum. The light red line is the (smoothed) difference spectrum of the first two spectra, which we interpret as the phase background of brookite. The intensities are shifted by 200, 100 and 50 units.

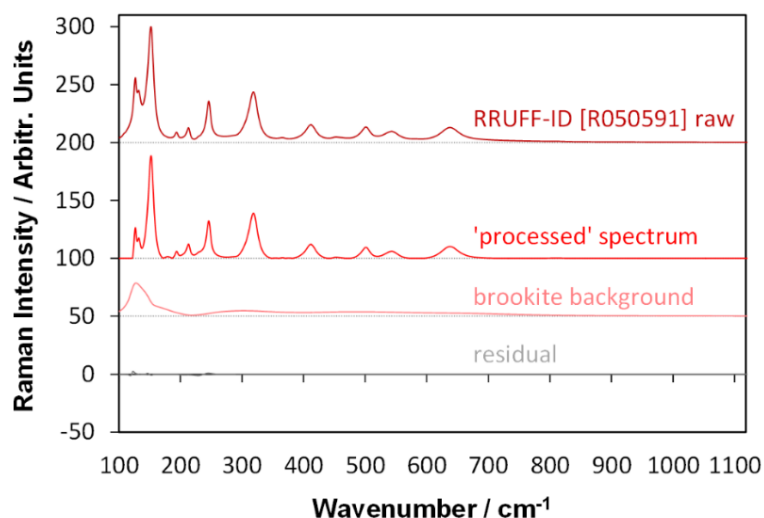


Fig. 40: Decomposition of a raw brookite TiO₂ Raman spectrum taken with a 780 nm laser (dark red) into the 'processed' spectrum (red), both available at RRUFF database,¹²⁵ and their smoothed difference spectrum (light red), which we interpret as the phase background spectrum of brookite.

If raw spectra are available only or reference spectra are measured, the spectral contributions of first-order and the phase background have to be separated manually. This procedure is demonstrated for anatase. Again, the reference spectrum is taken from RRUFF database.¹²⁶ We have fitted Lorentzian functions of the first-order scattering model to the literature spectrum by hand until artefacts were minimized in the residual spectrum around the center of the peaks. We consider this residual spectrum as the phase background spectrum of the reference anatase sample. Fig. 41 (I) shows the 780 nm literature Raman spectrum (black), the modeled anatase first-order scattering Lorentzian peaks of Eg (red), A1g (blue), and B1g (green) phonons and the residual spectrum that remains after subtracting the Lorentzian peaks, which we interpret as the phase background spectrum (dashed black line).

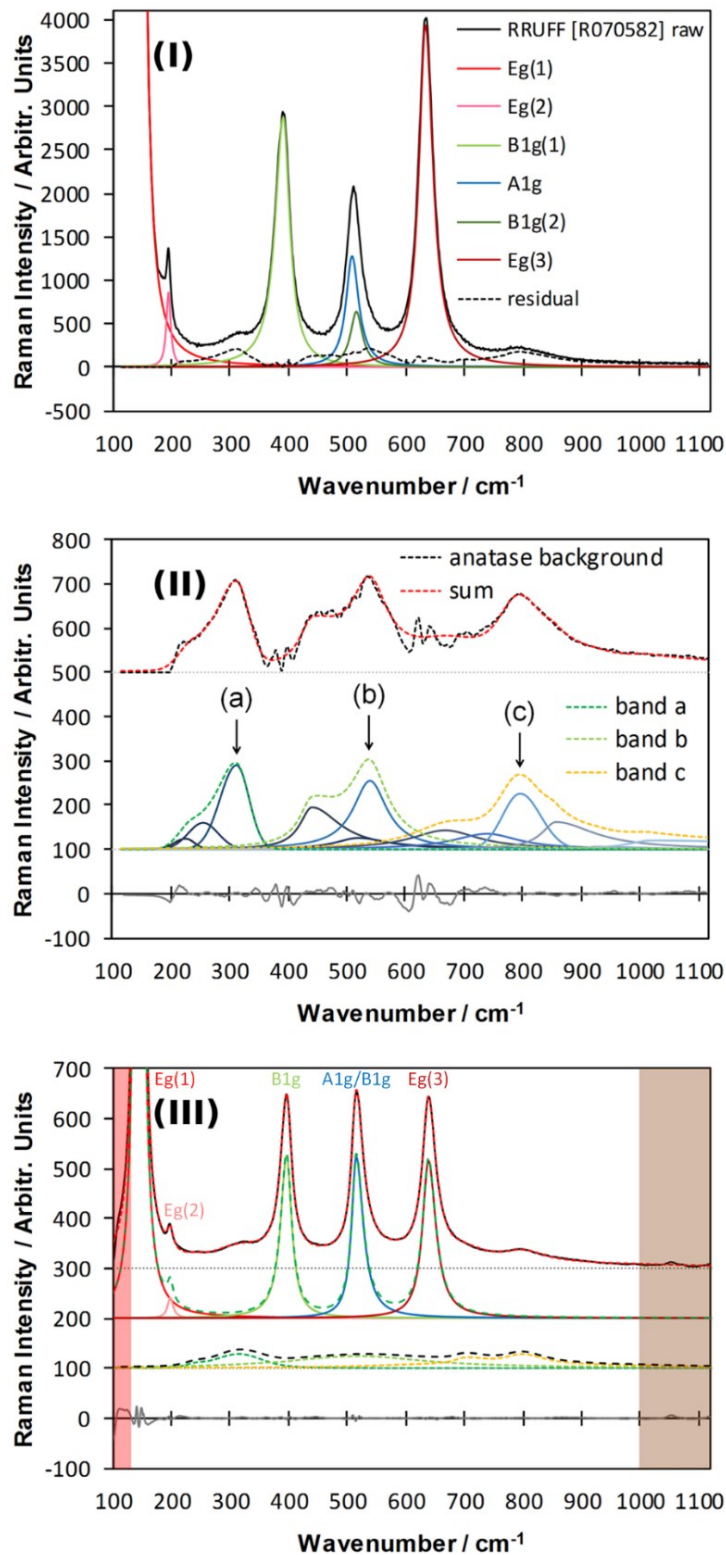


Fig. 41: (I) Decomposition of a reference monocrystalline bulk anatase raw spectrum¹²⁶ into first-order Lorentzian peaks and the residual spectrum (dashed black line), which we interpret as the anatase background spectrum. The Eg peak at 143 cm^{-1} has an intensity of $50\,000\text{ units}$; (II) pseudo-Voigt peaks, grouped to three bands (a), (b), and (c) as models for the anatase background spectrum (for 780 nm laser excitation). The black dashed line (anatase background) is the residual spectrum in Fig. 41 (I); (III) TiO₂ anatase spectrum derived by subtraction of the substrate and amorphous spectrum from a measured spectrum, decomposed into modeled anatase first-order and background spectra. The Eg peak at 145 cm^{-1} has an intensity of $3\,200\text{ units}$. The excluded range is light red and the low priority range is light brown.

3.1.4.4.2 Adjustable spectral bands for phase backgrounds

Anatase is the strongest phase in our films and will serve as an example for a phase background model with individually adjustable spectral bands. As described above, we consider the residual spectrum of Fig. 41 (I) as the phase background spectrum of anatase. We modeled it by a set of 12 pseudo-Voigt functions as depicted in Fig. 41 (II). The pseudo-Voigt functions are grouped to form three bands around 300 cm^{-1} , 530 cm^{-1} and 800 cm^{-1} , which are also discussed in literature. A further band occurs around 700 cm^{-1} , especially in Nb-doped films, which might be attributed to defects, such as oxygen vacancies.²⁸ This will be discussed in a following publication. Kontos et al. described Raman bands as broad peaks for N-doped TiO₂ at 328 cm^{-1} , 585 cm^{-1} , 680 cm^{-1} and 815 cm^{-1} with a 459.9 nm laser, and similar bands were found by Liu et al. around the wavenumbers 289 cm^{-1} , 600 cm^{-1} , and 800 cm^{-1} using a 514.5 nm laser.^{27,124} Zeng et al. describe two distinct bands at 803 cm^{-1} and 918 cm^{-1} for undoped TiO₂ in spectra measured using a 473 nm laser.²⁹ In certain of our spectra an individual band occurred around 930 cm^{-1} , also. The band around 300 cm^{-1} is associated with A1g vibrations by Giarola et al.,¹⁰⁷ yet in our spectra it still occurs when neither A1g nor B1g first-order peaks are present.

In Fig. 41 (II), the dashed black line is the phase background spectrum of Fig. 41 (I), the thin blue lines are the pseudo-Voigt functions, the green and orange lines are the modeled phase background bands, the dashed red line is the sum of the three bands and the gray line is the new residual spectrum. The bulk anatase background spectrum as well as the sum of the modeled phase background are shifted by 500 units and the pseudo-Voigt functions as well as the corresponding bands are shifted by 100 units on the intensity axis.

The positions of our first-order scattering spectra are generally different from the reference spectrum.¹²⁶ We therefore adapt the positions of the phase background bands corresponding to the neighboring first-order peaks. The fit parameters are the height ratios of the bands, one variable for the width of all bands and one for the total height of the spectrum.

Fig. 41 (III) shows the decomposition of a measured Raman spectrum of a strongly crystallized TiO₂ anatase thin film (black) after the subtraction of the substrate spectrum and the spectrum of the amorphous phase into the modeled anatase first-order scattering (green) and anatase background (light green) spectra. The dashed red line is the sum of both anatase spectra (fit), the gray line is the residual spectrum and the transparent brown area is excluded (below 130 cm^{-1}) or fitted with less priority (above 1000 cm^{-1}). The measured and fit spectra are shifted by 300, the modeled first-order spectrum by 200, and the anatase background spectrum by 100 units on the intensity axis.

3.1.4.4.3 Simplified models for phase backgrounds

In the samples with more than one crystalline phase, the number of parameters should be reduced. Rutile and brookite are present in our films to only a small degree ($< 20\%$) and their models are simplified as compared to anatase. The rutile background model was derived the same way as shown for anatase and agrees well with a study of Nicola et al.¹²⁹ In the fitting routine, the widths of the bands are kept constant. The model for the complex phase brookite is more simplified: in the fitting routine, the brookite background spectrum of Fig. 40 is added to the total modeled spectrum with a linear factor. The total intensities of the simplified phase background models depend on the ratios of the crystalline phases in the first-order scattering models. Thus, the simplified phase background models have no own fitting parameters and are indirectly manipulated by the fit parameters of the first-order scattering fitting routine.

3.1.5 Models for substrate spectra

Raman measurements of thin films often are superimposed by the spectra of the substrate onto which they are coated. Depending on the substrate, two kinds of issues have to be met: difficulties occur 1) when sharp Raman peaks of substrates are orders of magnitude more intense than the spectra of the thin films or 2) when substrates show strong luminescence in addition to their Raman spectra. Both types of substrates need an individual approach. Si wafers are an example for non-luminescent substrates with strong and sharp peaks, while B270 (crown glass) and fused silica are examples for substrates that feature Raman active modes as well as luminescence.

The Raman spectrum of a certain substrate depends on structural properties, such as local chemical composition (vacancies, doping) or variations in bonding angles; as well as on the experimental setup, such as laser intensity, focus, wavelength, irradiation time, grit or an offset. The structural properties and the laser focus may vary not only from substrate to substrate, but also between measurements on the same sample. That is why building a model for substrates has to be a compromise between flexibility and robustness. On the one hand, the model for a substrate should interfere as little as possible with the fitting routines of the film, and, on the other hand, the complexity of the substrate's spectrum has to be taken into account.

For variations in the experimental setup such as laser wavelength, laser power, irradiation time, or the choice of the grit, it is necessary to prepare individual models by repeating the procedure presented here.

3.1.5.1 Substrates with strong and sharp Raman peaks

We demonstrate means for fitting Raman spectra of thin films that are superimposed with strong Si wafer substrate spectra over a wide range covering most of the TiO₂ anatase and rutile Raman peaks. This is realized by excluding ranges from the fit, in which the substrate's Raman signals are either very sharp or orders of magnitudes more intense than the spectrum of the thin film.

The model for non-luminescent substrates with strong and sharp Raman peaks consists of a set of reference spectra. We measured five different Si wafers and varied the focus of the laser on the fifth Si wafer to produce a range of reference spectra for the generation of a modeled Si Raman spectrum. The measured Si spectra are shown in Fig. 42 (I). That range of spectra has to be considered in the fitting procedure.

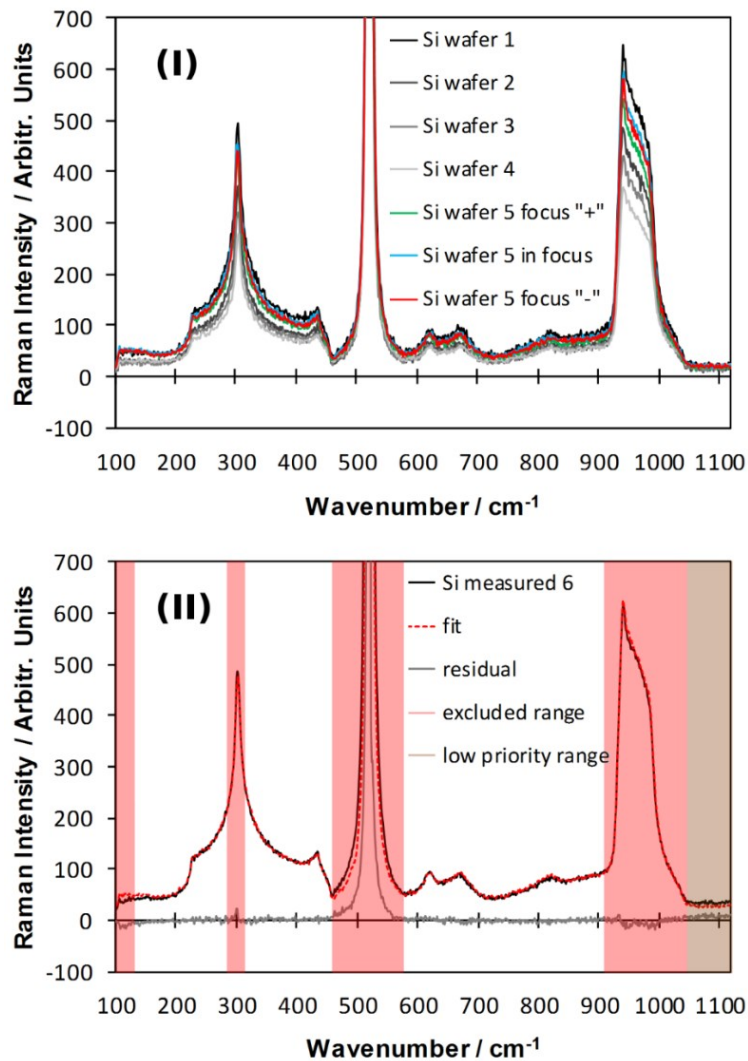


Fig. 42: (I) Spectra of five individual Si wafers and a variation of the laser focus on wafer 5; (II) measured Raman spectrum of a sixth Si substrate (black), modeled by seven reference spectra of five reference substrates with varying laser focus. The excluded range is light red and the low priority range is light brown.

The main fitting routine is straightforward: each of the seven reference spectra is added to the whole spectrum with a fitting factor and can additionally be shifted on the wavenumber axis by $\pm 1 \text{ cm}^{-1}$. However, the peak around 300 cm^{-1} is very sharp, the first-order peak at 520.7 cm^{-1} is orders of magnitudes more intense than the other peaks, and there is heavy variance in the height of the band between 900 cm^{-1} and 1050 cm^{-1} . These are factors that cause artefacts that corrupt the whole fitting routine. The least square method would rather minimize these artefacts than provide a setting for a fitting of the film spectrum. To meet these requirements, the spectral ranges in which these artefacts occur are excluded from the fitting procedure. Fig. 42 (II) shows a successful fit to a measured Si substrate by the described procedure with excluded ranges of $100 \text{ cm}^{-1} - 130 \text{ cm}^{-1}$, $285 \text{ cm}^{-1} - 315 \text{ cm}^{-1}$, $460 \text{ cm}^{-1} - 575 \text{ cm}^{-1}$, and $910 \text{ cm}^{-1} - 1045 \text{ cm}^{-1}$. The Si peak at 520.7 cm^{-1} is cut off in both graphs of Fig. 42. In Fig. 42 (II), one can see that also the residual spectrum of the fit exceeds the graph and thus all Si peaks of the measured spectrum. The variation of these peaks in the reference spectra and the fit to the measured sixths spectrum that are cut off in Fig. 42 (I) and (II) are shown in Fig. 43 (I) and (II). The error of the modeled peak is more than one third of the measured intensity, while the residual spectrum is nearly zero in all non-excluded ranges. This demonstrates the benefit of excluding ranges within the fit. Without excluding these ranges, the fit as shown in Fig. 60 would not be realizable, because the error in these ranges (especially around 520.7 cm^{-1}) is enormous as compared to the spectral features of the TiO_2 thin film.

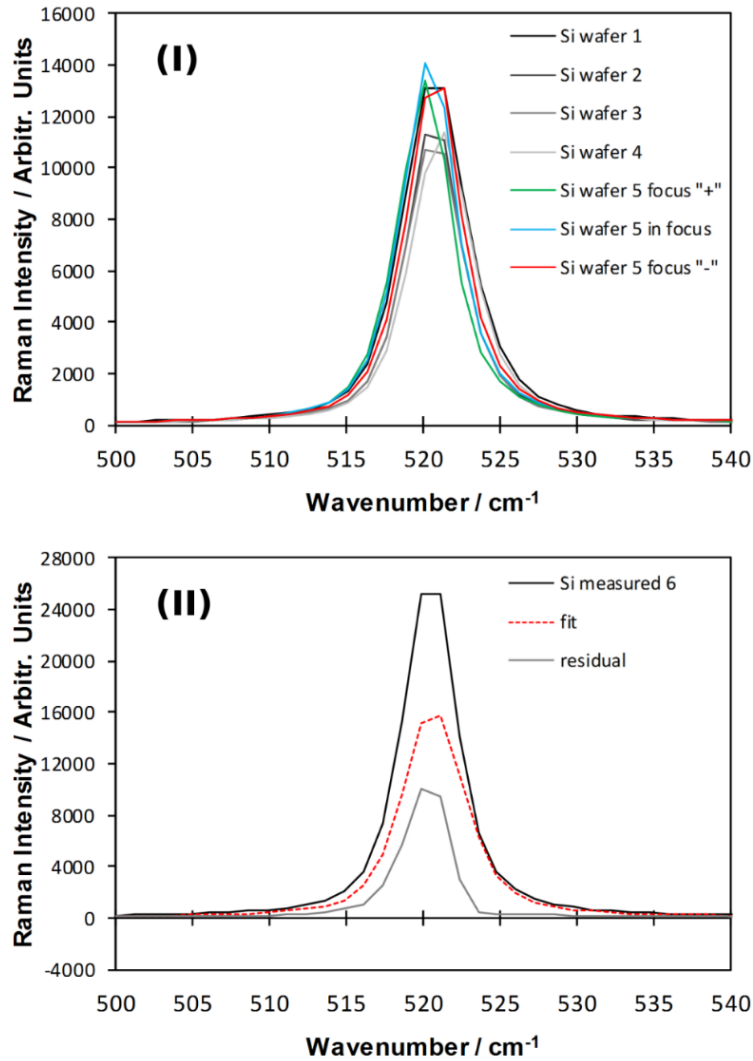


Fig. 43: (I) Variation of the Si peak around 520 cm^{-1} of the spectra shown in Fig. 42; (II) measured and modeled ('fit') Si peak around 520.7 cm^{-1} , which was excluded from the fit, of the spectrum shown in Fig. 42 (II) – the error of the modeled peak is more than one third of the measured intensity.

3.1.5.2 Models for luminescent substrates

For substrates that show Raman scattering as well as luminescence, both vary independently of each other from sample to sample or depending on the experimental setup. Further aspects that affect the relative intensities of a substrate's measured Raman and luminescence spectrum are the properties of the thin films that are coated onto the substrate – such as the degree of crystallinity or electrical and optical properties, which influence the absorption behavior of the film. This becomes evident in our work with electron beam evaporated Nb-doped and undoped TiO₂ films, which will be published later.

Thus, the main procedure for obtaining a model for luminescent substrates is to split the substrate's spectrum into a luminescence background and Raman active modes. In order to obtain the Raman active modes, the luminescence background has to be stripped off the spectrum. The often-complex shapes of the Raman bands make it difficult to differentiate

between both. We use a standard routine to deconvolute the reference substrate spectra by modeling the luminescence background with a polynomial function, assuming that between certain Raman bands there are spectral ranges in which the Raman signal is zero or close to zero. This assumption agrees with works on silica-based glass substrates in literature.^{130–136} Seuthe et al. discuss the deconvolution of Raman bands and their physical origins for silica glass samples with varying composition.^{134,135}

In detail, the luminescence spectra were obtained as follows. Fig. 44 (I) shows the spectra of four individual B270 glass samples (gray). At fixed wavenumbers where there are local minima of the bands, we take the intensity of the spectra as function values of polynomial functions that lie below the measured spectra (blue lines). The base points for the functions are at 250 cm^{-1} , 730 cm^{-1} , 845 cm^{-1} , and 1015 cm^{-1} . Then, these functions are treated as the reference luminescence spectra of our model. The spectra that remain after subtracting the luminescence from the measured spectra are what we consider as the Raman active bands (green lines).

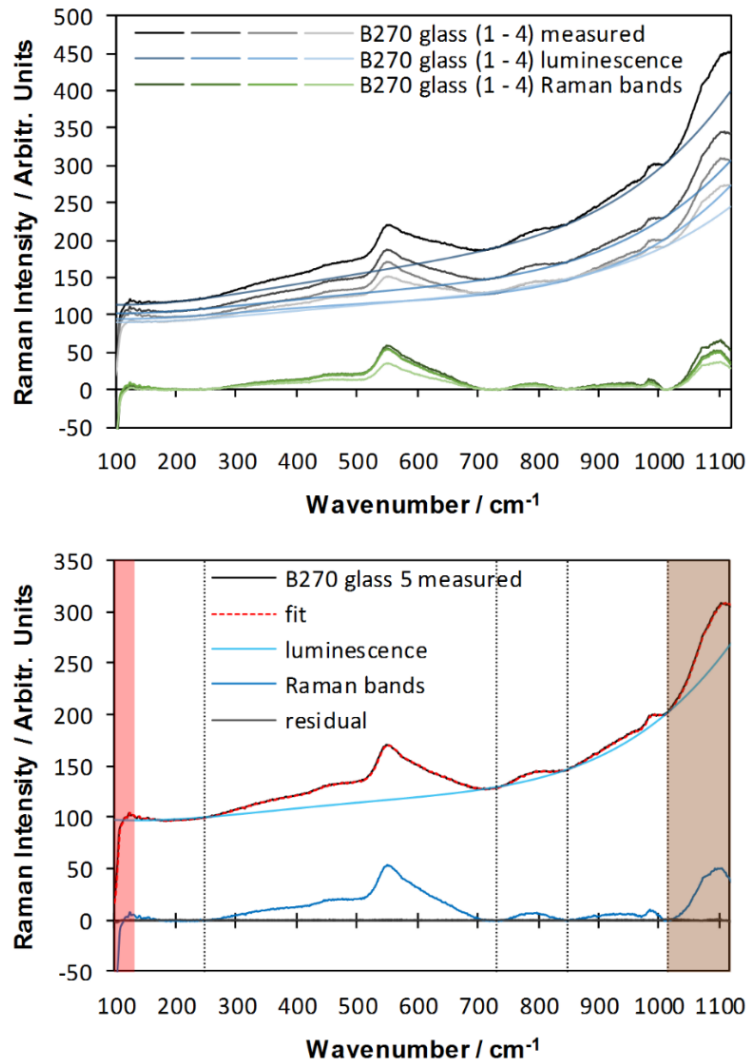


Fig. 44: (I) Decomposition of measured B270 glass substrate spectra into luminescence and Raman active modes. (II) Measured (black) and modeled (red) Raman spectra of a B270 glass substrate composed by luminescence (light blue) and Raman bands (blue). The vertical dotted lines mark the base points of the luminescence spectrum, where the Raman spectrum is zero, and they separate the spectral ranges to be fitted individually. The excluded range is light red and the low priority range is light brown.

The described approach to discriminate between Raman bands and luminescence of substrates is often implemented into standard Raman evaluation software. However, such a direct decomposition of the substrate spectra into Raman active bands and luminescence spectra within thin film Raman spectra is not possible, because there are no base points where a polynomial function for the luminescence could be anchored. Our approach to overcome this problem is to treat the four luminescence spectra that were obtained by the decomposition of the reference measurements as *reference luminescence spectra*, which are added to the fit with one fitting factor for intensity, each. Thus, there is no polynomial function applied in the fitting of the spectra of thin films on luminescent substrates, but the aforementioned reference spectra.

This approach is possible because all spectra, including all sub-spectra of the thin films are fitted simultaneously.

Again, we use versions with varying complexity of the model for luminescent substrates. We use a simple model which is less accurate but a reasonable choice for modelling spectra of mixed-phase films, and a more flexible model which treats certain Raman bands of the substrate individually. The last one is more suitable for films that consist of only one crystalline phase (plus amorphous content) and results in clearer spectra. Furthermore, the flexible model permits to compensate a variation of the thin film's absorption.

3.1.5.2.1 Simple model for luminescent substrates

When modelling the measured spectrum of a substrate, the spectrum is built up in two steps. The luminescence background is the sum of the four reference luminescence spectra which are each multiplied by a fitting factor. The substrate's Raman bands are treated in the same way.

3.1.5.2.2 Individual-band model for luminescent substrates

The individual-band model for luminescent substrates treats the Raman bands individually. Therefore, the spectrum of the substrate Raman bands are split into five bands. This approach allows to model the measured spectrum of a new substrate without considerable inaccuracy as we will demonstrate below.

As a compromise between accuracy and robustness, the shapes of the Raman bands are not modeled in a way that take into account the physical properties that affect the individual modes but are manipulated in a more simplified way. We split the spectra of the Raman bands, shown as green lines in Fig. 44 (I) into the spectral ranges that lie between the minima. The limits of these intervals are at the same wavenumbers as the base points used for obtaining the polynomial functions for the luminescence spectra, and are shown as vertical lines in Fig. 44 (II).

The height of the five bands in these intervals can be individually adjusted by a factor (in our case between 0.8 and 1.2). Additionally, the spectrum can be slightly shifted on the spectral axis by $\pm 1 \text{ cm}^{-1}$ to compensate an offset.

By this combination of four individual luminescence backgrounds and four footprints with adjustment factors for the five spectral ranges, a Raman spectrum of a further glass sample can be successfully modeled without significant deviations. This is demonstrated in Fig. 44 (II), which shows a measured spectrum of a B270 glass sample (black), a modeled luminescence spectrum (light blue), the modeled Raman bands (dark blue) and the sum of both, which is the

simulated spectrum of the glass (dashed red line). The residual spectrum, the difference between the measured and the modeled spectrum (dark gray), is nearly zero for the whole spectrum below 1000 cm^{-1} and only weak inaccuracies are visible above the main fit interval. While the adjustment factors for the five spectral ranges work well with films containing mainly one phase (this will be presented in a forthcoming paper), there are too many fit parameters for mixed-phase films. Omitting these factors result in inaccuracy of the fit in Fig. 61. at 550 cm^{-1} .

We used the same procedure to build a model for fused silica as a further luminescent substrate in order to assess the reproducibility of the procedure with another substrate material. We measured and decomposed four spectra of fused silica substrates into luminescence and Raman bands, shown in Fig. 45 (I).

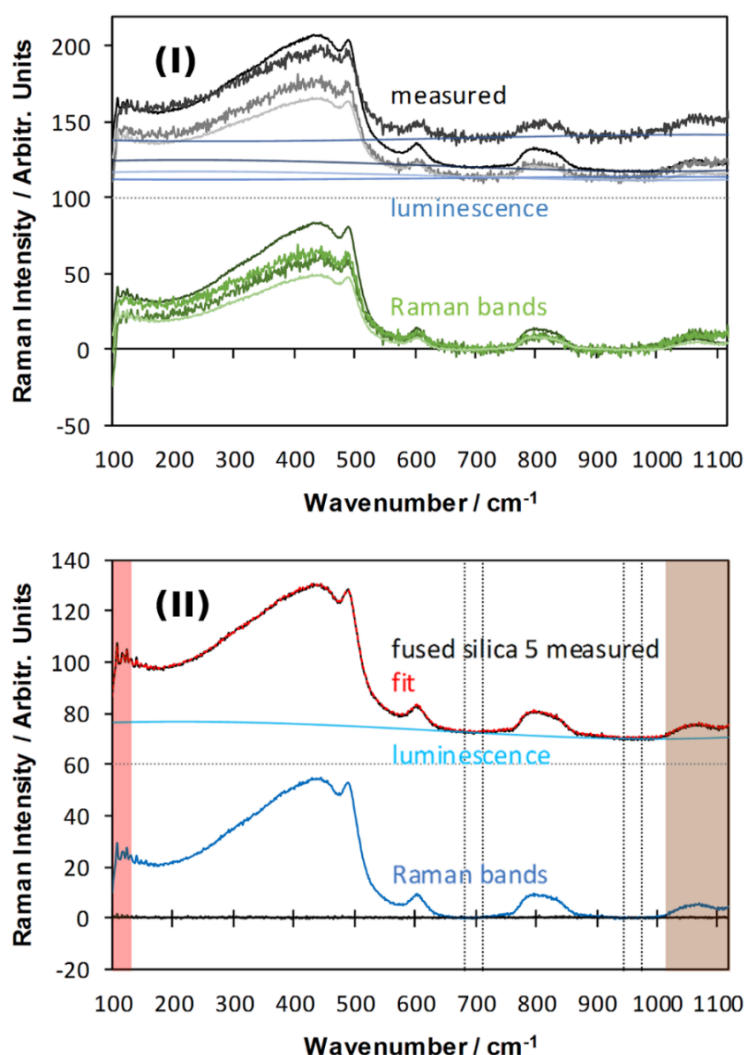


Fig. 45: (I) Decomposition of measured fused silica substrate spectra (gray) into luminescence (blue) and Raman bands (green); the measured and luminescence spectra are shifted by 100 units on the intensity axis. (II) Measured (black) and modeled (red) Raman spectra of fused silica substrate composed by luminescence (light blue) and Raman bands (blue). The vertical dotted lines mark the base points of the luminescence spectrum, where the Raman spectrum is zero, and they separate the spectral ranges to be

fitted individually. The measured, fit, and luminescence spectra are shifted by 60 units on the intensity axis.

Then we modeled a fit to a fifth measured fused silica substrate with a combination of the reference luminescence spectra and the Raman band with almost zero background, as shown in Fig. 45 (II). This model is applied to the fit in Fig. 62.

3.1.6 Conclusions

The most noticeable aspect of our work is to demonstrate a model that allows a *simultaneous* decomposition of a measured thin film Raman spectrum over a wide range into various components arising from thin film and substrate. The model for thin films considers mixed-phase, amorphous content, first-order Raman scattering and additional bands of each phase. Concerning substrate models, there is a distinction between luminescence and Raman activity of the substrate or an exclusion of ranges in which the substrate Raman features are either sharp or orders of magnitude more intense than the thin film spectrum.

We described an approach for designing least squares models for a complete decomposition of measured TiO₂ thin film Raman spectra into their components using the *solver* plugin of the widely available spreadsheet *Microsoft Excel*. The spectra are split into substrate signals and thin film signals. The thin film signals are separated into an amorphous spectrum and spectra for the crystalline phases: anatase, rutile, and brookite. All crystalline spectra are furthermore split into first-order scattering and a phase background (covering second-order scattering and disorder-induced scattering). The many fit parameters are handled reasonably by introducing physically based limits. We successfully fitted model spectra to Raman measurements of TiO₂ thin films prepared by e-beam evaporation and sputtering containing mixtures of varying amorphous, anatase, rutile, and brookite contents on the substrates Si, fused silica and B270 crown glass.

We assume that the described procedure for building fit models is also applicable to other materials or mixture of materials on further substrates, but this has to be proven experimentally. Limitations of the model are accuracy in the simultaneous fit of luminescence, crystalline phase backgrounds, and the amorphous content. When this model gets applied to other materials further limitations can occur caused by films which are highly fluorescing, dark in color or contain materials with low Raman cross-section, such as metals or with mono-atomic ions. On the one hand, the models must be flexible enough to cover the complexity of the involved spectra, but on the other hand, one must prevent the models to interference with each other. The choice of appropriate simplifications and simultaneous modeling of all components are the key

factors to both issues. The result provides separated spectra suitable for individual qualitative characterization and for quantification of the composition. The correlation of the decomposition of the Raman spectra with the decomposition of X-ray diffractograms will be discussed in forthcoming chapters.

3.2 Models for the simulation of Raman spectra

In this chapter, we describe adjustable models for the simulation of TiO₂ thin film Raman spectra on various substrates. The models consist of fit parameters which are to be manipulated by the *solver* plugin in Microsoft Excel, linked parameters that are depending on certain fit parameters and fixed parameters which are not manipulated during the fitting routine. We used Excel for the calculations because it is widely used, but the models can also be implemented in other programs, such as Python. The main concepts of the fitting routine are presented and discussed in chapter 3.1, which was published in the Journal of Raman spectroscopy.¹ In the following, we will often refer to this chapter/publication.

We have built the models with rigid and flexible options for different fitting purposes. The rigid models are used for simulating highly complex spectra or spectra with a low signal-to-noise ratio, while the models are more flexible for simpler (yet still complex) spectra with a high signal-to-noise ratio. The mathematical ideas behind the models are given and the fit parameters of each model are described and listed in tables. The white columns of the tables sum up the main fit parameters of the models while the gray columns show additional fit parameters for more flexible fitting or further parameters, such as for Nb-doped films. This chapter is structured into an overview on the concept of the Raman fitting model, followed by the description of the models of the TiO₂ phases and the models for various substrates.

3.2.1 Main concept of the thin film Raman fitting model

The main concept of the *thin film Raman fitting model* is a general model that should be applicable to all kinds of thin film Raman spectra: the full Raman spectrum consists of a spectrum of the thin film and a spectrum of the substrate. The thin film spectrum may contain crystalline as well as amorphous contents and the substrate spectra contain Raman bands and/or a luminescence background spectrum. An overview of the concept is shown in a flowchart in Fig. 46.

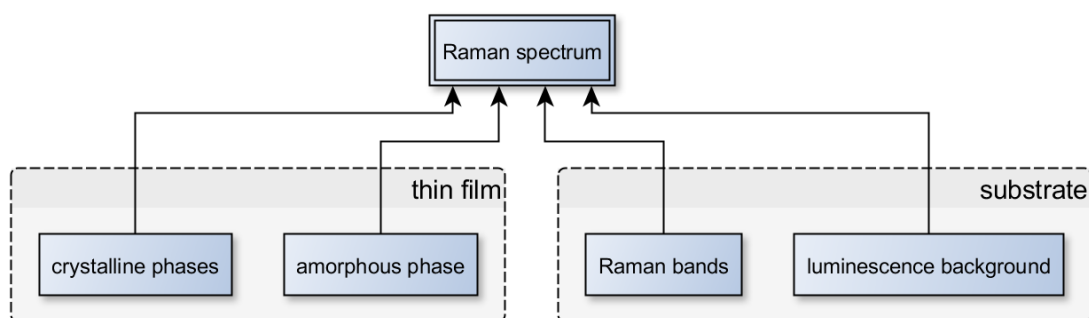


Fig. 46: Overview of the thin film Raman fitting model.

3.2.2 Raman models for TiO₂ thin films

The TiO₂ models include amorphous TiO₂ as well as the crystalline TiO₂ phases, anatase, brookite, and rutile. The models for the crystalline phases differentiate between first-order Raman scattering and phase background for each phase.

3.2.2.1 Amorphous TiO₂ model

The Raman spectrum of the amorphous TiO₂ phase is fitted by multiplying a reference spectrum of amorphous TiO₂, with a fit parameter I_{Nb0} . For Nb-doped films, also the spectra of Nb-doped amorphous Ti_{0.92}O_{2.25}Nb_{0.08} and Ti_{0.84}O_{2.25}Nb_{0.16} thin films are added with fit parameters I_{Nb1} and I_{Nb2} . An overview about the fit parameters is given in Table 5.

Table 5: Fit parameters of the amorphous phase model

Fit parameters	Description
I_{Nb0}	for undoped TiO ₂ films: Intensity of amorphous TiO ₂ reference spectrum
$I_{Nb0}, I_{Nb1}, I_{Nb2}$	for Nb-doped TiO ₂ films: Intensity factors for reference spectra of amorphous TiO ₂ , Ti _{0.92} O _{2.25} Nb _{0.08} , Ti _{0.84} O _{2.25} Nb _{0.16}

The reference spectrum of the amorphous TiO₂ thin film was derived by performing Raman spectroscopy of 1) an e-beam evaporated amorphous TiO₂ thin film on a B270 glass substrate and 2) the blank backside of the glass sample. The Raman spectrum of the substrate backside was multiplied by a certain factor and stripped from the first Raman spectrum. The factor was varied until the remaining spectrum did not contain visible Raman features of the second (pure glass) spectrum. Reference spectra of amorphous Ti_{0.92}O_{2.25}Nb_{0.08} and Ti_{0.84}O_{2.25}Nb_{0.16} thin films were derived in the same way.

The (normalized) reference spectra for amorphous TiO₂, Ti_{0.92}O_{2.25}Nb_{0.08}, Ti_{0.84}O_{2.25}Nb_{0.16} thin films are shown in Fig. S2. One can see that the intensity of the spectra of amorphous TiO₂ shows a plateau below 650 cm^{-1} , a strong decrease for values up to 700 cm^{-1} , followed by a rather straight slope down to zero intensity at around 1100 cm^{-1} . For the Nb-doped films, the plateau is below and the slope is above that of the spectrum of undoped TiO₂.

3.2.2.2 Models for crystalline phases

For TiO₂ thin films, the crystalline phases are anatase, brookite, and rutile. The total spectrum of the crystalline phases is the sum of the spectra of each individual phase. The spectra of each phase are fitted individually and consist of first-order Raman scattering and a phase

background (which contains second-order scattering and disorder-induced scattering). These aspects are summed up in the flowchart of the *crystalline phases model* as in Fig. 47.

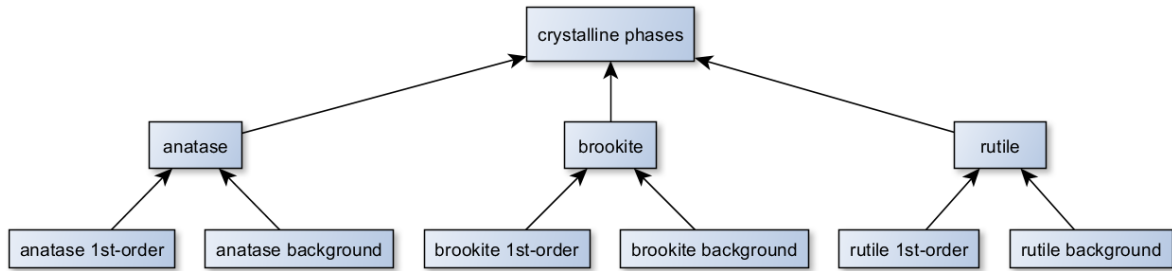


Fig. 47: Flowchart of the crystalline phases model.

The first-order models for anatase, brookite, and rutile are described below, followed by the models for the phase backgrounds of each phase.

3.2.2.3 First-order scattering models

We use first-order Raman scattering models with varying amount of simplification depending on the complexity of the spectra to be fitted. As described in chapter 3.1.4.3, the first-order scattering peaks of all Raman active modes are represented as asymmetric Lorentzian functions. The four parameters peak position x_0 on the wavenumber axis, the peak height A , and the peak widths on the left-side Δx_l and on the right-side Δx_r , are used to simulate the spectral intensity I of the first-order Raman peaks. The mathematical expression in equation (42) (in chapter 3.1.4.3) is assigned to each wavenumber in the sheet for each peak. The parameters of such a peak are depicted in Fig. S3. For the fitting routine, minimum and maximum values are defined for each of the four peak parameters. The start positions of the simulated Raman modes are taken from literature.^{8,73,76}

A model with asymmetric Lorentzian peaks is used solely for spectra that contain only one crystalline phase (in our case anatase) and an amorphous content. When we simulate spectra of multiphase films which contain more than traces ($< 1\%$) of two or more crystalline phases (anatase plus brookite and/or rutile), the spectra become more complex and a fit of asymmetric peaks is not feasible anymore and the formula of (42) is simplified to:

$$I = \frac{A}{1 + \left(\frac{x - x_0}{\Delta x}\right)^2}, \quad (43)$$

Phases which are present only as traces are fitted by adding a reference spectrum multiplied with a fitting factor for the intensity. The individual models are described below.

3.2.2.3.1 First-order scattering model of anatase

The first-order scattering model of anatase consists of five or six peaks (as described in chapter 3.1.4) each with a position x_{0i} , an amplitude $A_{i(an)}$, and an half-width $\Delta x_{i(an)}$ (or two half-widths, $\Delta x_{i,l(an)}$ and $\Delta x_{i,r(an)}$) and has 12 or 16 fit parameters, depending on the complexity of the film's Raman spectrum. The Raman active modes Eg(1) (144 cm^{-1}), Eg(2) (196 cm^{-1}), B1g (399 cm^{-1}), and Eg(3) (639 cm^{-1}) are modeled by asymmetric Lorentzian peaks using equation (42). The A1g and B1g peaks at around 513 cm^{-1} and 519 cm^{-1} are modeled as one peak which we call an A1g/B1g doublet peak. The peak asymmetry is omitted for multi-phase TiO₂ films using equation (43). The fit parameters of the first-order scattering model of anatase are listed and described in Table 6 (with $i = \text{Eg}(1), \text{Eg}(3), \text{B1g}(1), \text{A1g/B1g}$).

Table 6: Fit parameters of the first-order scattering model of anatase

Fit parameters	Description
$x_{0i(an)}, A_{i(an)}, \Delta x_{i(an)}$	Eg(1), B1g, A1g/B1g, Eg(3): peak position, amplitude, half-width
$\Delta x_{i,l(an)}/\Delta x_{i,r(an)}$	for single-phase anatase films only: ratio of left-side and right-side half-width

The parameters of the weak Eg(2) peak around 196 cm^{-1} are excluded from the *solver* calculation. Its peak widths on the left-side and right side $\Delta x_{l,\text{Eg}(2)(an)}$ and $\Delta x_{r,\text{Eg}(2)(an)}$ are linked to the peak widths of the Eg(1) peak. The relations of the two linked parameters are defined in equations (44) and (45) in Table 7.

Table 7: Linked parameters of the first-order scattering model of anatase

Linked parameters	Description	
$\Delta x_{l,\text{Eg}(2)(an)}, \Delta x_{r,\text{Eg}(2)(an)}$	$\Delta x_{l,\text{Eg}(2)(an)} = 1.1 \times \Delta x_{l,\text{Eg}(1)(an)}$	(44)
	$\Delta x_{r,\text{Eg}(2)(an)} = 1.1 \times \Delta x_{r,\text{Eg}(1)(an)}$	(45)

3.2.2.3.2 First-order scattering model of rutile

Rutile occurs only in multi-phase Raman spectra in this work and it is never the main phase. Taking this into account, the first-order scattering model of rutile is simplified by reducing the number of fit parameters. In the first place, this is done by omitting peak asymmetry. Thus, the four Raman active modes (Eg, B1g, A1g, B2g) are modeled by Lorentzian functions using equation (43). Furthermore, certain parameters are linked or fixed to standard values.

With these simplifications, the first-order scattering model of rutile has four fit parameters: peak position $x_{0,Eg(ru)}$, height $A_{Eg(ru)}$ and half-width $\Delta x_{Eg(ru)}$ of the Eg mode around 447 cm^{-1} , as well as the peak position $x_{0,A1g(ru)}$ of the A1g mode around 612 cm^{-1} (see Table 8).

Table 8: Fit parameters of the first-order scattering model of rutile

Fit parameters	Description
$x_{0,Eg(ru)}, A_{Eg(ru)}, \Delta x_{Eg(ru)}$	Eg: position, height, and half-width
$x_{0,A1g(ru)}$	A1g: position

The peak heights $A_{A1g(ru)}, A_{B1g(ru)}, A_{B2g(ru)}$ and widths $\Delta x_{A1g(ru)}, \Delta x_{B1g(ru)}, \Delta x_{B2g(ru)}$ of the A1g, B1g, and B2g modes are linked to the peak height $A_{Eg(ru)}$ and width $\Delta x_{Eg(ru)}$ of the Eg mode as defined in the equations (46) to (51) in Table 9.

Table 9: Linked parameters of the first-order scattering model of rutile

Linked parameters	Description	
$A_{A1g(ru)}$	$A_{A1g(ru)} = A_{Eg(ru)}$	(46)
$\Delta x_{A1g(ru)}$	$\Delta x_{A1g(ru)} = \Delta x_{Eg(ru)}$	(47)
$A_{B1g(ru)}$	$A_{B1g(ru)} = 0.08 \times A_{Eg(ru)}$	(48)
$\Delta x_{B1g(ru)}$	$\Delta x_{B1g(ru)} = 0.1 \times \Delta x_{Eg(ru)}$	(49)
$A_{B2g(ru)}$	$A_{B2g(ru)} = 0.03 \times A_{Eg(ru)}$	(50)
$\Delta x_{B2g(ru)}$	$\Delta x_{B2g(ru)} = 1.5 \times \Delta x_{Eg(ru)}$	(51)

The positions of the weak B1g and B2g peaks, $x_{0,B1g(ru)}$ and $x_{0,B2g(ru)}$, are fixed to the standard positions at 143 cm^{-1} and 626 cm^{-1} , respectively (Table 10).⁷⁶

Table 10: Fixed parameters of the first-order scattering model of rutile

Fixed parameters	Description
$x_{0,B1g(ru)}$	143 cm^{-1} (standard position)
$x_{0,B2g(ru)}$	626 cm^{-1} (standard position)

If there are only traces of rutile present, the peak positions of the Eg and the A1g peaks are fixed to the standard values 447 cm^{-1} and 612 cm^{-1} , and the Eg peak width is set to a certain value a priori by hand and excluded from the automated fitting routine. This strict simplification leaves only one fit parameter (A_{Eg}) for the automated fitting routine of the rutile first-order Raman spectrum.

3.2.2.3.3 First-order scattering model of brookite

Brookite, like rutile, also occurs only in multi-phase Raman spectra in this work and is never the main phase. Furthermore, it is the phase with the most complex Raman spectra. Thus, the first-order Raman scattering model of brookite has strong simplifications.

The model is fitted automatically by varying a prepared set of Lorentzian peaks using only one to five fit parameters, depending on the intensity of the brookite spectra. The parameters $A_{(br)}$ and $\Delta x_{(br)}$ are global factors which are multiplied with the heights and widths of each Lorentzian peak of the model (Table 11).

Table 11: Fit parameters of the first-order scattering model of brookite

Fit parameters	Description
$A_{(br)}$	multiplied with the height of each Lorentzian peak
$\Delta x_{(br)}$	<i>multiplied with the width of each Lorentzian peak (excluded if traces of brookite are present only)</i>
$x_{0,A1g(br)}$	<i>position of the A1g peak around 155 cm^{-1} (excluded if traces of brookite are present only)</i>

In general, the peak positions are fixed – with a few exceptions. If more than traces are present, the position $x_{0,A1g(br)}$ of the most intense A1g peak around 155 cm^{-1} is a fit parameter. For strong brookite spectra, the individual height ratios $h_{i,200-350}$ and peak positions $x_{i,200-350}$ of the most intense peaks in the range from 200 cm^{-1} to 350 cm^{-1} are adjusted by hand. The various individual fixed ratios of the peak parameters are not discussed in detail.

Table 12: Fixed parameters of the first-order scattering model of brookite

Fixed parameters	Description
$h_{i,200-350}$	for strong spectra: height ratios (of the most intense peaks between 200 cm^{-1} and 350 cm^{-1}), fitted manually
$x_{i,200-350}$	for strong spectra: Peak positions (of the most intense peaks between 200 cm^{-1} and 350 cm^{-1}), fitted manually

Instead, we describe how the model was developed for both laser wavelengths (532 nm and 633 nm) used for the experimental Raman spectra in this work. The model for simulating 532 nm laser Raman spectra was derived by fitting a set of Lorentzian peaks to a reference spectrum of brookite (RRUFF ID R050591) taken with a 532 nm laser, as shown in Fig. 49

(medium green line). We could not find a reference Raman spectrum for a 633 nm laser but a 780 nm reference spectrum (medium red line in Fig. 49 in chapter 3.2.2.4.2) was available for the same sample of the 532 nm spectrum.¹²⁵ Another set of Lorentzian peaks was fitted to the 780 nm Raman spectrum. The model for the 633 nm laser Raman spectrum was derived by averaging each parameter of the both sets of Lorentzian peaks from the 532 nm and the 780 nm model.

If traces of brookite are present only, the global peak width factor $\Delta x_{(br)}$ is set to a certain value a priori by hand and excluded from the automated fitting routine. This strict simplification leaves only one fit parameter (A) for the automated fitting routine of the brookite first-order Raman spectrum.

3.2.2.4 Models for phase background spectra

In chapters 3.1.4.2 and 3.1.4.4, we discuss the nature of the “phase backgrounds” occurring in Raman spectra of crystalline phases. We built individual models for the phase backgrounds of anatase, brookite, and rutile. While the anatase background model has three or more fit parameters that change the shape and intensity of the model spectrum (see chapter 3.2.2.4.1), the background spectra of the weaker phases, brookite and rutile, have no fit parameters that are manipulated directly by the fitting routine. Instead, the intensities of the brookite background spectrum $I_{bg(br)}$ and the rutile background spectrum $I_{bg(ru)}$ are linked to the intensity of the anatase background spectrum $I_{bg(an)}$ as well as to the intensity ratios of the first-order Raman spectra of brookite and anatase $I_{1st-order(br)}/I_{1st-order(an)}$, and of rutile and anatase $I_{1st-order(ru)}/I_{1st-order(an)}$. The intensities of the first-order spectra ($I_{1st-order(an)}$, $I_{1st-order(br)}$, and $I_{1st-order(ru)}$), result from the area under the spectra that are modeled in chapters 3.2.2.3.1 to 3.2.2.3.3. The phase-background intensity of anatase ($I_{bg(an)}$) results from the area under the spectrum that is modeled in chapter 3.2.2.4.1.

The intensities of the brookite and rutile background spectra are shown in the equations (52) and (53) in Table 13 as functions of the intensity of the anatase phase background spectrum and the intensity ratios of first-order Raman spectra. The background of rutile is described to be high in intensity in literature – even higher than the first-order spectrum.⁷³ Thus, the intensity of the rutile phase background is multiplied by an arbitrary factor of 2 in equation (53). The factor might be inaccurate, but the spectra analyzed in this work do not provide enough information on the rutile phase background.

Table 13: Linked parameters of the phase background spectra

Linked parameters	Description	
$I_{bg(br)}$	$I_{bg(br)} = 1 \cdot I_{bg(an)} \cdot \left(\frac{I_{1st-order(br)}}{I_{1st-order(an)}} \right)$	(52)
$I_{bg(ru)}$	$I_{bg(ru)} = 2 \cdot I_{bg(an)} \cdot \left(\frac{I_{1st-order(ru)}}{I_{1st-order(an)}} \right)$	(53)

3.2.2.4.1 Crystalline background of anatase

The anatase phase background model for a certain laser wavelength consists of 12 peaks expressed by asymmetric Pseudo-Voigt functions. A Pseudo-Voigt function approximates the Voigt function and is the combination of a Lorentzian and a Gaussian function. Equation (54) shows the intensity of a peak simulated with this function, where I is the total intensity, I_L the intensity of a Lorentzian function, I_G the intensity of a Gaussian function, and η a number between 0 and 1:

$$I = \eta \cdot I_L + (\eta - 1) \cdot I_G, \text{ with } 0 < \eta < 1. \quad (54)$$

An asymmetric peak is then simulated by equations (55) and (56):

$$I = A \left(\eta \cdot \left(\frac{1}{1 + \left(\frac{x-x_0}{\Delta x_l} \right)^2} \right) + (\eta - 1) \cdot \left(\exp \left[-\ln(2) \cdot \left(\frac{x-x_0}{\Delta x_l} \right) \right] \right) \right) \text{ for } x \leq x_0, \quad (55)$$

$$I = A \left(\eta \cdot \left(\frac{1}{1 + \left(\frac{x-x_0}{\Delta x_r} \right)^2} \right) + (\eta - 1) \cdot \left(\exp \left[-\ln(2) \cdot \left(\frac{x-x_0}{\Delta x_r} \right) \right] \right) \right) \text{ for } x \geq x_0. \quad (56)$$

This provides the intensity at a certain wavenumber x with the peak position x_0 on the wavenumber axis, the peak height A , and the peak widths on the left-side Δx_l and on the right-side Δx_r . The fit parameters of the anatase phase background model are listed in Table 14.

Table 14: Fit parameters of the anatase phase background model

Fit parameters	Description
$I_{anbg532}, I_{anbg780}$	multiplied with the height of each Pseudo-Voigt peak of the 532 nm or the 780 nm background model
W_{anbg}	multiplied with the width of each Pseudo-Voigt peak values: $0.5 < I_{anbg1}, I_{anbg3} < 2$
$I_{anbg,a}, I_{anbg,c}$	for single-phase anatase films only: multiplied with the heights of the peaks that are components of the bands a and c values: $0.8 < I_{anbg1}, I_{anbg3} < 1.2$
$W_{anbg,a}, W_{anbg,c}$	for single-phase anatase films only: multiplied with the widths of the peaks that are components of the bands a and c values: $0.8 < I_{anbg1}, I_{anbg3} < 1.2$
$x_{0,930}, h_{930}, \Delta x_{930}$	optional, for single-phase anatase films only: position, height, and width of a Pseudo-Voigt ($\eta = 0.5$) peak around 930 cm^{-1}
$x_{0,Nb}, h_{Nb}, \Delta x_{Nb}$	for Nb-doped TiO_2 films: position, height, and width of a broad Gaussian peak between 700 cm^{-1} and 850 cm^{-1}

Anatase background models were built for the wavelengths 532 nm and 780 nm. A detailed description on the preparation of these models is given in chapter 3.1.4.4.1. Thus, in this chapter, there is only a summary: we subdivide a raw reference anatase Raman spectrum (RRUFF-ID R070582) into a first-order and a phase background spectrum. Therefore, the first-order peaks are fitted by hand and we interpret the remaining spectrum as the anatase phase background spectrum. The reference raw anatase Raman spectra for the wavelengths 532 nm and 780 nm (light green and light red lines) and the corresponding anatase phase background spectra (dark green and dark red lines) are shown in Fig. 48.

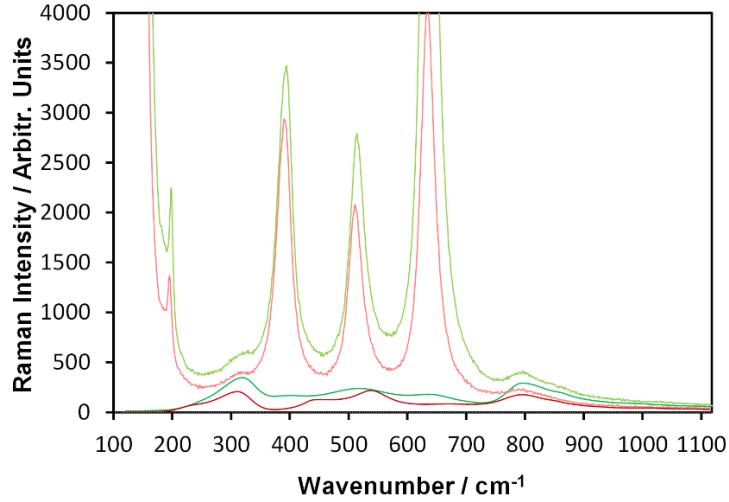


Fig. 48: Literature raw anatase Raman spectra (RRUFF-ID R070582)¹²⁶ produced with a 532 nm (light green line) and a 780 nm (light red line) laser and the corresponding phase backgrounds in dark green and dark red. The phase backgrounds are obtained in our work from the remaining spectra after fitting first-order Raman peaks to the reference spectra.

The anatase phase backgrounds for 633 nm and 532 nm lasers are fitted by a set of 11 Pseudo-Voigt functions each and are grouped to three bands (a, b, c), which is exemplarily shown for the 780 nm anatase phase background in Fig. 41 (II) in chapter 3.1.4.4.1. The bands are located around 300 cm^{-1} , 530 cm^{-1} , and 800 cm^{-1} (the bands are discussed in chapter 3.1.4.4.2). In the fitting routine, the peak positions $x_{anbg,i}$ of the peaks corresponding to the bands are shifted according to the peak shifts of the neighboring first-order Raman peaks that are fitted in the first-order anatase Raman scattering model (see Table 15). In the model for the simulation of 633 nm Raman spectra, both model spectra are added with a certain factors $I_{anbg532}$ and $I_{anbg780}$ that are multiplied with all peak heights in the models. In the fitting routine, the widths of these peaks can be globally changed by multiplying all widths with the fit parameter w_{anbg} . The model for anatase phase backgrounds have these three fit parameters for multi-phase films.

Table 15: Linked parameters of the anatase phase background model

Linked parameter	Description
$x_{anbg,i}$	Positions of the Pseudo-Voigt peaks, linked to the peak shifts of the neighboring first-order Raman peaks that are fitted in the first-order anatase Raman scattering model

We use five more fit parameters for the spectra of films that consist of only anatase and amorphous TiO₂ to make the model more flexible. In this case, the heights and widths of the three bands a, b, and c are treated individually to a certain extent. The heights and widths of the

peaks corresponding to the bands *a* and *c* are multiplied by the factors $I_{anbg,a}$ resp. $I_{anbg,c}$ as well as $w_{anbg,a}$ resp. $w_{anbg,c}$ with lower and upper limits of 0.8 and 1.2.

A further band can be found around 930 cm^{-1} in the spectra of anatase TiO_2 films of this work. A band around 918 cm^{-1} was found by Zeng et al. in undoped TiO_2 in Raman spectra measured with a 473 nm laser.²⁹ This band is simulated by a Pseudo-Voigt peak with $\eta = 0.5$ using the fit parameters position $x_{0,930}$, height h_{930} , and width Δx_{930} . The same applies to a broad band occurring in the spectra of Nb-doped TiO_2 anatase films, which is simulated by a Gaussian function with fit parameters for position $x_{0,Nb}$, height h_{Nb} , and width Δx_{Nb} .

3.2.2.4.2 Crystalline background of brookite

Reference brookite Raman spectra of a 532 nm and a 780 nm laser are available on the RRUFF database as raw and processed spectra.¹²⁵ The processed spectra consist of a first-order Raman spectrum while the raw spectra contain also a background which we interpret as the phase background of brookite. The raw reference spectra of the 532 nm and a 780 nm laser are shown as a light green and a light red line in Fig. 49 (shifted by 800 units on the intensity axis). The corresponding processed reference spectra are shown as a medium green and a medium red line. For both laser wavelengths, we built an individual phase background model spectrum by subtracting the processed spectra from the raw spectra. The resulting spectra were smoothed by averaging the Raman intensity values of adjacent wavenumbers and are used as the brookite background spectra for a 532 nm and a 780 nm laser in our model (dark green and a dark red line, shifted by 800 units on the intensity axis). For the simulation of spectra taken with a 633 nm laser, a new spectrum was generated by taking half of the sum of the 532 nm and 780 nm spectra. [Note: Fig. 40 already depicts the 780 nm spectra¹, but they are shown here again together with the 532 nm spectra for clearer presentation.]

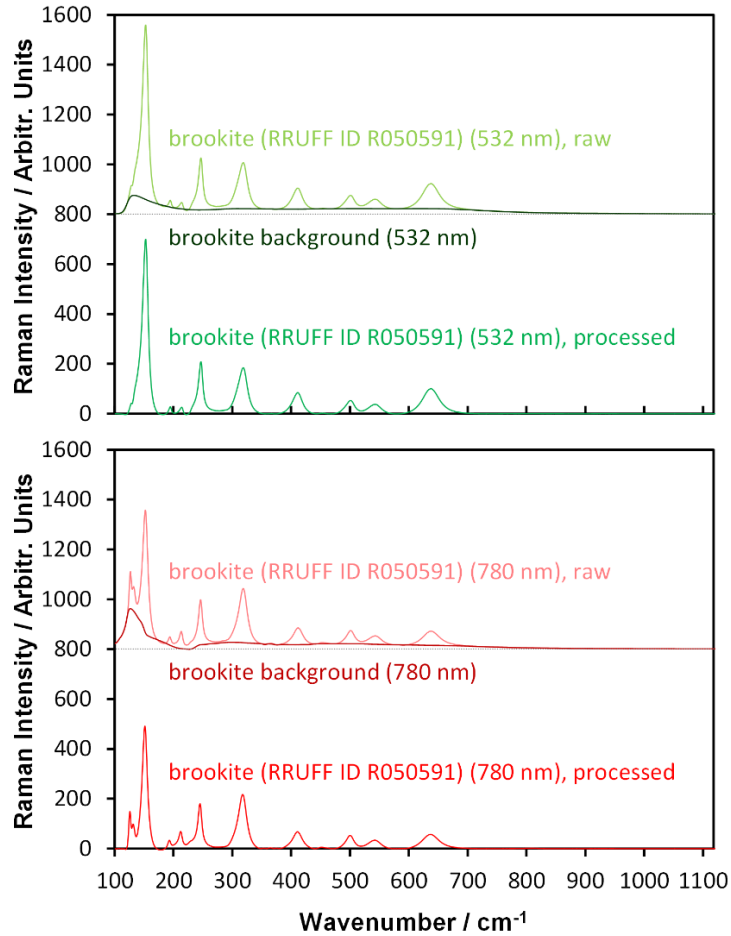


Fig. 49: Literature raw brookite Raman spectra (RRUFF-ID R050591)¹²⁵ produced with a 532 nm (light green line) and a 780 nm (light red line) laser, the corresponding literature ‘processed’ spectra¹²⁵ in medium green and red as well as the corresponding smoothed phase backgrounds in dark green and dark red (raw and processed spectra are shifted by 800 on the intensity axis). The phase background signals are obtained in our work from the remaining spectra after fitting first-order Raman peaks to the reference spectra.

3.2.2.4.3 Crystalline background of rutile

The rutile phase background Raman spectrum was derived analogously to the anatase phase background spectrum. We fitted Lorentzian-peaks for the first-order Raman active modes of rutile to the spectrum by hand until artifacts in the remaining spectrum around the center of the peaks were minimized. The reference spectrum was taken with a 514.5 nm laser and can be found at the Handbook of Raman spectra of the Laboratoire de Géologie, Ecole normale supérieure de Lyon.¹³⁷ Here, only one wavelength was available. Fig. 50 shows the reference spectrum in light blue, the fitted first-order spectrum in medium blue, and the residual rutile phase background spectrum.

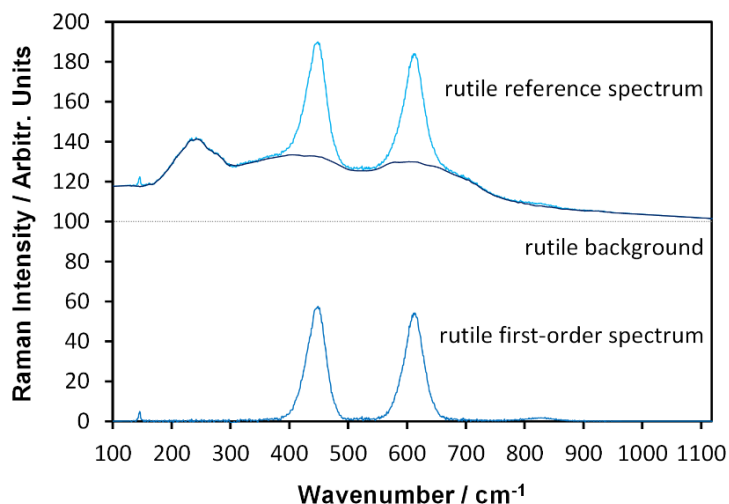


Fig. 50: Rutile reference spectrum (light blue)¹³⁷, rutile phase background (dark blue), both shifted by 100 on the intensity axis; and rutile first-order Raman spectrum (blue). The phase background is obtained in our work from the remaining spectrum after fitting first-order Raman peaks to the reference spectrum.

3.2.3 Raman models for substrate spectra

The TiO_2 thin films analyzed in this work are coated onto three different substrates: Si wafers, B270 glass (crown glass), and fused silica. Fig. 51 shows the Raman spectra of TiO_2 thin films coated simultaneously by diode sputtering onto Si, B270, and fused silica. The left blue intensity-axis is for the spectra of TiO_2 on B270 glass and on fused silica and the right red axis is for the spectrum of TiO_2 on Si. We assign the substrates to two categories: substrates with sharp and intense peaks on the one hand and luminescent substrates on the other hand. Si is a substrate that has intense peaks that are either orders of magnitudes higher (sharp peak at 520.7 cm^{-1}) or in the same order of magnitude (bands around 300 cm^{-1} and 950 cm^{-1}) than the most intense TiO_2 peak. B270 glass and fused silica belong to the luminescent substrates, which show both, Raman activity as well as luminescence. For these substrates, the luminescence is broad and the intensity of the Raman bands is in the order of magnitude of the weak Raman modes of TiO_2 thin film. The models for both types of substrates are described below.

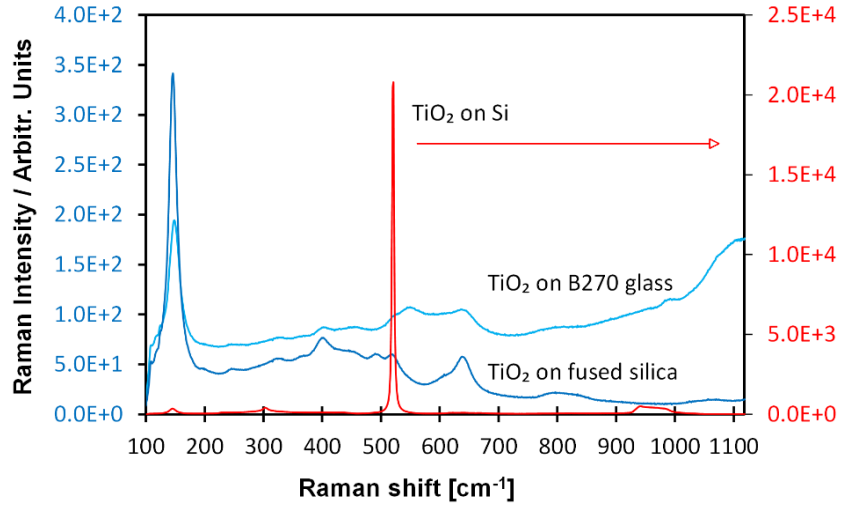


Fig. 51: Raman spectra (produced in this work) of TiO₂ thin films that were simultaneously coated on Si, B270 crown glass, and fused silica in the master’s thesis of M.Sc. Jingyi Shi.

3.2.3.1 Si substrate model

The model for Si substrates has four to seven fit parameters depending on the complexity of the TiO₂ thin film. We measured reference spectra of four individual Si wafers using a 633 nm laser. In the fitting routine, these four reference spectra are added to the total spectrum with a factor I_{Si1} , I_{Si2} , I_{Si3} , or I_{Si4} each. For spectra of TiO₂ films on Si that contain anatase as the only crystalline phase (plus an amorphous content), three more reference spectra are added with the factors I_{Si5-} , I_{Si5} , or I_{Si5+} . These spectra were prepared by measuring a fifth Si wafer in-focus and out-of-focus (in positive and negative z-direction perpendicular to the sample surface). The fit parameters are shown in Table 16.

Table 16: Fit parameters of the anatase phase background model

Fit parameters	Description
$I_{Si1}, I_{Si2}, I_{Si3}, I_{Si4}$	multiplied with the measured reference spectra of 4 individual Si wafers
$I_{Si5-}, I_{Si5}, I_{Si5+}$	for anatase single phase films only: multiplied with 3 reference spectra of a Si wafer with varying laser focus

The wavenumber ranges where the Si peaks are strong (285 cm^{-1} to 315 cm^{-1} , 460 cm^{-1} to 575 cm^{-1} , and 910 cm^{-1} to 1045 cm^{-1}) are excluded from the fit. For further information see the discussion of Fig. P2 and Fig. S5 in chapter 3.1.5.1. A model for the simulation of 532 nm Si spectra was prepared analogously.

3.2.3.2 Models for luminescent substrates

The model for luminescent substrates has 8 fit parameters. The model consists of the spectra of four individual substrates, which we split into a Raman spectrum and a luminescence background, each. The preparation of the spectra is explained in the discussion of Fig. P3 and Fig. S6 in chapter 3.1.5.2. There are four factors ($I_{B270R-1}$, $I_{B270R-2}$, $I_{B270R-3}$, $I_{B270R-4}$) that are multiplied with the corresponding Raman reference spectra and four factors ($I_{B270I-1}$, $I_{B270I-2}$, $I_{B270I-3}$, $I_{B270I-4}$) which are multiplied with the corresponding reference luminescence spectra.

For single-phase films (that consist of an anatase and an amorphous content only) a fit parameter Δx_{B270R} is introduced, which shifts the substrate Raman spectrum by values up to $\pm 1 \text{ cm}^{-1}$ on the wavenumber-axis. The fit parameters are listed in Table 17. For spectra with a high signal-to-noise ratio, the intensities of the individual Raman bands are adjusted by factors between 0.8 and 1.2 (not listed). Four such models were prepared individually: for 532 nm and 633 nm Raman spectra of B270 glass as well as fused silica substrates.

Table 17: Fit parameters of the B270 glass model

Fit parameters	Description
$I_{B270I-1}$, $I_{B270I-2}$, $I_{B270I-3}$, $I_{B270I-4}$	multiplied with the prepared luminescence reference spectra of 4 individual B270 glass samples
$I_{B270R-1}$, $I_{B270R-2}$, $I_{B270R-3}$, $I_{B270R-4}$	multiplied with the prepared reference Raman spectra of 4 individual B270 glass samples
Δx_{B270R}	for anatase single phase films only: shift of the B270 glass Raman spectrum on the wavenumber-axis by $\pm 1 \text{ cm}^{-1}$

3.3 Models for the simulation of X-ray diffractograms

In this chapter, we describe adjustable models for the simulation of TiO₂ thin film X-ray diffractograms. We used the models for the simulation of TiO₂ thin film coated onto B270 glass as well as for fused silica substrates in the range from $2\theta = 22^\circ - 87^\circ$ in chapters 4, 5, and 6. The diffractograms to be fitted contain signals from crystalline phases and from amorphous structures of the TiO₂ thin films as well as from the substrates. An instrument background – and the substrate-holder in θ - θ geometry – are further sources of signals contributing to a measured diffractogram.

In order to analyze the crystalline phases qualitatively or to quantify the various TiO₂ phases within a diffractogram, the measured diffractograms are decomposed into several components by models which are simultaneously fitted to the measured diffractogram by a least squares method. The mathematics behind the fitting routine is done by the *solver* plugin in Microsoft Excel and is similar to the routine described in chapters 3.1.3 and 3.2. The models were developed for two geometries (θ - θ and *grazing incidence* θ - 2θ geometry) analogously. In general, θ - θ geometry provides more reliable information on texture while *grazing incidence* θ - 2θ geometry has a considerably higher signal-to-noise ratio, especially when thin films are measured.

All models were built by analyzing two sets of films. The first set consists of undoped and Nb-doped TiO₂ anatase thin films on B270 glass and fused silica substrates that were prepared by e-beam evaporation by Dipl.-Phys.Ing. Martin Jerman in the optical workshop at the University of Duisburg-Essen and post-heated in this dissertation in the thin film technology group. The second set consists of multi-phase TiO₂ thin films that were prepared by RF magnetron sputtering during the master's thesis *Strukturelle und optische Eigenschaften von RF-Dioden-gesputterten TiO₂-Schichten der Dicke von 2 bis 200 nm* by M.Sc. Jingyi Shi (2015) as well as in the current work in the thin film technology group at the University of Duisburg-Essen.

3.3.1 Main concept of the thin film XRD fitting model

The XRD fitting model consists of models for a TiO₂ thin film, a B270 substrate, and an instrument background (plus a substrate holder in θ - θ geometry). The diffractogram of the TiO₂ thin film is furthermore decomposed into: an amorphous phase diffractogram and diffractograms for the crystalline phases: anatase, brookite, and rutile.

An overview of this thin film XRD fitting model is shown in a flowchart in Fig. 52.

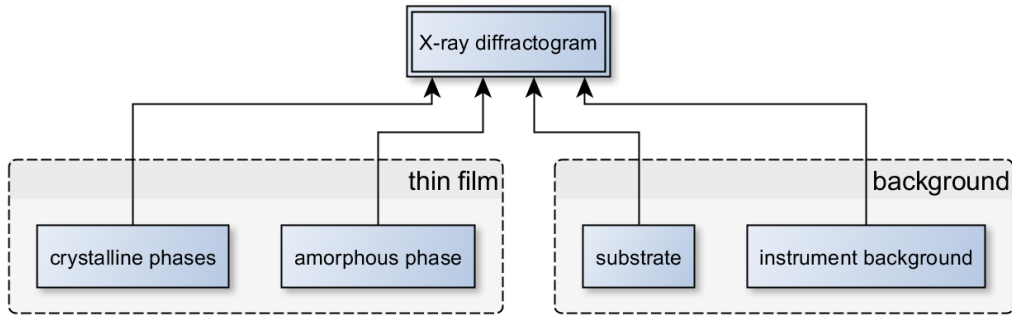


Fig. 52: Overview of the thin film XRD fitting model. The X-ray diffractogram is decomposed into a thin film and a background. The thin film is divided into diffractograms of crystalline phases and an amorphous phase, and the background is divided into diffractograms of the substrate and an instrument background (plus a substrate holder when measured in θ - θ geometry).

Fig. 53 shows an example of a measured *grazing incidence* θ - 2θ X-ray diffractogram of an anatase TiO₂ thin film on a B270 glass substrate and the sub-diffractograms that do not contribute to the TiO₂ thin film diffractogram. Depicted are the diffractogram of a measured TiO₂ thin film on a B270 glass substrate (black), the fit (dashed red), the diffractograms of the substrate (light blue), of the instrument background (dashed blue), and the residual diffractogram (gray) after fitting. The anatase diffractogram (not shown) was fitted by the XRD model for single-phase anatase (see chapter 3.3.3.1).

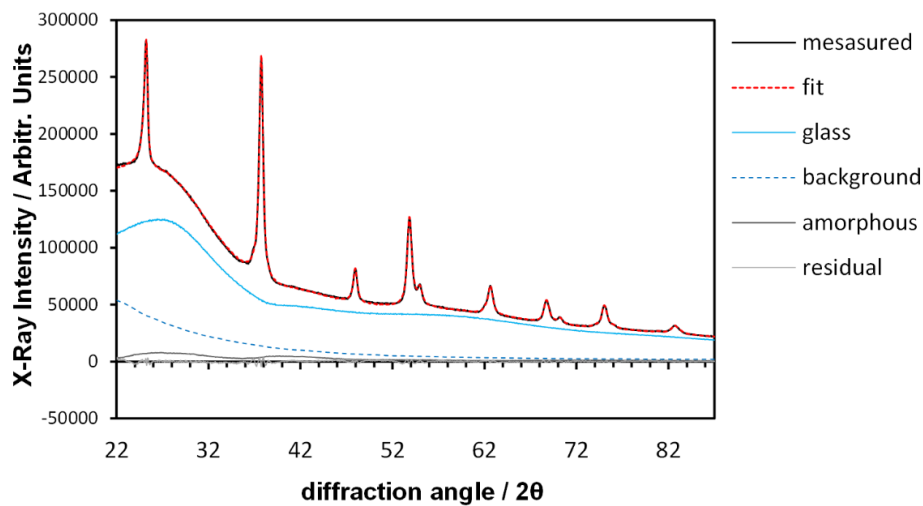


Fig. 53: Example of a measured X-ray diffractogram of an anatase TiO₂ thin film on a B270 glass substrate prepared by e-beam evaporation in the optical workshop at the University of Duisburg-Essen: (black), the fit (dashed red), the diffractograms of the substrate (light blue), of the instrument background (dashed blue), and the residual diffractogram (gray). The anatase diffractogram that contributes to the fit is not shown.

3.3.2 XRD model for the amorphous TiO₂ phase

The amorphous TiO₂ phase XRD model consists of two experimental reference diffractograms and three bands. We derived the ‘reference’ diffractograms of the amorphous TiO₂ thin films analogously to the models for amorphous Raman reference spectra (see chapters 3.1.4.1 and 3.2.2.1). Therefore, we measured X-ray diffractograms of e-beam evaporated undoped and Nb-doped amorphous TiO₂ thin films on B270 glass substrates and diffractograms on the blank backsides of the corresponding substrates. The film of the first diffractogram was coated at a substrate temperature of 250 °C. The diffractogram of the substrate backside was used as a substrate reference diffractogram that was multiplied by a certain factor and stripped from the diffractogram of the coated side of the sample. The factor was varied until the remaining diffractogram did not contain visible features of the pure glass diffractogram. Analogously, a second reference diffractogram was produced for an amorphous Nb-doped TiO₂ film that was post-heated at 350 °C. Both reference diffractograms are shown in Fig. 54.

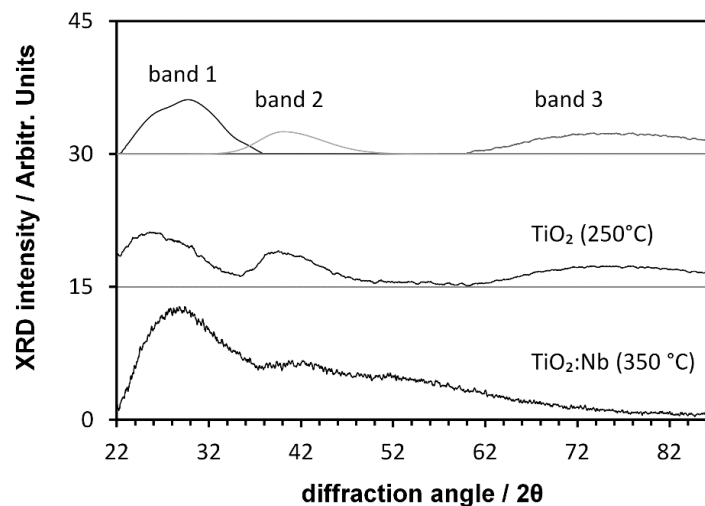


Fig. 54: Reference diffractograms of amorphous TiO₂ samples prepared by e-beam evaporation in the optical workshop at the University of Duisburg-Essen and additional bands modeled by the XRD model of amorphous TiO₂.

In the amorphous TiO₂ phase XRD model, both diffractograms are added to the total diffractogram after multiplying it with the parameter I_{am250} or I_{am350} . As one can see in Fig. 54, the characteristics of the diffractograms of amorphous TiO₂ differ more than the Raman spectra of amorphous TiO₂ (cf. Fig. 38). The main differences of the two are a broad band between $2\theta = 60^\circ - 90^\circ$ which occurs in the diffractogram of the as-deposited TiO₂ film and a broad increase of intensity to smaller diffraction angles in diffractogram of the Nb-doped TiO₂ film (post-heated at 350 °C).

The diffractograms of the amorphous phase in the films analyzed in the work differ from both diffractograms. Therefore, three bands are added to this model (see Fig. 54). Band 1 lies in the range $2\theta = 22^\circ - 38^\circ$. It was derived from the difference-diffractograms of a further Nb-doped TiO₂ thin film on B270 glass post-heated at 500 °C (not shown) and of the above-mentioned second diffractogram of the Nb-doped TiO₂ film that was post-heated at 350 °C. Band 2 is a Gaussian peak that is modeled with the fit parameters (left and right) half-widths $\Delta x_{l,am2}$ and $\Delta x_{r,am2} > 3^\circ$, a peak position $40^\circ < x_{0am2} < 55^\circ$, and a peak height A_{am2} . Band 3 is copied from the reference diffractogram of the as-deposited TiO₂ film (250 °C) in the range $2\theta = 60^\circ - 90^\circ$. Band 1 and 3 are added to the model after multiplying the band 1 and band 3 diffractograms with the parameters I_{am1} or I_{am3} . The discussed fit parameters are listed in Table 18.

Table 18: Fit parameters of the amorphous TiO₂ phase XRD model

Fit parameters	Description
I_{am250}, I_{am350}	multiplied with the reference diffractograms of the amorphous films coated at 250 °C as-deposited or post-heated at 350 °C
I_{am1}	multiplied with the intensity of band 1 at $\theta = 20^\circ - 30^\circ$
$x_{0am2}, A_{am2}, \Delta x_{l,am2}, \Delta x_{r,am2}$	position, height, and widths (left & right) of band 2 (Gaussian peak) at $\theta = 40^\circ - 55^\circ$
I_{am1}	multiplied with the intensity band 3 at $\theta = 60^\circ - 90^\circ$

3.3.3 XRD models of crystalline phases

The adjustable model diffractograms used for simulating the crystalline TiO₂ phases are of varying simplifications depending on the complexity of the diffractogram to be simulated. Anatase and rutile are simulated by manipulating Lorentzian functions for each individual peak while brookite is simulated by reference diffractograms which are manipulated by global parameters. All XRD peaks of anatase and rutile are fitted by asymmetric Lorentzian peaks. Equations (57) and (58) are used to simulate each XRD peak as a doublet that considers the splitting of the Cu K_α line into Cu K_{α1} and Cu K_{α2} emission:

$$I = A \left[\left(\frac{\frac{100}{151}}{1 + \left(\frac{x - x_0}{\Delta x_l} \right)^2} \right) + \left(\frac{\frac{51}{151}}{1 + \left(\frac{x - \sin^{-1} \left(\frac{1.54433}{1.54051} \sin \left(\frac{x_0}{2} \right) \right)}{\Delta x_l} \right)^2} \right) \right] \text{ for } x \leq x_0, \quad (57)$$

$$I = A \left[\left(\frac{\frac{100}{151}}{1 + \left(\frac{x-x_0}{\Delta x_r} \right)^2} \right) + \left(\frac{\frac{51}{151}}{1 + \left(\frac{x - \sin^{-1} \left(\frac{1.54433}{1.54051} \sin \left(\frac{x_0}{2} \right) \right)}{\Delta x_r} \right)^2} \right) \right] \text{ for } x \geq x_0. \quad (58)$$

with the diffraction angle x and the four peak parameters amplitude A , peak position x_0 , and half-widths Δx_l and Δx_r , an intensity ratio of $100/51$ and a wavelength ratio of $1.54433/1.54041$ the $Cu K_{\alpha 1}$ and $Cu K_{\alpha 2}$ emission.¹³⁸ Each peak parameter is corrected by polynomial functions which are based on measurements that we performed on LaB_6 660 a standard reference powder individually for both geometries. Therefore, the peak positions, heights, and half-widths (left and right) were fitted to the LaB_6 diffractograms. The fit results of the LaB_6 diffractograms are used for the polynomial correction of the measured diffractograms in our studies. In the fitting routine, the corrected peaks are then fitted to the measured diffractograms. Single phase anatase films are simulated by adjusting each peak parameter separately while the peaks of anatase and rutile are simulated by global parameters.

3.3.3.1 XRD model for single-phase anatase

In the XRD model for single-phase anatase each peak parameter is fitted separately. This model was used for fitting measured diffractograms of e-Beam evaporated TiO_2 thin films. Table 19 shows the fit parameters used for each diffraction peak.

Table 19: Fit parameters for each individual peak of the single-phase anatase XRD model

Fit parameters	Description
$x_{0i(an)}, A_{i(an)}, \Delta x_{i,l(an)}, \Delta x_{i,r(an)}$	peak position, amplitude, half-width (left & right)

For the three series of experiments of undoped and Nb-doped films each peak was fitted individually for the most crystalline films post-heated at 640 °C and 750 °C. The ratios of the peak widths between the weakest and the neighboring stronger peaks were kept constant for each experimental series and used for the films post-heated at lower temperatures.

3.3.3.2 XRD models for multi-phase anatase and rutile

For multi-phase TiO_2 films, the models for anatase and rutile are simplified as compared to the single-phase anatase XRD model. Here, the models for both phases are analogous. Before fitting, the peak positions and intensity ratios are set to the values of standard powder anatase or rutile. The peak positions are calculated according to the fit parameters, $a_{(an)}$, $c_{(an)}$, or $a_{(ru)}$, $c_{(ru)}$, which are the lattice parameters of anatase and rutile. The height and width of the (101) anatase peak and (110) rutile peak are fitted by one parameter each $A_{(101)(an)}$, $\Delta x_{(101)(an)}$ or

$A_{(110)(ru)}$, $\Delta x_{(110)(ru)}$. These peaks are at the lowest diffraction angle of the corresponding phase and are the most intense for powder samples. Another parameter, $\Delta x_{(x)(an)}$ or $\Delta x_{(x)(ru)}$, is for peak broadening with increasing diffraction angle. A parameter for simulating texture is $\Delta A_{(c)(an)}$ or $\Delta A_{(c)(ru)}$ which increases the height of the (hkl) peaks with increasing $l^2/(h^2+k^2)$. This simulates the preference ($\Delta A_{(c)} > 1$) or suppression ($\Delta A_{(c)} < 1$) of c -oriented grains. The parameters are listed in Table 20.

Table 20: Fit parameters of the multi-phase anatase and rutile XRD models

Fit parameters	Description
$a_{(an)}, c_{(an)},$ $a_{(ru)}, c_{(ru)}$	lattice parameters a and c of anatase or rutile
$A_{(101)(an)}, \Delta x_{(101)(an)},$ $A_{(110)(ru)}, \Delta x_{(110)(ru)}$	anatase (101) height & width rutile (110) height & width
$\Delta x_{(\theta)(an)},$ $\Delta x_{(\theta)(ru)}$	parameters for varying anatase or rutile peak widths with increasing diffraction angle
$\Delta A_{(c)(an)}$ $\Delta A_{(c)(ru)}$	parameters for varying anatase or rutile (hkl) peak heights of c -oriented reflections with increasing l

3.3.3.3 XRD models for minor-phase brookite

In this work, brookite is weakly present in a small number of diffractograms. Brookite diffractograms have a high number of peaks. Considering both aspects, the brookite XRD model is kept simple. That is why the model of this phase is rather mathematical than physical. The brookite model was designed by manipulating a reference diffractogram found in the RRUFF database.¹²⁵ The square root of the intensity was taken at each diffraction angle in order to build an artificial second reference diffractogram in which the peak heights of the weaker peaks are relatively higher. The second model aims at taking relative peak heights into account that do not match with powder diffractograms, which might be caused for example by texture. Both reference diffractograms are shown in Fig. 55 normalized to a maximum intensity of 1000 cps as a black and a gray line. The reference diffractograms are multiplied with a fit factor each, $I_{br(lit.)}$ or $I_{br(mod.)}$, and then summed to the brookite model diffractogram. This brookite model diffractogram is shifted on the 2θ -axis by the fit parameter Δd . A global factor w_{br} simulates peak broadening by adding multiple copies of the simulated brookite model diffractogram to a certain amount in the range of plus and minus 0.2° on the 2θ -axis. The manipulation of the width is adjusted a priori by hand. The fit parameters are listed in Table 21

Table 21.

Table 21: Fit parameters of the minor-phase brookite XRD model

Fit parameters	Description
$I_{br(lit.)}, I_{br(mod.)}$	multiplied with the literature diffractogram or the artificial reference diffractogram
Δd	parameter for shifting the modeled diffractogram along the diffraction axis
w_{br}	parameter for varying the widths in the modeled brookite diffractogram (adjusted a priori by hand)

Examples of simulated brookite diffractograms with broad and narrow peaks are shown in Fig. 55 as a dark green and a medium green line (shifted by 1000 cps). This model is not suitable for modeling precise brookite diffractograms but is used for the quantification of the brookite content only. Anyway, the measured diffractograms do not contain adequate brookite features to be fitted. In this work, qualitative analysis of the brookite diffractograms is done by manually measuring the peak widths of the strongest peaks by hand independently of this model.

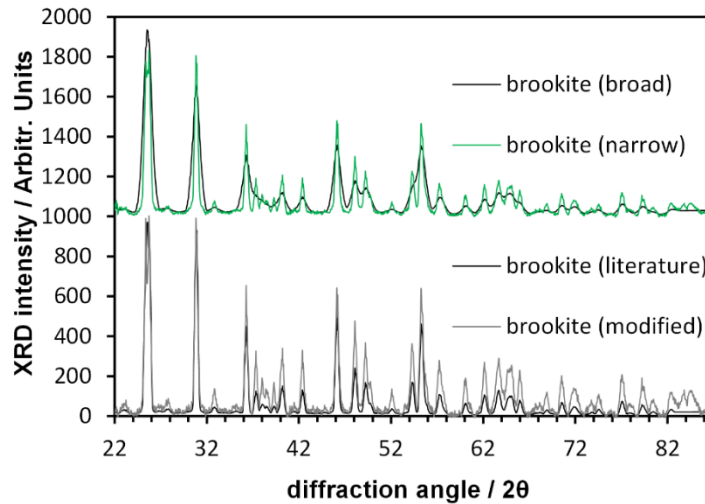


Fig. 55: Brookite diffractograms: examples of a broad (dark green) and a narrow (medium green) modeled diffractogram (shifted by 1000 on the intensity axis), a literature diffractogram (black)¹²⁵ and a modification (done in the current work) of the literature diffractogram normalized to 1000 intensity units.

3.3.4 XRD models for substrates and background

There are two or three fit parameters for the diffractograms of the substrates and background signals model depending on the geometry of the diffraction scan. In both

geometries used in this work (*grazing incidence θ - 2θ* and *θ - θ* geometry), an instrument background and the substrate contribute to the measured diffractograms. In diffractograms measured in *θ - θ* geometry, also signals for the substrate holder are present.

The instrument background depends on various parameters used in the experiments, such as the choice of the X-ray source, the detector, divergence slits, collimators, and the geometry of the experimental setup. A reference instrument background was measured after dislocating the sample and the sample-holder from the X-ray beam. We furthermore measured reference substrate diffractograms of uncoated B270 glass, fused silica ('quartz'), and Si wafers individually for each of both geometries. A reference diffractogram of a self-made substrate holder was measured in *θ - θ* geometry. The corresponding diffractograms are shown in Fig. 56.

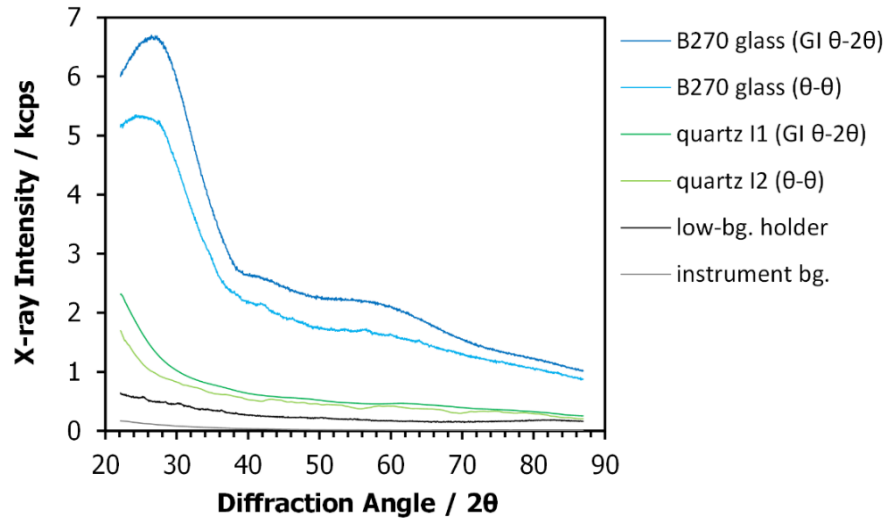


Fig. 56: X-ray diffractograms of a B270 glass substrate in *grazing incidence θ - 2θ* geometry (dark blue) and in *θ - θ* geometry (light blue), of a fused silica substrate in *grazing incidence θ - 2θ* geometry (dark green) and in *θ - θ* geometry (light green), a self-made low-background holder in *θ - θ* geometry (black), and the instrument background (gray).

For the simulation of diffractograms in both geometries, the reference instrument-background diffractogram and the reference substrate diffractogram are added to the total diffractogram by multiplying the corresponding reference diffractograms with the factors $I_{instr.bg}$, and $I_{sub(\theta-2\theta)}$ or $I_{sub(\theta-\theta)}$. Additionally, for the simulation of *θ - θ* gonio diffractograms, the substrate holder reference diffractogram is added with the factor I_{holder} . The fit parameters are listed in Table 22.

Table 22: Fit parameters for the substrate and background XRD models

Fit parameters	Description
$I_{instr.bg}, I_{sub(\theta-2\theta)}$	multiplied with reference diffractograms of: - the instrument background - the substrate in <i>grazing incidence</i> $\theta-2\theta$ geometry (model for <i>grazing incidence</i> $\theta-2\theta$ geometry)
$I_{instr.bg}, I_{sub(\theta-\theta)},$ I_{holder}	multiplied with reference diffractogram of: - the instrument background - the substrate in $\theta-\theta$ geometry - substrate holder in $\theta-\theta$ geometry (model for $\theta-\theta$ geometry)

4 Decomposed X-ray diffractograms and Raman spectra

In the following, we demonstrate measured X-ray diffractograms and Raman spectra of TiO₂ thin films on B270 glass, fused silica and Si wafers decomposed into several components arising from the thin films, the substrates, and from experimental backgrounds. The thin film diffractograms and spectra are subdivided into contributions from anatase, brookite, rutile, and amorphous TiO₂. For the decomposition, we simulate adjustable models of X-ray diffractograms and Raman spectra and fit them to the measured X-ray diffractograms and Raman spectra as developed in chapter 3.

We decomposed X-ray diffractograms measured in *grazing incidence* θ - 2θ as well as in θ - θ geometry. In this chapter we focus on the *grazing incidence* θ - 2θ diffractograms. They were used for the quantification of the TiO₂ phases because they do not show signals arising from the substrate holder and they have a significantly higher signal-to-noise ratio than the θ - θ diffractograms. An example of a θ - θ diffractograms is shown in the appendices in Fig. 168. It shows the diffractogram of a Ti_{0.84}O_{2.25}Nb_{0.16} film on B270 glass containing strong substrate holder signals.

The measurements and decompositions of X-ray diffractograms and Raman spectra were performed on two set of samples: rf-diode sputtered films and films prepared by reactive e-beam evaporation. The sputtered films are multi-phase TiO₂ and the evaporated films are – partly amorphous – anatase films that contain traces of brookite and rutile. A further decomposed Raman spectrum of the best conducting rf-magnetron sputtered film (placed *12.5 mm* horizontally from the Nb wire coated with a target oxidation of *68%*) is shown in Fig. 169 in the appendices.

The preparation of the thin films is described in chapter 2.1 and measurement details are described in chapter 2.2. Quantitative analysis on the individual Raman spectra X-ray diffractograms can be found in chapter 5, and qualitative analysis in chapter 6.

The decomposition of the PEM rf-magnetron sputtered films are performed analogously and not shown here. Instead, the resulting TiO₂ thin film spectra are directly presented in Fig. 124 in chapter 6.1.3.3.

4.1 Decomposed X-ray diffractograms and Raman spectra of rf-diode sputtered multi-phase TiO₂ films

In this chapter, we demonstrate the decomposition of measured diffractograms and measured Raman spectra (using *532 nm* and *633 nm* laser excitation) of multi-phase TiO₂ thin films that were rf-diode sputter coated onto B270 glass at various substrate temperatures. The

deposition parameters are given in chapter 2.1.1. The diffractogram and Raman spectra of the sample deposited at a substrate temperature of $310\text{ }^{\circ}\text{C}$ are discussed in detail. This sample was chosen because it showed the most distinct brookite signals in the X-ray diffractogram. The Raman spectra and X-ray diffractograms are evaluated quantitatively in chapter 5.2 and qualitatively in chapter 6.1.1.

Raman spectra of TiO_2 thin films deposited at a substrate temperature of $415\text{ }^{\circ}\text{C}$ are chosen to demonstrate the decomposition of multi-phase TiO_2 Raman spectra on various substrates because they show the most pronounced multi-phase TiO_2 Raman spectra. These spectra are quantitatively evaluated in chapter 5.3.

4.1.1 Decomposed multi-phase TiO_2 X-ray diffractograms

The X-ray diffractograms are decomposed into sub-diffractograms represented by adjustable model diffractograms including anatase, rutile, brookite, amorphous TiO_2 , substrate, and instrument background. Adjustable model spectra were fitted simultaneously to the experimental diffractograms, with good results. The models used are described in chapter 3.3. The diffractograms of anatase and rutile are decomposed by the multi-phase model as described in chapter 3.3.3.2, in which the (hkl) peak positions are modeled by the lattice parameters, a and c , as the only adjustable parameters. LaB_6 correction (see chapter 2.2.3) is implemented into the fitting routine. The X-ray diffractograms were measured in grazing incidence θ - 2θ geometry with a constant incident angle of 7° . This geometry provides a higher signal-to-noise ratio for thin films than the symmetrical goniometry, which is more suitable for the analysis of texture. The decomposition of an X-ray diffractogram of a TiO_2 thin film on a B270 crown glass substrate deposited at $310\text{ }^{\circ}\text{C}$ is shown in Fig. 57.

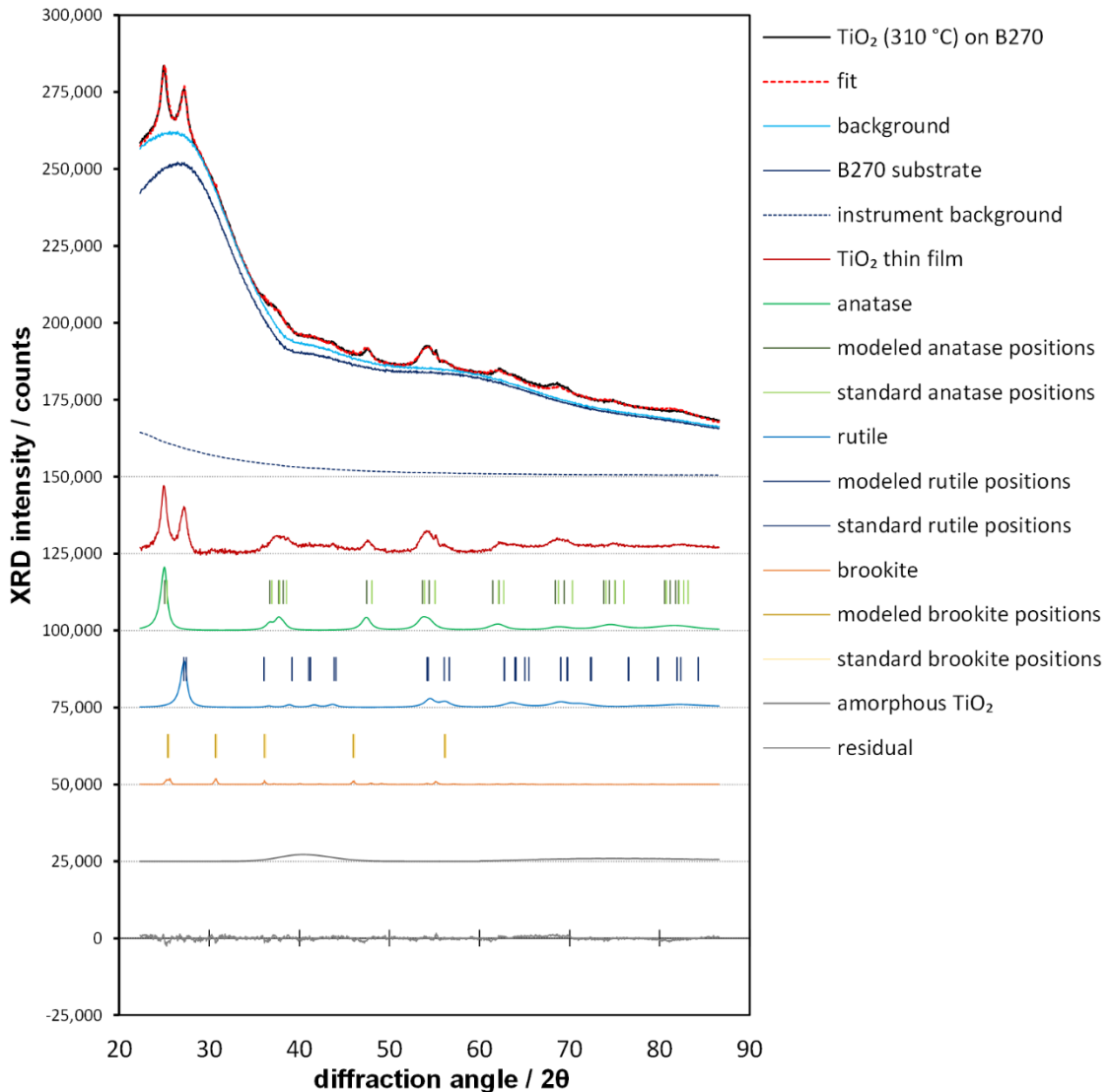


Fig. 57: Decomposition of a measured X-ray diffractogram of a rf-sputter coated TiO₂ thin film on a B270 crown glass substrate deposited at 310 °C (black) into a background (light blue) and the thin film (dark red). The background is split into the B270 substrate (medium blue) and an instrument background (dashed dark blue). The film is further decomposed into anatase (green), brookite (orange), rutile (blue), and amorphous TiO₂ (medium gray). The residual diffractogram is light gray and the fit of the modeled diffractogram to the measured one is the dashed red line. Peak positions of standard powder are added as light and the modeled peak positions are added as vertical lines. The graphs are shifted on the intensity axis (indicated by dotted baselines) as described in the text.

The measured diffractogram (black line) is split into a background (light blue) and a TiO₂ thin film diffractogram (dark red). The background diffractogram is composed of an instrument background (dashed blue) and a B270 substrate diffractogram (dark blue). The TiO₂ thin film diffractogram is composed of anatase (green), brookite (orange), rutile (blue), and amorphous TiO₂ (gray) diffractograms. The fit (dashed red line) is the sum of all sub-diffractograms, and the residual diffractogram (light gray) is the difference diffractogram of the measured diffractogram and the fit. The standard peak positions of the crystalline phases are indicated as

light vertical lines and the fitted positions as dark vertical lines (both after LaB₆ correction). For brookite, only the most intense peaks of powder diffractograms are indicated. The TiO₂ sub-diffractograms are each shifted in steps of 25 000 counts, and the measured diffractogram, the fit, and the background diffractograms are shifted by 150 000 counts on the XRD intensity Axis. The decomposed diffractograms of the films deposited with the substrates temperatures 155 °C, 200 °C, 275 °C, and 415 °C can be found in the appendices in (Fig. 170 to Fig. 173).

The model XRD diffractograms could be fitted to the measured diffractograms with a low residual signal. Anatase, rutile and amorphous TiO₂ is detected in all diffractograms. The diffractograms of anatase and rutile are well distinguishable. Certain individual peak positions, such as the anatase (004) peak at $2\theta = 37^\circ$, the anatase (200) peak at $2\theta = 48^\circ$, or the peaks in the range of diffraction angles of $2\theta > 60^\circ$, do not fit well with the measured diffractograms. This trend increases with increasing deposition temperature and thus with increasing anatase and brookite content in the films (see chapter 5.2). For further analysis of the lattice, they have to be corrected by hand after the fitting routine. The discrepancies are most likely not an artefact of poor LaB₆ peak position correction, because the peak positions of the multi-phase model fit well for an e-beam coated TiO₂ anatase thin film with an undistorted lattice (see chapter 4.2.1). We suppose that the peak shifts are caused by asymmetric lattice distortion. This is not implemented into the models. There measured diffractograms of the films also differ in the range of $2\theta = 60^\circ - 70^\circ$. Here, the measured diffractograms of the films deposited at 310 °C and 415 °C have a plateau between the peaks, which could be caused by an inhomogeneous distribution of phase boundaries or an indication of texture.

Brookite is found in the diffractograms of the samples deposited at 310 °C and 415 °C (see Fig. 173 in the appendices), but is not detected in the diffractograms deposited at 155 °C, 200 °C, and 275 °C (see Fig. 170, Fig. 171, and Fig. 172). In the diffractogram of the film deposited at 310 °C, there is a considerable and sharp peak at 55°, which can be attributed to brookite, but most brookite peaks are not visible. In the diffractograms of the film deposited at 415 °C, only traces of brookite can be found with a few visible peaks with intensities that are close to the photon shot noise. The findings imply that the sensitivity of XRD to brookite is low as compared to Raman spectroscopy, where we found brookite signals in the spectra of all samples (see chapter 4.1.2). A similar result was found for partially crystallized TiO₂ anatase thin films that contain traces of brookite (see chapter 4.2.2). The sensitivities to the various TiO₂ phases are analyzed in the chapter 5.2 and 5.4 for both sets of TiO₂ films. The brookite (210) peak at $2\theta = 25.4^\circ$, which is the most intense peak of brookite powder diffractograms, is superimposed by the anatase (101) peak, which is the most intense peak of anatase powder

diffractograms. Anyway, the position of the second strongest brookite peak (*211*), at $2\theta = 30.8^\circ$, is not superimposed by any anatase or rutile peak. Yet, XRD is ill suited for the detection of small brookite amounts in TiO₂ diffractograms because of the low signal-to-noise ratio caused by the low intensity of brookite.

4.1.2 Decomposed multi-phase TiO₂ 633 nm and 532 nm Raman spectra

The Raman spectra are decomposed into sub-spectra represented by adjustable model spectra that are discussed in chapter 3.1 and defined in chapter 3.2. Fig. 58 and Fig. 59 show the decomposition of a 633 nm Raman spectrum and, respectively, a 532 nm Raman spectrum of a TiO₂ thin film on a B270 crown glass substrate deposited at 310 °C. The decomposed Raman spectra of the films deposited with the substrates temperatures 155 °C, 200 °C, 275 °C, and 415 °C can be found in the appendices in Fig. 174 to Fig. 177 (633 nm laser) and in Fig. 178 to Fig. 181 (532 nm laser). The Raman spectra measured with the 532 nm laser has a higher relative amount of photon shot noise because it was measured for 100 s while the spectra taken with the 633 nm laser were iterated from measurements adding up to 14641 s (see chapter 2.2.1).

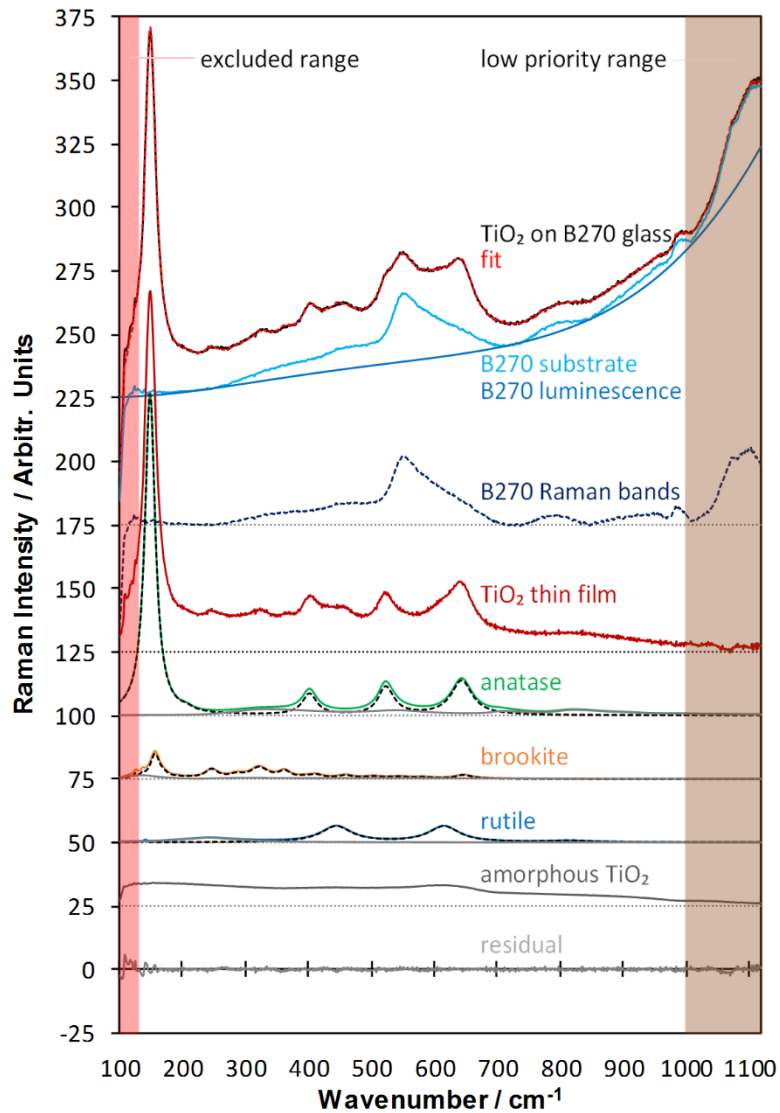


Fig. 58: Decomposition of a TiO₂ film 633 nm Raman spectrum (on B270 deposited at 310 °C) into anatase, rutile, brookite, amorphous TiO₂, substrate, and instrument background (intensity shift: see text).

The measured Raman spectrum (black line) is decomposed into a B270 glass substrate spectrum (light blue) and a TiO₂ thin film spectrum (dark red). The substrate spectrum is composed of a Raman footprint (dashed blue) and a luminescence spectrum (dark blue). The TiO₂ thin film spectrum is split into spectra of anatase (green), brookite (orange), rutile (blue), and amorphous TiO₂ (gray). The first-order Raman spectra of the crystalline phases are indicated as dashed black lines and the phase backgrounds are shown as gray lines. The fit (dashed red line) is the sum of all sub-spectra, and the residual spectrum (light gray) is the difference spectrum of the measured spectrum and the fit. The TiO₂ sub-spectra are each shifted in steps of 25 counts (in Fig. 58) or 15 counts (in Fig. 59) and the measured spectrum, the fit, and the glass spectra are shifted by 175 counts (in Fig. 58) or 105 counts (in Fig. 59) on the Raman intensity axis.

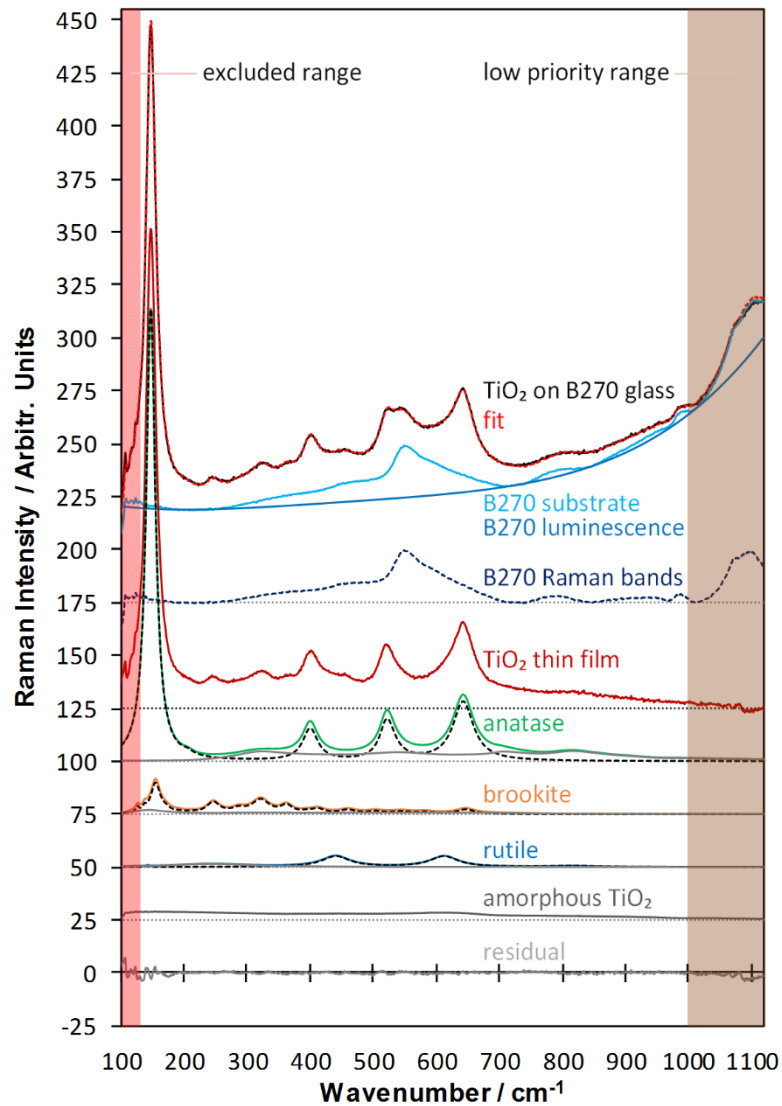


Fig. 59: Decomposition of a TiO₂ film 532 nm Raman spectrum (on B270 deposited at 310 °C) into anatase, rutile, brookite, amorphous TiO₂, substrate, and instrument background (intensity shift: see text).

Each of the TiO₂ phases, anatase, rutile, brookite and amorphous TiO₂ is visible in all Raman spectra. The most intense brookite Raman peak, A1g at 155 cm⁻¹ is overlain by the anatase Eg(1) peak at 146 cm⁻¹. Yet, the spectral range of the brookite Raman modes A1g at 247 cm⁻¹, B3g at 287 cm⁻¹, B1g at 322 cm⁻¹, and B2g at 364 cm⁻¹ do overlay neither with the first-order Raman spectra of the other TiO₂ phases nor with sharp features of the B270 glass footprints. As we will discuss in the chapter 5.2 and 5.4, Raman is highly sensitive to brookite. With the strong intensity of brookite, this constellation of peak positions makes Raman suitable for detecting small contents of brookite in TiO₂ Raman spectra.

4.1.3 Decomposed TiO₂ spectra on Si, crown glass, and fused silica

*[This chapter is part of a publication in the Journal of Raman Spectroscopy, Volume 49, Issue 7, 1217-1229 (2018).]*¹ Copyright © 2018 John Wiley & Sons, Ltd.

Fig. 60, Fig. 61, and Fig. 62 show measured Raman spectra of mixed-phase TiO₂ thin films that were deposited onto Si, B270 glass, and fused silica, respectively, by rf-diode sputtering at the same time in one deposition process. Each of the three spectra are decomposed into substrate and thin film, and the film further into the various TiO₂ phases. The transparent red areas are excluded from the fitting routine and the brown areas are fitted with low priority (10%). Each figure shows a measured (black) and modeled (dashed red) spectrum of mixed-phase TiO₂ thin film on the corresponding substrate decomposed into substrate (light blue) and thin film (dark red). The thin film is decomposed into anatase (green), brookite (orange), rutile (blue), and amorphous (dark gray) spectra. The crystalline spectra are divided into first-order scattering (black dashed lines) and phase background (light gray lines). In Fig. 61 and Fig. 62, the substrate spectrum is split into luminescence (mid blue) and Raman bands (dashed dark blue).

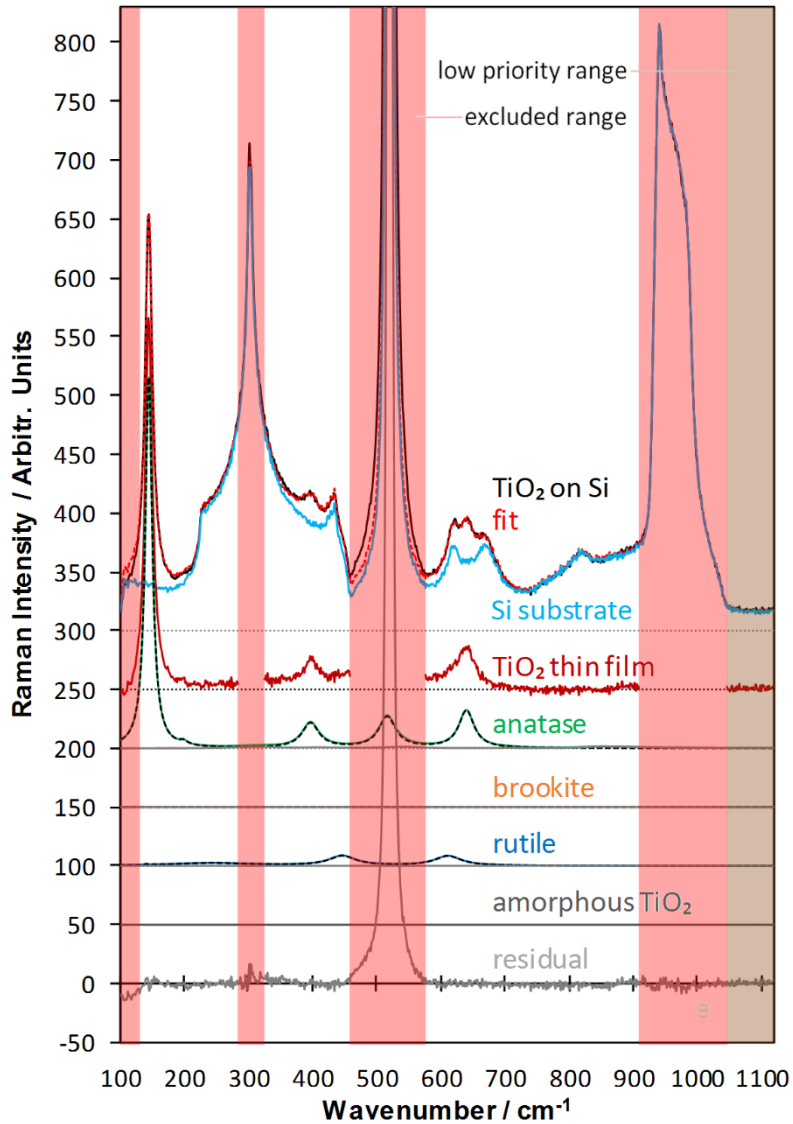


Fig. 60: Measured (black) and modeled (dashed red) Raman spectrum of an rf-diode sputtered mixed-phase TiO₂ thin film on a Si substrate decomposed into substrate (light blue) and thin film (dark red). The thin film is decomposed into anatase (green), brookite (orange), rutile (blue), and amorphous TiO₂ (dark gray) spectra. The residual spectrum is medium gray. The crystalline spectra are divided into first-order scattering (black dashed lines) and phase background (light gray lines). The heights of the Si peak and the residual spectrum at 520.7 cm⁻¹ are 21000 and 10000 Raman intensity units. The excluded ranges are light red and the low priority range is light brown. Intensity shifts are indicated by dotted lines.

In Fig. 60, the fit is successful in the ranges that are not excluded from the fit. The huge error of the Si peak around 520.7 cm⁻¹ clearly indicates that the exclusion of this peak from the fit is necessary to apply the fitting model to the spectrum. Also, the artefacts in the residual spectrum within the other excluded ranges (red) show that not omitting these ranges would corrupt the fit.

The exclusion of the range around the sharp edge of the Si spectrum at 300 cm⁻¹ does not strongly interfere with the amorphous thin film spectrum. However, the high number of excluded ranges hinder accuracy in the fitting of the amorphous spectrum. Furthermore, the

anatase A1g/B1g doublet around 517 cm^{-1} is completely overlain by the 520.7 cm^{-1} Si peak. For a quantification of the anatase content, we model the doublet with a fixed position at 517 cm^{-1} and fixed width and height ratios between the doublet and the single B1g peak around 400 cm^{-1} . After the subtraction of the substrate spectrum, the pure TiO_2 thin film spectrum remains without strong artefacts of the Si spectrum in the non-excluded fit ranges. The peaks of the main phase, anatase, as well the strongest rutile peaks are clearly visible in the TiO_2 thin film spectrum, and are fitted to the spectrum.

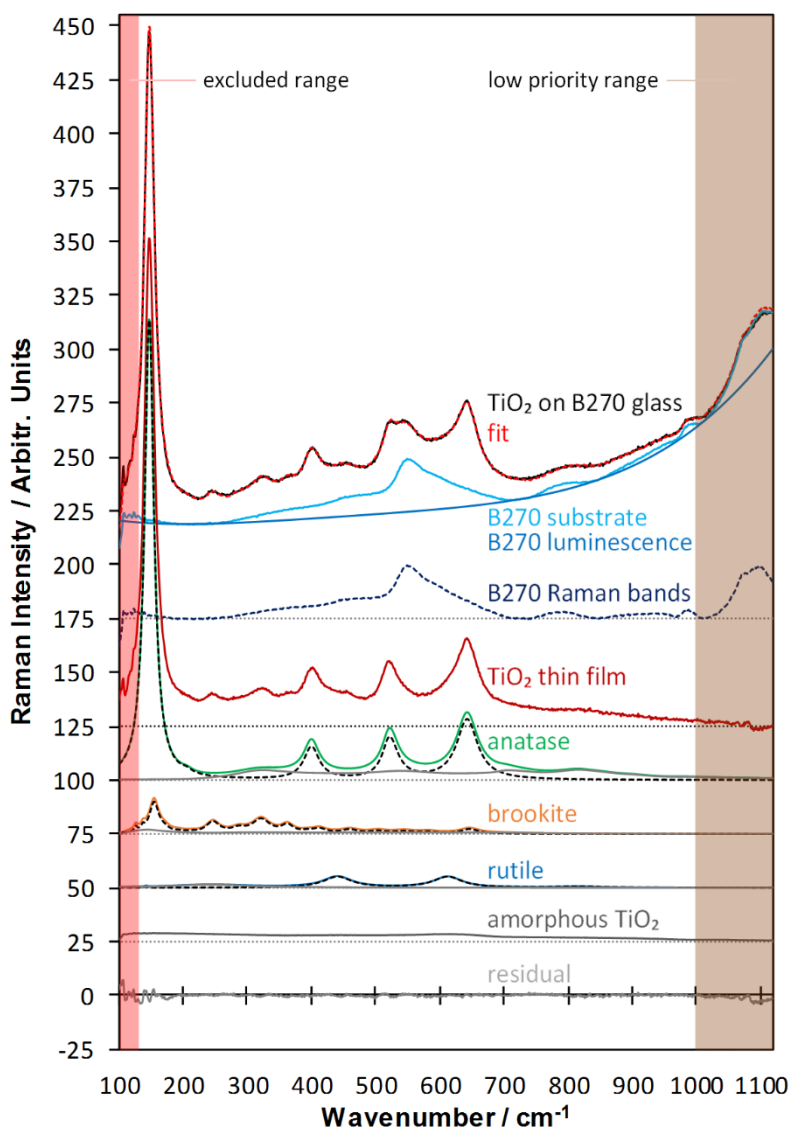


Fig. 61: Measured (black) and modeled (dashed red) Raman spectrum of an rf-diode sputtered mixed-phase TiO_2 thin film on B270 glass decomposed into substrate (light blue) and thin film (dark red). The substrate spectrum is split into luminescence (mid blue) and Raman bands (dashed dark blue) and the thin film is decomposed into anatase (green), brookite (orange), rutile (blue), and amorphous TiO_2 (dark gray) spectra. The residual spectrum is medium gray. The crystalline spectra are divided into first-order scattering (black dashed lines) and phase background (light gray lines). The excluded range is light red and the low priority range is light brown. Intensity shifts are indicated by dotted lines.

In Fig. 61 and Fig. 62, all four TiO₂ phases that occur at ambient pressure contribute to the thin film spectrum. While anatase is also the main phase and the broad peaks around 445 cm⁻¹ and 611 cm⁻¹ indicate the presence of rutile, the peaks at 247 cm⁻¹, 325 cm⁻¹, and 364 cm⁻¹ indicate the presence of brookite.

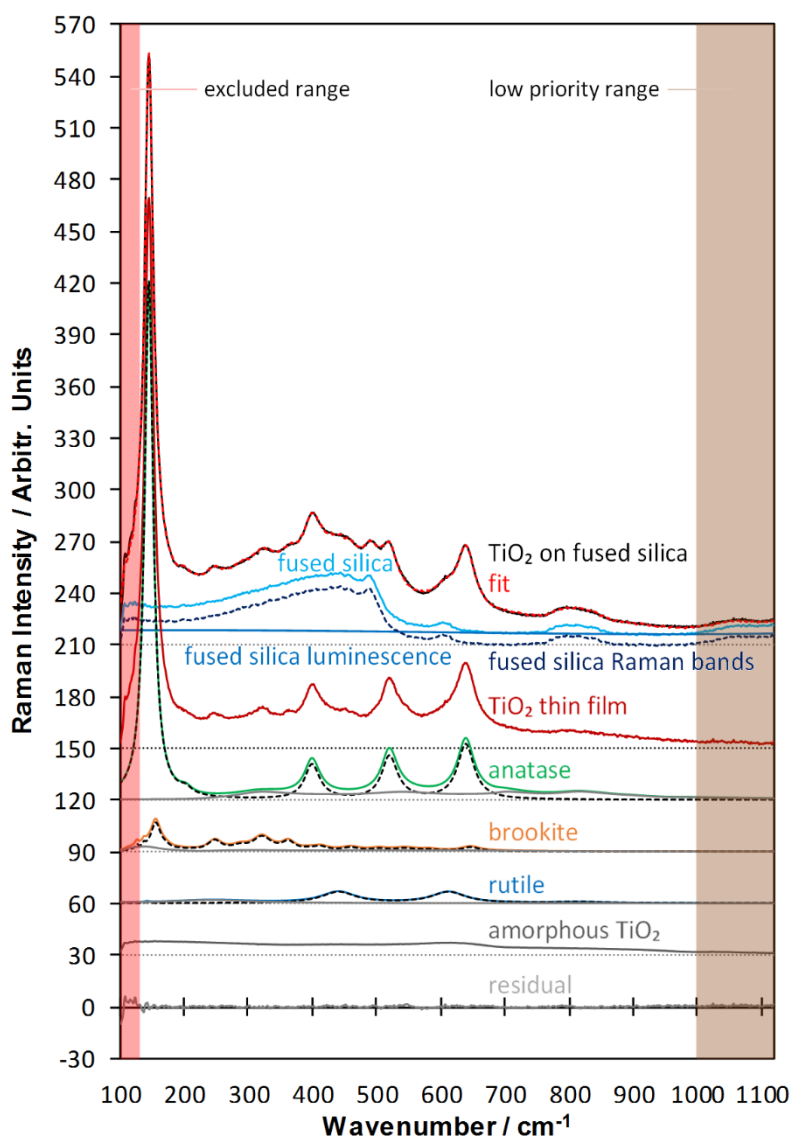


Fig. 62: Measured (black) and modeled (dashed red) Raman spectrum of an rf-diode sputtered mixed-phase TiO₂ thin film on fused silica decomposed into substrate (light blue) and thin film (dark red). The substrate spectrum is split into luminescence (mid blue) and Raman bands (dashed dark blue) and the thin film is decomposed into anatase (green), brookite (orange), rutile (blue), and amorphous TiO₂ (dark gray) spectra. The residual spectrum is medium gray. The crystalline spectra are divided into first-order scattering (black dashed lines) and phase background (light gray lines). The excluded range is light red and the low priority range is light brown. The spectra are shifted on the intensity axis as indicated by dotted lines.

The content and characteristics of each TiO₂ phase vary between the different substrates. The thin film spectrum on Si contains anatase and rutile while the thin films spectra on B270 glass and on fused silica contain anatase, rutile, brookite, as well as amorphous spectra. The

amorphous content is strongest in the spectrum of the TiO₂ thin film on fused silica. Interference of the phases' spectra in mixed-phase spectra as well as the various simplifications of the models limit the precision of fitting the position and shapes of the Raman peaks for the minor phases. Furthermore, accuracy of the distinction between amorphous content, the substrate's luminescence, and additional signals of the thin film are limited. The models for the substrates and the TiO₂ phases are fitted to the measured spectra of TiO₂ thin films on the substrates Si, B270 glass, and fused silica with nearly zero baseline in all non-excluded ranges.

4.2 Decomposed X-ray diffractograms and Raman spectra of e-beam evaporated anatase TiO₂ films

In this chapter, we demonstrate the decomposition of measured diffractograms and measured Raman spectra (using 633 nm laser excitation) of partly-amorphous anatase TiO₂ thin films that were coated onto B270 glass (and fused silica) by reactive e-beam evaporation and post-heated at temperatures of 350 °C – 750 °C. The deposition parameters are given in chapter 2.1.2. The films contain 0 at.%, 8 at.%, or 16 at.% of Nb and have the stoichiometries TiO₂, Ti_{0.92}O_{2.25}Nb_{0.08}, or Ti_{0.84}O_{2.25}Nb_{0.16}.

For the decompositions, we used the adjustable models for single-phase anatase films with individual peak fitting as described in the chapters 3.1.4.3, 3.2.2.3.1, and 3.3.3.1. The modeling procedure was successful for all samples and the simulated diffractograms and Raman spectra are fitted to the measurements with low residual signals.

Exemplarily, we show the X-ray diffractograms and Raman spectra of the samples that cover the most interesting features of this study. These samples are an Ti_{0.92}O_{2.25}Nb_{0.08} film post-heated at 375 °C (showing initial crystallization of anatase), an undoped anatase TiO₂ film post-heated at 420 °C (containing a small amount of brookite), and highly crystalline anatase TiO₂, Ti_{0.92}O_{2.25}Nb_{0.08}, and Ti_{0.84}O_{2.25}Nb_{0.16} films post-heated at 640 °C (highest temperature used for the films on B270 glass substrates).

In the appendices, there is an example of a decomposed diffractogram and a decomposed Raman spectrum (633 nm) of a Ti_{0.92}O_{2.25}Nb_{0.08} film on fused silica post-heated at 750 °C, in Fig. 182 and Fig. 183, respectively.

All anatase XRD and Raman peaks are visible in all films that are not fully amorphous (thus in all films that are post-heated at temperatures above 350 °C). Anatase first-order Raman peaks become wider and smaller in height with increasing Nb content and the intensity anatase phase background spectrum increases drastically with increasing Nb content. Both indicate disorder, which is most probably caused by Nb incorporation. Strong texture is found in the X-ray diffractograms of the undoped TiO₂ films: the c-orientation is favored. In contrast, less texture is found in the Nb doped films (with slightly favored a-orientation, see chapter 6.1.1).

Brookite peaks are present in the diffractograms and Raman spectra of the undoped samples, which disappear at higher temperatures. Though, brookite is more clearly visible in Raman than in XRD. Brookite is not visible in the diffractograms or Raman spectra of the undoped samples.

Traces of rutile are visible, and the intensity increases slightly with increasing temperature and decreasing Nb content. All diffractograms and Raman spectra contain a certain amount of contributions from the amorphous phase.

Details on the apparent phase contents in the Raman spectra and X-ray diffractograms are discussed in chapter 5.4. We furthermore evaluate the fitted Raman and XRD peak parameters in chapter 6.1.2.

4.2.1 Decomposed undoped and Nb-doped anatase TiO₂ X-ray diffractograms

The figures in this chapter show the decomposition of measured X-ray diffractograms of TiO₂, Ti_{0.92}O_{2.25}Nb_{0.08}, and Ti_{0.84}O_{2.25}Nb_{0.16} films (that were coated onto B270 glass using reactive e-beam evaporation post-heated at various temperatures). In each figure, the measured diffractogram is a black line and the modeled ‘fit’ diffractogram is a dashed red line that was fit to the measured one by simulating adjustable model diffractograms containing components from various origins.

The fit diffractogram is the sum of these components and it is composed of a background (light blue) and a thin film (dark red) diffractogram. The background diffractogram is the sum of contributions from the B270 substrate (medium blue) and from an instrument background (dashed dark blue). The film diffractogram is composed of anatase (green), brookite (orange), rutile (blue), and amorphous TiO₂ (dark gray). The residual diffractogram is medium gray.

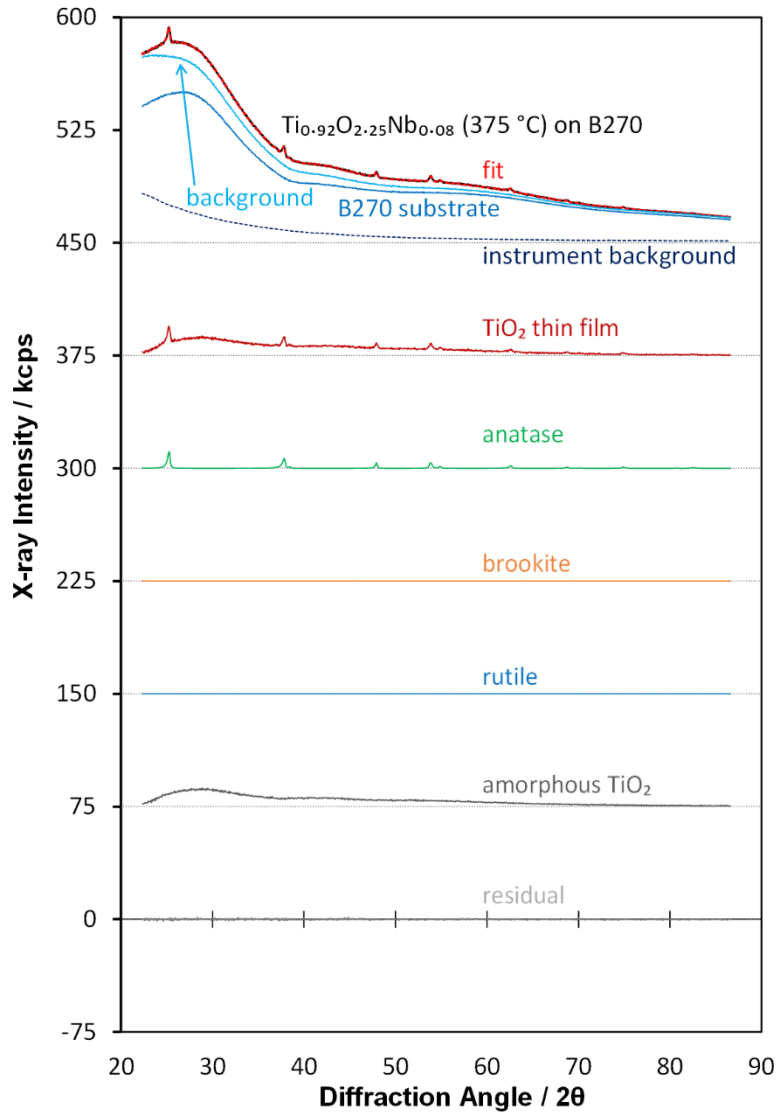


Fig. 63: Measured (black) and modeled (dashed red) X-ray diffractogram of a titanium oxide thin film with 8 at.% Nb – e-beam evaporated onto a B270 crown glass substrate and post-heated at 375°C – decomposed into a background (light blue) and a thin film (dark red). The background is split into the B270 substrate (medium blue) and an instrument background (dashed dark blue). The film is decomposed into anatase (green), brookite (orange), rutile (blue), and amorphous TiO_2 (dark gray). The residual diffractogram is medium gray. The diffractograms are shifted on the intensity axis as indicated by dotted lines.

Fig. 63 shows the diffractogram of an e-beam coated $\text{Ti}_{0.92}\text{O}_{2.25}\text{Nb}_{0.08}$ film on B270 glass post-heated at 375°C that contains anatase islands in an amorphous matrix (see chapter 7.2). The thin film diffractogram is composed of strong contributions arising from the amorphous phase as well as of anatase peaks with low intensity. Brookite or rutile are not detected.

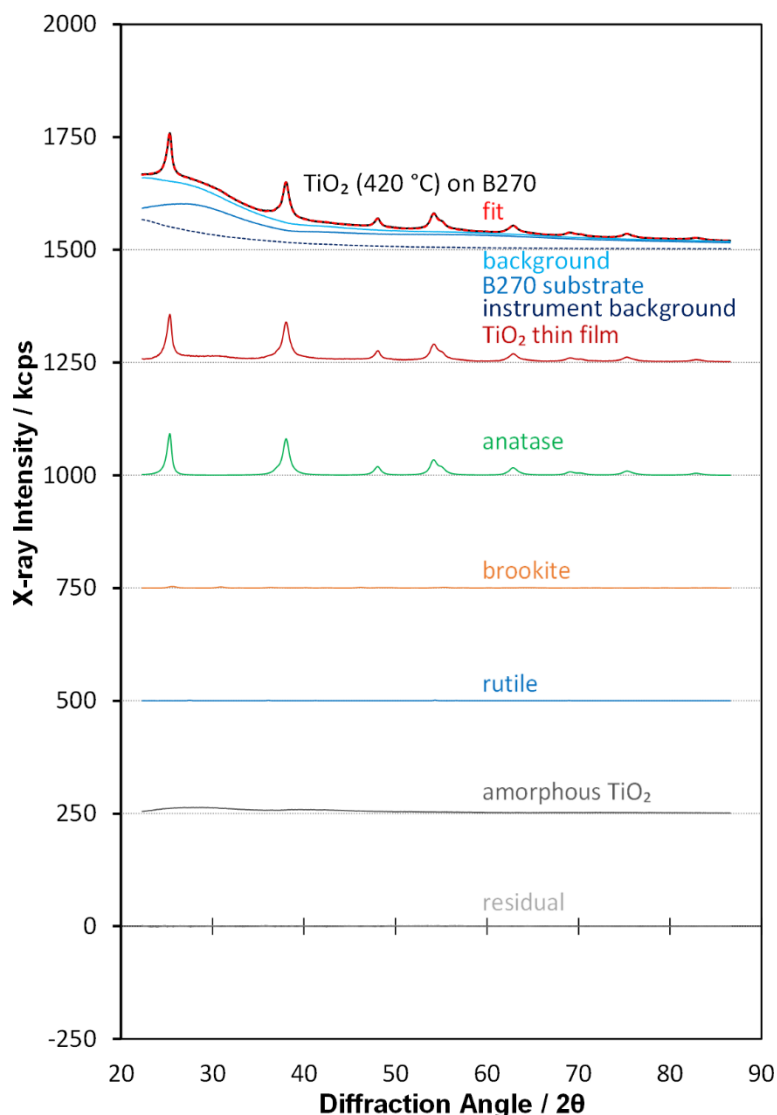


Fig. 64: Measured (black) and modeled (dashed red) X-ray diffractogram of an undoped TiO₂ thin film – e-beam evaporated onto a B270 crown glass substrate and post-heated at 420 °C – decomposed into a background (light blue) and a thin film (dark red). The background is split into the B270 substrate (medium blue) and an instrument background (dashed dark blue). The film is decomposed into anatase (green), brookite (orange), rutile (blue), and amorphous TiO₂ (dark gray). The residual diffractogram is medium gray. The diffractograms are shifted on the intensity axis as indicated by dotted lines.

Fig. 64 shows the diffractogram of an e-beam coated undoped TiO₂ film that was coated onto B270 glass and post-heated at 420 °C. Here, anatase is the dominating phase and the signals from amorphous titanium oxide are smaller than in the Ti_{0.92}O_{2.25}Nb_{0.08} film (post-heated at 375 °C) shown in Fig. 63. Anatase peaks of *c*-oriented planes are favored. The peak of the (004) reflex at a diffraction angle of 37.8° for example superimposed its neighboring peaks, (103) at 36.9° and (112) at 38.5°, and its intensity is comparable to the (101) peak at 25.3°. Brookite is visible with low intensity and also traces of rutile are found (for details on brookite and rutile peaks see Fig. 92).

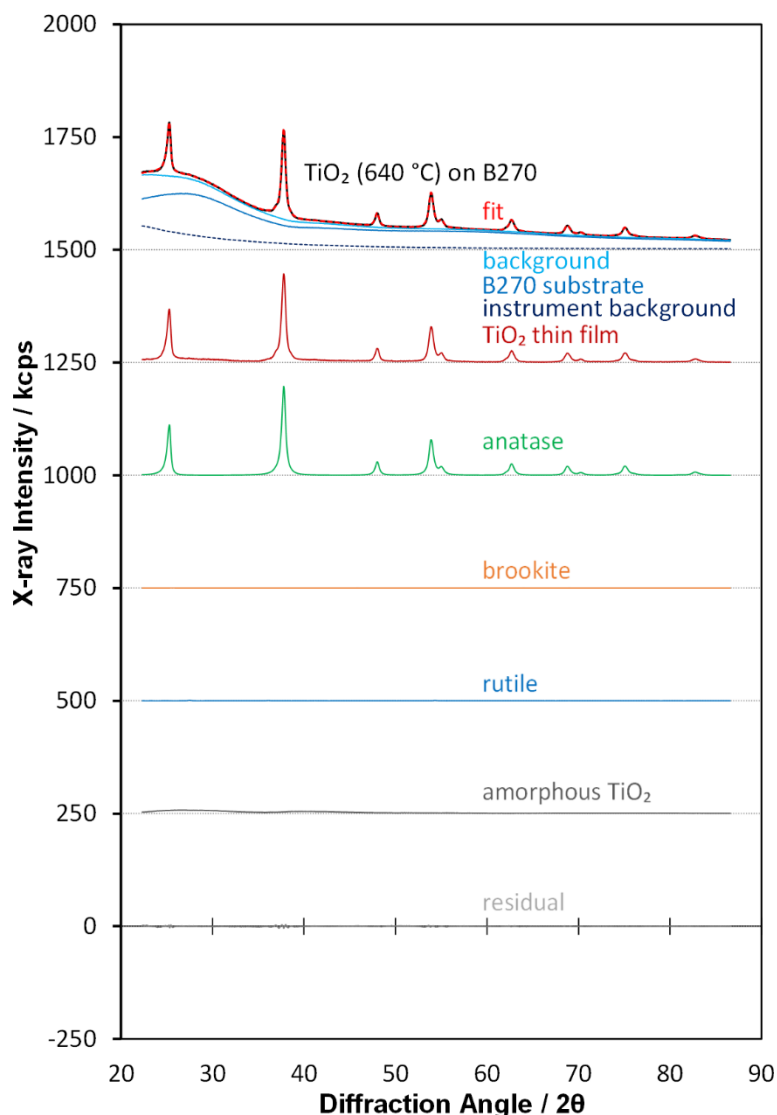


Fig. 65: Measured (black) and modeled (dashed red) X-ray diffractogram of an undoped TiO₂ thin film – e-beam evaporated onto a B270 crown glass substrate and post-heated at 640 °C – decomposed into a background (light blue) and a thin film (dark red). The background is split into the B270 substrate (medium blue) and an instrument background (dashed dark blue). The film is decomposed into anatase (green), brookite (orange), rutile (blue), and amorphous TiO₂ (dark gray). The residual diffractogram is medium gray. The diffractograms are shifted on the intensity axis as indicated by dotted lines.

Fig. 65 shows the diffractogram of an e-beam coated undoped TiO₂ film that was coated onto B270 glass and post-heated at 640 °C. The anatase peaks are stronger and the contribution of amorphous TiO₂ to the measured diffractogram is weaker as compared to the TiO₂ film post-heated at 420 °C (shown in Fig. 64). Also, the anatase peaks of *c*-oriented planes are even more favored. Here, the peak intensity of the (004) reflex at a diffraction angle of 37.8° is even higher than the intensity of the (101) peak at 25.3°.

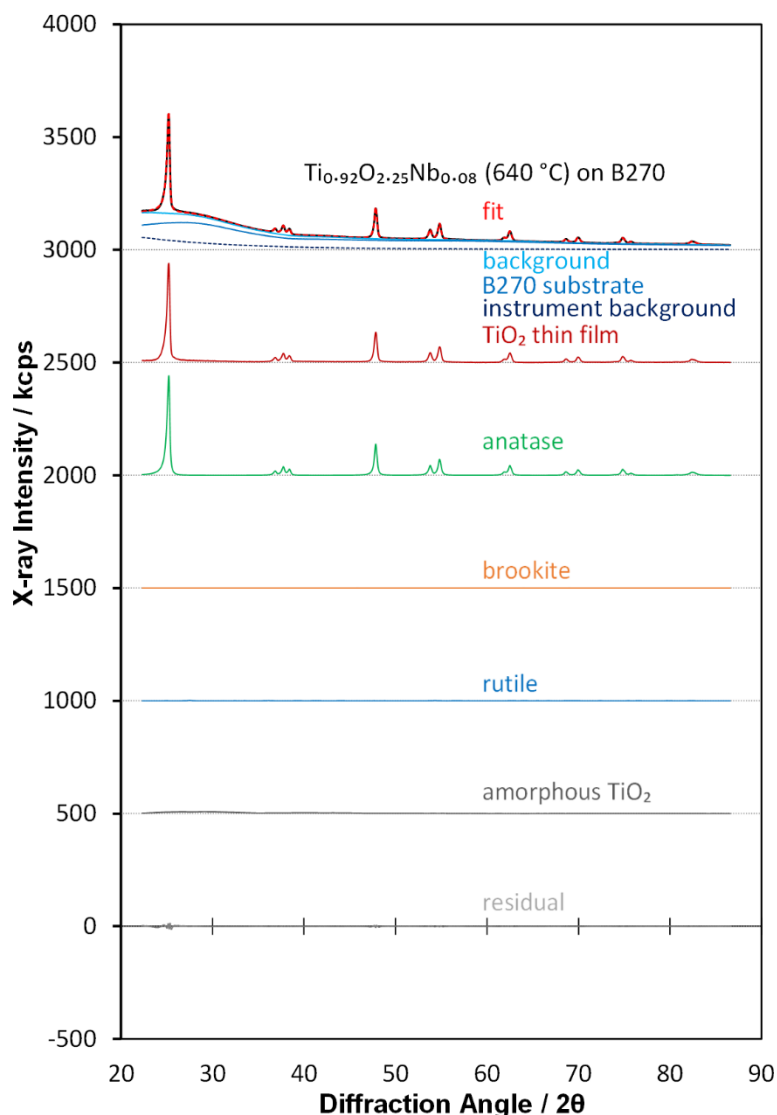


Fig. 66: Measured (black) and modeled (dashed red) X-ray diffractogram of a titanium oxide thin film with 8 at.% Nb – e-beam evaporated onto a B270 crown glass substrate and post-heated at 640 °C – decomposed into a background (light blue) and a thin film (dark red). The background is split into the B270 substrate (medium blue) and an instrument background (dashed dark blue). The film is decomposed into anatase (green), brookite (orange), rutile (blue), and amorphous TiO₂ (dark gray). The residual diffractogram is medium gray. The diffractograms are shifted on the intensity axis as indicated by dotted lines.

Fig. 66 shows the diffractogram of an e-beam coated $\text{Ti}_{0.92}\text{O}_{2.25}\text{Nb}_{0.08}$ film that was coated onto B270 glass and post-heated at 640 °C. The overall anatase and amorphous TiO₂ intensities are comparable to that of the undoped film post-heated at the same temperature (see Fig. 65). Yet, the peaks are narrower, and the ratios of the peak intensities are closer to that of standard anatase powder (see chapter 6.1.2). Brookite is not present and traces of rutile are modeled by the fitting routine, but cannot be confirmed by eye (cf. Fig. 93 in chapter 6.1.2). Thus, rutile is either not present or the intensity is so low that the intensity is close to the measurements noise.

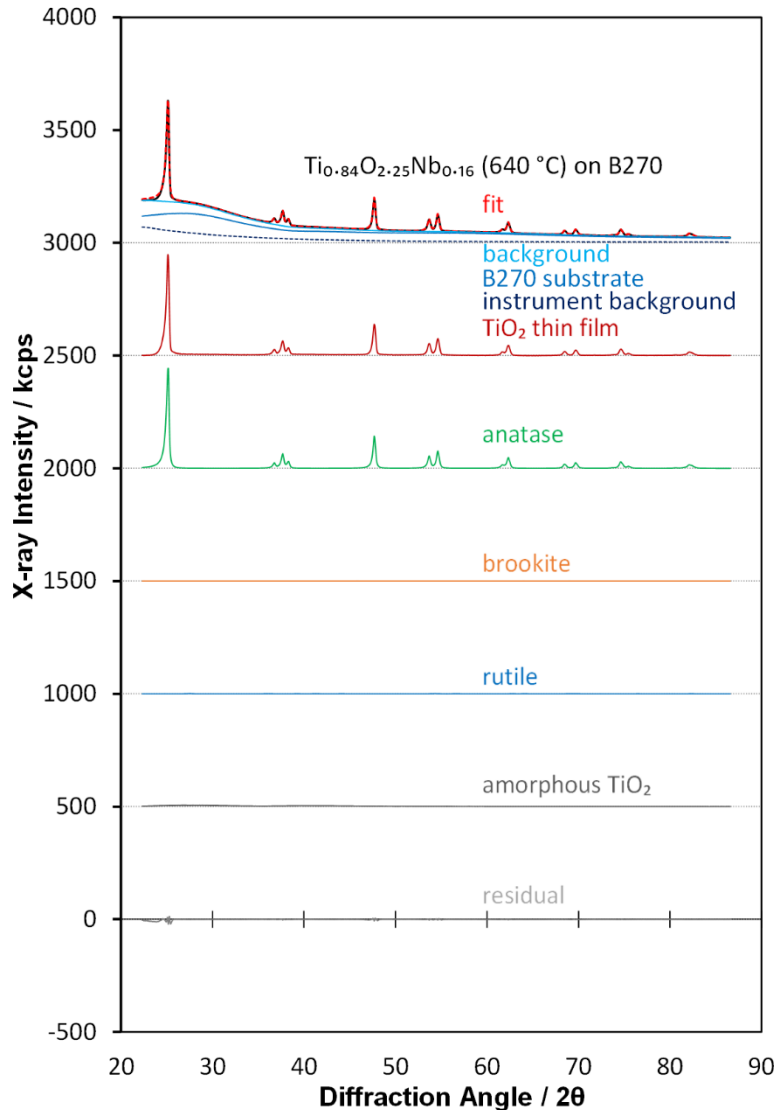


Fig. 67: Measured (black) and modeled (dashed red) X-ray diffractogram of a titanium oxide thin film with 16 at.% Nb – e-beam evaporated onto a B270 crown glass substrate and post-heated at 640 °C – decomposed into a background (light blue) and a thin film (dark red). The background is split into the B270 substrate (medium blue) and an instrument background (dashed dark blue). The film is decomposed into anatase (green), brookite (orange), rutile (blue), and amorphous TiO₂ (dark gray). The residual diffractogram is medium gray. The diffractograms are shifted on the intensity axis as indicated by dotted lines.

Fig. 67 shows the diffractogram of an e-beam coated Ti_{0.84}O_{2.25}Nb_{0.16} film that was coated onto B270 glass and post-heated at 640 °C. The phase composition of the film is comparable to that of the Ti_{0.92}O_{2.25}Nb_{0.08} film post-heated at the same temperature (Fig. 66). Also, no crystal orientation is strongly preferred.

4.2.2 Decomposed undoped and Nb-doped anatase TiO₂ Raman spectra

The figures in this chapter show the decomposition of measured Raman spectra (633 nm) of TiO₂, Ti_{0.92}O_{2.25}Nb_{0.08}, and Ti_{0.84}O_{2.25}Nb_{0.16} films (that were coated onto B270 glass using

reactive e-beam evaporation post-heated at various temperatures). In each figure, the measured Raman spectrum is a black line and the modeled 'fit' spectrum is a dashed red line that was fit to the measured one by simulating adjustable model spectrum containing components from various origins.

The fit spectrum is the sum of these components and it is composed of a substrate spectrum (light blue) and a thin film (dark red) spectrum. The substrate spectrum is the sum of contributions from substrate's luminescence (medium blue) and its Raman bands (dashed dark blue). The film spectrum is composed of anatase (green), brookite (orange), rutile (blue), and amorphous TiO₂ (dark gray). The residual spectrum is medium gray.

Fig. 63 shows the spectrum of a Ti_{0.92}O_{2.25}Nb_{0.08} film post-heated at 375 °C that contains anatase islands in an amorphous matrix (see chapter 7.2). The thin film spectrum is composed of strong contributions arising from the amorphous phase as well as of anatase peaks with low intensity. Brookite or rutile are not detected.

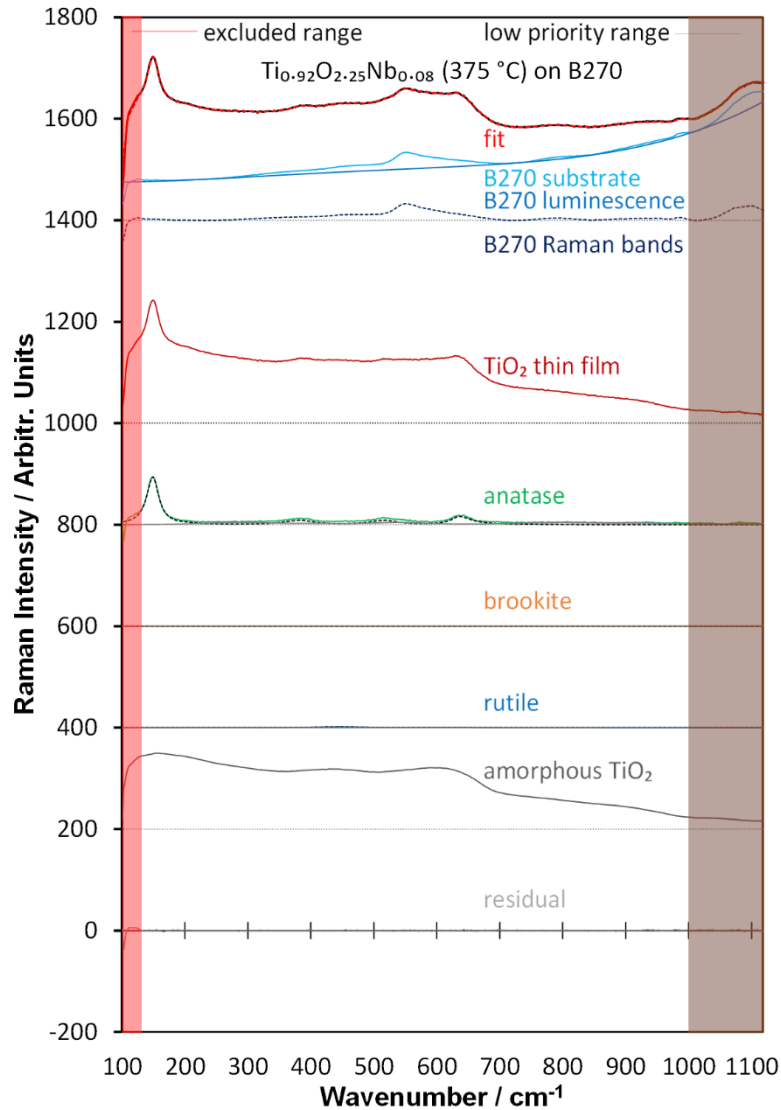


Fig. 68: Measured (black) and modeled (dashed red) Raman spectrum of an e-beam coated titanium oxide thin film doped with 8 at.% Nb on B270 glass post-heated at 375 °C – decomposed into substrate (light blue) and thin film (dark red). The substrate spectrum is split into luminescence (mid blue) and Raman bands (dashed dark blue) and the thin film is decomposed into anatase (green), brookite (orange), rutile (blue), and amorphous TiO₂ (dark gray) spectra. The crystalline spectra are divided into first-order scattering (black dashed lines) and phase background (light gray lines). The excluded range is light red and the low priority range is light brown. Same sample as in Fig. 63. The spectra are shifted on the intensity axis as indicated by dotted lines.

This is the Raman spectrum of a film that contains anatase islands in an amorphous matrix (see chapter 7.2). The thin film spectrum is composed of strong contributions arising from the amorphous phase as well as of anatase peaks with lower intensity. Brookite is not detected. Rutile is found to little or no amount.

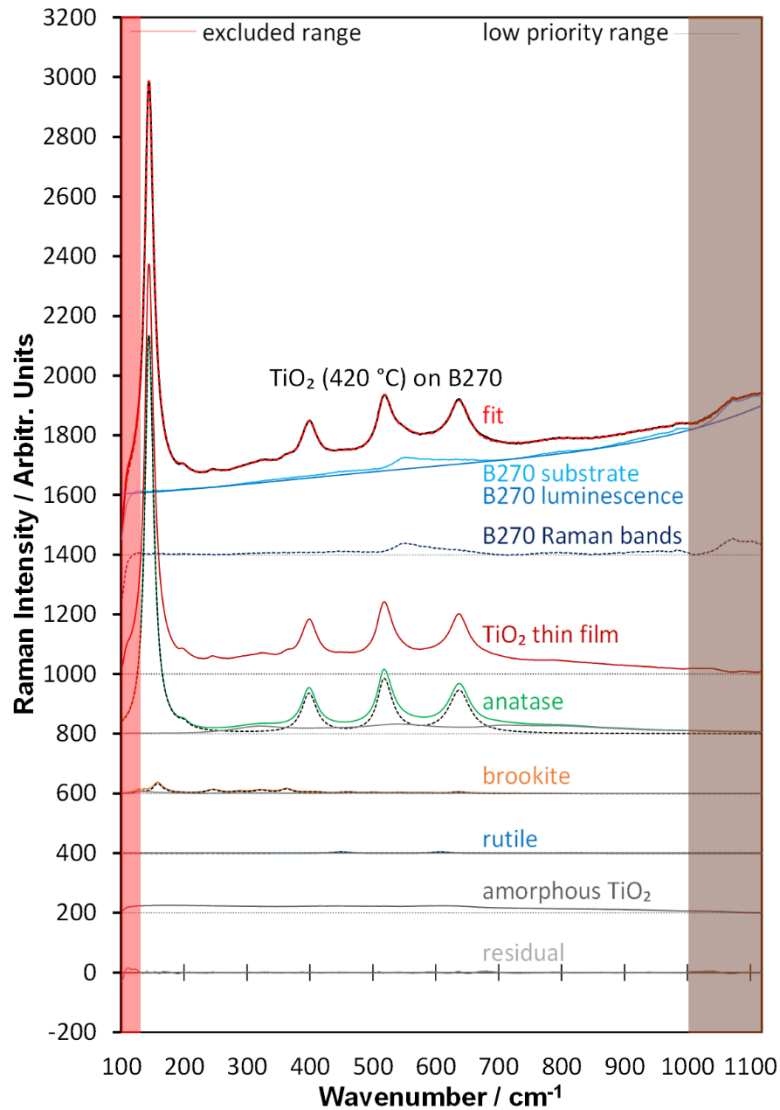


Fig. 69: Measured (black) and modeled (dashed red) Raman spectrum of an e-beam coated undoped TiO₂ thin film on B270 glass post-heated at 420 °C – decomposed into substrate (light blue) and thin film (dark red). The substrate spectrum is split into luminescence (mid blue) and Raman bands (dashed dark blue) and the thin film is decomposed into anatase (green), brookite (orange), rutile (blue), and amorphous TiO₂ (dark gray) spectra. The crystalline spectra are divided into first-order scattering (black dashed lines) and phase background (light gray lines). The excluded range is light red and the low priority range is light brown. Same sample as in Fig. 64. The spectra are shifted on the intensity axis as indicated by dotted lines.

Fig. 69 shows the Raman spectrum of an e-beam coated undoped TiO₂ film that was coated onto B270 glass and post-heated at 420 °C. Anatase is the dominating phase and the signals from amorphous titanium oxide are smaller than in the Ti_{0.92}O_{2.25}Nb_{0.08} film (post-heated at 375 °C) shown in Fig. 68. Brookite is visible and its peaks between 200 cm⁻¹ and 400 cm⁻¹ (A1g at 246 cm⁻¹, B1g at 322 cm⁻¹, B2g at 363 cm⁻¹) are clearly distinct from the signals of the other components. Also, small traces of rutile are found.

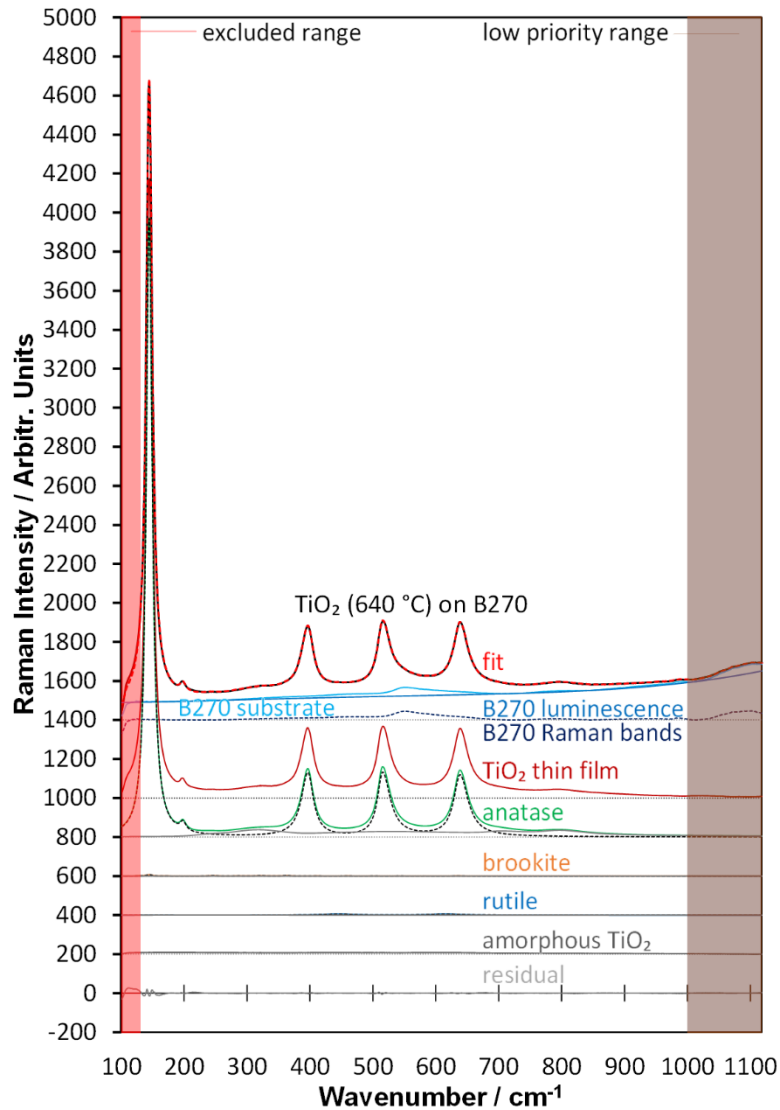


Fig. 70: Measured (black) and modeled (dashed red) Raman spectrum of an e-beam coated undoped TiO₂ thin film on B270 glass post-heated at 640 °C – decomposed into substrate (light blue) and thin film (dark red). The substrate spectrum is split into luminescence (mid blue) and Raman bands (dashed dark blue) and the thin film is decomposed into anatase (green), brookite (orange), rutile (blue), and amorphous TiO₂ (dark gray) spectra. The crystalline spectra are divided into first-order scattering (black dashed lines) and phase background (light gray lines). The excluded range is light red and the low priority range is light brown. Same sample as in Fig. 65. The spectra are shifted on the intensity axis as indicated by dotted lines.

Fig. 70 shows the Raman spectrum of an e-beam coated undoped TiO₂ film that was coated onto B270 glass and post-heated at 640 °C. This sample was coated in the same deposition process as the sample in Fig. 69, but post-heated at a higher temperature. The anatase peaks are stronger and the contribution of amorphous TiO₂ to the measured Raman spectrum is weaker as compared to the TiO₂ film post-heated at 420 °C. Little to no brookite is found in this sample.

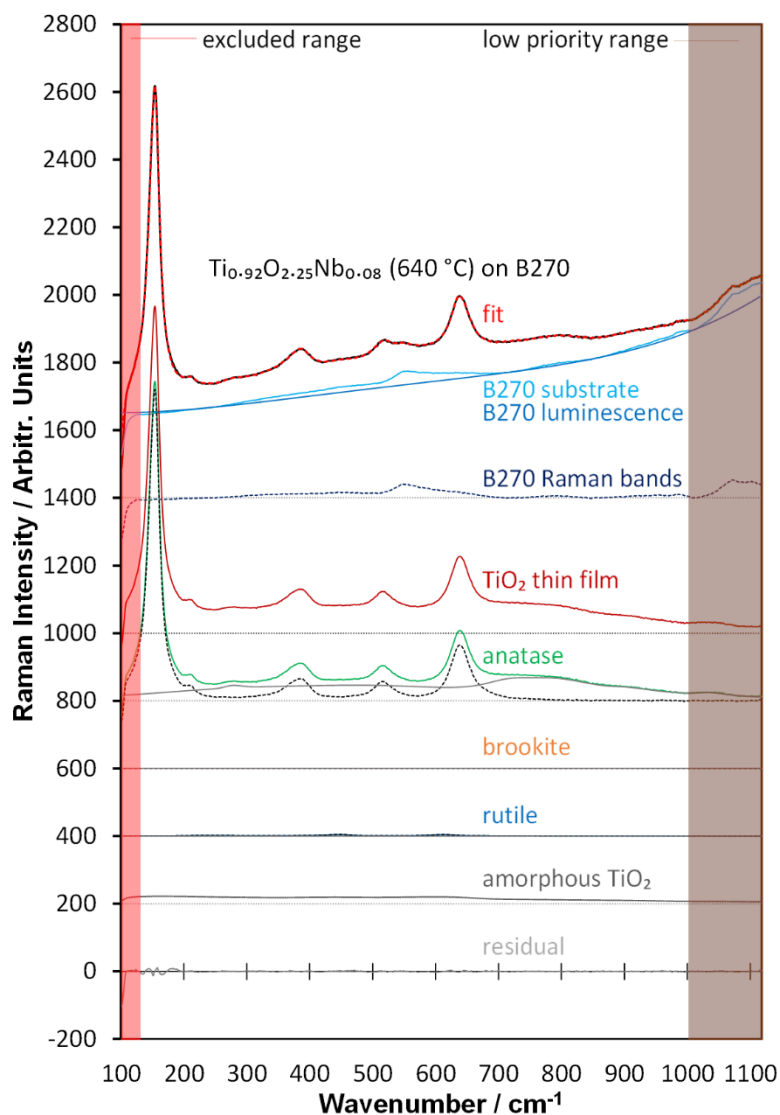


Fig. 71: Measured (black) and modeled (dashed red) Raman spectrum of an e-beam coated titania film doped with 8 at.% Nb on B270 glass post-heated at 640 °C – decomposed into substrate (light blue) and film (dark red). The substrate spectrum is split into luminescence (mid blue) and Raman bands (dashed dark blue) and the film is decomposed into anatase (green), brookite (orange), rutile (blue), and amorphous TiO₂ (dark gray). The crystalline spectra are divided into first-order scattering (black dashed lines) and phase background (light gray lines). The excluded range is light red and the low priority range is light brown. Same sample as in Fig. 66. Intensity shifts of the spectra are indicated by dotted lines.

Fig. 71 shows the Raman spectrum of an e-beam coated Ti_{0.92}O_{2.25}Nb_{0.08} film that was coated onto B270 glass and post-heated at 640 °C. Anatase is the main phase and the anatase phase background spectrum is significantly more intense than in the spectrum of the undoped film post-heated at the same temperature (cf. Fig. 70). Also, the first-order Raman peaks are wider and smaller in height as the peaks of the undoped film. Both are indications of disorder, most probably caused by the incorporation of niobium. We found the amorphous content to be higher than in the undoped film. Brookite is not found in the films doped with 8 at.% Nb and rutile is found as traces.

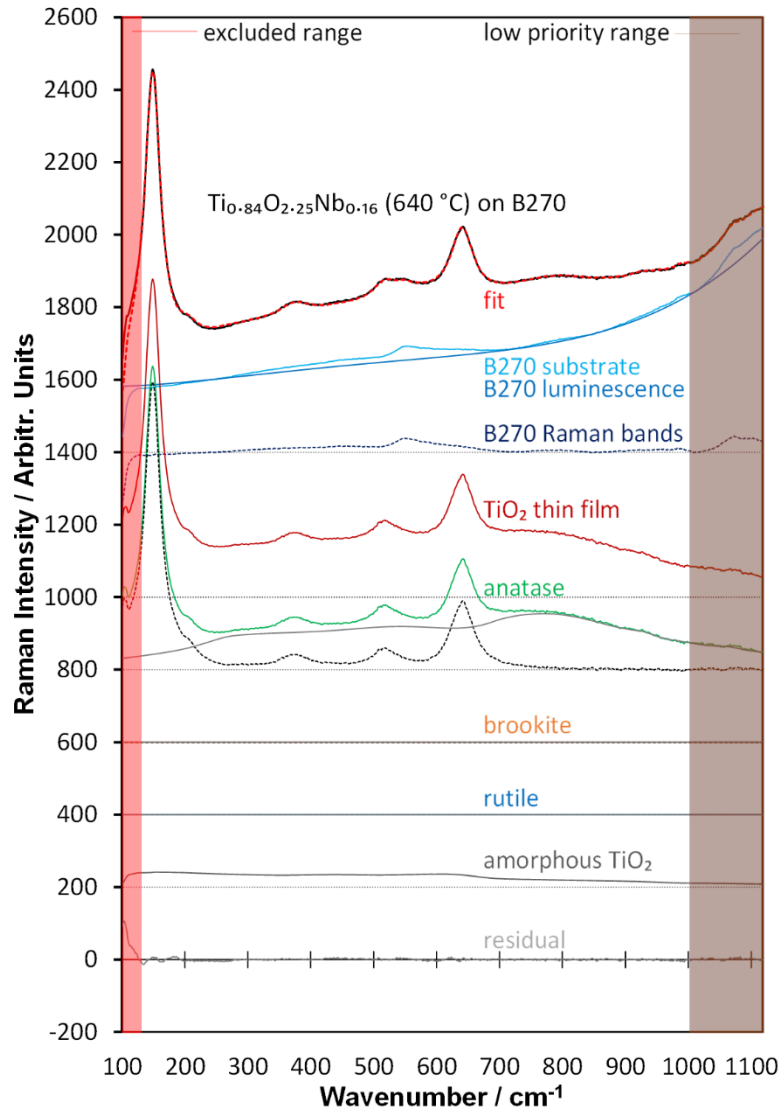


Fig. 72: Measured (black) and modeled (dashed red) Raman spectrum of an e-beam coated titania film doped with 8 at.% Nb on B270 glass post-heated at 640 °C – decomposed into substrate (light blue) and film (dark red). The substrate spectrum is split into luminescence (mid blue) and Raman bands (dashed dark blue) and the film is decomposed into anatase (green), brookite (orange), rutile (blue), and amorphous TiO₂ (dark gray). The crystalline spectra are divided into first-order scattering (black dashed lines) and phase background (light gray lines). The excluded range is light red and the low priority range is light brown. Same sample as in Fig. 67. Intensity shifts of the spectra are indicated by dotted lines.

Fig. 72 shows the Raman spectrum of an e-beam coated Ti_{0.84}O_{2.25}Nb_{0.16} film that was coated onto B270 glass and post-heated at 640 °C. The phase composition of this film with 16 at.% Nb is comparable to that of the Ti_{0.92}O_{2.25}Nb_{0.08} film with 8 at.% Nb (cf. Fig. 71), but we found no traces of rutile. The anatase peaks are wider than those of the Ti_{0.92}O_{2.25}Nb_{0.08} film post-heated at the same temperature (cf. Fig. 71) and the phase background is so intense that its height is higher than the height of the A1g and B1g peaks. This indicates increasing disorder in the TiO₂ film with increasing Nb content.

We discuss the behavior of the anatase first-order Raman peak parameters with the temperature and the Nb content in chapter 6.1.2 and the behavior of the anatase phase backgrounds in chapter 6.2.

5 Quantitative evaluation of decomposed Raman spectra and X-ray diffractograms

In the following, we present quantitative studies on measured TiO₂ thin film Raman spectra, which were decomposed into various sub-spectra in chapter 4. Additional qualitative studies on these spectra are discussed in chapter 6. The sub-spectra are simulated simultaneously by adjustable model spectra, which were presented and discussed in chapter 3.1 and mathematically defined in chapter 3.2. In chapter 5.1, we introduce general aspects that have to be considered when Raman spectra and X-ray diffractograms are quantitatively analyzed.

In chapter 5.2, we compare the quantification of TiO₂ phases in Raman spectra and in X-ray diffractograms of multi-phase TiO₂ thin films. The films are rf-diode sputtered and consist of anatase, brookite, rutile, as well as amorphous TiO₂. The phase contents are varied by depositing the samples at various substrate temperatures. This set of multi-phase films was chosen for further studies on a variation of the Raman laser wavelength. The cross-sections of the used measurement methods are considered. In chapter 5.3, we study the influence of the substrate material on the phase composition of rf-diode sputtered multi-phase TiO₂ thin films using Raman spectrometry.

In chapter 5.4, we compare the contributions of TiO₂ phases in Raman spectra and in X-ray diffractograms of e-beam coated undoped and Nb-doped TiO₂ thin films. The films are amorphous as deposited and crystallize to mainly anatase with increasing post-heating temperatures.

In chapter 5.5, we compare the quantitative results of chapter 5.2 with chapter 5.4, and discuss the advantages and disadvantages of both methods, XRD and Raman.

5.1 Quantification of Raman spectra and X-ray diffractograms

This work aims at the decomposition of Raman spectra of TiO₂ on various substrates and their numerical evaluation. The results presented here do not provide the total amount of atoms/molecules or the weight ratios of the phases in the measured samples. In future work, in which actual amounts of the individual TiO₂ phases are to be determined, the actual cross-sections of the various materials must be identified from measurements of standard materials and mixtures of standard materials.

In general, the X-ray or Raman intensity of a given material is proportional to the amount of the measured material. However, in mixtures of materials, the intensity ratios are not

necessarily proportional to the weight fractions.^{19,139} The intensity ratio of X-ray diffractograms is proportional to the weight fraction of different materials if the X-ray absorption power of the materials is similar.¹³⁹ The X-ray photons of the $CuK\alpha$ radiation (0.154 nm) have energy of around 8000 eV . This is above the Ti K-edge, which is between 4900 eV and 5000 eV (equivalent to a wavelength of 0.25 nm) for the four TiO_2 allomorphs. The X-ray absorbance of anatase, rutile, brookite and amorphous TiO_2 is in the same range.^{140,141}

In such a case, the ratio of weight fractions w_1/w_2 and the X-ray intensity ratios I_1/I_2 of two materials are proportionally linked with a constant factor K:

$$\frac{w_1}{w_2} = K \frac{I_1}{I_2} \quad (59)$$

Spurr and Myers showed that for mixtures of anatase and rutile powder, the coefficient K between the weight ratio w_A/w_R and the X-ray anatase/rutile peak intensity I_A/I_R ratio of the most intense peak of both phases was almost constant, around $K = 0.8$, for all anatase/rutile weight fractions.¹⁴²

Raman intensities of a given material are also proportional to the amount of the measured material. Other factors that contribute to the Raman intensity are most notably temperature, density, refractive index, and optical absorption. The measuring temperature contribution is described by the Boltzmann factor:

$$1 - e^{-\frac{h\nu}{kT}}, \quad (60)$$

which affects lower frequency vibrations stronger. The density of the films can also be affected by the measurement temperature. The density alters the number of molecules that are irradiated by the Raman laser. Yet, this should not affect the measurements of films that are thinner than the penetration depth of the Raman laser or the X-ray beam. The refractive index changes the integrated Raman peak area by a factor L by:

$$L = \left(\frac{n_s}{n_0}\right) \frac{(n_s^2+2)^2 (n_0^2+2)^2}{81}, \quad (61)$$

with the refractive index n_s of the sample of the Raman scattering light, and the refractive index n_0 of the sample of the exciting light. Optical absorption leads to attenuation of the laser or of Raman photons (self-absorption). Self-absorption often distorts relative band areas.

Further inherent parameters of the samples also alter the X-ray diffractograms and Raman spectra in varying ways and to varying degrees. These are for example preferred orientation, crystal morphology, grain size, residual strain, and impurities.¹⁴³

The measurements were performed on varying days. Thus, the total measured intensities of Raman spectra and X-ray diffractograms are altered by several experimental factors. Such factors are for example instrument parameters such as the instrument calibration, optical alignment within the instrument, a drift in the performance of the spectrometer/diffractometer, or errors due to dead time. Further aspects that influence the measured intensities are sample alignment and the focus of the Raman laser spot or the X-ray beam.

Therefore, we calibrated the sample placement and measurement equipment before each measurement for Raman and XRD. Many Raman spectra contain bands that do not change in intensity with increasing analyte concentration and they can be used as internal standards for calibration. In TiO₂ Raman spectra, there is no such internal standard, so we measured a Si reference sample before each measurement and the peak parameters/intensities were analyzed for the calibration of the spectrometer so that it yields comparable results for each measurement.

In order to lower the impact of the variance of the total measured intensities on the interpretation of the data, we use two ways to quantify the same set of Raman and XRD data, as was suggested by Pelletier.¹⁹ Firstly, we compare the total intensities of the individual TiO₂ phases in *kcps*, and secondly we compare the relative amounts of X-ray or Raman photon counts.

5.2 Quantitative comparison of Raman with XRD on diode sputtered multi-phase TiO₂ films

In this chapter, we compare the intensities in Raman spectra and X-ray diffractograms of the TiO₂ phases, anatase, brookite, rutile, and amorphous TiO₂ of diode-sputtered multi-phase TiO₂ thin films (for deposition parameters see chapter 2.1.1). Therefore, the measured X-ray diffractograms and Raman spectra are decomposed into their components by the simulation of adjustable model diffractograms or spectra as demonstrated in chapter 4. The models that we used for the decompositions are described in chapters 3.1 – 3.3. The Raman spectra were taken individually with two different excitation wavelengths, *633 nm* and *532 nm* (for the measurement procedure see chapter 2.2.1). As shown in the Raman maps of chapter 7.1, the four TiO₂ phases are homogeneously distributed over the sample surface. The same set of Raman spectra and X-ray diffractograms are analyzed qualitatively in chapter 6.1.1.

5.2.1 Phase quantification with XRD and Raman

For the measured diffractograms or Raman spectra, we assign a certain amount of X-ray or Raman photons to the TiO₂ phases, anatase, brookite, rutile, or amorphous TiO₂. We quantify the contributions of the various TiO₂ phases to the total diffractograms or spectra by calculating the areas under the corresponding graphs of the adjustable model X-ray diffractograms and Raman spectra. For the Raman quantification of crystalline phases, the number of counts of a certain phase is a sum of the counts arising from first-order Raman scattering and from the phase background (e.g. second-order scattering and disorder- and defect-induced scattering). For better comparability, the *532 nm* Raman intensities are then multiplied by a factor of *10* because the power output of the laser was ten times lower than that of the *633 nm* laser.

We have decomposed the X-ray diffractograms as well as the *633 nm* and *532 nm* Raman spectra of *70 nm* thick TiO₂ thin films on B270 glass that were diode-sputtered at substrate temperatures of *155 °C*, *200 °C*, *275 °C*, *310 °C*, and *415 °C* (± 20 °C). The contributions to the diffractograms and Raman spectra were quantified for each TiO₂ phase. The left side of Fig. 73 shows the intensities of anatase, brookite, rutile, and amorphous TiO₂ in thousand counts per second (*kcps*) as measured by XRD, *633 nm* Raman, and *532 nm* Raman versus the deposition temperature. The right side of Fig. 73 displays the relative amount of counts we assign to the individual phases that contribute to the X-ray diffractograms and Raman spectra (calculated from the data of the left column).

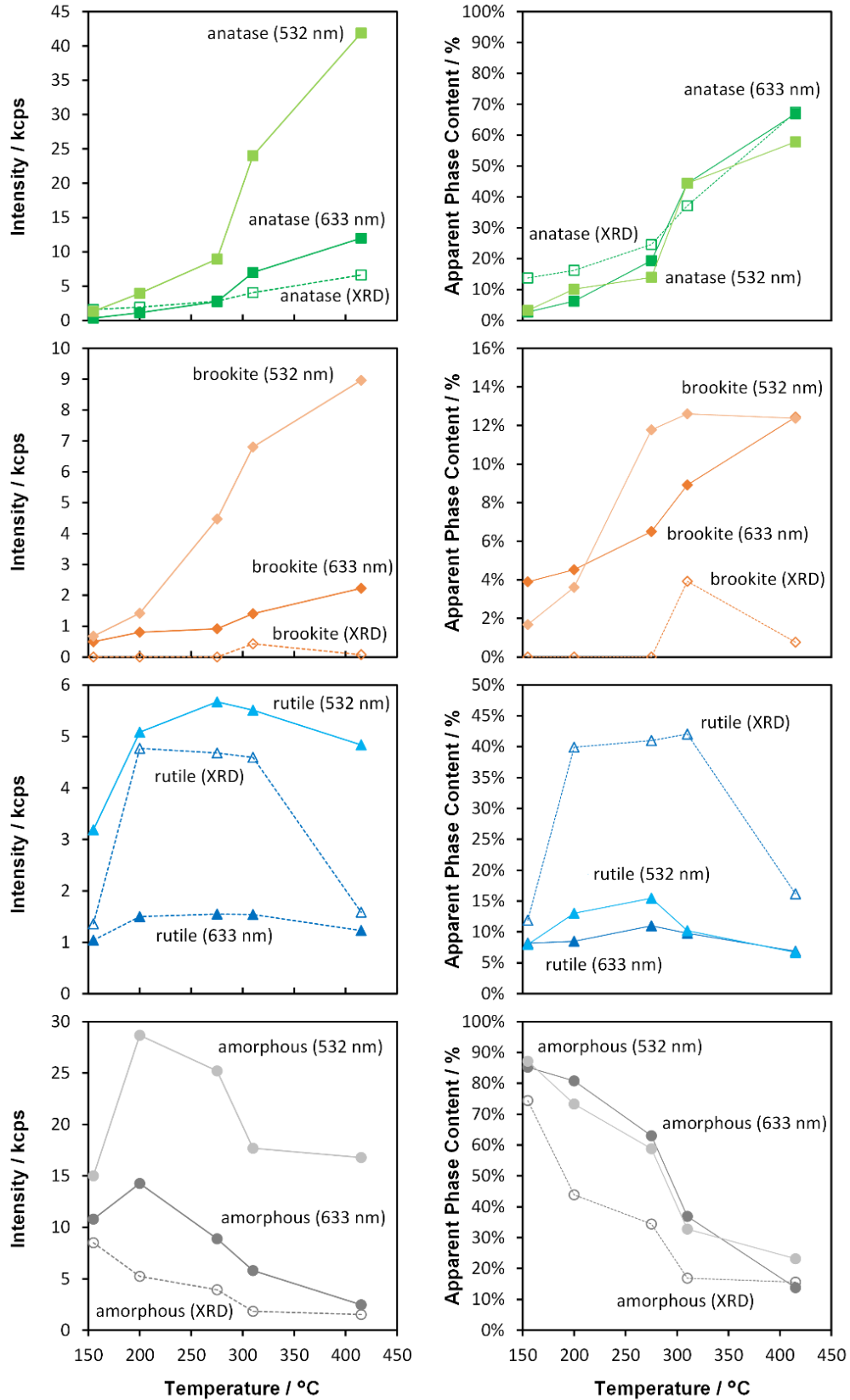


Fig. 73: Left column: Contributions (in thousand counts per second) of anatase, brookite, rutile, and amorphous TiO₂ to XRD diffractograms and (633 nm and 532 nm) Raman spectra of TiO₂ thin films diode-sputtered at temperatures of 155 °C – 415 °C. Right column: Apparent relative phase contents (relative number of X-ray or Raman photon counts) in the XRD diffractograms and (633 nm and 532 nm) Raman spectra. The lines are added to guide the eye.

Each of the four TiO₂ phases, anatase, brookite, rutile, and amorphous TiO₂ was detected by Raman with both laser wavelengths in all samples. In the X-ray diffractograms we found anatase, rutile, and amorphous TiO₂, as well, but brookite was visible in the diffractograms of the films deposited at temperatures above 300 °C only.

The relative amount of photon counts that we assign to amorphous TiO₂ decreases with increasing deposition temperature from 155 °C to 415 °C and decreases in the diffractograms as well as in the Raman spectra from around 80% to around 20%. The total intensity that we attribute to amorphous TiO₂ in the X-ray diffractograms decreases from 8 *kcps* to 2 *kcps*. The intensity of amorphous TiO₂ in the Raman spectra shows the same trend at temperatures above 200 °C. It decreases from 15 *kcps* to 2 *kcps* in the 633 nm Raman spectra and from around 30 *kcps* to 15 *kcps* in the 532 nm Raman spectra. Yet, the intensity of amorphous TiO₂ increases with increasing deposition temperature from 155 °C to 200 °C from 10 *kcps* to 15 *kcps* in the 633 nm Raman spectra and from 15 *kcps* to around 30 *kcps* in the 532 nm Raman spectra.

The total and relative number of counts that we assign to anatase increases with increasing deposition temperature from 155 °C to 415 °C for all three measurement techniques. That is 0.3 *kcps* – 12 *kcps* in the 633 nm Raman spectra, 2 *kcps* – 42 *kcps* in the 532 nm Raman spectra, and 2 *kcps* – 7 *kcps* in the X-ray diffractograms. The apparent relative anatase content in the diffractograms and the Raman spectra of both laser wavelengths increases from around 10% to around 60% of the total number of TiO₂ counts with increasing temperature.

The counts assigned to brookite show the same trend in the Raman spectra of both laser wavelengths and increases from 0.7 *kcps* to 2 *kcps* in the 633 nm Raman spectra, and from 0.5 *kcps* to 9 *kcps* in the 532 nm Raman spectra. This is an increase of an apparent phase content from approximately 3% to 12% for both wavelengths. Concerning X-ray diffractometry, brookite is present only in the diffractograms of the films produced above 300 °C, with values below 0.5 *kcps* and apparent phase contents below 5%. The XRD data do not contradict the Raman findings of increasing brookite content with the deposition temperature, but are not sufficient for a clear interpretation.

From the low and partly non-identifiable intensities of brookite in the X-ray diffractograms, we conclude that Raman is more sensitive for brookite than XRD. This is supported by the quantitative analysis described in chapter 4.1.1 and 4.1.2. This makes Raman spectroscopy more suitable for detecting the presence of traces or small amounts of brookite.

The rutile content increases in the Raman spectra of both wavelengths and in the diffractograms with the temperature increasing from 155 °C to 200 °C and is maximum for the samples prepared at substrate temperatures between 200 °C and 310 °C and decreases again for

samples prepared at 415 °C. The described trend ranges from 1 *kcps* to 5 *kcps* in the XRD diffractograms, from 1 *kcps* to 1.5 *kcps* in the 633 nm Raman spectra, and from 3 *kcps* to 6 *kcps* in the 532 nm Raman spectra. This equals an apparent phase contents of about 10% – 40% in the X-ray diffractograms, 7% – 11% in the 633 nm Raman spectra, and 7% – 15% in the 532 nm Raman spectra.

According to literature, the temperature at which rutile is obtained from anatase-to-rutile transition starts at around 600 °C – 700 °C at pressures below atmospheric pressure.⁵ In our sputter-deposited films, rutile formation is most probably supported by kinetic particle impact into the films during the deposition, as was suggested by Löbl et al.¹⁴⁴ Our interpretation of the decrease of rutile at higher temperatures is that fast-growing anatase leaves no space for rutile generation.

5.2.2 Influence of laser wavelength on the intensity of TiO₂ phases in Raman spectra

The left side of Fig. 74 shows the number of Raman photon counts that we account to the phases, anatase, brookite, rutile, and amorphous TiO₂, taken with a 532 nm (multiplied by a factor of 10, see chapter 5.2.1) vs. a 633 nm laser. The right side of Fig. 74 shows the relative intensities $I_{(532)}$ and $I_{(633)}$ of the Raman photon counts that we assign to each phase (or the 'apparent phase contents') from spectra measured with a 532 nm and 633 nm laser. The plotted values follow immediately from the data of Fig. 73.

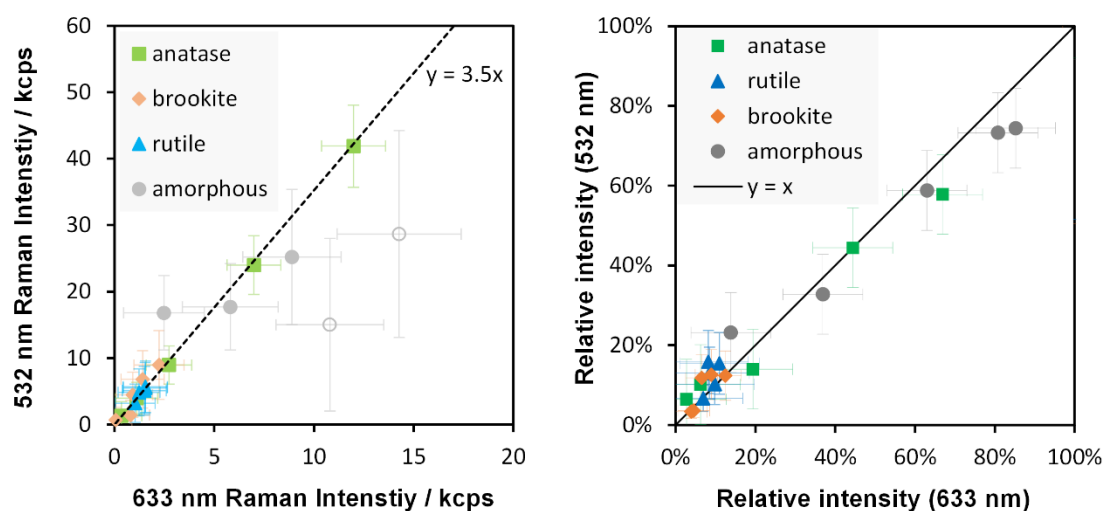


Fig. 74: left side: Raman intensity of anatase, brookite, rutile, and amorphous TiO₂ in multi-phase thin films as derived from Raman spectra measured with a 532 nm laser versus a 633 nm laser; right side: same data plotted as relative intensities (relative apparent phase contents).

In the right graph of Fig. 74, the data points are close to the diagonal line. Thus, the apparent phase contents in the Raman spectra are nearly identical for both laser wavelengths. In the left graph of Fig. 74, one can see that the intensities of the crystalline phases, anatase,

brookite and rutile follow an identical linear relationship for the two laser wavelengths. From the straight trendline it follows that the intensities $I_{cryst.(532)}$ of the crystalline phases in the 532 nm Raman spectra is $K_{cryst.(532/633)} = 3.5$ times the intensities $I_{cryst.(633)}$ in the 633 nm Raman spectra:

$$I_{cryst.(532)} = 3.5 \cdot I_{cryst.(633)}, \quad (62)$$

According to equation (31) in chapter 1.4.2.5, the Raman cross-section and thus the measured intensity has a $1/\lambda^4$ relationship with the laser wavelength λ . Adding the factor $(532\text{ nm})^4/(633\text{ nm})^4$, we get a remaining proportionality factor $K'_{cryst.(532/633)}$ of $K'_{532/633} = 1.8$:

$$I_{cryst.(532)} = 1.8 \cdot I_{cryst.(633)} \cdot \frac{(633\text{nm})^4}{(532\text{nm})^4}, \quad (63)$$

Several aspects contribute to the remaining factor of 1.8 between the Raman intensities of the two laser wavelengths. Such factors are a variance of the reflectance of the thin films or the film/substrate interface for the different laser wavelengths, or geometrical factors such as the laser spot size and the energy distribution within the laser spot.

The number of photons that we assign to the amorphous phase using 532 nm and 633 nm laser has a high variance and does not follow the trend of the crystalline phases. Especially the values for the highly amorphous films (marked with open circles) deposited at $155\text{ }^\circ\text{C}$ and $200\text{ }^\circ\text{C}$ are not close to the trendline. A trendline for amorphous TiO_2 (not shown in Fig. 74) gives a ratio of the number of counts that our simulation models assigned to the amorphous phase as measured with a 532 nm and a 633 nm laser $I_{am.(532)}/I_{am.(633)}$ of approximately 2. Considering the wavelength dependent change in Raman cross-section with $1/\lambda^4$, equation (64) gives a laser-dependent proportionality factor for the amorphous phase as $K'_{am.(532/633)} = 1$:

$$I_{am.(532)} = 1 \cdot I_{am.(633)} \cdot \frac{(633\text{nm})^4}{(532\text{nm})^4}. \quad (64)$$

An explanation for the variance in the intensities of the amorphous TiO_2 phase might be the high signal-to-noise ratio of the 532 nm spectra, which hinders the identification of the broad features of the amorphous Raman bands. This assumption is supported by Fig. 75, in which the amorphous content as measured with the 532 nm laser has a higher variance. Interestingly, the apparent phase contents (relative content) of the amorphous phase in the Raman spectra of both laser wavelengths agrees well for both laser wavelengths (see the right side of Fig. 74).

5.2.3 Correlation between total XRD and Raman intensities

Fig. 75 depicts the Raman intensities (633 nm and 532 nm) versus the corresponding X-ray intensities of the TiO₂ allomorphs, anatase, brookite, rutile, and amorphous TiO₂ of the data shown in Fig. 73.

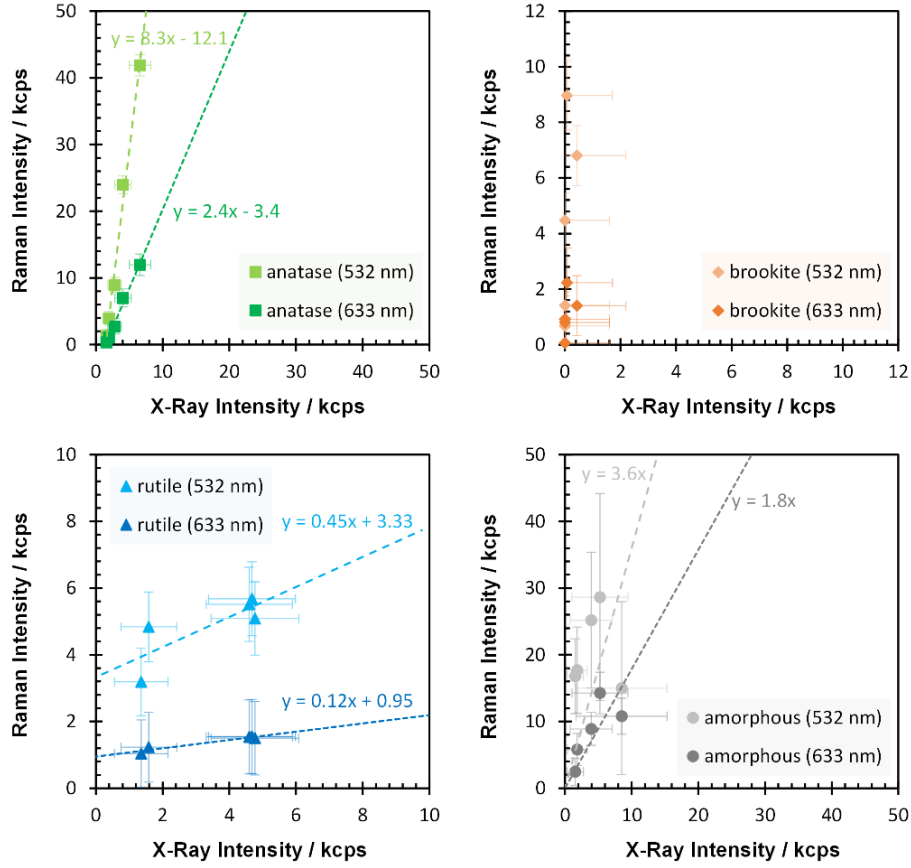


Fig. 75: Intensities (number of counts) of the TiO₂ phases, anatase, brookite, rutile, and amorphous TiO₂ in the 633 nm and 532 nm spectra Raman spectra vs. in the X-ray diffractograms in one thousand counts per second (kcps).

For each phase, the X-ray intensity axis and the Raman intensity axis are equal. So, one can directly see that the ratios of the Raman and the XRD intensities of brookite $I_{Raman(br)}/I_{XRD(br)}$ is highest, followed by the intensity ratios of anatase $I_{Raman(an)}/I_{XRD(an)}$, and the intensity ratio of amorphous TiO₂ $I_{Raman(am)}/I_{XRD(am)}$, while the Raman to XRD intensity ratio $I_{Raman(ru)}/I_{XRD(ru)}$ of rutile is the lowest:

$$\frac{I_{Raman(br)}}{I_{XRD(br)}} > \frac{I_{Raman(an)}}{I_{XRD(an)}} > \frac{I_{Raman(am)}}{I_{XRD(am)}} > \frac{I_{Raman(ru)}}{I_{XRD(ru)}}. \quad (65)$$

The anatase Raman intensities increase from 0.3 kcps to 12 kcps (633 nm) and from 1.3 kcps to 42 kcps (532 nm) with the XRD intensity increasing from 1.6 kcps to 6.6 kcps . Although the anatase Raman intensities increase strongly with the anatase XRD intensity, with factors of 2.4 (633 nm) and 8 (532 nm), the XRD intensity is relatively large as compared to the anatase Raman intensity for the weakly crystallized film deposited at $155 \text{ }^\circ\text{C}$.

The brookite Raman counts increase from 0.5 kcps to 2.2 kcps (633 nm) and from 0.7 kcps to 9.0 kcps (532 nm), while brookite was detected by XRD only in the two films deposited at the highest temperatures, $310 \text{ }^\circ\text{C}$ and $415 \text{ }^\circ\text{C}$, with values of 0.4 kcps and 0.1 kcps , respectively. The Raman intensities of the brookite phase in the sample deposited at $310 \text{ }^\circ\text{C}$ are 1.2 kcps (633 nm) and 6.8 kcps (532 nm). For these two samples, the brookite grain size is 60 nm as determined from X-ray diffractograms using the Scherrer method (in chapter 6.1.1). The absence or low intensity of brookite in the X-ray diffractograms could be caused by crystal sizes that are so small that most crystals are X-ray amorphous and only the biggest crystals are visible.

The rutile Raman intensity increases from 1.2 kcps to 1.5 kcps (633 nm) and from 4.0 kcps to 5.5 kcps (532 nm) with increasing X-ray intensity from 1.3 kcps to 4.7 kcps .

The 633 nm and 532 nm Raman intensities of the amorphous TiO_2 phase have increasing trends with increasing XRD intensities, but show high variance, especially in the Raman spectra that were taken with a 532 nm laser.

Straight trendlines are added to Fig. 75 for both laser wavelengths for each phase except for brookite, where the X-ray intensity was too low or mostly absent in the diffractograms. Pelletier suggests to fit the relation of phase contents in Raman spectra with a straight line with a slope a and intersect b by $y = ax + b$.¹⁹ We used this kind of trendlines for anatase and rutile. The trendlines for amorphous TiO_2 was forced to intersect both axes at 0 because of the high variance in the data points.

The slopes and intersects of the trendlines (of the Raman intensity axis) of anatase and rutile are 3.5 times higher for the Raman spectra taken with a 532 nm laser than for the Raman spectra taken with a 633 nm laser. This agrees with equation (62).

The trendlines that are applied to the data for anatase and rutile do not go through 0 for both lasers (633 nm and 532 nm). The anatase trendlines intersect the XRD-axis at 1.5 kcps for both laser wavelengths, and the rutile trendlines intersect the Raman-axis at 1 kcps and 3 kcps . Yet, the relation of Raman and XRD is nearly proportional for anatase.

As mentioned in chapter 5.2, the X-ray or Raman intensity should be proportional to the amount of the measured material. Thus, if the Raman and X-ray intensities are not proportional,

there must be further aspects that alter the measured intensities. This discrepancy could be caused by intrinsic properties of the analyzed films, by limitations of the experimental setup, or by errors in the quantitative evaluation of the Raman spectra and X-ray diffractograms.

The low Raman intensities of anatase in the weakly crystallized films coated at $155\text{ }^{\circ}\text{C}$ and $200\text{ }^{\circ}\text{C}$ indicate that the activation of phonons is inhibited in these films. This correlates with three observations: Firstly, the anatase lattice is distorted and relaxes with the deposition temperature, and thus with the anatase content (see Fig. 85 in chapter 6.1.1). Secondly, in chapter 6.2, we observed that disorder-induced Raman scattering becomes less in the anatase phase background spectra of evaporated single-phase anatase thin films with increasing crystallization due to increasing annealing temperature. Thirdly, anatase is surrounded by a relatively high amount of brookite and rutile in the films coated at $155\text{ }^{\circ}\text{C}$ and $200\text{ }^{\circ}\text{C}$. Thus, phonons in the anatase crystallites might be suppressed by adjacent brookite and rutile crystallites.

The relatively low rutile intensity in the X-ray diffractograms of the weakly crystallized films could be caused by a very small crystallite size of rutile. As mentioned in chapter 5.2.1, rutile formation takes place most probably by particle impact in our films. This was suggested by Löbl et al. for sputtered TiO_2 thin films, where TEM imaging revealed that the rutile crystals were considerably smaller than the anatase crystals.¹⁴⁴

Actually, the low rutile intensity in the X-ray diffractograms of the weakly crystallized films correlate with small crystallite sizes as determined from the Raman peak widths of the rutile E_g and A_{1g} modes arising from phonon confinement (see chapter 6.1.1). The crystallite sizes as determined from the Raman spectra increases from 1.7 nm to 3.3 nm for rutile and from 5.2 nm to 6.6 nm for anatase with the deposition temperature increasing from $155\text{ }^{\circ}\text{C}$ to $415\text{ }^{\circ}\text{C}$ while the anatase as well as rutile crystallite size as determined from X-ray diffractograms using the Scherrer method increases from 7 nm to 16 nm .

In a study of Viana et al. on the average sizes of anatase nanoparticles synthesized by a solvothermal method, the crystal size as determined from Raman spectra by the phonon confinement model were closer to the average size as determined by TEM, as compared to X-ray diffraction.¹⁴⁵ If in our work the crystallite sizes that were determined by Raman spectroscopy are also more accurate than grain sizes that were determined by the volume weighted Scherrer method, a significant amount of rutile crystallites should be significantly smaller than 2 nm in the less crystallized films deposited below $250\text{ }^{\circ}\text{C}$. Such small crystals are most probably *X-ray amorphous*, but Raman active as crystalline modes. This leads to an

underrepresentation of rutile in the X-ray diffractograms and an overestimation of grain size using the Scherrer equation.

A further reason for the non-linear relation between the Raman and X-ray intensities of rutile could lie in the rutile phase background Raman model spectrum. Fig. 76 (top) illustrates that the rutile phase background model spectrum resembles the Raman spectrum of amorphous TiO_2 . The figure shows a typical rutile Raman spectrum (blue) with a strong rutile phase background spectrum (light blue). For comparison, a simulated spectrum of amorphous TiO_2 is added to the figure. The intensity of the amorphous spectrum is chosen so that one can see the similarities with the phase background model of rutile. From this depiction, one can follow that there is an uncertainty in distinguishing between rutile and amorphous TiO_2 .

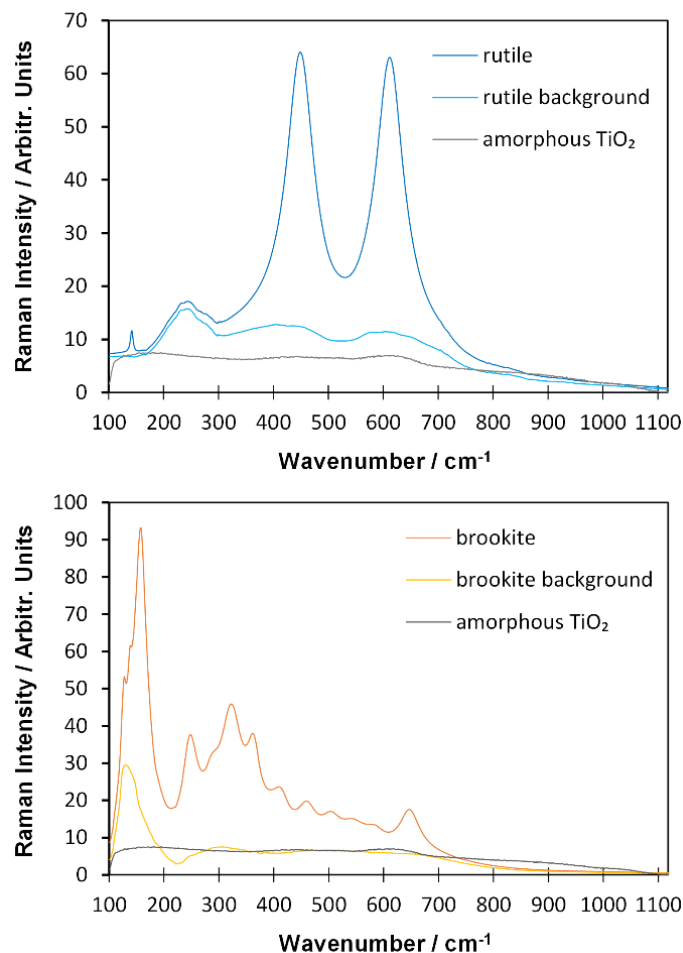


Fig. 76: Top: a simulated rutile Raman spectrum (blue) with its phase background (light blue) compared to a simulated Raman spectrum of amorphous TiO_2 (gray), bottom: simulated brookite Raman spectrum (orange) with its phase background (light orange) compared to a simulated Raman spectrum of amorphous TiO_2 (gray).

It is possible that either the phase background of rutile resembles the spectrum of amorphous TiO₂ or that the literature rutile spectrum that was used to build the rutile phase background model contains a considerable amount of amorphous TiO₂.

Furthermore, the low increase of rutile Raman intensity as compared to X-ray intensity with increasing deposition temperature correlates with a strong increase in anatase content, thus the rutile phonons might be suppressed by adjacent anatase content.

In Fig. 76 (bottom), one can see a certain similarity of the brookite phase background model spectrum (light orange) with the amorphous TiO₂ Raman spectrum. Yet here, above 800 cm⁻¹ and around 210 cm⁻¹ they are clearly distinct.

An interpretation of the cross-sections of Raman and XRD measurements on the various TiO₂ phases is not simple in the analyzed set of samples, because of the non-linear relation of anatase and rutile intensities. When for each phase the slopes of the trendlines in Fig. 75 are interpreted as the ratios of the Raman and the XRD cross-section, one would get Raman/XRD intensity ratios of:

$$\frac{I_{Raman(br)}}{I_{XRD(br)}} : \frac{I_{Raman(an)}}{I_{XRD(an)}} : \frac{I_{Raman(am)}}{I_{XRD(am)}} : \frac{I_{Raman(ru)}}{I_{XRD(ru)}} = 30 : 20 : 10 : 1. \quad (66)$$

The ratio of the rutile Raman intensity and XRD intensity $I_{Raman(ru)}/I_{XRD(ru)}$ is normalized to a value of 1. For this estimation, a slope is missing for brookite. We therefore took the ratios of the brookite Raman and X-ray intensities for the sample with the most pronounced brookite diffractogram, deposited at 310 °C.

Anyway, using the slope of the trendlines as estimates for the ratio of Raman and XRD cross sections is not accurate in this study. The estimation of the crystal size using XRD (Scherrer) does not agree with the crystal size determined by Raman (phonon confinement model). The XRD intensity might be underestimated due to the small crystallite sizes of the samples deposited at low temperatures.

In order to avoid the impact of small crystals on the X-ray intensity and possible weakening of Raman intensity caused by a distorted lattice, we consider only the intensities of the samples deposited at 310 °C and 415 °C, which are most crystalline and have the largest crystals. Comparing the Raman and XRD intensity ratios of these samples, we get Raman/XRD intensity ratios of:

$$\frac{I_{abs,Raman(br)}}{I_{abs,XRD(br)}} : \frac{I_{abs,Raman(an)}}{I_{abs,XRD(an)}} : \frac{I_{abs,Raman(am)}}{I_{abs,XRD(am)}} : \frac{I_{abs,Raman(ru)}}{I_{abs,XRD(ru)}} = 12 : 6 : 3 : 1, \quad (67)$$

where the ratio of the rutile Raman intensity and XRD intensity $I_{Raman(ru)}/I_{XRD(ru)}$ is normalized to a value of I .

5.2.4 Correlation between relative XRD and Raman intensities

A comparison of the relative Raman intensity (or apparent phase content) in the Raman spectra vs. the X-ray diffractograms is shown in Fig. 77.

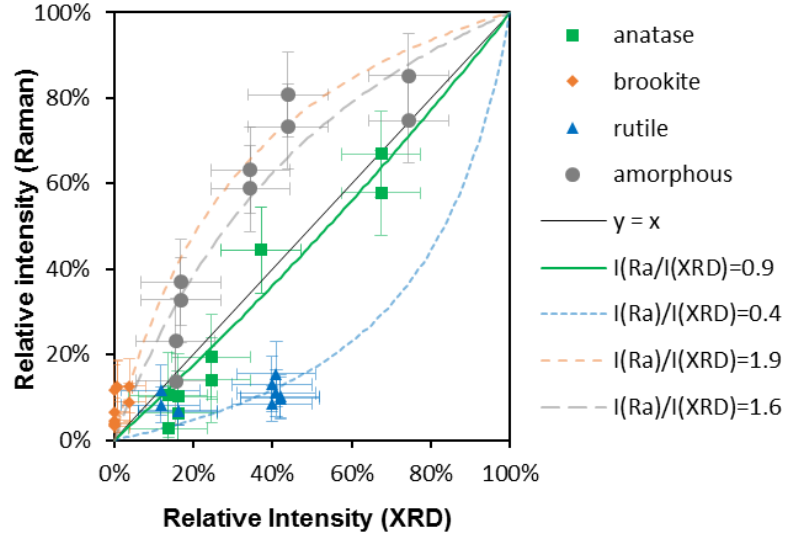


Fig. 77: Apparent phase contents of the TiO₂ phases, anatase, brookite, rutile, and amorphous TiO₂ in the Raman spectra (including 633 nm and 532 nm spectra) vs. in the X-ray diffractograms.

The shown data points include the apparent phase contents in the Raman spectra of both laser wavelength, 633 nm as well as 532 nm. A distinction between both laser wavelengths would provide similar results because they are almost equal for each phase, as can be seen in the right side of Fig. 74.

Simulated lines are added to the figure that give relative Raman intensities $I_{rel,Raman}$ for relative XRD intensities $I_{rel,XRD}$ from 0% to 100% corresponding to certain cross-section ratios k of Raman spectroscopy and XRD intensities with $k = I_{Raman}/I_{XRD}$. These lines are simulated by:

$$I_{rel,Raman} = 1 - \frac{(1-I_{rel,XRD})}{k^2 \cdot I_{rel,XRD} + (1-I_{rel,XRD})}, \quad (68)$$

and are fitted to the data shown in Fig. 77 for each phase with *solver* using the least-square method. These simulated trendlines give ratios of relative Raman and XRD phase contents $I_{rel,Raman}/I_{rel,XRD}$ for brookite, anatase, amorphous TiO₂, and rutile as:

$$\frac{I_{rel,Raman(br)}}{I_{rel,XRD(br)}} : \frac{I_{rel,Raman(an)}}{I_{rel,XRD(an)}} : \frac{I_{rel,Raman(am)}}{I_{rel,XRD(am)}} : \frac{I_{rel,Raman(ru)}}{I_{rel,XRD(ru)}} = 5 : 2 : 4 : 1, \quad (69)$$

which differs strongly from equations (66) and (67). If, again, the values of the weakly crystallized samples are omitted and solely the values for the highest crystalline films with the largest crystals are compared, we get relative $I_{rel,Raman}/I_{rel,XRD}$ ratios of

$$\frac{I_{rel,Raman(br)}}{I_{rel,XRD(br)}} : \frac{I_{rel,Raman(an)}}{I_{rel,XRD(an)}} : \frac{I_{rel,Raman(am)}}{I_{rel,XRD(am)}} : \frac{I_{rel,Raman(ru)}}{I_{rel,XRD(ru)}} = 10 : 4 : 3 : 1, \quad (70)$$

where the ratio of the rutile Raman intensity and XRD intensity $I_{Raman(ru)}/I_{XRD(ru)}$ is normalized to a value of 1, which agrees quite well with equation (67).

5.2.5 Conclusions

TiO₂ thin films were rf-diode sputtered onto B270 glass at substrate temperatures of 155 °C to 415 °C. The films are multiphase, including anatase, brookite, rutile, and amorphous TiO₂. The film thickness is 70 nm, and the density increases from 3.8 g/cm³ to 4.0 g/cm³ as the films gain crystallinity with increasing substrate temperature. For a quantitative comparison of Raman spectroscopy with X-ray diffraction (XRD), each sample was analyzed by XRD as well as by Raman, with two different lasers (532 nm and 633 nm). Adjustable model diffractograms and model spectra for multi-phase thin films have been used to determine the relative content of X-ray counts or photon counts of the individual TiO₂ phases in the X-ray diffractograms and in the Raman spectra. The corresponding models are described in chapters 3.2 and 3.3.

The overall trends of the phase intensities with increasing deposition temperature are similar for all three measurement methods. The intensity of the anatase phase is growing while the intensity of the amorphous phase decreases with the deposition temperature. Brookite is found in all Raman spectra of both laser wavelengths and the (absolute and relative) intensity of counts that we assign to brookite increases with the deposition temperature. However, in the X-ray diffractograms, only a few brookite peaks become visible, for deposition temperatures above 300 °C. The intensity of the rutile phase reaches its maximum already at 200 °C and decreases strongly at 415 °C to a value almost as low as the minimum value at 155 °C in the X-ray diffractograms as well as in the Raman spectra.

As mentioned in chapter 5.1, we use two different methods to interpret one set of data of X-ray diffractograms and Raman spectra of multi-phase TiO₂ thin films that we decomposed into various components including anatase, brookite, rutile, and amorphous TiO₂. In chapter 5.2.3, we compared and discussed the total numbers of photon counts that we assign to each phase. The same is done with the relative amount of photon counts assigned to each phase in chapter 5.2.4.

The ratios of the intensity ratios of Raman and X-ray intensities of the TiO₂ phases is similar for both methods. Combining the values of equations (67) and (70), we get:

$$\frac{I_{Raman(br)}}{I_{XRD(br)}} : \frac{I_{Raman(an)}}{I_{XRD(an)}} : \frac{I_{Raman(am)}}{I_{XRD(am)}} : \frac{I_{Raman(ru)}}{I_{XRD(ru)}} = 10 : 5 : 3 : 1. \quad (71)$$

The value for rutile is normalized to 1. The values are very imprecise, especially for brookite, and we therefore have rounded each value to one digit. We suggest that the ratios in equation (71) can be interpreted as a conservative estimate for the ratios of Raman and XRD cross sections. In chapter 5.5, these results will be further discussed and compared to the results of chapter 5.4.

When further factors that vary Raman or XRD intensities (for example phonon confinement or disorder) are ignored, the results imply that the ratio of Raman and XRD sensitivities (or cross-sections) to brookite is *ten* times higher than to rutile.

Brookite was found in the Raman spectra of all samples, while it was detected in the X-ray diffractograms of the most crystalline films only. Thus, Raman is more suitable than XRD to detect and characterize small amounts of brookite.

The estimated apparent phase contents of anatase, brookite, rutile, and amorphous TiO₂ are similar for both Raman laser wavelengths, 633 nm and 532 nm. The most notable result of the comparison of the phase quantification using two different laser wavelengths is that there is a linear relationship between the total intensities that our models assigned to the crystalline TiO₂ phases. This implies two things: firstly, between the crystalline TiO₂ phases, there is most probably no notable variation of the wavelength-dependency of the Raman cross-section. Secondly, the linearity of the total Raman photon intensities (and thus also the matching relative intensities) that our models assign to the various phases suggests that the models for anatase, rutile, and brookite are well suited for the decomposition of mixed-phase TiO₂ Raman spectra. Crystalline phases are easier quantifiable than the amorphous phase.

The ratios of amorphous TiO₂ Raman intensity and X-ray intensity have a high variance, especially in the Raman spectra taken with a 532 nm laser, which have a low signal-to-noise ratio. These spectra were taken 100 times for 1 s at one fixed position. The variance is smaller in the 633 nm Raman spectra, which were average spectra of Raman spectra taken at 121 × 121 positions (laser spot size ca. 0.6 μm) in an area of 30 μm × 30 μm for 1 s each. This suggests that quantifiability of amorphous TiO₂ by Raman or XRD is limited as compared to the crystalline phases. The quantification of amorphous TiO₂ by XRD and Raman becomes more

consistent when Raman spectra have a high signal-to-noise ratio and/or when the (micro-)Raman measurements are not limited to one position.

The weakly crystallized films deposited at $155\text{ }^{\circ}\text{C}$ and $200\text{ }^{\circ}\text{C}$ have a distorted anatase lattice and show a relatively low first-order anatase Raman intensity while the anatase phase background is strong, presumably containing intense disorder-induced scattering. This suggests that the intensity of first-order Raman scattering needs a certain degree of order within the crystals.

The X-ray intensity of rutile is low in the same two weakly crystallized samples. The average crystallite size in such samples of rutile is $< 2\text{ nm}$ as determined by Raman (phonon confinement model using peak position and peak width) and around 7 nm as determined by XRD (Scherrer method). A certain amount of crystals could be too small to be detected by XRD ('X-ray amorphous'). Thus, XRD underestimates the amount of the phases with very small crystals and is suitable for phase quantification for larger crystals only.

5.2.6 Suggested further studies

Future studies should perform 532 nm Raman measurements with varying positions on the samples with a higher signal-to-noise ratio in order to assess the quantifiability of the amorphous phase. In the discussed set of samples, the signal-to-noise ratio is the more crucial source of error because the Raman measurements do not vary with the position of the measurement – as can be seen in the Raman maps taken with the 633 nm laser (see chapter 7.1).

A further aspect that generally could hinder an accurate simulation of the Raman spectra and X-ray diffractograms of the amorphous TiO_2 phase is a possible interaction of the model spectra/diffractograms for the substrates and the spectra/diffractograms of the amorphous TiO_2 phase. Both kinds of spectra/diffractograms are modeled over the whole measured wavenumber range and use simple, rigid models (see chapters 3.2.2.1 and 3.2.3.2 as well as 3.3.2 and 3.3.4). The luminescence spectra in the Raman measurements vary with the laser wavelengths (compare the luminescence spectra derived from measurements with 633 nm excitation in Fig. 44 in chapter 3.1.5.2 and with and 532 nm excitation in Fig. 184 in the appendices). The models for amorphous TiO_2 could be revised by studying Raman spectra and X-ray diffractograms of amorphous and partly crystalline TiO_2 material that is thicker than the penetration depth of the Raman laser or the XRD beam. In this way, one can avoid a superposition of substrate signals with the signals arising from the TiO_2 samples.

The model for rutile Raman background spectra should be improved in following studies. In order to prepare new models for rutile phase backgrounds, one could use group-theory

analysis of the selection rules for the first-order and second-order scattering processes and perform ab initio calculations on phonon dispersion relations using density functional theory. These kinds of simulations are complex and need a high amount of computing power, so this should be used for the preparation of the model spectra and should not be implemented into the fitting routine for the decomposition of measured Raman spectra. Studies on the second-order spectrum of rutile can be found in an article of Nicola et al.¹²⁹ Anyway, further (non-second-order) phase background has also be added to such a model.

Also, more experiments should be done with high numbers of samples in order to get a higher number of statistical values for the phase quantification.

5.3 Influence of the substrate on the phase composition of multi-phase TiO₂ films

In this chapter, Raman spectra (*633 nm*) of TiO₂ films on various substrates are quantified and discussed. Therefore, three different substrates, B270 glass, Si wafers, and fused silica, were simultaneously rf-sputter coated with TiO₂. The spectra were decomposed into various components which are simulated by adjustable model spectra using the methods discussed in chapters 3.1 and 3.2.

The Raman spectra of the TiO₂ films on B270 glass have already been discussed and compared to *532 nm* Raman spectra and to X-ray diffractograms in chapter 5.2. Here, they are compared to Raman spectra of TiO₂ on fused silica and on Si.

We measured, decomposed and quantified Raman spectra using a *633 nm* laser on TiO₂ thin films that were coated onto the substrates Si, fused silica, and B270 glass at various temperatures ranging from *155 °C* to *415 °C*. The films were coated simultaneously during the deposition processes that is described in chapter 2.1.1 onto the three different kinds of substrates. The Raman spectra are quantified by decomposing the measured spectra into various components that were simulated by adjustable model spectra as described in chapters 3.1 and 3.2. The decomposition of the Raman spectra of the films coated onto Si, B270, and fused silica into their sub-spectra are shown in the figures Fig. 60, Fig. 61, and Fig. 62, respectively, in chapter 4.1.3.

We quantified Raman spectra of TiO₂ thin films that were rf-diode sputtered onto the substrates Si, fused silica, and B270 glass, coated at various substrate temperatures from *155 °C* to *415 °C*. On all substrates, the Raman intensity of the amorphous phase decreases with increasing temperature while the intensities of anatase and brookite increase. The relative amount of brookite Raman counts increases from around *5%* to *10%*, the rutile Raman counts are around *8%* of the TiO₂ thin film counts. On the crystalline Si substrates, the anatase content is higher and the amorphous content is lower in the Raman spectra of TiO₂ than on the glassy substrates, B270 and fused silica. On B270 and fused silica, the Raman intensity that we attribute to the anatase phase, accounts for *10% (±8%)* of the total counts of the TiO₂ thin film coated at *155 °C*, and increases to *65%* with the substrate temperature increasing to *415 °C*. On the Si substrate, the anatase counts increase from *35%* to *80%*.

The main difference that we found in the phase composition of the TiO₂ films is that the amorphous amount is lower on the Si substrate than on the glassy substrates, B270 and fused silica.

The absolute and the relative Raman intensities of the four TiO₂ phases, anatase, brookite, rutile, and amorphous TiO₂ are shown in Fig. 78 (in *kcps* and in percent). The values of anatase

are marked as green squares, brookite as orange rhombuses, rutile as blue triangles, and amorphous TiO₂ as gray circles.

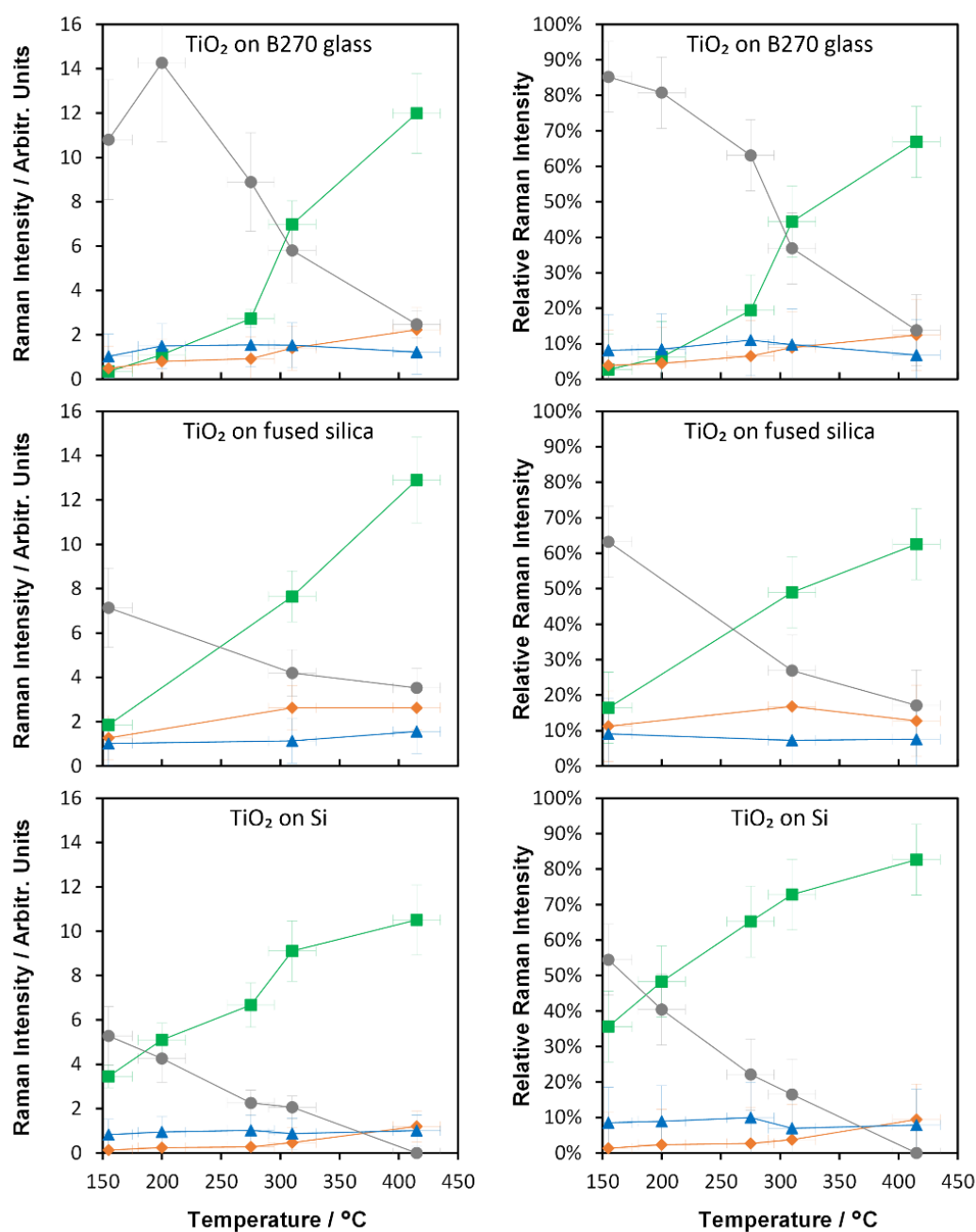


Fig. 78: Quantification of 633 nm Raman spectra of TiO₂ phases in thin films that were diode-sputtered onto B270, fused silica, and Si substrates at various substrate temperatures of 155 °C – 415 °C. The values of anatase are marked as green squares, brookite as orange rhombuses, rutile as blue triangles, and amorphous TiO₂ as gray circles. The left side shows contributions (in thousand counts per second) of anatase, brookite, rutile, and amorphous TiO₂ to the Raman. The right side depicts the same values as relative contents.

All TiO₂ allomorphs that exist at room temperature at atmospheric pressure are present in the Raman spectra of each film. The TiO₂ films coated at 155 °C are predominately amorphous

on all three substrates and they become more crystalline with increasing temperature and are mainly crystalline (anatase) at a substrate temperature of 415 °C. This was confirmed by XRD for the set of TiO₂ thin films on B270 glass in chapter 5.2. The number of counts that we attribute to the amorphous phase decreases from 9 *kcps* (± 2 *kcps*) to 3 *kcps* (± 0.5 *kcps*) or from 75% ($\pm 10\%$) to 15% ($\pm 5\%$) with increasing temperature on the two glassy substrates, B270 and fused silica. The amorphous content is lower on the Si substrate: the total amount of counts from the amorphous phase decreases from 5 *kcps* to almost 0 *kcps* or from 55% to almost 0%. On B270 and fused silica, the Raman intensity that we attribute to the anatase phase, accounts for 10% ($\pm 8\%$) for the film coated at 155 °C, and increases to 65% with the substrate temperature increasing to 415 °C. On the Si substrate, the anatase Raman counts are higher and increase from 35% to 80% of the TiO₂ counts. Besides anatase, the brookite Raman spectra also become more intense with increasing temperature. The relative amount of Raman counts assigned to the brookite phase increases from 5% to 10% and the rutile counts are around 8% in the Raman spectra of the TiO₂ films on all three substrates.

5.4 Quantitative comparison of Raman with XRD on e-beam evaporated TiO₂ anatase films

In this chapter, we compare the intensities in Raman spectra and X-ray diffractograms of the TiO₂ phases, anatase, brookite, rutile, and amorphous TiO₂ for e-beam evaporated undoped and Nb-doped TiO₂ thin films – analogously to the work presented in chapter 5.2. The preparation of the films is described in chapter 2.1.2.

The films are amorphous as-deposited and crystallize to mainly anatase with increasing annealing temperature. First crystallization starts at 375 °C as crystalline anatase islands, as we will see in the Raman maps in chapter 7.2. At 400 °C and above the whole surface is covered with anatase. The same set of Raman spectra and X-ray diffractograms that are quantitatively analyzed here, are qualitatively analyzed in chapter 6.1.2.

5.4.1 Phase quantification with XRD and Raman

We have decomposed X-ray diffractograms as well as 633 nm Raman spectra of 300 nm thick TiO₂ thin films on B270 glass that were e-beam evaporated at 250 °C and post-heated at various temperatures up to 750 °C (± 20 °C). The films that were post-heated at 750 °C, were coated onto fused silica because this temperature is too high for the B270 glass samples. For each of the temperatures 250 °C, 420 °C, 530 °C, 640 °C, and 750 °C, there are values for three samples with different degrees of Nb-doping, TiO₂ (undoped), Ti_{0.92}O_{2.25}Nb_{0.08} (8 at.% Nb), and Ti_{0.84}O_{2.25}Nb_{0.16} (16 at.% Nb). See chapter 2.1.2 for the deposition parameters and sample preparation and see chapter 6.1.2 for the stoichiometry. For Ti_{0.92}O_{2.25}Nb_{0.08}, there are also values given for 350 °C, 375 °C, 400 °C, and 450 °C.

The contributions to the diffractograms and Raman spectra were quantified for each TiO₂ phase. The left side of Fig. 79 shows the intensities of anatase, brookite, rutile, and amorphous TiO₂ in thousand counts per second (*kcps*) as measured by XRD and Raman spectroscopy (633 nm) versus the annealing temperature. The right side of Fig. 79 displays the relative amount of counts that we assign to the individual phases in the X-ray diffractograms and Raman spectra (calculated from the data of the left column).

Raman intensities are represented by closed symbols and XRD intensities by open symbols. Anatase is represented by green squares, brookite by orange rhombuses, rutile by blue triangles, and amorphous TiO₂ by gray circles. Lines are added to each graph to guide the eye – solid lines represent Raman and dashed lines represent XRD intensities. The lines that are added to the graphs of anatase and amorphous TiO₂ connect the averaged values of the three differently doped samples for each temperature. For brookite, the added lines connect the data

points for the undoped samples (TiO_2). For rutile, straight trendlines are added to each set of TiO_2 thin films with different Nb contents for Nb0 (light blue), $\text{Ti}_{0.92}\text{O}_{2.25}\text{Nb}_{0.08}$ (medium blue), and $\text{Ti}_{0.84}\text{O}_{2.25}\text{Nb}_{0.16}$ (dark blue). The trendlines are forced to intersect the temperature axis at $250\text{ }^\circ\text{C}$, which is the deposition temperature of the samples prior to the post-heating. For rutile, the error bars are left out for clarity. Here, the error bars are in the order of 2 kcps for Raman and 0.5 kcps for XRD.

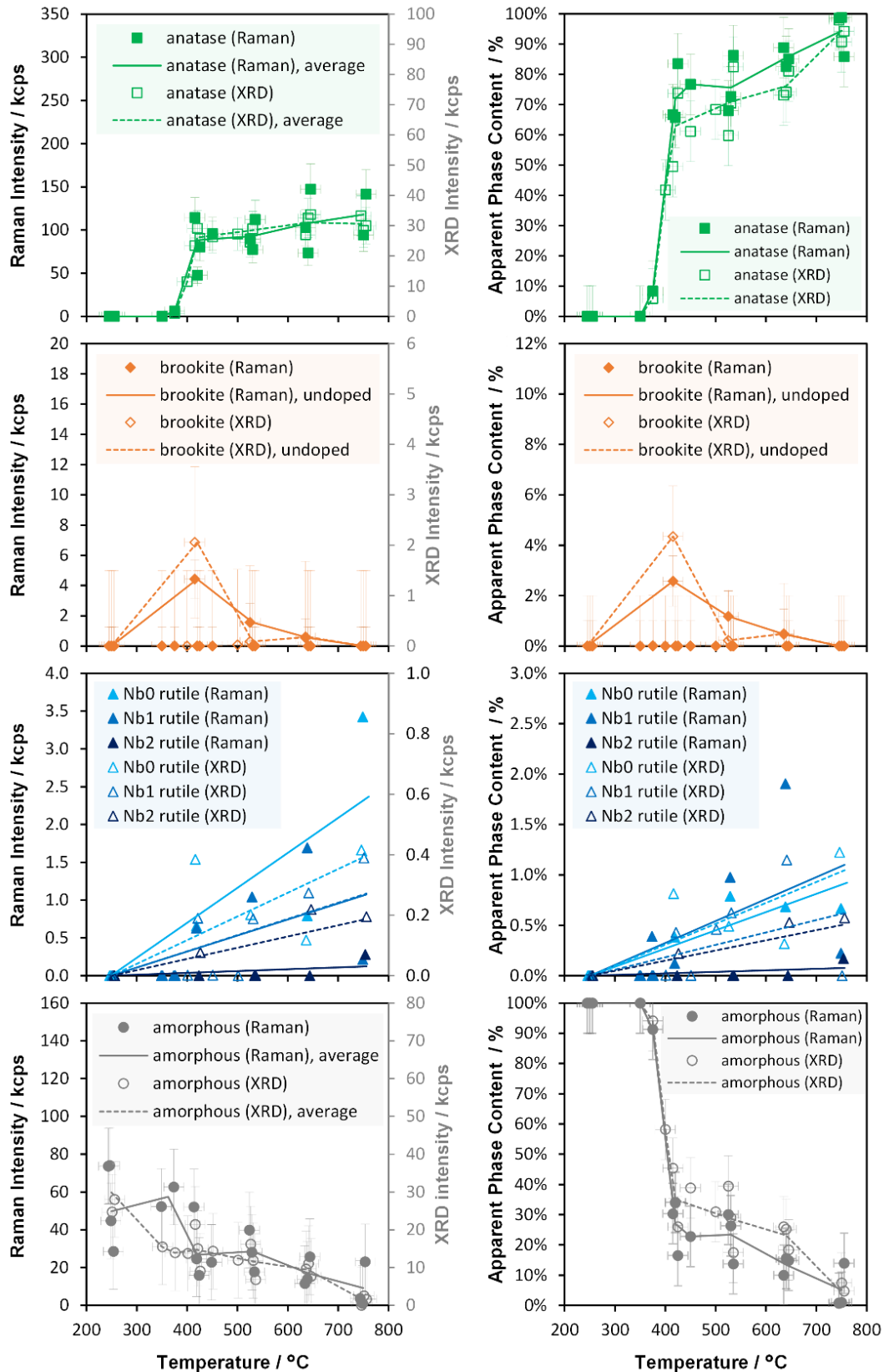


Fig. 79: Left side: contributions (in thousand counts per second) of anatase, brookite, rutile, and amorphous TiO₂ to XRD diffractograms and (633 nm) Raman spectra of e-beam evaporated TiO₂ thin films post-heated at temperatures of 250 °C – 750 °C. For each phase, the Raman intensities refer to the left axis and the X-ray intensities refer to the right axis. Right side: apparent phase content (= relative amount of counts) of the TiO₂ phases in the XRD diffractograms and (633 nm) Raman spectra.

All films are amorphous after deposition at 250 °C. Below annealing temperatures of 375 °C, the films do not show any crystallinity neither in the X-ray diffractograms nor in the Raman spectra. The total and the relative intensities of anatase and amorphous TiO₂ in the Raman spectra and diffractograms are independent of the Nb content. The variance of the intensities of anatase and amorphous TiO₂ is higher in the Raman spectra than in the X-ray diffractograms.

Anatase is found in all X-ray diffractograms and Raman spectra of the films post-heated at temperatures of 375 °C and above. The anatase content in the spectra and diffractograms of the film post-heated at 375 °C is very low with 1 *kcps* in the diffractogram and 7 *kcps* in the Raman spectrum. The intensity increases strongly to values of 90 *kcps* in the Raman spectra and 25 *kcps* in the diffractograms with annealing temperature increasing to 420 °C. This correlates with the strong increase in the area of anatase on the Raman maps in chapter 7.2. There, we present that anatase islands are formed in a matrix of amorphous TiO₂ at 375 °C and that the films become crystalline over the whole area at temperatures of 400 °C and higher. The anatase intensity increases slightly further to values of 120 *kcps* in the Raman spectra and 30 *kcps* in the X-ray diffractograms with the temperature increasing to 750 °C.

Analogously to the total intensities, the apparent phase content of anatase (right column of Fig. 79) stays at 0% up to an annealing temperature of 350 °C and grows slightly to values below 10% at an annealing temperature of 375 °C and increases strongly to values around 70% with the annealing temperature increasing to 420 °C. The apparent anatase intensities increase further to a value of 90% at an annealing temperature of 750 °C in both, the Raman spectra as well as in the X-ray diffractograms. In the range in between it is slightly stronger in the Raman spectra than in the X-ray diffractograms.

Brookite is weakly present only in the X-ray diffractograms and Raman spectra of the undoped films and is strongest at the lowest post-heating temperature of 420 °C at which the full area is covered with crystalline phases. It decreases from 4 *kcps* to 0 *kcps* in the Raman spectra and from 2 *kcps* to 0 *kcps* in the X-ray diffractograms, which corresponds to a decrease of the apparent phase content from 2% to 0% in the Raman spectra and from 4% to 0% in the X-ray diffractograms.

Traces of rutile are found in all Raman spectra as well as in the X-ray diffractograms of the undoped films (TiO₂) annealed at temperatures above 400 °C. The intensities increase with the annealing temperature and decrease with the Nb content. In the Raman spectra, rutile is found in the films with 8 *at.%* Nb only at annealing temperatures above 500 °C and in the films with 16 *at.%* Nb only above 700 °C. With the annealing temperature increasing to 750 °C, the

linear trendlines of the rutile Raman intensities increase to 2.4 kcps for the undoped (TiO_2) films, to 1.1 kcps for the films with $8 \text{ at.}\%$ Nb ($\text{Ti}_{0.92}\text{O}_{2.25}\text{Nb}_{0.08}$), and to 0.2 kcps for the films with $16 \text{ at.}\%$ Nb ($\text{Ti}_{0.84}\text{O}_{2.25}\text{Nb}_{0.16}$). With increasing temperature, the rutile X-ray intensity increases to 0.4 kcps for the undoped films and becomes lower with the Nb content and decreases to 0.3 kcps for the $\text{Ti}_{0.92}\text{O}_{2.25}\text{Nb}_{0.08}$ films and 0.2 kcps for the $\text{Ti}_{0.84}\text{O}_{2.25}\text{Nb}_{0.16}$ films. A similar trend is visible for the apparent phase content of rutile in the Raman spectra and in the X-ray diffractograms with a maximum value of 1% for the undoped films.

The amorphous TiO_2 phase is strongest in the as-deposited films with an average Raman intensity of 50 kcps and an average X-ray intensity of 25 kcps . The amorphous features in the X-ray diffractograms and Raman spectra decrease with the annealing temperature to values close to 0 kcps at a temperature of $750 \text{ }^\circ\text{C}$. The amorphous intensity in the X-ray diffractograms gets closer to zero than in the Raman spectra. The trend of the apparent phase content of amorphous TiO_2 in the diffractograms and spectra is the opposite of that of anatase because brookite and rutile are present only as traces.

5.4.2 Correlation between total XRD and Raman intensities

Fig. 80 shows the Raman intensities (633 nm) versus the corresponding X-ray intensities of the TiO_2 allomorphs, anatase, brookite, rutile, and amorphous TiO_2 of the data shown in Fig. 79.

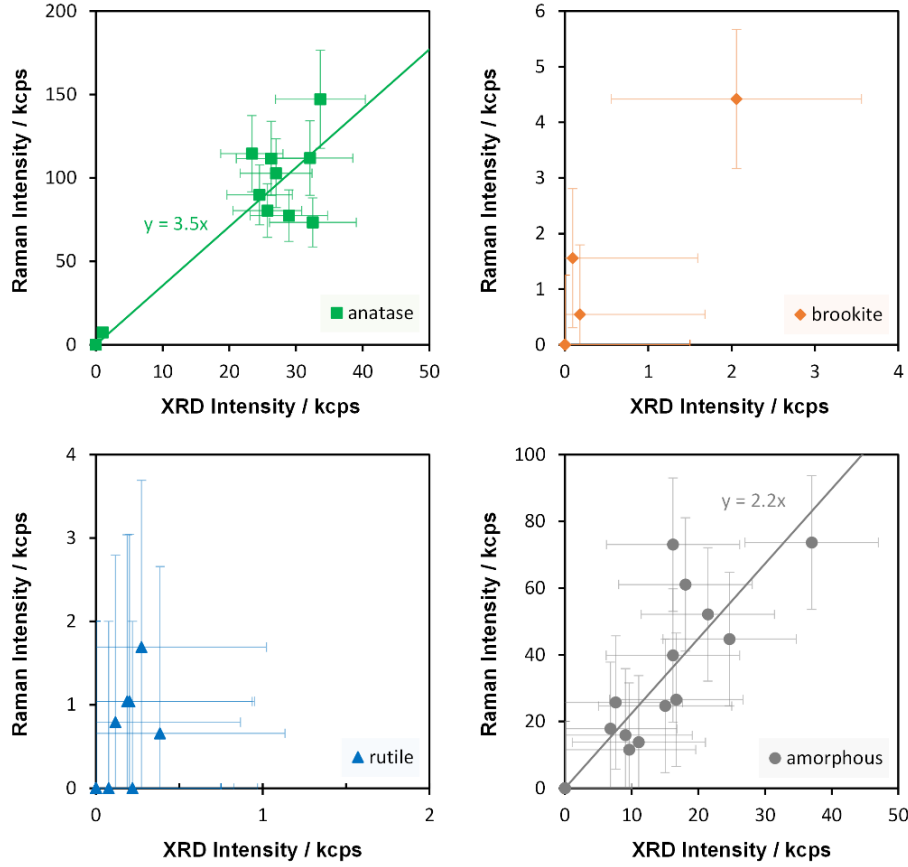


Fig. 80: Raman Intensities (633 nm) of the TiO₂ phases, anatase, brookite, rutile, and amorphous TiO₂ in the X-ray diffractograms e-beam of e-beam evaporated TiO₂ thin films post-heated at temperatures of 250 °C – 750 °C in one thousand counts per second (kcps).

The Raman intensities of anatase and amorphous TiO₂ have high intensities but show a certain variance. Straight trendlines are given for both phases. The equation of the trendline for anatase is

$$I_{abs,Raman(an)} = 3.5 \cdot I_{abs,XRD(an)}, \quad (72)$$

with the absolute anatase Raman intensity $I_{abs,Raman(an)}$ and the absolute anatase X-ray intensity $I_{abs,XRD(an)}$. The equation of the trendline for amorphous TiO₂ is

$$I_{abs,Raman(am)} = 2.2 \cdot I_{abs,XRD(am)}, \quad (73)$$

with the absolute amorphous TiO₂ Raman intensity $I_{abs,Raman(am)}$ and the absolute amorphous TiO₂ X-ray intensity $I_{abs,XRD(am)}$.

Thus, the Raman/XRD intensity ratio is higher for anatase than for amorphous TiO₂. If we interpret the slopes of the trendlines (equations (72) and (73)) as the general intensity ratio

of Raman and XRD in these measurements, the Raman/XRD intensity ratios of anatase and amorphous TiO₂ relate as

$$\frac{I_{abs,Raman(an)}}{I_{abs,XRD(an)}} : \frac{I_{abs,Raman(am)}}{I_{abs,XRD(am)}} = 5 : 3, \quad (74)$$

as an integer ratio. This accounts for the films that are post-heated above temperatures of 400 °C. The anatase Raman intensity $I_{abs,375^{\circ}C,Raman(an)}$ (7 *kcps*) of the film deposited at 375 °C is seven times higher than the anatase X-ray intensity $I_{abs,375^{\circ}C,XRD(an)}$ (1 *kcps*):

$$I_{abs,375^{\circ}C,Raman(an)} = 7 \cdot I_{abs,375^{\circ}C,XRD(an)}. \quad (75)$$

For brookite there are only three values above 0 *kcps* available. There are only traces of brookite and rutile present in the X-ray diffractograms and in the Raman spectra, so the signal-to-noise ratio is low, and the errors are high. Thus, trendlines cannot be given for brookite and rutile.

5.4.3 Correlation between relative XRD and Raman intensities

Fig. 81 shows the relative Raman Intensity vs. the relative X-ray intensity (or apparent phase contents).

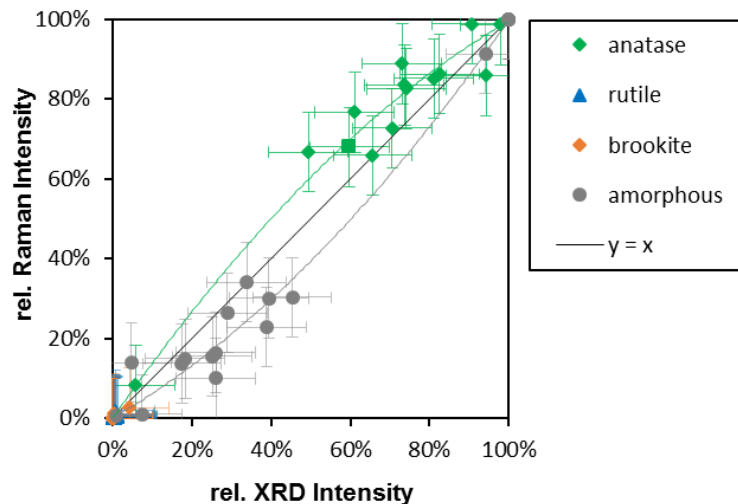


Fig. 81: Apparent phase contents of the TiO₂ phases, anatase, brookite, rutile, and amorphous TiO₂ in the Raman spectra (633 nm) vs. in the X-ray diffractograms of e-beam evaporated films.

The data shown in Fig. 81 are evaluated analogously to the data of Fig. 77 in chapter 5.2.4. The plots indicate a slightly over-linear anatase intensity, 60% in XRD corresponds to 70% in Raman. Yet, apparent phase contents of anatase between 10% and 50% and of

amorphous TiO₂ between 50% and 90% are not given. The values for rutile and brookite are too low for evaluation. The trendlines of the relative contents of amorphous TiO₂ and anatase are described by

$$I_{rel,Raman(am)} = 0.8 \cdot I_{rel,XRD(am)}, \quad (76)$$

with the relative Raman intensity of amorphous TiO₂ $I_{rel,Raman(am)}$ and the relative X-ray intensity of amorphous TiO₂ $I_{rel,XRD(am)}$ and

$$I_{rel,Raman(an)} = 1.2 \cdot I_{rel,XRD(an)}, \quad (77)$$

with the relative Raman intensity of anatase $I_{rel,Raman(an)}$ and the relative X-ray intensity of anatase $I_{rel,XRD(an)}$. This gives a relation of the Raman and XRD intensity ratios for anatase and amorphous TiO₂ of

$$\frac{I_{rel,Raman(an)}}{I_{rel,XRD(an)}} : \frac{I_{rel,Raman(am)}}{I_{rel,XRD(am)}} = 5 : 3, \quad (78)$$

which is equal to the ratio of the absolute values in equation (74). This was to be expected because rutile and brookite are present only as traces.

5.4.4 Conclusions

Undoped and Nb-doped TiO₂ thin films were evaporated by reactive e-beam evaporation onto B270 glass and fused silica with Nb contents of 0 at.%, 8 at.%, and 16 at.%. They were coated at a substrate temperature of 250 °C and individually post-heated at temperatures from 350 °C to 640 °C on B270 glass, and additionally at 750 °C on fused silica.

Each sample was measured by XRD as well as by Raman (633 nm) and the spectra were evaluated quantitatively. Adjustable model diffractograms and model spectra have been used to determine the relative content of X-ray counts or photon counts of the individual TiO₂ phases in the X-ray diffractograms and in the Raman spectra. The corresponding models are described in chapters 3.2 and 3.3. The overall trends of the phase intensity with increasing deposition temperature is similar for both measurement methods.

The main contributions to the X-ray diffractograms and Raman spectra are from anatase and amorphous TiO₂, while the photon counts that we assign to brookite plus rutile contribute to less than 5% of the TiO₂ diffractograms or Raman spectra. The films are amorphous as-deposited and crystallization in Ti_{0.92}O_{2.25}Nb_{0.08} films starts at a temperature of 375 °C (as

crystalline anatase islands in an amorphous matrix, see chapter 7.2.4). The films are mainly anatase after post-heating at temperatures above 400 °C.

The ratio of the anatase Raman intensity $I_{375^{\circ}\text{C},\text{Raman}(\text{an})}$ and the anatase X-ray intensity $I_{375^{\circ}\text{C},\text{XRD}(\text{an})}$ of the films post-heated at 375 °C is *twice* as high as the intensity ratio $I_{\text{Raman}(\text{an})}/I_{\text{XRD}(\text{an})}$ of the films post-heated at temperatures above 400 °C. Combining the equations (72) and (75), we get:

$$\frac{I_{375^{\circ}\text{C},\text{Raman}(\text{an})}}{I_{375^{\circ}\text{C},\text{XRD}(\text{an})}} = 2 \cdot \frac{I_{\text{Raman}(\text{an})}}{I_{\text{XRD}(\text{an})}}. \quad (79)$$

As we will see in the Raman maps in chapter 7.2, crystallization starts as anatase islands in an amorphous matrix. SEM images of this film (also in chapter 7.2) show island sizes between 50 nm and 700 nm. Thus, the islands are too large to be X-ray amorphous and they are mostly smaller than the spatial resolution of the 633 nm Raman maps (ca. 0.6 μm). This suggests that the high Raman to XRD intensity ratio of this sample might be caused not by relatively low X-ray intensity but by a high Raman intensity. The relatively high Raman intensity might lie in the nature of the islands: they are surrounded by an amorphous phase and not by grain boundaries (in the sense of a two-dimensional lattice defect between crystallites) which occur in the films that are crystallized over the whole surface.

Brookite is found in the X-ray diffractograms and the Raman spectra of the undoped TiO₂ films only. The apparent phase content is 3% (±1%) in both, the X-ray diffractogram and the Raman spectrum of the undoped film post-heated at 420 °C. The brookite content decreases with the temperature and disappears at 750 °C.

Rutile is present as traces in the crystalline films post-heated at temperatures above 400 °C. The apparent phase content increases with the temperature and is 1% at the highest post-heating temperature of 750 °C in the X-ray diffractogram as well as in the Raman spectra. The rutile content decreases with the Nb content.

Thus, Nb favors anatase, suppresses brookite and diminishes rutile. For the absolute as well as for the relative intensities, the relation of the Raman and XRD intensity ratios of anatase $I_{\text{Raman}(\text{an})}/I_{\text{XRD}(\text{an})}$ and of amorphous TiO₂ $I_{\text{Raman}(\text{am})}/I_{\text{XRD}(\text{am})}$ is:

$$\frac{I_{\text{Raman}(\text{an})}}{I_{\text{XRD}(\text{an})}} : \frac{I_{\text{Raman}(\text{am})}}{I_{\text{XRD}(\text{am})}} = 5 : 3. \quad (80)$$

5.5 Comparison of the quantitative studies on rf-sputtered and evaporated TiO₂ films

In the following we compare the quantitative Raman and XRD studies of the rf-diode sputtered (DS) and reactive e-beam evaporated (EB) films discussed in chapters 5.2 and 5.4. Fig. 82 shows the Raman intensities and XRD intensities of DS and EB films in *kcps* in logarithmic scale. The values of the rf-diode sputtered films are represented by open symbols and of the e-beam evaporated films by closed symbols. For three rf-diode sputtered films, brookite is found in Raman spectra while it is not found in the corresponding X-ray diffractograms. The absent X-ray intensities are set to 0.02 kcps , so that they are also displayed in the logarithmic scale of Fig. 82. A black diagonal line represents values with $I_{Raman} = I_{XRD}$.

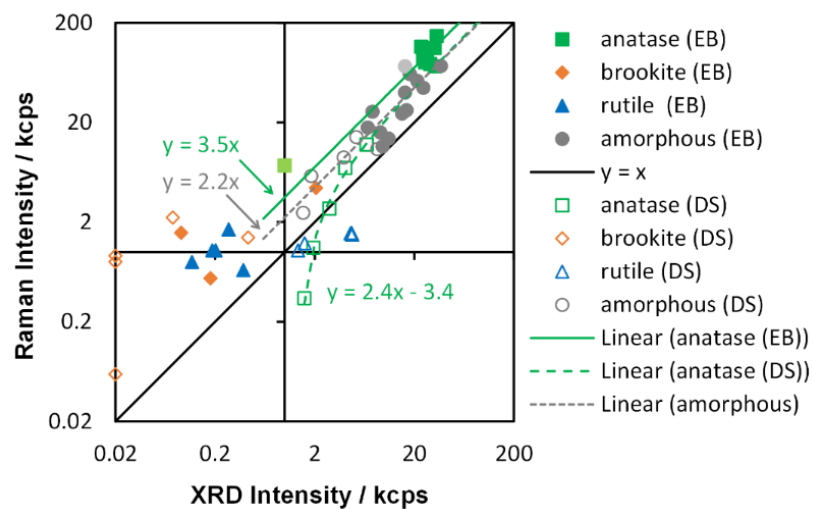


Fig. 82: Raman intensity vs. XRD intensity of anatase, brookite, rutile, and amorphous TiO₂ of rf-diode sputtered (DS) films as open symbols and e-beam evaporated (EB) films as closed symbols. The values of the e-beam coated film with crystalline islands are indicated by light colors.

Linear trendlines are added to the figure for the anatase intensities of the e-beam evaporated films (green solid line), for the anatase intensities of the multi-phase rf-diode sputtered films (green dashed line), and for the intensities of amorphous TiO₂. The trendline of the amorphous phase is equal for both sets of films (the rf-diode sputtered and the e-beam evaporated films), with

$$I_{DS,Raman(am)} = I_{EB,Raman(am)} = 2.2 \cdot I_{XRD(am)}. \quad (81)$$

The trendline of the anatase Raman intensity $I_{EB,Raman(an)}$ vs. the corresponding X-ray $I_{EB,XRD(an)}$ of the films prepared by reactive e-beam evaporation is described by

$$I_{EB,Raman(an)} = 3.5 \cdot I_{EB,XRD(an)}. \quad (82)$$

The anatase Raman intensity of the diode sputtered films $I_{DS,Raman(an)}$ is not proportional to the X-ray intensity $I_{DS,XRD(an)}$ and the trendline is described by

$$I_{DS,Raman(an)} = 2.4 \cdot I_{DS,XRD(an)} - 3.4 \text{ kcps}. \quad (83)$$

The trendline is extrapolated for values above the intensities of the diode sputtered films and it approaches the trendline of amorphous TiO₂ at an XRD intensity of *20 kcps* and the lower values of anatase in the e-beam coated films at an XRD intensity of *40 kcps*. With increasing crystallinity or increasing anatase content, the Raman/XRD intensity ratio of the rf-diode sputtered films gets closer to the Raman/XRD intensity ratios of the e-beam coated films.

Brookite occurs only in undoped samples and is more consistently detected in Raman spectroscopy than in XRD. The brookite intensity increases with the deposition temperature in the rf-diode sputtered samples (with *60 nm* grains) and decreases with the post-heating temperature in the e-beam evaporated samples.

Most brookite intensities and the rutile intensities of the e-beam evaporated films are below *2 kcps* in the Raman spectra as well as in the X-ray diffractograms. Their Raman/XRD intensity ratios are in the order of magnitude as the Raman/XRD intensity ratios of anatase or amorphous TiO₂. Yet the low intensities result in low signal-to-noise ratios. Thus, relating Raman intensities with the X-ray intensities from these values is unreliable.

The intensity of rutile of the rf-diode sputtered films is relatively high in the X-ray diffractograms as compared to the Raman spectra, but the X-ray intensity declines in the diffractograms of films with crystal sizes below *2 nm* (as evaluated with the phonon confinement model).

The rutile Raman/XRD intensity ratios of the rf-diode sputtered films are below those of the e-beam films and become even smaller with increasing X-ray intensity.

The TiO₂ thin film intensity (sum of all four TiO₂ phases) of the rf-diode sputtered films is in average *12 kcps* in the X-ray diffractograms and *18 kcps* in the (*633 nm*) Raman spectra and the thin film intensity of the e-beam evaporated films (post-heated at temperatures above *420 °C*) is in average *42 kcps* in the X-ray diffractograms and *130 kcps* in the (*633 nm*) Raman spectra.

The average X-ray intensity of the e-beam evaporated films is 3.5 times higher than the average X-ray intensity of the rf-diode sputtered films, which is equal to the ratio of the film thicknesses (the EB films are around 250 nm and the films are 70 nm thick). In contrast, the average Raman intensities of the e-beam evaporated films are 7 times higher than those of the rf-diode sputtered films. Thus, in average, the ratio of Raman and XRD intensities $I_{Raman(EB)}$ and $I_{XRD(EB)}$ of the e-beam coated films is twice as high as the ratio of Raman and XRD intensities $I_{Raman(DS)}$ and $I_{XRD(DS)}$ of the diode sputtered films:

$$\frac{I_{Raman(EB)}}{I_{XRD(EB)}} = 2 \cdot \frac{I_{Raman(DS)}}{I_{XRD(DS)}} \quad (84)$$

This must be due to structural differences of the two types of films, not only their thickness: the studies on chapter 6.1 suppose that the diode sputtered films consist of smaller crystallites with a higher defect ratio as compared to the e-beam coated films, which both decrease the lifetime of optical phonons. These findings are supported by the relatively low Raman intensities of the diode sputtered films.

Concerning the intensities of the individual phases there are four remarkable behaviors that we should point out:

1. The rutile Raman/XRD intensity ratio of the rf-sputtered multi-phase films decreases with a decreasing rutile/anatase phase content ratio (the rutile signal is suppressed by other phases).
2. The anatase Raman/XRD intensity ratio of the rf-sputtered multi-phase films decreases with decreasing phase content ratios of anatase/brookite or anatase/rutile (the anatase signal is suppressed by other phases).
3. With increasing apparent anatase phase content (in Raman as well as in XRD) of the rf-sputtered multi-phase films the Raman/XRD intensity ratio gets closer to the Raman/XRD intensity ratio of the e-beam coated films which are mainly anatase.

Thus, the Raman intensity of a certain phase is relatively low when other TiO₂ allomorphs are present.

4. The e-beam coated film post-heated at 375 °C with anatase islands in an amorphous matrix has twice the anatase Raman/XRD intensity ratio than the e-beam coated films which are crystallized over the whole surface.

The intensity of Raman vibrations seems to depend on the environment of the active crystals. Grain boundaries (or two-dimensional lattice defects) between crystallites might suppress phonons as compared to crystallites that are surrounded by an amorphous matrix.

In future studies, a tip-enhanced Raman spectroscopy coupled with a scanning tunneling microscope should be used to measure the Raman intensities of individual crystallites in multi-phase TiO₂ films. Then one should measure Raman intensities of – for example – anatase crystallites which are surrounded by only anatase crystallites and compare these intensities to the Raman intensities of anatase crystallites that are surrounded by amorphous content or by further crystallites. This should be performed for rutile and brookite as well.

6 TiO₂ studies including decomposed TiO₂ Raman spectra

In this chapter we use the decomposed thin film Raman spectra and X-ray diffractograms (see chapter 4) to investigate how the properties of the various crystal phases change with the deposition parameters or post-heating. The studies include a variation of the coating temperature of rf-diode sputtered films (6.1.1), the annealing temperature and Nb incorporation of reactive e-beam evaporated films (6.1.2), or the variation of target oxidation and sample position, annealing temperature, and deposition time of Nb-doped rf-magnetron sputtered TiO₂ thin films (6.1.3).

Chapters 6.2 and 6.3 present further studies on the undoped and Nb-doped reactive e-beam evaporated films. In chapter 6.2 we deduce information about local disorder from the anatase phase backgrounds that occur in the measured Raman spectra. In chapter 6.3 we interpret amorphous TiO₂ as a combination of highly disordered crystalline phases.

6.1 Studies including first-order spectra from decomposed TiO₂ Raman spectra

In this chapter, we study the influence of the deposition temperature on the structural properties of the same rf-diode sputtered multi-phase TiO₂ films that are quantitatively analyzed in chapter 5.2. We mainly discuss X-ray diffractograms, Raman spectra, and use the combination of both methods in order to investigate the crystallite size and defect density in the films.

6.1.1 Structural effects of the deposition temperature on diode-sputtered multi-phase TiO₂ films

Rf-diode sputtered TiO₂ films were deposited as described in chapter 2.1.1. The films have a thickness of 70 nm ($\pm 3\text{ nm}$) and a mass of $134\text{ }\mu\text{g}$ ($\pm 3\text{ }\mu\text{g}$). The thicknesses estimated from optical spectra (simulated in SCOUT) agree well with those measured by the profiler. The film density is between the values of anatase (3.8 g/cm^3)¹⁴⁶ and rutile (4.2 g/cm^3)¹⁴⁶ and grows from 3.8 g/cm^3 ($\pm 0.2\text{ g/cm}^3$) to 4.0 g/cm^3 ($\pm 0.2\text{ g/cm}^3$) with increasing temperature from $155\text{ }^\circ\text{C}$ to $415\text{ }^\circ\text{C}$. The refractive index behaves likewise: it is between the literature values of anatase (2.55) and rutile (2.90) at 550 nm ¹⁴⁶ and grows from 2.55 to 2.72 with increasing deposition temperature. Optical absorption spectra indicate that the band gap becomes sharper and increases with the deposition temperature.¹⁰²

Films deposited for 2 minutes with a thickness of $3\text{ nm} - 4\text{ nm}$ (as estimated by ellipsometry and XPS) are already compact. AFM scans reveal a closed film on the surface of the substrate of the sample coated for 2 minutes. AFM images taken with a height sensor as

well as with an adhesion sensor are shown in Fig. 185 in the appendices. Using XPS on the same sample, we detected a TiO₂ film with a thickness of ca. 4 nm. The corresponding spectrum is shown in Fig. 186 in the appendices.

We analyzed structural properties with XRD and Raman. Diffractograms and spectra were taken as described in chapter 2.2 and decomposed into their components (chapter 4.1). Reflections of anatase, rutile, and amorphous TiO₂ are found in all Raman spectra and X-ray diffractograms. Brookite was found in all Raman spectra as well, but by XRD they are detected only in the diffractograms deposited at deposition temperatures above 300 °C. Quantitative evaluation of XRD and Raman indicate increasing crystallinity with increasing deposition temperature (for more details on the phase composition see chapter 5.2). The increase of crystallinity with the deposition temperature correlates with increasing density and refractive index.

Below, we discuss X-ray diffractograms and Raman spectra of the samples. Furthermore, crystallite sizes are estimate from the XRD measurements and defect density is estimated by comparing Raman with XRD measurements using a phonon confinement model.

6.1.1.1 X-ray diffractograms

Fig. 83 shows the diffractograms of the multi-phase TiO₂ thin films rf-diode sputtered at temperatures between 155 °C and 415 °C (after the B270 glass substrate diffractograms and the instrument backgrounds were subtracted from the measured diffractograms). A detailed view on the range of the anatase (101), the rutile (110), and the brookite (211) reflection (22° – 32°) is shown in the middle. On the right-hand side, the figure presents a detailed view on the range around the brookite (421) reflection (50° – 60°). Literature positions of anatase are marked by green solid lines, rutile by blue dashed lines and brookite by narrowly dashed orange lines.^{125–127} The corresponding Raman spectra of the same samples are shown in Fig. 86.

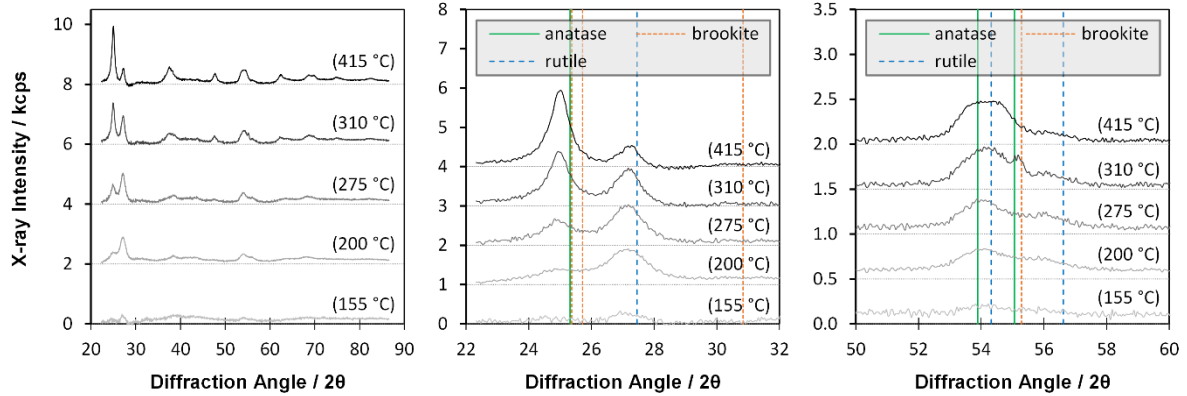


Fig. 83: Diffractograms of multi-phase TiO₂ thin films diode sputtered at temperatures between 155 °C and 415 °C after subtracting the B270 glass substrate diffractograms and the instrument backgrounds from the measured diffractograms. Left: whole range, mid: anatase (101) peak around 25.0° and rutile (110) peak around 27.2°, including the range around the brookite (211) peak position in literature at 30.8°. Right: range around the brookite (421) peak position in literature at 55.2°.¹²⁵

The anatase (101) reflection becomes more intense with increasing temperature while the rutile (110) peak is strongest at deposition temperatures between 200 °C and 275 °C and its intensity decreases with the temperature above 300 °C.

Brookite has 62 *hkl*-reflections of which the strongest brookite peaks in literature are a (210)/(111) doublet at 25.4°/25.7° and the (211) reflection at 30.8°, followed by the (321) reflection at 48.1° and (421) at 55.2°.¹²⁵ The position of the brookite (211) reflection is the only one of these peaks that is not superimposed by anatase or rutile reflections and is not visible in any of the measured diffractograms. In the diffractogram of the film deposited at 310 °C appears a peak at 55.2° that is narrower than the neighboring peaks. This peak can be attributed to brookite (narrowly dashed orange line), but is also close to the standard position of the anatase (211) reflection (solid green line).

Yet, the fitting routine that was used for the decomposition of the X-ray diffractogram (see Fig. 57) implies strongly that this is a brookite peak. This is demonstrated in Fig. 84, which shows the thin film diffractogram of the film deposited at 310 °C (black), the simulated ‘fit’ TiO₂ diffractogram (dashed red), the anatase (105) and (211) peaks (solid green), the rutile (211) and (220) peaks (dashed blue), and the brookite diffractogram (narrowly dashed orange).

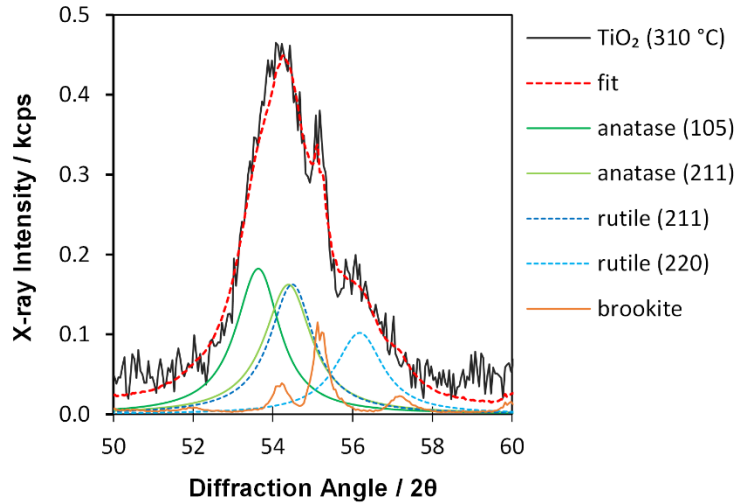


Fig. 84: Diffractogram of a diode sputtered multi-phase TiO_2 thin film deposited at $310\text{ }^\circ\text{C}$ (black), the simulated ‘fit’ TiO_2 diffractogram (dashed red), the anatase (105) and (211) peaks (green), the rutile (211) and (220) peaks (dashed blue), and the brookite diffractogram (orange).

The peak positions of anatase and rutile were manipulated only by the lattice parameters, a and c , over the whole range of the measurement (22° to 87°) and the brookite diffractogram was simulated by a rigid routine as described in chapter 3.3.3.3.

Fig. 85 shows the lattice parameters, a and c , of anatase and of rutile as well as the unit cell volume of anatase, rutile, and brookite. Lines are added to guide the eye. The unit cell volumes of anatase and rutile follow from the lattice parameters, a and c . The brookite lattice volume was determined from all brookite-like structures found in the diffractograms of the films deposited at $310\text{ }^\circ\text{C}$ and $415\text{ }^\circ\text{C}$.

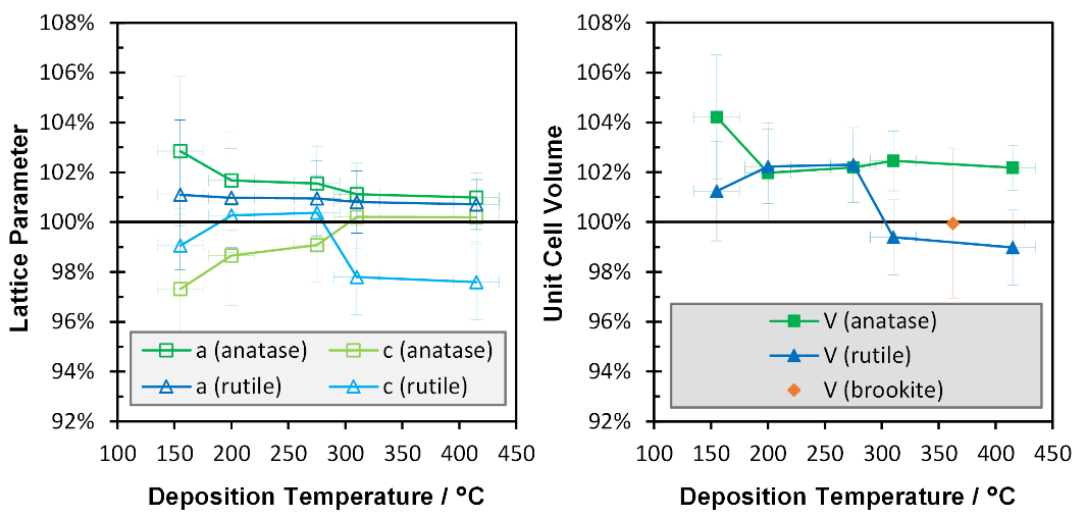


Fig. 85: Left side: lattice parameters a and c of anatase and rutile in rf-diode sputtered TiO_2 films on B270 glass, right side: unit cell volume of anatase, rutile, and brookite.

The anatase lattice of the film deposited at $155\text{ }^{\circ}\text{C}$ is distorted, with the lattice parameter a being 2% larger (3.88 \AA) and c 2% (9.31 \AA) smaller than the standard anatase values ($a = 3.785\text{ \AA}$, $c = 9.514\text{ \AA}$).¹⁴⁷ Both lattice parameters relax and get close to the standard value with the deposition temperature increasing to $415\text{ }^{\circ}\text{C}$. The unit cell volume of anatase is (139.1 \AA^3), 2% bigger than the standard value, for all films deposited at temperatures above $200\text{ }^{\circ}\text{C}$.

The rutile lattice parameters of the film deposited at $155\text{ }^{\circ}\text{C}$ are close to the values of rutile standard powder.¹⁴⁷ The rutile lattice parameter a decreases insignificantly (from 4.64 \AA to 4.63 \AA) and stays around 101% of the standard value ($a = 4.593\text{ \AA}$) while the lattice parameter c decreases from 100% to 98% (from 2.96 \AA to 2.89 \AA) with the temperature increasing to $415\text{ }^{\circ}\text{C}$. The unit cell volume of rutile decreases with increasing deposition temperature from 64.1 \AA^3 to 61.7 \AA^3 (102% to 99% of the standard value 62.409 \AA^3).¹⁴⁷

Brookite could not be detected in all diffractograms. Some peaks appear in the diffractograms of the samples prepared at $310\text{ }^{\circ}\text{C}$ and $415\text{ }^{\circ}\text{C}$. All peaks found in the diffractogram of both samples were used to estimate the brookite unit cell volume (independently of the temperature). We estimated the unit cell volume of brookite to be around the literature value (257 \AA^3).¹²⁵

6.1.1.2 Raman spectra

Fig. 86 shows the Raman spectra of rf-diode sputtered multi-phase TiO_2 thin films deposited at substrate temperatures between $155\text{ }^{\circ}\text{C}$ and $415\text{ }^{\circ}\text{C}$ (after the B270 glass substrate spectra were subtracted from the measured spectra). A detailed view on the range of the anatase $\text{Eg}(1)$ peak ($100\text{ cm}^{-1} - 200\text{ cm}^{-1}$) is shown in the middle. On the right-hand side, the figure presents a detailed view on the range that shows most TiO_2 Raman peaks ($100\text{ cm}^{-1} - 700\text{ cm}^{-1}$). The spectra are shifted apart by 10 cm^{-1} on the Raman intensity axis. Standard positions of bulk material are shown for the anatase Eg peaks, B1g peak, and the A1g/B1g doublet (green solid lines), for the most intense brookite (narrowly dashed orange lines), and for the A1g and Eg rutile peaks (blue dashed lines). The corresponding X-ray diffractograms of the same samples can be found in Fig. 83.

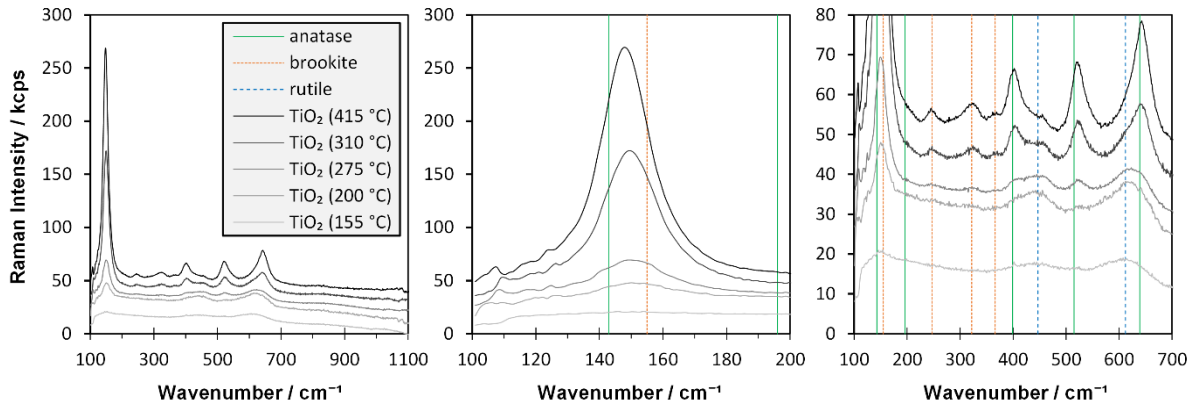


Fig. 86: Raman spectra (633 nm) of multi-phase TiO₂ thin films rf-diode sputtered at temperatures between 155 °C and 415 °C after subtracting the B270 glass substrate spectra from the measured spectra. Left: whole range, mid: anatase Eg peak, right: detailed view in the range of 100 cm⁻¹ – 700 cm⁻¹. All spectra are shifted upwards on the intensity axis in steps of 10 cm⁻¹. Vertical lines indicate standard peak positions of each anatase (green) and the most intense brookite (narrowly dashed orange) and rutile (dashed blue) peaks.

The Raman spectrum of the sample deposited at 155 °C is mainly amorphous and the peaks of the crystalline phases become sharper and more intense with increasing deposition temperature – except for the rutile peaks which become less intense at deposition temperatures above 300 °C. The anatase Eg peak is strongly blueshifted and relaxed slightly with deposition increasing temperature. The main peaks of anatase, brookite, and rutile are clearly distinct by eye at temperatures above 250 °C.

Raman peak positions (in relation to standard values) and shifts are presented in Fig. 87 for the anatase Eg(1) (143 cm⁻¹), B1g (399 cm⁻¹), A1g+B1g-doublet (514 cm⁻¹), the brookite A1g (155 cm⁻¹), A1g (247 cm⁻¹), and the rutile Eg (447 cm⁻¹), A1g (612 cm⁻¹) vibrations. Increasing deposition temperature from 155 °C to 415 °C is indicated by arrows.

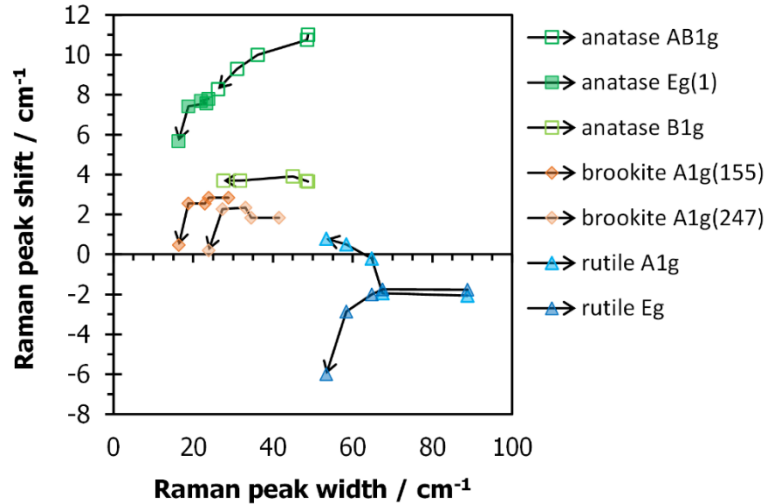


Fig. 87: Raman peak shifts (in relation to standard values) vs. (full) widths of various anatase, brookite, and rutile peaks in Raman spectra of diode-sputtered multi-phase TiO₂ thin films measured with a 633 nm laser. Increasing deposition temperature from 155 °C – 415 °C is indicated by arrows.

All peaks become sharper with increasing deposition temperature. This indicates an increase in crystallite size, which is also supported by an increase of the optical band gap with the deposition temperature reported above. The effect of the deposition temperature on Raman line width is about half as strong (factor 1.4) than on XRD peak width (factor 2.5). Crystallite sizes are discussed below.

6.1.1.3 Crystallite size and defect density

Crystallite sizes were determined by evaluating X-ray diffractograms (and Raman spectra) and the defect density was estimated by comparison of Raman with XRD measurements. An upper limit of grain sizes were determined by SEM for the film deposited at 200 °C. The grain size or particle size found by SEM is usually bigger or the same size than the crystallite size determined by XRD or Raman. Two main reasons are discussed in literature. On the one hand, grain structures or particles which are visible in SEM images might consist of several crystallites. On the other hand, defects within the crystallites lower the correlation length and lower the sizes determined by XRD and especially Raman.^{99,148–152}

Simplified, SEM gives an upper limit while Raman and XRD provide lower limits of crystallite sizes. Furthermore, one can gain information on defect density when crystal sizes from SEM, XRD, and Raman are compared.

Fig. 138 in chapter 7.1 shows an SEM image of a polycrystalline rf-diode sputtered TiO₂ film (deposited at 200 °C) in 200 k magnification taken at a working distance of 6.0 mm with an acceleration voltage of 30 keV. Grains are visible with grain sizes of 10 nm – 40 nm and an average grain size of 18 nm. The particles are arbitrarily distributed and around half of the

visible area is amorphous. An evaluation of smaller grains would need higher magnification, for which the samples would have been coated with a conducting film. A conducting Pt layer was added, but it was nanostructured, which made it impossible to distinguish between the TiO₂ film and the extra coating. We therefore focus on the comparison of grain sizes as determined by XRD and Raman only.

The crystallite sizes as determined by Scherrer (see chapter 1.4.5.2) are similar for anatase and rutile and they increase ca. from *6 nm* to *16 nm* with the deposition temperature increasing from *155 °C* to *415 °C* (see the discussion on Fig. 89).

The Scherrer method neglects strain, and the measured X-ray diffractograms of the multi-phase films are too complex to provide suitable information for methods that consider strain, such as the Williamson-Hall plot. Furthermore, peak asymmetry is neglected in the fitting routine of the multi-phase Raman spectra. Thus, we cannot differentiate between asymmetric broadening due to crystallite size or inhomogeneous strain and symmetric broadening caused by other actors. Because of this, stress/strain is not considered in the evaluation of both, the Raman spectra and the X-ray diffractograms.

In the following chapters, the *q* vector relaxation model (or phonon confinement model) is presented and then applied for the Raman peak parameters in combination with the crystallite sizes as determined by XRD.

6.1.1.4 *Q-vector relaxation models*

We determined crystallite size from Raman measurements with the q vector relaxation model (QVRM) – also referred to as phonon confinement model (PCM) or spatial correlation model (SCM). The model allows to estimate crystallite sizes from Raman peak position, width, (and asymmetry).

For anatase, the Eg(1) peak provides the most intense signal, and thus gives the most reliable values for peak position and width fitting. It is furthermore the most discussed peak in literature concerning the QVRM. We therefore focus on the Eg(1) peak in this study.

The QVRM describes nanocrystals as an intermediate state between an infinite crystal and amorphous material.⁸⁶ In an infinite crystal, conservation of phonon momentum requires that only optic phonons near the center of the Brillouin zone ($q \approx 0$) contribute to first-order Raman scattering, which is called the selection rule.¹⁵³ In amorphous material, the interatomic bonding forces are similar to those in crystals. Yet, due to the lack of long-range order the q -vector selection rule breaks down and the Raman spectra are described in literature to resemble the phonon density of states.⁷⁰

In nanocrystals with a diameter L , the periodicity of the lattice is interrupted at the surface and the phonon wave function decays to a small value at the crystal boundary, and the phonon gets confined inside the crystal. This causes an uncertainty in phonon momentum and the selection rule becomes ‘relaxed’ and, thus, a range of q -vectors contribute to Raman scattering:

$$\Delta q \sim \frac{2\pi}{L}. \quad (85)$$

This results in Raman peak shift and asymmetric broadening. Richter et al. described the Raman intensity of confined phonons with a Gaussian confinement model for spherical particles,¹⁵⁴ which has been extended by Campbell and Fauchet for columnar structures and thin films.⁸⁰ This model has been used extensively with a Gaussian weighting function to describe the Raman intensity profile $I(\omega)$ of nanocrystals, including TiO₂.^{78,155}

$$I(\omega) = \sum_{i=1}^2 \iiint_{BZ} \frac{e^{-\frac{q^2 L^2}{4}}}{[\omega - \omega_i(q)]^2 + \left(\frac{\Gamma_0}{2}\right)^2} d^3 q, \quad (86)$$

with the wavevector q , the nanocrystals with the diameter (or correlation length) L , the phonon dispersion curve $\omega(q)$, and the linewidth of the zone center phonon Γ_0 of bulk material (e.g. 7 cm^{-1} for the anatase Eg mode at $d_0 = 143 \text{ cm}^{-1}$ at room temperature).

Two empirical formulas, equation (87) and later, additionally (88), have been introduced to describe the effect of phonon confinement on Raman peak widths and positions:^{151,156}

$$\Gamma(L) = \Gamma_0 + k_1 \cdot \left(\frac{1}{L}\right)^{\gamma_1}, \quad (87)$$

$$p(L) = p_0 + k_2 \cdot \left(\frac{1}{L}\right)^{\gamma_2}, \quad (88)$$

with full peak width $\Gamma(L)$, peak position $p(L)$, crystallite size L , and width-vs.-size scaling exponent $\gamma_{1,2}$. The formulas had been established for the classification of the behavior of Raman line shape as compared to optical measurements, such as TEM or SEM. Yet, in literature, it is used also for the comparison with crystallite sizes that were determined indirectly by other methods, such as XRD.^{78,86,153,155–157}

The scaling exponent γ_1 was found to be around 1.5 in 3D covalently bonded semiconductors and around 1.0 in 2D or layered materials, such as graphite or BN. Thus, it should be 1.5 for spherical TiO₂ nano crystals. When the shapes of the crystals are rather columns than spheres, γ_1 can become as low as 1.0 instead of 1.5 for example in Si. Zhu et al. suggest that defects, such as oxygen vacancies, might lower the scaling factor to $\gamma_1 = 1.32$ and $\gamma_2 = 1.29$ for their TiO₂ nano crystals.¹⁵⁵ Kelly et al. found γ_1 as 1.55 in aerogel anatase.¹⁵³

Werninghaus et al. suggested that a high density of defects (such as stacking faults, impurities, or dopants), within a crystal causes the same or similar effects in Raman line shape as small crystallite sizes: shift of the peak position, increase of width and asymmetry as well as a decrease of intensity – which are all caused by decreasing correlation lengths. Thus for real crystals, L is rather the correlation length than the actual crystallite size in equations (85), (87), and (88).¹⁵²

Iida et al. suggested that Raman should be more sensitive to such defects (that occur additionally to grain boundaries) than XRD.¹⁵¹ Their correlation curves of Raman peak width vs. crystallite size as determined by XRD (Scherrer method) varied for two sets of TiO₂ nanoparticles that were synthesized in different ways. The corresponding graphs are shown in Fig. 187 in the appendices. When defects affect XRD reflections to a smaller degree than Raman peaks, samples with a high defect density move the correlation curve upwards in such a plot of Raman peak width vs. the particle sizes as determined by XRD (Scherrer) (in Fig. 187).¹⁵¹

Assuming that the defect density depends on the way that samples are synthesized, they treated the bulk peak width Γ_0 as a variable that depends on the defect density. They postulated $\gamma_1 = 1.5$ and fitted the constants constant k_1 and the bulk peak width Γ_0 to their data using least squares regression. For the two sets of samples, they determined k_1 as $200 \text{ nm}^{1.5}/\text{cm}^{-1}$ or

$170 \text{ nm}^{1.5}/\text{cm}^{-1}$ and Γ_0 as 8.1 cm^{-1} or 6.5 cm^{-1} . Yet, the analysis did not consider peak position and the lower value of Γ_0 (6.5 cm^{-1}) is below the standard peak width of bulk anatase at room temperature (7 cm^{-1}).⁹

Later studies expected an increase in defect density (for example oxygen vacancies) with decreasing anatase nanoparticle size which is caused by a higher volume-to-surface ratio.^{78,157} The formulas (87) and (88) were modified by treating Γ_0 to and p_0 as constants; and a factor α was introduced, which can be understood as a degree of confinement^{80,154}

The constants k_1 and k_2 were then replaced by $A_1 \cdot \alpha$ and $A_2 \cdot \alpha$. The resulting formulas were successfully implemented in literature:^{86,153,155,158,159}

$$\Gamma(L) = \Gamma_0 + A_1 \cdot \left(\frac{\alpha}{L}\right)^{\gamma_1}, \quad (89)$$

$$p(L) = p_0 + A_2 \cdot \left(\frac{\alpha}{L}\right)^{\gamma_2}. \quad (90)$$

The constants A_1 , A_2 and α have to be found before we can use equations (89) and (90) for the peak parameters found in our Raman spectra. Also, the scaling exponent γ can vary between different sets of samples. This causes a certain arbitrariness in the evaluation of the equations – a problem that the PCM generally has to face.⁸³

The parameter α has a value of $\alpha = 4$ in the Richter phonon confinement model for Si nanocrystals,¹⁵⁴ and $\alpha = 8\pi^2 \approx 79$ in the Campbell model for strongly confined phonons in ZnO_2 , CdSe , c-BN nanocrystals where only a few atoms in the central part of the crystal can vibrate.⁸⁰ It was found to be around 30 for TiO_2 by Zhu et al.¹⁵⁵ They set p_0 to 143 cm^{-1} and Γ_0 to 7 cm^{-1} and determined $A_1 = 27.0$ and $A_2 = 12.7$ (in nm scale) for their samples of nanocrystals that were mainly anatase and additionally contained brookite and rutile. Note: Zhu et al. calculate with crystal sizes in \AA but describe their results in nm , which can lead to a confusion by a factor of 10 in the confinement model.¹⁵⁵

6.1.1.5 Application of the QVRM

Fig. 88 presents the anatase Eg(1) Raman peak positions versus their widths of this work (green squares) in comparison with literature values: filled diamonds¹⁵³, hollow squares¹⁶⁰, filled triangles¹⁶¹, filled circles¹⁶², and values marked by letters⁸⁶. A linear QVRM correlation suggested by Kelly et al. is shown in gray.¹⁵³ Parts of a figure of Swamy et al.¹⁶³ are copied into the figure.

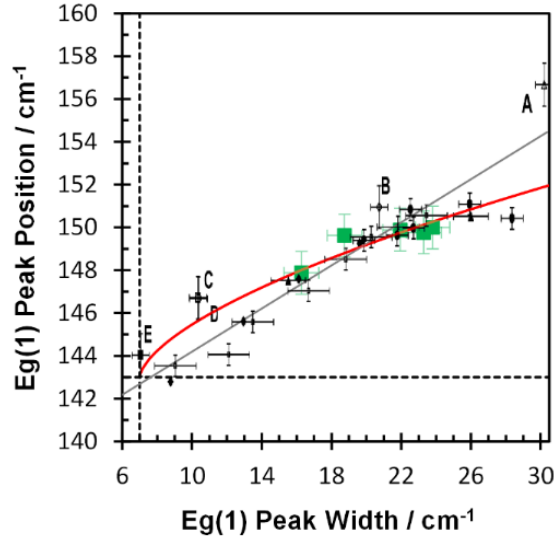


Fig. 88: Anatase Eg(1) Raman peak positions and widths of diode sputtered TiO₂ thin films on B270 glass (green) compared to literature values (black), a straight trendline of Kelly et al.¹⁵³ (gray) and the QVRM used in this work (red) with $A_1 = 28.8$, $A_2 = 10.2$, and $\gamma_2 = 0.63 \cdot \gamma_1$. The position (143 cm^{-1}) and width (7 cm^{-1}) of bulk material at room temperature are marked by dashed black lines. Parts of a figure of Swamy et al.¹⁶³ are copied into the figure

Most of the displayed literature data points show a linear relationship of peak position and width below 20 cm^{-1} and a kink at 20 cm^{-1} (especially for thin films of Barborini et al., which contain anatase as well as rutile).¹⁶² This kink is confirmed by our data, supporting a relationship different from the linear one of Kelly et al.¹⁵³ (gray line). Thus, for most of the displayed data, the peak position increases less than proportionally to the peak width. This is also predicted by the phonon confinement model of Bersani^{77,90} and Ivanda^{77,164}.

Ager et al. pointed out that there are effects that result in an increase of Raman peak widths but do not change the positions, for example a variance in lattice size or in crystallite size, a stress gradient within the crystallites, or thin film-substrate interaction.⁸² An inhomogeneous distribution of stress⁸² or stoichiometry⁸³ can cause peak broadening without resulting peak shifts.

Considering that such effects occur additionally to size effects, we fit a trendline that follows our data. We therefore suggest to use an *effective* scaling factor of the peak position γ_2 that differs from the scaling factor of the peak width γ_1 . Otherwise a plot of $p(L)$ vs. $\Gamma(L)$ (equation (89) vs. (90)) would result in a straight line.

Our measurements were performed at room temperature, for which the Eg(1) peak has a position d_0 of 143 cm^{-1} and a full width at half maximum Γ_0 of 7 cm^{-1} in bulk material.⁹ A least squares fit of the empirical QVRM equations (89) and (90) to our data points gives $A_1 = 28.8$, $A_2 = 10.2$, and $\gamma_2 = 0.63 \cdot \gamma_1$. The resulting trendline is presented in Fig. 88 as a red line.

Presuming that the crystallites in our films are not perfect spheres, we postulate $\gamma_1 = 1.40$, which is a value between those determined (or postulated) by Zhu et al., Kelly et al., and Iida et al.^{151,153,155} This results in an *effective* peak position scaling factor of $\gamma_2 = 0.88$.

We will now use these values and resolve equations (89) and (90) to the crystallite size L , with the Eg peak width Γ_i , and p_i with the Eg peak position p_i for each sample deposited at a substrate temperature of T_i . with $T_1 = 155$ °C, $T_2 = 200$ °C, $T_3 = 275$ °C, $T_4 = 310$ °C, and $T_5 = 415$ °C. This results in:

$$L_{\Gamma_i} = \alpha \cdot \left(\frac{A_1}{\Gamma_i - \Gamma_0} \right)^{1/\gamma_1}, \quad (91)$$

$$L_{p_i} = \alpha \cdot \left(\frac{A_2}{p_i - p_0} \right)^{1/\gamma_2}. \quad (92)$$

The Eg peak width Γ_i and position p_i used here, were provided for each sample by the fitting routine for multi-phase films (presented in Fig. 87 in chapter 6.1.1.2). The further variables are already determined except for the parameter α , which is now altered by a simultaneous least squares fit of L_{Γ_i} and L_{p_i} against the corresponding crystallite sizes as determined by Scherrer (from XRD) for each sample:

$$\min \left(\sum_{i=1}^5 \left(L_{L_{p_i}} - L_{i_{Scherrer}} \right)^2 + \left(L_{\Gamma_i} - L_{i_{Scherrer}} \right)^2 \right). \quad (93)$$

From this results $\alpha = 56$ for the rf-diode sputtered TiO₂ films of this study. A plot of the Raman Eg(1) peak widths vs. the crystallite size as determined by XRD is presented as open green squares in Fig. 89 (A) and the same values in Fig. 89 (B) and a plot of Raman Eg(1) peak positions vs. the crystallite size as determined by XRD in Fig. 89 (C). Values corresponding to the QVRM (equations (89) and (90)) with $\alpha = 56$ are added as a red line. As mentioned earlier, $\alpha = 30$ is considered the value for ‘defect free’ TiO₂ crystals¹⁵⁵. Graphs of the QVRM used here with $\alpha = 30$ are presented as light blue lines.

For a comparison with literature values, parts of the above mentioned figure of Iida et al.¹⁵¹ (see Fig. 187 in the appendices) are added to Fig. 89 (A), and figures of Swamy et al.⁸⁶ are added to Fig. 89 (B) and (C).

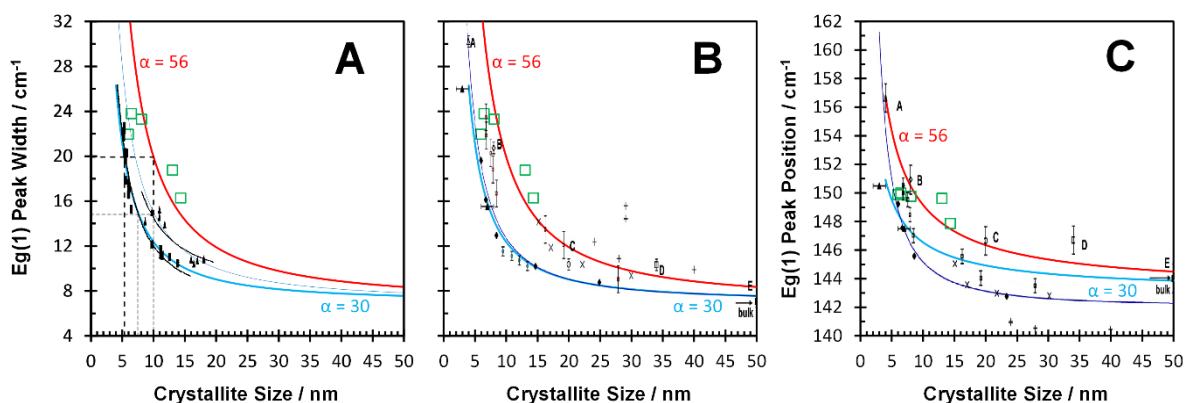


Fig. 89: (A) & (B): Anatase Eg(1) peak width vs. crystallite size (from XRD), (C): anatase Eg(1) peak position vs. crystallite size (from XRD). The crystallite sizes are as determined by XRD the peak position are fitted by the Raman fit models for multi-phase TiO₂. Values of this study are represented by open green squares. Trendlines as predicted by equations (89) and (90) with $\alpha = 30$ (light blue), $\alpha = 56$ (red) are added. (A) is a comparison with a figure of Iida et al.¹⁵¹, their trendlines are black. Horizontal and vertical dashed lines are added at 5.4 nm, 7.5 nm, and 10 nm. (B) & (C) are comparisons to figures of Swamy et al.⁸⁶ Values of Swamy et al. are marked by letters A-E. The QVRM trendlines of Kelly et al.¹⁵³ in (B) and (C) are dark blue.

The red QVRM graphs for $\alpha = 56$ describe our data well, except for the samples deposited at 155 °C and 200 °C, which have the highest errors in the peak fitting of XRD as well as Raman. The graphs are closer the widths of Swamy's samples B, C, and D and describe all of their peak positions (marked by letters in Fig. 89 (B) and (C)) better than the graphs of Kelly et al. for defect free crystals.

The light blue QVRM graphs for $\alpha = 30$ in Fig. 89 (A) is in most parts identical to the lower curve of Iida et al. below crystallite sizes of 10 nm and fits better than their graph to the data of the samples which they consider to be close to defect free crystals (filled black squares). A thin blue line for $\alpha = 40$ is added to the figure using equation (89), which describes the data of their set of disordered samples (filled black triangles) also better than their black line calculated by equation (87).

This supports the assumption that the extended empirical QVRM equations (89) and (90) are more accurate than the simpler equations (87) and (88), which do not consider an increase of defects arising from a higher fraction of surface atoms.

The same light blue graph for $\alpha = 30$ is also shown in Fig. 89 (B) and is nearly identical with the QVRM graph for peak width of Kelly et al.¹⁵³ (purple line) above a crystallite size of 5 nm, and thus also describe the values of Kelly et al. (filled diamonds) well.

Yet, the values of nanoparticles by Bersani et al. (open circles in Fig. 89 (B) around a crystallite size of 12 nm), which they consider defect free, are below the graph of Kelly et al.

The same accounts for the values of Lei et al.¹⁶¹ (filled triangles in Fig. 89 (B) and (C)). Thus, the actual value of α for defect free nanocrystals might be below 30.

The light blue graph for $\alpha = 30$ in Fig. 89 (C) calculated with equation (90) does not fit with the QVRM trendline of Kelly et al. that predicts the positions of defect free crystallites (where $\gamma_2 = \gamma_1$). γ_2 should be equal to γ_1 in defect free crystals. This is not the case in our films. Thus, the light blue line does not provide values for defect free crystallites in Fig. 89 (C). It is presented anyway to illustrate a trendline that would result from $\alpha = 30$ for $\gamma_2 = 0.88$.

The crystallite sizes of anatase estimated from XRD using Scherrer (green crosses) and from Raman using equation (91) (light green squares) and (92) (medium green squares) are presented in Fig. 90. The crystallite sizes of rutile as determined by XRD and Raman are presented by blue crosses and pyramids, respectively.

Rutile crystallite size was estimated from peak widths of the A1g and Eg mode predicted by a PCM of Mazza et al.⁴⁸ The rutile peak positions do not follow the trends predicted by the phonon confinement model (see Fig. 188 in the appendices), which indicates that the peak shift is strongly affected by aspects other than crystallite size. These are most likely strain (because the lattice is distorted and unit cell volume changes with the deposition temperature, see chapter 6.1.1.1) and defects (because we determined a high defect density also for anatase).

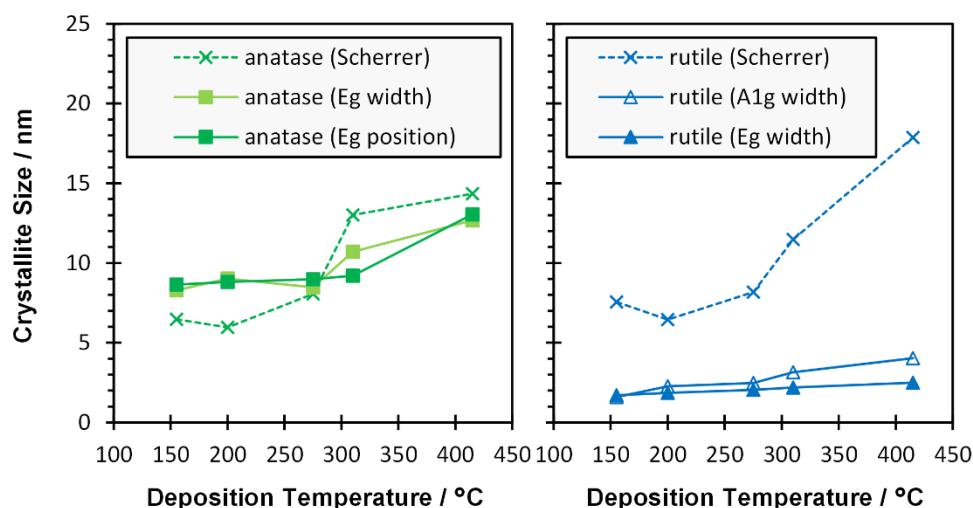


Fig. 90: Crystallite sizes of anatase (left-side) and rutile (right-side) as determined by XRD using the Scherrer formula (marked by crosses connected with dashed lines) and by Raman using models for phonon confinement: anatase estimated from Eg(1) peak width using equation (91) (light green squares) and Eg(1) peak position (92) (medium green squares), rutile estimated by PCM of Mazza et al.⁴⁸

The crystallite sizes of anatase and rutile as determined by XRD and Raman show increasing trends with the deposition temperature. As mentioned in chapter 6.1.1.3, the sizes as determined by Scherrer are similar for anatase and rutile and they increase from around 6 nm to

16 nm with the deposition temperature increasing from 155 °C to 415 °C. Due to the QVRM calculations, the anatase crystallite sizes as determined by Raman is in the same range, and they are very similar for the values determined from peak widths and from positions. Yet, the increase (from 9 nm to 13 nm) is smaller as compared to XRD.

The rutile crystallite size as determined from the Eg and A1g Raman peak widths increases from below 2 nm to 3 nm (Eg) or 4 nm (A1g). The values for the films deposited at 155 °C and 200 °C are rough extrapolations from the trend of the PCM (cf. see Fig. 188 in the appendices), but they are actually below the minimum values the PCM is applicable for. The discrepancy between the crystallite sizes determined from XRD and Raman might be a hint that XRD overestimates the crystallite size or that massive Raman peak broadening occurs additionally to grain size effects. Both is plausible, because on the one hand, the average crystallite size as determined from Raman is so small that a considerable amount of rutile crystallites could be X-ray amorphous. On the other hand, likewise anatase, the rutile phase could have a high defect density – which was not considered in the evaluation of the rutile crystallite size by Raman.

The crystallite size of brookite was determined by only XRD because we could not find literature on phonon confinement in brookite crystals. The brookite crystallite size was determined to be 60 nm in the films deposited at 310 °C and 415 °C.

6.1.1.6 Defect density

The defect density ρ_{def} is often defined as:

$$\rho_{def} = N \cdot \left(\frac{D}{L}\right)^3, \quad (94)$$

with the approximate number N of crystallites per cm^3 , the grain size D (mostly obtained from an SEM image) and the correlation length L obtained from a Raman spectrum. Iida et al. suggested to calculate the defect density of the two black regression curves in Fig. 89 (A) as follows. The lower curve (black squares) is postulated as being close to the ideal case for which the correlation length L is equal to the crystal size D . Then the defect density for a 10 nm crystal (or particle) would be $1.0 \cdot 10^{18} cm^{-3}$. If then a horizontal line is drawn through the upper curve (triangles) starting at 10 nm, it cuts the lower curve at 7.5 nm (dashed gray line). This results in a defect density ratio of $(10)^3/(7.5)^3 = 2.4$ and $\rho_{def} = 2.4 \cdot 10^{18} cm^{-3}$.

If we apply the same for our QVRM with $\alpha = 56$ (red line), a horizontal line starting at 10 nm cuts the lower black line at 5.4 nm, which results in a defect density ratio of

$(10)^3/(5.4)^3 = 6.5$ as (supposedly) compared to an ideal nanocrystal. This would be a defect density in the diode sputtered anatase content $\rho_{def,DS}$ of

$$\rho_{def,DS} = 6.5 \cdot 10^{18} \text{ cm}^{-3}. \quad (95)$$

In a plot of Raman peak width (or shift) vs. crystallite size, an increase of the parameter α moves the graph upwards. An upwards shift in such a plot is a measure of disorder according to Iida et al.¹⁵¹

We therefor consider defining parameter α as $\alpha = \alpha_0 + \alpha_{def}$, which we treat as a measure for disorder, with the material specific degree of confinement α_0 and a parameter for the defect density α_{def} . We then roughly estimate the average defect distance in a nanocrystal of size L by

$$D_{def} = \frac{\alpha_0}{\alpha_{def}} \cdot L, \quad (96)$$

or likewise the average number of defects n_{def} in a nanocrystal (in one dimension):

$$n_{def} = \frac{\alpha_{def}}{\alpha_0}. \quad (97)$$

Crystallite sizes are usually given in one dimension (for example $x \text{ nm}$ instead of a cube of $(x \text{ nm})^3$ or a sphere of $4/3 \pi (x/2 \text{ nm})^3$). Therefore, to us it is more convenient to treat defects in the same manner. It is not clear if defects distances cause the exact same amount of Raman peak broadening as crystallite size, but for an estimation of the number of defects in a nanocrystal we assume that it is roughly in the same scale. If we interpret the correlation length as the average distance between defects L_{def} , the number of defects n_{def} inside a crystal of a given size L_{crys} is $n_{def} = L_{crys}/L_{def}$. Then equation (89) can be written as

$$\Gamma(L_{def}) = \Gamma_0 + A \cdot \left(\frac{\alpha_0}{L_{crys}/n_{def}} \right)^{\gamma_1}, \quad (98)$$

with the degree of confinement $\alpha_0 = 30$ for a perfect TiO_2 crystal in a crystallite with size L_{crys} that contains n_{def} defects with average defect distance L_{def} . From equations (89) and (98) follows that the number of defects n_{def} is the quotient of α/α_0 . Thus, we estimate the number of defects in the rf-diode sputtered films as:

$$n_{def} = \frac{\alpha}{\alpha_0} = \frac{56}{30} \approx 2. \quad (99)$$

Which are in average *two* defects inside of a nanocrystal (or $2^3 = 8$ defects in three dimensions).

We suggest to extend equations (89) and (90) by $\alpha = n_{def} \cdot \alpha_0$, which results in equations (100) and (101):

$\Gamma(L) = \Gamma_0 + A_1 \cdot \left(\frac{n_{def} \cdot \alpha_0}{L} \right)^{\gamma_1}, \quad (100)$
$p(L) = p_0 + A_2 \cdot \left(\frac{n_{def} \cdot \alpha_0}{L} \right)^{\gamma_2}. \quad (101)$

These formulas assume that defects (such as stacking errors, interstitials, and so on) alter Raman peak parameters to the same degree as crystallite sizes. Future studies should focus on the amount of peak broadening (and shift) that arise from defects (stacking, interstitials, ...) as compared to crystallite sizes. This could result in a weighting factor or scaling exponent that has to be added to the equation.

6.1.1.7 Diode Sputtered films – connection between quantitative and qualitative Raman and XRD studies

Inhomogeneous stress distribution⁸² or compositional defects cause anharmonic decay of optical phonons into two or more phonons with lower energies, which decreases the phonon lifetime and results in peak broadening.¹⁶⁵ A decrease in lifetime should result in a decrease of the measured Raman intensity.

Thus, for a given crystallite size, an increase of Raman peak width and a decrease in Raman intensity can be indicators of an increase of the defect density. The high defect density estimated for the rf-diode sputtered TiO₂ films in chapter 6.1.1 correlates with a relatively low Raman intensity as compared to e-beam coated films (see chapter 5.5).

Hence, the findings of the quantitative studies in chapter 5 and the qualitative studies in chapter 6 provide complementary information about the same phenomenon.

6.1.1.8 Conclusions

We used Raman, XRD and SEM to determine grain size, lattice parameters, crystallite size, and to estimate defect density in rf-diode sputtered multi-phase TiO₂ thin films on B270

glass (produced in the master's thesis of M.Sc. Jingyi Shi, and in this work by the author). Films are already compact after deposition for 2 minutes with a thickness of $3\text{ nm} - 4\text{ nm}$.

The anatase Raman peaks are wider than expected from the crystallite size determined by X-ray diffraction: a trendline of anatase peak width (or peak position) vs. the crystallite size (determined by XRD) is higher than would be expected from perfect crystals. We interpret this by a high defect density which affects the phonon vibrations but reduces the coherence length of X-ray diffraction to a lesser extent. The defects are probably incorporated by ion bombardment during the coating process.

We suggest to introduce a new parameter $n_{def} = \alpha/\alpha_0$ to the QVRM, with the defect density n_{def} as a degree for the approximate number of defects inside a crystal, the degree of confinement α resulting from the trendlines of peak width (or peak position) vs. the crystallite size, and the material specific degree of confinement α_0 . The estimated defect density in our samples is *twice* as high as would be the case for defects occurring at surfaces of perfect crystals of the same size.

The assumption of a high defect density is supported by the results of the quantitative evaluation of the Raman spectra and X-ray diffractograms. The ratio of Raman intensity to XRD intensity I_{Raman}/I_{XRD} of the diode-sputtered films is smaller than I_{Raman}/I_{XRD} of the e-beam samples – by a factor of *two*. Defects (like grain boundaries or point defects) reduce the number of phonons that contribute to a Raman spectrum.

The defects affect the peak shift to a smaller degree than the peak width (the scaling factor γ_2 is smaller than γ_1). Therefore, the low peak shift could result from point defects with counteracting influence on the peak position or from stress. These defects could be a combination of vacancies and interstitials, for example.

At low substrate temperatures, the anatase lattice is distorted (with large lattice parameter c and small lattice parameter a). The lattice parameters relax with increasing deposition temperature, but the unit cell volume stays 2% above the standard. All Raman peaks become narrower with increasing deposition temperature. Anatase and brookite Raman peak positions approach the standard.

The lattice of the rutile phase is closer to the ideal value at low temperatures, but c becomes smaller (tension) with increasing deposition temperature. The rutile Raman A_{1g} peak (in c -direction) experiences a blue shift towards the ideal position, while the E_g peak (in a -direction) undergoes a red shift, away from the ideal position.

The anatase crystallite size increases from 7 nm to 14 nm with deposition temperature increasing from $155\text{ }^\circ\text{C}$ to $415\text{ }^\circ\text{C}$ as determined by Raman and XRD. Rutile crystallites with a

size of 2 *nm* (according to Raman) already show crystalline Raman vibrations, while they still appear amorphous in X-ray diffraction.

6.1.2 Structural, electrical, and optical properties of Nb doped e-beam evaporated TiO₂ films

In this chapter, we study the influence of Nb doping onto structural and electrical properties of the same e-beam evaporated TiO₂ thin films that are qualitatively analyzed in chapter 6.1.2. This chapter focuses mainly on the discussion of X-ray diffractograms, Raman spectra, optical measurements and four-point-probe cd measurements.

6.1.2.1 Stoichiometry

The stoichiometries of the three sets of reactive e-beam coated films are TiO₂ (“Nb0”), Ti_{0.92}O_{2.25}Nb_{0.08} (“Nb1”), and Ti_{0.84}O_{2.25}Nb_{0.16} (“Nb2”), as obtained from RBS measurements. These samples were annealed at 420 °C, 530 °C or 640 °C (B270 glass substrate), or 750 °C (fused silica substrate). A further set of samples was produced with a stoichiometry of Ti_{0.93}O_{2.25}Nb_{0.07}. This set was annealed at 350 °C, 375 °C, 400 °C, 450 °C, and 500 °C.

$Nb/(Ti+Nb)$ ratios obtained from EDX differ by ± 0.01 as compared to the RBS values. The chemical composition did not change upon annealing. The oxygen content is over-stoichiometric in the Nb-doped films. The same was reported by Atashbar et al.¹⁶⁶ for sol-gel films by and Mukherjee et al.¹⁰⁴ for sputtered films. Three additionally produced films have stoichiometric oxygen contents, with chemical compositions of TiO₂, Ti_{0.95}O₂Nb_{0.05} and Ti_{0.84}O₂Nb_{0.16}, and were post-heated at 350 °C.

The B270 glass substrates consist of 62 at.% O, 27 at.% Si, 6 at.%, 3 at.% Na, and 0.4 at.% Ba as obtained from RBS.

6.1.2.2 Film thickness

The as-deposited films are 300 nm (TiO₂) and 235 nm (Ti_{0.92}O_{2.25}Nb_{0.08}, Ti_{0.84}O_{2.25}Nb_{0.16}) thick, as determined by profilometry, optical NIR-UV-VIS spectroscopy, RBS, and SEM. The films become more compact with the annealing temperature and decrease to 95% of the initial thickness for all three Nb contents (Nb0, Nb1, Nb2). The thicknesses obtained by RBS agree well with the average thicknesses measured by SEM and profilometry, while thicknesses obtained by optical spectroscopy are 5% higher.

6.1.2.3 XRD

Fig. 91 shows the diffractograms of the e-beam coated Nb0 (green), Nb1 (blue), and Nb2 (red) films measured in grazing-incidence (7°) geometry after decomposition of the measured diffractograms into thin film and substrate (plus background), see chapter 4.2.1.

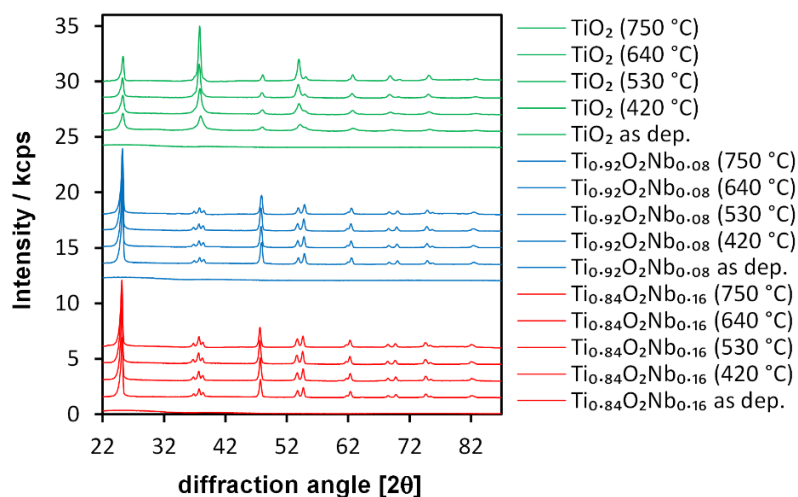


Fig. 91: Grazing-incidence (7°) diffractograms of TiO_2 , $\text{Ti}_{0.92}\text{O}_2\text{Nb}_{0.08}$, and $\text{Ti}_{0.84}\text{O}_2\text{Nb}_{0.16}$ (shifted on the intensity axis in steps of 1.5 kcps).

The films are amorphous as-deposited and are crystalline after post-heating. The X-ray diffractograms of the films that are annealed at temperatures of $420 \text{ }^\circ\text{C}$ to $750 \text{ }^\circ\text{C}$ show reflections of all anatase crystal orientations.¹⁴⁷ Traces of brookite and rutile are also visible, as can be seen in Fig. 92.

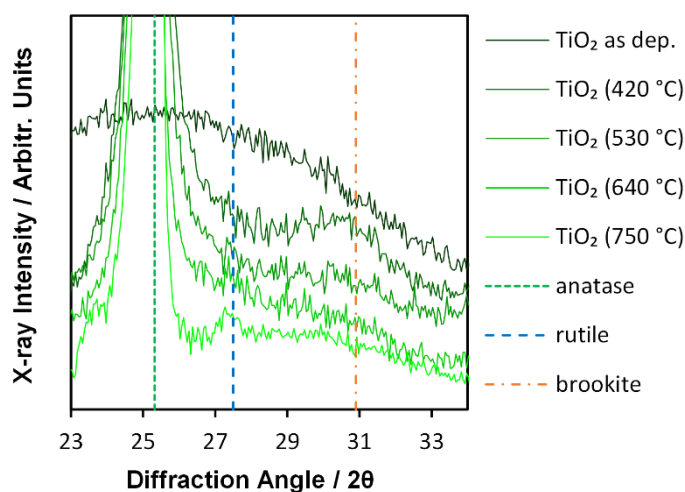


Fig. 92: Grazing-incidence diffractograms (low intensity-range) of e-beam evaporated TiO_2 films as-deposited and post heated at various temperatures (not shifted). The powder standard positions of the anatase (101), rutile (110), and brookite (211) are marked by vertical dashed lines.

The position of the brookite XRD doublet (strongest in powder brookite), consisting of (210) at 25.4° and (111) at 25.7° , is heavily superimposed by the anatase (101) peak. But at the position of the second main XRD brookite peak, (211) at 30.8° , a brookite-like nearest-neighbor-coordination is visible in the diffractogram of the TiO_2 film annealed at $420 \text{ }^\circ\text{C}$, which disappears with increasing annealing temperature.

A rutile (*110*) reflection becomes increasingly visible with increasing annealing temperature, and is most pronounced in the diffractogram of the film on fused silica annealed at 750 °C.

The broad amorphous underground decreases steadily with increasing annealing temperature. In contrast, in the diffractograms of the Nb-doped TiO₂ films, no further crystallization takes place at temperatures above 420 °C (see figures Fig. 93 and Fig. 94). Clear signals of brookite and rutile are not visible.

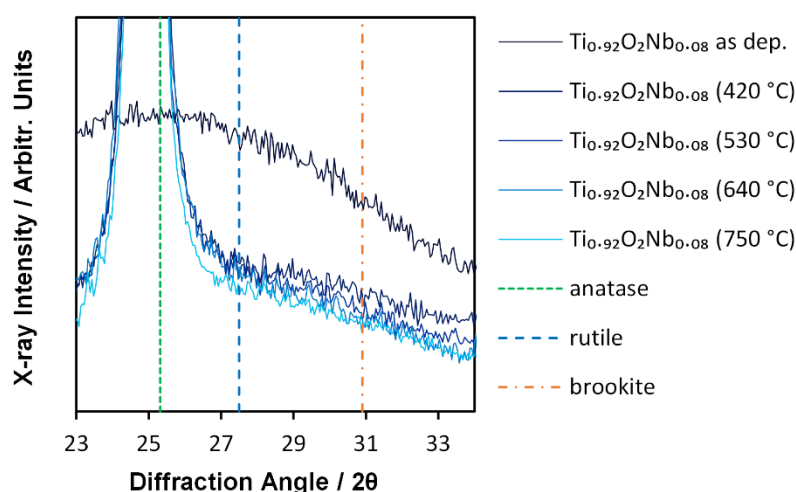


Fig. 93: Grazing-incidence diffractograms (low intensity-range) of e-beam evaporated Ti_{0.92}O₂Nb_{0.08} films as-deposited and post heated at various temperatures (not shifted). The powder standard positions of the anatase (*101*), rutile (*110*), and brookite (*211*) are marked by vertical dashed lines.

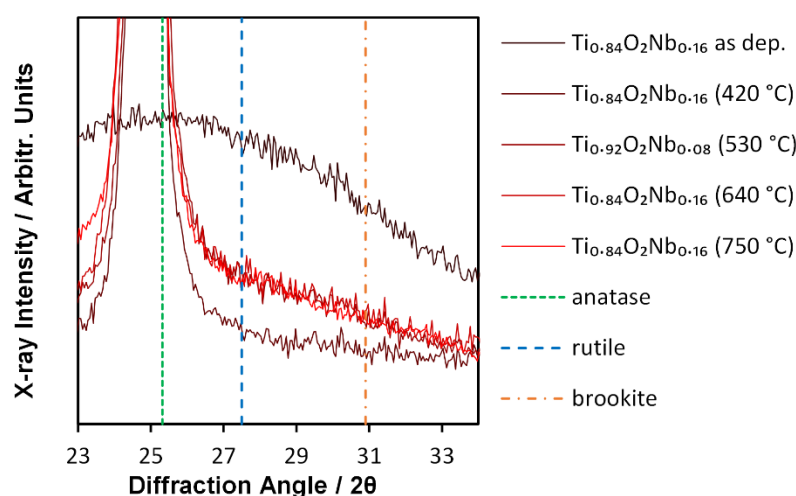


Fig. 94: Grazing-incidence diffractograms (low intensity-range) of e-beam evaporated Ti_{0.84}O₂Nb_{0.16} films as-deposited and post heated at various temperatures (not shifted). The powder standard positions of the anatase (*101*), rutile (*110*), and brookite (*211*) are marked by vertical dashed lines.

At the beginning of the crystallization, the peaks of the TiO₂ films in *a*-direction have a slight shift towards higher d-spacing while the peaks in *c*-direction have a strong shift towards smaller d-spacing and get close to the standard value at higher annealing temperatures. With higher annealing temperatures, the peaks shift closer to the standard value. This is most pronounced for the (004) orientation, which experiences the strongest shift of -1.3 pm as compared to the standard spacing of 237.8 pm after annealing at $420 \text{ }^\circ\text{C}$ and grows to a shift as small as -0.2 pm upon annealing at $640 \text{ }^\circ\text{C}$. For the doped films, all peaks shift to smaller diffractions angles with increasing temperature.

It is hardly detectable if traces of the Ti₂O₃ coating material are present in an anatase matrix by XRD because the positions of the strongest Ti₂O₃ peaks of standard powder, (012), (104), (110), (113), (024), (116), (214), (300) at 24° , 34° , 35° , 40° , 48° , 54° , 61° , and 62° are each superimposed by anatase peaks positions.^{147,167} Anyway, the Raman spectra reveal that Ti₂O₃ is not present in the films.

6.1.2.3.1 Lattice parameters and unit cell volume

The lattice parameters *a* and *c* are determined by a least-squares fit of the (*hkl*) positions that result from *a* and *c* versus the determined positions as described elsewhere.¹⁰⁴ An example of such a fit is shown in Fig. 189 in the appendices. The lattice parameters and the resulting unit cell volumes are shown in Fig. 95.

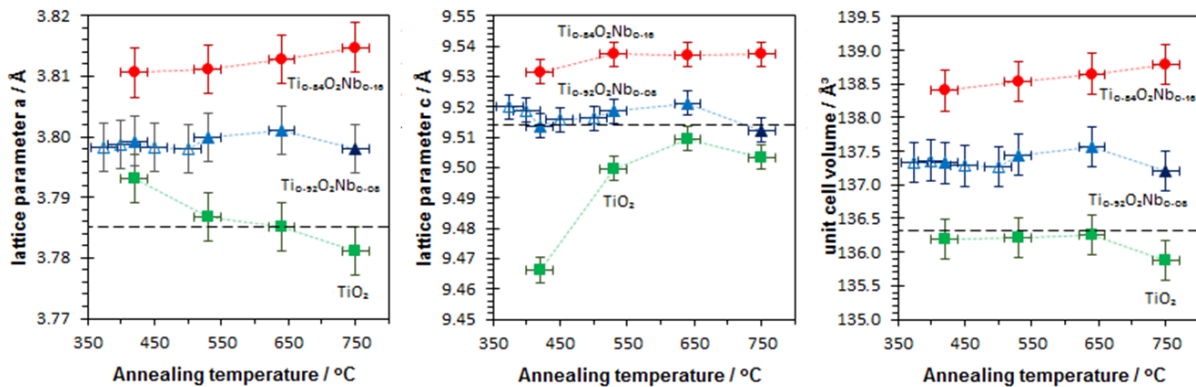


Fig. 95: Lattice parameters *a* and *c*, and unit cell volume *V* vs. annealing temperature

The lattice of the undoped TiO₂ film annealed at $420 \text{ }^\circ\text{C}$ is highly distorted. The lattice parameter *a* is 0.01 \AA higher, the parameter *c* is 0.05 \AA lower than the standard values of 3.785 \AA and 9.514 \AA , and both get closer to the standard values with increasing annealing temperatures and reach the standard when annealed at $640 \text{ }^\circ\text{C}$.

The lattice parameter *a* is 3.80 \AA for the films doped with 8% Nb and 3.81 \AA for the films doped with 16% Nb and are slightly growing with the annealing temperature for temperatures

up to 640 °C. The lattice parameter c is between 9.51 Å and 9.52 Å for the films with 8% Nb as well as 9.53 Å for the film with 16% Nb annealed at 420 °C and 9.54 Å for those annealed at higher temperatures.

Both lattice parameters decrease in the films with 0% and 8% Nb when the annealing temperature is increased to 750 °C, while the lattice parameter c does not change and a increases further in the 16% Nb films. A phase transition from anatase nanoparticles to rutile is around 800 °C.^{7,18} The decrease of the unit cell volume can be an indication that the binding energies begin to change in favor of a rutile formation at 750 °C. The high Nb content of 16% seems to hinder that trend. Rutile was found to become unstable with high Nb doping by Trenzcek-Zajac and Rekas, who found TiNb₂O₇ in sol-gel prepared polycrystalline rutile with Nb content above 10%.³¹

Nb⁵⁺ ions (64.0 pm) have a larger radius than Ti⁴⁺ ions (60.5 pm).³² According to Vegard's "law" (or rather "approximation")¹⁶⁸, the lattice parameter should increase linearly with the Nb content incorporated into the Ti lattice sites. We compare the variation of the lattice parameters with the Nb content of the films that were annealed at 640 °C, because we consider those films to have the most relaxed lattice. Here, lattice parameters, a and c , both increase by ca. 0.17 pm per Nb-at.%, which follows Vegard's Law. This is slightly below a trend of the samples of Furubajashi et al. (around 0.22 pm per Nb-at.%).⁵⁶ When both lattice parameters are compared for each annealing temperature and the values are averaged, the lattice parameters increase by ca. 0.21 pm per Nb-at.%. The unit cell volume increases by 0.12% (or ca. 16 pm³) per Nb-at.%.

The unit cell volume in the undoped TiO₂ films is slightly smaller (0.1 Å³) than that of anatase in literature (136.3 Å³)¹⁴⁷ after crystallization at 420 °C and gets closer to the literature value with increasing temperature. The decreasing strain correlates with the decreasing brookite content. This supports findings in literature: in a study of Rezaee, brookite that was attached to the {112} surface of anatase also disappears with decreasing strain with increasing annealing temperature.⁷

6.1.2.3.2 Texture

For the Nb-doped films, the (101) reflection is the strongest one, as is the case for standard powder samples. The undoped samples have a pronounced preference for c -oriented crystallites. The (004)₁ reflection is the strongest one, but also (103)₁, (105)₁, (116)₁ are stronger than in powder diffractograms. Texture is analyzed quantitatively in theta-theta geometry. Here, the (004)₁ reflection is superimposed by signals from the substrate holder. We therefore compare

the peak intensity ratio $I_{(105)}/I_{(101)}$ of the (105) and the (101) reflection with their ratio in standard powder diffractograms, which is displayed in Fig. 96.

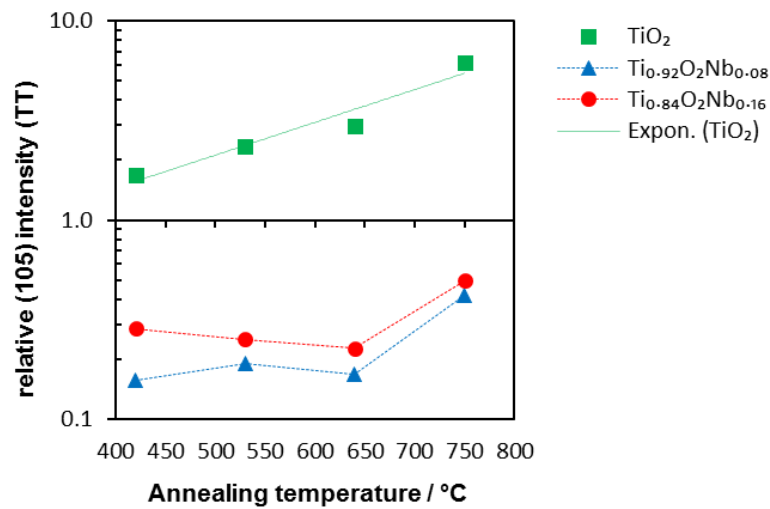


Fig. 96: Intensity ratio of the (105) and the (101) peak $I_{(105)}/I_{(101)}$ in the X-ray diffractograms in relation to the $I_{(105)}/I_{(101)}$ ratio in standard powder diffractograms vs. the annealing temperature.

Growth in c -direction is strongly favored in undoped films. This trend increases with the annealing temperature. In contrast, the growth of c -oriented grains is suppressed in the Nb-doped films. The relative intensity of the (105) reflection does not change with increasing annealing temperature in the diffractograms of the Nb-doped films which are coated on B270 glass and annealed at 420 °C to 640 °C. It is highest in the diffractograms of the undoped and the Nb-doped TiO₂ films on fused silica (annealed at 750 °C).

For the undoped films, the peak intensity ratios $I_{(105)}/I_{(101)}$ increases from 1.5 to 5 in θ - θ geometry as compared to the literature ratios of anatase powder.¹⁴⁷ The trend is even stronger in grazing incidence geometry, where $I_{(105)}/I_{(101)}$ increases from 2 to 10 with the annealing temperature. From this, we conclude that in the undoped films, c -orientated grains are more pronounced in horizontal direction. In chapter 6.1.2.4.1 we compare texture found in XRD and Raman.

6.1.2.3.3 Crystallite size and strain

The variation of the (101) peak widths with annealing temperature is shown in Fig. 190 in the appendices. The peak width of the (101) reflex of the undoped films decreases from 0.4° to 0.15° with annealing temperature increasing from 420 °C to 750 °C. It is *four* times the width as compared to the Nb-doped films annealed at 420 °C and twice the width as compared to the undoped films annealed at 750 °C. Crystallite sizes that follow directly from these values as calculated with the Scherrer method are presented in Fig. 191. The resulting crystallite size of

the Nb0 films increases nearly linearly from 20 nm to 50 nm. It stays around 75 nm for the Nb1 films and 80 nm for the Nb2 films on B270 glass and is 90 nm (Nb1) or 100 nm (Nb2) on the fused silica substrates annealed at 750 °C.

Grain size was also evaluated using Williamson-Hall-Plots (in grazing incidence as well as in θ - θ geometry). Grain sizes as determined using Williamson-Hall-Plots are shown in Fig. 97.

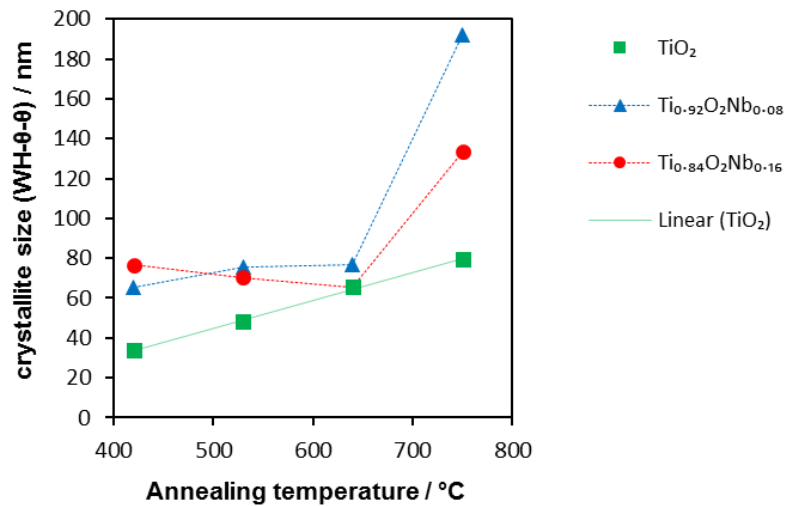


Fig. 97: Average crystallite size of Nb0, Nb1, and Nb2 films according to Williamson-Hall plots vs. annealing temperature.

In the undoped films, the resulting crystallite size increases linearly from around 35 nm to 80 nm with annealing temperature increasing from 420 °C to 750 °C. In the Nb-doped films, crystallite size is around 70 nm, independent of the Nb content, and it does not change upon annealing up to a temperature of 640 °C on B270 glass. The crystallite size is drastically increased (to 130 nm and 190 nm) in the Nb-doped films on fused silica substrates annealed at 750 °C. The crystallite sizes determined by both methods have comparable trends, but the determined values differ by a factor of up to almost two.

Fig. 98 shows the statistical microstrain as a function of the temperature, averaged over all crystalline orientations resulting from the Williamson-Hall-Plots.

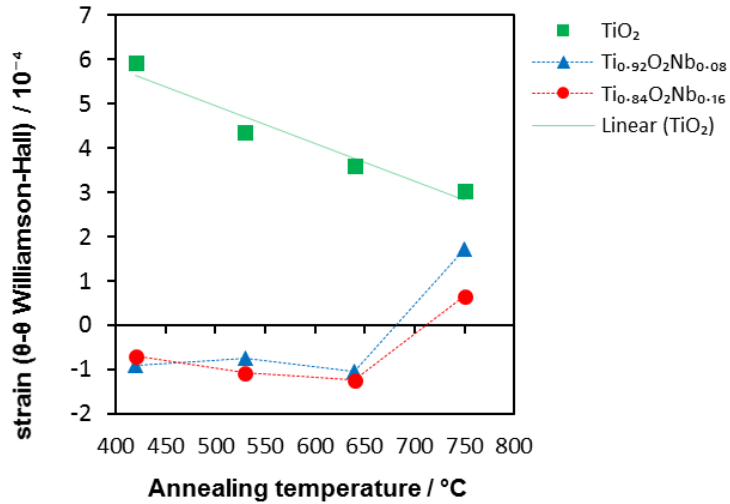


Fig. 98: Strain of Nb0, Nb1, and Nb2 films as obtained from Williamson-Hall vs. annealing temperature.

According to the Williamson-Hall plots, a strong tensile strain is reduced upon annealing in the undoped films, which correlates with the decreasing lattice distortion with the temperature. There is compressive strain in the Nb-doped films on B270 glass, independent of Nb content and it does not change with increasing annealing temperature on B270 glass, but is tensile in the films on fused silica annealed at 750 °C.

Yet as one can see, the actual trend of the peak parameters in the Williamson-Hall plots does not follow the straight trendline. For example, the (101) peak at around $4 \cdot \sin(0.9)$ does not lie close to the line. A direct strain comparison of the (101) reflection with the (105) strong *c*-orientation) and the (200) (*a*-orientation) peaks is presented in Fig. 99. The presented values for strain are derived from $\varepsilon = \Delta d/d_0$ (with $\Delta d = d_{\text{experiment}} - d_{\text{literature}}$).

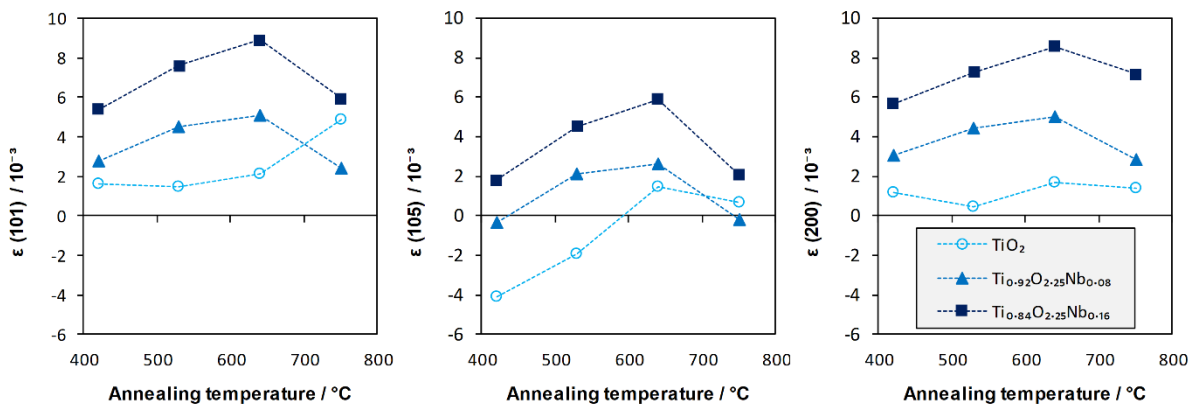


Fig. 99: Strain of θ - θ XRD (101), (105), and (200) reflections of Nb0, Nb1, and Nb2 films.

As a general trend, the XRD peak positions are shifted linearly with increasing Nb content. A further trend is similar for all three peaks of the three sets of samples (especially for Nb1 and Nb2): strain shows an increasing trend with annealing temperature increasing from

420 °C to 640 °C and a decrease with temperature rising higher to 750 °C (and with the substrate material changing from B270 glass to fused silica). An exception is the Nb0 (101) peak, which increases further.

Yet, for each doping concentration, there is an offset when the strain of the different peaks is compared. Furthermore, these trends behave not completely like the lattice parameters (cf. Fig. 95), which were from all X-ray reflections. Thus, strain estimation using the Williamson-Hall method may be used for the determination of average strain, but it provides actual values only when it is performed on single crystalline orientations if peaks of various order (e.g. (200) and (400)) are available.

The trends of strain of the single peaks shown in Fig. 99 with the annealing temperature is opposing to the behavior statistical microstrain found by the Williamson-Hall plot shown in Fig. 98. Thus, using the Williamson-Hall method with all XRD peaks simultaneously is inaccurate if the samples are textured.

The findings suggest that strain as well as crystallite size differs for grains of different crystalline orientations.

6.1.2.4 Raman spectra

Fig. 100 shows the Raman spectra of Nb0 samples and Fig. 101 of the Nb1 and Nb2 samples (as deposited at 250 °C, annealed at 420 °C, 530 °C and 640 °C). The spectra are as measured; thus, they include substrate and they are not shifted on the intensity axis.

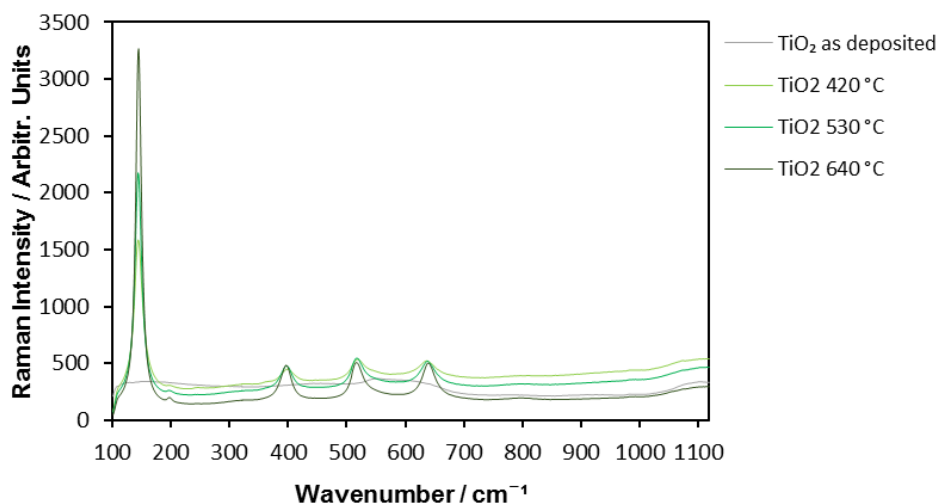


Fig. 100: Raman spectra of Nb0 films on B270 glass (not shifted).

One can see that the all anatase peaks Eg(1) peak at 143 cm⁻¹ of the Nb0 becomes stronger with increasing annealing temperature. The Raman intensity of the substrate gets stronger after the first crystallization of the Nb0 films and decreases with further annealing temperature.

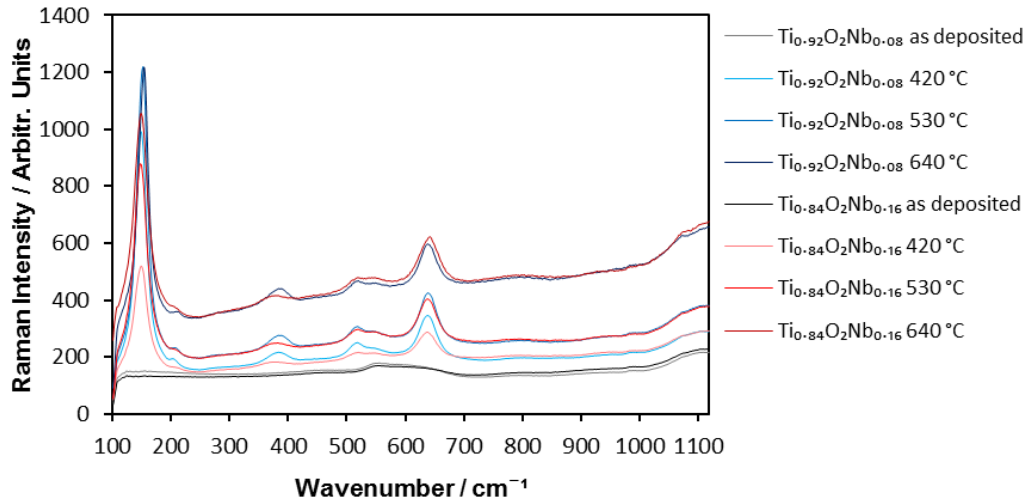


Fig. 101: Raman spectra Nb1 and Nb2 films on B270 glass (not shifted).

The B270 glass substrate spectra are similar for both Nb contents and become more intense with increasing annealing temperature. One can already see by eye that the B1g peak becomes broader and strongly red shifted with increasing Nb content.

The corresponding Nb0, Nb1, and Nb2 thin film Raman spectra plus the spectra of the films deposited onto fused silica annealed at 750 °C are presented in Fig. 102. The Raman spectrum of the Nb0 film on fused silica (annealed at 750 °C) was measured after a new Raman laser has been installed, which seems to have a higher intensity. The intensity of the measured signal was afterwards arbitrarily divided by a factor of 2 to be better comparable to the other spectra in the figure.

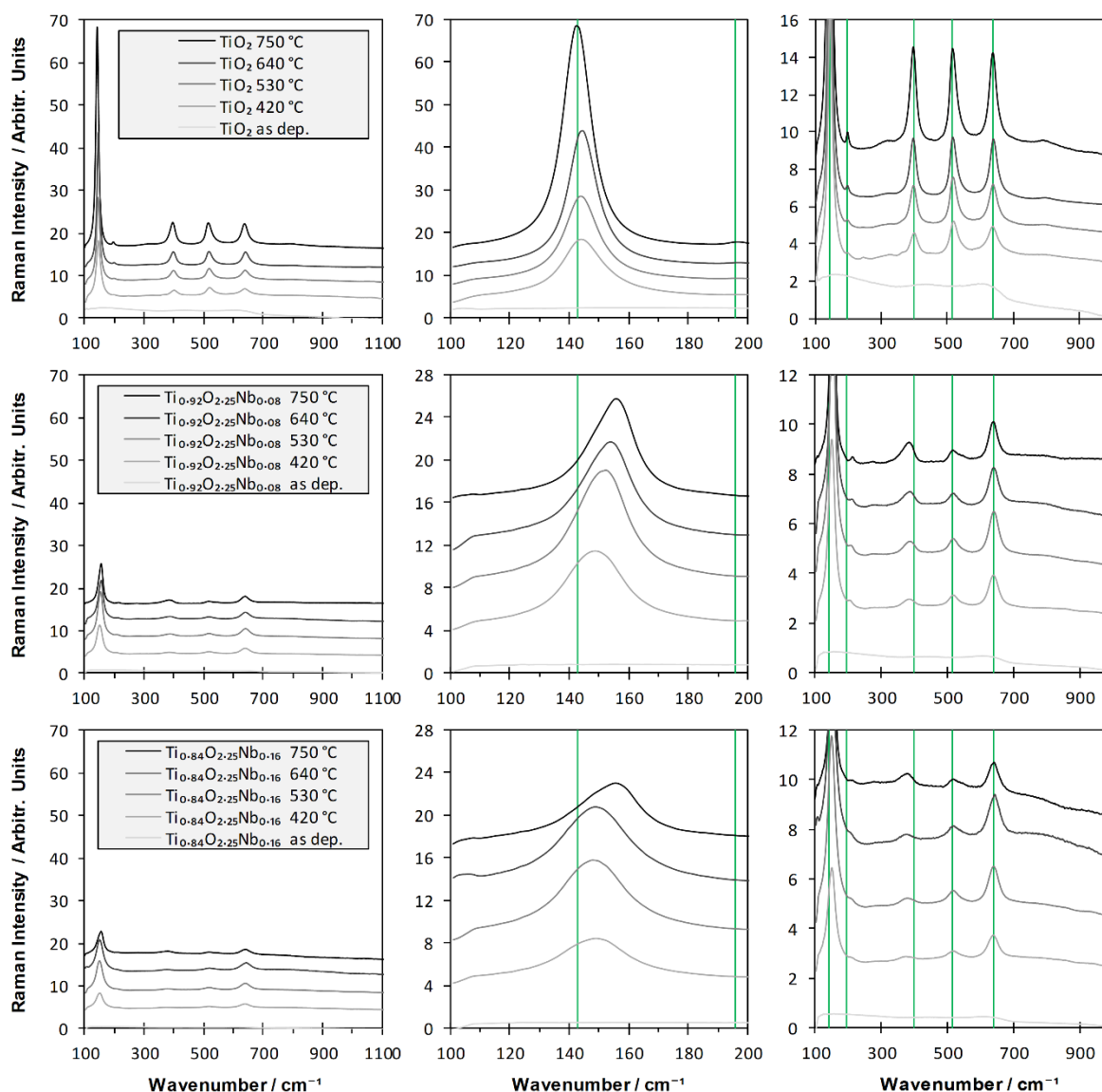


Fig. 102: Thin film Raman spectra (633 nm) of Nb0, Nb1, and Nb2 films; full range (left), Eg(1) peak (middle), detailed view on lower intensity ranges (right); each spectrum is shifted in steps of 4 units on the intensity axis (left and middle column) or 2 units (right column).

Left column of Fig. 102: All thin film spectra consist of mainly anatase. Traces of brookite are found in the Nb0 spectra, which are most pronounced in the 420 °C film, and they diminish with increasing annealing temperature. Traces of rutile become visible in the Nb0 spectra with increasing annealing temperature. See the black line in Fig. 103 (top) for the traces of both phases (the spectra are not shifted on the intensity axis in that picture; colors of the spectra are the same than in Fig. 102). For details on the phase quantification, see chapter 5.4.

No traces of the evaporation materials Ti_2O_3 or Nb_2O_5 are found in the spectra. The spectra of the coating materials (see Fig. 21 and Fig. 22) were added to the Raman models as reference spectra. This is not mentioned in chapters 3 and 4, because these materials do not contribute to the Raman spectra.

The Raman spectra of the Nb-doped films have significant lower intensity than the undoped ones and the peaks are broadened. The broadening and decrease in intensity are most probably due to decreasing phonon lifetime or a decrease in the phonon density of states caused by Nb atoms, oxygen interstitials or Ti vacancies.

Middle column of Fig. 102: in the spectra of the undoped films (Nb0), all anatase peaks become more intense with increasing temperature. This is not the case in the Nb1 and Nb2 spectra, here the peaks become only sharper, but not more intense. The Eg(1) peaks of the Nb-doped films on fused silica that were annealed at 750 °C, are blueshifted.

Right column of Fig. 102: also, the phase backgrounds of the Nb1 and Nb2 samples on fused silica that were annealed at 750 °C differ in their nature from those of the films on B270 glass substrate annealed at lower temperatures.

In the Raman spectra of the undoped films, the B1g peak at 399 cm^{-1} and the A1g/B1g doublet at 517 cm^{-1} (oscillations in *c*-direction) have about the same intensity than the Eg(3) peak at 639 cm^{-1} (oscillations in *a*-direction) – while they are weaker in anatase standard powder of *Sigma-Aldrich*.¹⁶⁹ For further details, see the discussion of Fig. 107.

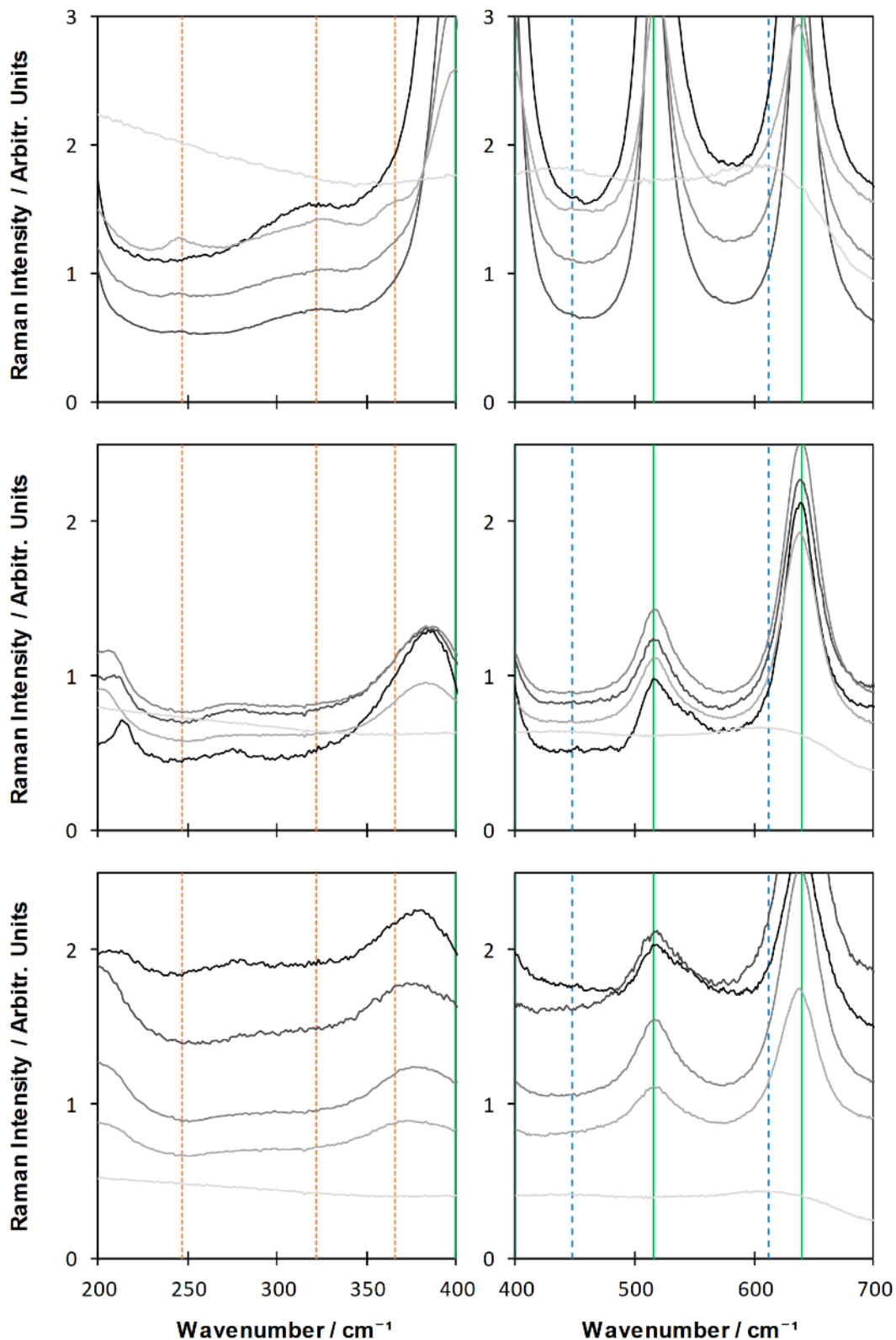


Fig. 103: Thin film Raman spectra (633 nm) of Nb0 (top), Nb1 (mid), and Nb2 (bottom) films – range of main brookite and rutile peak positions. The spectra are not shifted on the intensity axis. Colors of the spectra are the same than in Fig. 102. Brookite standard positions are marked by narrowly dotted orange, and rutile by widely dotted blue vertical lines.

6.1.2.4.1 Raman peak intensities

Fig. 104 shows the variation of Raman peak intensities (area under the modeled Lorentzian peaks) with the annealing temperature. The Raman spectra are average spectra of Raman maps that include the $121 \cdot 121 = 14641$ single spectra and thus take into account the distribution of crystals in the thin films. Each map contains several micrograins of varying crystal orientations (see the maps in 7.2).

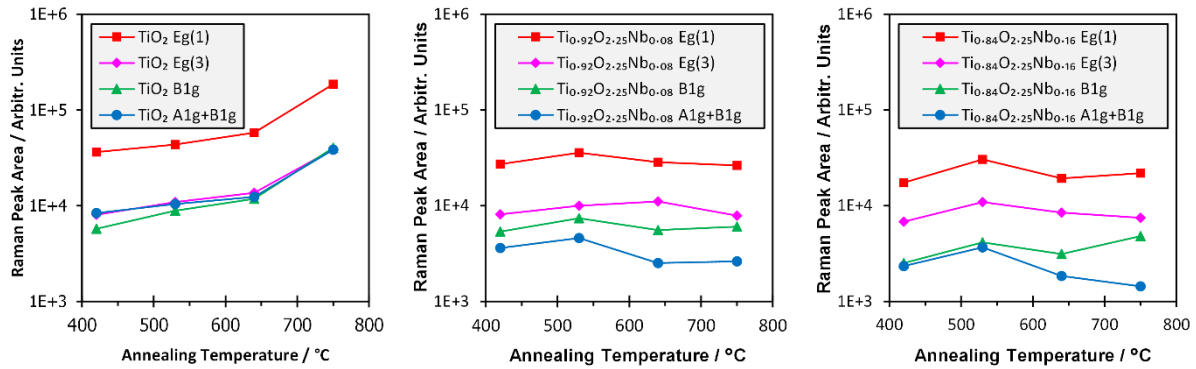


Fig. 104: Anatase Raman peak areas of e-beam evaporated Nb0, Nb1, and Nb2 films on B270 glass (and fused silica, 750 °C) vs. annealing temperature. The spectra of the Nb0 film annealed at 750 °C was taken with a newly installed laser.

The Raman peak intensities of the undoped films increase steadily with increasing temperature. The intensities increase potentially with the annealing temperature up to 640 °C (probably also up to 750 °C: the increase of intensity from 640 °C to 750 °C is doubled as compared to the other temperatures, but the latter sample was measured with a newly installed laser, which might have caused a higher intensity). In contrast to the undoped films, the Raman peak intensities of the doped films do not show clear trends with annealing temperature.

The peak intensity in relation to the Eg(1) intensities of the Nb0, Nb1, and Nb2 films is presented in Fig. 105. Ratios of the B1g peak at 399 cm^{-1} and the A1g/B2g-doublet intensities with the Eg(1) peak intensity of anatase nano particles prepared by hydrothermal method by Yan et al. are added as comparison to the ratios of the Nb0 films.¹⁷⁰

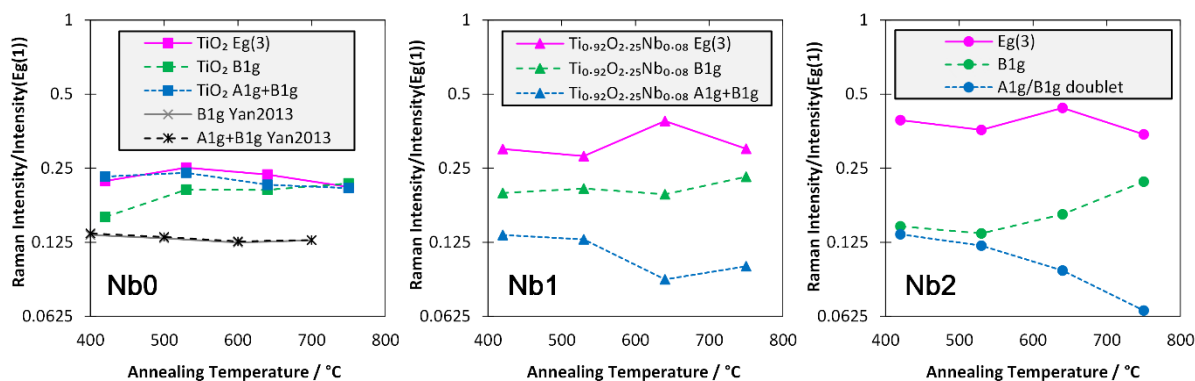


Fig. 105: Raman $Eg(3)/Eg(1)$ (pink), $B1g/Eg(1)$ (green), and $(A1g/B1g\ doublet)/Eg(1)$ peak intensity ratios of Nb0, Nb1, and Nb2 films. $B1g/Eg(1)$ (gray crosses with solid line) and $(A1g/B1g\ doublet)/Eg(1)$ (black stars with dashed line) intensity ratios of anatase nano particles by Yan et al.¹⁷⁰ are added to the graph of the undoped TiO_2 films.

The intensity ratios are almost equally around 0.2 of the Nb0 films for $Eg(3)/Eg(1)$ as well as for the c -oriented $B1g/Eg(1)$ and $(A1g/B1g\ doublet)/Eg(1)$, which is ca. twice the value of the ratios of Yan et al. In The Nb doped films, the $Eg(3)/Eg(1)$ ratio (0.35) is higher and the $(A1g/B1g\ doublet)/Eg(1)$ ratio (0.1) is lower as compared to Nb0.

The Raman A1g mode corresponds to O anti-symmetric bending vibrations along the c -axis, the B1g modes to O—Ti—O symmetric bending vibrations along the c -axis, and the Eg modes correspond to Ti—O—Ti symmetric stretching vibrations along the a -axis.

Thus, like in XRD, a preference of c -oriented signals of Nb0 as compared to the doped films is also found in Raman spectra. Fig. 106 gives a quantitative comparison of θ - θ XRD and Raman for signals in the direction of the lattice parameters, a and c .

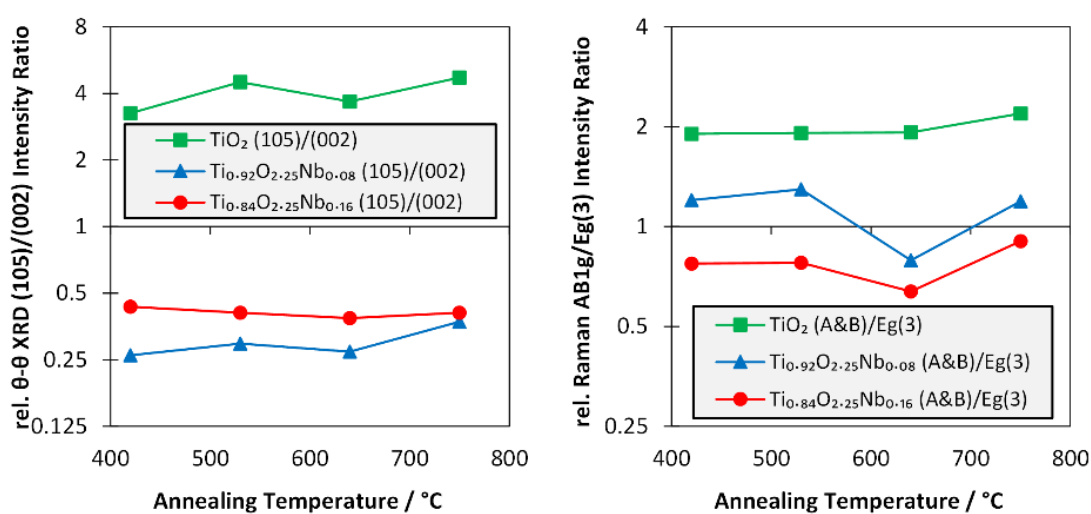


Fig. 106: Relative peak intensity ratios of Nb0, Nb1, and Nb2 films: θ - θ XRD (105)/(002) intensity ratio (left), Raman (B1g & A1g/B1g doublet)/Eg(3) (right) vs. the annealing temperature. The ratios are in relation to standard (XRD) and to Raman *Sigma-Aldrich* anatase powder.^{147,169}

The given values are relative ratios as compared to ‘standard’ ratios in literature. The standard ratio of the intensity of the XRD (105) and (002) peaks is $I_{(105)}/I_{(002)} \approx 33/21 \approx 1.6$. A ratio higher than 1.6 results in a relative ratio higher than 1, which refers to a preferred growth of *c*-oriented grains. For the undoped films the ratio is $I_{(105)}/I_{(002)} \approx 4 \cdot 1.6$, which is a relative ratio of $I_{rel(105)/(002)} \approx 4$. The relative ratio is below 0.5 for the doped films. Thus, in XRD, the growth in *c*-direction is strongly preferred, while a growth in *a*-direction is preferred in the Nb-doped films.

The same is done for Raman peaks. Here, we took the average intensities of both *c*-oriented ‘peaks’ (the B1g peak and the A1g/B1g-doublet) together and divided them by the intensity of the Eg(3) peak. The Eg(3) peak was chosen as comparison, because it is similar in the spectra of two literature samples, which we consider representative for anatase Raman spectra. The ratio of the average A&B peak intensities and the Eg(3) peak intensity is around 0.5 for *Sigma-Aldrich* anatase powder (taken with a 785 nm laser),¹⁶⁹ as well as for RRUFF-ID R070582 (532 nm and 768 nm, unoriented), which we used to build the anatase phase background models in chapter 3.1.4.:¹²⁶ The relative intensities of the reflections in the corresponding X-ray diffractogram of the RRUFF sample are almost identical to those of anatase standard X-ray diffraction powder patterns published by the United States National Bureau of Standards.¹⁴⁷

In Fig. 106, the $(A\&B)/Eg(3)$ ratio of the undoped films is 2, thus as in XRD, signals arising from vibrations in *c*-direction is also relatively strong in Raman, but it is stronger in XRD by a factor of *two*. The $(A\&B)/Eg(3)$ ratio of the doped films are close to one and the ratio of the Nb1 films is in between that of Nb0 and Nb2. A preference of *a*-orientation in the doped films found in XRD is not reflected in Raman.

There are clear trends in peak ratios with the Nb content, which is shown in Fig 77. It depicts the intensity ratios of *c*-oriented modes (averaged over the intensities of the B1g peak and the A1g/B1g doublet for all temperatures) and the Eg(1) and Eg(3) modes vs. the Nb content.

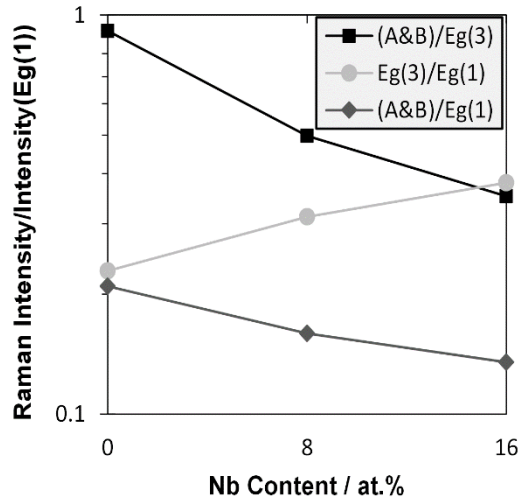


Fig. 107: Raman peak intensity ratios of (A&B)/Eg(3) (black), (A&B)/Eg(1) (medium gray), and Eg(3)/Eg(1) (light gray) vs. the Nb content (*at. %* in relation to the Ti content). “A&B” is the average intensity of the B1g peak at 399 cm^{-1} and the A1g/B1g-doublet at 517 cm^{-1} . The values are averaged over all temperatures.

The displayed ratios show continuous trends with the Nb content and vary by a factor of around 2 with the Nb content increasing to 16 at. % . The intensity ratios of the *c*-oriented modes (A1g & B1g) with the *a*-oriented modes, Eg(1) and Eg(2), have decreasing trends with increasing Nb content.

The intensity ratio of the *c*-oriented peaks with the Eg(1) peak, $I_{(A1g+AB1g)/2}/I_{Eg(1)}$, decreases from ca. 0.2 in the Nb0 films to ca. 0.1 in the Nb2 films. The intensity ratio of the *c*-oriented peaks with the Eg(3) peak is almost 1 in the Nb0 films and decreases to 0.4 in the Nb2 films. Thus, like in XRD, signals arising from the *c*-axis are strong in the undoped films.

Also, the intensity ratio of the Eg(3) and Eg(1) peak varies with the Nb content and increases from 0.2 to 0.4 with increasing Nb content.

The described behavior can be caused by the direction of growth in the thin films, but can also be caused by the volume fraction of crystal orientations, which can be also found in powder diffractograms or Raman spectra of powder samples.¹⁷¹

6.1.2.4.2 Raman peak positions and widths

The positions and widths of the Eg(1), Eg(3), and B1(g) Raman peaks are shown in Fig. 108. Linear trend lines with arrows indicate the variation with the temperature. No trendline is given for the Eg(3) peak of the Nb2 ($\text{Ti}_{0.84}\text{O}_{2.25}\text{Nb}_{0.16}$) films, because it shows no trend with the temperature. The peak widths are the actual values (minus 1 cm^{-1} instrument broadening) peaks shifts are given in relation to the literature values of 143 cm^{-1} , 639 cm^{-1} , and 399 cm^{-1} , respectively.

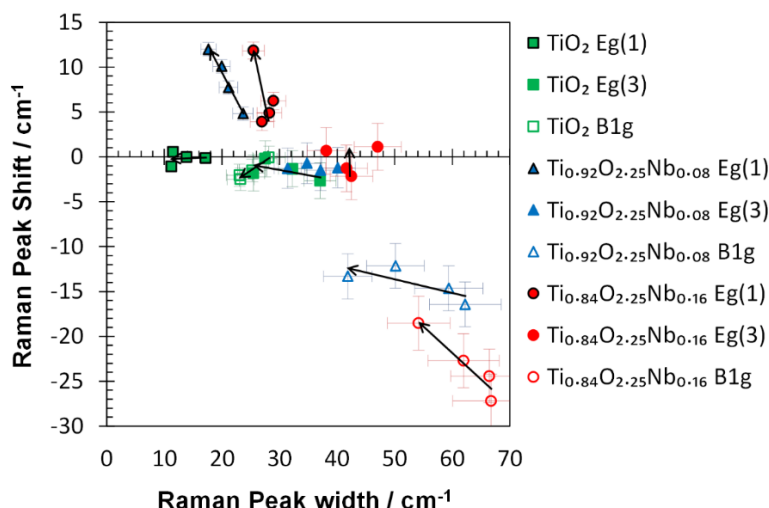


Fig. 108: Positions vs. widths of the Eg(1), Eg(3), and B1(g) Raman peaks. Linear trend lines with arrows indicate the variation with the temperature.

(Nearly) all peaks become narrower with increasing annealing temperature. This could indicate decreasing disorder, which is also confirmed by the behavior of the phase background of the undoped films, but not of the doped films (see chapter 6.2).

Raman peak parameters of the undoped films:

The peaks are nearly at standard positions and vary barely with the annealing temperature. The Eg(3) peak experiences a slight blueshift with increasing temperature, while the B1g peak and the A1g/B1g doublet slightly shift towards lower wavenumbers. The directions of the B1g and A1g/B1g peak shifts agree with the phonon confinement model resulting from a growth in crystallite size. Yet, there is almost no shift in the Eg(1) peak.

In the Raman spectrum of the 420 °C Nb0 film, the Eg(3) peak width is 37 cm^{-1} , and is higher than the width of the B1g peak and the A1g/B1g doublet (28 cm^{-1}). The widths decrease with increasing annealing temperature and the Eg(3), B1g, and A1g/B1g full widths are almost equal 25 cm^{-1} in the spectrum of the Nb0 film annealed at 750 °C, which agrees with literature spectra.⁸⁶

Raman peak parameters of the Nb-doped films:

In average, the Eg(1) peak width increases by 0.9 cm^{-1} per Nb *at.%*. It decreases from 24 cm^{-1} to 17 cm^{-1} for Ti_{0.92}O_{2.25}Nb_{0.08} and from 28 cm^{-1} to 25 cm^{-1} for Ti_{0.84}O_{2.25}Nb_{0.16}. The Eg(1) peak positions of the doped films is blueshifted by 4 cm^{-1} – 5 cm^{-1} in the spectra of the 420 °C films, which increases to 12 cm^{-1} upon annealing to 750 °C, irrespectively of the Nb

content. A blueshift and an increase of the width of the Eg(1) peak was also observed in literature.¹⁷²

The average Eg(3) width increases by 0.7 cm^{-1} per Nb-*at.*%. The Eg(3) peak positions are close to standard values and show no clear trend with the deposition temperature.

The B1g peak undergoes a strong red shift with Nb-doping of -1.5 cm^{-1} per Nb *at.*% doping in average. For an annealing temperature of $420\text{ }^{\circ}\text{C}$, the redshift is -16 cm^{-1} for the Nb1 and -27 cm^{-1} for the Nb2 films. It decreases to $2/3$ of the values with the annealing temperature increasing to $640\text{ }^{\circ}\text{C}$ or $750\text{ }^{\circ}\text{C}$.

A1g/B1g doublet:

The A1g/B1g doublet peak around 514 cm^{-1} is close to intense signals in the Raman footprint of B270 glass, which might result in inaccurate fitting. IT is therefore not shown in Fig. 108. Its position is fitted to be blue shifted by 3 cm^{-1} for the doped as well as undoped films post-heated at $420\text{ }^{\circ}\text{C}$. The shift decreases to 1 cm^{-1} for the undoped films with increasing temperature and stays around 3 cm^{-1} for the Nb-doped films.

For the undoped films, the estimated width has about the same value (or slightly higher) than the B1g peak and decreases from 30 cm^{-1} to 25 cm^{-1} with annealing temperature increasing to $750\text{ }^{\circ}\text{C}$. The A1g/B1g width decreases from 48 cm^{-1} to 36 cm^{-1} for the Nb1 films and from 50 cm^{-1} to 31 cm^{-1} in the Nb2 films.

6.1.2.4.3 Causes of Raman peak shifts

Variation in peak widths and positions can be assigned to a combination of nanosize effects, such as phonon-confinement, strain, stoichiometry, defects, and phonon coupling.⁷⁷

The crystallite sizes as determined by XRD are so large that there should not be recognizable peak shift and broadening caused by phonon confinement. Thus, variation in peak width and position with the temperature should mainly be caused by other factors. This is indeed indicated by the Raman peak parameters as the peak positions do not follow the trend predicted by phonon confinement models.

Changes in Stoichiometry result in opposing directions of peak shifts for Eg(1) and B1g modes. Yet, our samples were annealed in vacuum at 10^{-4} Pa , and stoichiometry did not vary upon annealing as determined from RBS. Peak shifts with the annealing temperature might be caused by variation in strain, which could explain the similar trend in the Eg(1) and the B1g peak of the doped films with increasing annealing temperature, but not the opposing trends of the B1g and the Eg(3) peak in the undoped films.

As a general trend, the Eg peaks as well the B1g peak in the doped films shift to higher wavenumbers with increasing annealing temperature, which indicates a variation of stress to a more compressive state. This correlates with increasing unit cell volume, and thus, variation of strain to a more compressive state. After an increase with annealing temperature, the unit cell volume of the Nb1 film decreases with the annealing temperature increasing from 640 °C to 750 °C, which is also indicated by the variation of the B1g position (increasing redshift), but does not agree with the Eg(1) peak position.

In summary, the peak shifts with the annealing temperature cannot be explained by phonon-confinement, homogenous strain, stoichiometry, or introduction of defects. One peak parameter has not been regarded so far: peak asymmetry.

6.1.2.4.4 Raman peak asymmetry

The Raman peaks of this study are asymmetric, and asymmetry varies with the annealing temperature, which is presented in Fig. 109. We quantify asymmetries by a ratio of the half-width on the right side and the half-width on the left side w_r/w_l . A value of 1/2 means that a peak is half as broad on the right side than on the left side; or, a value above 1 stands for a peak that is broader on the right-side (higher wavenumbers) of the peak center. In the fitting routine, the lower asymmetry limit is 0.5 in order to minimize interference of the B1g peak with the anatase phase background model, and the higher limit is 1.5 in order to minimize interference of the A1g/B1g doublet with the substrate's Raman footprint.

In the spectra of this study, the Eg(1) peak around 143 cm^{-1} provides most reliable values for asymmetry, followed by the B1g peak around 399 cm^{-1} and the Eg(3) peak around 639 cm^{-1} . Yet, the fits of the B1g and Eg(3) peaks might interfere with the anatase phase background and the fit of the Eg(3) peak might further interfere with the shoulder of the amorphous spectrum in the same range. The relative positions of the peaks contributing to the A1g/B1g doublet might shift, their intensity ratios might vary, and their asymmetries might vary independently of each other. Furthermore, the B270 and fused silica Raman footprints have their sharpest features in the range of the doublet. These critical spectral features that might lead to errors in the deconvolution of the spectra can for example be seen in Fig. 70 and Fig. 183.

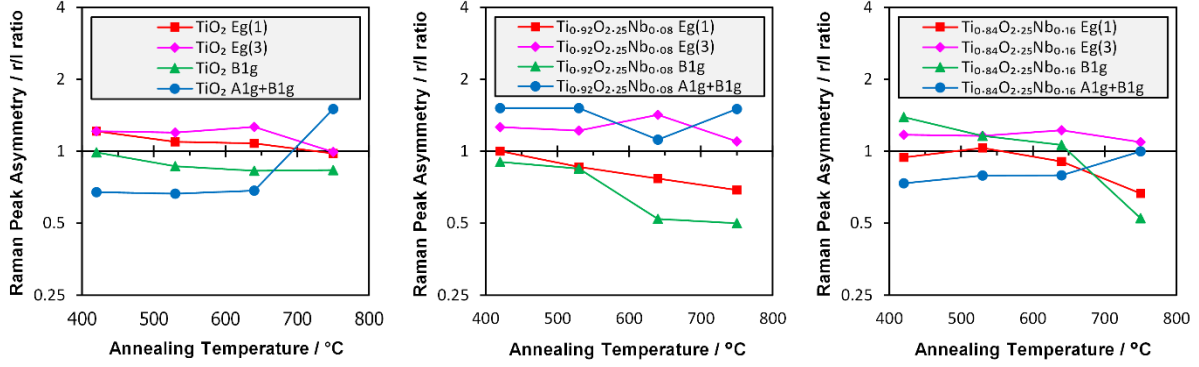


Fig. 109: Raman peak asymmetries of e-beam evaporated Nb0 (left), Nb1 (mid), and Nb2 (right) films on B270 glass (and fused silica, 750 °C) vs. annealing temperature.

In the Raman spectra of the undoped films, the Eg(1) and Eg(3) peak asymmetries are 1.2 for the film annealed at 420 °C and are symmetric (1.0) in the spectrum of the film annealed at 750 °C. The B1g is symmetric in the spectrum of the film annealed at 420 °C, and gradually becomes more asymmetric to a value of 0.8 with the annealing temperature increasing to 750 °C. This is due to a stronger decrease on the right side (from 14 cm^{-1} to 10.5 cm^{-1}) than on the left side (from 14 cm^{-1} to 12.5 cm^{-1}) of the peak center.

For the Nb-doped films, the Eg(1) peak is symmetric in the Raman spectra of the films annealed at 420 °C and become asymmetric to a value of 0.7 with annealing temperature increasing to 750 °C. Asymmetry of the Eg(3) peak is around 1.2. The B1g peak asymmetry of the Nb1 films “increases” from 0.9 to 0.5, which is mainly due to the width decreasing drastically on the right side from 30 cm^{-1} to 14 cm^{-1} . The B1g asymmetry of the Nb2 films varies from 1.4 to 0.5 with increasing annealing temperature. This is due to the half-width of the B1g peak increasing from 28 cm^{-1} to 36 cm^{-1} on the left side, while it decreases from 39 cm^{-1} to 19 cm^{-1} on the right side.

For all films (Nb-doped and undoped), the Eg(1) and B1g peak widths decrease stronger on the right-hand side of the peak center than on the lower wavenumber side with increasing annealing temperature.

A comparison of Fig. 109 with Fig. 106 shows that for all films, the variation of the Eg(3)/Eg(1) peak intensity ratio is proportional to the variation of the peak asymmetry value. Thus, an increasing Eg(3)/Eg(1) intensity ratio correlates with the peak becoming relatively stronger on the right side of the peak center. The B1g peak shows the opposite trend. It becomes relatively weaker on the right-hand side of the peak center with increasing B1g/Eg(1) intensity ratio.

It is stated in literature that peak asymmetry can only be induced by phonon confinement, asymmetric distribution of crystallite sizes, or inhomogeneous strain.^{77–79} A change in peak

asymmetry was observed for crystallite sizes only below 10 nm by Georgescu et al. in anatase aerogels prepared by sol-gel.⁷⁷ Thus, crystallite size should not play a role in peak asymmetry here.

To us, “inhomogeneous strain” is a rather vague term. By XRD, we found that strain differs between varying crystal orientations in the strongly textured films, and that texture as well as strain of the crystal orientations vary with the annealing temperature. Thus, the peak asymmetries and their variation with the annealing temperature is most probably caused by texture: a mixture of crystallites with varying orientation and size resulting in crystallites with a broad distribution of strains. We focused on this by measuring Raman spectra of phonons in varying directions within different micro grains using different Raman polarizations.

6.1.2.4.5 Polarized Raman spectra

In order to analyze the strain in different crystal orientations, Raman spectra with three different polarization states (*unpolarized*, *circular polarization* and *orthogonal polarization*) were taken at *ten* different positions on the sample surface of an Nb₂ film that had been annealed at $640\text{ }^{\circ}\text{C}$. We chose this sample because it has the largest “micro-domains” ($2\text{ }\mu\text{m}$, see chapter 7.2), which are larger than the laser spot ($0.6\text{ }\mu\text{m}$). The distance between the measurement points is $10\text{ }\mu\text{m}$ perpendicular to the sample surface. Thus, each measurement point provides Raman spectra from different micro domains. There is a probability of ca. $(0.6\text{ }\mu\text{m})/(2\text{ }\mu\text{m}) = 0.3$ that a spectrum contains considerable amounts of signals scattered from more than one domain.

The resulting Raman spectra (three for each measurement point: unpolarized (black), circularly polarized (red), orthogonally polarized (green)) are shown in Fig. 192 in the appendices. They are sorted from bottom to the top by the intensity of the Eg(1) peak in the unpolarized Raman spectra. On the left-hand side, the Eg(1) peaks are shown, and on the right-hand side there is a more detailed view on the whole range of measurement (same spectra). The displayed spectra are as measured and include the B270 glass substrate spectra. Thus, a peak is visible (to varying degree) at 550 cm^{-1} , which arises from the Raman footprint of the substrate – it should not be confused with the A1g/B1g doublet at 517 cm^{-1} .

The Raman spectra measured with orthogonal polarization display the vibrations that take place orthogonally to the direction of the measurement. Thus, they show the signals of the phonon vibrations perpendicular to the sample surface. One can see that the intensity of the Eg(1) peaks in orthogonal polarization behaves inversely proportional to the intensity in the unpolarized spectra. The peak intensities of all peaks in the Raman spectra taken with circular polarization always are between those of the unpolarized and the orthogonally polarized

spectra. Therefore, we suppose that the “unpolarized” spectra in the *Renishaw* spectrometer are polarized in the direction of the laser beam. The variation of peak intensity with the polarization indicates the measurements in varying directions of the crystal lattice.

Fig. 110, Fig. 111, and Fig. 112 show the same spectra but for each polarization the spectra are sorted by the position of the Eg(1) peak. The spectra are sorted from low peak positions (bottom) to high peak positions (top). Thick lines indicate the spectra that were used for sorting.

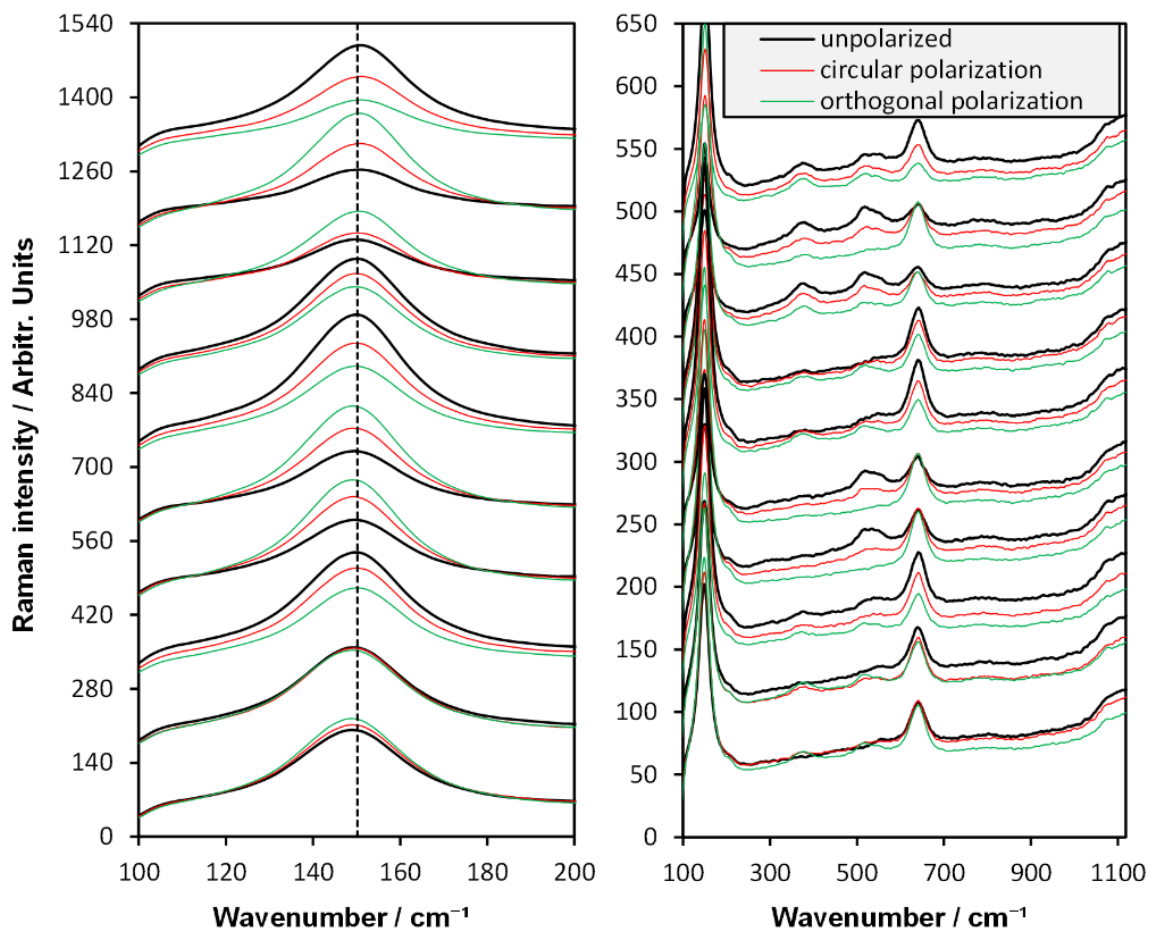


Fig. 110: Raman spectra of varying polarization (unpolarized (black), circularly polarized (red), orthogonally polarized (green)) on various positions on a $\text{Ti}_{0.84}\text{O}_{2.25}\text{Nb}_{0.16}$ film that was annealed at $640\text{ }^\circ\text{C}$, sorted by the Eg(1) peak position of the unpolarized spectra. Left: Eg(1) peak with average peak position of the whole sample at 150.2 cm^{-1} (dashed vertical line). The spectra of each position are shifted by 140 units on the intensity axis. Right: detailed view on the whole range of measurement (same spectra), shifted by 50 units for each position.

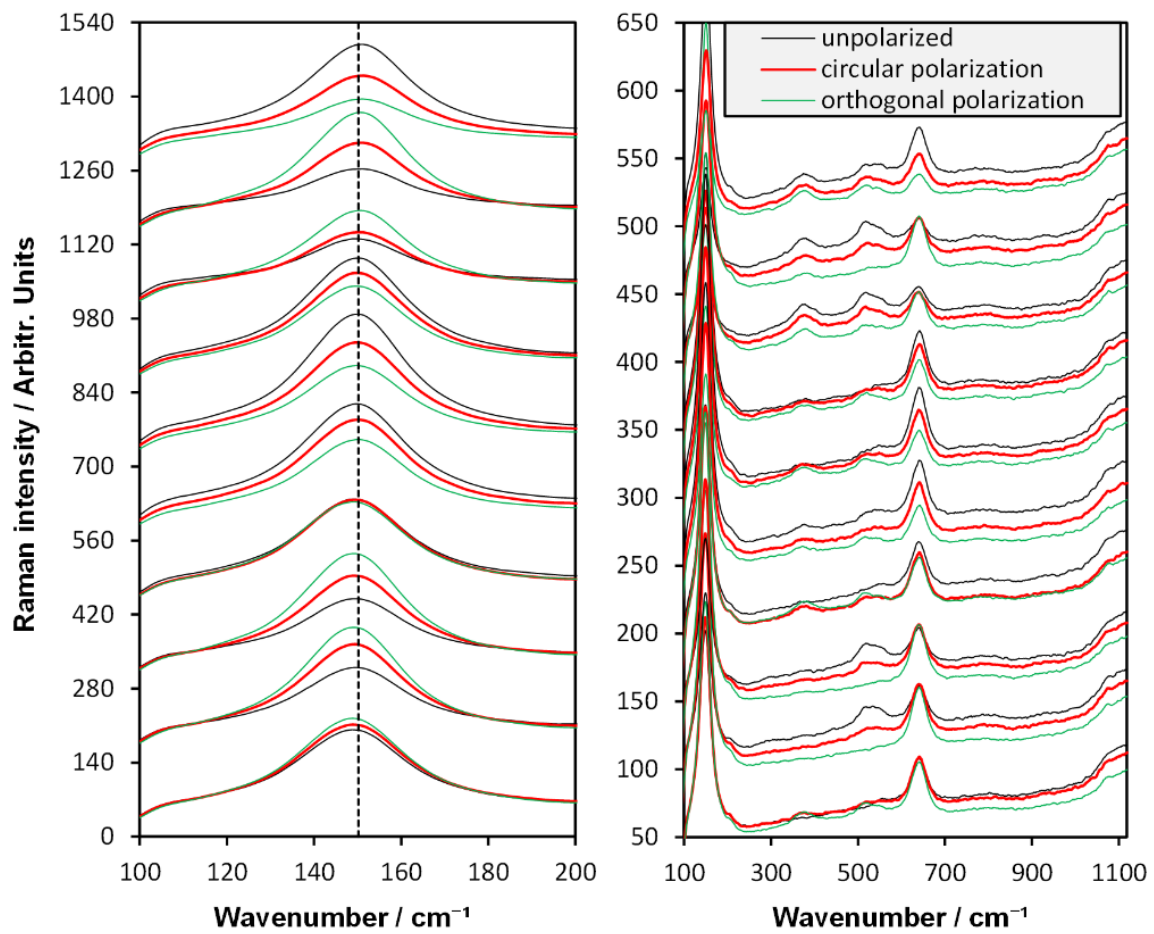


Fig. 111: Same spectra as in Fig. 110, sorted by the $E_g(1)$ peak position of the spectra taken with circular polarization. Left: $E_g(1)$ peak with average peak position of the whole sample at 150.2 cm^{-1} (dashed vertical line). The spectra of each position are shifted by 140 units on the intensity axis. Right: detailed view on the whole range of measurement (same spectra), shifted by 50 units for each position.

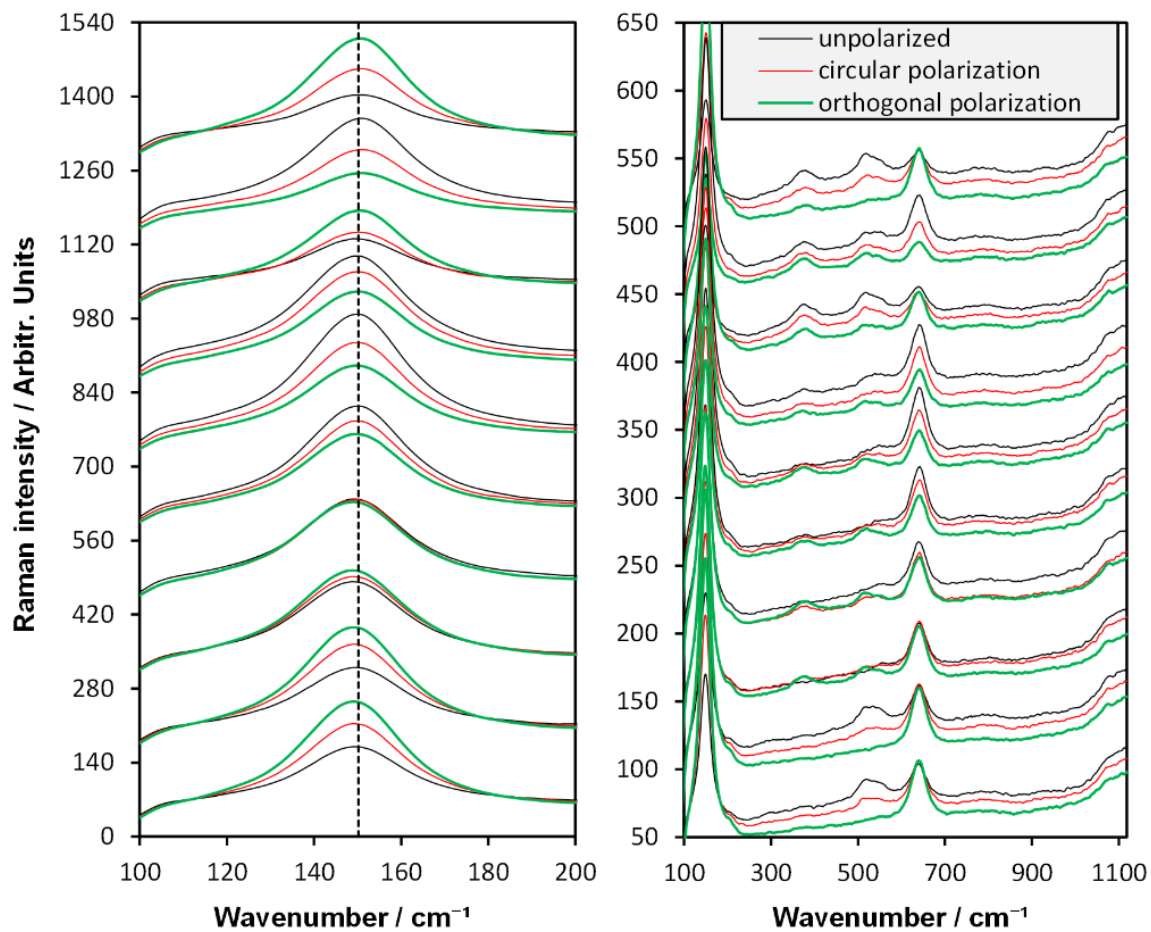


Fig. 112: Same spectra as in Fig. 110, sorted by the Eg(1) peak position of the spectra taken with orthogonal polarization. Left: Eg(1) peak with average peak position of the whole sample at 150.2 cm^{-1} (dashed vertical line). The spectra of each position are shifted by 140 units on the intensity axis. Right: detailed view on the whole range of measurement (same spectra), shifted by 50 units for each position.

The Eg(1) peak positions of the three differently polarized Raman spectra are not equal for each measurement point. For each polarization, the shift of the peak position varies by 2 cm^{-1} (from -1 cm^{-1} to $+1\text{ cm}^{-1}$) around the average peak position of the sample of 150.2 cm^{-1} determined in chapter 6.1.2.4.2. Although such a shift might be close to the tolerance of measurement errors, the intensity of the B1g peak at 375 cm^{-1} shows a clear trend with the Eg(1) peak position: the B1g is absent when the Eg(1) peak is redshifted and strongest for a blueshifted Eg(1) peak (in relation to the average peak position). This accounts for each polarization state.

Thus, in Raman spectra that are taken nearly parallel to the c -direction (high B1g (and A1g) intensity), the Eg(1)-peak shifts to higher wavenumbers, which is associated with compressive stress. In the Raman spectra taken nearly parallel to the a -direction (absent B1g and A1g peaks), the Eg(1)-peak shifts to lower wavenumbers, which is associated with tensile stress. This agrees with the strain found in XRD, where the (105) reflection has lower tensile

strain than the (200) reflection in the diffractogram of the Nb2 film annealed at 640 °C (see Fig. 99).

We took such spectra for only one sample. Future studies should do more measurements with various samples in order to make reliable conclusions. However, we can say that at varying measurement positions the crystalline orientations and the peak positions vary from each other. More information on the spatial distribution of the crystalline orientations (or the relative intensities of the various anatase Raman peaks) are discussed in chapter 7.2.2, without variation of polarization.

6.1.2.5 Optical measurements

Optical UV-VIS-NIR reflectance, transmittance, and the resulting absorbance spectra of the Nb0, Nb1, and Nb2 films are presented in Fig. 113.

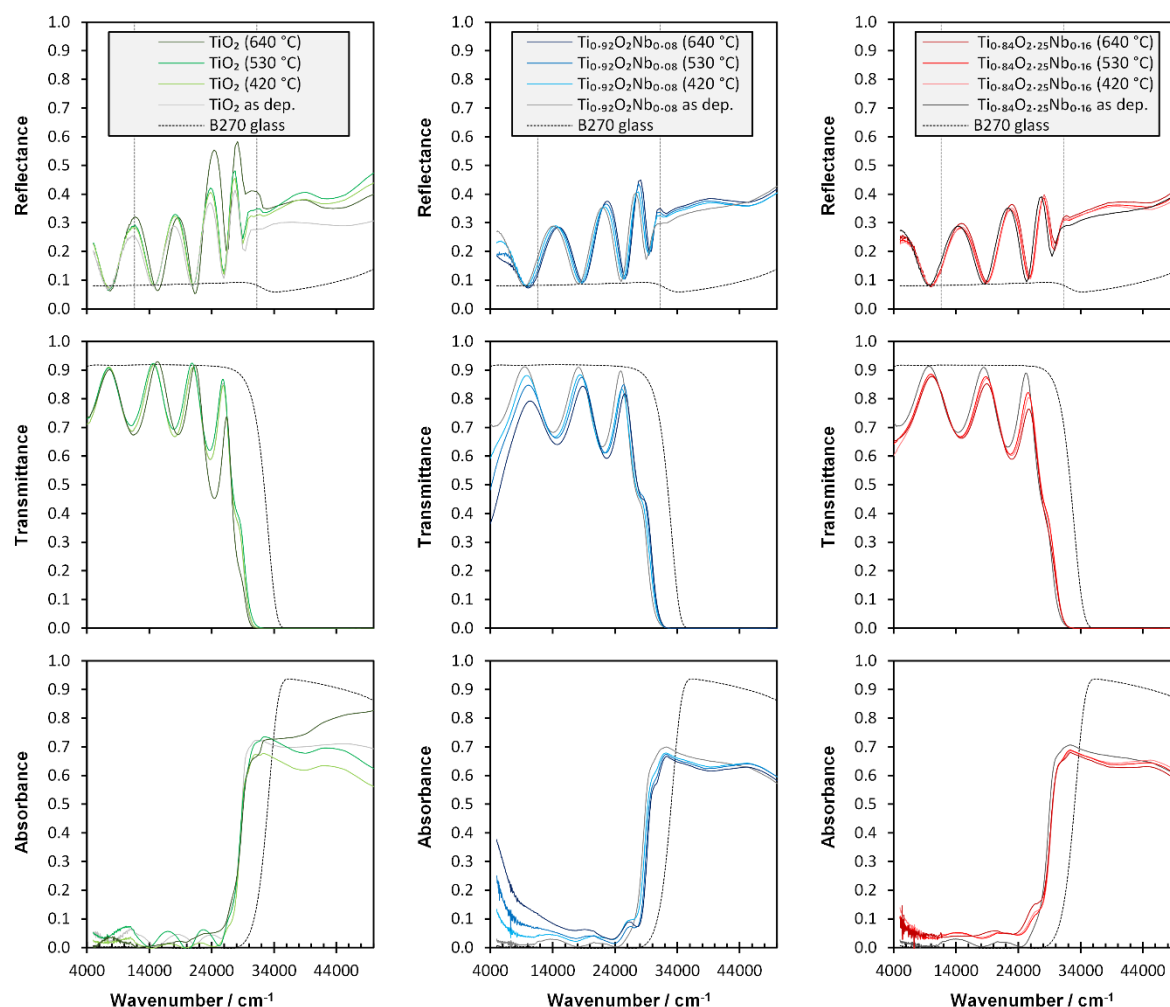


Fig. 113: Reflectance (R), transmittance (T), and the resulting absorbance spectra ($I-R-T$) of reactive e-beam evaporated Nb0 (green), Nb1 (blue), and Nb2 (red) thin films on B270 glass (dashed black). Amorphous spectra of as deposited films (250 °C) are gray and crystalline spectra are colored. Increasing annealing temperatures is indicated by darker colors. Vertical lines mark the wavenumbers at which the light source was switched.

The maxima in the transmittance and reflectance spectra of all three sets films shift to higher wavenumbers with increasing annealing temperature, which indicates decreasing film thickness and thus increasing density. All films have an absorption edge that shifts to higher wavenumbers for the Nb-doped sets after crystallization and shifts further with increasing annealing temperature for the Nb1 samples, indicating an increase of the band gap energies. The absorption edges do not go straight to zero and show further steps or wave-like structures at lower wavenumbers, which indicates the presence of further states.

A plasma edge becomes visible in the IR range with crystallization of the Nb-doped films. The absorbance of the $\text{Ti}_{0.92}\text{O}_{2.25}\text{Nb}_{0.08}$ films increases with increasing temperature to 38% at 5000 cm^{-1} for the film annealed at $640\text{ }^\circ\text{C}$. The absorbance is 10% for the crystalline $\text{Ti}_{0.84}\text{O}_{2.25}\text{Nb}_{0.16}$ films and does not change with the annealing temperature.

Fig. 114 shows the average transmittance of e-beam evaporated Nb0 (green), Nb1 (red), Nb2 (blue) thin films on B270 in the visible range ($380\text{ nm} - 780\text{ nm}$) vs. the annealing temperature. The data are calculated from the transmittance spectra shown in Fig. 113. As in all other pictures, the Nb0 films are displayed as green squares, Nb1 by blue triangles, and Nb2 by red squares.

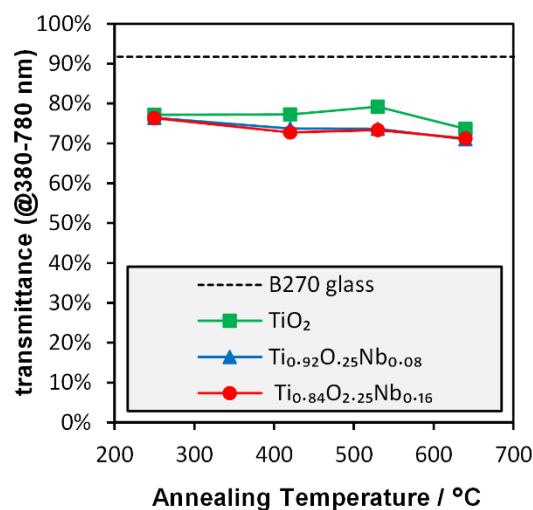


Fig. 114: Average transmittance of e-beam evaporated Nb0 (green squares), Nb1 (blue triangles), Nb2 (red circles) thin films on B270 glass (black dashed line) in the visible range ($380\text{ nm} - 780\text{ nm}$) versus the annealing temperature.

The transmittance is 78% ($\pm 2\%$) for all three amorphous samples and the undoped samples annealed at $420\text{ }^\circ\text{C}$ and $530\text{ }^\circ\text{C}$. The same films have a resistivity above the critical value of $0.3\ \Omega\text{cm}$ (see the discussion on Fig. 119). The sample with the TiO_2 film annealed at $640\text{ }^\circ\text{C}$ has an average transmittance of 74%, and the doped samples have transmittances of 73% for an annealing temperature of $420\text{ }^\circ\text{C}$ and $530\text{ }^\circ\text{C}$ and of 71% for an annealing

temperature of 640 °C. The glass substrate has a transmittance of 92%, thus the transmittances of the films should be around 8% (= 100% – 92%) higher than those of the samples (film + substrate).

6.1.2.5.1 Optical band gap

We obtained the optical band gap E_g with the Tauc method, which is based on the Davis-Mott relation:

$$(\alpha h\nu)^n = K \left(\frac{hc}{\lambda} - E_g \right), \quad (102)$$

with the absorption coefficient α , the Planck constant h ($= 6.6263 \times 10^{-37} \text{ Js} = 4.136 \times 10^{-15} \text{ eVs}$), the incident photon energy $h\nu$ (or hc/λ), and a constant K (which arises from the conversion of the natural constants units used). The exponent n represents the type of transition and is 2 for direct band gaps and $1/2$ for indirect band gaps. In order to find the indirect band gap in our (mainly) anatase films, we plot $(\alpha h\nu)^{0.5}$ vs. the energy and draw the tangents to the straight parts of the plots. The point at which the tangents cross the energy-axis are the band edge energies of the samples.

The Tauc plots are shown in Fig. 115. The samples are displayed as: Nb0 (green), Nb1 (blue), and Nb2 (red) films on B270 substrates, amorphous as deposited (gray), and post-heated at 420 °C (light colors), 530 °C (medium colors), and 640 °C (dark colors). The upper half of the figure shows the full range displaying several states at lower energies than the main band gaps. The lower half shows a detailed view of the main band edges with the tangents of the Tauc plots.

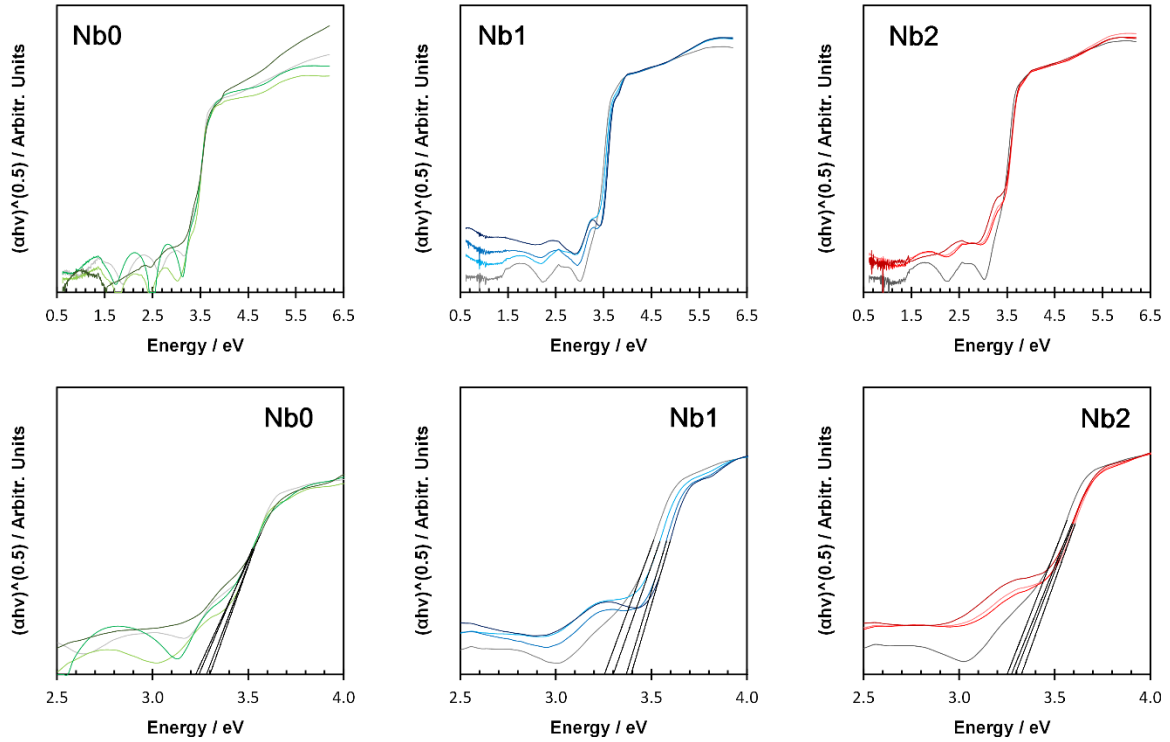


Fig. 115: Tauc plots of e-beam evaporated Nb0 (green), Nb1 (blue), and Nb2 (red) films on B270 substrates, amorphous as deposited (gray), and post-heated at 420 °C (light colors), 530 °C (medium colors), and 640 °C (dark colors). Top: Full range displaying several states at lower energies than the main band gaps; bottom: detailed view of the main band edges.

To the left of the band gaps there are several intermediate states visible in the amorphous spectra (gray) of which most disappear with increasing annealing temperature in the Nb-doped films, but disappear in the undoped films only at 750 °C. The (main) band gaps that result from the Tauc plots are shown in Fig. 116.

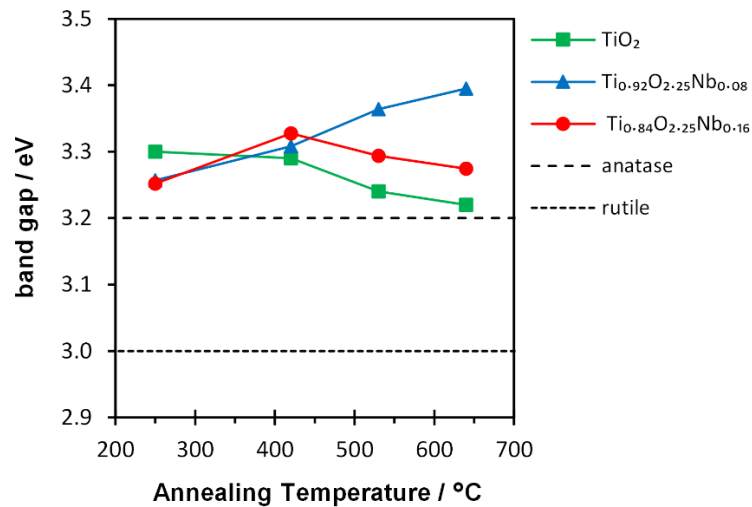


Fig. 116: Band gaps vs. annealing temperature of e-beam evaporated Nb0 (green), Nb1 (blue), and Nb2 (red) films on B270 substrates as determined by Tauc plots (see Fig. 115), compared to anatase (3.2 eV) and rutile (3.0 eV) standard values.¹⁷³

The band gaps are above that of anatase (3.2 eV) in literature.¹⁷³ The band gaps of the amorphous as-deposited films are lower in the Nb-doped than in the undoped films. This trend is consistent with experiments by Mattson et al. with sol gel prepared Nb doped TiO_2 films.¹⁷⁴

The band gaps are around 3.3 eV in all films annealed at $420\text{ }^\circ\text{C}$. It gets close to the standard value in the undoped films with the deposition temperature increasing to $640\text{ }^\circ\text{C}$.

6.1.2.5.2 SCOUT fits

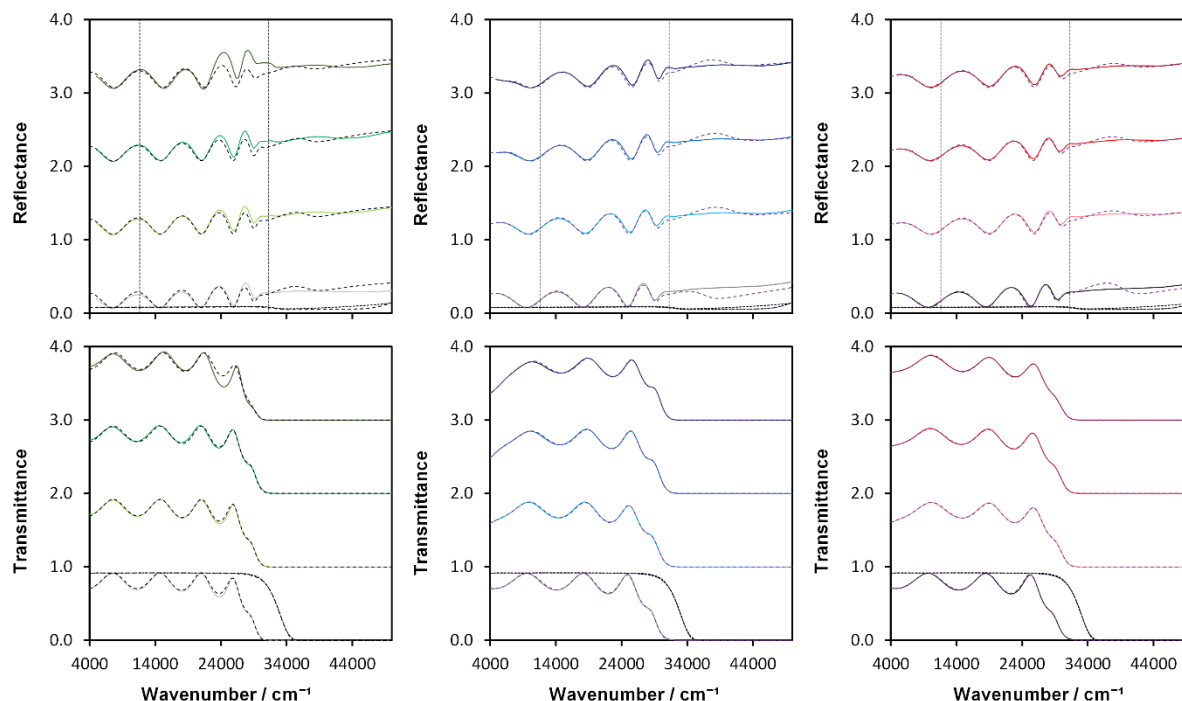


Fig. 117: Measured and modeled reflectance and transmittance spectra. The colors of the spectra are the same as in Fig. 113. The modeled spectra using SCOUT are shown as dashed lines. Spectra are shifted by I upwards each. 270 glass spectra are added without shift.

For the SCOUT fit, the band gaps of the crystalline films were derived from the Tauc-Lorentz model¹⁷⁵, while in general amorphous films get a better fit with an OJL model, which is expected for amorphous films.¹⁷⁶ The range of the band gap (above 22000 cm^{-1} or below 500 nm) does not agree well with the measured data, which might be caused by the additional states (that are visible in the absorbance spectra in Fig. 113 or in the Tauc plots in Fig. 115). Most parts of the visible and IR range agree better. The fit quality improves with the Nb content.

Considering the qualities of the SCOUT fits, the only information that we gain from the data of all samples are the refractive indices in the visible range (see discussion of Fig. 118). The best agreement of the fit with the measurement in the range of the VIS and the IR light sources can be found for the Nb1 and Nb2 films on B270 glass that were annealed at $420\text{ }^\circ\text{C}$ and $530\text{ }^\circ\text{C}$. These four SCOUT fits were used to estimate the charge carrier density n , the

charge carrier mobility μ , and the resistivity σ using the Drude model and a harmonic oscillator. These models are discussed by Qiao.¹⁷⁷ The resulting electrical properties are presented in Fig. 119.

6.1.2.5.3 Refractive index

The refractive index n of the films at 550 nm is around 2.28 , which is below that of the anatase literature value (2.55).¹⁴⁶ For each Nb doping level, it shows an increasing trend with the mass density, which is shown in Fig. 118. The refractive index n of the undoped films increases from 2.25 to 2.30 with the density increasing from 3.4 g/cm^3 to 3.6 g/cm^3 .

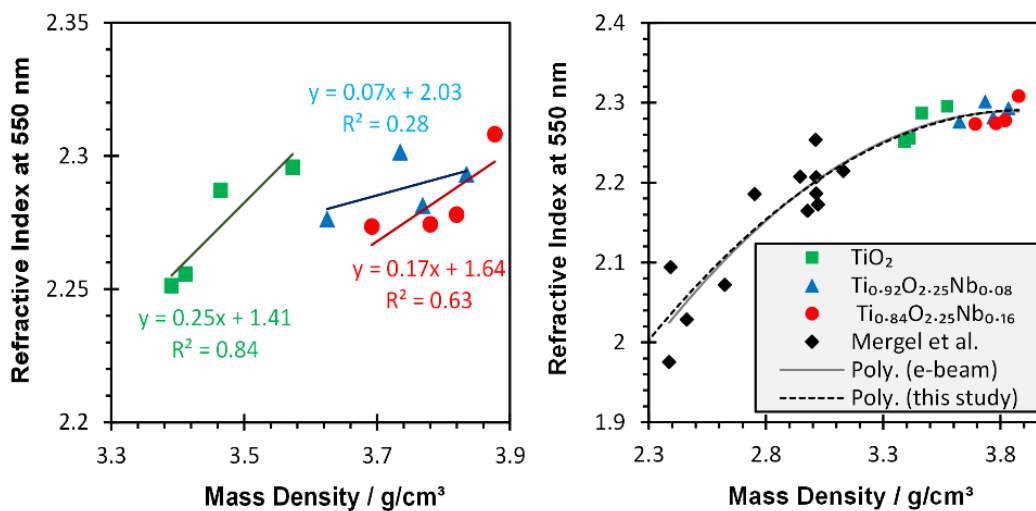


Fig. 118: refractive index n compared to Mergel et al.⁵³

On the right-hand side, the refractive indices are compared to those of e-beam evaporated undoped TiO_2 thin films by Mergel et al.⁵³, which show the trend of n (also at 550 nm) with the mass density at a lower densities (2.3 g/cm^3 to 3.1 g/cm^3). We added a polynomial trendline ($n = -0.11\rho^2 + 0.87\rho + 0.59$) to our data, and it also describes the trend of Mergel et al.⁵³ More samples and data would be necessary to interpret the impact of Nb-doping on n .

Lorentz-Lorentz-plots are shown in Fig. 193 in the appendices. The deviation of the trendlines is high, which is also the case in literature. The trendlines for the undoped films are compared to literature values in Fig. 194 and are in between those of Khawaja and Laube. A discussion on such plots can be found in Mergel et al.⁵³

6.1.2.6 DC conductivity

We performed four-point-probe measurements as described in chapter 2.2.7. Additional I - U -characteristics (two-point-probe) were taken between $0\text{ V} - 50\text{ V}$. The measured samples can be grouped into two groups of similar current-voltage characteristics, which are presented

in Fig. 195 (double-logarithmic) and Fig. 196 (linear) in the appendices. Both figures show straight lines for each displayed sample. Fig. 195 depicts the current-voltage characteristics of all crystalline doped samples (annealed above $400\text{ }^{\circ}\text{C}$) and of the undoped Nb0 film that was annealed at $640\text{ }^{\circ}\text{C}$. Each of the samples shows a potential I - U -relationship with a power of $1.3 (\pm 0.1)$. The *space charge limited current* theory interprets potential I - U -characteristics to be caused by current induced effects arising from traps.¹⁷⁸

Fig. 196 shows linear (ohmic) behavior of the amorphous samples and of the undoped films annealed at $420\text{ }^{\circ}\text{C}$ and $530\text{ }^{\circ}\text{C}$, each with slopes of $3 \times 10^{-11}\text{ A/V}$ ($\pm 1\text{ A/V}$). Yet, the measured currents of these samples are in the lowest measurement range and the trend might be caused by the measurement equipment.

A distinction between the two groups of samples can also be found in the results of the four-point-probe measurements, which are presented in Fig. 119. The figure shows the electrical resistivity of Nb0 (green squares), Nb1 (blue triangles), Nb2 (red circles) thin films versus the annealing temperature as determined by a four-point-probe (connected with solid lines). A horizontal dashed black line is added at a resistivity of $0.3\ \Omega\text{cm}$, which is a critical value that discriminates between the samples that show linear (resistivity $> 0.3\ \Omega\text{cm}$) or potential (resistivity $< 0.3\ \Omega\text{cm}$) I - U -characteristics in the two-point-probe measurements.

Three additional samples were deposited (also at $250\text{ }^{\circ}\text{C}$) and post-heated at $350\text{ }^{\circ}\text{C}$ with stoichiometric oxygen content ($(\text{Ti}+\text{Nb})/\text{O} = 1/2$), TiO_2 (open green square), $\text{Ti}_{0.95}\text{O}_2\text{Nb}_{0.05}$ (open blue triangle), $\text{Ti}_{0.84}\text{O}_2\text{Nb}_{0.16}$ (open red circle).

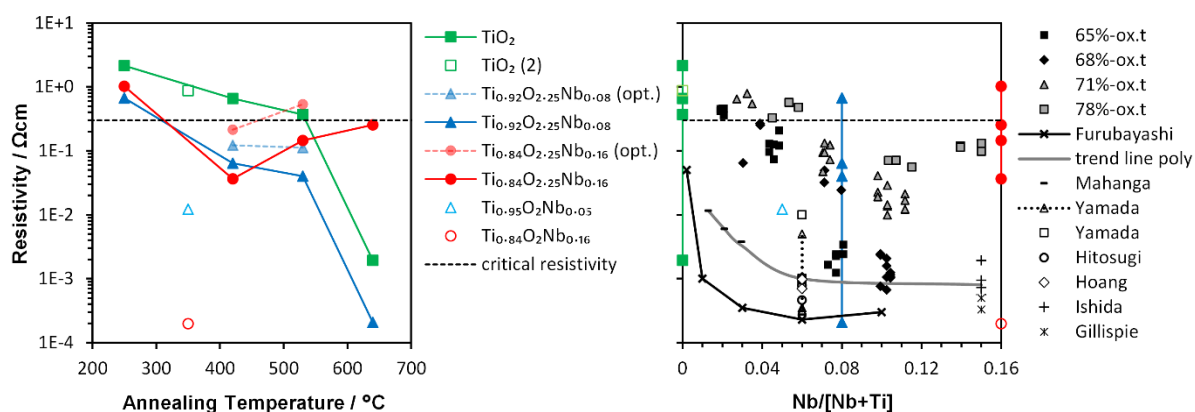


Fig. 119: Left: Electrical resistivity of Nb0 (green), Nb1 (red), Nb2 (blue) thin films versus the annealing temperature as determined using a four-point-probe (solid lines). Three additional samples were prepared with stoichiometric oxygen content (open symbols). Values as determined by modeling optical transmittance and reflectance spectra to measured spectra using SCOUT (dashed lines) are added for the spectra of crystalline samples with the most precise fit (see Fig. 117). A dashed black line marks a critical resistivity that discriminates between samples with potential and linear current-voltage characteristics.

Right: values compared to previously published work in Mukherjee et al.¹⁰⁴

The resistivities decrease with the annealing temperature increasing from 250 °C to 750 °C for the Nb0 films (from 2 Ωcm to 3·10⁻³ Ωcm) and Nb1 films (from 1 Ωcm to 2·10⁻⁴ Ωcm). The resistivity of the Nb2 film also decreases with first crystallization after annealing at 420 °C, but it increases further with increasing deposition temperature and is in the range of (2·10⁻² Ωcm and 1 Ωcm).

The Nb-doped films with stoichiometric oxygen content, Ti_{0.95}O₂Nb_{0.05} and Ti_{0.84}O₂Nb_{0.16} have a resistivities (1·10⁻² Ωcm and 2·10⁻⁴ Ωcm, respectively) already after post-heating at 350 °C.

Dashed lines are added for the resistivities resulting from the SCOUT plots, which are slightly higher than the corresponding measured *dc*-resistivity.

The data of Furubayashi et al. suggest that there is an optimal unit cell volume around 138 Å³ ± 0.5 Å³ with the highest resistivity in their Nb-doped TiO₂ thin films prepared by pulsed laser deposition.⁵⁶ Fig. 120 shows the conductivities of this study vs. the unit cell volume. The two highest conducting films, Ti_{0.84}O₂Nb_{0.16} and Ti_{0.92}O_{2.25}Nb_{0.08}, have unit cell volumes of 137.8 Å³ ± 0.2 Å³. A trendline by Furubayashi et al. (gray) also has a maximum around 138 Å³.⁵⁶ In a study with Nb-doped TiO₂ films deposited by rf-magnetron sputtering (see chapter 6.1.3), we found that the films with the maximum conductivity also had the largest unit cell volumes in the same range (137.7 Å³ ± 0.2 Å³).¹⁰⁴

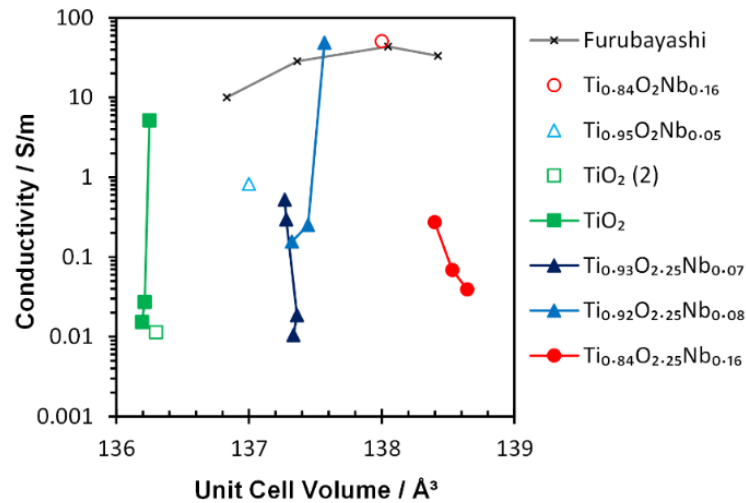


Fig. 120: Electrical conductivity vs. unit cell volume (*a²c*), compared to monocrystalline films of Furubayashi et al.⁵⁶

6.1.2.7 Conclusions

Nb-doped and undoped TiO₂ thin films were prepared by reactive e-beam evaporation in the optical workshop of the University of Duisburg-Essen by Dipl.-Phys. Ing. Martin Jerman

and have been post-heated by the author. We have analyzed the films by XRD, Raman, RBS, EDX, four-point-probe, and optical (UV-VIS-NIR) measurements.

The films are well conducting but less transparent as compared to literature. The average transparency of the films is 82% in the visible range at 550 nm (or 75% for film and substrate). UV-VIS-NIR spectra suggest that there might be intermediate states in the band gap in the undoped films.

The conductivity depends on Nb content, annealing temperature, and the unit cell volume. The two films with the lowest resistivities are $\text{Ti}_{0.84}\text{O}_2\text{Nb}_{0.16}$ on B270 glass annealed at 350 °C ($2 \cdot 10^{-4} \Omega\text{cm}$) and $\text{Ti}_{0.92}\text{O}_{2.25}\text{Nb}_{0.08}$ on fused silica annealed at 750 °C ($2 \cdot 10^{-4} \Omega\text{cm}$). These well conducting films have unit cell volumes of $137.8 \text{ \AA}^3 \pm 0.2 \text{ \AA}^3$. This is in the range of well conducting films described in literature.

The Nb-doped films with stoichiometric oxygen contents ($(\text{Ti}+\text{Nb})/\text{O} = 1/2$) have high conductivities already at low temperatures. Future studies should do experiments with film that contain stoichiometric oxygen contents at higher annealing temperatures.

The TiO_2 films (undoped and Nb-doped) have a relatively high mass density compared to previous studies reported in the literature.¹⁰³ The refractive index increases with increasing mass density and continues a trend that was described in literature for films with lower mass densities.¹⁰³

According to XRD, the nanocrystals of the films are so large that phonon confinement caused by crystallite size should be insignificant. Indeed, the Raman peak positions and widths cannot be explained by crystallite size and homogeneous stress. The XRD peak positions and the Raman peaks asymmetries suggest that stress and strain are inhomogeneously distributed in the films. Stress is more tensile in *c*-direction than in *a*-direction, which is reflected in X-ray diffractograms as well as in Raman spectra. Peak asymmetry is most probably caused by preference of one crystal orientation. Our hypothesis is that texture might cause Raman peak asymmetry by inhomogeneous distribution of grain sizes and orientations accompanied by varying strain.

Undoped TiO_2 films:

In the undoped films, anatase crystallization increases steadily with the annealing temperature. At 420 °C, 30% of the Raman and XRD signals arise from amorphous TiO_2 . Traces of brookite are found in the undoped TiO_2 films and are strongest at the lowest annealing temperature of 420 °C. They vanish upon increasing annealing temperature to 750 °C and

decreasing strain, while traces of rutile become more pronounced with increasing deposition temperature. The traces of brookite and rutile phases are found by Raman as well as XRD.

The lattice is distorted at the lowest annealing temperature of 420 °C, with a large lattice parameter a and a small lattice parameter c , and it relaxes with increasing annealing temperature, which is reflected in XRD as well as in Raman.

The X-ray diffractograms reveal a strong preference of c -oriented grains in the undoped films. This is also reflected in the Raman spectra: the B1g peak at 399 cm^{-1} and the A1g/B1g doublet at 517 cm^{-1} (both oscillations in c -direction) have the same intensity than the Eg(3) peak at 639 cm^{-1} (in a -direction), which is twice the relative intensity that we consider as ‘standard’ anatase.^{126,169,170}

Nb-doped films:

The Nb-doped films are already strongly crystalized as anatase at 420 °C. Other phases are generally not present in the Nb-doped films. Thus, Nb stabilizes the anatase phase, and suppresses all other phases, confirming findings in literature. For example, Ahmad et al. reported a stabilization of the anatase phase caused by Nb doping,¹⁷⁹ and a suppression of rutile at high Nb contents was also reported by Trenzcek-Zajac.³¹

Both lattice parameters, a and c , increase by around 0.2 pm per Nb-at.%, which confirms Vegard’s law and is close to the increase in thin films of Furubayashi et al. produced by pulsed laser deposition.⁵⁶ Correspondingly, the unit cell volume increases by ca. 0.12% (or 16 pm³) per Nb-at.%. The lattice of the Nb-doped films shows no pronounced effect caused by heating.

The distribution of crystal orientation is closer to powder samples as compared to the undoped films. In the X-ray diffractograms of the Nb-doped films, a -oriented grains are preferred, which is opposite to the trend in films of Gardecka et al. prepared by aerosol assisted chemical vapor deposition.¹⁷² Also in the Raman spectra with increasing Nb content, the intensity of the oscillations in a -direction (Eg) becomes relatively stronger as compared to those in c -direction (A1g, B1g). The intensity ratios of a -oriented and c -oriented XRD peaks does not change with increasing annealing temperature.

The influence of Nb incorporation on the anatase Raman peak positions is as expected from literature. It leads to a *blue* shift of the Eg(1) Raman peak (independent of the Nb content) and the Eg(3) peak (0.7 cm^{-1} per Nb-at.%) and a strong *red* shift of the Raman B(1g) peak (1.5 cm^{-1} per Nb at.% in relation to Ti atoms). The redshift of the B1g peak is about twice as high as the blueshift of the Eg(3) peak. The Eg(1) peak width increases by 0.9 cm^{-1} per Nb at.%.

6.1.3 Nb-doped TiO₂ films sputtered with plasma emission control

This chapter gives an overview about nano-, and micro- structural and electrical properties of Nb-doped TiO₂ films rf-magnetron sputtered with plasma emission control. In the following, we use the common abbreviation *PEM* (plasma emission monitoring) for a sputter coating process in which the oxidation state of the Ti target is controlled using plasma emission monitoring. All PEM films were produced as described in chapter 2.1.3.

In chapter 6.1.3.1, we give a summary on published work (and also a few non-published aspects of the work), in which we found that there is an optimum oxidation state of the metallic Ti target (of around 68%) that leads to well conducting films. Also, we provide 2D representations of the Nb content, the O content, the unit cell volume and the conductivity for the varied deposition parameters (oxidation state of the target and sample position during deposition).

Chapter 6.1.3.3 presents an electrical and Raman study on similar films, with a lower post-heating temperature, which confirms a target surface oxidation of 68% for well conducting films. The structural studies of this chapter mainly focuses on Raman spectra that were derived as average spectra from Raman maps (see chapter 2.2.1), and which were decomposed into their components as described in the chapters 3 and 4.

The two chapters provide information on structural and electrical properties, but cannot explain the good conductivity of the films deposited with 68% target oxidation. Further insight will be given in chapter 7.3, in which the micro-structure of the films is studied by Raman mapping.

Chapter 6.1.3.4 studies the structural effects of the deposition time (or the film thickness) on films coated with a 71% oxidized Ti target surface.

6.1.3.1 Structural and electrical properties of PEM sputtered Nb-doped TiO₂ films

This chapter contains a summary of a work led by Dr. rer. nat. Sanat Kumar Mukherjee that was published in *Thin Solid Films, Volume 568, Issue 1, 94-101 (2014)*.¹⁰⁴ Although in the published work, the oxidation state was varied from 0% to 100%, we will here focus on the window of parameters that result in well conducting films (65% to 78%). We will present additional (new) analysis on these films in chapter 6.1.3.2.

We applied a technique to rf-magnetron sputter Nb-doped TiO₂ anatase thin films by putting Nb wires onto the sputter track and controlling the oxidation state of the metallic Ti target by the intensity of the Ti 453 nm plasma line. The films were coated using a sputter coater

by *von Ardenne Anlagentechnik GmbH* with a sputter power of 300 W and post-heated the films at $530\text{ }^{\circ}\text{C}$ (the publication says $400\text{ }^{\circ}\text{C}$, but we have re-calibrated the heating afterwards).

We successfully controlled the oxygen flow by monitoring the intensity of the Ti 453 nm plasma line. We found that for optimum conductivity of the PEM controlled rf-sputtered Nb-doped thin films there is a sweet spot of the oxidation state of the Ti target and the position of the substrate to be coated. Firstly, the Ti target surface should be between metallic and oxidic mode, with an oxidation state of the around 68% and 71% . This corresponds to a relative intensity of the 453 nm Ti plasma emission line of 0.35 or 0.375 – with the intensities 0 for a fully oxidized Ti target and 1 for an oxygen-free Ti target. Secondly, the substrate position of the film to be coated should not be too far away (horizontally) from the Nb wire. Although the oxidation state was varied from 0% to 100% , we will here focus on the window of parameters that result in well conducting films (65% to 78%).

As in the publication¹⁰⁴, we name the films according to the approximate *oxidation state* of the target during deposition and by their *position* ((a) 12.5 mm , (b) 42.5 mm , and (c) 72.5 mm horizontally away from the Nb wire). For example, we name the film deposited with a 65% oxidized Ti target surface that was deposited at position (a), 12.5 mm horizontally from the Nb wires, as “ 65-ox.t (a) ”.

Stoichiometry was measured by *RBS* (at the surface and at the interface), and *EDX*. Fig. 197 in the appendices shows the determined oxygen content by *RBS* at the film surface and the interface, and by *EDX* vs. the average of both *RBS* values. The films have over-stoichiometric oxygen contents, which is in the range of $O/(Ti+Nb) = 2.15 - 2.45$. The average deviation of the O content as measured by *EDX* from the *RBS* average is 0.04 and the average deviation of the *RBS* surface and *RBS* interface O content is also in average 0.04 . In average, the oxygen content is the same at the surface than at the interface.

The films that were coated between 65% and 78% target oxidation contain $2\text{ at.}\%$ – $16\text{ at.}\%$ of Nb (in relation to the Ti content). *RBS* indicates that the Nb content is higher at the surface than in the “bulk” of the films. According to *XPS* analysis, more than 95% of the Nb is in Nb^{5+} oxidation state and Ti^{3+} is only weakly present in the films.

6.1.3.2 2D representations of film parameters

Fig. 121 presents 2D representations of the Nb (left) and O content (right) vs. the oxidation state of the target and the sample position.

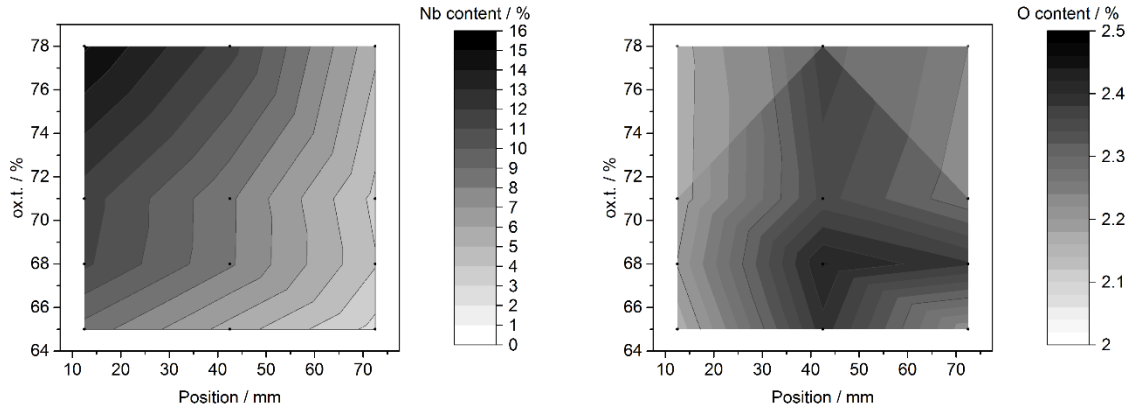


Fig. 121: Nb content (left) and O content (right) in PEM controlled rf-sputter coated Nb-doped TiO₂ thin films on B270 glass. The samples are placed (a) 12.5 mm, (b) 42.5 mm, and (c) 72.5 mm horizontally from the Nb wire, and the Ti target surface is oxidized by 65%, 68%, 71%, or 78%. Oxygen values for 78%-ox.t (a) and 78%-ox.t (c) were not measured and are extrapolated.

The films that were coated closest to the Nb wires contain the highest Nb content and the Nb content increases with the oxidation state of the target. The oxygen content in the films is lowest at position (a) and highest at position (b).

The films 68%-ox.t (a) and 65%-ox.t (a) with the best conductivities (around 10 S/m) have Nb contents of 10 at.% and 8 at.%, as well as O contents of 2.2 and 2.4 respectively. The two films have unit cell volumes of about $137.5 \text{ \AA}^3 \pm 0.2 \text{ \AA}^3$, which agrees with the unit cell volume of well conducting films in literature⁵⁶ and which is also the case in our work with e-beam evaporated TiO₂ films in chapter 6.1.2. The density of the two films is 4.3 g/cm³, which corresponds roughly to the mass density of Nb_{0.16}Ti_{0.84}O_{2.4} calculated as 4.4 g/cm³.

Yet, the conductivity does not correlate strictly with the unit cell volume. Fig. 122 presents the relation of the unit cell volume (on the left) and the conductivity (on the right) with the two deposition parameters %-ox.t and sample position.

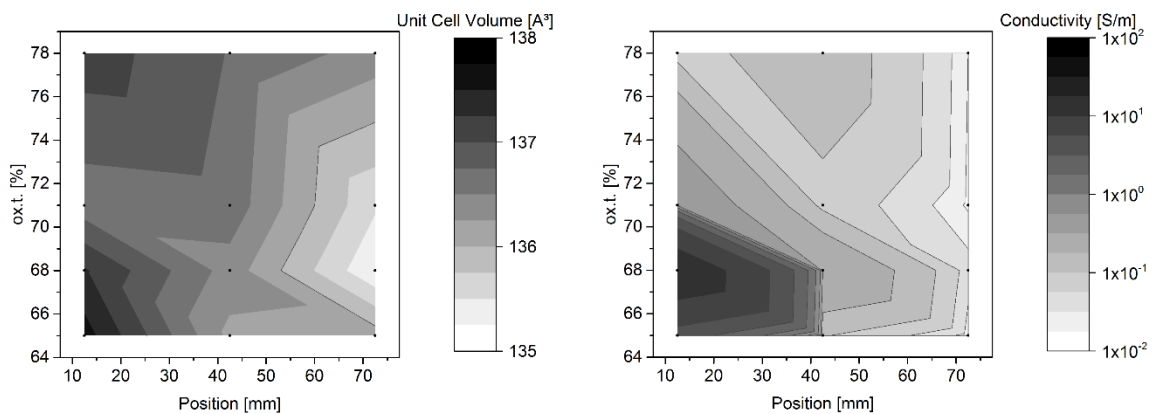


Fig. 122: 2D representation of unit cell volume (left) and conductivity (right) vs. the oxidation state of the Ti target surface and the position of the sample horizontally from the Nb wires.

In general, the unit cell volume increases with a sample position closer to the Nb wires, but is also influenced by the oxidation state of the Ti target. On the right side of Fig. 122 one can see the “region” of good conductivity around 65%-ox.t (a) (between the parameters 65%-ox.t and 71%-ox.t and the positions (a) and (b)).

The best conducting films have a transmittance of 70% in the visible range and an absorbance of 5% – 10% (at 250 nm film thickness). An as-deposited films 68%-ox.t film (substrate temperature around 50 °C during deposition) is X-ray amorphous and has a columnar nano structure of 15 nm thick columns visible by SEM. After post-heating at around 530 °C, the nano structure is less columnar and consists of more randomly oriented grains with a size of around 10 nm.

According to literature, small grains and extended grain boundaries might lead to a low mobility of the charge carriers and result in high resistivity.¹⁸⁰ Yet, the 68%-ox.t films are well conducting. Another explanation for high resistivity in the films with: Ti vacancies act as electron acceptors & counteract the donor behavior of Nb⁵⁺.

6.1.3.3 Electrical and Raman properties of PEM sputtered Nb-doped TiO₂ films

In the following we present further studies that aim on a better understanding the mechanisms that lead to the variation of conductivity between the PEM sputtered films and to the good conductivity the 68%-ox.t and 65%-ox.t films.

We have prepared similar films to the ones in chapter 6.1.3.1 using the same equipment (see chapter 2.1.3) with the same deposition parameters and with a lower post-heating temperature of around 475 °C. We used four different oxidation states (65%, 68%, 71%, or 78%) of the Ti target around the range that resulted in the best conducting films produced for chapter 6.1.3.1.

We performed DC conductivity measurements using a four-point-probe as described in chapter 2.2.7. Fig. 123 shows the conductivities of the films that were coated at the positions (a) 12.5 mm (red), (b) 42.5 mm (green), and (c) 72.5 mm (blue) horizontally from the Nb wires, with Ti target surface is oxidations of 65%, 68%, 71%, or 78%.

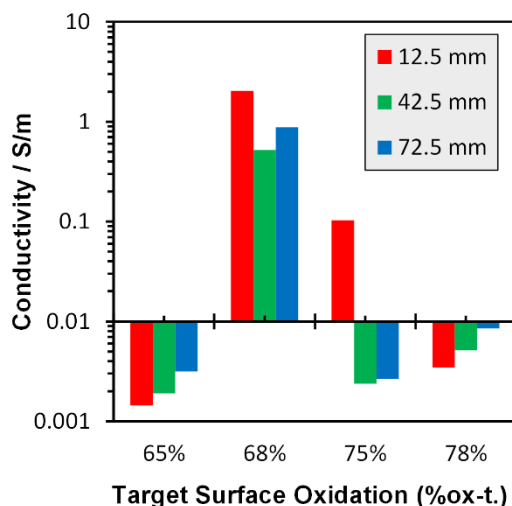


Fig. 123: Conductivities of the films that coated at the positions (a) 12.5 mm (red), (b) 42.5 mm (green), and (c) 72.5 mm (blue) horizontally from the Nb wires, with Ti target surface is oxidation states of 65%, 68%, 71%, or 78%.

The conductivity is highest for the 68%-ox.t films, with values of (a) 2 S/m, (b) 0.5 S/m, and (c) 1 S/m. For the 71%-ox.t (a) film, we measured a conductivity of 0.1 S/m. All other films have conductivities below 0.01 S/m.

The transmittance of the films and the B270 substrates together are in average 89%. The transmittance of an uncoated substrate is 92%. Thus, the transmittance of *film+substrate* is in average equal to 97% of the transmittance of the substrate without film. The transmittance Φ of the best conducting film is the lowest one ($\Phi_{film+substrate} = 93\% \cdot \Phi_{substrate}$).

XRD was performed for the 68%-ox.t (a) film. The lattice parameters are $a = 3.80 \text{ \AA}$ and $c = 9.52 \text{ \AA}$, and the unit cell volume is $V = 137.7 \text{ \AA}^3$. V is 1% larger and a is 0.5% larger than the standard value.

Raman spectra were taken with 633 nm excitation described in chapter 2.2.1. The spectra are average spectra of Raman maps, which are presented and discussed in chapter 7.3. Fig. 124 shows the Raman spectra of the thin films (after the subtraction of the substrate spectra from the measured spectra).

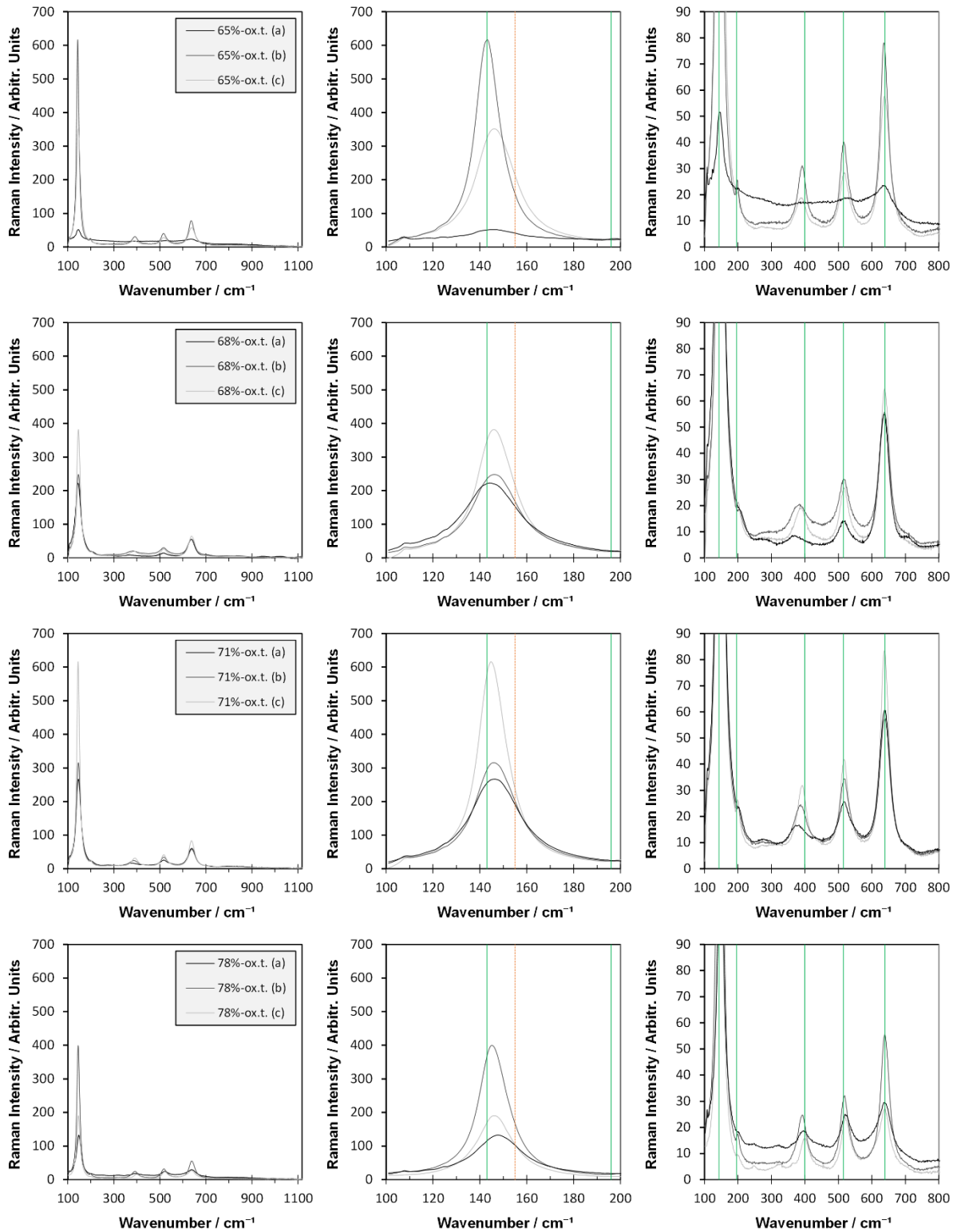


Fig. 124: Raman spectra (633 nm) of PEM controlled rf-sputter coated Nb-doped TiO_2 thin films (after subtraction of the substrate spectra from the measured spectra). The samples were placed (a) 12.5 mm , (b) 42.5 mm , and (c) 72.5 mm horizontally from the Nb wire, and the Ti target surface was oxidized by 65%, 68%, 71%, or 78%. The standard positions of anatase are marked green and of the strongest brookite peak is marked by a dotted orange line.

The films contain mainly anatase. The Eg(1) peak is blueshifted and the B1g peak is redshifted to various degrees, which is to be expected for varying amounts of Nb incorporation and a variation of O content. For each of the four oxidation states, the sample coated at position (a) has the broadest and least intense peaks. The intensity ratio $I_{Eg(3)}/I_{(A\&B)}$ of the Eg(3) phonon and the average of the B1g peak and the A1g/B1g-doublet is around 2 – 2.5 for most films. For each *ox.t.*, it is highest for the (a) films and lowest for the (c) films. The peak ratio is highest in the Raman spectrum the best conducting film 68%-*ox.t (a)*, with $I_{Eg(3)}/I_{(A\&B)} = 4$.

Fig. 125 presents a detailed view on the spectra of Fig. 124 in the range of the main brookite and rutile peak positions above 200 cm^{-1} . The 65%-*ox.t (a)* film has a high amorphous content. In Fig. 157 in chapter 7.3.1 one can see that the film consists of anatase islands in an amorphous matrix. In several spectra, elevations of the intensities around 440 cm^{-1} suggest that traces of rutile are present, most prominently in the spectrum of the 68%-*ox.t (a)* film. Traces of brookite are clearly visible in the 78%-*ox.t* films.

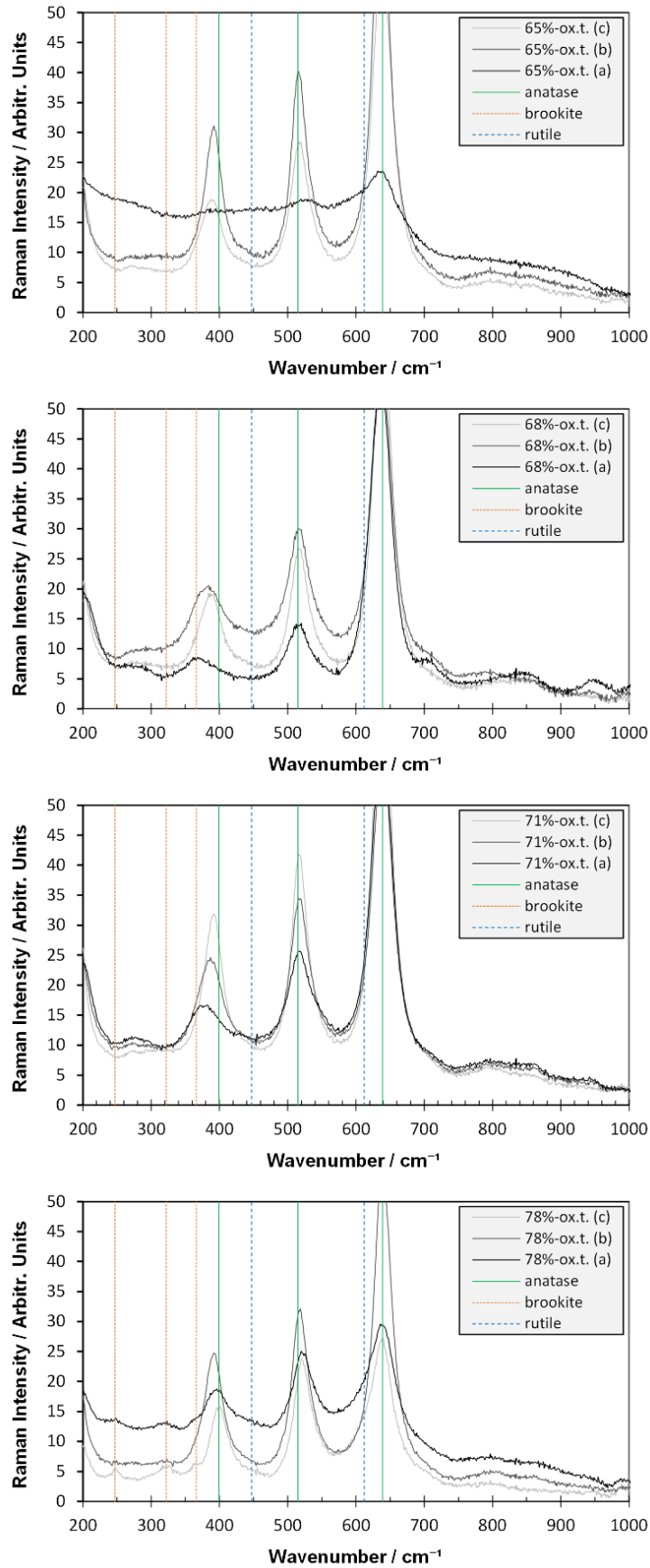


Fig. 125: Detailed view on the spectra of Fig. 124 in the range of the main brookite and rutile peak positions above 200 cm^{-1} . Brookite standard positions are marked by narrowly dotted orange, and rutile by widely dotted blue vertical lines.

Fig. 198 in the appendices shows various Raman peak parameters: the Eg(1) position vs. the Eg(1) width; the conductivity vs. the Eg(1) position and the Eg(1) width; the B1g position vs. the Eg(1) position; the Eg(1) width vs. the B1g width; as well as the conductivity vs. the B1g width. None of these parameters shows a clear trend that accounts for all oxidation states, except of a rough correlation of the Eg(1) and the B1g peak width.

Fig. 126 shows the B1g width (left) and the conductivity (right) vs. the B1g position. The B1g peak is redshifted by $3\text{ cm}^{-1} - 30\text{ cm}^{-1}$ from the standard position of 399 cm^{-1} . The redshift of the anatase B1g position correlates with an increasing B1g width. There is a rough trend of increasing conductivity with a decreasing B1g peak position. The four best conducting films have B1g peak positions between 370 cm^{-1} and 390 cm^{-1} and the poorly conducting films have B1g peak positions between 385 cm^{-1} and 400 cm^{-1} . Yet, the oxidation state of the Ti target has a stronger influence on the conductivity than the B1g peak position.

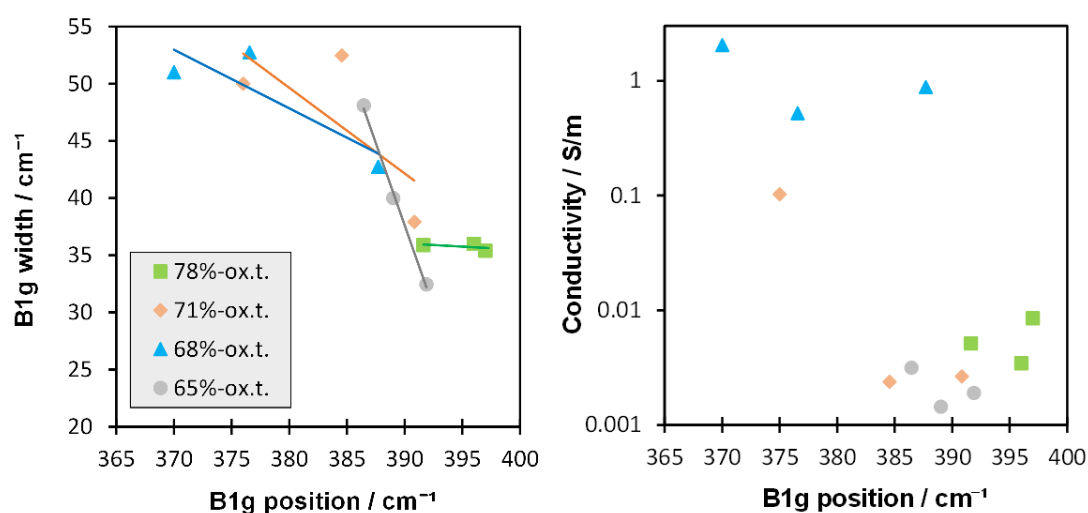


Fig. 126: Anatase B1g position vs. B1g width (left) and Raman phonon domain size vs. the B1g position of the PEM films.

6.1.3.4 Variation of film thickness

The deposition time was varied for PEM films with a 71% oxidized Ti target. The films were produced by M.Sc. Shixun Cui for his master's thesis. Fig. 127 shows the film thicknesses for each of the three sample positions (see chapter 2.1.3) vs. the deposition time.

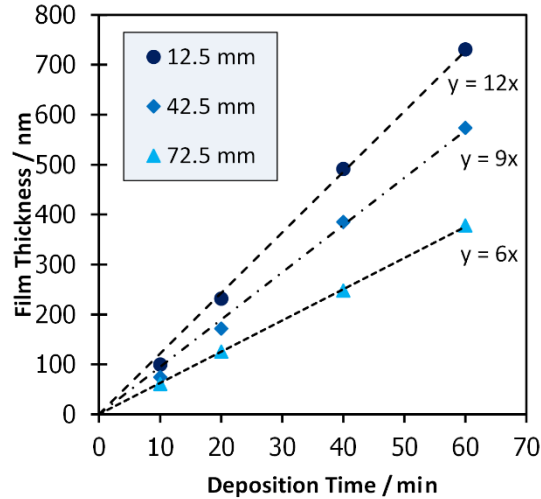


Fig. 127: Film thicknesses of PEM controlled rf-sputter coated Nb-doped TiO₂ thin films on B270 glass, with 71% oxidation of the Ti target surface. The samples are placed (a) 12.5 mm, (b) 42.5 mm, and (c) 72.5 mm horizontally from the Nb wires are deposited for 10, 20, 40, or 60 minutes.

After a delay of about two minutes, the deposition rates are constant. The approximate deposition rate of position (a) is 12 nm/min, of position (b) is 9 nm/min, and of position (c) is 6 nm/min. Thus, the deposition rate increases with closeness to the Nb wire or with increasing Nb content in the films. Fig. 128 shows the mass densities, which initially increase with increasing deposition time. They approach the density of anatase (3.8 g/cm³)¹⁴⁶ with increasing deposition time. Lines are added to the figure to guide the eye.

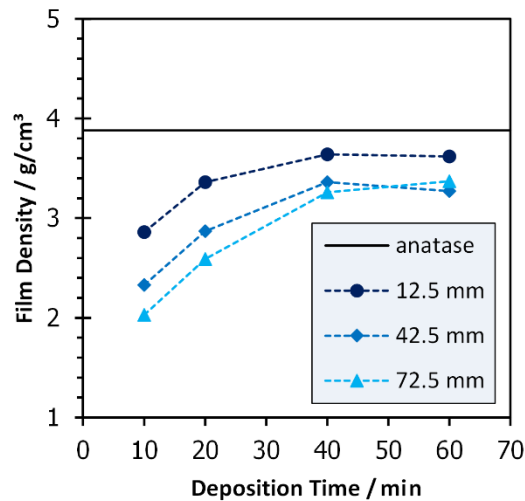


Fig. 128: Mass densities of PEM controlled rf-sputter coated Nb-doped TiO₂ thin films on B270 glass, with 71% oxidation of the Ti target surface. The samples are placed (a) 12.5 mm, (b) 42.5 mm, and (c) 72.5 mm horizontally from the Nb wires are deposited for 10, 20, 40, or 60 minutes.

Above 40 minutes, the density does not increase anymore with increasing deposition time. The films at position (a) have the highest density of 3.6 g/cm^3 . We have further prepared *combined anatase phonon maps* of these films, which are presented in Fig. 163 in chapter 7.3.2.

6.1.3.5 Conclusions

We produced Nb-doped TiO_2 thin films using rf-magnetron sputtering by placing Nb wires onto the sputter track and controlling the target oxidation by varying the oxygen flow according to the intensity of a Ti plasma emission line at 453 nm .¹⁰⁵

Chapter 6.1.3.1 contains published information.¹⁰⁴ We estimated an optimum Ti target oxidation state of around 68%. The films post-heated at $530 \text{ }^\circ\text{C}$ have high conductivities up to 7 S/m and a low optical transmission of 75% in the visible range at 550 nm . Samples that are positioned closely to the Nb wire (position (a)) are the most conducting ones.

In chapter 6.1.3.3, we confirmed the parameter window of the best conductivity around 68%-ox.t. (a). The films post-heated at $475 \text{ }^\circ\text{C}$ have conductivities up to 2 S/m and a high optical transmittance of 95% in the visible range at 550 nm .

The best conducting films, 68%-ox.t (a)-(530 °C), 65%-ox.t (a)-(530 °C), 68%-ox.t (a)-(475 °C), have unit cell volumes of $137.5 \text{ \AA}^3 \pm 0.2 \text{ \AA}^3$. This is in the same range as the best conducting e-beam coated films in chapter 6.1.2.

There is a correlation of high conductivity with a strong B1g redshift: The films with a B1g redshift $> 20 \text{ cm}^{-1}$ have a high conductivity ($\geq 0.1 \text{ S/m}$) while the films with a B1g redshift $< 10 \text{ cm}^{-1}$ have a low conductivity ($\leq 0.01 \text{ S/m}$).

The Nb content was determined only for the set of films that were annealed at $530 \text{ }^\circ\text{C}$. The films contain 2 at.% to 16 at.% of Nb. There is a clear trend that the Nb content increases with increasing Ti target oxidation and with decreasing distance to the Nb wires. The B1g peak position of the films annealed at $475 \text{ }^\circ\text{C}$ does not correlate with the Nb content determined for the films that were annealed at $530 \text{ }^\circ\text{C}$. A redshift of the anatase B1g position might indicate the efficiency (or amount) of Nb ion incorporation into the TiO_2 lattice, rather than the Nb content.

The films produced with the highest target oxidation (78%-ox.t.) are the least conducting films for each sample position and contain traces of brookite (visible in the Raman spectra). Also, for each coating position, these films have the lowest Nb contents. This supports the assumption made in chapter 6.1.2 that Nb doping of TiO_2 stabilizes the anatase phase.

In chapter 6.1.3.4, we varied the deposition time. After a delay of about 2 minutes, the deposition time is constant for each sample position. The deposition rate and the mass density

are highest for position (a). The mass density increases initially whereas it approaches the density of anatase (3.8 g/cm^3) and it is constant when the films are thicker than 150 nm .

6.2 Phase background spectra of undoped and Nb-doped TiO₂ anatase films

As described in chapter 3.1.4.2, the Raman spectra of a crystalline phase consists of not only first-order Raman scattering, but also of further signals arising from various origins, which we sum up as “phase background”. The phase background can include signals of for example second-order Raman scattering, defect or disorder induced scattering, overtones, dopant-specific vibrations, Raman inactive phonons (after a breakdown of selection rules), acoustic phonons, or phonon coupling.

Anatase-phase background spectra of e-beam evaporated undoped and Nb-doped TiO₂ thin films were derived by the fitting routine with adjustable spectral bands for phase backgrounds that are described in chapters 3.1.4.4.2 and 3.2.2.4.1. The phase background spectra are decomposed from the same measured Raman spectra (see chapter 4.1.3) than the first-order anatase spectra that are discussed in chapter 6.1.2. Spectral artefacts are visible around 144 cm^{-1} , 397 cm^{-1} , 516 cm^{-1} , and 637 cm^{-1} arising from the fit to the anatase first-order Raman peaks with asymmetric Lorentzian functions.

The modeled phase background spectra are least reliable in the ranges around the intense Eg peaks at 143 cm^{-1} and 639 cm^{-1} and in the range of 530 cm^{-1} ($\pm 30\text{ cm}^{-1}$), which overlaps with the sharp B270 glass Raman band at 550 cm^{-1} (see Fig. 44 in chapter 3.1.5.2) and the A1g/B1g anatase first-order Raman peaks around 517 cm^{-1} . Spectral features above 1000 cm^{-1} cannot be evaluated here because of artefacts in the spectra discussed in chapter 2.2.1. Anyway, peaks in that range can be either attributed to the spectral artefacts, to features of the B270 glass substrate or to incorporation of dopants.

6.2.1 Phase background spectra of e-beam evaporated undoped TiO₂ films

Below, the phase backgrounds of the undoped and Nb-doped TiO₂ anatase films are discussed separately. Fig. 129 shows Raman spectra containing the modeled anatase phase backgrounds of the undoped TiO₂ films annealed at $420\text{ }^{\circ}\text{C}$, $530\text{ }^{\circ}\text{C}$, and $640\text{ }^{\circ}\text{C}$. The spectra of the $420\text{ }^{\circ}\text{C}$ film is shown as a light green line, $530\text{ }^{\circ}\text{C}$ medium green, and $640\text{ }^{\circ}\text{C}$ dark green. The *Raman Intensity* axis is set to the same values as Fig. 131. The spectra are overlain by the same spectra plus the residual spectra (thin lines) that remained in the whole fitting routine.

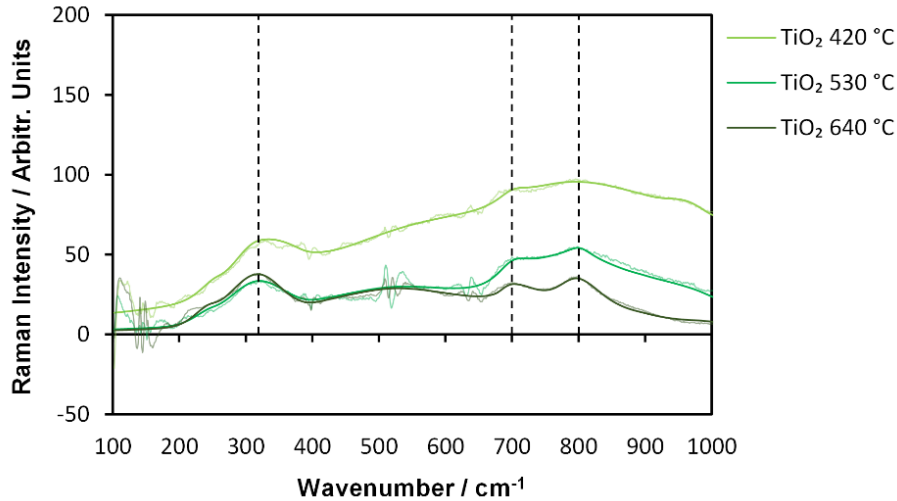


Fig. 129: Anatase phase backgrounds of e-beam evaporated undoped TiO₂ films. Peak positions of supposed second-order Raman peaks (or other coupled vibrations) are indicated by dashed lines.

The main features of the anatase Raman phase backgrounds of the undoped TiO₂ films are three peaks at 320 cm^{-1} , 700 cm^{-1} , and 800 cm^{-1} (positions indicated by vertical dashed lines in Fig. 129), and a broad band centered around 850 cm^{-1} (indicated by a dashed-dotted vertical line in Fig. 130). There is also a plateau visible between 400 cm^{-1} and 650 cm^{-1} that has an intensity lower than the three bands, but it contains three major artefacts from the fitting of the first-order peaks at 399 cm^{-1} , 514 cm^{-1} , and 639 cm^{-1} and will not be discussed further.

The peaks around 320 cm^{-1} , 700 cm^{-1} and 800 cm^{-1} become narrower and higher with increasing temperature. They behave similar to the first-order Raman peaks of anatase and thus, we consider that they arise from coupled vibrations. Such vibrations could be second-order scattering, overtones, or non-Raman allowed vibrations. The peak position around 800 cm^{-1} is double of the wavenumber of the B1g peak at 399 cm^{-1} . This peak is attributed to the first overtone of the B1g by Ohsaka et al.⁷³

The broad band at 850 cm^{-1} becomes visible when we look at the *difference spectra* of the phase backgrounds. The lower half of Fig. 130 shows phase background of the film annealed at 420 °C minus the phase background of the film annealed at 640 °C (light green), and the *difference spectrum* of the films annealed at 530 °C and 640 °C (dark green). For both *difference spectra*, a symmetric Gaussian band was added (by eye) as dashed lines centered at 850 cm^{-1} . Two sinks appear in the difference spectra below the Gaussian bands at 700 cm^{-1} and 800 cm^{-1} , which indicate that the described narrow peaks are strongest in the 640 °C spectrum.

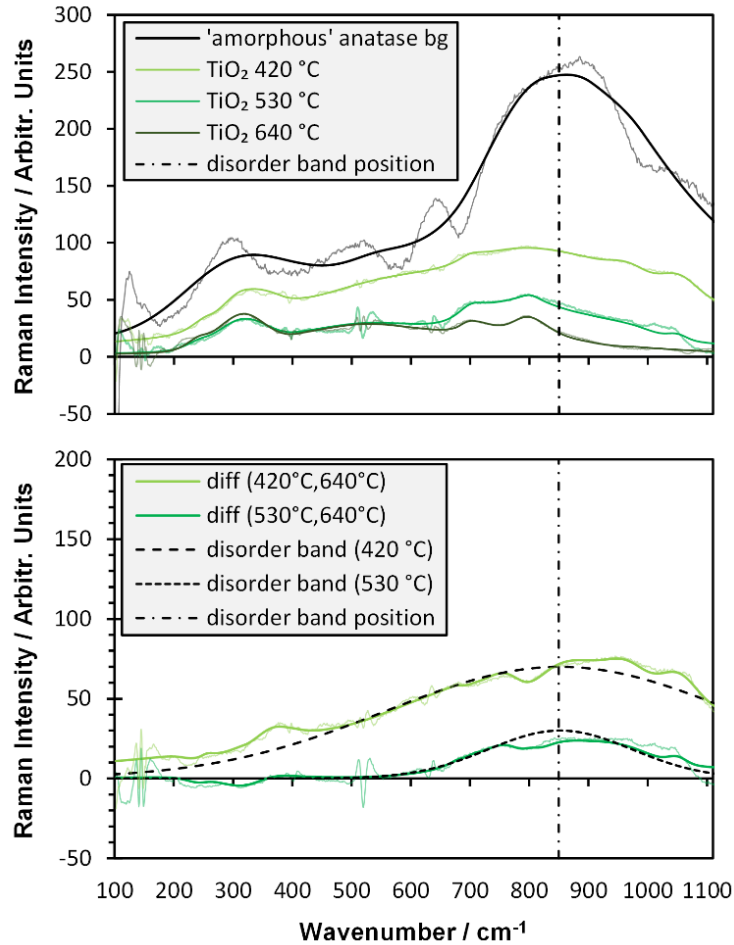


Fig. 130: Top: A nominal ‘amorphous’ phase background compared to anatase phase backgrounds of e-beam evaporated undoped TiO₂ films (already shown in Fig. 129) with a supposed position of a disorder band; bottom: difference spectra of the phase backgrounds of the TiO₂ films that were annealed 420 °C and 640 °C (light green) as well as of 530 °C and 640 °C. Gaussian bands which we consider as disorder-induced scattering are added by eye centered at 850 cm⁻¹.

The band at 850 cm⁻¹ is the major contribution to the intensity of the phase background of the film annealed at 420 °C (see lower and upper half of Fig. 130) and is wider than the measured range. It decreases drastically in width and height with increasing annealing temperature to 530 °C. At this temperature, the band becomes so narrow and weak that the spectra of the films annealed at 530 °C and 640 °C are nearly identical for wavenumbers below 600 cm⁻¹. We suggest considering the Gaussian band at 850 cm⁻¹ as a ‘disorder band’.

The upper half of Fig. 130 compares the TiO₂ phase backgrounds of Fig. 129 (green) with a *nominal* (anatase) phase background spectrum (black) that we found in chapter 6.3 by simulating the Raman spectrum of amorphous TiO₂ by extremely disordered structures that resemble the atomic bonds of the crystalline TiO₂ phases (anatase, brookite, rutile). The nominal anatase background is scaled arbitrarily and represented by a black line. The same

spectrum plus the residual spectrum of the simulation is a gray line. Future studies could check if such a TiO_2 disorder band is independent of the crystalline phase.

The occurrence of an intense band around 850 cm^{-1} in the nominal phase background in the Raman spectrum of amorphous TiO_2 supports our suggestion to classify the band as disorder-induced scattering, which decreases with increasing order.

6.2.2 Phase background spectra of e-beam evaporated Nb-doped TiO_2 films

Fig. 131 shows the anatase phase backgrounds of e-beam evaporated Nb-doped TiO_2 films annealed at $420\text{ }^\circ\text{C}$, $530\text{ }^\circ\text{C}$, and $640\text{ }^\circ\text{C}$. They are a sum of the background model spectra and the residual spectra of the whole fitting routine, each. The spectra of the films with $8\text{ at.}\%$ Nb are shown in blue and with $16\text{ at.}\%$ Nb in red. The spectra of the films annealed at $420\text{ }^\circ\text{C}$ are in light colors and at $640\text{ }^\circ\text{C}$ in dark colors.

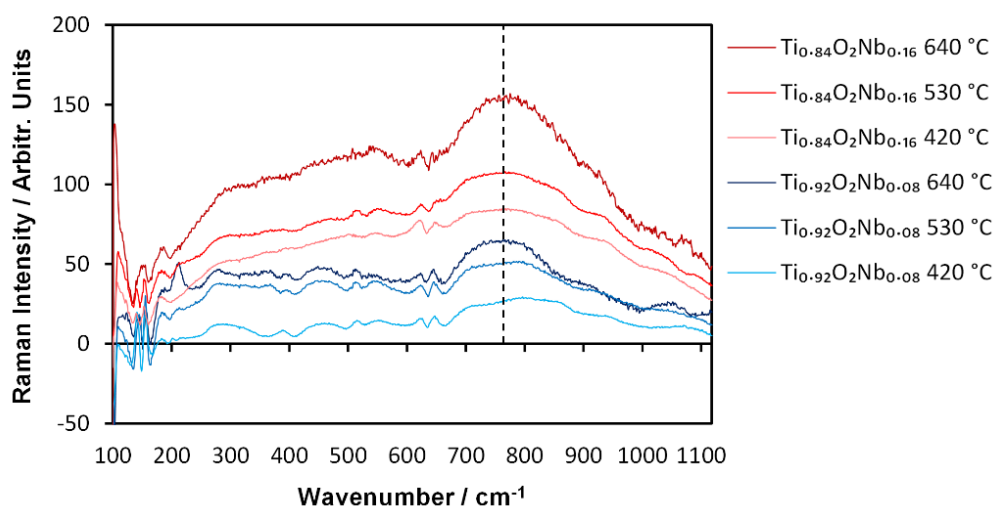


Fig. 131: Anatase phase backgrounds of e-beam evaporated Nb-doped TiO_2 films.

The phase backgrounds of Nb-doped TiO_2 have a band around 760 cm^{-1} (indicated by a vertical dashed line) that becomes more pronounced with increasing annealing temperature. In literature it is argued whether doping promotes the appearance of additional specific peaks in the background of anatase Raman spectra.

A vibration at around 690 cm^{-1} was found by Zhang et al. in nanocrystalline Fe-doped anatase thin films prepared by a facile nonhydrolytic sol-gel process, which they attribute to a two-phonon scattering process related to the surface morphology and oxygen vacancies. Kontos et al. doubt that a peak at 680 cm^{-1} (and at around 330 cm^{-1} , 585 cm^{-1} , and 815 cm^{-1}) in N doped films is dopant specific, because similar peaks were also found in undoped films by Balachandran and Eror.^{124,181}

The band at 760 cm^{-1} in the phase backgrounds of our doped films is at the double wavenumber than the B1g peak, and could be the first overtone, which occurs in the background of the undoped films (see Fig. 129 in chapter 6.2.1). Anyway, the band at 760 cm^{-1} increases with annealing temperature, while the B1g first-order peak does not become more intense. Furthermore, the band is the most intense feature of the phase background of the undoped films while the first-order anatase B1g peak is less intense than in the undoped samples. Thus, the high intensity in the range around 760 cm^{-1} most probably arises from a further cause in addition to signals from the first overtone of the B1g vibration. Actually, the flat or broad nature of the peak suggests that signals arise from two or more vibrations.

A plateau in a range of around $280\text{ cm}^{-1} - 900\text{ cm}^{-1}$ is present and its intensity increases with the Nb content as well as with the deposition temperature – followed by a ‘wavy’ downwards slope for increasing wavenumbers. For both Nb concentrations, the phase background intensity increases by roughly a factor of 2 in the full range of wavenumbers with temperatures increasing from $420\text{ }^{\circ}\text{C}$ to $640\text{ }^{\circ}\text{C}$. For each annealing temperature, the $\text{Ti}_{0.84}\text{O}_{2.25}\text{Nb}_{0.16}$ background spectra have about 2.5 times the intensity of the $\text{Ti}_{0.92}\text{O}_{2.25}\text{Nb}_{0.08}$ background spectra over the whole range.

6.2.3 Conclusions

We have analyzed the phase background of reactive e-beam evaporated anatase thin films. The material-specific background of a Raman spectrum provides information about local disorder in addition to the signals arising from first-order Raman scattering.

We suggest categorizing the features of the anatase phase backgrounds of undoped TiO_2 into two independent aspects: (1) distinct peaks around 320 cm^{-1} , 700 cm^{-1} and 800 cm^{-1} that become more pronounced (stronger and narrower) with increasing deposition temperature (like the first-order Raman peaks), while (2) an intense and broad Gaussian band around 850 cm^{-1} decreases heavily in width and height. We interpret the three distinct peaks as coupled vibrations and the Gaussian band at 850 cm^{-1} band as disorder-induced scattering. The assumption of a disorder-band at 850 cm^{-1} is supported by a nominal phase background spectrum that we found in chapter 6.3 in the Raman spectrum of amorphous TiO_2 .

The two described trends ((1) and (2)) with the annealing temperature correlate with increasing grain size indicated by SEM (cf. Fig. 151 in chapter 7.2.3), increasing crystallite size and decreasing lattice distortion indicated by XRD (chapter 6.1.2), stronger and narrower first-order anatase Raman peaks, as well as decreasing brookite and amorphous content (chapter 5.4). All of these are factors associated with increasing order.

In the Nb-doped films, the intensity of the whole phase backgrounds increases with Nb content and with annealing temperature. Strong vibrations occur in the phase backgrounds of the Nb-doped TiO₂ films as a band around 760 cm^{-1} , which also become more pronounced with increasing Nb content and annealing temperature. This is around the double wavenumber of the anatase B1g peak. The band might be partially caused by the first overtone of the B1g vibration. Its flat shape suggests that additionally further vibrations (for example two-phonon vibrations) might contribute to the band.

6.3 Raman spectrum and XRD of amorphous TiO₂

In amorphous material, the interatomic bonding forces are similar to those in crystals, yet, there is no long-distance order.⁷⁰ Interpreting this in terms of a ‘lattice’, the distribution of the bonding forces are often considered as a disordered elementary cell of infinite size – which can be seen as a Brillouin zone that is reduced to zero. This results in a diffuse Raman spectrum that resembles the phonon density of states rather than individual lines.^{70,153}

Exarhos et al. compared Raman spectra of crystalline and amorphous/vitreous (KPO₃)_n, which produces extremely sharp peaks in crystalline state (see Fig. 132). They demonstrated clearly that the amorphous Raman spectrum is closely related to the crystalline spectrum and described the amorphous spectrum as ‘essentially the envelope’ of the crystalline spectrum.¹⁸² They found the same in infrared spectra of the same materials.

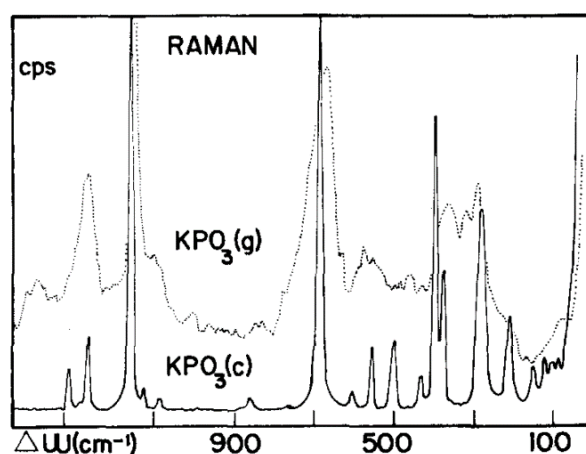


Fig. 132: Raman spectral comparison between crystalline and amorphous KPO₃ (taken from Exarhos et al.).¹⁸²

Similar ‘envelopes’ around allowed Raman bands were also found for BeO and for TiO₂ coatings. Exarhos et al. described broad Raman peaks of amorphous TiO₂ around 440 cm⁻¹ and 600 cm⁻¹ close to the rutile Eg (447 cm⁻¹) and A_{1g} (612 cm⁻¹) vibrations, which was also pointed out by Iida et al.^{151,183} From this, Exarhos et al. suggest that amorphous TiO₂ contains the same localized structural groups that are found in rutile (octahedral co-ordination of titanium with oxygen).

Our Raman spectra are taken in a broader range (100 cm⁻¹ – 1100 cm⁻¹) and are similar to Raman spectra of amorphous TiO₂ thin films and powder in literature.¹⁸⁴⁻¹⁸⁷ These spectra feature a band located around 160 cm⁻¹ in addition to the bands around 440 cm⁻¹ and 600 cm⁻¹. The three bands are located on a plateau, which changes to a downwards-slope above 700 cm⁻¹ with a weak but broad shoulder around 850 cm⁻¹.

The band at around 160 cm^{-1} is close to a blue-shifted anatase Eg(1) peak position typical for small crystallites. Not only the rutile A1g peak (612 cm^{-1}) is close to the band around 600 cm^{-1} , but also the anatase Eg(3) peak (639 cm^{-1}). The broad shoulder around 850 cm^{-1} is close to the rutile B2g position (826 cm^{-1}) and also resembles the band at 850 cm^{-1} in anatase phase background spectra (see chapter 6.2).

This suggests that the interatomic bonding forces of amorphous TiO₂ are also similar to those of anatase, not only of rutile. From this we assume that the interatomic bonding forces are similar to those of all three TiO₂ (normal pressure) allomorphs, thus brookite-like bonds might be also included.

6.3.1 Decomposition of an amorphous TiO₂ Raman spectrum into nominal crystalline Raman spectra

In order to check the plausibility of these assumptions, we simulated the spectrum of amorphous TiO₂ by the sum of anatase-, brookite-, and rutile-like features. In this simulation we treat these features as nominal crystalline phases with extremely broad Raman peaks. We fit this simulated spectrum to an experimental spectrum. The experimental spectrum is the average spectrum of all amorphous spectra obtained in this work from Raman measurements of reactive e-beam coated undoped TiO₂ thin film spectra. This also includes the amorphous content in partly crystallized films.

We used the models for multi-phase TiO₂ (see chapter 3.2.2) with additional simplifications/assumptions: we assume the distribution of bonds to be arbitrary and we simplify all peak widths Γ to have the same (extremely high) value. Thus, the widths of all first-order Raman ‘peaks’ together are fitted by one parameter only.

The peak positions and peak asymmetries are set to values that correspond to the smallest crystals that can be calculated using phonon confinement models (4 nm for anatase and 2 nm for rutile). For example, in 4 nm defect free nanocrystals, the nominal peak position of anatase Eg(1) vibrations is blue-shifted (by $+17\text{ cm}^{-1}$) to 161 cm^{-1} (see Fig. 89).

The brookite positions are fixed to those of the fit results to the Raman spectrum of a multi-phase TiO₂ thin film that contains a high amorphous content, small crystallites, high crystalline backgrounds and broad yet still rather distinguishable first-order Raman peaks. We therefore chose the peak positions of the Raman spectrum of an rf-diode sputtered TiO₂ thin film coated at $200\text{ }^\circ\text{C}$ (see Fig. 175 in the appendices), which has such properties.

The anatase Eg(1) peak is the TiO₂ vibration with the highest Raman cross section. Its height $I_{an,Eg1}$ is fitted individually. All further peak height ratios within each nominal phase are

taken from the literature spectra that have already been used to prepare the phase background spectra.^{125–127} Thus, the intensity of the nominal first-order Raman spectra of each phase is fitted by one factor, each: $I_{an,1st}$, $I_{br,1st}$, $I_{ru,1st}$.

Likewise, the intensity of the nominal phase backgrounds of the three phases are fitted by one factor, each: $I_{an,bg}$, $I_{br,bg}$, $I_{ru,bg}$. The factors are multiplied with ‘reference’ phase backgrounds. The nominal phase background reference spectra were created by broadening the original phase backgrounds (see chapter 3.1.4.4) by a factor of 3.

The anatase phase background spectrum of the e-beam deposited TiO₂ thin film annealed at 420 °C (see Fig. 129 in chapter 6.2) was used as the nominal anatase background reference spectrum. This spectrum was chosen because it is the most intense anatase phase background spectrum of undoped TiO₂ that was simulated earlier in this work in detail using the *anatase phase background model with adjustable spectral bands* (see chapter 3.1.4.4.2).

The decomposition of an amorphous TiO₂ spectrum by simulating extremely broadened nominal anatase, brookite, and rutile phases using the described model is shown in Fig. 133.

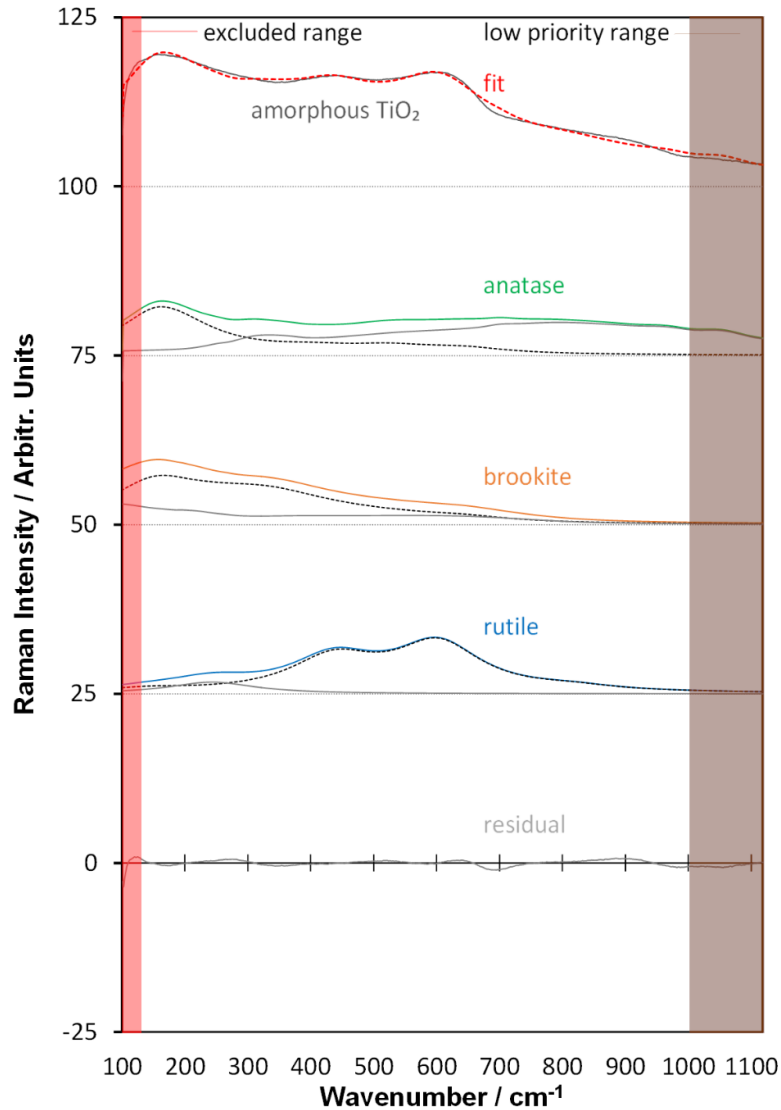


Fig. 133: Measured Raman spectrum of an amorphous TiO₂ thin film decomposed into spectra of nominal anatase, brookite, and rutile structures. The corresponding nominal first-order spectra are black dashed and the nominal phase backgrounds are gray lines.

The measured amorphous TiO₂ spectrum is dark gray and the fit is a dashed red line. The nominal anatase, brookite and rutile ‘phases’ are green, orange, and blue, respectively. The corresponding nominal ‘first-order Raman spectra’ are medium gray and the nominal ‘phase backgrounds’ are dashed black lines. The residual spectrum is light gray.

The modeled spectrum is close to the experimental amorphous TiO₂ spectrum. This suggests that the interatomic bonding forces of amorphous TiO₂ are similar to those present in all three TiO₂ allomorphs that occur at normal pressure: anatase, brookite, and rutile. Thus, seemingly the short-range order is reflected in the Raman spectra of amorphous TiO₂. The peak widths are extremely wide. Thus, the material lacks long range-order.

The simulated global peak width of the nominal first-order Raman peaks of amorphous TiO_2 , Γ_{am} , and the ratios of the total intensities I_{an} , I_{br} , I_{ru} of the contributions from the nominal phases, anatase, brookite, and rutile, are shown in Table 23.

Table 23: Fit results of the decomposition of amorphous TiO_2 into nominal crystalline phases

Parameter	Value
Γ_{am}	170 cm^{-1}
I_{an}, I_{br}, I_{ru}	$1 : 1 : 1$

The total intensities of each nominal ‘phase’ in the simulated spectra are almost identical and the intensities of the nominal ‘phase backgrounds’ are in the same order of magnitude than the nominal ‘first-order spectra’. The global peak width for all peaks is $\Gamma_{am} = 170 \text{ cm}^{-1}$.

6.3.2 Interpretation of the fit parameters as disordered nanoparticles

We will now interpret the structural effects of the peak width of $\Gamma_{am} = 170 \text{ cm}^{-1}$ in the QVRM. 170 cm^{-1} is around 6 times the width ($\Gamma_{an, Eg(4 \text{ nm})} = 30 \text{ cm}^{-1}$) of the anatase Eg(1) peak that corresponds to a 4 nm ‘defect free’ anatase nanocrystal with $\alpha_0 = 30$ (see Fig. 89 in chapter 6.1.1) or 2.5 times the width ($\Gamma_{ru, A1g(2 \text{ nm})} = 70 \text{ cm}^{-1}$) of the rutile A1g vibration in a phonon confinement model for a 2 nm rutile crystal.¹⁶³ Below these crystallite sizes, phonon confinement models cannot be applied because the dispersion curve and the shape of the Brillouin zone become critical (the Brillouin zone becomes extremely large and the phonon density approaches infinity).¹⁸⁸

Amorphous TiO_2 structures of 3 nm seem to be relatively stable: we measured the size of grain boundaries in our e-beam coated TiO_2 films to be around 3 nm – 4 nm using SEM images (see chapter 7.2.3). Therefore, we consider sizes of 3 nm \pm 1 nm as useful values for the calculation of (nominal disordered crystalline) amorphous TiO_2 clusters.

We estimate the number of defects $n_{def,an}$ in a nominal anatase crystal with a size of $L_{crys,an} = 4 \text{ nm}$ that corresponds to a peak width of $\Gamma_{am} = 170 \text{ cm}^{-1}$ by resolving equation (100) to $n_{def,an}$ with $\Gamma_0 = 7 \text{ cm}^{-1}$, $A_1 = 27.0$, $\gamma_1 \approx 1.3$, and $\alpha_0 = 30$ (or $\alpha_0 = 3 \cdot (10 \text{ \AA/nm})$):

$$n_{def,an} = \left(\frac{\Gamma_{am} - \Gamma_0}{A_1} \right)^{1/\gamma_1} \cdot \frac{L_{crys,an}}{\alpha_0} \approx 5.4. \quad (103)$$

Thus, a peak width of $\Gamma_{am} = 170 \text{ cm}^{-1}$ corresponds to 5 defects in a nominal 4 nm anatase crystal or to an average defect distance of approximately 0.8 nm. This is about 1.5 times the size of an anatase unit cell with $(a_{an}^2 c_{an})^{1/3} = 0.5 \text{ nm}$ (in 1-dimensional view).

A simpler estimation assuming a proportional increase of peak width with the number of defects in a crystal (in one dimension) gives about the same result.

$$\alpha_{am,ru} = \frac{\Gamma_{am}}{\Gamma_{an,Eg(4 \text{ nm})}} \cdot \alpha_0 = \frac{170 \text{ cm}^{-1}}{30 \text{ cm}^{-1}} \cdot \alpha_0 \approx 5.7 \cdot \alpha_0. \quad (104)$$

An equivalent estimation for a nominal 2 nm rutile crystal is:

$$\alpha_{am,ru} = \frac{\Gamma_{am}}{\Gamma_{ru,A1g(2 \text{ nm})}} \cdot \alpha_{0,ru} = \frac{170 \text{ cm}^{-1}}{70 \text{ cm}^{-1}} \cdot \alpha_{0,ru} \approx 2.4 \cdot \alpha_{0,ru}, \quad (105)$$

with the value $\alpha_{am,ru}$ that corresponds to a peak width of 170 cm^{-1} , and the value for a defect free rutile crystal $\alpha_{0,ru}$. Thus, a peak width of $\Gamma_{am} = 170 \text{ cm}^{-1}$ roughly corresponds to in average 2.4 defects in a nominal 2 nm rutile crystal or an average defect distance of 0.8 nm. This is around twice the size of a rutile unit cell $(a_{ru}^2 c_{ru})^{1/3} = 0.4 \text{ nm}$ (in one dimension).

6.3.3 Disorder-band at 850 cm^{-1}

The same fitting procedure was performed again with a slightly more flexible anatase background spectrum. Here, the anatase background is not simulated by a reference spectrum, but by a simplified version of the *anatase phase background model with adjustable spectral bands* (see chapter 3.1.4.4.2). The width of the anatase background is treated in the same way as the brookite and rutile phase backgrounds: by multiplying the widths of all pseudo-Voigt functions with an arbitrary factor of 3 – as compared to the phase-backgrounds derived for the literature reference spectra.¹²⁶ The intensities of the three bands are now fitted individually by the parameters $A_{bg,an1}$, $A_{bg,an2}$, $A_{bg,an3}$.

The resulting fit is shown in Fig. 134. The derived phase background is presented in Fig. 130 (top) and discussed in chapter 6.2.1. It contains an intense and broad band at 850 cm^{-1} , which supposedly is an indicator of disorder.

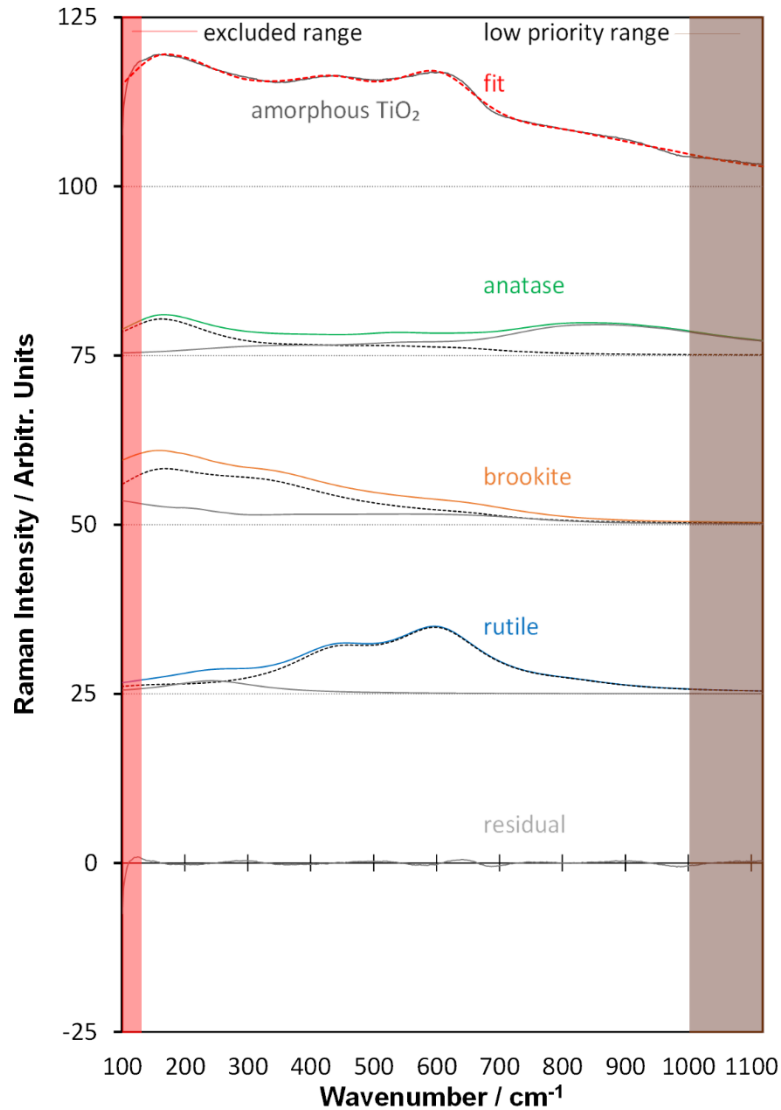


Fig. 134: Measured Raman spectrum of an amorphous TiO₂ film decomposed into nominal crystalline phases (with individual band heights in the anatase phase background model).

6.3.4 Conclusions

An amorphous TiO₂ spectrum was simulated by the sum of broad nominal anatase, brookite, and rutile Raman spectra including first-order Raman scattering and phase background spectra. We used the fitting models for multiphase TiO₂ Raman spectra introduced in chapters 3.1.4 and 3.2.2. The anatase-, brookite, and rutile-like vibrations contribute to the total spectrum to about the same amount.

The results confirm the presumption made in literature that interatomic bonds in amorphous structures are comparable to the bonds in the crystalline structures and that this is reflected in Raman spectra.

The nominal crystalline spectra are extremely broad, and the phase backgrounds are intense – both indicating highly disordered material. A fit of a global peak width for all peaks

resulted in a width of 170 cm^{-1} , and the peak position of the nominal anatase Eg(1) is located at 161 cm^{-1} . The peak position corresponds to a nominal anatase crystallite size of 4 nm . The width was fed into a q -vector relaxation model (QVRM) that contains a parameter α used for the estimation of defect densities.

We interpreted the fit results for nominal anatase crystals as well as for nominal rutile crystals with an average size of around 3 nm with defect distances of around 0.8 nm . This can be seen as clusters of $5 - 8$ unit cells with defect distances of $1 - 2$ unit cells.

Amorphous TiO_2 appears to be relatively stable in structures with a size of approximately $3\text{ nm} - 4\text{ nm}$. The thickness of the grain boundaries in the crystalline e-beam evaporated TiO_2 films is in the same scale.

Instead of arising from nominal “grain sizes”, the broad bands in the Raman spectra of the nominal phases could also be interpreted by a distribution of peaks around an average peak position. Then one could presume a Gaussian distribution of overlapping Lorentz peaks, which results in Gaussian functions⁷¹. Anyway, the modeled nominal crystalline spectra would look similar.

There appears an intense band at 850 cm^{-1} in the nominal crystalline Raman background of amorphous TiO_2 . This supports the assumption made in Chapter 7.2 that a band at 850 cm^{-1} might indicate disorder.

In literature, amorphous structures are often interpreted as an infinitely large unit cell. Apparently, one can also describe amorphous material as disordered small clusters of nominal unit cells.

7 Analysis of microstructure including Raman maps

We produced oversampled Raman maps using a 633 nm laser in areas of $30\ \mu\text{m} \times 30\ \mu\text{m}$ in steps of $0.25\ \mu\text{m}$ as described in chapter 2.2.1. The lateral resolution of the Raman maps taken with a 633 nm Raman laser is around $0.6\ \mu\text{m}$. This is the minimum size of crystalline anatase island displayed in the Raman maps of an e-beam coated $\text{Ti}_{0.92}\text{O}_{2.25}\text{Nb}_{0.08}$ film annealed at $375\text{ }^\circ\text{C}$ and of a PEM sputter coated $78\%\text{-ox.t. (a)}$ film. Thus, there are $121 \times 121 = 14641$ individual spatially resolved spectra that contain a certain amount of spectral information of the adjacent measurement points.

The spectra of each measurement point can be broken down into the TiO_2 phases (anatase, brookite, rutile, amorphous TiO_2), or into the intensities of individual Raman active phonons of the main phase, anatase. The maps display the spatial distribution of TiO_2 phases or of micrometer-sized domains, in which the intensities of anatase phonons in the Raman spectra are homogeneously distributed. These phonon domains include multiple nano-sized crystallites which are most probably homogeneously aligned. SEM images (in chapter 7.2.3) confirm that the domains consist of parallel aligned columnar structures.

Textures of the crystal phases and crystal orientation can be determined if they are inhomogeneous on a μm -scale. However, there are already visible differences in maps in with the structures a presumably more fine-grained versus more coarse grained in a scale smaller than $1\ \mu\text{m}$ (examples are the anatase phonon maps of the $65\%\text{-ox.t. (b)}$, $71\%\text{-ox.t. (c)}$ and the $78\%\text{-ox.t. (b)}$ films in Fig. 157 in chapter 7.3.1). The analyzed films are either amorphous, contain crystalline islands in an amorphous matrix, or are crystalline over the whole measured area.

All crystalline films are nano-structured; thus, the laser spot captures several nano-crystals. In partially crystallized mainly amorphous maps, we found by SEM that several crystallites are actually smaller than the smallest islands that appear in the Raman maps. The variation of the nuclei size below the spatial Raman resolution is reflected to a certain degree in the Raman maps by a variation in intensity.

Chapter 7.1 presents homogeneous Raman TiO_2 *phase maps* of rf-diode sputtered thin films. Chapter 7.2 presents Raman TiO_2 *phase maps* as well as (mainly) micro-structured *anatase Raman phonon maps* of reactive e-beam evaporated undoped and Nb-doped TiO_2 thin films. Chapter 7.3 presents (mainly) micro-structured *anatase Raman phonon maps* of Nb-doped TiO_2 films coated by rf-magnetron sputtering controlled by plasma-emission-monitoring.

All maps were taken at normal pressure and a constant room temperature of $20\text{ }^{\circ}\text{C}$. Given temperatures refer to either deposition temperatures (diode sputtered films) or annealing temperatures prior to the measurement (e-beam coated or PEM controlled rf-sputtered films).

For each map, average spectra have been calculated. The average spectra as well as the nanostructure are analyzed further in the chapters 4, 5, and 6.

7.1 Raman maps of diode sputtered multi-phase TiO_2 films

In this chapter we briefly present Raman TiO_2 phase maps of the rf-diode sputtered TiO_2 thin films that were deposited as described in chapter 2.1.1. The Raman spectra of each measurement point of the maps sum up to the average spectra presented in chapter 4.1.2. Thus, the maps are from the same samples of which the average Raman spectra are discussed quantitatively in chapter 5.2 and qualitatively in chapter 6.1.1.

Fig. 135 shows normalized ratio maps of the distribution of anatase (I_{150}/I_{270} , green), brookite (I_{244}/I_{270} , orange), and rutile (I_{440}/I_{270} , blue) in an rf-diode sputtered TiO_2 film coated onto a B270 glass substrate at a substrate temperature of $155\text{ }^{\circ}\text{C}$. For each phase, the ratio maps are made for the Raman peaks that are most distinct from the other two phases (cf. Fig. 86 in chapter 6.1.1.2).

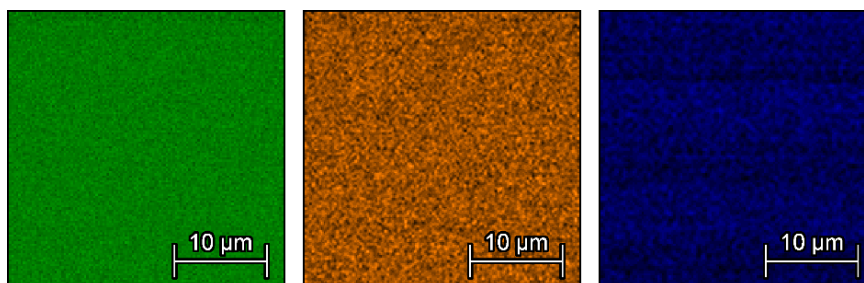


Fig. 135: Raman maps of rf-diode sputtered TiO_2 films on a B270 glass substrate deposited at $155\text{ }^{\circ}\text{C}$ with ratio maps in the ranges of the following peaks: anatase Eg (I_{150}/I_{270} , green), brookite A1g (I_{244}/I_{270} , orange), and rutile Eg (I_{440}/I_{270} , blue).

No structures that are larger than the resolution of the maps (ca. $0.6\text{ }\mu\text{m}$) are visible. The relative amount of noise in the anatase map is lower because it has the highest intensity. The same is the case for all other deposition temperatures of the set. Fig. 136 shows the same kind of maps for the temperatures $200\text{ }^{\circ}\text{C}$, $275\text{ }^{\circ}\text{C}$, $310\text{ }^{\circ}\text{C}$, and $415\text{ }^{\circ}\text{C}$ exemplarily for anatase.

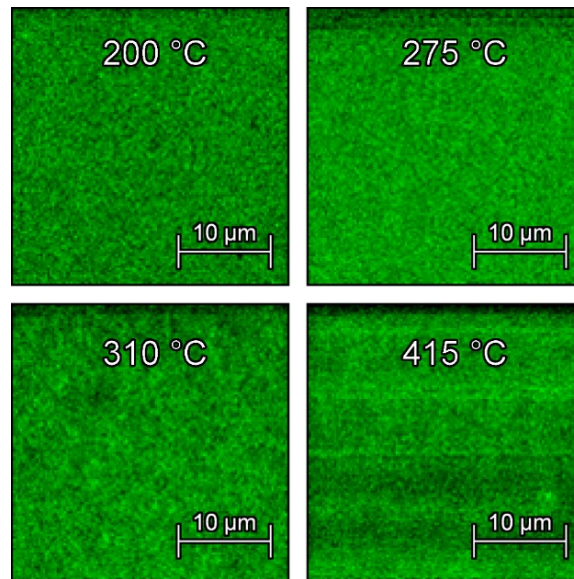


Fig. 136: Anatase Raman maps of rf-diode sputtered TiO₂ films on a B270 glass substrate deposited at temperatures of 200 °C – 415 °C.

These maps also show a homogeneous phase distribution in the lateral resolution of the Raman maps ($0.5 \mu\text{m} - 1 \mu\text{m}$). Also, brookite and rutile maps also show no structures. The surface of the film deposited at 310 °C also shows no structure in a SEM image in the same resolution, (Fig. 137).

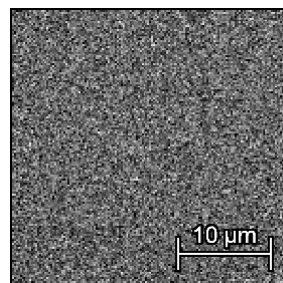


Fig. 137: SEM image of a diode sputtered thin film coated at 310 °C.

Fig. 138 displays a SEM image with 200 k magnification that shows nano-structures in a diode sputtered film coated at 200 °C. The nano-structures are interpreted by XRD and Raman in chapter 6.1.1.

Thus, the structures of the diode sputtered films are finer than the resolution of the Raman maps. The focus area of each measurement point in the Raman maps (around $0.6 \mu\text{m}$) captures several grains.

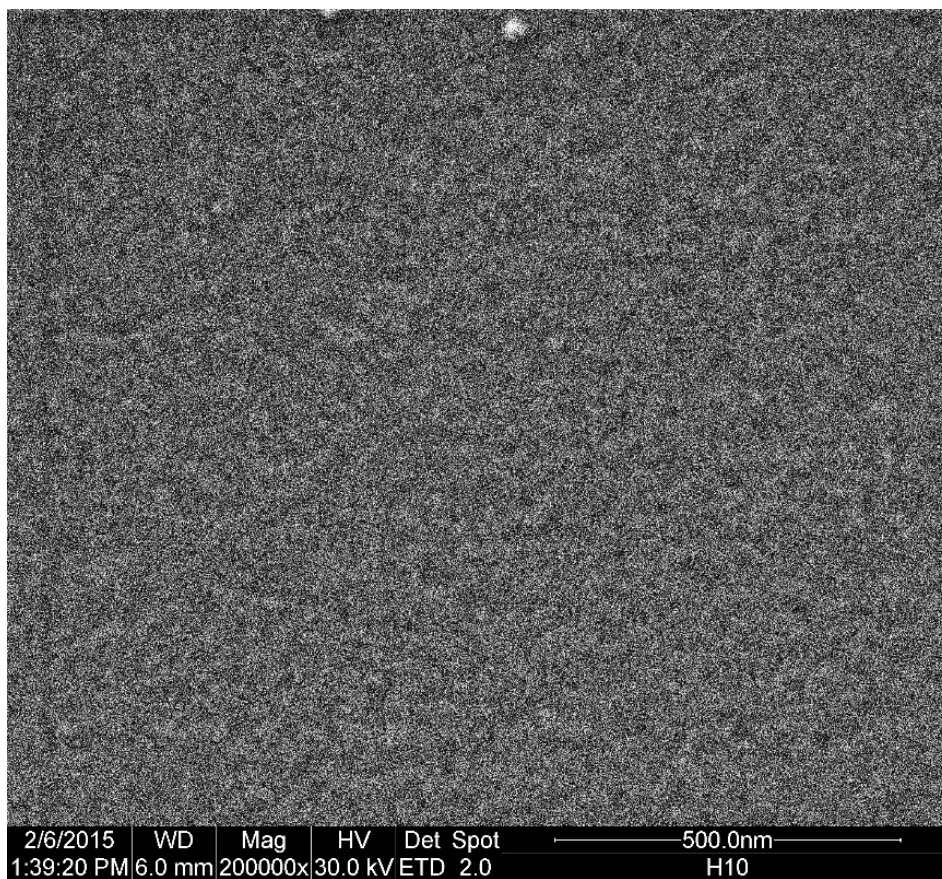


Fig. 138: SEM image of a polycrystalline rf-diode sputtered 70 nm thick TiO₂ thin film deposited at 200 °C in 200 k magnification.

7.2 Raman maps of reactive e-beam evaporated TiO₂ anatase films

In this chapter we discuss *Raman TiO₂ phase maps* and *Raman anatase phonon maps* of the e-beam evaporated undoped and Nb-doped TiO₂ thin films that were deposited as described in chapter 2.1.2. The Raman spectra of each measurement point of the maps sum up to the average spectra that are decomposed in chapter 4.2. Thus, the maps are from the same samples of which the average Raman spectra are discussed quantitatively in chapter 5.4 and qualitatively in chapter 6.1.2.

7.2.1 TiO₂ phase composition maps

Fig. 139 shows *TiO₂ phase maps* of e-beam evaporated undoped films on B270 glass (deposited at 250 °C, annealed at 420 °C, 530 °C, 640 °C) or on fused silica (annealed at 750 °C). The *TiO₂ phase maps* are prepared as described in chapter 2.2.2.2. The first three columns are overlay *phase maps* of anatase (red) and amorphous TiO₂ (green). The last column shows phase maps of the TiO₂ film on fused silica annealed at 750 °C of anatase (red) and brookite (green), rutile (blue), and the resulting *combined phase map*.

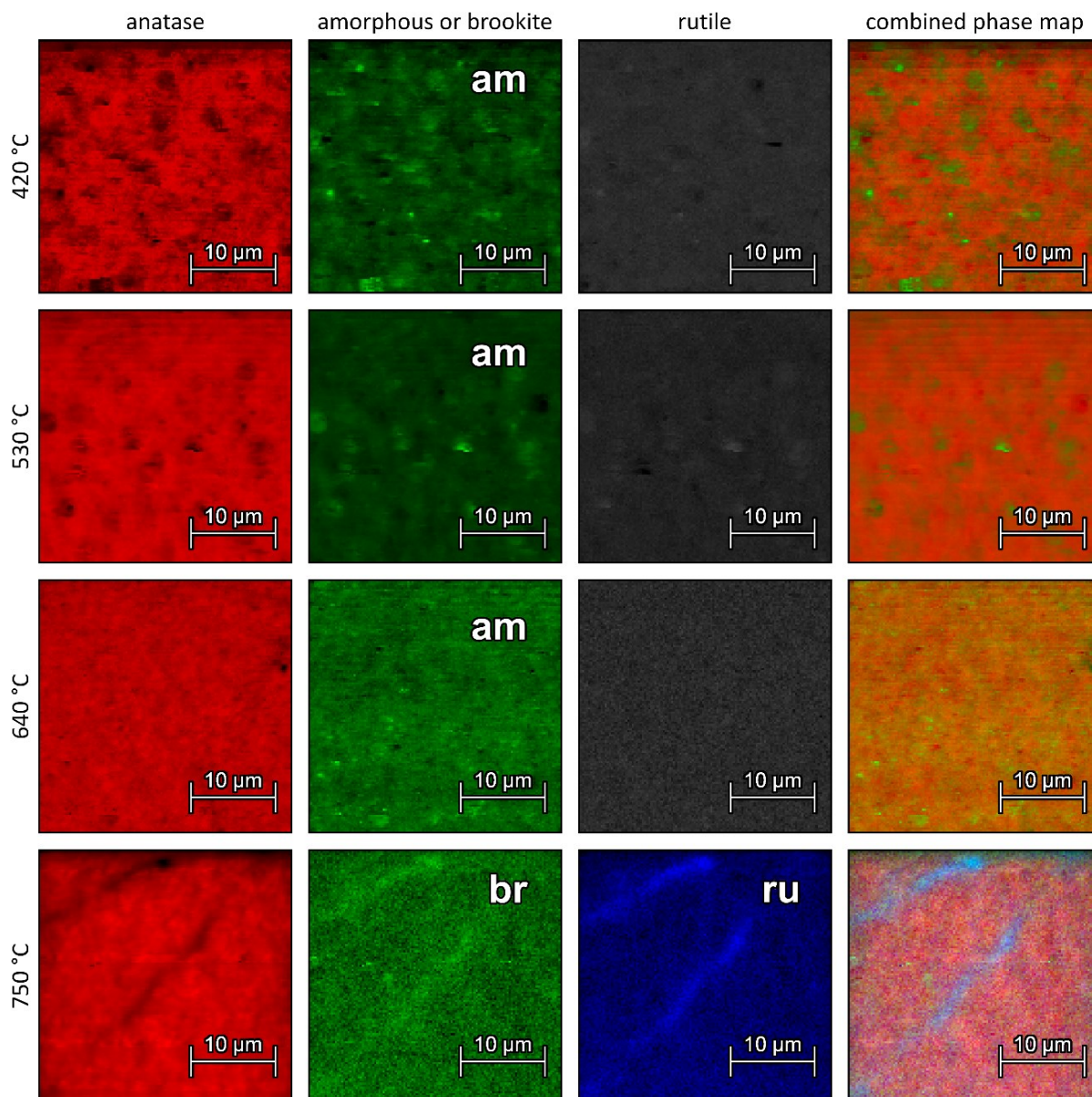


Fig. 139: *TiO₂ phase maps* (anatase (red), amorphous TiO_2 or brookite (green), rutile (blue)) of e-beam evaporated undoped TiO_2 films on B270 glass (deposited at $250\text{ }^\circ\text{C}$, annealed at $420\text{ }^\circ\text{C}$, $530\text{ }^\circ\text{C}$, $640\text{ }^\circ\text{C}$) or on fused silica (annealed at $750\text{ }^\circ\text{C}$).

All anatase phase maps of the undoped films include dark areas. In the films on B270 glass ($420\text{ }^\circ\text{C} - 640\text{ }^\circ\text{C}$), the intensity of amorphous TiO_2 is stronger in these areas, while in the maps of the film on fused silica ($750\text{ }^\circ\text{C}$) rutile is relatively strong in the areas with lower anatase intensity. The maps of the film annealed at $640\text{ }^\circ\text{C}$ shows homogeneous anatase intensity over almost the whole area.

The *combined phase maps* of the films on B270 glass that were annealed at $420\text{ }^\circ\text{C}$, $530\text{ }^\circ\text{C}$, and $640\text{ }^\circ\text{C}$ show the special distribution of the intensities in the *anatase phase maps* and of the intensities in the *amorphous phase maps*. Brookite is present in the spectra of all

measurement points. In the maps of the same films, no clearly distinct spectral information of rutile present in the individual locally resolved Raman spectra. Here, the I_{447}/I_{467} maps are gray.

The intensity of amorphous TiO_2 content is highest in the areas in which the anatase content is lowest: in the dark areas of the anatase maps in Fig. 139, the ratios of the first-order Raman peak intensities and the intensity in the range of $270 \text{ cm}^{-1} \pm 10 \text{ cm}^{-1}$ are lower than in the areas with strong red color, yet anatase is still present in the spectra. In general, at 270 cm^{-1} , Raman signals of the crystalline TiO_2 phases are low while in this range amorphous TiO_2 has a high Raman intensity. This makes the intensity in this range relatively suitable for distinguishing between crystalline and amorphous TiO_2 (for more information, see chapter 2.2.2.2).

Fig. 140 shows four representative positions on the *combined phase map* of the film annealed at $420 \text{ }^\circ\text{C}$ with intense green or red color. The corresponding locally resolved spectra are displayed in Fig. 141 (as red and green graphs, respectively) in comparison to the average spectrum (black) of the maps.

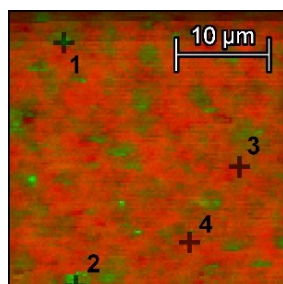


Fig. 140: *Combined TiO_2 phase maps* (overlay of anatase (red) and amorphous (green)) of a reactive e-beam coated TiO_2 thin film annealed at $420 \text{ }^\circ\text{C}$. This map appears already in Fig. 139. Positions 1 – 4 mark the measurement points of the corresponding spectra in Fig. 141.

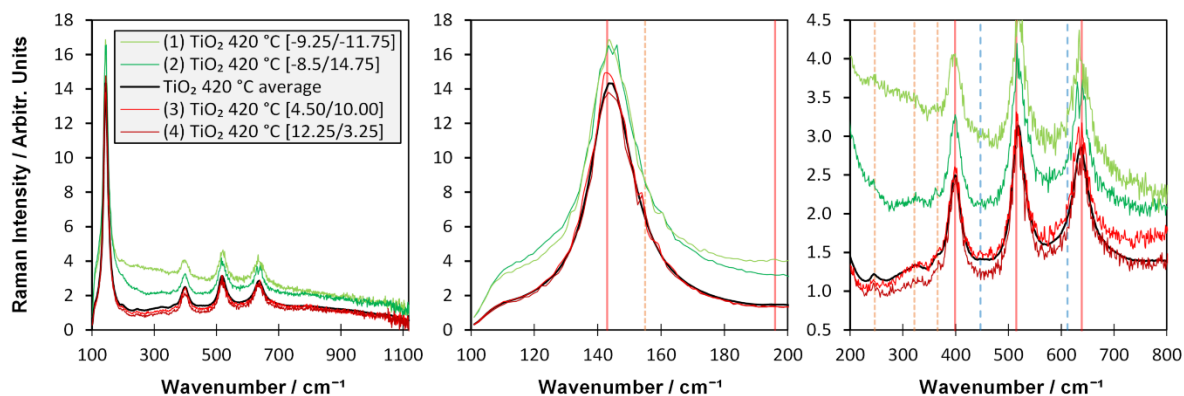


Fig. 141: Locally resolved Raman spectra taken at the four positions that are marked in Fig. 140 and average spectrum of NbO annealed at $420 \text{ }^\circ\text{C}$. Literature positions are marked by vertical transparent lines for anatase (red solid), brookite (orange narrowly dashed), and rutile (blue widely dashed).

The red spectra are close to the average spectrum. Brookite present in all spectra (several spectra were examined, but for clarity only the displayed four locally resolved spectra are presented). Thus, brookite homogeneously distributed in the resolution of the maps ($0.5\ \mu\text{m} - 1\ \mu\text{m}$). No clearly distinct spectral information of rutile is present. In the green spectra, strong broad features superimpose the anatase spectra. These features resemble amorphous TiO_2 .

In the rutile map (I_{447}/I_{467}) of the film annealed at $750\ ^\circ\text{C}$, high intensity is visible along straight lines. The corresponding brookite map shows few positions with high intensity. Also, medium high intensities are visible at the same positions at which the rutile map is strong, which might be caused by the rutile multi-phonon peak at $245\ \text{cm}^{-1}$. The positions with the highest intensity of each *Raman phase map* (anatase, brookite, rutile) are marked in the *combined phase map* in Fig. 142.

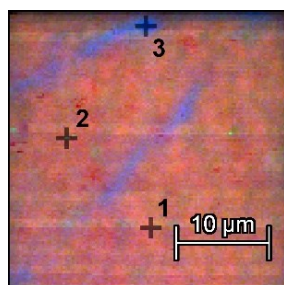


Fig. 142: *Combined TiO_2 phase maps* (overlay of anatase (red), amorphous or brookite (green), rutile (blue)) of a reactive e-beam coated TiO_2 thin film annealed at $750\ ^\circ\text{C}$. This map appears already in Fig. 139. Positions 1 – 3 mark the measurement points of the corresponding spectra in Fig. 143.

Fig. 143 shows the corresponding spectra with the highest intensity in the phase maps of anatase (red), brookite (green), and rutile (blue), and the average spectrum (black) of the map.

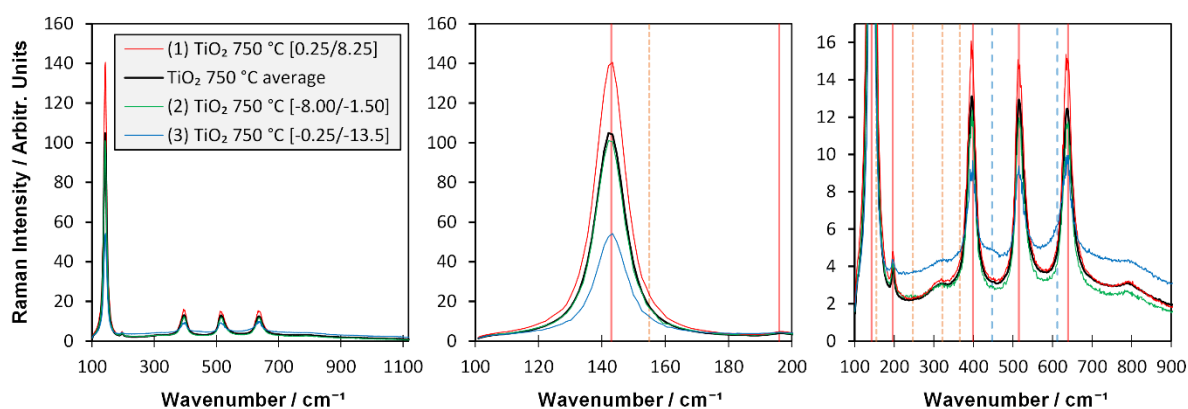


Fig. 143: *Locally resolved Raman spectra* taken at the three positions that are marked in Fig. 142 and average spectrum of NbO annealed at $750\ ^\circ\text{C}$. Literature positions are marked by vertical transparent lines for anatase (red solid), brookite (orange narrowly dashed), and rutile (blue widely dashed).

The spectrum of position (1) (red spectrum), is similar to the average spectrum (black) with more intense first-order anatase Raman peaks. The spectrum of position (2) (green) is also comparable to average spectrum. It is slightly lower in most parts of the spectral range, except for the range $150\text{ cm}^{-1} - 380\text{ cm}^{-1}$, in the range of the most intense brookite peaks in literature. A small bump at 245 cm^{-1} might indicate the existence of brookite.

The spectrum of position (3) (blue) includes weak but sharp spectral information of the rutile Eg and A1g phonon at 447 cm^{-1} and 612 cm^{-1} . The anatase first-order Raman peaks are weaker than in average spectrum (half of the intensity). The spectral background is more intense and broader as compared to other spectra, indicating disorder.

7.2.2 Anatase phonon maps: variation of Nb content and annealing temperature

Fig. 144 shows *combined phonon maps* of e-beam evaporated Nb0, Nb1, and Nb2 films on B270 glass (deposited at $250\text{ }^{\circ}\text{C}$, annealed at $420\text{ }^{\circ}\text{C}$, $530\text{ }^{\circ}\text{C}$, $640\text{ }^{\circ}\text{C}$) or on fused silica (annealed at $750\text{ }^{\circ}\text{C}$). They are overlay *phonon maps* of the Eg(1) (red), B1g (green), A1g/B1g-doublet (blue) vibrations. The *combined phonon maps* were prepared as described in chapter 2.2.2.1.

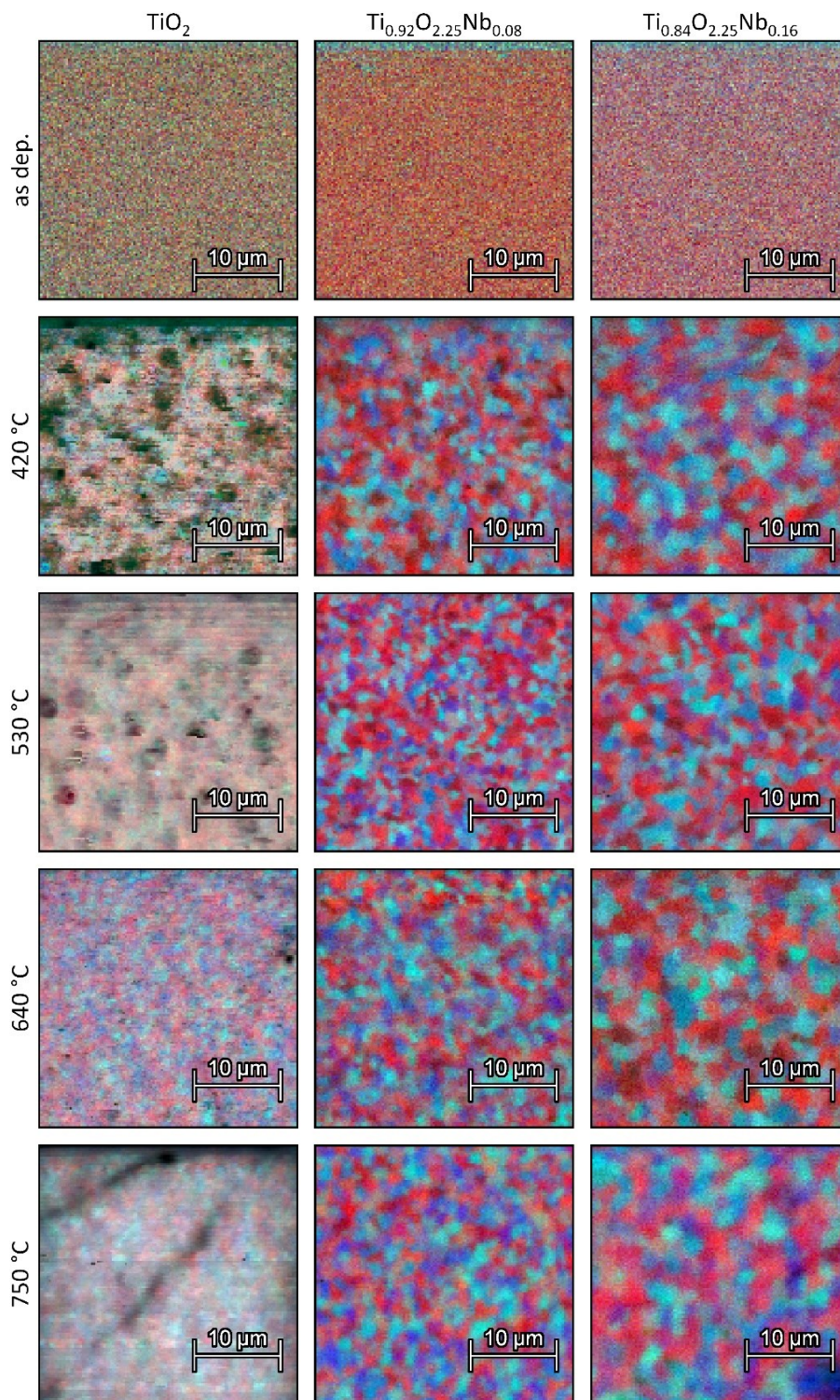


Fig. 144: Combined phonon maps of anatase (Eg(1) (red), B1g (green), A1g/B1g-doublet (blue)) of e-beam evaporated Nb0 (left), Nb1 (mid), and Nb2 (right) films on B270 glass (deposited at 250 °C, annealed at 420 °C, 530 °C, 640 °C) or on fused silica (annealed at 750 °C).

The as deposited films are amorphous (see Fig. 102 in chapter 6.1.2.4) and the Raman maps do not show any structure beyond noise.

The anatase phonon maps of the crystalline films (post-heated above 400 °C) show microstructures of homogeneous anatase peak intensities. In the red areas, the Eg(1) peak at

143 cm^{-1} is strongest (also the E(2) and Eg(3) peak, not shown); in the blue areas, the B1g peak at 399 cm^{-1} is strongest; and in the cyan areas, the B1g peak as well as the A1g/B1g doublet at 517 cm^{-1} are strong.

The structure of anatase is nearly homogenous in the undoped films. The size of the visible domains of the films are in the range of the lateral resolution of the maps, but when compared to the diode sputtered films, a certain kind of structure is visible. The domains of the Nb-doped films have a higher contrast and they become larger with increasing Nb-doped films. The structures in the Nb0 films are below $1\ \mu\text{m}$, while the average domain sizes are around $1.5\ \mu\text{m}$ (Nb1), $2.5\ \mu\text{m}$ (Nb2).

The anatase *phonon maps* of the undoped films have dark areas that are not found in the doped films. The Nb0 films that were post-heated at $420\text{ }^\circ\text{C}$ and $530\text{ }^\circ\text{C}$ are not completely crystalline. The dark area in the Nb0 film post-heated at $750\text{ }^\circ\text{C}$ show rutile structures (in addition to anatase) – as will be shown in chapter 7.2.1. As mentioned in chapter 2.2.2, the maps are normalized to the color intensities: the weakest values are black and the strongest values are full color. Thus, black does not mean zero intensity, but relatively low intensity for each of the three anatase phonons.

The Nb-doped films are fully crystalline already at the lowest annealing temperature ($420\text{ }^\circ\text{C}$). So, the maps confirm the assumption (in chapter 5.4) that Nb stabilizes anatase and suppresses the other TiO_2 phases.

The maps reveal that the relative intensities of the individual anatase oscillations vary along the sample surface. Example spectra are shown in Fig. 145. The figure displays arbitrarily chosen micro Raman spectra of various positions (gray) and the average spectrum (green) of the Nb2 $640\text{ }^\circ\text{C}$ anatase *phonon map* (Fig. 144). The spectra are sorted by the intensity of the Eg(1) peak at 143 cm^{-1} , noise-filtered, and the substrate spectra are stripped from the measured spectrum.

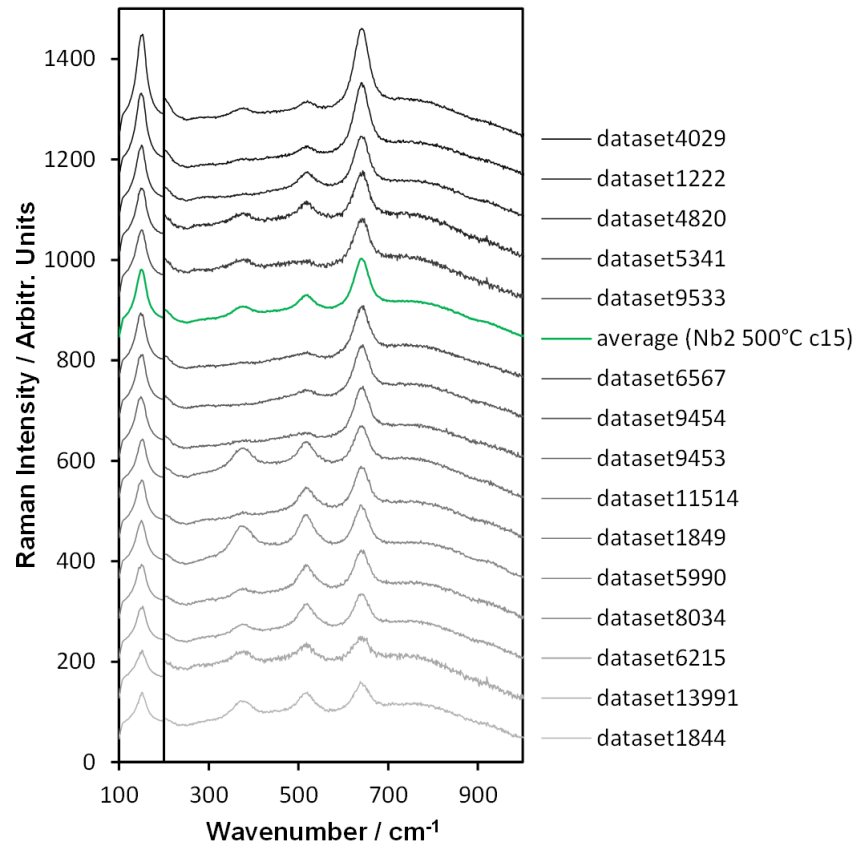


Fig. 145: Micro Raman spectra of various positions on the anatase Nb2 640 °C map. The spectra are sorted by the Eg(1) height, shifted on the intensity axis by 80 each, and the Eg(1) peak is multiplied by a factor of 0.25 with an offset of +60, normalized to the intensity at 1000 cm⁻¹. (Temperature set point of 500 °C resulted in an annealing temperature of 640 °C ± 20 °C.

The Raman spectra differ heavily depending on the position of the measurement. Thus, average spectra are different from locally resolved spectra. For statistical evaluation of the films a Raman map provides more information than a single measurement at one position.

7.2.3 Topographical analysis using SEM & EDX

We took SEM images of films on Si wafers that were simultaneously coated with the films on B270 glass. The films on Si provide high contrast SEM images. The images show structures of nano topography (Fig. 146) as well as micro topography (Fig. 149): small grains in the nm scale and domains in the μm scale which are larger with increasing Nb content. The micro-structures found in SEM images have comparable size to those found in the Raman phonon maps.

Fig. 146 shows SEM images of the nano-structure taken in 200000 x magnification of (a) TiO₂, (b) Ti_{0.92}O_{2.25}Nb_{0.08}, and (c) Ti_{0.84}O_{2.25}Nb_{0.16} films on Si wafers annealed at 640 °C. Fig.

146 (d) show the boundaries between micro-domains of $\text{Ti}_{0.84}\text{O}_{2.25}\text{Nb}_{0.16}$ films displayed in Fig. 149.

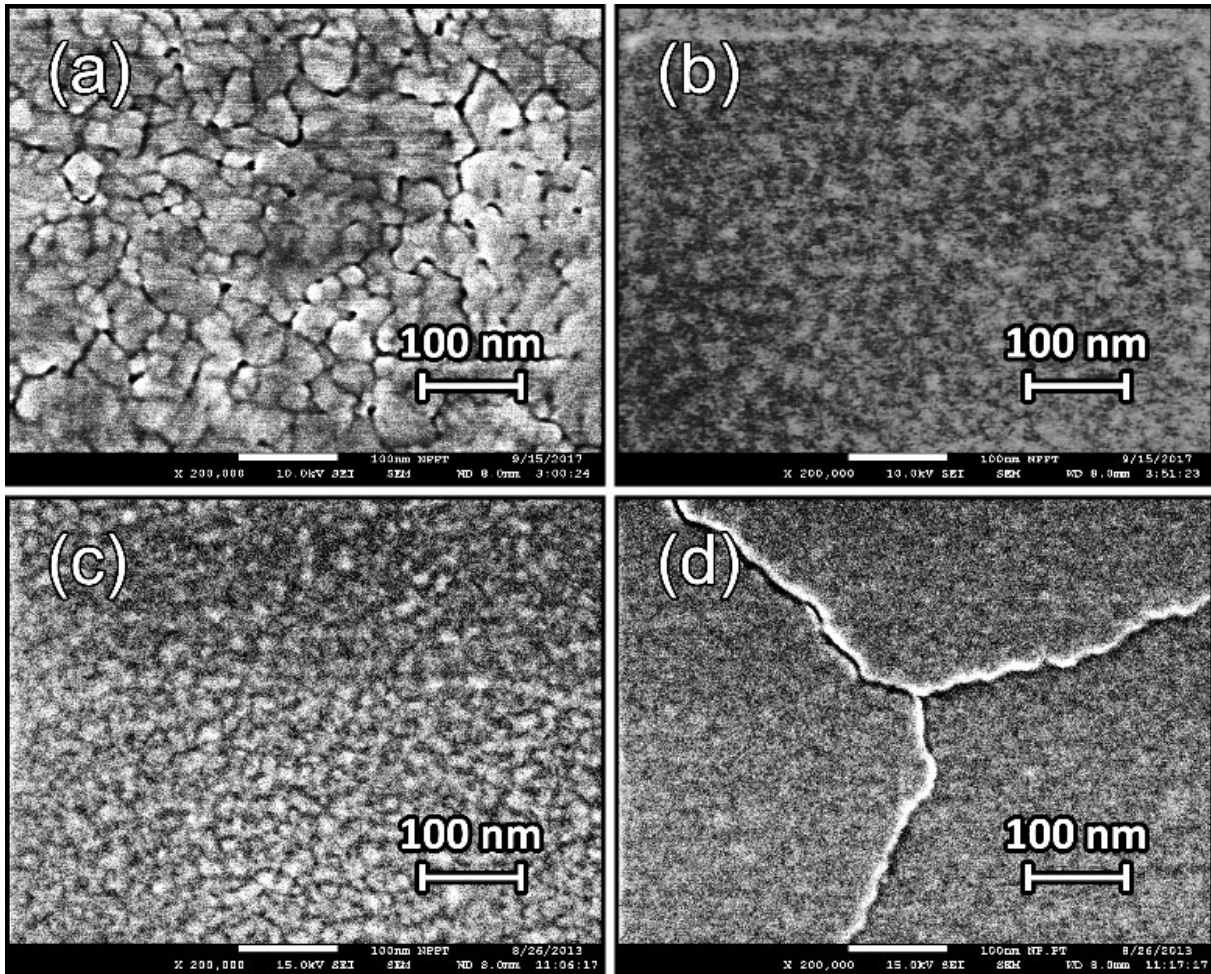


Fig. 146: SEM images (200000 x) of (a) TiO_2 , (b) $\text{Ti}_{0.92}\text{O}_{2.25}\text{Nb}_{0.08}$, and (c) $\text{Ti}_{0.84}\text{O}_{2.25}\text{Nb}_{0.16}$ films annealed at 640°C , (d) micro-grain boundaries in the $\text{Ti}_{0.84}\text{O}_{2.25}\text{Nb}_{0.16}$ film.

The surfaces of the undoped films have sinter structures of partly agglomerated grains with a mean size of 50 nm (distributed from $10\text{ nm} - 400\text{ nm}$) and sub-grains of 20 nm ($10\text{ nm} - 40\text{ nm}$). The grains of the doped films have a mean size of ca. 10 nm ($5\text{ nm} - 15\text{ nm}$) in the Nb1 films and of ca. 15 nm ($5\text{ nm} - 20\text{ nm}$) in the Nb2 films. The grain size of the undoped films is significantly smaller than the crystallite size estimated from XRD, yet the SEM figures show films grown on Si, and XRD was performed on films that were coated onto B270 glass.

The boundaries between the sintered structures in the undoped films are 6 nm broad (and vary between $3\text{ nm} - 20\text{ nm}$), as was determined by various SEM pictures of films on B270 glass and Si wafers taken at magnifications of 100000 , 200000 , and 1000000 . Examples of such SEM pictures can be found in the appendices in and Fig. 199 to Fig. 201.

Fig. 146 (d) shows another area of the same Nb2 film annealed at 640°C shown in Fig. 146 (c). Clear boundaries are visible in the figure. These boundaries separate micro-domains

(see Fig. 148 and Fig. 149) that resemble the structures found in the Raman anatase *phonon maps* (chapter 7.2.2). The boundaries between the microstructures in the Nb-doped films are also 6 nm ($\pm 1\text{ nm}$) broad, as was determined from SEM pictures taken at magnifications of 100000 and 200000 . Example figures are shown in Fig. 202 and in Fig. 203 in the appendices.

We performed an EDX linescan across such a boundary, which reveals that the Si substrate is more visible in the boundary. Fig. 147 shows the position of the linescan and the normalized intensities (*average* = 1) of Ti, O, Nb and Si.

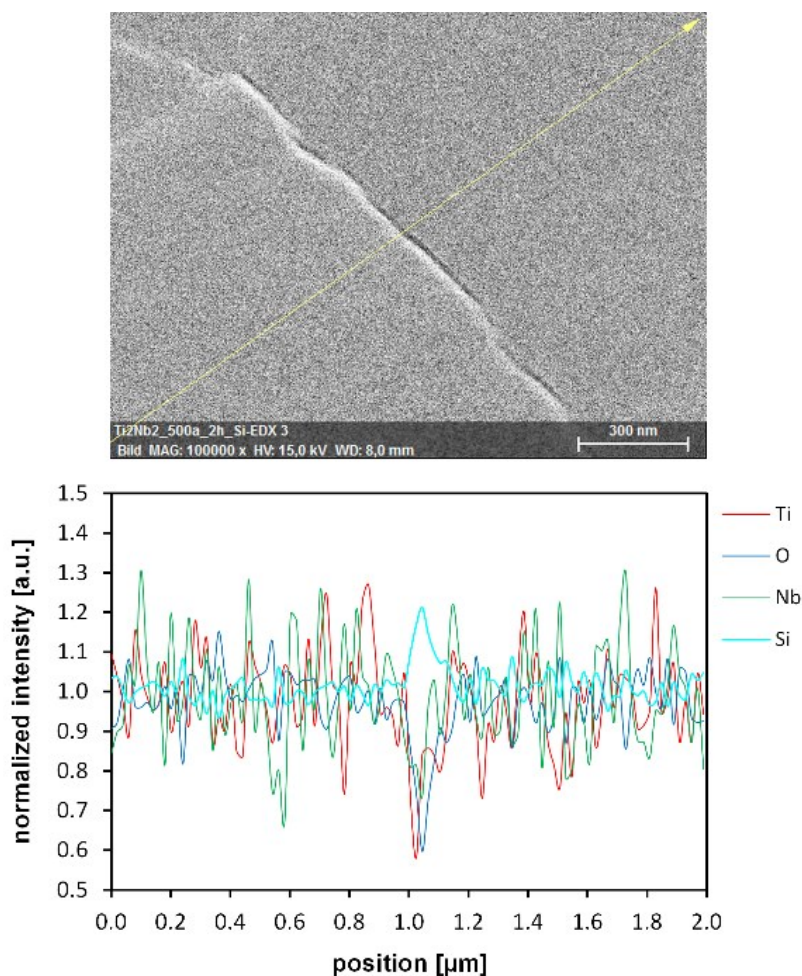


Fig. 147: EDX linescan across a domain boundary of as $\text{Ti}_{0.84}\text{O}_{2.25}\text{Nb}_{0.16}$ film annealed at $640\text{ }^\circ\text{C}$, and normalized intensities (*average* = 1) of Ti, O, Nb and Si.

The measurements were taken in 20 nm steps and the theoretical lower limit of lateral resolution is around $10\text{ nm} - 40\text{ nm}$ for the elements (Ti, O, Nb, Si). A clear trend is visible for all elements at the boundary. In the edge, the Si sample is more visible.

Fig. 148 (a) shows several micro-domains of a $\text{Ti}_{0.84}\text{O}_{2.25}\text{Nb}_{0.16}$ film annealed at $640\text{ }^\circ\text{C}$ in 10000 x magnification. Each of the domains is characterized by an individual brightness which is rather homogeneous within the individual domains. The boundaries between the domains have either high contrast or are barely visible. High- as well as low-contrast boundaries

are visible in the SEM image in Fig. 148 (b) ($100000\times$ magnification). One reason might be that the electron conductivity of the various boundaries could differ. The absence of high contrast might also be caused by sample alignment in the SEM.

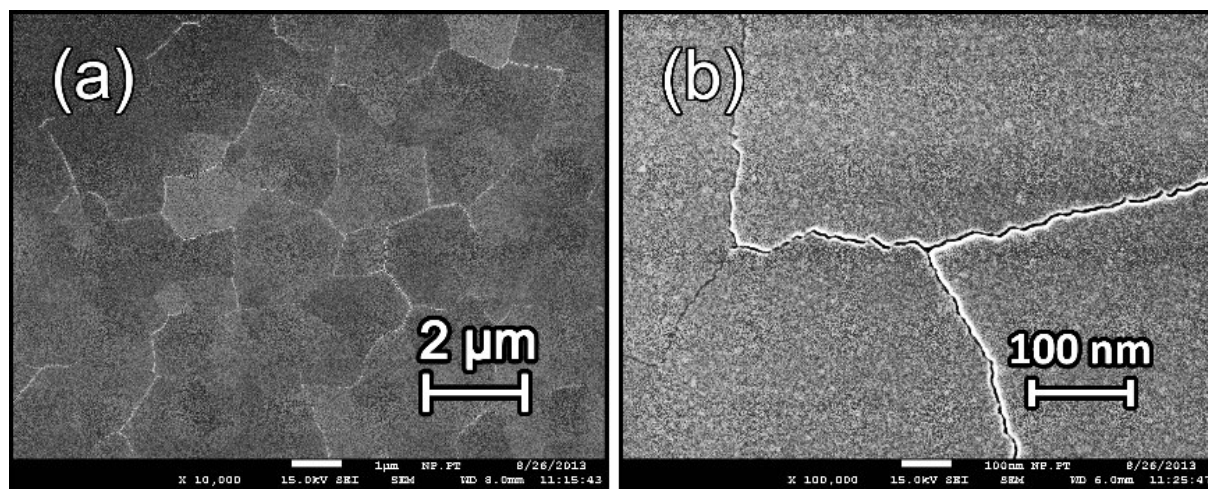


Fig. 148: SEM images of a $\text{Ti}_{0.84}\text{O}_{2.25}\text{Nb}_{0.16}$ film annealed at 640°C in (a) $10000\times$ and (b) $100000\times$ magnification, providing a detailed view on the micro-domains.

Fig. 149 shows SEM images taken in $4000\times$ magnification, which show topographies in micro-scale of (a) TiO_2 , (b) $\text{Ti}_{0.92}\text{O}_{2.25}\text{Nb}_{0.08}$, (c) $\text{Ti}_{0.84}\text{O}_{2.25}\text{Nb}_{0.16}$ films on Si substrates annealed at 640°C . Fig. 149 (d) shows the area of (c) scanned with a LBE (low angle backscatter electron) detector, which is highly sensitive to the chemical composition of the surface.

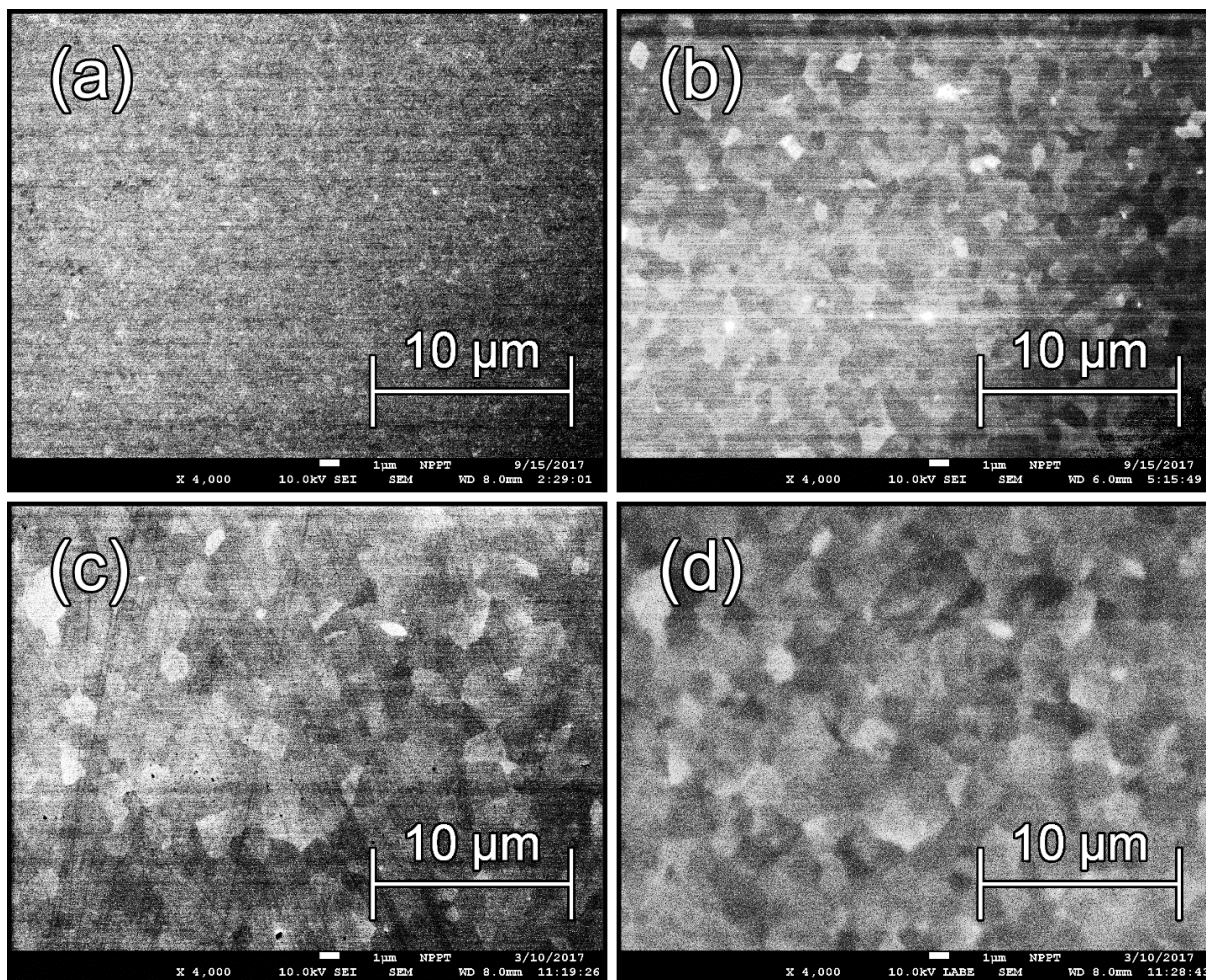


Fig. 149: SEM images (4000 x) of (a) TiO₂, (b) Ti_{0.92}O_{2.25}Nb_{0.08}, (c) Ti_{0.84}O_{2.25}Nb_{0.16} films annealed at 640 °C using the standard SEI (secondary electron imaging) detector, (d) the area of (c) scanned with a LABE (low angle backscatter electron) detector.

The size of the micro-structures in the Nb0 films is around $0.5 \mu m$, and the mean sizes of the micro domains of the doped samples are $1 \mu m$ ($0.5 \mu m - 2 \mu m$) in the Nb1 films and $1.5 \mu m$ ($0.5 \mu m - 3 \mu m$) in the Nb2 films.

The sizes of the domains are in the same order than the ones found in the anatase phonon maps on B270 glass and fused silica in Fig. 144. Yet, they are around $2/3$ the size, which could be caused by the different measurement techniques or also by varying film growths on different kinds of substrates (B270 glass or Si wafer).

The LABE image looks similar to the one scanned with the standard SEI (secondary electron imaging) detector, but with low contrast. This indicates that the LABE image does not provide additional (chemical) information to the SEI image.

Also, a variation of chemical composition between the domains was not found by EDX maps (see Fig. 205 in the appendices). We performed an EDX mapping at a magnification of $16000 x$ in an area of $4 \mu m \times 4 \mu m$, which contains *four* facets. The measurement was performed

with an acceleration voltage of 5 kV with $1000\text{ counts per second}$ and was limited to 8 minutes in order to avoid an impact of sample shift. Fig. 205 shows the measured distribution of (a) Ti, (b) O, (c) Nb, and (d) Si, each as semi-transparent layers on top of the SEM map image of the scanned area. The elements are uniformly distributed and do not correlate with the facets visible in the SEM images. Further mappings at a magnification of $4000\times$ showed the same results.

The SEM images in Fig. 150 show inclined views on the films edges and surfaces of (a) TiO_2 , (b) $\text{Ti}_{0.92}\text{O}_{2.25}\text{Nb}_{0.08}$, and (c) $\text{Ti}_{0.84}\text{O}_{2.25}\text{Nb}_{0.16}$ films on Si annealed at $640\text{ }^\circ\text{C}$. The micro domains are visible as topographically distinct areas on the Nb-doped films. The film edges of the doped films are partly in line with the edge of the Si substrate and partly split off along the boundaries of the domains. Fig. 150 (d) shows an intact domain that broke off during the preparation of the film edge and lies on top of the $\text{Ti}_{0.84}\text{O}_{2.25}\text{Nb}_{0.16}$ film. This demonstrates strong bonds within the domains.

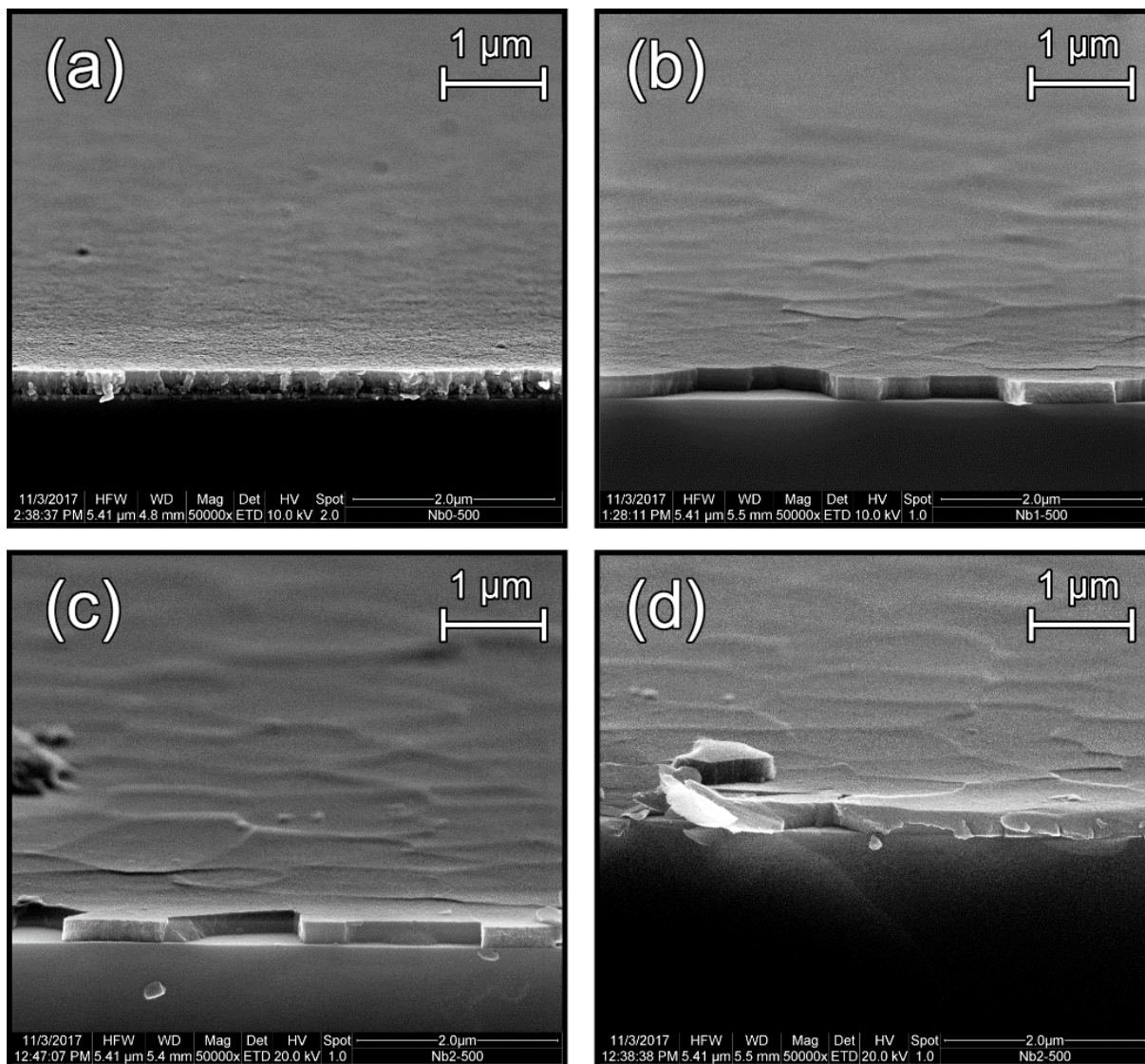


Fig. 150: SEM images (50000 x) of film edges of e-beam coated films on Si substrates annealed at 640 °C: (a) TiO_2 , (b) $\text{Ti}_{0.92}\text{O}_{2.25}\text{Nb}_{0.08}$, and (c) $\text{Ti}_{0.84}\text{O}_{2.25}\text{Nb}_{0.16}$. (d) shows another part of the edge shown in (c) with an intact domain that was broken off the edge.

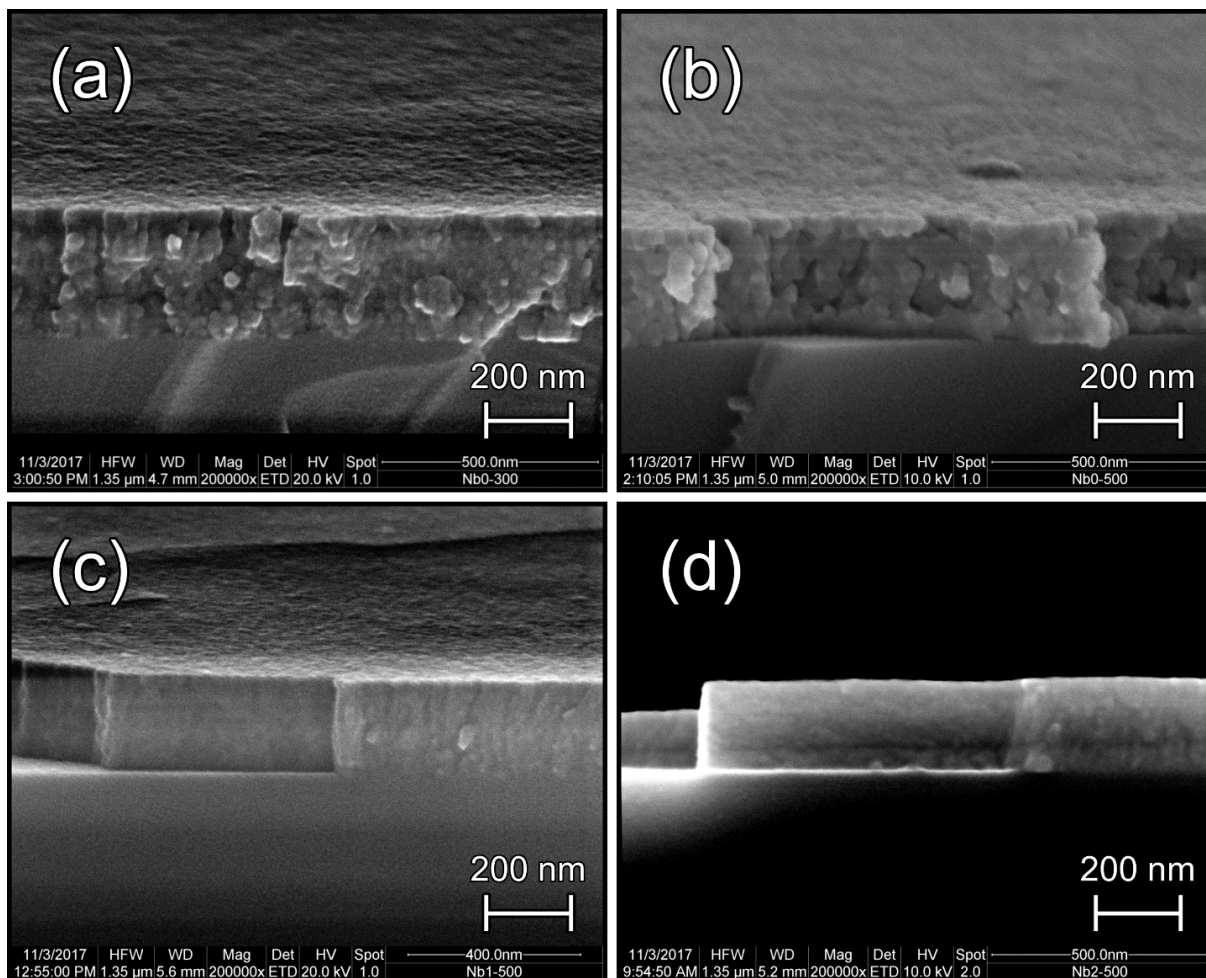


Fig. 151: SEM images ($200,000\times$) of film edges of (a) TiO_2 annealed at $420\text{ }^\circ\text{C}$, (b) TiO_2 annealed at $640\text{ }^\circ\text{C}$ (c) $\text{Ti}_{0.92}\text{O}_{2.25}\text{Nb}_{0.08}$ annealed at $640\text{ }^\circ\text{C}$, and (d) $\text{Ti}_{0.84}\text{O}_{2.25}\text{Nb}_{0.16}$ annealed at $640\text{ }^\circ\text{C}$.

Fig. 151 shows films edges of (a) a TiO_2 thin film annealed at $420\text{ }^\circ\text{C}$; as well as (b) TiO_2 , (c) $\text{Ti}_{0.92}\text{O}_{2.25}\text{Nb}_{0.08}$, and (d) $\text{Ti}_{0.84}\text{O}_{2.25}\text{Nb}_{0.16}$ thin films annealed at $640\text{ }^\circ\text{C}$. Porous structures are visible in the undoped films, with grain size growing from 25 nm ($10\text{ nm} - 40\text{ nm}$) to 50 nm ($20\text{ nm} - 130\text{ nm}$) with the annealing temperature increasing from $420\text{ }^\circ\text{C}$ to $640\text{ }^\circ\text{C}$. Thereby the films become more compact and the thickness decreases from 300 nm to 285 nm . The displayed edges of the Nb doped films have mainly columnar structures with parallel grains aligned horizontally or tilted by 45° .

The strong bonds within the micro-domains, the parallel alignment of the grains in the domains, as well as the homogeneous Raman spectra within the domains indicate that the micro-domains are crystallites.

7.2.4 Crystallization process of $\text{Ti}_{0.92}\text{O}_{2.25}\text{Nb}_{0.08}$ films

We have observed the crystallization process of e-beam coated $\text{Ti}_{0.92}\text{O}_{2.25}\text{Nb}_{0.08}$ films on B270 glass in dependence on the annealing temperature. Fig. 152 shows anatase Raman *phonon maps* of $\text{Ti}_{0.92}\text{O}_{2.25}\text{Nb}_{0.08}$ films annealed at 350 °C, 375 °C, 400 °C, and 450 °C.

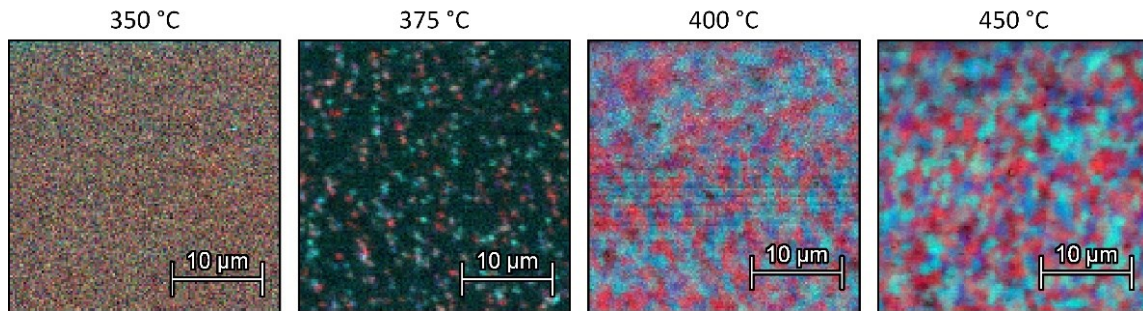


Fig. 152: anatase Raman *phonon maps* of $\text{Ti}_{0.92}\text{O}_{2.25}\text{Nb}_{0.08}$ films annealed at 350 °C, 375 °C, 400 °C, and 450 °C.

At 350 °C, only amorphous TiO_2 spectra are found, no Raman domains are resolved. At 375 °C, the film has nuclei in an amorphous matrix (which are also observed in SEM, see in Fig. 155). The Raman spectra are amorphous or crystalline depending on the position at which the spectrum was measured (see Fig. 154).

The film that was annealed at 400 °C is completely crystallized and domains of around 1 μm size with homogeneous phonon intensities are visible in the anatase *phonon maps*. At 450 °C, the anatase first-order intensity is higher and the edges of the domains are sharper on the map, which indicates more ordered structures.

Fig. 153 shows the anatase *phonon maps* of a $\text{Ti}_{0.92}\text{O}_{2.25}\text{Nb}_{0.08}$ film annealed at 375 °C: (a) Eg(1) (red), (b) AB1g (blue), (c) B1g (green), and (d) *combined phonon map* (already shown in Fig. 152).

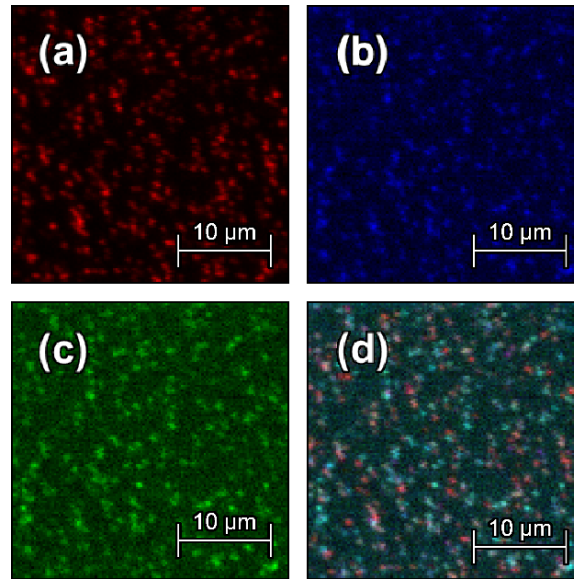


Fig. 153: Anatase *phonon maps* of a $\text{Ti}_{0.92}\text{O}_{2.25}\text{Nb}_{0.08}$ film annealed at $375\text{ }^\circ\text{C}$: (a) Eg(1) (red), (b) AB1g (blue), (c) B1g (green), and (d) *combined phonon map*.

Small crystalline islands are clearly visible with sizes mainly below $1\ \mu\text{m}$. Considering a variation of brightness in the smaller crystals, several should be smaller than the lateral resolution of the maps ca. $0.6\ \mu\text{m}$. Indeed, we found smaller crystalline islands by SEM (see Fig. 155). In the *combined phonon map* (Fig. 153 (d)), the crystalline structures are either red, blue, or cyan. This implies that in the individual Raman spectra either (1) the Eg vibrations are strong (red), (2) the A1g/B1g-doublet is strong (blue), or (3) the A1g/B1g-doublet as well as the B1g peak at $399\ \text{cm}^{-1}$ are strong (cyan). Eg modes are vibrations in *a*-direction and A1g in *c*-direction. B1g vibrations are also in *c*-direction, but the detected Raman intensity varies by $\cos(2\theta)_a$ with a rotation by around the *a*-axis. This is a simplified description of the behavior of crystalline orientation with Raman. For more details, see Giarola et al.¹⁰⁷

Fig. 154 shows Raman spectra of randomly chosen coordinates of the map in Fig. 153 which contain bright spots or dark areas after stripping the substrate spectra. As for each map, beforehand the cosmic rays had been removed and the noise filter had been applied (see chapter 2.2.1). The spectra in the dark area show amorphous TiO_2 and reveal that the bright areas are crystalline islands in an amorphous matrix. Non-localized spectra average over the whole sample and intermingle topographic differences.

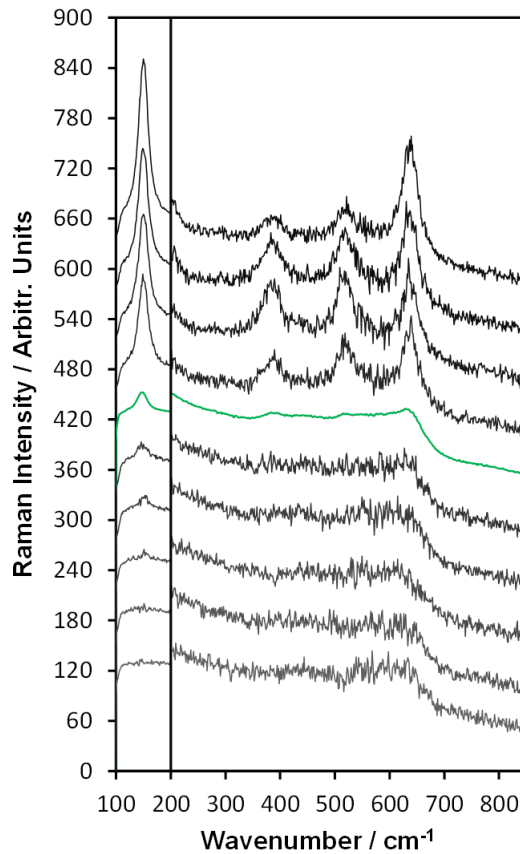


Fig. 154: Various crystalline anatase and amorphous TiO_2 spectra that correspond to randomly chosen coordinates of the map in Fig. 153 (sorted by the intensity of the Eg(1) peak). The spectra are shifted by 60 units on the Raman intensity axis, the range between 100 cm^{-1} and 200 cm^{-1} is divided by 4 and then shifted upwards by 90 units.

SEM confirms crystalline islands in amorphous matrix in the $\text{Ti}_{0.92}\text{O}_{2.25}\text{Nb}_{0.08}$ film annealed at $375 \text{ }^\circ\text{C}$, as can be seen in Fig. 155.



Fig. 155: SEM image of $\text{Ti}_{0.92}\text{O}_{2.25}\text{Nb}_{0.08}$ film annealed at $375 \text{ }^\circ\text{C}$ (same resolution as in Fig. 153).

7.2.5 Crystallization of films with stoichiometric oxygen content

In contrast to the films with over-stoichiometric O content ($\text{Ti}_{0.92}\text{O}_{2.25}\text{Nb}_{0.08}$), a film that contains stoichiometric O content $[(\text{Ti}+\text{Nb})_1\text{O}_2]$ film is completely crystallized already after annealing at $350 \text{ }^\circ\text{C}$, as can be seen in the anatase *phonon map* in Fig. 156.

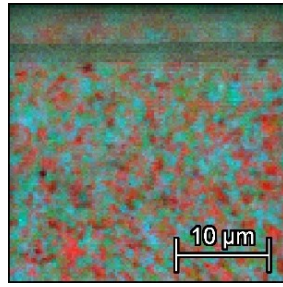


Fig. 156: Raman anatase *phonon map* of an e-beam coated $\text{Ti}_{0.92}\text{O}_2\text{Nb}_{0.08}$ (right) film on B270 glass after annealing at $350\text{ }^\circ\text{C}$.

Thus, over-stoichiometric oxygen content seems to hinder nucleation. Future experiments should do more studies on oxygen content.

7.2.6 Conclusions

We produced Raman TiO_2 phase maps and Raman anatase phonon maps of as-deposited and post-heated reactive e-beam evaporated undoped and Nb doped TiO_2 thin films. The Raman maps of the films are amorphous over the whole area after deposition. The maps are produced with a 633 nm laser in areas of $30\text{ }\mu\text{m} \times 30\text{ }\mu\text{m}$ in $0.25\text{ }\mu\text{m}$ steps and a lateral resolution of around $0.6\text{ }\mu\text{m}$.

Undoped TiO_2 films crystallize continuously with the post-heating temperatures increasing from $420\text{ }^\circ\text{C}$ to $640\text{ }^\circ\text{C}$. At $420\text{ }^\circ\text{C}$, the maps contain areas in which the amorphous TiO_2 content is larger than in the average of the map. At $640\text{ }^\circ\text{C}$ they consist almost entirely of anatase. Traces of brookite are homogeneously distributed (in the resolution of the maps) and disappear with increasing post-heating temperature (and with a relaxing anatase lattice, see chapter 6.1.2.3.1). Rutile appears aligned in thin strings in the map of the undoped film annealed at $750\text{ }^\circ\text{C}$.

In the chapters 5.4 (quantitative analysis) and 6.1.2 (qualitative analysis), we found that Nb favors anatase growth and suppresses the other phases. This is also reflected in the Raman maps of the Nb-doped films: the whole area of the map is crystallized already at $400\text{ }^\circ\text{C}$.

Over-stoichiometric O content hinders initial crystallization. Films with stoichiometric O content $[(\text{Ti}+\text{Nb})_1\text{O}_2]$ are crystalline already after post-heating at $350\text{ }^\circ\text{C}$, while in the films with higher oxygen content crystallization starts at around $375\text{ }^\circ\text{C}$. Crystallites evolve from nuclei in an amorphous matrix.

SEM figures of the films show nanostructures and additionally reveal distinct areas in μm size. The areas differ from each other in contrast and they are separated by boundaries with a width of around 4 nm . The chemical composition is homogeneous over the sample surface and

does not differ from domain to domain. The anatase Raman phonon maps deliver additional information about the areas found in SEM.

The anatase Raman phonon maps contain domains on a μm scale, revealing a texture of *a* and *c* phonons. The intensity ratios of anatase Eg(1), B1g, and AB1g phonons are homogeneous within the domains and vary between the individual domains. These domains become larger with increasing Nb content and do not change significantly with increasing annealing temperature. When the samples are broken apart in liquid nitrogen, the films break along the domain boundaries with the domains remaining intact.

7.3 Plasma-emission controlled rf-magnetron sputtered Nb-doped TiO₂ films

In this chapter we discuss *Raman anatase phonon maps* of the PEM rf-magnetron sputtered Nb-doped TiO₂ thin films that were deposited as described in chapter 2.1.3. The Raman spectra of each measurement point of the maps sum up to the average spectra that are discussed quantitatively in chapter 5.4 and qualitatively in chapter 6.1.2.

7.3.1 Anatase Raman phonon maps of PEM sputtered Nb-doped TiO₂ films

Fig. 157 shows the *combined anatase phonon maps* of PEM controlled rf-sputter coated Nb-doped TiO₂ thin films on B270 glass. The samples are placed (a) *12.5 mm*, (b) *42.5 mm*, and (c) *72.5 mm* horizontally from the Nb wires and the Ti target surface is oxidized by *65%*, *68%*, *71%*, or *78%*. The substrate temperature was around *50 °C* during the deposition, and the samples were post-heated at *475 °C (±20 °C)*.

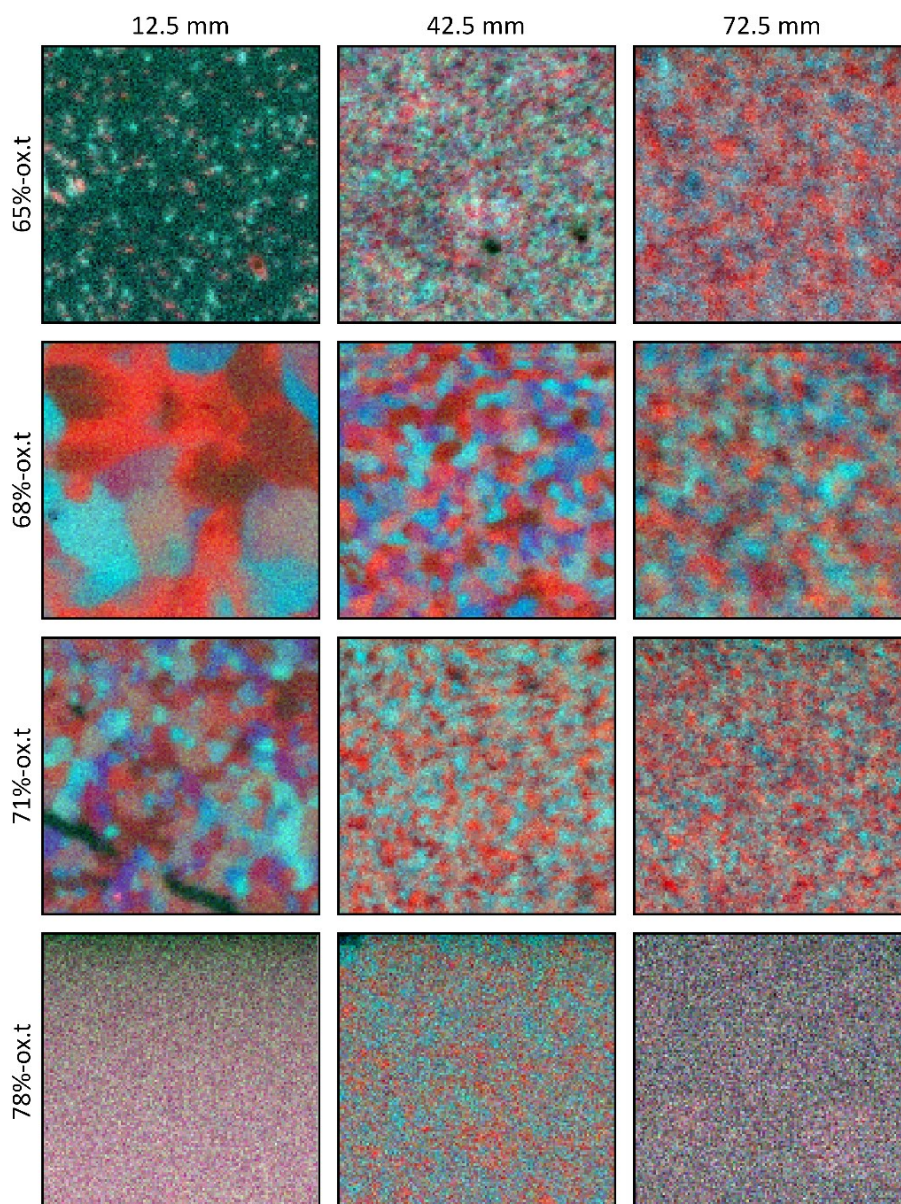


Fig. 157: Combined anatase phonon maps of PEM controlled rf-sputter coated Nb-doped TiO_2 thin films on B270 glass. The samples are placed (a) 12.5 mm, (b) 42.5 mm, and (c) 72.5 mm horizontally from the Nb wire, and the Ti target surface is oxidized by 65%, 68%, 71%, or 78%.

The *combined anatase phonon maps* mainly consist of anatase with phonon domains of various sizes. The map of the 65%-ox.t (a) shows crystalline islands in an amorphous matrix. No growth of the islands occurs upon further post-heating at 530 °C (not shown). All other films are completely crystalline. The 78%-ox.t films are crystalline but has no domain structure beyond the resolution of Raman mapping. They have the finest crystalline structure.

Not shown in the maps is the following. In the 65%-ox.t (a) map there is a defect in the glass between the center and the right bottom corner (small round black area). There the intensity of the glass spectrum is very high. The largest anatase crystallite of this map formed around this defect. In the dark areas in the 65%-ox.t (b) map there are defects in the glass. We

found brookite in the spectrum of the 78%-ox.t (a) and (c) films (see Fig. 124 in chapter 6.1.3.3). In the resolution of the map, brookite is evenly distributed (as is anatase).

In the 71%-ox.t (a) phonon map contains areas of the dark straight lines. There, we could not find anatase. In these lines there are no changes in the range of 1000 cm^{-1} . In the spectrum of the average spectrum of that map we found rutile (see Fig. 124 in chapter 6.1.3.3). We therefore made a “rutile” I_{447}/I_{467} map. In that map (not shown) noise is strong. Here, the area around the lines are more intense than the average spectrum. Also other structures of $10\ \mu\text{m}$ size are visible within the whole map. The spectrum in the dark lines resemble those of glass. Thus, there might be either broad rutile peaks with low intensity or there could be a scratch in the sample which goes into the bulk glass and thus only glass might be visible in the spectra of that areas.

The 68%-ox.t and the 71%-ox.t films have the clearest domain structures. The 68%-ox.t (a) film has the largest domains. Fig. 158 shows the average domain sizes of each map. A dashed horizontal black line is added at $2\ \mu\text{m}$ that discriminates the best conducting samples (with clear micro domains larger than $2\ \mu\text{m}$) from the weakly conducting ones (see Fig. 159).

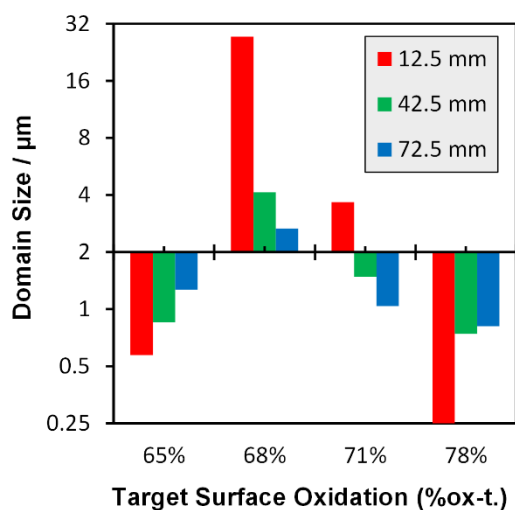


Fig. 158: Phonon domain sizes in the *combined anatase phonon maps* of PEM controlled rf-sputter coated Nb-doped TiO_2 thin films on B270 glass. The samples are placed (a) 12.5 mm, (b) 42.5 mm, and (c) 72.5 mm horizontally from the Nb wire, and the Ti target surface is oxidized by 65%, 68%, 71%, or 78%.

All 68%-ox.t films and the 71%-ox.t (a) film have phonon domain sizes larger than $2\ \mu\text{m}$. The largest domains are found for the 68%-ox.t (a) film with a domain size of around $25\ \mu\text{m}$. This film is also the best conducting film of this set of samples. Fig. 159 shows the conductivity vs. the phonon domain size (as a double logarithmic plot). Potential trendlines are added to guide the eye.

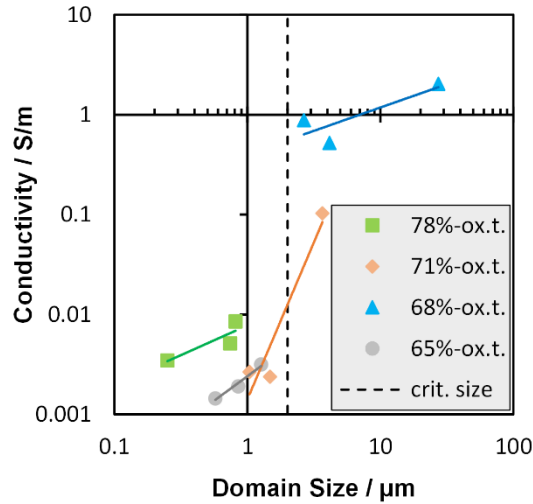


Fig. 159: Conductivity vs. phonon domain of PEM controlled rf-sputter coated Nb-doped TiO₂ thin films on B270 glass. The samples are placed (a) 12.5 mm, (b) 42.5 mm, and (c) 72.5 mm horizontally from the Nb wire, and the Ti target surface is oxidized by 65%, 68%, 71%, or 78%.

For each of the four oxidation states of the Ti target, the conductivity increases with increasing phonon domain size. There might be a critical domain size of 2 μm above which the conductivity drastically improves.

Fig. 160 shows the conductivity of the samples that were annealed at 475 °C. The conductivities are lower than those of the films annealed at 530 °C (see Fig. 122 in chapter 6.1.3.1), but it confirms the trend of a region around 68%-ox.t. (a) for optimum coating conditions that lead to well conducting films.

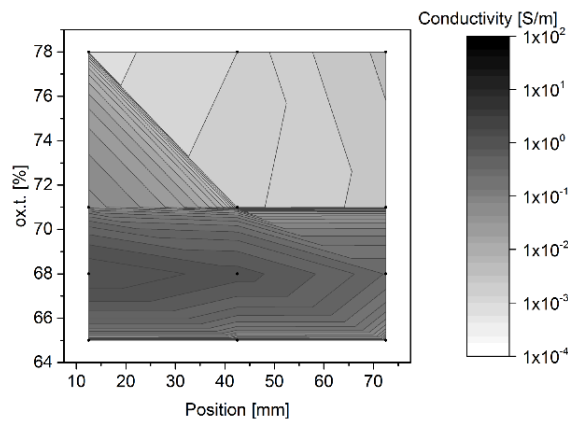


Fig. 160: 2D representation of the conductivity of the films annealed at 475 °C vs. the oxidation state of the Ti target surface and the position of the sample horizontally from the Nb wires.

Fig. 161 compares the average conductivities of the films annealed at 530 °C (chapter 6.1.3.1) and at 475 °C (chapter 6.1.3.3) (top) with the anatase phonon domain sizes (bottom) as 2D functions of the Ti target oxidation and the position of the sample horizontally from the Nb wires.

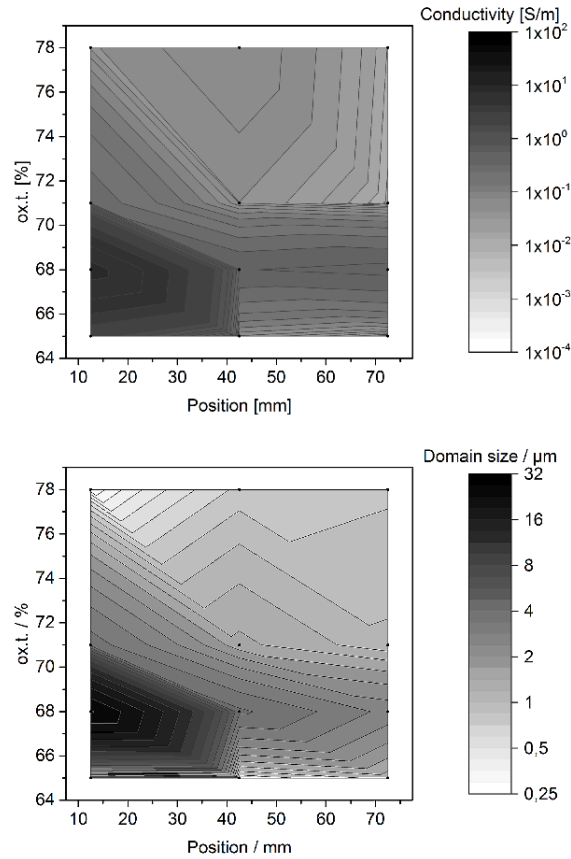


Fig. 161: 2D representations of the average conductivity of both annealing temperatures (530 °C and at 475 °C) (top), and the Raman domain size (bottom) vs. the oxidation state of the Ti target surface and the position of the sample horizontally from the Nb wires.

In these 2D representations a strong correlation is visible: the “region” of good conductivity around 68%-*ox.t.* (a), (i.e. a film with a high Nb content produced with a 68% oxidized target surface) agrees well with the region of high phonon domain size. Fig. 162 shows 2D representations of Raman anatase peak parameters of the Eg(1) peak (left) and the B1g peak (right) vs. the *ox.t.* and the sample position. The figures show the peak widths (top), positions (middle), and intensities (bottom).

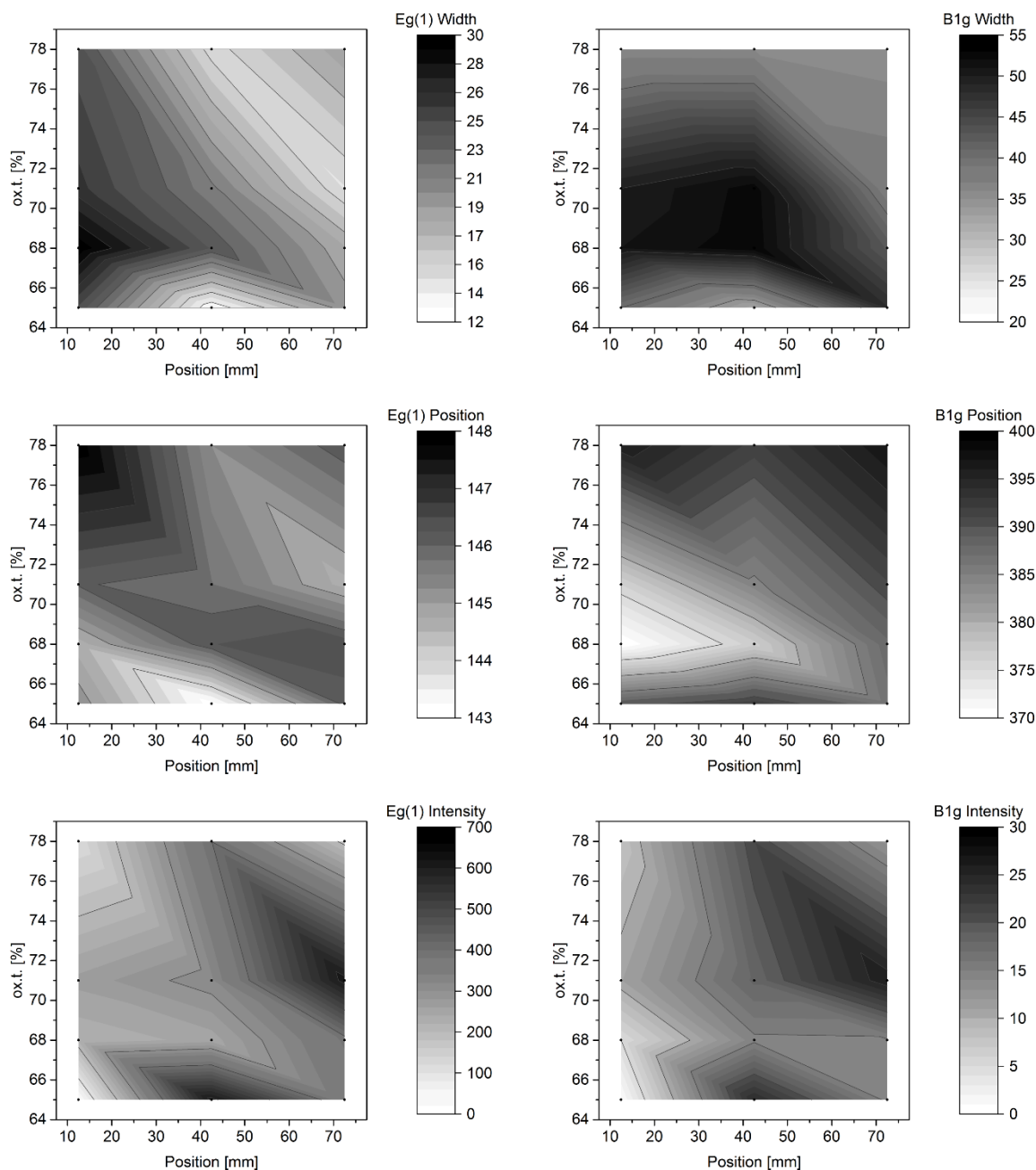


Fig. 162: 2D representations of Raman anatase peak parameters of the Eg(1) peak (left) and the B1g peak (right) vs. the *ox.t.* and the sample position. The figures show the peak widths (top), positions (middle), and intensities (bottom).

A comparison of Fig. 162 and Fig. 161 indicates that an anatase B1g redshift, the and Eg(1) peak width correlate with large phonon domains and good conductivity. Also, the B1g peak width shows a certain correlation with the conductivity and the phonon domain size. The Eg(1) peak position does not correlate with the conductivity or the phonon domain size. The Eg(1) and B1g Raman line intensities of the well conducting films are low (see also Fig. 124 in chapter 6.1.3.3).

The intensity of the A1g/B1g-doublet behaves similar to the B1g peak – the corresponding 2D representation is shown in Fig. 206 the appendices. The stoichiometry was not measured for this set. The B1g position does not correlate with the Nb or O content of the films that were post-heated at 530 °C presented in Fig. 121. Gautam et al. assign a redshift (and asymmetric broadening) of the B1g position to a reduction of Ti^{4+} ions to Ti^{3+} ions by Nb^{5+} incorporation into the lattice.¹⁸⁹ Thus, the B1g position might be seen as an indicator for the amount of efficiency of Nb^{5+} incorporation into the titania lattice.

7.3.2 Variation of the sample position and film thickness

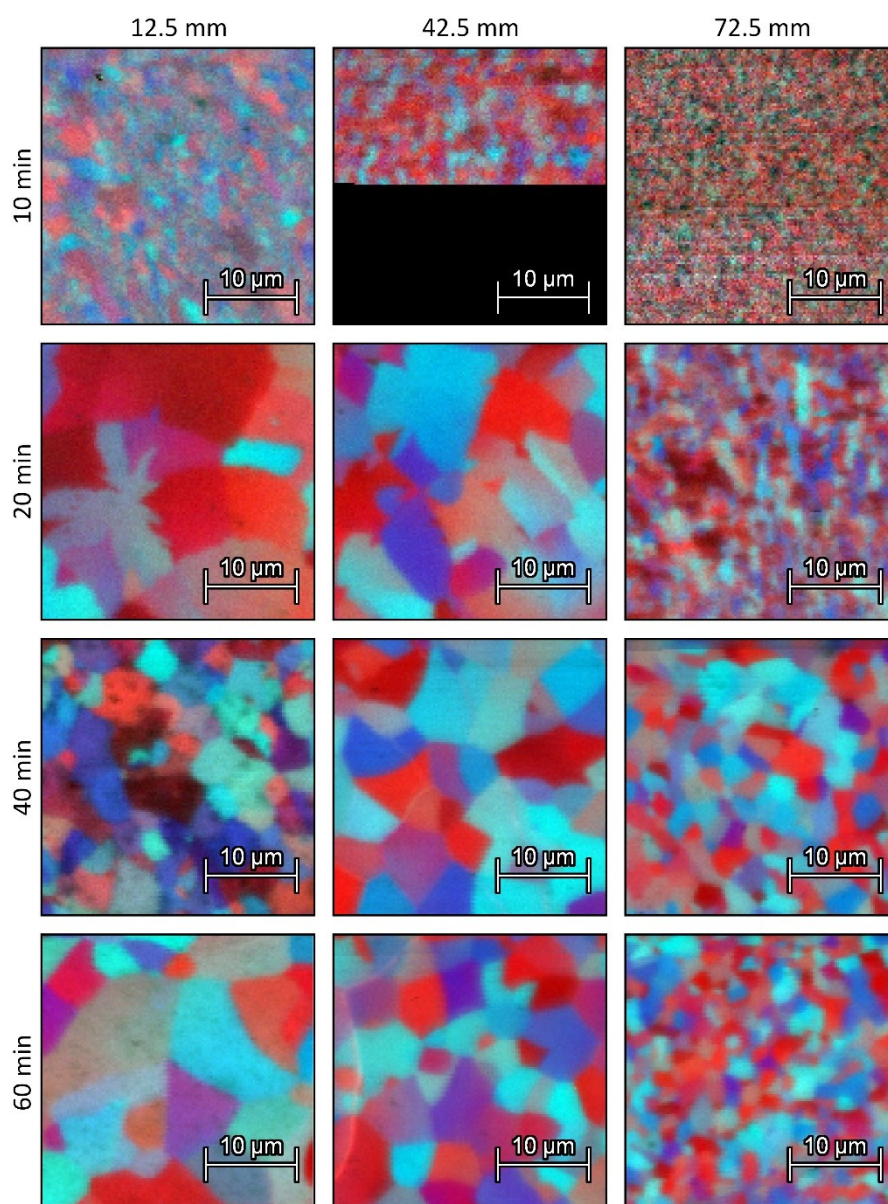


Fig. 163: Combined anatase phonon maps of PEM controlled rf-sputter coated Nb-doped TiO_2 thin films on B270 glass, with 71% oxidation of the Ti target surface. The samples are placed (a) 12.5 mm, (b) 42.5 mm, and (c) 72.5 mm horizontally from the Nb wires are deposited for 10, 20, 40, and 60 minutes.

The *combined anatase phonon maps* show domains of homogeneous phonon intensities in the Raman spectra. The domains of the films deposited for *20 min* or more are larger and have simpler geometric structures as compared to the films deposited for *10 min*. The domain size seems to be independent of the mass density. Fig. 164 shows the mean sizes of the phonon domains in each *combined anatase phonon map*.

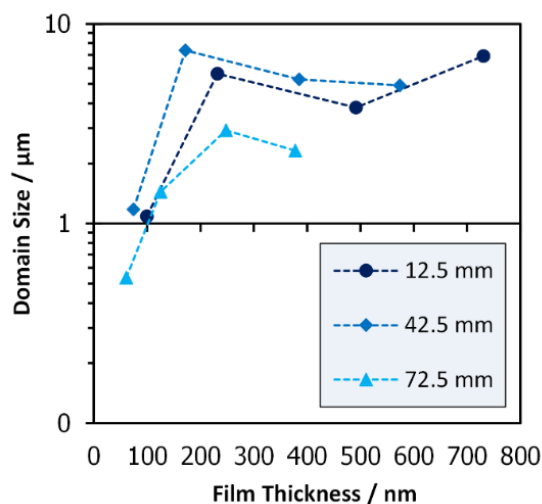


Fig. 164: S1-S4: Phonon domain size vs. film thickness, in the Raman maps of the samples coated at positions (a) 12.5 mm, (b) 42.5 mm, and (c) 72.5 mm horizontally from the Nb wires.

A film thickness above *150 nm* (or a deposition time of *20 minutes*) provides films with large phonon domains (*2 µm* to *8 µm*) in position (a) and (b) films. More Nb and thicker films lead to larger domains with regular shape. The domains at position (c) are the smallest. Thus, in the films deposited at positions (a) and (b) grain growth seems to be favored among nucleation as compared to the films deposited at position (c). The films deposited at position (c) seem to have a higher density of nuclei during the film growth.

7.3.3 Conclusions

We created anatase Raman phonon maps of Nb doped TiO₂ thin films coated with PEM controlled rf-magnetron sputtering. The maps reveal that the films contain micro domains in which the phonon vibrations are homogeneous. The domain size depends on the film thickness. Above a thickness of *150 nm*, textures in the *µm* range are created. With a favorably chosen degree of oxidation of the sputtering target (around *68%*), textures of *a* and *c* phonon domains are observed on a scale of *10 µm*. Such layers have a high conductivity up to approximately *2 S/m* for a post-heating temperature of *475 °C* and up to *7 S/m* for a post-heating temperature of *530 °C*. Layers produced under other conditions also show exceptionally high conductivities if the domain sizes exceed the critical value of *2 µm*.

Crystallization in the PEM controlled rf-magnetron sputter coated post-heated films evolves from nuclei in an amorphous matrix – like in the as deposited amorphous e-beam coated Nb doped thin films in chapter 7.2. This is visible in the Raman map of the *65%-ox.t (a)* film. All other maps show that the films are fully crystallized and consist of mainly anatase. Brookite is found in the films coated with a high oxidized Ti target (*78%-ox.t.*) with low Nb content and cannot be spatially resolved.

The phonon domain size in the *combined Raman anatase phonon maps* correlates positively with increasing conductivity, a redshift of the B1g peak and an increase of the Eg(1) peak width found in chapter 6.1.2.4. The redshift does not strictly correlate with the Nb content in the films but might indicate the efficiency of Nb incorporation into the TiO₂ lattice.

8 Complementary findings of chapters 4, 5, 6, and 7

In the following, we emphasize a selection of findings in the different studies that correlate or complement each other. The studies are: the decomposition of TiO₂ thin film Raman spectra (chapter 4), quantitative evaluation of the decomposed Raman spectra (chapter 5), characterization of structural properties of the TiO₂ thin films that include the decomposed Raman spectra (chapter 6), and the Raman maps (chapter 7).

8.1 Correlations in the studies of the rf-diode sputtered films

In chapter 5.5 we found a relatively low Raman/XRD intensity ratio of the crystalline phases in spectra/diffractograms of the rf-diode sputtered TiO₂ films as compared to e-beam coated films. The Raman/XRD intensity ratio is smaller by a degree of *two*. This correlates with the high defect density in these films, which we estimated in chapter 6.1.1. The estimated defect density in the rf-diode sputtered films is *twice* as high as would be expected from perfect crystals. The presence of rutile (found in chapter 5.2) in all films (coated at 155 °C – 415 °C) suggest that the films were bombarded by ions with a high kinetic energy, which probably also incorporate defects into the film.

Thus, for a given crystallite size, Raman peaks that are broader than predicted by the *q*-vector relaxation model as well as a decrease in Raman intensity can indicate high defect density. We follow the interpretation in literature that defects (additionally to those arising from crystallite boundaries) affect phonon vibrations (peak width and intensity) to a larger degree than the coherence length of XRD. We suggest extending the *q*-vector relaxation model by a parameter α that affects the Raman peak width and represents the average number of defects in a polycrystalline material. Future studies should evaluate in which way (or in how far) the parameter should be implemented into the model.

8.2 Correlations in the studies of the reactive e-beam coated films

The Raman/XRD intensity ratio of anatase of the Ti_{0.92}O_{2.25}Nb_{0.08} film post-heated at 375 °C is about *twice* as high as those of the fully crystallized films (see chapter 5.4). The corresponding Raman maps revealed that the film consists of anatase crystals in an amorphous matrix, while the other films are (vastly or) fully crystallized over the whole surface (chapter 7.2). This suggests that either a high amount of the crystals in the film are so small that they are X-ray amorphous or that phonons of crystals that are surrounded by amorphous material are weakened when the crystallites are separated from surrounding crystallites by grain boundaries.

8.3 Correlation between the Raman spectra of amorphous and crystalline TiO₂ phases

In chapter 6.3, we simulated a Raman spectrum composed of broad spectra arising from “nominal crystalline” structures that resemble those of anatase, brookite and rutile, and fit the model spectrum to an experimental Raman spectrum of amorphous TiO₂. We used models to simulate the nominal crystalline phases similar to those used for the decomposition of the measured Raman presented in chapter 4. The modeled spectra suggest that amorphous TiO₂ can be decomposed into broad spectra arising from anatase, brookite and rutile that contain high intense nominal phase backgrounds – indicating a large amount of disorder.

From the fit results we estimated a size of $3\text{ nm} - 4\text{ nm}$ with the q -vector relaxation model for the structures that resemble disordered anatase or rutile crystallites. Arbitrarily assuming that the parameter α in the model affects the peak width linearly with the number of defects, we estimated a defect distance in the nominal crystallites of 0.8 nm , which corresponds to the size of 1-2 anatase or rutile unit cells.

We are aware that the broad features in the Raman spectra could also be a Gaussian distribution of Lorentz peaks and rather describe the distribution of the binding forces rather than to arise from “defects”. The peaks then should be simulated by Gaussian or Pseudo-Voigt profiles. Yet, still, the resulting model spectra (not shown) look similar. Anyway, we can at least conclude that the Raman spectrum of amorphous TiO₂ can be simulated by a sum of Raman spectra that resemble those of anatase, brookite and rutile, which suggests that the atomic binding forces of amorphous TiO₂ resemble those of crystalline TiO₂.

8.4 Correlations in the studies of the PEM controlled rf-magnetron sputtered films

The electrical conductivity of the Nb-doped rf-magnetron sputtered TiO₂ thin films increases with a redshift of the anatase B1g position, but not with the Nb content (chapter 6.1.3). The B1g position might indicate the efficiency of Nb⁵⁺ incorporation into the TiO₂ lattice. The Raman maps reveal that the films consist of micrograins (or anatase phonon domains) that contain nanocrystallites with homogeneous orientation (chapter 7.3). Such microstructures are also visible in SEM images. The phonon domains are absent or smaller than the resolution of the Raman maps when brookite is present in the films. A certain degree of Ti target oxidation (68%-ox.t) produces films with the largest micrograins. The electrical conductivity increases drastically with the anatase phonon domain size. As the conductivity correlates the strongest with the anatase phonon domain size, manufacturers that produce Nb-doped anatase for electrical applications should have a focus on maximizing the anatase phonon domain size.

Appendices

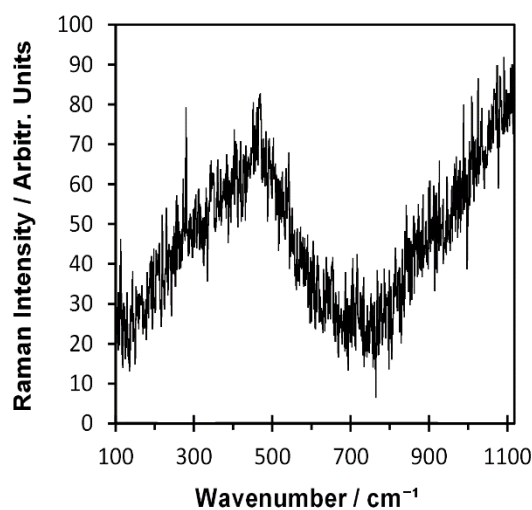


Fig. 165: Darkfield spectrum measured inside of a *Renishaw InVia μ Raman* spectrometer (without incident laser beam).

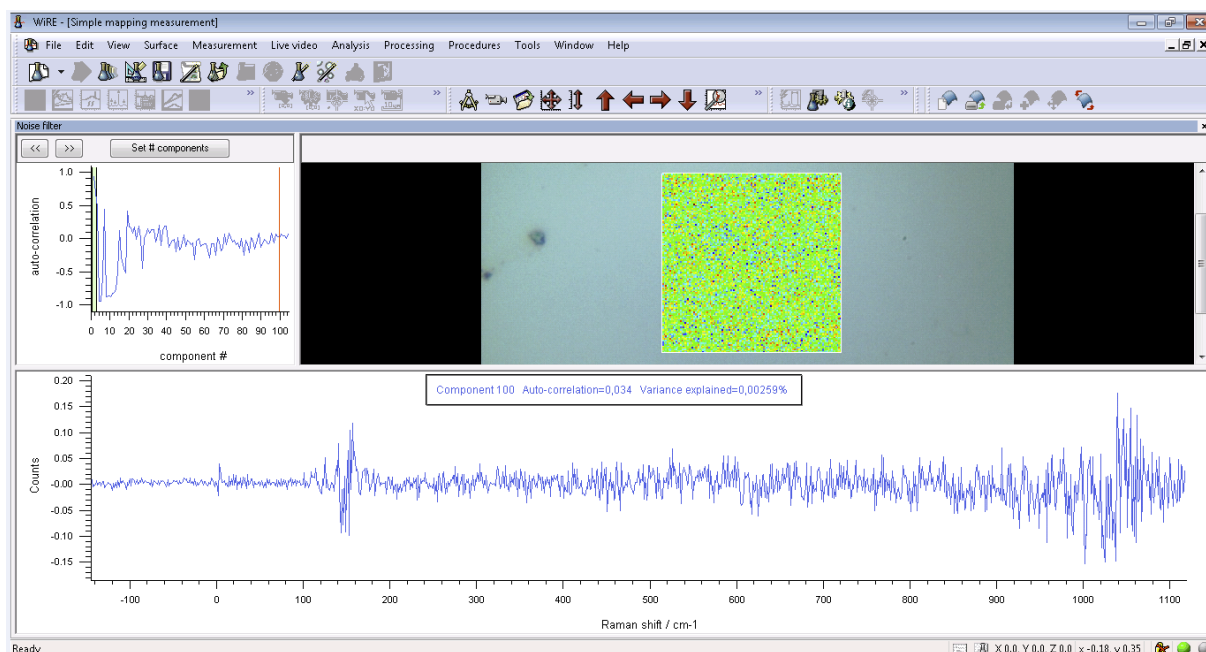


Fig. 166: Screenshot of the Renishaw noise filter program. The top left window shows the correlation function, the top right figure is the map and the amount of signal (low = green, high = red) that is affected by the PCA component (here, component 100 is shown). The lower window shows the residual signal that remains when all higher components are deleted.

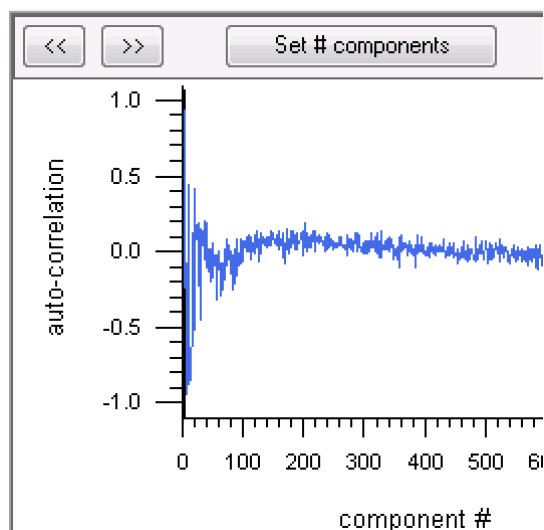


Fig. 167: Example of an auto-correlation function that becomes stationary above 100 components.

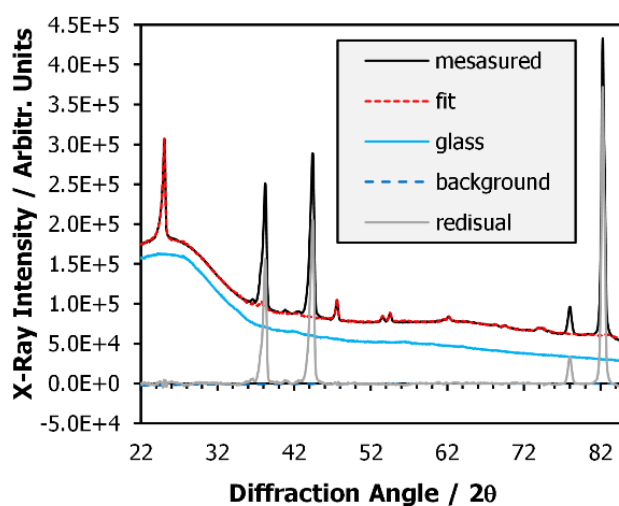


Fig. 168: Measured (black) and modeled (dashed red) X-ray diffractogram of a $\text{Ti}_{0.84}\text{O}_{2.25}\text{Nb}_{0.16}$ film on B270 glass (light blue) measured in θ - θ geometry. The film was e-beam evaporated and post-heated at 640°C . The residual spectrum contains strong signals arising from the substrate holder.

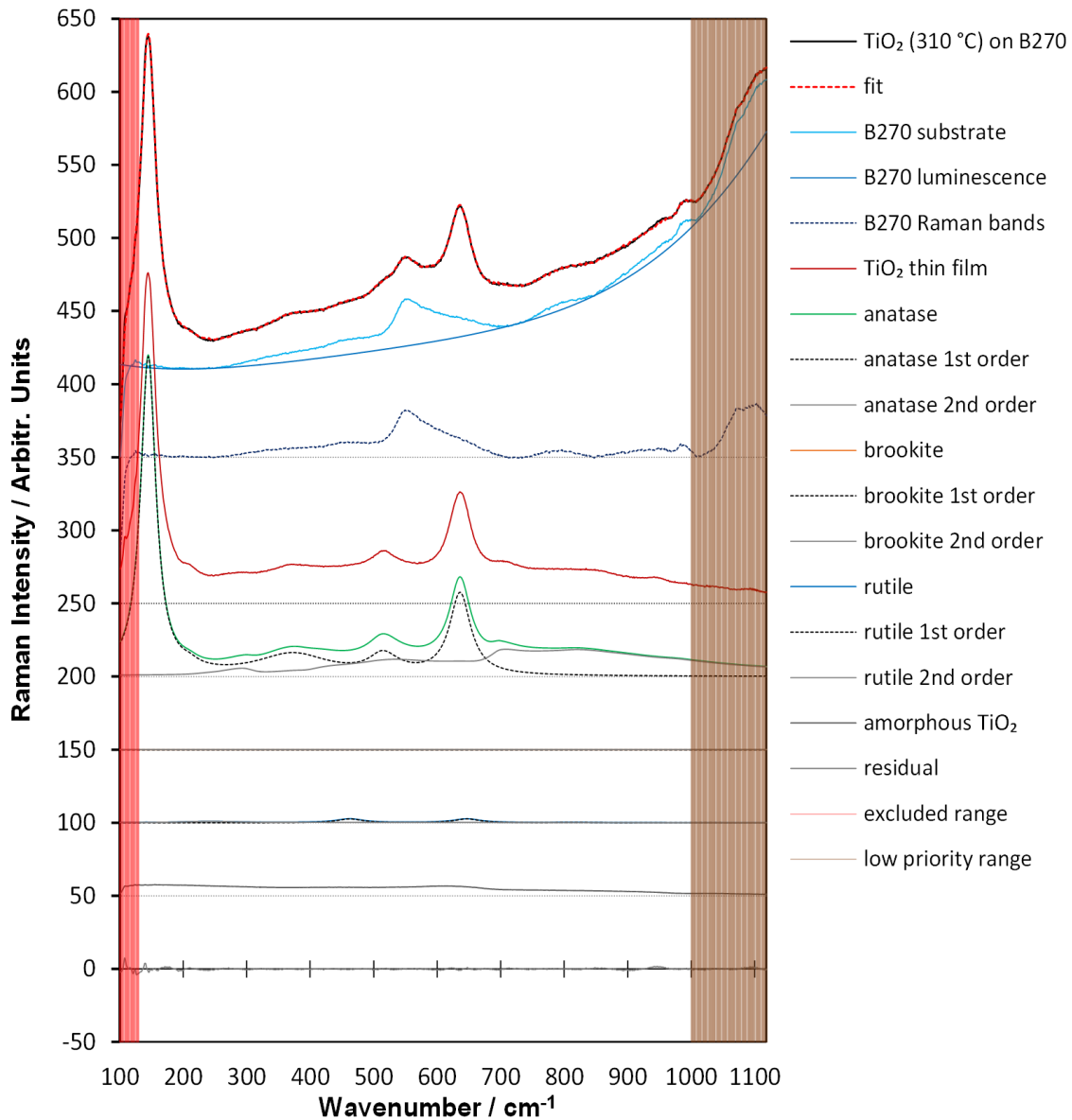


Fig. 169: Decomposition of a 633 nm Raman spectrum of an rf-magnetron sputtered Nb-doped TiO₂ thin film on a B270 crown glass substrate (deposited 12.5 mm horizontally from the Nb wire with an estimated target surface oxidation of 68%) into anatase, rutile, brookite, amorphous TiO₂, substrate, and the substrate. The main phase, anatase, has a strong phase background. The anatase phase background is so intense that it can hardly be separated from the extremely weak anatase B1g peak or from possible small rutile or amorphous TiO₂ contents. The Raman spectra are shifted on the intensity axis in (1, 2, 3, 4, 5, and 7) steps of 50 units as indicated by dotted lines.

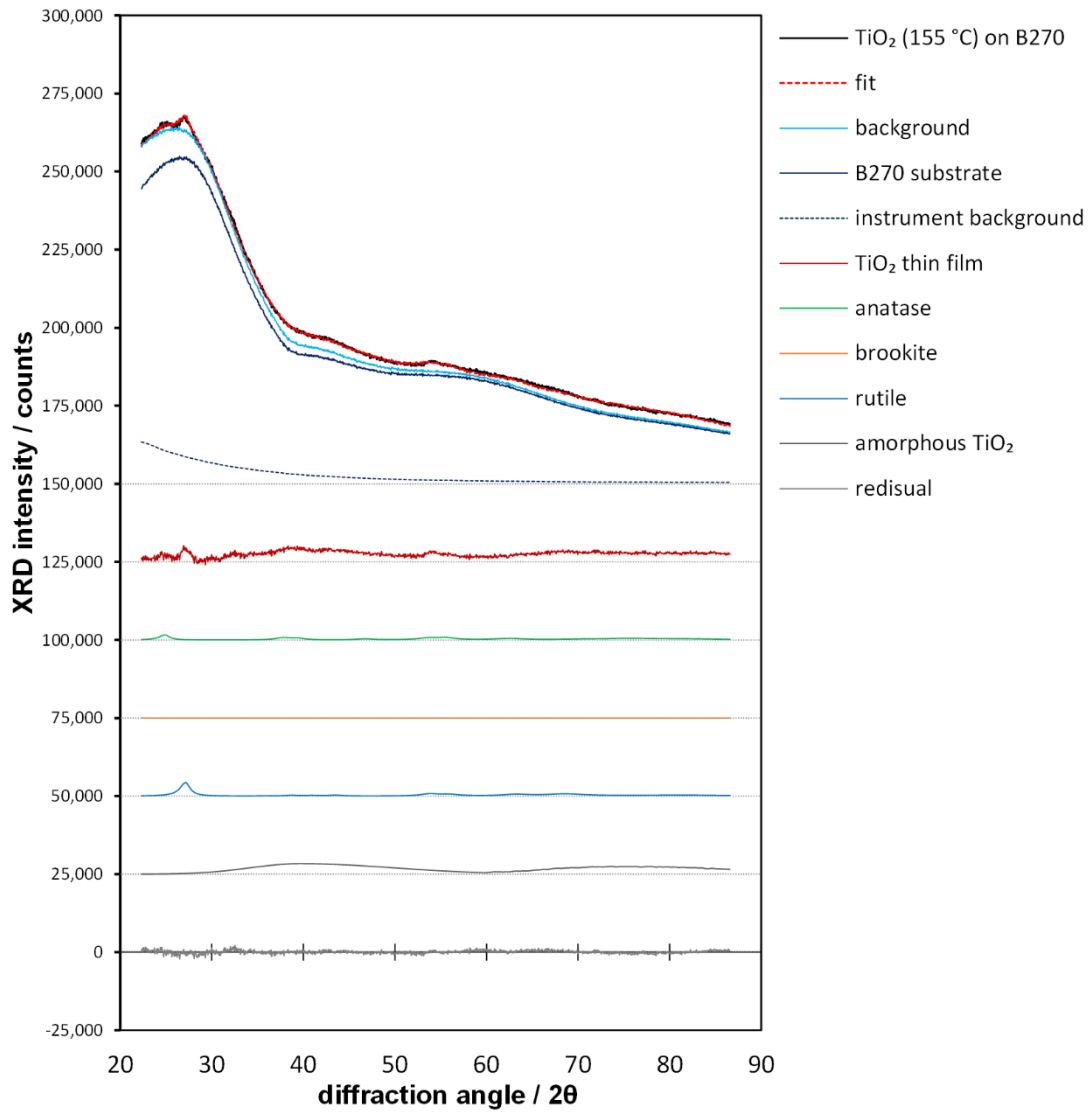


Fig. 170: Decomposition of an X-ray diffractogram of an rf-diode-sputtered TiO₂ thin film on a B270 crown glass substrate deposited at 155 °C into anatase, rutile, brookite, amorphous TiO₂, substrate, and instrument background. The diffractograms are shifted on the intensity axis in steps of 25 000 counts as indicated by dotted lines.

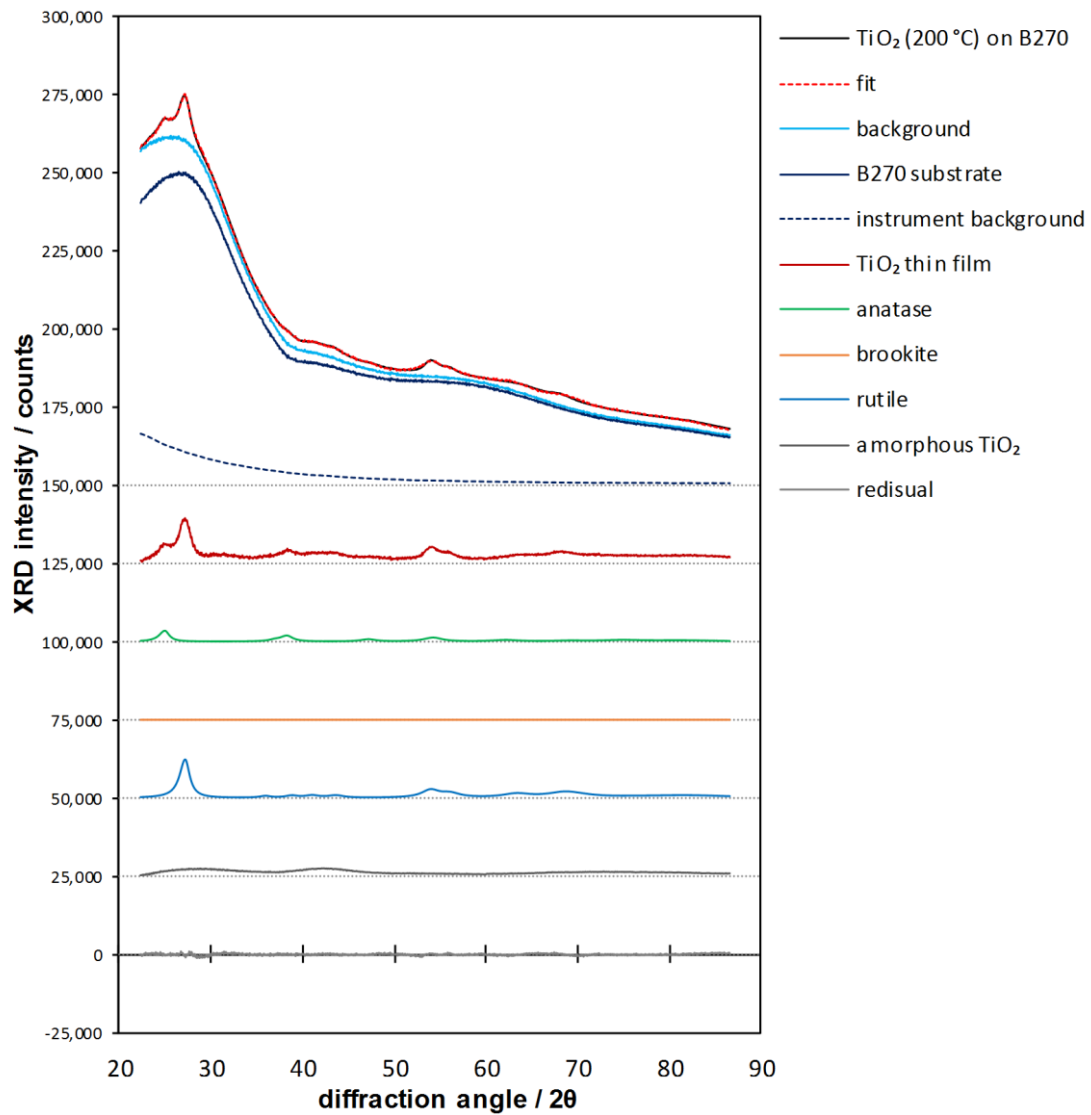


Fig. 171: Decomposition of an X-ray diffractogram of an rf-diode-sputtered TiO₂ thin film on a B270 crown glass substrate deposited at 200 °C into anatase, rutile, brookite, amorphous TiO₂, substrate, and instrument background. The diffractograms are shifted on the intensity axis in steps of 25 000 counts as indicated by dotted lines.

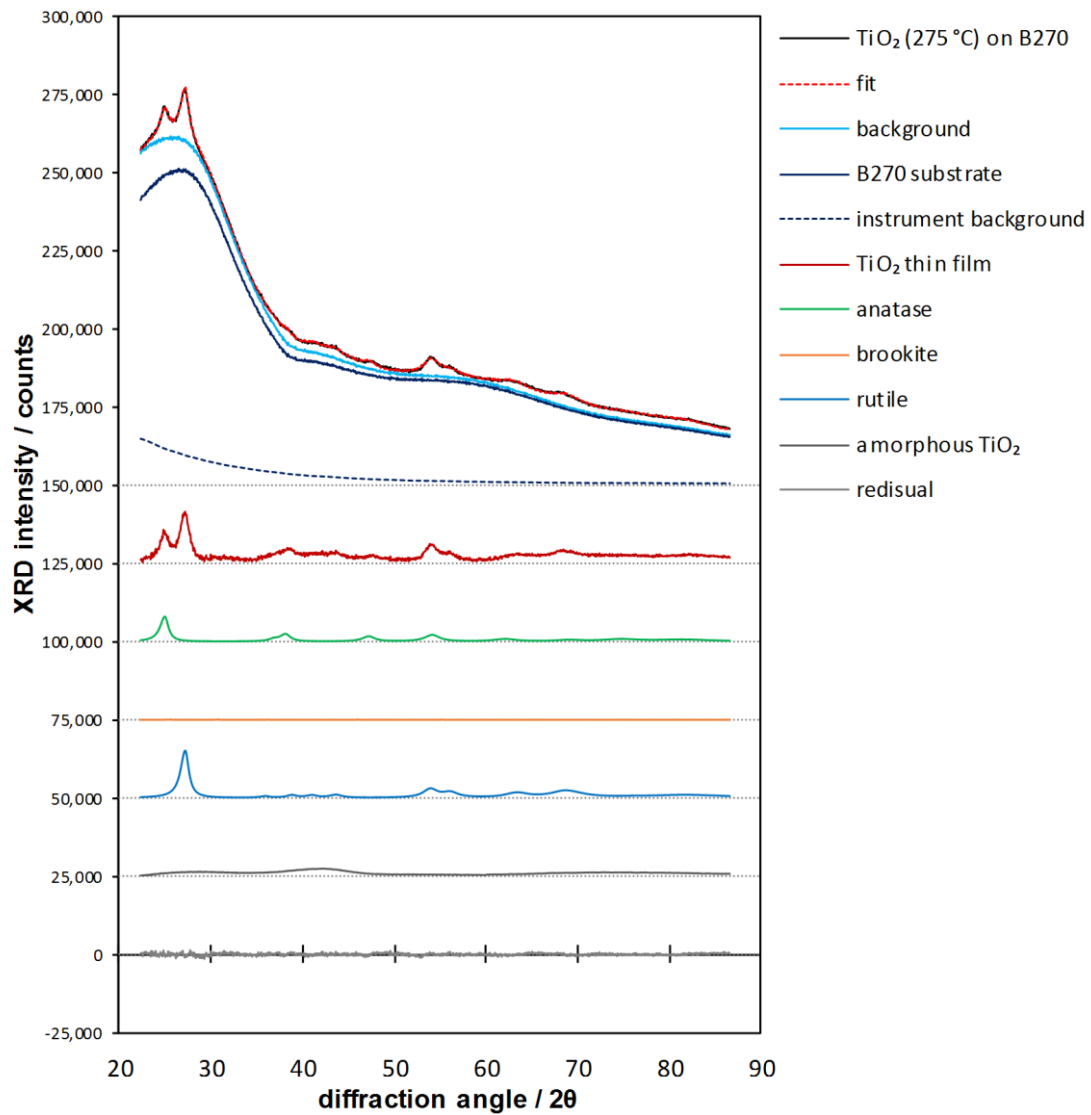


Fig. 172: Decomposition of an X-ray diffractogram of an rf-diode-sputtered TiO₂ thin film on a B270 crown glass substrate deposited at 275 °C into anatase, rutile, brookite, amorphous TiO₂, substrate, and instrument background. The diffractograms are shifted on the intensity axis in steps of 25 000 counts as indicated by dotted lines.

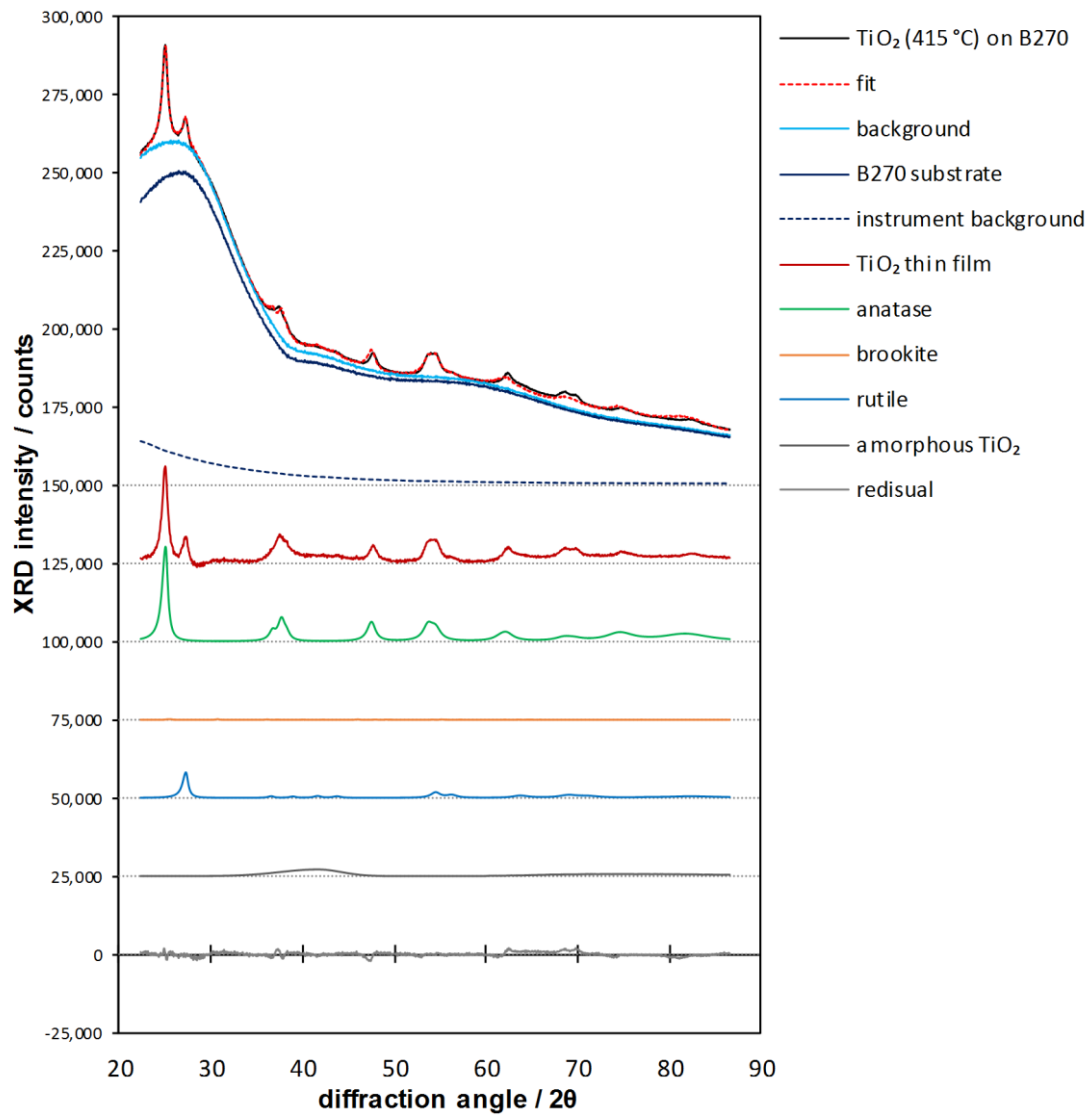


Fig. 173: Decomposition of an X-ray diffractogram of an rf-diode-sputtered TiO₂ thin film on a B270 crown glass substrate deposited at 415 °C into anatase, rutile, brookite, amorphous TiO₂, substrate, and instrument background. The diffractograms are shifted on the intensity axis in steps of 25 000 counts as indicated by dotted lines.

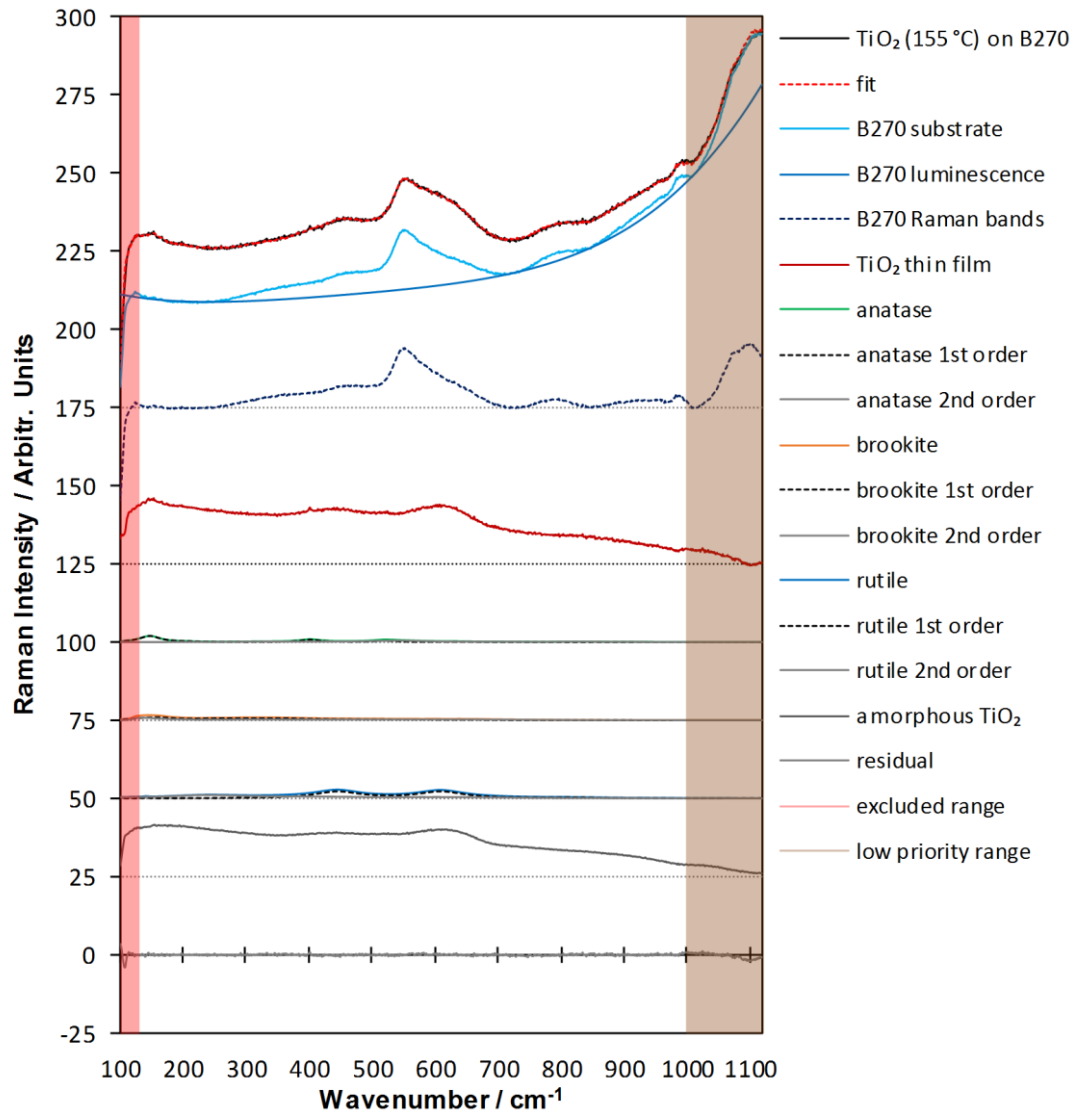


Fig. 174: Decomposition of a 633 nm Raman spectrum of an rf-diode-sputtered TiO_2 thin film on a B270 crown glass substrate deposited at 155 °C into anatase, rutile, brookite, amorphous TiO_2 , and the substrate. The Raman spectra are shifted on the intensity axis in (1, 2, 3, 4, 5, and 7) steps of 25 units as indicated by dotted lines.

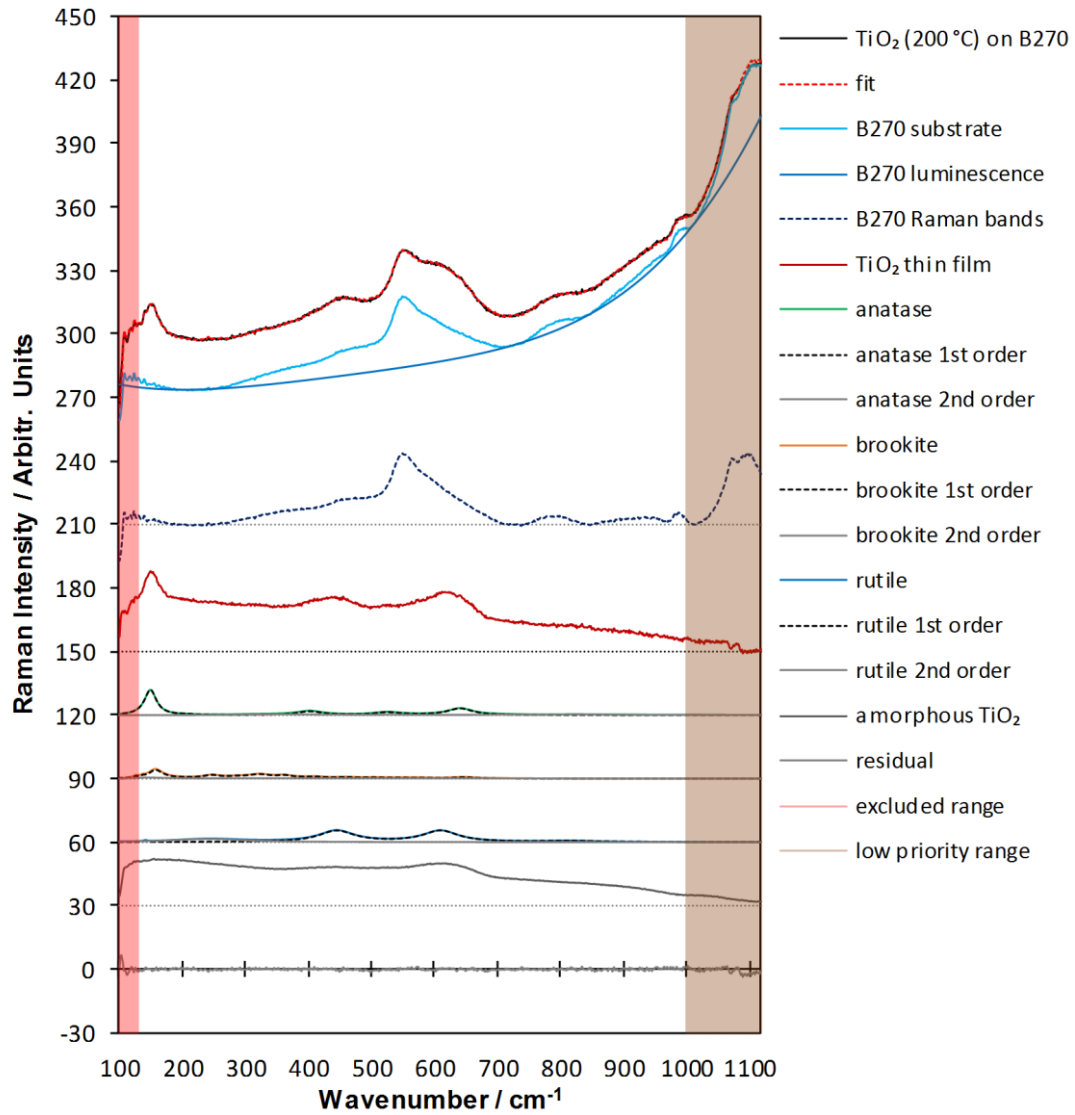


Fig. 175: Decomposition of a 633 nm Raman spectrum of an rf-diode-sputtered TiO_2 thin film on a B270 crown glass substrate deposited at $200 \text{ }^\circ\text{C}$ into anatase, rutile, brookite, amorphous TiO_2 , and the substrate. The Raman spectra are shifted on the intensity axis in (1, 2, 3, 4, 5, and 7) steps of 30 units as indicated by dotted lines.

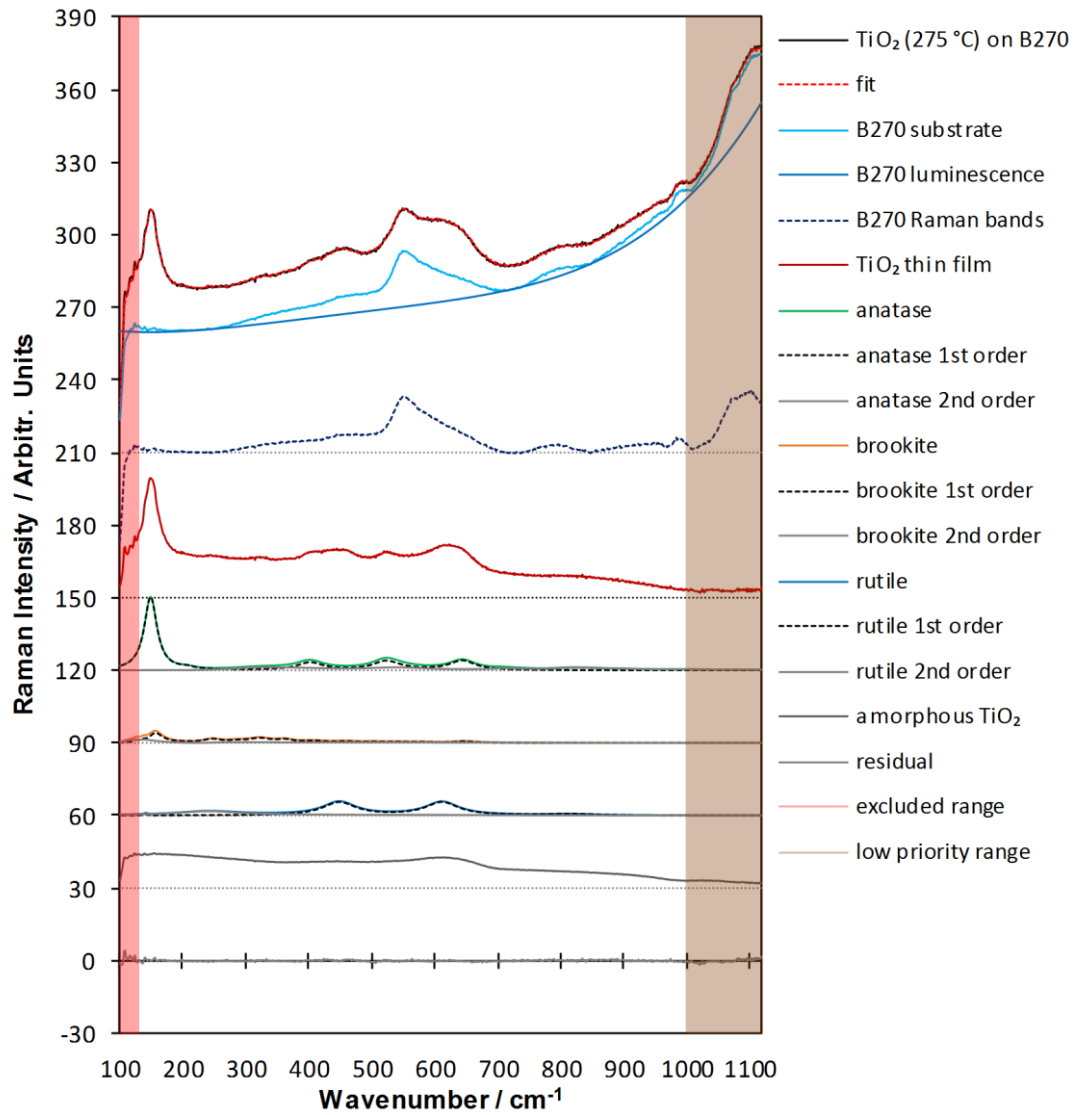


Fig. 176: Decomposition of a 633 nm Raman spectrum of an rf-diode-sputtered TiO_2 thin film on a B270 crown glass substrate deposited at 275 °C into anatase, rutile, brookite, amorphous TiO_2 , and the substrate. The Raman spectra are shifted on the intensity axis in (1, 2, 3, 4, 5, and 7) steps of 30 units as indicated by dotted lines.

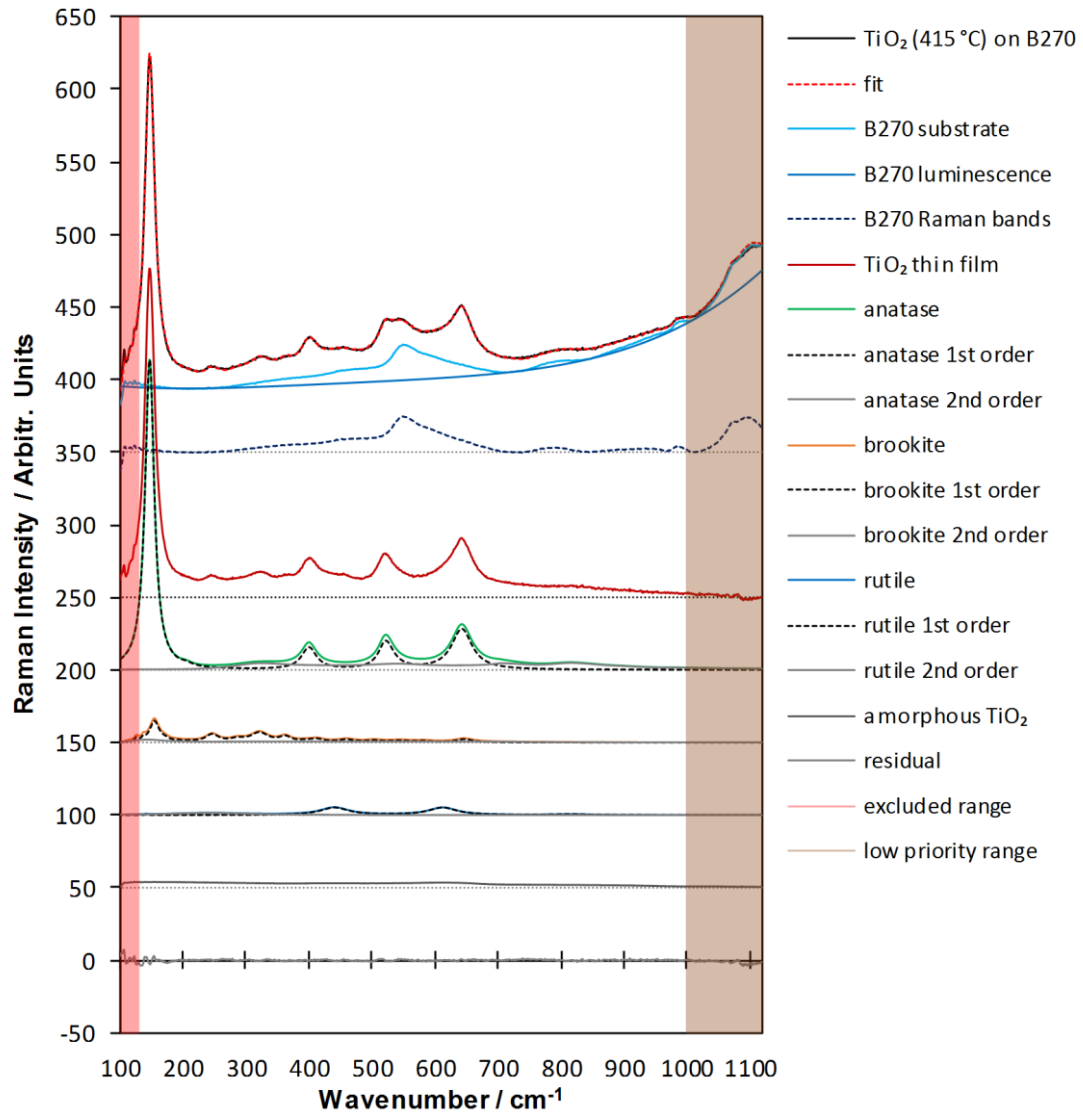


Fig. 177: Decomposition of a 633 nm Raman spectrum of an rf-diode-sputtered TiO_2 thin film on a B270 crown glass substrate deposited at 415 °C into anatase, rutile, brookite, amorphous TiO_2 , and the substrate. The Raman spectra are shifted on the intensity axis in (1, 2, 3, 4, 5, and 7) steps of 50 units as indicated by dotted lines.

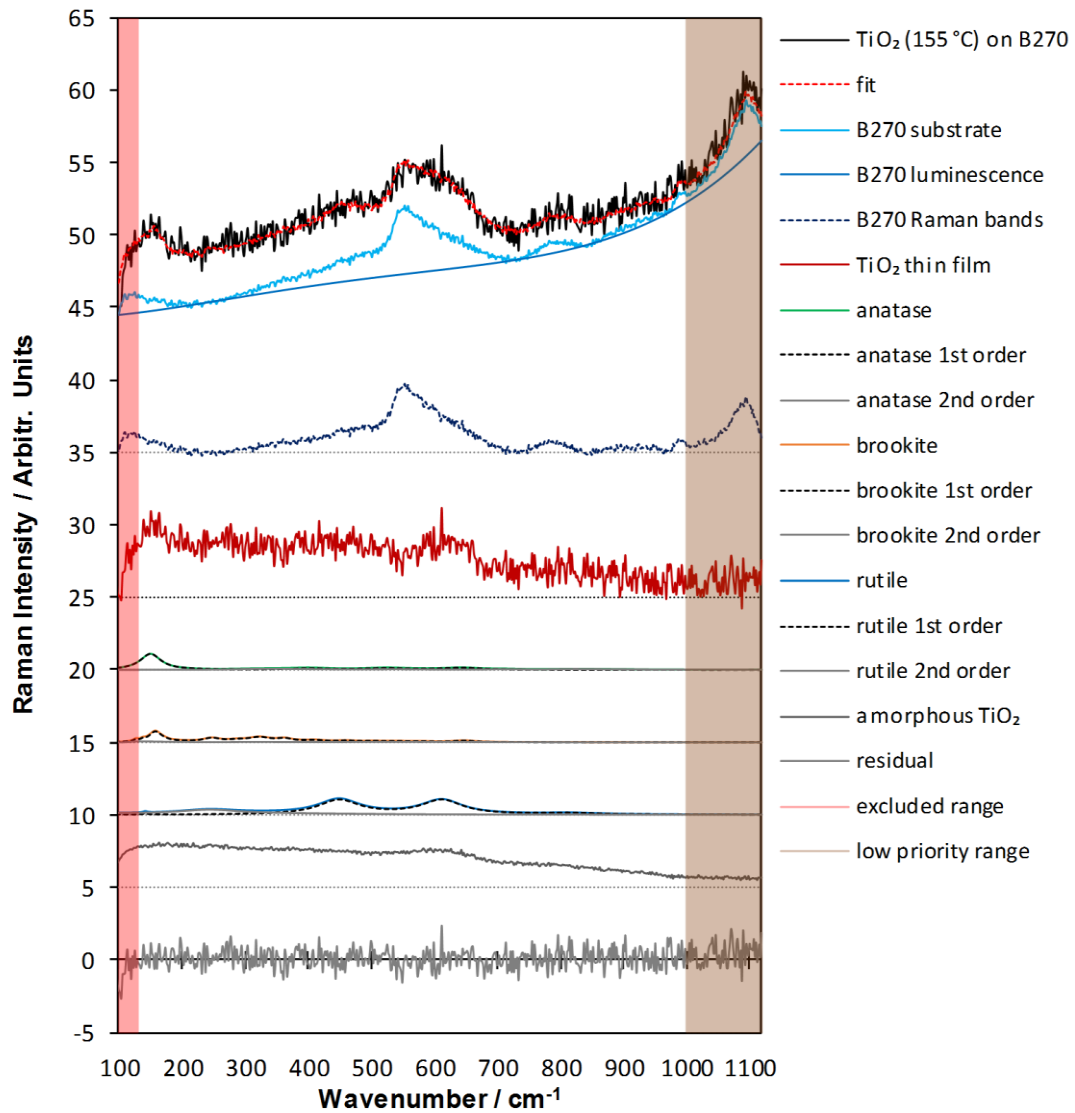


Fig. 178: Decomposition of a 532 nm Raman spectrum of an rf-diode-sputtered TiO₂ thin film on a B270 crown glass substrate deposited at 155 °C into anatase, rutile, brookite, amorphous TiO₂, and the substrate. The Raman spectra are shifted on the intensity axis in (1, 2, 3, 4, 5, and 7) steps of 5 units as indicated by dotted lines.

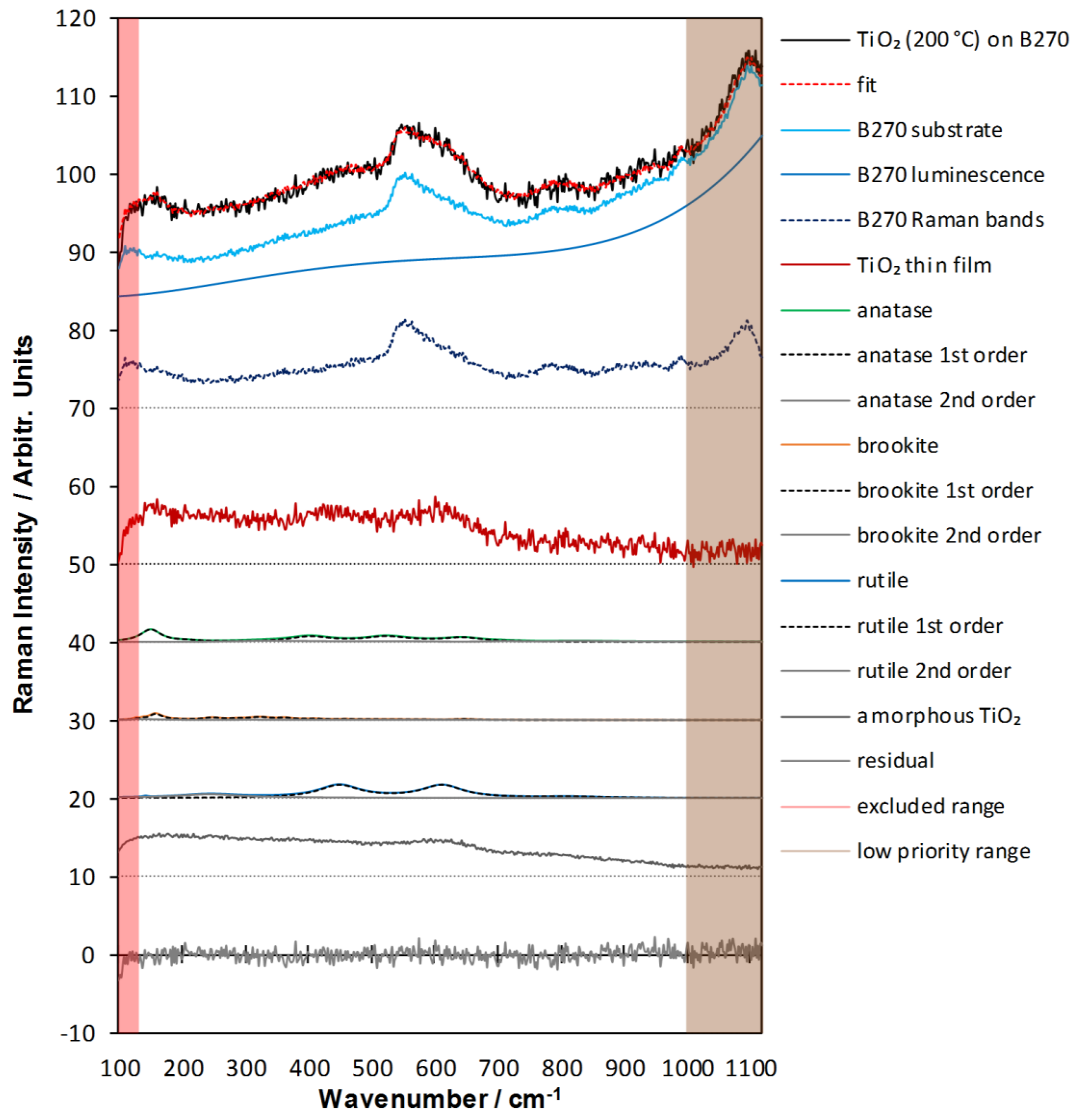


Fig. 179: Decomposition of a 532 nm Raman spectrum of a TiO_2 thin film on an rf-diode-sputtered B270 crown glass substrate deposited at 200 °C into anatase, rutile, brookite, amorphous TiO_2 , and the substrate. The Raman spectra are shifted on the intensity axis in (1, 2, 3, 4, 5, and 7) steps of 10 units as indicated by dotted lines.

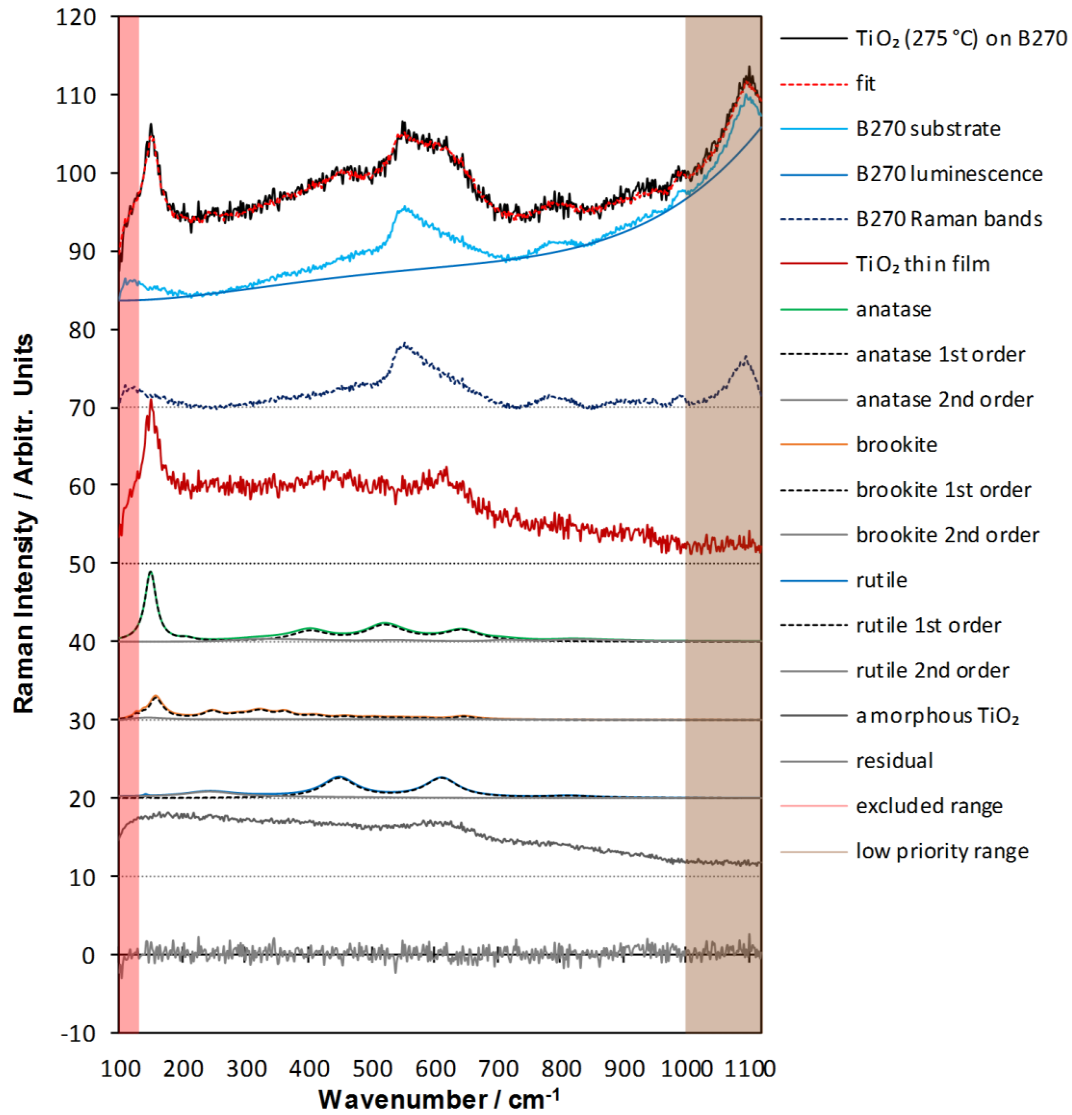


Fig. 180: Decomposition of a 532 nm Raman spectrum of an rf-diode-sputtered TiO_2 thin film on a B270 crown glass substrate deposited at 275 °C into anatase, rutile, brookite, amorphous TiO_2 , and the substrate. The Raman spectra are shifted on the intensity axis in (1, 2, 3, 4, 5, and 7) steps of 10 units as indicated by dotted lines.

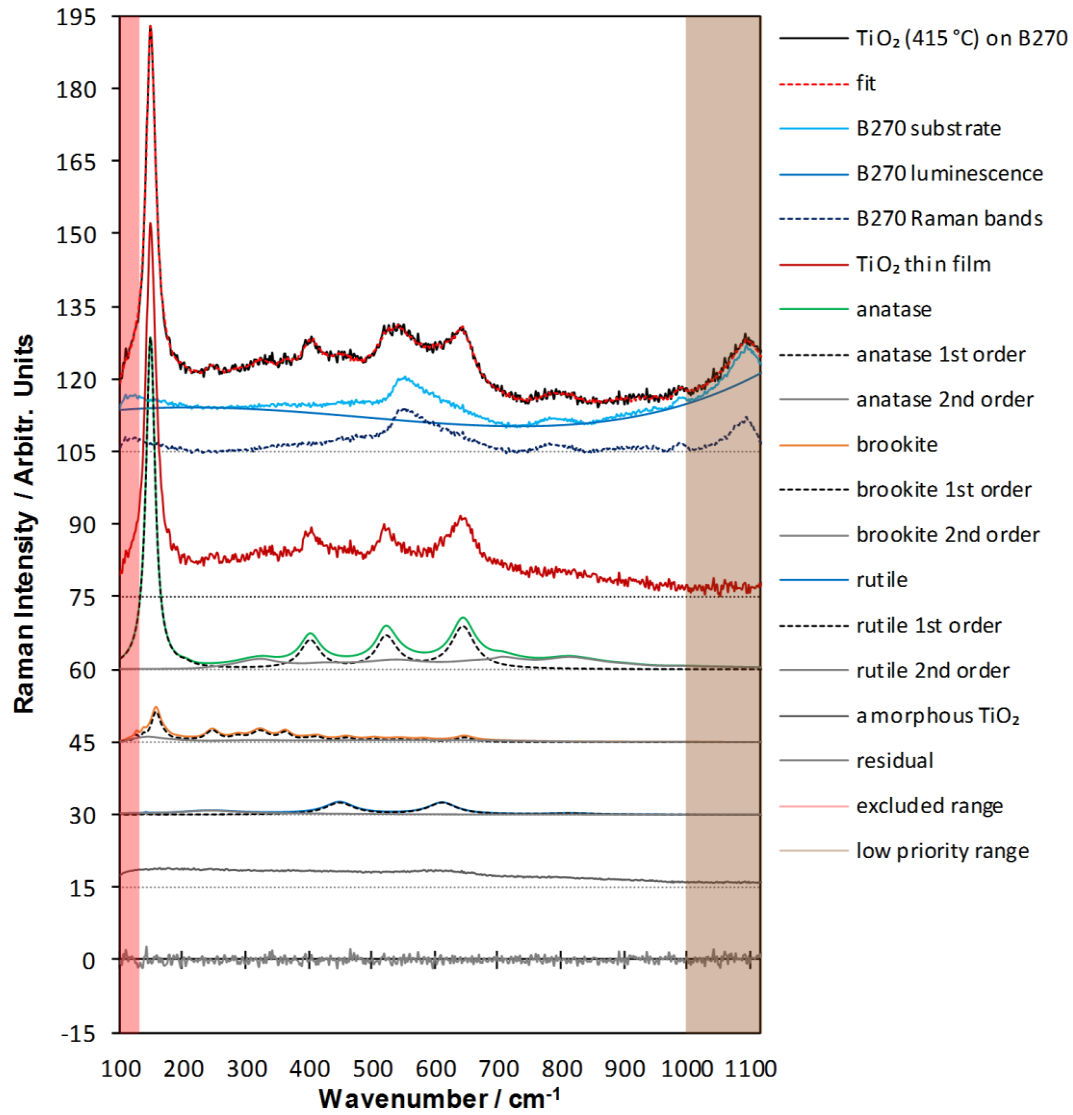


Fig. 181: Decomposition of a 532 nm Raman spectrum of a TiO_2 thin film on an rf-diode-sputtered B270 crown glass substrate deposited at 415 °C into anatase, rutile, brookite, amorphous TiO_2 , and the substrate. The Raman spectra are shifted on the intensity axis in (1, 2, 3, 4, 5, and 7) steps of 15 units as indicated by dotted lines.

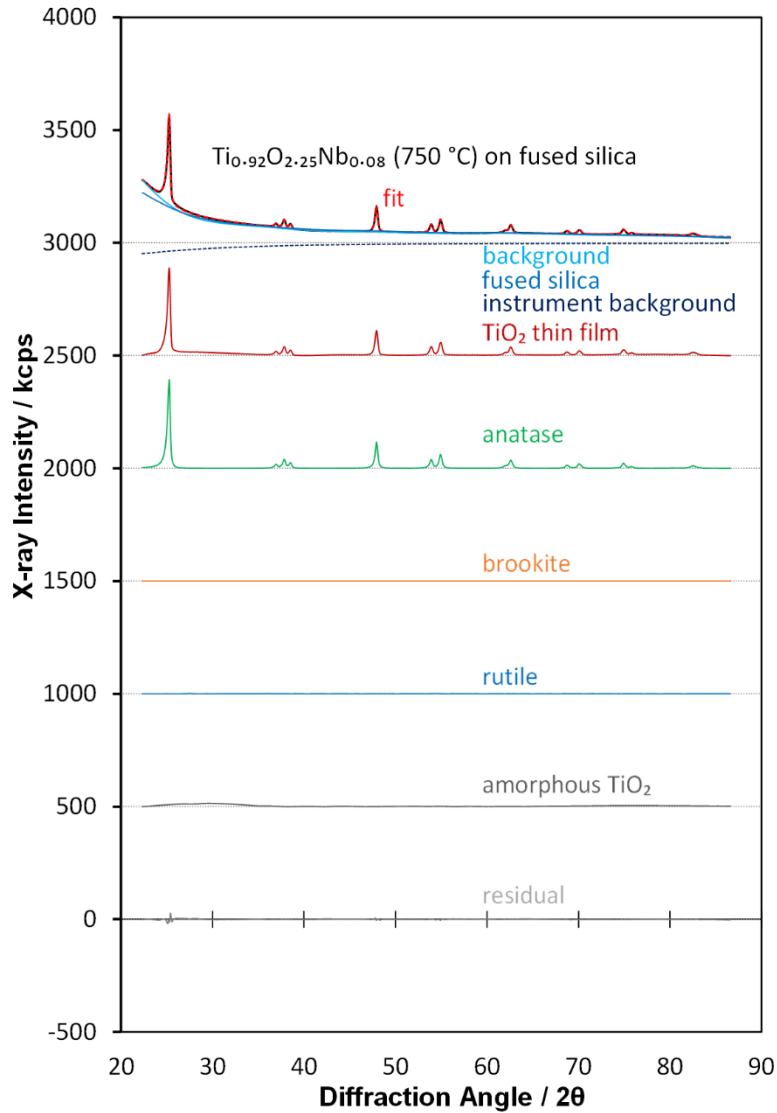


Fig. 182: Measured (black) and modeled (dashed red) X-ray diffractogram of a titanium oxide thin film with 8 at.% Nb – e-beam evaporated onto a fused silica substrate and post-heated at 750 °C – decomposed into a background (light blue) and a thin film (dark red). The background is split into the fused silica substrate (medium blue) and an instrument background (dashed dark blue). The film is decomposed into anatase (green), brookite (orange), rutile (blue), and amorphous TiO₂ (dark gray). The residual diffractogram is medium gray. The diffractograms are shifted on the intensity axis in steps of 10 kcps as indicated by dotted lines.

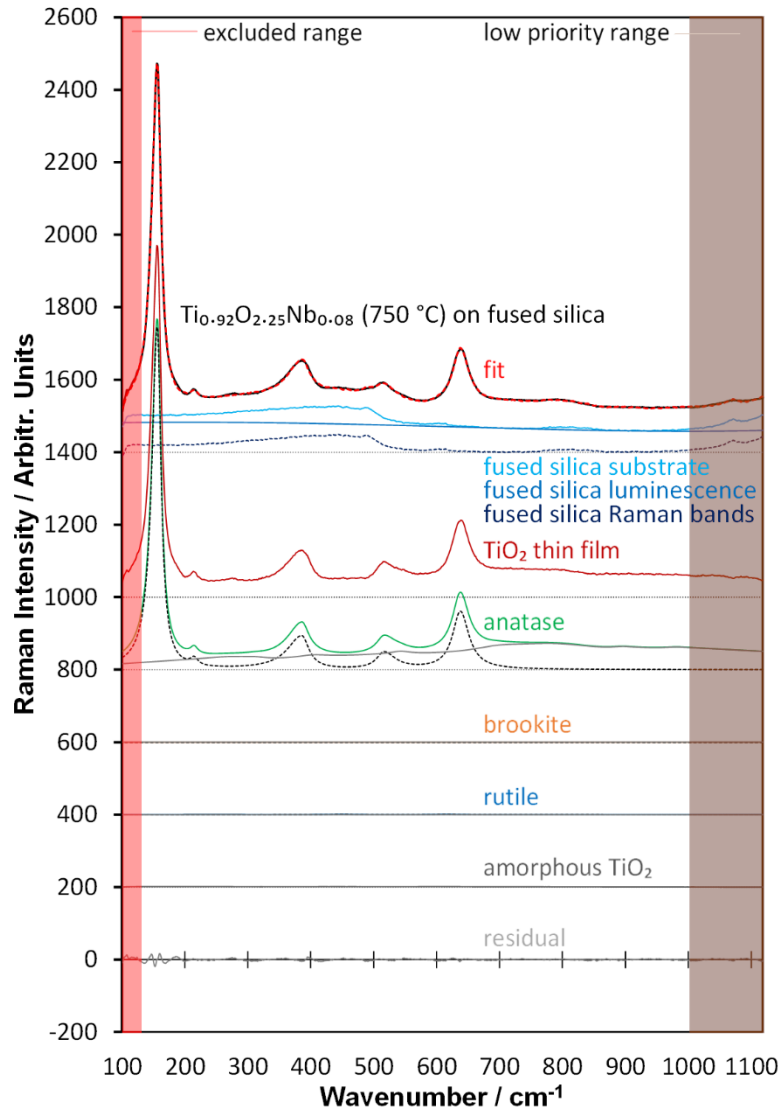


Fig. 183: Measured (black) and modeled (dashed red) spectrum of an e-beam coated titanium oxide thin film doped with 8 at.% Nb on fused silica post-heated at 750 °C – decomposed into substrate (light blue) and thin film (dark red). The substrate spectrum is split into luminescence (mid blue) and Raman bands (dashed dark blue) and the thin film is decomposed into anatase (green), brookite (orange), rutile (blue), and amorphous TiO₂ (dark gray) spectra. The crystalline spectra are divided into first-order scattering (black dashed lines) and phase background (light gray lines). The excluded range is light red and the low priority range is light brown. The Raman spectra are shifted on the intensity axis in (1, 2, 3, 4, 5, and 7) steps of 200 units as indicated by dotted lines.

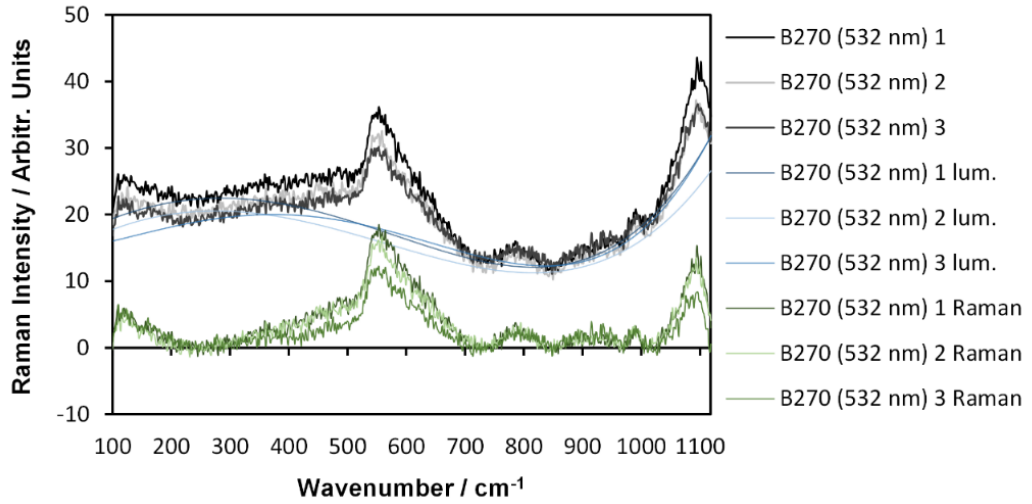


Fig. 184: Decomposition of measured B270 glass substrate Raman spectra (532 nm) into luminescence and Raman active modes.

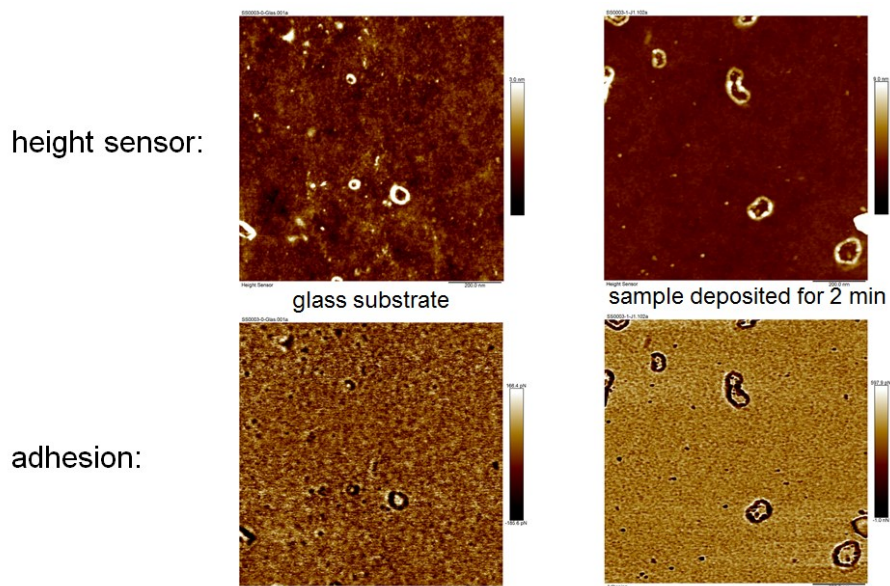


Fig. 185: AFM images of an uncoated B270 glass substrate (left) and a substrate that was coated with TiO₂ for 2 minutes by rf-diode sputtering (right). The images have areas of 1 μm × 1 μm and were taken using a height sensor (top) as well as an adhesion sensor (bottom).

name	position (eV)	FWHM (eV)	area (CPS eV)
Ti 2p	458,38	1,14	12845
Ti 2p	464,05	2,1	6423

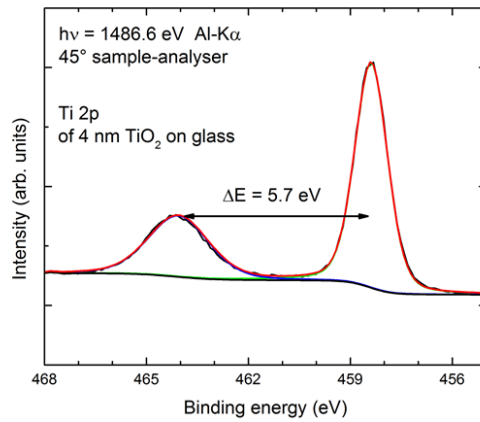


Fig. 186: XPS spectrum of a TiO₂ thin film rf-diode sputtered for 2 minutes onto a B270 glass substrate.

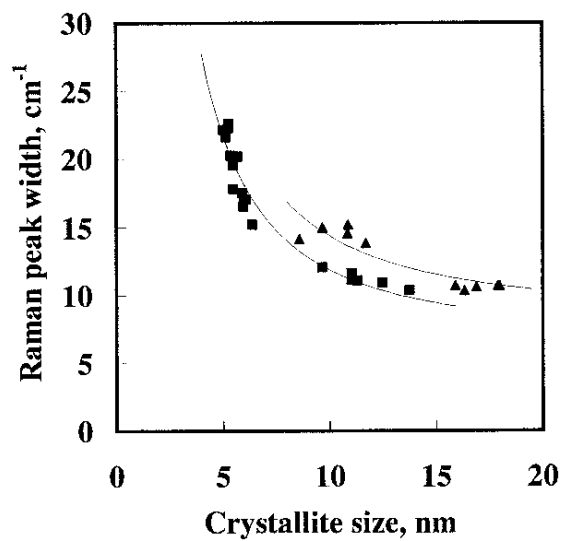


Fig. 187: Relationship between the Raman peak width and the crystallite size (as estimated by XRD with the Scherrer method) of two sets of nano powders differently synthesized from hydrolysis of alkoxide.

Figure taken from Iida et al.¹⁵¹

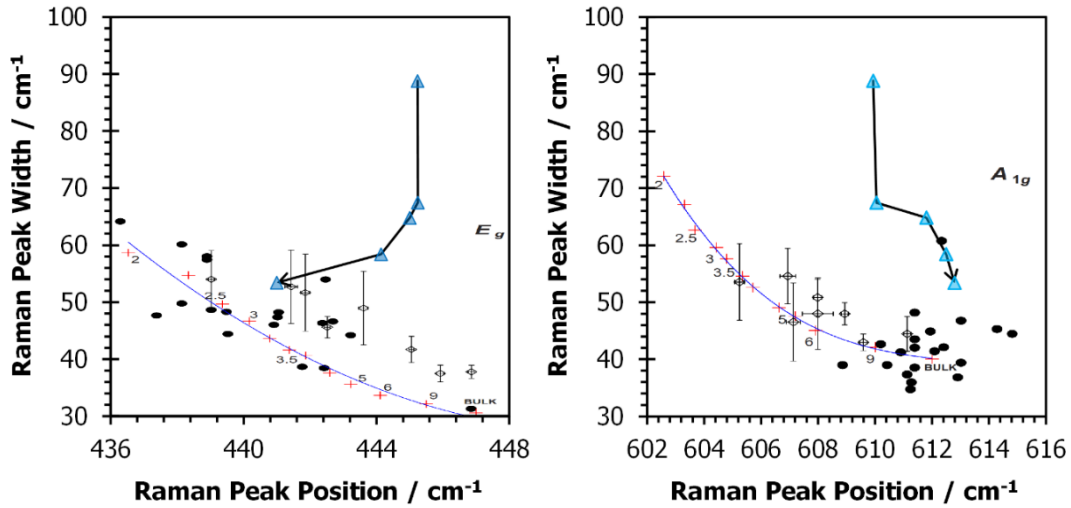


Fig. 188: Rutile Raman peak positions vs. widths of diode sputtered mixed-phase TiO_2 thin films on B270 glass (E_g : left side, A_{1g} : right side) marked as blue triangles. The arrows indicate increasing deposition temperature ($155\text{ }^\circ\text{C} - 415\text{ }^\circ\text{C}$). The figure contains literature values of Swamy et al. (open symbols) and of Mazza et al. (closed symbols) as well as the values calculated with a phonon confinement model by Mazza et al. Parts of a figure of Swamy et al. is added to this figure.^{48,163}

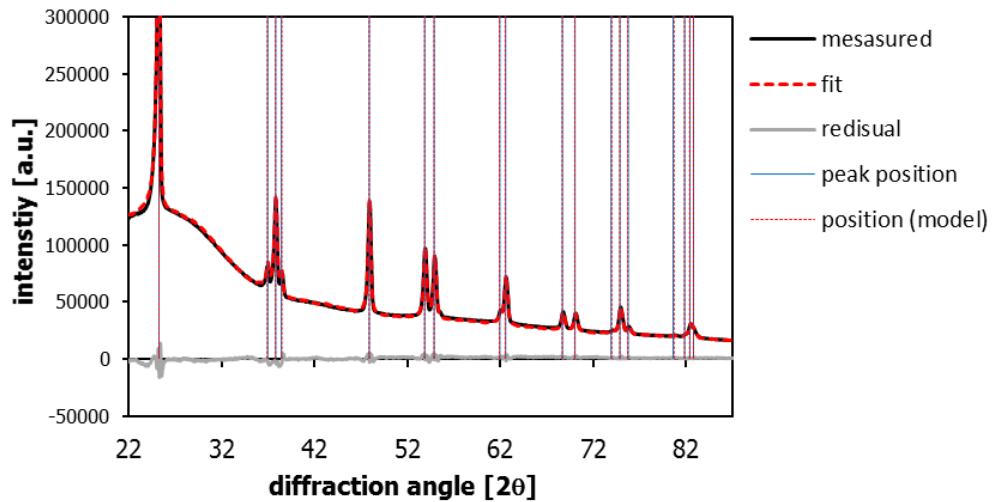


Fig. 189: Measured (black) and modeled (“fit”, dashed red) XRD diffractograms of an undoped TiO_2 film on B270 glass annealed at $640\text{ }^\circ\text{C}$ (black), fitted peak positions (blue), and peak positions (dotted red) modeled by lattice parameters a and c . The fitted and the modeled positions are less than 0.01° apart.

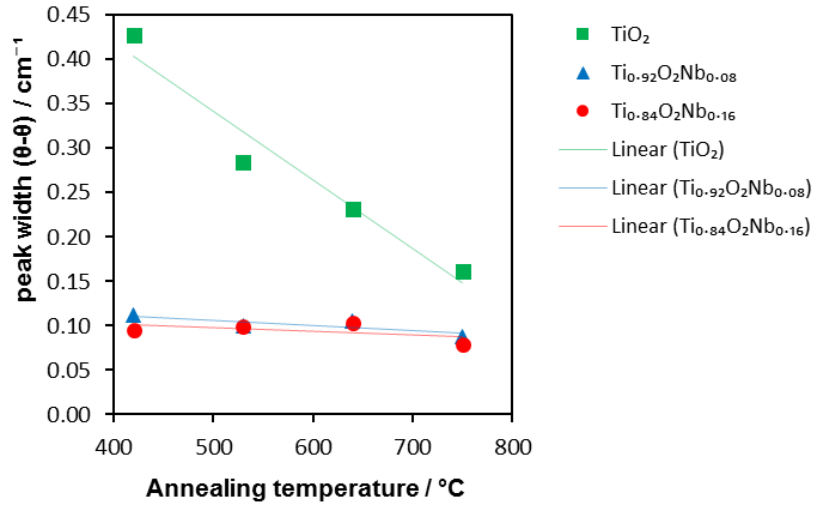


Fig. 190: XRD (101) peak width of e-beam evaporated Nb0, Nb1, and Nb2 thin films in theta-theta geometry vs. annealing temperature.

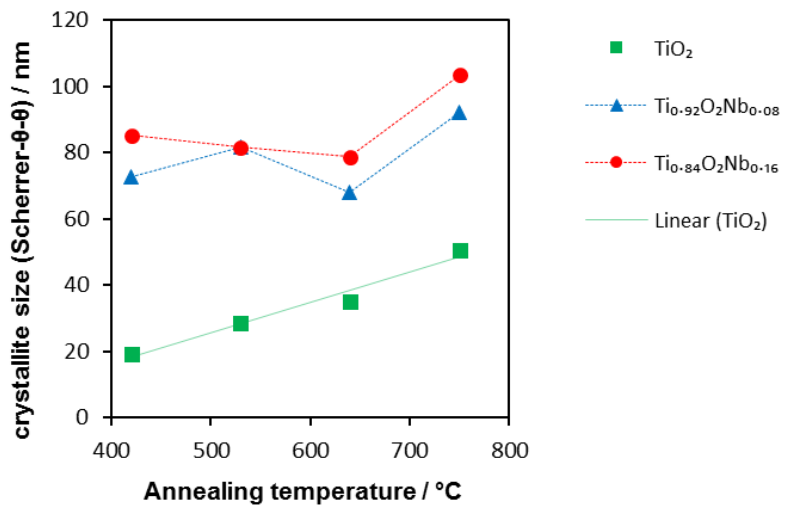


Fig. 191: Crystallite size of (101)-oriented grains according to Scherrer in e-beam evaporated Nb0, Nb1, and Nb2 films vs. annealing temperature.

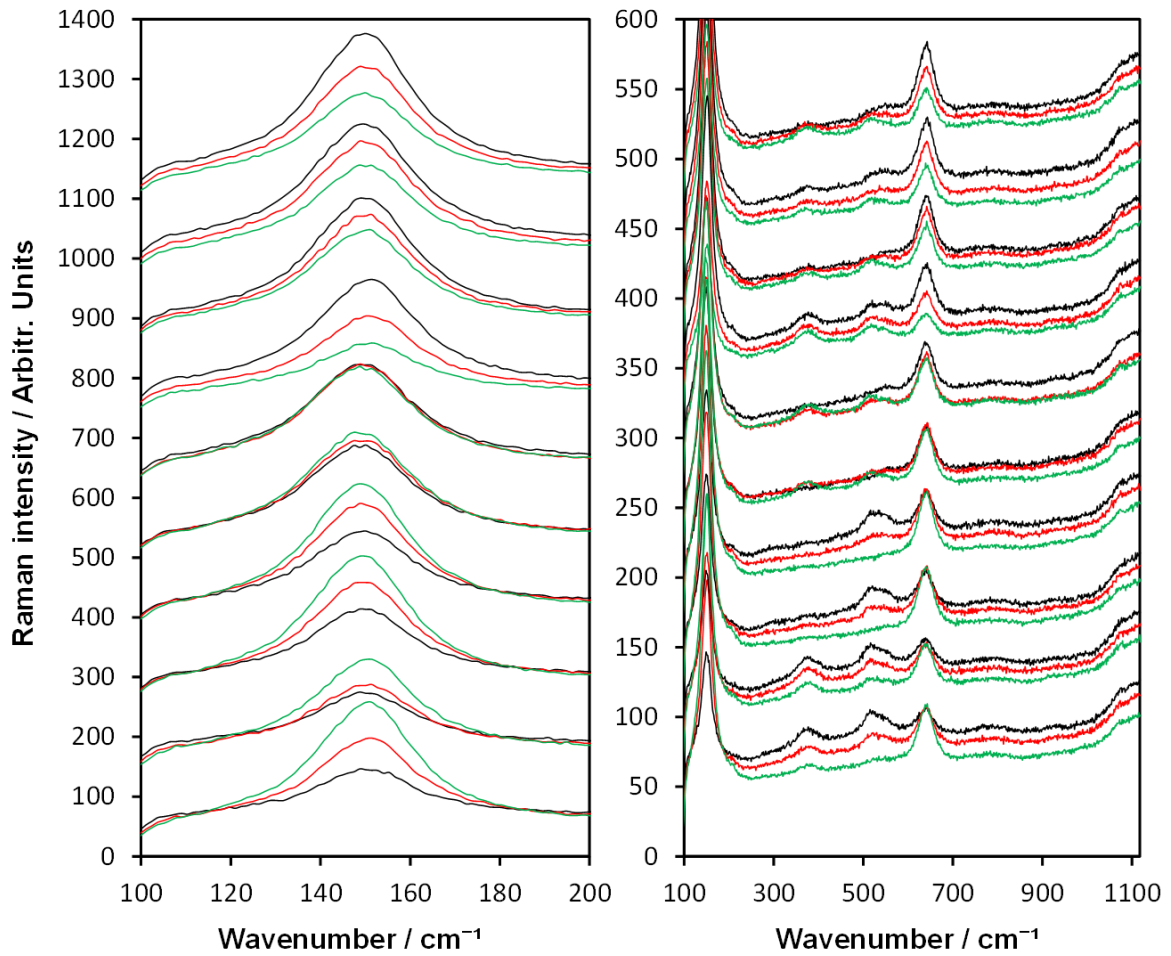


Fig. 192: Raman spectra of varying polarizations (unpolarized (black), circularly polarized (red), orthogonally polarized (green)) on various positions on a $\text{Ti}_{0.84}\text{O}_{2.25}\text{Nb}_{0.16}$ film that was annealed at $640\text{ }^\circ\text{C}$, sorted by the height of the $\text{E}_g(1)$ peak in the unpolarized spectra. Left: $\text{E}_g(1)$ peak. The spectra of each position are shifted on the intensity axis. Right: detailed view on the whole range of measurement (same spectra), shifted by 50 units on the intensity axis for each position.

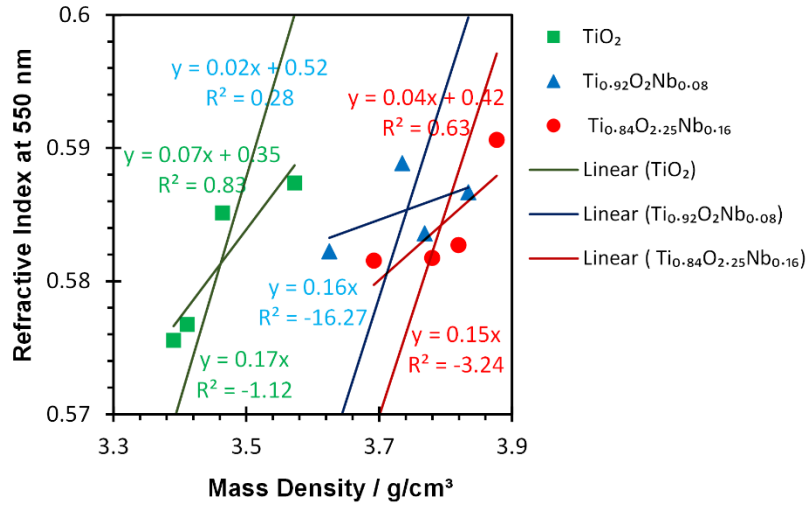


Fig. 193: Lorentz-Lorentz plots of the refractive indices of Nb0, Nb1, Nb2 with two trendlines each, of which one goes through zero.

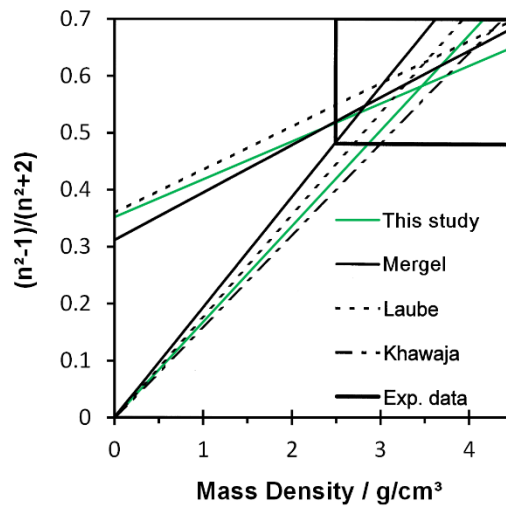


Fig. 194: Comparison of the Nb0 trendlines from Fig. 193 with literature values. Parts of Fig. 12 of Mergel et al. were copied into this figure.⁵³

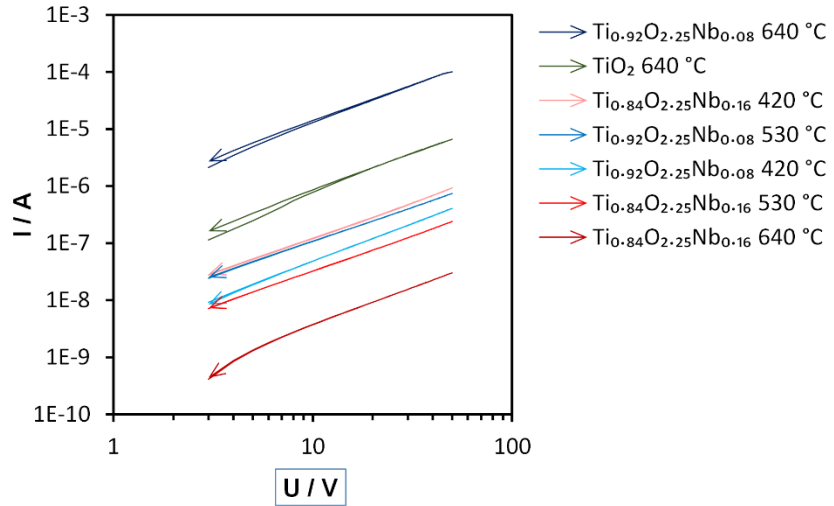


Fig. 195: Potential current-voltage characteristics of e-beam coated crystalline Nb0, Nb1, and Nb thin films on B270 glass. All displayed films show a power of 1.3 (± 0.1) relationship.

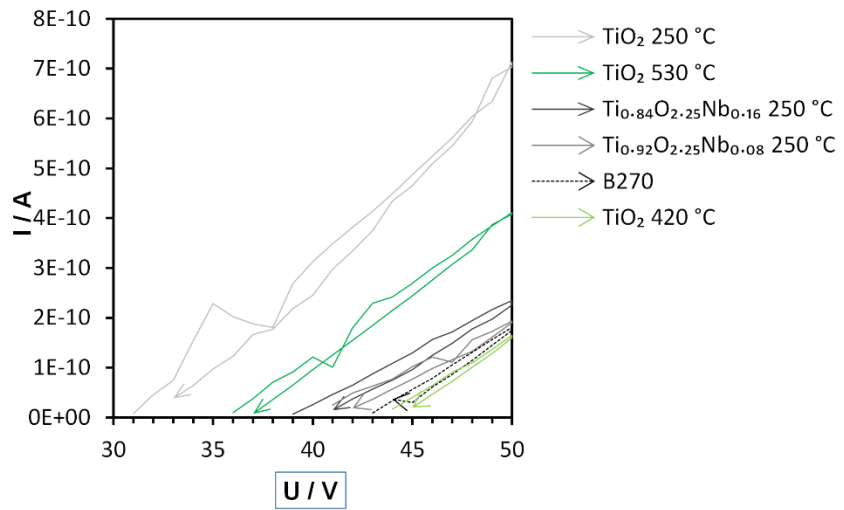


Fig. 196: Linear current-voltage characteristics of e-beam coated Nb0, Nb1, and Nb thin films, and of the B270 glass substrate. The films are amorphous and not post-heated, except of the crystalline undoped films post-heated at 420 °C and 530 °C (light and medium green lines).

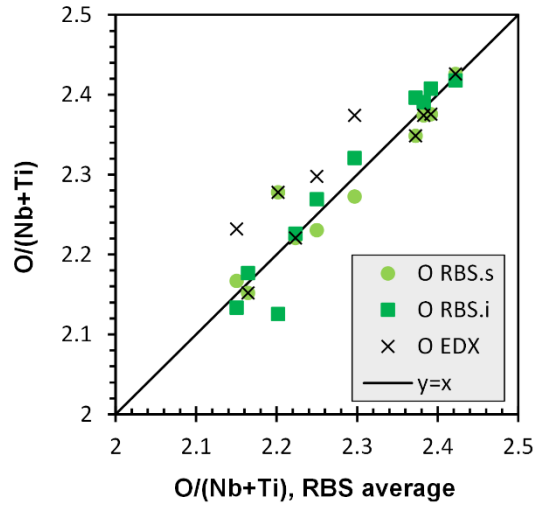


Fig. 197: Oxygen content of PEM controlled rf-sputter coated Nb-doped TiO₂ thin films on B270 glass as determined by RBS at the surface (RBS.s), at the interface (RBS.i) and by EDX vs. the average of both RBS values.

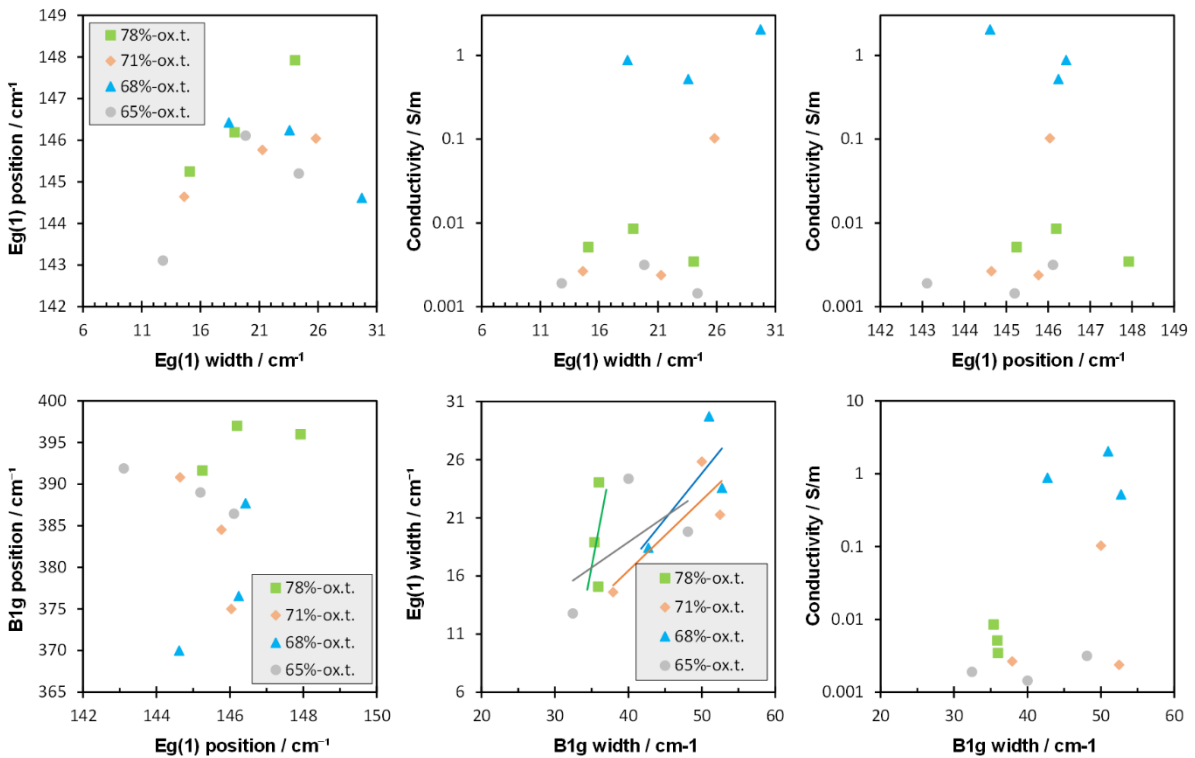


Fig. 198: Comparison of Raman peak parameters and conductivities of PEM controlled rf-sputter coated Nb-doped TiO₂ thin films on B270 glass. The Ti target surface is oxidized by 65%, 68%, 71%, or 78%. The samples are placed 12.5 mm, 42.5 mm, and 72.5 mm horizontally from the Nb wires and the film thickness decreases with the distance from the wire.

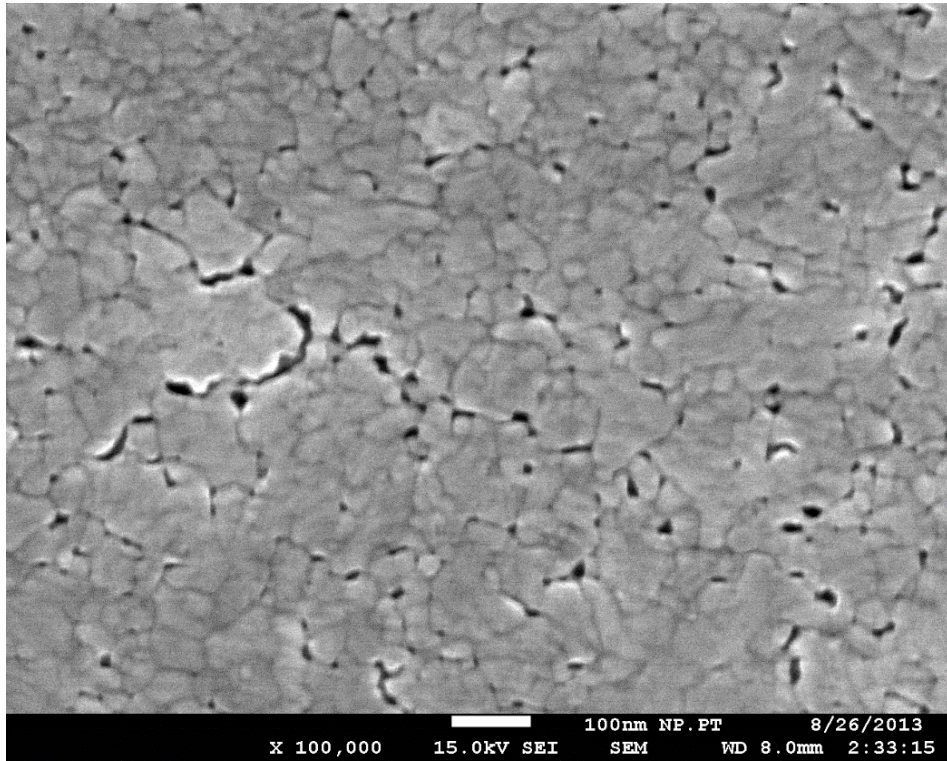


Fig. 199: SEM image (100000 x) of a TiO₂ film annealed at 640 °C.

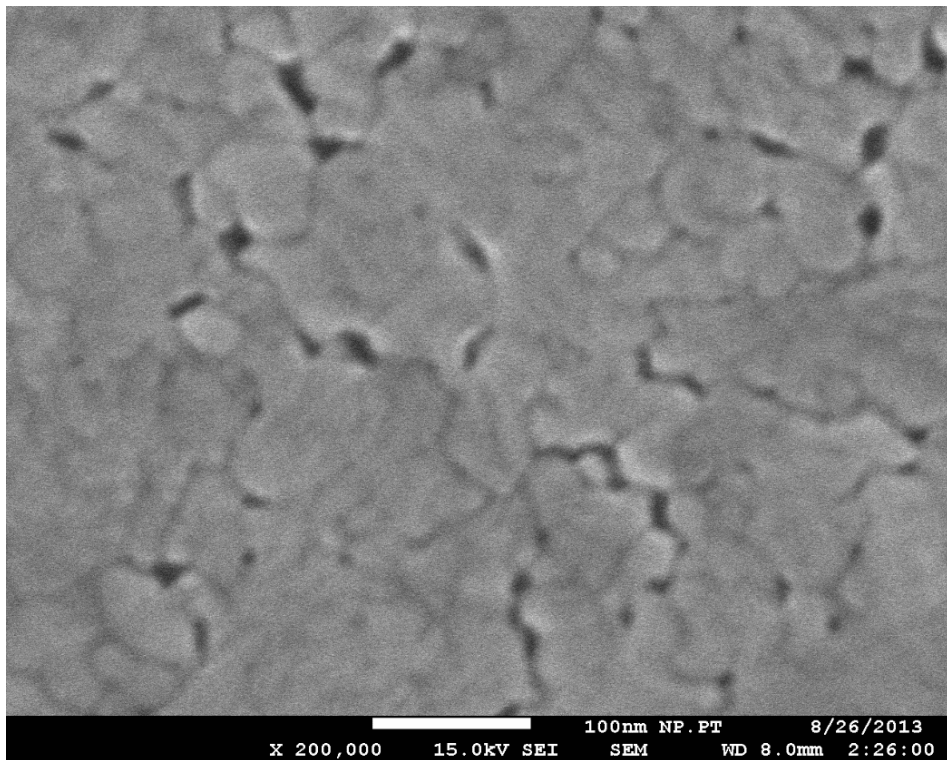


Fig. 200: SEM image (200000 x) of a TiO₂ film annealed at 640 °C.

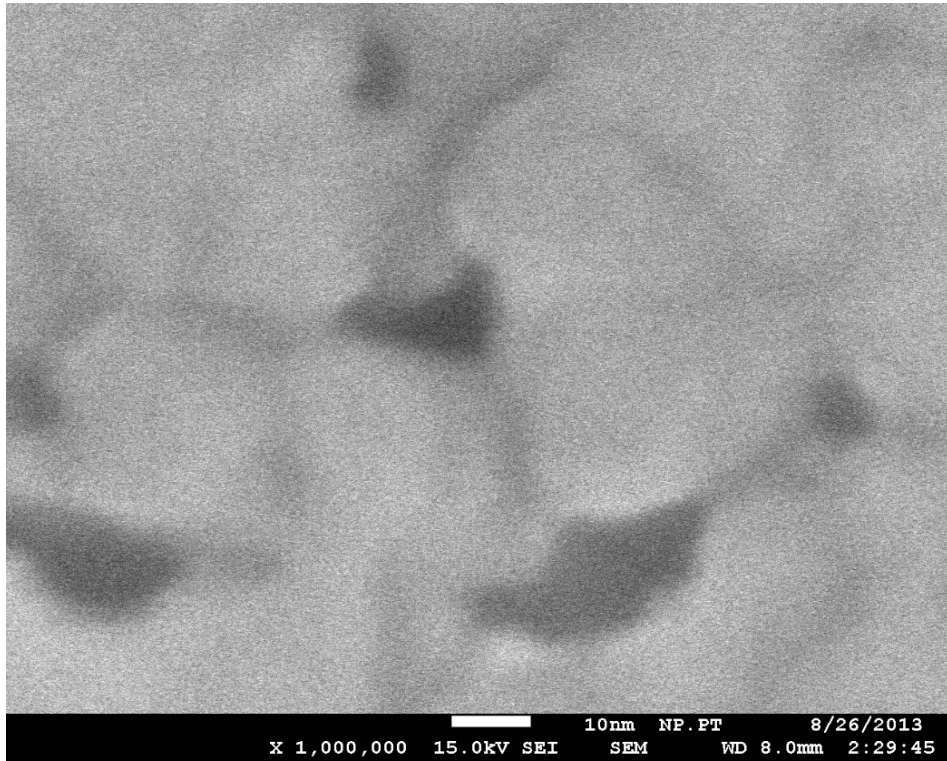


Fig. 201: SEM image (*1000000 x*) of a TiO₂ film annealed at 640 °C.

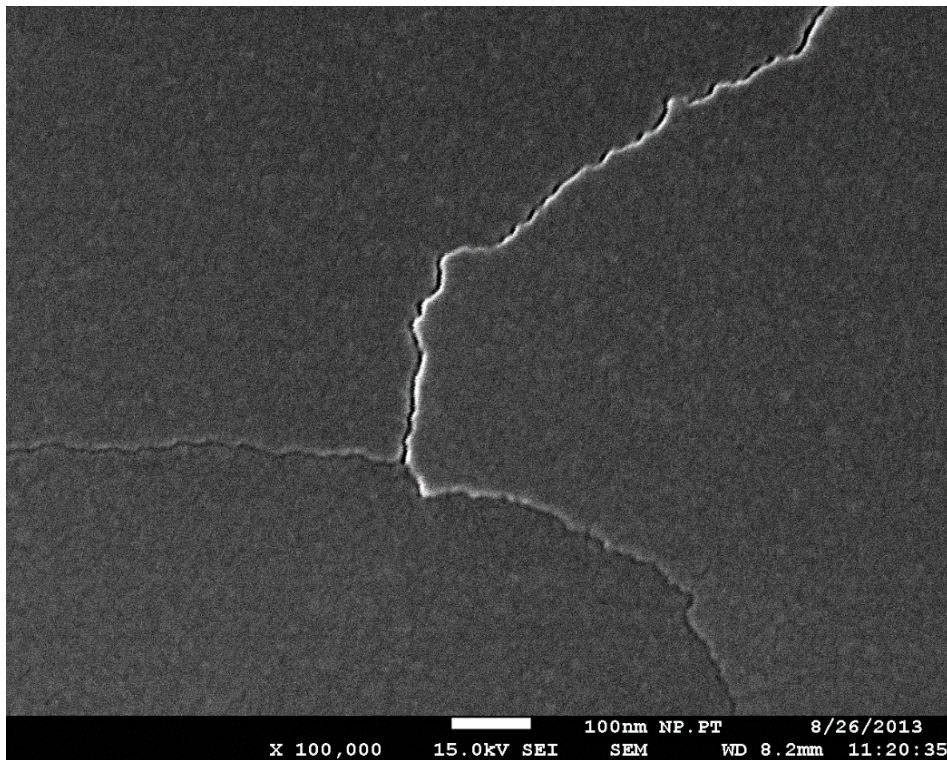


Fig. 202: SEM image (*100000 x*) of a Ti_{0.92}O_{2.25}Nb_{0.08} film annealed at 640 °C.

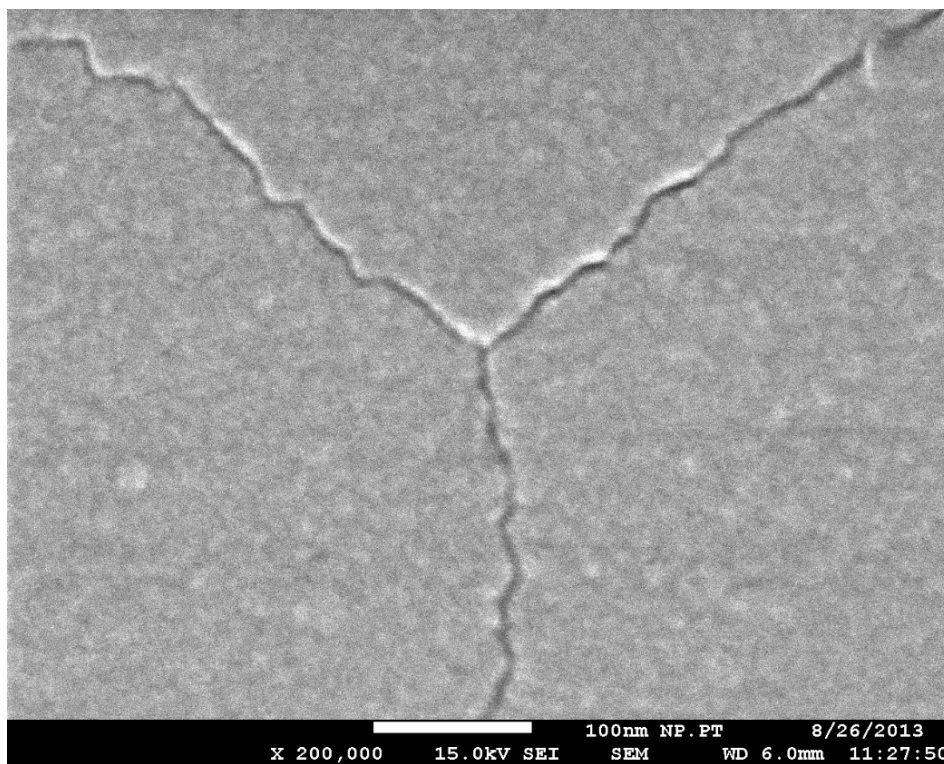


Fig. 203: SEM image (200000 x) of a $\text{Ti}_{0.92}\text{O}_{2.25}\text{Nb}_{0.08}$ film annealed at 640 °C.

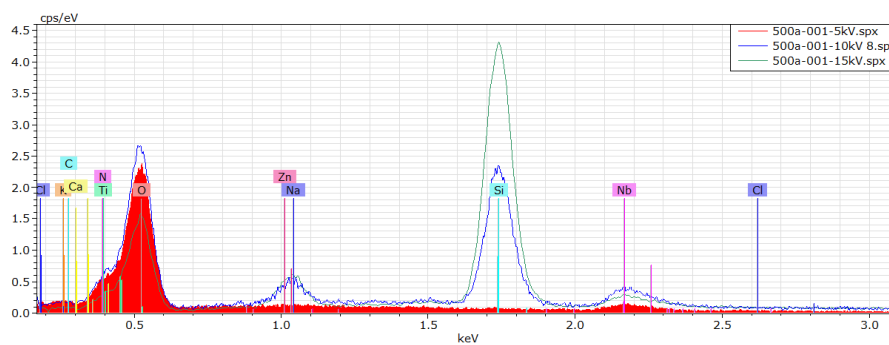


Fig. 204: EDX spectra of Nb_2 (640 °C) with acceleration voltages of 5 kV (red), 10 kV (blue), and 15 kV (green).

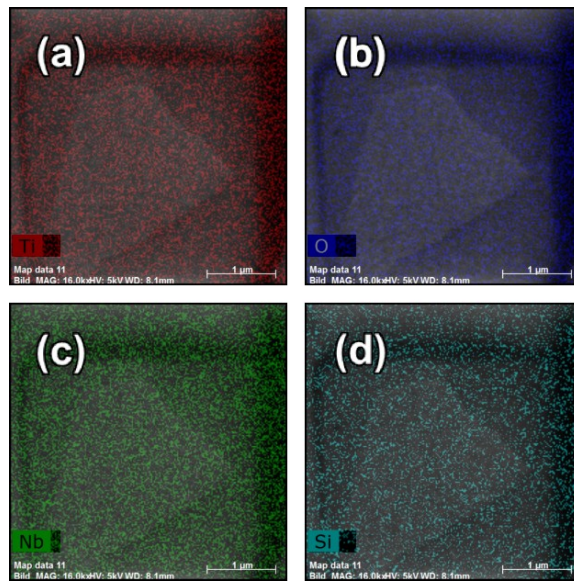


Fig. 205: EDX maps ($4\ \mu\text{m} \times 4\ \mu\text{m}$) of $\text{Ti}_{0.84}\text{O}_{2.25}\text{Nb}_{0.16}$ film annealed at $640\ \text{°C}$ of (a) Ti, (b) O, (c) Nb, and (d) Si.

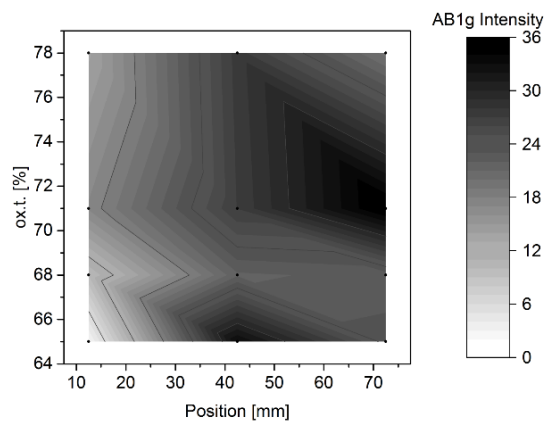


Fig. 206: 2D representations of Raman anatase peak parameters of the Eg(1) peak (left) and the B1g peak (right) vs. the *ox.t.* and the sample position. The figures show the peak widths (top), positions (middle), and intensities (bottom).

References

- (1) Schipporeit, S.; Mergel, D. Spectral decomposition of Raman spectra of mixed-phase TiO₂ thin films on Si and silicate substrates. *J. Raman Spectrosc.* **2018**, *49* (7), 1217–1229. DOI: 10.1002/jrs.5369.
- (2) Schipporeit, S.; Mergel, D. Cover Image. *J. Raman Spectrosc.* **2018**, *49* (7), I-I. DOI: 10.1002/jrs.5453.
- (3) Fujishima, A.; Honda, K. Electrochemical photolysis of water at a semiconductor electrode. *Nature* **1972**, *238* (5358), 37–38. DOI: 10.1038/238037a0.
- (4) Di Paola, A.; Bellardita, M.; Palmisano, L. Brookite, the Least Known TiO₂ Photocatalyst. *Catalysts* **2013**, *3* (1), 36–73. DOI: 10.3390/catal3010036.
- (5) Hanaor, D. A. H.; Sorrell, C. C. Review of the anatase to rutile phase transformation. *J. Mater. Sci.* **2011**, *46* (4), 855–874. DOI: 10.1007/s10853-010-5113-0.
- (6) Beltrán, A.; Gracia, L.; Andrés, J. Density functional theory study of the brookite surfaces and phase transitions between natural titania polymorphs. *The journal of physical chemistry. B* **2006**, *110* (46), 23417–23423. DOI: 10.1021/jp0643000.
- (7) Rezaee, M.; Mousavi Khoie, S. M.; Liu, K. H. The role of brookite in mechanical activation of anatase-to-rutile transformation of nanocrystalline TiO₂: An XRD and Raman spectroscopy investigation. *Cryst. Eng. Comm.* **2011**, *13* (16), 5055. DOI: 10.1039/c1ce05185g.
- (8) Tompsett, G. A.; Bowmaker, G. A.; Cooney, R. P.; Metson, J. B.; Rodgers, K. A.; Seakins, J. M. The Raman spectrum of brookite, TiO₂ (Pbc₂, Z = 8). *J. Raman Spectrosc.* **1995**, *26* (1), 57–62. DOI: 10.1002/jrs.1250260110.
- (9) Bersani, D.; Antonioli, G.; Lottici, P. P.; Lopez, T. Raman study of nanosized titania prepared by sol–gel route. *J. Non-Cryst. Solids* **1998**, *232–234*, 175–181. DOI: 10.1016/S0022-3093(98)00489-X.
- (10) Djaoued, Y.; Brüning, R.; Bersani, D.; Lottici, P. P.; Badilescu, S. Sol–gel nanocrystalline brookite-rich titania films. *Mater. Lett.* **2004**, *58* (21), 2618–2622. DOI: 10.1016/j.matlet.2004.03.034.
- (11) Kandiel, T. A.; Robben, L.; Alkaim, A.; Bahnemann, D. Brookite versus anatase TiO₂ photocatalysts: phase transformations and photocatalytic activities. *Photochem. Photobiol. Sci.* **2013**, *12* (4), 602–609. DOI: 10.1039/c2pp25217a.
- (12) Tomić, N.; Grujić-Brojčin, M.; Finčurb, N.; Abramović, B.; Simović, B.; Krstić, J.; Matović, B.; Šćepanović, M. Photocatalytic degradation of alprazolam in water suspension of brookite type TiO₂ nanopowders prepared using hydrothermal route. *Mater. Chem. Phys.* **2015**, *163*, 518–528. DOI: 10.1016/j.matchemphys.2015.08.008.
- (13) Vuong, T. H.; Radnik, J.; Schneider, M.; Atia, H.; Armbruster, U.; Brückner, A. Effect of support synthesis methods on structure and performance of VO_x/CeO₂ catalysts in low-temperature NH₃-SCR of NO. *Catal. Commun.* **2016**, *84*, 171–174. DOI: 10.1016/j.catcom.2016.07.002.
- (14) Xin, X.; Xu, T.; Wang, L.; Wang, C. Ti³⁺-self doped brookite TiO₂ single-crystalline nanosheets with high solar absorption and excellent photocatalytic CO₂ reduction. *Sci. Rep.* **2016**, *6*, 23684. DOI: 10.1038/srep23684.
- (15) Zhao, H.; Liu, L.; Andino, J. M.; Li, Y. Bicrystalline TiO₂ with controllable anatase–brookite phase content for enhanced CO₂ photoreduction to fuels. *J. Mater. Chem. A* **2013**, *1* (28), 8209. DOI: 10.1039/c3ta11226h.
- (16) El-Sheikh, S. M.; Zhang, G.; El-Hosainy, H. M.; Ismail, A. A.; O'Shea, K. E.; Falaras, P.; Kontos, A. G.; Dionysiou, D. D. High performance sulfur, nitrogen and carbon doped mesoporous anatase-brookite TiO₂ photocatalyst for the removal of microcystin-LR under visible light irradiation. *J. Hazard. Mater.* **2014**, *280*, 723–733. DOI: 10.1016/j.jhazmat.2014.08.038.
- (17) Hou, H.; Shang, M.; Wang, L.; Li, W.; Tang, B.; Yang, W. Efficient Photocatalytic Activities of TiO₂ Hollow Fibers with Mixed Phases and Mesoporous Walls. *Sci. Rep.* **2015**, *5*, 15228. DOI: 10.1038/srep15228.
- (18) Ohno, T.; Tokieda, K.; Higashida, S.; Matsumura, M. Synergism between rutile and anatase TiO₂ particles in photocatalytic oxidation of naphthalene. *Appl. Catal. A. Gen.* **2003**, *244* (2), 383–391. DOI: 10.1016/S0926-860X(02)00610-5.
- (19) Pelletier, M. J. Quantitative analysis using Raman spectrometry. *Appl. Spectrosc.* **2003**, *57* (1), 20A–42A. DOI: 10.1366/000370203321165133.
- (20) Ramoji, A.; Galler, K.; Glaser, U.; Henkel, T.; Mayer, G.; Dellith, J.; Bauer, M.; Popp, J.; Neugebauer, U. Characterization of different substrates for Raman spectroscopic imaging of eukaryotic cells. *J. Raman Spectrosc.* **2016**, *47* (7), 773–786. DOI: 10.1002/jrs.4899.

- (21) Gasparov, L.; Jegorel, T.; Loetgering, L.; Middey, S.; Chakhalian, J. Thin film substrates from the Raman spectroscopy point of view. *J. Raman Spectrosc.* **2014**, *45* (6), 465–469. DOI: 10.1002/jrs.4487.
- (22) Kiefer, J.; Noack, K.; Leipertz, A. Background suppression for raman analysis of pharmaceutically active compounds in fluorescing media. *Am. Pharmaceut. Rev.* **2013**, *16* (4).
- (23) Krishna, H.; Majumder, S. K.; Gupta, P. K. Range-independent background subtraction algorithm for recovery of Raman spectra of biological tissue. *J. Raman Spectrosc.* **2012**, *43* (12), 1884–1894. DOI: 10.1002/jrs.4127.
- (24) Vickers, T. J.; Wambles, R. E.; Mann, C. K. Curve Fitting and Linearity: Data Processing in Raman Spectroscopy. *Appl. Spectrosc.* **2001**, *55* (4), 389–393.
- (25) Cordero, E.; Korinth, F.; Stiebing, C.; Krafft, C.; Schie, I. W.; Popp, J. Evaluation of Shifted Excitation Raman Difference Spectroscopy and Comparison to Computational Background Correction Methods Applied to Biochemical Raman Spectra. *Sensors (Basel, Switzerland)* **2017**, *17* (8). DOI: 10.3390/s17081724.
- (26) *Wire(TM) [Software]*; Renishaw plc, Spectroscopy Products Division, 2017.
- (27) Liu, S.; Yu, J.; Wang, W. Effects of annealing on the microstructures and photoactivity of fluorinated N-doped TiO₂. *Phys. Chem. Chem. Phys.* **2010**, *12* (38), 12308–12315. DOI: 10.1039/c0cp00036a.
- (28) Zhang, J.; Chen, X.; Shen, Y.; Li, Y.; Hu, Z.; Chu, J. Synthesis, surface morphology, and photoluminescence properties of anatase iron-doped titanium dioxide nano-crystalline films. *Phys. Chem. Chem. Phys.* **2011**, *13* (28), 13096–13105. DOI: 10.1039/c0cp02924f.
- (29) Zeng, G.; Li, K.-K.; Yang, H.-G.; Zhang, Y.-H. Micro-Raman mapping on an anatase TiO₂ single crystal with a large percentage of reactive (001) facets. *Vib. Spectrosc.* **2013**, *68*, 279–284. DOI: 10.1016/j.vibspec.2013.08.012.
- (30) Bertoni, G.; Beyers, E.; Verbeeck, J.; Mertens, M.; Cool, P.; Vansant, E. F.; van Tendeloo, G. Quantification of crystalline and amorphous content in porous samples from electron energy loss spectroscopy. *Ultramicroscopy* **2006**, *106* (7), 630–635. DOI: 10.1016/j.ultramic.2006.03.006.
- (31) Trenczek-Zajac, A.; Rekas, M. Electrical properties of Nb-doped titanium dioxide TiO₂ at room temperature. *Mater Sci-Poland* **2006**, *24* (1), 53–60.
- (32) Liu, Y.; Szeifert, J. M.; Feckl, J. M.; Mandlmeier, B.; Rathousky, J.; Hayden, O.; Fattakhova-Rohlfing, D.; Bein, T. Niobium-doped titania nanoparticles: synthesis and assembly into mesoporous films and electrical conductivity. *ACS nano* **2010**, *4* (9), 5373–5381. DOI: 10.1021/nn100785j.
- (33) Mei, B.; Sánchez, M. D.; Reinecke, T.; Kaluza, S.; Xia, W.; Muhler, M. The synthesis of Nb-doped TiO₂ nanoparticles by spray drying: an efficient and scalable method. *J. Mater. Chem.* **2011**, *21* (32), 11781. DOI: 10.1039/c1jm11431j.
- (34) Frey, H.; Kienel, G. *Dünnschichttechnologie*; VDI Verlag, 1987.
- (35) Mazzi, A. Modeling and production of metal nanoparticles through laser ablation and applications to photocatalytic water oxidation. Dissertation, University of Trento,, Trento, Italy, 2017.
- (36) Filipov, O. Correlation of particle fluxes and film properties deposited by vacuum arc. Dissertation, University of Duisburg-Essen, Duisburg, Germany, 2013.
- (37) Sauerbrey, G. Verwendung von Schwingquarzen zur Wgung dner Schichten und zur Mikrowgung. *Z. Physik* **1959**, *155* (2), 206–222. DOI: 10.1007/BF01337937.
- (38) Kanazawa, K. K. Some basics for operating and analyzing data using the thickness shear mode resonator. *The Analyst* **2005**, *130* (11), 1459–1464. DOI: 10.1039/b506691n.
- (39) Janshoff, A.; Steinem, C. *Piezoelectric Sensors*, Vol. 5; Springer Berlin Heidelberg, 2007. DOI: 10.1007/978-3-540-36568-6.
- (40) Haefel, R. A. *Oberflächen- und Dünnschicht-Technologie:Teil I: Beschichtungen von Oberflächen*; WFT Werkstoff-Forschung und -Technik, Vol. 5; Springer Berlin Heidelberg, 1987.
- (41) Ziegler, J. F.; Biersack, J.; Ziegler, M. D. *SRIM - the stopping and range of ions in matter*; SRIM, 2015.
- (42) Jacob, W. Surface reactions during growth and erosion of hydrocarbon films. *Thin Solid Films* **1998**, *326* (1-2), 1–42. DOI: 10.1016/S0040-6090(98)00497-0.
- (43) Itoh, T. *Ion Beam Assisted Film Growth*; Beam Modification of Materials, v. 3; Elsevier Science, 2014.
- (44) Dzur, B. *Grundlagen der Oberflächentechnik:Physikalische Verfahren, Teil 2*. http://www.tuilmenau.de/fakei/fileadmin/template/fg/wt_pot/lehre/PhV-Handout-Teil2.pdf (accessed 2010-08-22).
- (45) Hawkeye, M. M.; Taschuk, M. T.; Brett, M. J. *Glancing angle deposition of thin films:Engineering the nanoscale*; Wiley series in materials for electronic and optoelectronic applications; Wiley, C 2014.

- (46) Thornton, J. A. High Rate Thick Film Growth. *Annu. Rev. Mater. Sci.* **1977**, *7* (1), 239–260. DOI: 10.1146/annurev.ms.07.080177.001323.
- (47) Zeeshan, A. Growth, transport, and magnetic properties of oblique-angle-deposited permalloy thin films. Master's thesis, Miami University, Miami, United States of America, 2018. https://www.researchgate.net/publication/334683586_GROWTH_TRANSPORT_AND_MAGNETIC_PROPERTIES_OF_OBLIQUE-ANGLE_DEPOSITED_PERMALLOY_THIN_FILMS (accessed 2020-03-21).
- (48) Mazza, T.; Barborini, E.; Piseri, P.; Milani, P.; Cattaneo, D.; Li Bassi, A.; Bottani, C. E.; Ducati, C. Raman spectroscopy characterization of TiO₂ rutile nanocrystals. *Phys. Rev. B* **2007**, *75* (4). DOI: 10.1103/PhysRevB.75.045416.
- (49) El Goresy, A.; Dubrovinsky, L.; Gillet, P.; Graup, G.; Chen, M. Akaogiite: An ultra-dense polymorph of TiO₂ with the baddeleyite-type structure, in shocked garnet gneiss from the Ries Crater, Germany. *American Mineralogist* **2010**, *95* (5-6), 892–895. DOI: 10.2138/am.2010.3425.
- (50) Cacciato, G.; Zimbone, M.; Ruffino, F.; Grimaldi, M. G. TiO₂ Nanostructures and Nanocomposites for Sustainable Photocatalytic Water Purification. In *Green Nanotechnology - Overview and Further Prospects*; Larramendy, M. L., Soloneski, S., Eds.; InTech, 2016. DOI: 10.5772/62620.
- (51) Ola, O.; Maroto-Valer, M.M. Review of material design and reactor engineering on TiO₂ photocatalysis for CO₂ reduction. *Journal of Photochemistry and Photobiology C: Photochemistry Reviews* **2015**, *24*, 16–42. DOI: 10.1016/j.jphotochemrev.2015.06.001.
- (52) Bundesmann, C.; Lautenschläger, T.; Spemann, D.; Finzel, A.; Thelander, E.; Mensing, M.; Frost, F. Systematic investigation of the properties of TiO₂ films grown by reactive ion beam sputter deposition. *Applied Surface Science* **2017**, *421*, 331–340. DOI: 10.1016/j.apsusc.2016.08.056.
- (53) Mergel, D.; Buschendorf, D.; Eggert, S.; Grammes, R.; Samset, B. Density and refractive index of TiO₂ films prepared by reactive evaporation. *Thin Solid Films* **2000**, *371* (1-2), 218–224. DOI: 10.1016/S0040-6090(00)01015-4.
- (54) Moellmann, J.; Ehrlich, S.; Tonner, R.; Grimme, S. A DFT-D study of structural and energetic properties of TiO₂ modifications. *Journal of physics. Condensed matter : an Institute of Physics journal* **2012**, *24* (42), 424206. DOI: 10.1088/0953-8984/24/42/424206.
- (55) Spickermann, D. *Werkstoffe der Bauelemente der Elektrotechnik und Elektronik*; Vogel-Verlag, 1978.
- (56) Furubayashi, Y.; Hitosugi, T.; Yamamoto, Y.; Inaba, K.; Kinoda, G.; Hirose, Y.; Shimada, T.; Hasegawa, T. A transparent metal: Nb-doped anatase TiO₂. *Appl. Phys. Lett.* **2005**, *86* (25), 252101. DOI: 10.1063/1.1949728.
- (57) Hitosugi, T.; Kamisaka, H.; Yamashita, K.; Nogawa, H.; Furubayashi, Y.; Nakao, S.; Yamada, N.; Chikamatsu, A.; Kumigashira, H.; Oshima, M.; Hirose, Y.; Shimada, T.; Hasegawa, T. Electronic Band Structure of Transparent Conductor: Nb-Doped Anatase TiO₂. *Appl. Phys. Express* **2008**, *1*, 111203. DOI: 10.1143/APEX.1.111203.
- (58) Mazzolini, P.; Russo, V.; Casari, C. S.; Hitosugi, T.; Nakao, S.; Hasegawa, T.; Li Bassi, A. Vibrational–Electrical Properties Relationship in Donor-Doped TiO₂ by Raman Spectroscopy. *J. Phys. Chem. C* **2016**, *120* (33), 18878–18886. DOI: 10.1021/acs.jpcc.6b05282.
- (59) Choudhury, B.; Verma, R.; Choudhury, A. Oxygen defect assisted paramagnetic to ferromagnetic conversion in Fe doped TiO₂ nanoparticles. *RSC Adv* **2014**, *4* (55), 29314. DOI: 10.1039/c3ra45286g.
- (60) Golubović, A.; Tomić, N.; Finčur, N.; Abramović, B.; Veljković, I.; Zdravković, J.; Grujić-Brojčin, M.; Babić, B.; Stojadinović, B.; Šćepanović, M. Synthesis of pure and La-doped anatase nanopowders by sol–gel and hydrothermal methods and their efficiency in photocatalytic degradation of alprazolam. *Ceramics International* **2014**, *40* (8), 13409–13418. DOI: 10.1016/j.ceramint.2014.05.060.
- (61) Lan, T.; Tang, X.; Fultz, B. Phonon anharmonicity of rutile TiO₂ studied by Raman spectrometry and molecular dynamics simulations. *Phys. Rev. B* **2012**, *85* (9), 279. DOI: 10.1103/PhysRevB.85.094305.
- (62) Anderson, A., Ed. *The Raman effect*; Dekker, 1971.
- (63) DARWIN, C. G. A Quantum Theory of Optical Dispersion. *Nature* **1922**, *110* (2773), 841–842. DOI: 10.1038/110841a0.
- (64) DARWIN, C. G. The Wave Theory and the Quantum Theory. *Nature* **1923**, *111* (2797), 771–773. DOI: 10.1038/111771b0.
- (65) Smekal, A. Zur Quantentheorie der Dispersion. *Naturwissenschaften* **1923**, *11* (43), 873–875. DOI: 10.1007/bf01576902.

- (66) Chimenti, R. V. Excitation source parameters dictate Raman spectroscopy outcomes. *Laser Focus World* **2017**, 77–79.
- (67) Gohn, P. Aufbau und didaktische Aufbereitung eines Experimentes zum Ramanereffekt, im Rahmen des Fortgeschrittenenpraktikum. Scientific work for the state examination in physics, Albert-Ludwigs-Universität Freiburg, Freiburg, 2011. <http://docplayer.org/3541685-Aufbau-und-didaktische-aufbereitung-eines-experimentes-zum-ramanereffekt-im-rahmen-des-fortgeschrittenenpraktikum.html> (accessed 2020-02-23).
- (68) Schilling, H. *Festkörperphysik: Physik in Beispielen*; VEB Fachbuchverlag, 1977.
- (69) Champion, P. M.; Albrecht, A. C. Resonance Raman Scattering: The Multimode Problem and Transform Methods. *Annu. Rev. Phys. Chem.* **1982**, 33 (1), 353–376. DOI: 10.1146/annurev.pc.33.100182.002033.
- (70) Lewis, I. R. *Handbook of Raman spectroscopy: From the research laboratory to the process line*; Practical spectroscopy, Vol. 28; CRC Pr, 2001.
- (71) Wu, G. *Vibrational spectroscopy*; De Gruyter graduate; De Gruyter, 2019.
- (72) Anderson, A. *Principles*; The Raman effect / ed. by A. Anderson, vol. 1; Dekker, 1971.
- (73) Ohsaka, T.; Izumi, F.; Fujiki, Y. Raman spectrum of anatase, TiO₂. *J. Raman Spectrosc.* **1978**, 7 (6), 321–324. DOI: 10.1002/jrs.1250070606.
- (74) Frank, O.; Zikalova, M.; Laskova, B.; Kürti, J.; Koltai, J.; Kavan, L. Raman spectra of titanium dioxide (anatase, rutile) with identified oxygen isotopes (16, 17, 18). *Physical chemistry chemical physics: PCCP* **2012**, 14 (42), 14567–14572. DOI: 10.1039/c2cp42763j.
- (75) Iliiev, M. N.; Hadjiev, V. G.; Litvinchuk, A. P. Raman and infrared spectra of brookite (TiO₂): Experiment and theory. *Vibrational Spectroscopy* **2013**, 64, 148–152. DOI: 10.1016/j.vibspec.2012.08.003.
- (76) S. P. S. Porto; P. A. Fleury; T. C. Damen. Raman Spectra of TiO₂, MgF₂, ZnF₂, FeF₂, and MnF₂. *Physical Review* **1967** (154, 2), 522–526.
- (77) Georgescu, D.; Baia, L.; Ersen, O.; Baia, M.; Simon, S. Experimental assessment of the phonon confinement in TiO₂ anatase nanocrystallites by Raman spectroscopy. *J. Raman Spectrosc.* **2012**, 43 (7), 876–883. DOI: 10.1002/jrs.3103.
- (78) Sahoo, S.; Arora, A. K.; Sridharan, V. Raman Line Shapes of Optical Phonons of Different Symmetries in Anatase TiO₂ Nanocrystals. *J. Phys. Chem. C* **2009**, 113 (39), 16927–16933. DOI: 10.1021/jp9046193.
- (79) Spanier, J. E.; Robinson, R. D.; Zhang, F.; Chan, S.-W.; Herman, I. P. Size-dependent properties of CeO₂-y nanoparticles as studied by Raman scattering. *Physical review. B, Condensed matter* **2001**, 64 (24), 307. DOI: 10.1103/PhysRevB.64.245407.
- (80) Campbell, I. H.; Fauchet, P. M. The effects of microcrystal size and shape on the one phonon Raman spectra of crystalline semiconductors. *Solid State Communications* **1986**, 58 (10), 739–741. DOI: 10.1016/0038-1098(86)90513-2.
- (81) Yin, W.-J.; Chen, S.; Yang, J.-H.; Gong, X.-G.; Yan, Y.; Wei, S.-H. Effective band gap narrowing of anatase TiO₂ by strain along a soft crystal direction. *Appl. Phys. Lett.* **2010**, 96 (22), 221901. DOI: 10.1063/1.3430005.
- (82) Joel W. Ager; III; D. Kirk Veirs; and Gerd M. Rosenblatt. Spatially resolved Raman studies of diamond films grown by chemical vapor deposition.
- (83) Gouadec, G.; Colombari, P. Raman Spectroscopy of nanomaterials: How spectra relate to disorder, particle size and mechanical properties. *Progress in Crystal Growth and Characterization of Materials* **2007**, 53 (1), 1–56. DOI: 10.1016/j.pcrysgrow.2007.01.001.
- (84) Dhanalakshmi, J.; Iyyapushpam, S.; Nishanthi, S. T.; Malligavathy, M.; Pathinettam Padiyan, D. Investigation of oxygen vacancies in Ce coupled TiO₂ nanocomposites by Raman and PL spectra. *Adv. Nat. Sci: Nanosci. Nanotechnol.* **2017**, 8 (1), 15015. DOI: 10.1088/2043-6254/aa5984.
- (85) Parker, J. C.; Siegel, R. W. Calibration of the Raman spectrum to the oxygen stoichiometry of nanophase TiO₂. *Appl. Phys. Lett.* **1990**, 57 (9), 943–945. DOI: 10.1063/1.104274.
- (86) Swamy, V.; Kuznetsov, A.; Dubrovinsky, L. S.; Caruso, R. A.; Shchukin, D. G.; Muddle, B. C. Finite-size and pressure effects on the Raman spectrum of nanocrystalline anatase TiO₂. *Phys. Rev. B* **2005**, 71 (18), 735. DOI: 10.1103/PhysRevB.71.184302.
- (87) Scepanovic, M.; Grujic-Brojcin, M.; Dohcevic-Mitrovic, Z. D.; Popovic, Z. V. Characterization of anatase TiO₂ nanopowder by variable-temperature Raman spectroscopy. *Sci Sintering* **2009**, 41 (1), 67–73. DOI: 10.2298/SOS0901067S.
- (88) Ohsaka, T. Temperature Dependence of the Raman Spectrum in Anatase TiO₂.

- (89) Hearne, G. R.; Zhao, J.; Dawe, A. M.; Pishedda, V.; Maaza, M.; Nieuwoudt, M. K.; Kibasomba, P.; Nemraoui, O.; Comins, J. D.; Witcomb, M. J. Effect of grain size on structural transitions in anatase TiO₂: A Raman spectroscopy study at high pressure. *Journal of Molecular Structure* **2004**, *70* (13), 717. DOI: 10.1103/PhysRevB.70.134102.
- (90) Bersani, D.; Lottici, P. P.; Ding, X.-Z. Phonon confinement effects in the Raman scattering by TiO₂ nanocrystals. *Appl. Phys. Lett.* **1998**, *72* (1), 73–75. DOI: 10.1063/1.120648.
- (91) S., A. B.; S., C. V.; S., N. C.; P., R. M.; S., J. H.; Lamani, A. R. Influence of particle size on band gap and dielectric properties of TiO₂ nanomaterials. In *INTERNATIONAL CONFERENCE ON CONDENSED MATTER AND APPLIED PHYSICS (ICC 2015): Proceeding of International Conference on Condensed Matter and Applied Physics*; Author(s), 2016; p 20347. DOI: 10.1063/1.4946398.
- (92) Guang-Lei, T.; Hong-Bo, H.; Jian-Da, S. Effect of Microstructure of TiO₂ Thin Films on Optical Band Gap Energy. *Chinese Phys. Lett.* **2005**, *22* (7), 1787–1789. DOI: 10.1088/0256-307X/22/7/062.
- (93) Li, W.; Liang, R.; Hu, A.; Huang, Z.; Zhou, Y. N. Generation of oxygen vacancies in visible light activated one-dimensional iodine TiO₂ photocatalysts. *RSC Adv* **2014**, *4* (70), 36959–36966. DOI: 10.1039/C4RA04768K.
- (94) Alhomoudi, I. A.; Newaz, G. Residual stresses and Raman shift relation in anatase TiO₂ thin film. *Thin Solid Films* **2009**, *517* (15), 4372–4378. DOI: 10.1016/j.tsf.2009.02.141.
- (95) Uchinokura, K.; Sekine, T.; Matsuura, E. Raman scattering by silicon. *Solid State Communications* **1972**, *11* (1), 47–49. DOI: 10.1016/0038-1098(72)91127-1.
- (96) Pecharsky, Vitaij, K.; Zavalij, P. Y. *Fundamentals of Powder Diffraction and Structural Characterization of Materials*; Springer US, 2009. DOI: 10.1007/978-0-387-09579-0.
- (97) Bragg, W. L. The Diffraction of Short Electromagnetic Waves by a Crystal. *Proceedings of the Cambridge Philosophical Society* **1913** (17), 43–57.
- (98) Scherrer, P. Bestimmung der Größe und der inneren Struktur von Kolloidteilchen mittels Röntgenstrahlen. In *Nachrichten von der Königlichen Gesellschaft der Wissenschaften zu Göttingen: Mathematisch-Physikalische Klasse*; Kaestner W. Fr., Ed.; Vandenhoeck & Ruprecht, 1918; pp 98–100.
- (99) Langford, J. I.; Wilson, A. J. C. Scherrer after sixty years: A survey and some new results in the determination of crystallite size. *J Appl Crystallogr* **1978**, *11* (2), 102–113. DOI: 10.1107/S0021889878012844.
- (100) Cowley, J. M. *Diffraction Physics*, 3rd ed.; Elsevier Science BV, 1995.
- (101) Williamson, G.K.; Hall, W.H. X-ray line broadening from filed aluminium and wolfram. *Acta Metallurgica* **1953**, *1* (1), 22–31. DOI: 10.1016/0001-6160(53)90006-6.
- (102) Shi, J. Strukturelle und optische Eigenschaften von RF-Dioden-gesputterten TiO₂-Schichten der Dicke von 2 bis 200 nm. Masterarbeit, University of Duisburg-Essen, Duisburg, 2015.
- (103) Jerman, M.; Mergel, D. Structural investigation of thin TiO₂ films prepared by evaporation and post - heating. *Thin Solid Films* **2007**, *515* (17), 6904–6908. DOI: 10.1016/j.tsf.2007.01.038.
- (104) Mukherjee, S. K.; Becker, H. W.; Cadiz Bedini, A. P.; Nebatti, A.; Notthoff, C.; Rogalla, D.; Schipporeit, S.; Soleimani-Esfahani, A.; Mergel, D. Structural and electrical properties of Nb-doped TiO₂ films sputtered with plasma emission control. *Thin Solid Films* **2014**, *568*, 94–101. DOI: 10.1016/j.tsf.2014.08.011.
- (105) Mukherjee, S. K.; Nebatti, A.; Mohtascham, F.; Schipporeit, S.; Notthoff, C.; Mergel, D. Influence of thickness on the structural properties of radio-frequency and direct-current magnetron sputtered TiO₂ anatase thin films. *Thin Solid Films* **2014**, *558*, 443–448. DOI: 10.1016/j.tsf.2014.02.048.
- (106) Shixun Cui. Sputter-deposited thin oxide films. Master's Thesis, University of Duisburg-Essen, Duisburg, 2015.
- (107) Giarola, M.; Sanson, A.; Monti, F.; Mariotto, G.; Bettinelli, M.; Speghini, A.; Salviulo, G. Vibrational dynamics of anatase TiO₂: Polarized Raman spectroscopy and ab initio calculations. *Phys. Rev. B* **2010**, *81* (17), 304. DOI: 10.1103/PhysRevB.81.174305.
- (108) Einasto, M.; Liivamagi, L. J.; Saar, E.; Einasto, J.; Tempel, E.; Tago, E.; Martinez, V. J. SDSS DR7 superclusters. Principal component analysis. *A&A* **2011**, *535*, A36. DOI: 10.1051/0004-6361/201117529.
- (109) Dieing, T.; Henrich, M.; Breuninger, S. Key Elements of Confocal Raman Microscopy for High-Resolution Imaging. *Spectroscopy* **2014**, *29* (s6), 42–54.
- (110) Adar, F.; Lee, E.; Mamedov, S.; Whitley, A. Raman Imaging: Defining the Spatial Resolution of the Technology. *Spectroscopy* **2006**, 18–24.

- (111) Gettings, R. J.; Trahay, N. M.; Freiman, S. W. *Certificate Standard Reference Material® 660a:Lanthanum Hexaboride Powder Line Position and Line Shape Standard for Powder Diffraction*. <https://www-s.nist.gov/srmors/certificates/archives/660a.pdf> (accessed 2020-02-27).
- (112) Clegg, I. M.; Everall, N. J.; King, B.; Melvin, H.; Norton, C. On-Line Analysis Using Raman Spectroscopy for Process Control during the Manufacture of Titanium Dioxide. *Appl. Spectrosc.* **2001**, *55* (9), 1138–1150. DOI: 10.1366/0003702011953388.
- (113) Beuvier, T.; Richard-Plouet, M.; Brohan, L. Accurate Methods for Quantifying the Relative Ratio of Anatase and TiO₂ (B) Nanoparticles. *J. Phys. Chem. C* **2009**, *113* (31), 13703–13706. DOI: 10.1021/jp903755p.
- (114) Castrejón Sánchez, V. H.; Camps, E.; Camacho-Lopez, M. Quantification of phase content in TiO₂ thin films by Raman spectroscopy. *Superficies y Vacío* **2014** (27), 88–92.
- (115) Mergel, D. *Physik mit Excel und Visual Basic: Grundlagen, Beispiele und Aufgaben*. ISBN: 978-3-642-37856-0; Springer Spektrum, 2017.
- (116) Balkanski, M.; Wallis, R. F.; Haro, E. Anharmonic effects in light scattering due to optical phonons in silicon. *Phys. Rev. B* **1983**, *28* (4), 1928–1934. DOI: 10.1103/PhysRevB.28.1928.
- (117) Alim, K. A.; Fonoberov, V. A.; Balandin, A. A. Origin of the optical phonon frequency shifts in ZnO quantum dots. *Appl. Phys. Lett.* **2005**, *86* (5), 53103. DOI: 10.1063/1.1861509.
- (118) Klemens, P. G. Anharmonic Decay of Optical Phonons. *Phys. Rev.* **1966**, *148* (2), 845–848. DOI: 10.1103/PhysRev.148.845.
- (119) Ridley, B. K. The LO phonon lifetime in GaN. *J. Phys.: Condens. Matter* **1996**, *8* (37), L511–L513. DOI: 10.1088/0953-8984/8/37/001.
- (120) Yadav, H. K.; Sreenivas, K.; Katiyar, R. S.; Gupta, V. Defect induced activation of Raman silent modes in rf co-sputtered Mn doped ZnO thin films. *J. Phys. D: Appl. Phys.* **2007**, *40* (19), 6005–6009. DOI: 10.1088/0022-3727/40/19/034.
- (121) Dresselhaus, M. S.; Jorio, A.; Souza Filho, A. G.; Saito, R. Defect characterization in graphene and carbon nanotubes using Raman spectroscopy. *Philosophical transactions. Series A, Mathematical, physical, and engineering sciences* **2010**, *368* (1932), 5355–5377. DOI: 10.1098/rsta.2010.0213.
- (122) Saviot, L.; Machon, D.; Debbichi, L.; Girard, A.; Margueritat, J.; Krüger, P.; Marco de Lucas, M. C.; Mermet, A. Optical and Acoustic Vibrations Confined in Anatase TiO₂ Nanoparticles under High-Pressure. *J. Phys. Chem. C* **2014**, *118* (19), 10495–10501. DOI: 10.1021/jp502409e.
- (123) Zhang, X.; Qiao, X.-F.; Shi, W.; Wu, J.-B.; Jiang, D.-S.; Tan, P.-H. Phonon and Raman scattering of two-dimensional transition metal dichalcogenides from monolayer, multilayer to bulk material. *Chem. Soc. Rev.* **2015**, *44* (9), 2757–2785. DOI: 10.1039/c4cs00282b. Published Online: Feb. 3, 2015.
- (124) Kontos, A. I.; Kontos, A. G.; Raptis, Y. S.; Falaras, P. Nitrogen modified nanostructured titania: Electronic, structural and visible - light photocatalytic properties. *Phys. Status Solidi (RRL)* **2008**, *2* (2), 83–85. DOI: 10.1002/pssr.200802006.
- (125) Thompson, W. *RRUFF Project [Internet]: Brookite R050591*. <http://rruff.info/Brookite/R050591> (accessed 2017 Jul 1).
- (126) Shigley, J. *RRUFF Project [Internet]: Anatase R070582*. <http://rruff.info/Anatase/R070582> (accessed 2017 Jul 1).
- (127) Shigley, J. *RRUFF Project [Internet]: Rutile R110109*. <http://rruff.info/Rutile/R110109> (accessed 2017 Jul 1).
- (128) Bob Downs. *RRUFF Project [Internet]*. <http://rruff.info/> (accessed 2017 Jul 1).
- (129) Nicola, J. H.; Brunharoto, C. A.; Abramovich, M.; Gonçalves da Silva, C. E. T. Second order Raman spectrum of rutile TiO₂. *J. Raman Spectrosc.* **1979**, *8* (1), 32–34. DOI: 10.1002/jrs.1250080108.
- (130) Furukawa, T.; White, W. B. Raman spectroscopic investigation of sodium borosilicate glass structure. *J. Mater. Sci.* **1981**, *16* (10), 2689–2700. DOI: 10.1007/BF00552951.
- (131) McMillan, P. A Raman spectroscopic study of glasses in the system CaO-MgO-SiO₂. *American Mineralogist* **1984** (69), 645–659.
- (132) McMillan, P. Structural studies of silicate glasses and melts - applications and limitations of Raman spectroscopy. *American Mineralogist* **1984** (69), 622–644.
- (133) Richet, P.; Mysen, B. O.; Andrault, D. Melting and premelting of silicates: Raman spectroscopy and X-ray diffraction of Li₂SiO₃ and Na₂SiO₃. *Appl. Spectrosc.* **1996** (23), 157–172.

- (134) Seuthe, T.; Grehn, M.; Mermillod-Blondin, A.; Eichler, H. J.; Bonse, J.; Eberstein, M. Structural modifications of binary lithium silicate glasses upon femtosecond laser pulse irradiation probed by micro-Raman spectroscopy. *Opt. Mater. Express* **2013**, *3* (6), 755. DOI: 10.1364/OME.3.000755.
- (135) Seuthe, T.; Grehn, M.; Mermillod-Blondin, A.; Bonse, J.; Eberstein, M. Compositional dependent response of silica-based glasses to femtosecond laser pulse irradiation. In *SPIE Laser Damage*; Exarhos, G. J., Gruzdev, V. E., Menapace, J. A., Ristau, D., Soileau, M. J., Eds.; SPIE, 2013; 88850M. DOI: 10.1117/12.2028713.
- (136) Toshiharu, F.; White, W. B. Raman spectroscopic investigation of sodium borosilicate glass structure. *J. Mater. Sci.* **1981** (16), 2689–2700.
- (137) Ecole normale supérieure de Lyon. *Handbook of Minerals Raman Spectra*. <http://www.ens-lyon.fr/LST/Raman/spectrum.php?nom=rutile> (accessed 2019-03-05).
- (138) Röhr, C. Werner Massa: Kristallstrukturbestimmung. Teubner-Verlag, Stuttgart, ISBN: 3-5 19-13527-2, DM 32,80. *Berichte der Bunsengesellschaft für physikalische Chemie* **1997**, *101* (3), 640–641. DOI: 10.1002/bbpc.19971010344.
- (139) Leroy, Alexander and H. P. Klug. Basic Aspects of X-Ray Absorption in Quantitative Diffraction Analysis of Powder Mixtures.
- (140) CHERGUI, M. Charge Carrier and Phonon Dynamics in Transition Metal Oxide and in Lead-Halide Perovskite Nanoparticles. In *Proceedings of the nanoGe Fall Meeting 2018*; Boettcher, S., Delerue, C., Egger, D., Herz, L., Jaegermann, W., Kaiser, B., Puiggollers, J., Vanmaekelbergh, D., Costa, R. D., Hens, Z., Houtepen, A., Ithurria, S., Lian, T., Perez-Rodriguez, A., Sadewasser, S., Sivula, K., Sum, T.-C., Walker, A., Berger, R., Bonn, M., Klinker, C., Quarti, C., Vilatela, J. J., Rabouw, F., Eds.; Fundació Scito: València, 2018 - 2018. DOI: 10.29363/nanoge.fallmeeting.2018.265.
- (141) Leitzke, F. P.; Fonseca, R. O. C.; Göttlicher, J.; Steininger, R.; Jahn, S.; Prescher, C.; Lagos, M. Ti K-edge XANES study on the coordination number and oxidation state of Titanium in pyroxene, olivine, armalcolite, ilmenite, and silicate glass during mare basalt petrogenesis. *Contrib Mineral Petrol* **2018**, *173* (12), 173. DOI: 10.1007/s00410-018-1533-7.
- (142) Spurr & Myers 1956 - Quantitative Analysis of Anatase-Rutile Mixtures with an X-Ray Diffractometer.
- (143) Zanatta, A. R. A fast-reliable methodology to estimate the concentration of rutile or anatase phases of TiO₂. *AIP Advances* **2017**, *7* (7), 75201. DOI: 10.1063/1.4992130.
- (144) Löbl, P.; Huppertz, M.; Mergel, D. Nucleation and growth in TiO₂ films prepared by sputtering and evaporation. *Thin Solid Films* **1994**, *251* (1), 72–79. DOI: 10.1016/0040-6090(94)90843-5.
- (145) Viana, B. C.; Gonçalves, J. S.; Santos, V. d.; Santos, M. R. d. M. C.; Longo, E.; Santos, F. E. P.; Matos, J. M. E. d. Phonon Confinement Model to Measure the Average Sizes of Anatase Nanoparticles Synthesized by a Solvothermal Method Using H₂O₂. *Journal of the Brazilian Chemical Society* **2013**. DOI: 10.5935/0103-5053.20130136.
- (146) Weast, R. C., Ed. *CRC handbook of chemistry and physics: A ready-reference book of chemical and physical data*, 63. ed.; CRC Press, 1983.
- (147) Swanson, H. E.; McMurdie, H. F.; Morris, M. C.; Evans, H. C. *Standard X-Ray Diffraction Powder Patterns*; U.S. Government Printing Office, 1969.
- (148) Gubicza, J. Correlation between Processing Conditions, Lattice Defect Structure and Mechanical Performance of Ultrafine-Grained Materials. *Acta Phys. Pol. A* **2015**, *128* (4), 479–487. DOI: 10.12693/APhysPolA.128.479.
- (149) Inamdar, S.; Ramudu, M.; Raja, M. M.; Kamat, S. V. Effect of process temperature on structure, microstructure, residual stresses and soft magnetic properties of sputtered Fe₇₀Co₃₀ thin films. *Journal of Magnetism and Magnetic Materials* **2016**, *418*, 175–180. DOI: 10.1016/j.jmmm.2016.02.081.
- (150) Keshvani, M. J.; Katba, S.; Jethva, S.; Udeshi, M.; Kataria, B.; Raval, A.; Kuberkar, D. G. Studies on structural, morphological and electroresistance properties of sol-gel grown nanostructured PrMnO₃. *Materials Science and Engineering: B* **2017**, *218*, 40–50. DOI: 10.1016/j.mseb.2017.02.006.
- (151) Iida, Y.; Furukawa, M.; Aoki, T.; Sakai, T. Raman Spectrum of Ultrafine Anatase Powders Derived from Hydrolysis of Alkoxide. *Appl. Spectrosc. (Applied Spectroscopy)* **1998**, *52* (5), 673–678.
- (152) Werninghaus, T.; Hahn, J.; Richter, F.; Zahn, D. R. T. Raman spectroscopy investigation of size effects in cubic boron nitride. *Appl. Phys. Lett.* **1997**, *70* (8), 958–960. DOI: 10.1063/1.118452.
- (153) Kelly, S.; Pollak, F. H.; Tomkiewicz, M. Raman Spectroscopy as a Morphological Probe for TiO₂ Aerogels. *The journal of physical chemistry. B* **1997**, *101* (14), 2730–2734. DOI: 10.1021/jp962747a.

- (154) Richter, H.; Wang, Z. P.; Ley, L. The one phonon Raman spectrum in microcrystalline silicon. *Solid State Communications* **1981**, *39* (5), 625–629. DOI: 10.1016/0038-1098(81)90337-9.
- (155) Zhu, K.-R.; Zhang, M.-S.; Chen, Q.; Yin, Z. Size and phonon-confinement effects on low-frequency Raman mode of anatase TiO₂ nanocrystal. *Physics Letters A* **2005**, *340* (1-4), 220–227. DOI: 10.1016/j.physleta.2005.04.008.
- (156) Doss; Zallen. Raman studies of sol-gel alumina: Finite-size effects in nanocrystalline AlO(OH). *Physical review. B, Condensed matter* **1993**, *48* (21), 15626–15637. DOI: 10.1103/PhysRevB.48.15626.
- (157) Zhao, Y.; Li, C.; Liu, X.; Gu, F.; Jiang, H.; Shao, W.; Zhang, L.; He, Y. Synthesis and optical properties of TiO₂ nanoparticles. *Materials Letters* **2007**, *61* (1), 79–83. DOI: 10.1016/j.matlet.2006.04.010.
- (158) Zi, J.; Büscher, H.; Falter, C.; Ludwig, W.; Zhang, K.; Xie, X. Raman shifts in Si nanocrystals. *Appl. Phys. Lett.* **1996**, *69* (2), 200–202. DOI: 10.1063/1.117371.
- (159) Zi, J.; Zhang, K.; Xie, X. Comparison of models for Raman spectra of Si nanocrystals. *Phys. Rev. B* **1997**, *55* (15), 9263–9266. DOI: 10.1103/PhysRevB.55.9263.
- (160) Zhang, W. F.; He, Y. L.; Zhang, M. S.; Yin, Z.; Chen, Q. Raman scattering study on anatase TiO₂ nanocrystals. *Berichte der Bunsengesellschaft für physikalische Chemie* **2000**, *33* (8), 912–916. DOI: 10.1088/0022-3727/33/8/305.
- (161) Lei, Y.; Zhang, L. D.; Fan, J. C. Fabrication, characterization and Raman study of TiO₂ nanowire arrays prepared by anodic oxidative hydrolysis of TiCl₃. *Chemical Physics Letters* **2001**, *338* (4-6), 231–236. DOI: 10.1016/S0009-2614(01)00263-9.
- (162) Barborini, E.; Kholmanov, I. N.; Piseri, P.; Ducati, C.; Bottani, C. E.; Milani, P. Engineering the nanocrystalline structure of TiO₂ films by aerodynamically filtered cluster deposition. *Appl. Phys. Lett.* **2002**, *81* (16), 3052–3054. DOI: 10.1063/1.1510579.
- (163) Swamy, V. Size-dependent modifications of the first-order Raman spectra of nanostructured rutile TiO₂. *Phys. Rev. B* **2008**, *77* (19), 2891. DOI: 10.1103/PhysRevB.77.195414.
- (164) Ivanda, M.; Musić, S.; Gotić, M.; Turković, A.; Tonejc, A. M.; Gamulin, O. The effects of crystal size on the Raman spectra of nanophase TiO₂. *Journal of Molecular Structure* **1999**, *480-481*, 641–644. DOI: 10.1016/S0022-2860(98)00921-1.
- (165) Ramkumar; Jain; Abbi. Raman-scattering probe of anharmonic effects due to temperature and compositional disorder in III-V binary and ternary alloy semiconductors. *Physical review. B, Condensed matter* **1996**, *53* (20), 13672–13681. DOI: 10.1103/PhysRevB.53.13672.
- (166) Atashbar, M. Z.; Sun, H. T.; Gong, B.; Wlodarski, W.; Lamb, R. XPS study of Nb-doped oxygen sensing TiO₂ thin films prepared by sol-gel method. *Thin Solid Films* **1998**, *326* (1-2), 238–244. DOI: 10.1016/S0040-6090(98)00534-3.
- (167) Afifi, M. A.; Abdel-Aziz, M. M.; Yahia, I. S.; Fadel, M.; Wahab, L. A. Transport properties of polycrystalline TiO₂ and Ti₂O₃ as semiconducting oxides. *Journal of Alloys and Compounds* **2008**, *455* (1-2), 92–97. DOI: 10.1016/j.jallcom.2007.01.156.
- (168) Jacob, K. T.; Raj, S.; Rannesh, L. Vegard's law: a fundamental relation or an approximation? *IJMR* **2007**, *98* (9), 776–779. DOI: 10.3139/146.101545.
- (169) Lagopati, N.; Tsilibary, E.-P.; Falaras, P.; Papazafiri, P.; Pavlatou, E. A.; Kotsopoulou, E.; Kitsiou, P. Effect of nanostructured TiO₂ crystal phase on photoinduced apoptosis of breast cancer epithelial cells. *International journal of nanomedicine* **2014**, *9*, 3219–3230. DOI: 10.2147/IJN.S62972.
- (170) Yan, J.; Wu, G.; Guan, N.; Li, L.; Li, Z.; Cao, X. Understanding the effect of surface/bulk defects on the photocatalytic activity of TiO₂: anatase versus rutile. *Physical chemistry chemical physics : PCCP* **2013**, *15* (26), 10978–10988. DOI: 10.1039/c3cp50927c.
- (171) Tian, F.; Zhang, Y.; Zhang, J.; Pan, C. Raman Spectroscopy: A New Approach to Measure the Percentage of Anatase TiO₂ Exposed (001) Facets. *J. Phys. Chem. C* **2012**, *116* (13), 7515–7519. DOI: 10.1021/jp301256h.
- (172) Gardecka, A. J.; Goh, G. K. L.; Sankar, G.; Parkin, I. P. On the nature of niobium substitution in niobium doped titania thin films by AACVD and its impact on electrical and optical properties. *J. Mater. Chem. A* **2015**, *3* (34), 17755–17762. DOI: 10.1039/c5ta03772g.
- (173) Luttrell, T.; Halpegamage, S.; Tao, J.; Kramer, A.; Sutter, E.; Batzill, M. Why is anatase a better photocatalyst than rutile?—Model studies on epitaxial TiO₂ films. *Sci. Rep.* **2014**, *4*, 4043. DOI: 10.1038/srep04043.

- (174) Mattsson, A.; Leideborg, M.; Larsson, K.; Westin, G.; Osterlund, L. Adsorption and solar light decomposition of acetone on anatase TiO₂ and niobium doped TiO₂ thin films. *The journal of physical chemistry. B* **2006**, *110* (3), 1210–1220. DOI: 10.1021/jp055656z.
- (175) Jellison, G. E. Spectroscopic ellipsometry data analysis: measured versus calculated quantities. *Thin Solid Films* **1998** (313-314), 33–39.
- (176) O’Leary, S. K.; Johnson, S. R.; Lim, P. K. The relationship between the distribution of electronic states and the optical absorption spectrum of an amorphous semiconductor: An empirical analysis. *Journal of Applied Physics* **1997**, *82* (7), 3334–3340. DOI: 10.1063/1.365643.
- (177) Zhaohui Qiao. Fabrication and Study of ITO thin films prepared by Magnetron Sputtering. Dissertation, Duisburg-Essen, Essen, 2003.
- (178) Bubel, S.; Mechau, N.; Hahn, H.; Schmechel, R. Trap states and space charge limited current in dispersion processed zinc oxide thin films. *Journal of Applied Physics* **2010**, *108* (12), 124502. DOI: 10.1063/1.3524184.
- (179) Ahmad, A.; Thiel, J.; Shah, S. I. Structural effects of niobium and silver doping on titanium dioxide nanoparticles. *J. Phys.: Conf. Ser.* **2007**, *61*, 11–15. DOI: 10.1088/1742-6596/61/1/003.
- (180) Hitosugi, T.; Ueda, A.; Nakao, S.; Yamada, N.; Furubayashi, Y.; Hirose, Y.; Konuma, S.; Shimada, T.; Hasegawa, T. Transparent conducting properties of anatase Ti_{0.94}Nb_{0.06}O₂ polycrystalline films on glass substrate. *Thin Solid Films* **2008**, *516* (17), 5750–5753. DOI: 10.1016/j.tsf.2007.10.028.
- (181) Balachandran, U.; Eror, N. G. Raman spectra of titanium dioxide. *Journal of Solid State Chemistry* **1982**, *42* (3), 276–282. DOI: 10.1016/0022-4596(82)90006-8.
- (182) Exarhos, G. J.; Miller, P. J.; Risen, W. M. Interionic vibrations and glass transitions in ionic oxide metaphosphate glasses. *The Journal of Chemical Physics* **1974**, *60* (11), 4145–4155. DOI: 10.1063/1.1680881.
- (183) Exarhos, G. J. Raman determination of molecular structure and physical properties of dielectric coatings. *Journal of Vacuum Science & Technology A: Vacuum, Surfaces, and Films* **1986**, *4* (6), 2962–2968. DOI: 10.1116/1.573609.
- (184) Anitha, V. C.; Banerjee, A. N.; Joo, S. W. Recent developments in TiO₂ as n- and p-type transparent semiconductors: synthesis, modification, properties, and energy-related applications. *J Mater Sci* **2015**, *50* (23), 7495–7536. DOI: 10.1007/s10853-015-9303-7.
- (185) Baszczuk, A.; Jasiorski, M.; Winnicki, M. Low-Temperature Transformation of Amorphous Sol–Gel TiO₂ Powder to Anatase During Cold Spray Deposition. *J Therm Spray Tech* **2018**, *27* (8), 1551–1562. DOI: 10.1007/s11666-018-0769-0.
- (186) Pisarek, M.; Roguska, A.; Marcon, L.; Andrzejczuk, M. Biomimetic and Electrodeposited Calcium-Phosphates Coatings on Ti - Formation, Surface Characterization, Biological Response. In *Biomedical Engineering - Technical Applications in Medicine*; Hudak, R., Ed.; InTech, 2012. DOI: 10.5772/48693.
- (187) Quesada-Cabrera, R.; Sotelo-Vazquez, C.; Bear, J. C.; Darr, J. A.; Parkin, I. P. Photocatalytic Evidence of the Rutile-to-Anatase Electron Transfer in Titania. *Adv. Mater. Interfaces* **2014**, *1* (6), 1400069. DOI: 10.1002/admi.201400069.
- (188) Venkatasubbu, G. D.; Ramakrishnan, V.; Sasirekha, V.; Ramasamy, S.; Kumar, J. Influence of particle size on the phonon confinement of TiO₂ nanoparticles. *Journal of Experimental Nanoscience* **2014**, *9* (7), 661–668. DOI: 10.1080/17458080.2012.689018.
- (189) Gautam, S. K.; Gautam, N.; Singh, R. G.; Ojha, S.; Shukla, D. K.; Singh, F. Anomalous behavior of B_{1g} mode in highly transparent anatase nano-crystalline Nb-doped Titanium Dioxide (NTO) thin films. *AIP Advances* **2015**, *5* (12), 127212. DOI: 10.1063/1.4938085.

List of Figures

Fig. 1: Schematic diagram of an electron beam chamber (adapted from Mazzi ³⁵ and Filipov ³⁶) with a mass flow controller (MFC), quartz crystal monitor (QCM), a turbo-molecular pump (TMP), and a rotary vane pump (RVP).	16
Fig. 2: Schematic representation of the atomistic processes that occur when energetic particles collide with a solid surface. This example shows a collision cascade in hydrocarbon. The incident particles are black, C atoms are white, and H atoms are small black circles. ⁴²	17
Fig. 3: Schematic diagram of a dc-diode sputter coating process. Atoms are marked as white circles, positive ions as circles with a plus sign, and electrons as e ⁻ ; adapted from Frey and Kienel. ³⁴	18
Fig. 4: Schematic diagram of dc-diode sputtering (left) and magnetron sputtering (right). The letters symbolize: (a) recipient wall, (b) substrates, (c) secondary electrons, (d) ions, (e) metal atoms, (f) target, (g) cathode, (h) magnetic field lines, (i) substrate holder, (j) anode, and (k) plasma. Adapted from Frey. ³⁴	19
Fig. 5: Process probability vs. kinetic particle energy of impact atoms resulting from collisions with a solid surface. Adapted from Dzur. ⁴⁴	21
Fig. 6: (a) Structure zone model by Movchan and Demchishin ⁴⁵ (b) Modified structure zone model by Thornton ⁴⁶ , (c) cross-section of the structure zones. Adapted from Zeeshan. ⁴⁷	22
Fig. 7: Unit cell balls and sticks schemes of anatase (left), brookite (mid), rutile (right). Large light spheres represent Ti atoms and small red spheres represent O atoms. Adapted from Moellmann et al. ⁵⁴	24
Fig. 8: Schematic representation of Stokes, Rayleigh, and Anti-Stokes frequencies.	27
Fig. 9: Schematic representations of ultraviolet/visible absorption, fluorescence, infrared absorption, Rayleigh scattering, Stokes Raman scattering, and Anti-Stokes Raman scattering. Taken from Chimenti. ⁶⁶	28
Fig. 10: Anatase vibrational Raman modes of anatase TiO ₂ – 3d vibrations projected to the (200)-plane, based on factor group analysis. ⁷³	34
Fig. 11: Scheme of Raman active atomic vibrations in anatase. Ti atoms are large black and O atoms are small red spheres. The arrows indicate the movements of the atoms. Adopted from Frank et al. ⁷⁴	35
Fig. 12: Scheme of Raman active atomic vibrations in brookite. Ti atoms are light gray and O atoms are red spheres. The green arrows indicate the movements of the atoms. The experimental and DFT values were obtained by Iliev et al. ⁷⁵	36
Fig. 13: Scheme of Raman active atomic vibrations in rutile. Ti atoms are large black and O atoms are small red spheres. The arrows indicate the movements of the atoms. Adopted from Frank et al. ⁷⁴	37
Fig. 14: a) Folding of a silica Brillouin zone towards zero, b) Raman spectra of amorphous (glass) and crystalline silica. ⁷⁰	41
Fig. 15: Williamson-Hall plot of an e-beam evaporated undoped TiO ₂ thin film after annealing at 640 °C.	45
Fig. 16: Perkin-Elmer PE 2400 sputter coater. ¹⁰²	47
Fig. 17: Geometry of the Perkin-Elmer PE 2400 sputter coater (left), sputter arrangement and area of homogeneous deposition rate (right). Taken from Shi and modified. ¹⁰²	47
Fig. 18: Balzers Process Systems BAK 640 coating system high vacuum chamber, with a calotte and quartz crystals.	48
Fig. 19: Crucibles to be filled with self-made Ti ₂ O ₃ or Nb ₂ O ₅ pellets.	49
Fig. 20: Rotatable calotte used as a substrate holder.	49
Fig. 21: Raman spectra of the Ti ₂ O ₃ coating material to be evaporated. The gray spectrum (shifted by 300 units) is the average spectrum of 80 measurements taken at distances of 1 μm. The other three spectra are taken at single grains found at the surface of a Ti ₂ O ₃ pellet.	50
Fig. 22: Raman spectra of the Nb ₂ O ₅ coating material to be evaporated. The black spectrum (shifted by 100 units) is the average spectrum of 80 measurements taken at distances of 1 μm. The other two spectra are taken at single grains found at the surface of the pellet.	51
Fig. 23: Von Ardenne Anlagentechnik GmbH LS500s sputter coater equipped with a PEM. ¹⁰⁶	52
Fig. 24: Sputter geometry including the placement of the Nb wire and the substrates. Taken from Mukherjee et al. and modified. ¹⁰⁴	52
Fig. 25: Raman spectra of a Nb doped TiO ₂ (Ox-65) thin film after cosmic ray removal and subtraction of the substrate spectrum. The gray spectra are from several positions measured for one second. The numbers in	

brackets are the position in μm from the center of the Raman map. The green spectrum is the average spectrum of the whole map.	56
Fig. 26: Three spectra of Fig. 25 without noise filter (gray), with a noise filter that deleted all components after the first 100 components "c100" (green), with noise filter keeping only 15 components "c15" (red).	57
Fig. 27: Map of the Raman intensity from 235 cm^{-1} to 255 cm^{-1} of a B270 glass substrate	59
Fig. 28: Spectra of a B270 glass substrate at four different positions marked on the map in Fig. 27. The coordinates in brackets are in μm in relation to the center of the map.	59
Fig. 29: Raman maps of a B270 glass substrate: (a) Raman intensity I_{270} (signal-to-axis $260\text{ cm}^{-1} - 280\text{ cm}^{-1}$), (b) focus track value, (c) Raman intensity I_{1000} (at $990\text{ cm}^{-1} - 1010\text{ cm}^{-1}$), (d) ratio map I_{270}/I_{1000} (a) vs. (c).	60
Fig. 30: Normalized maps of $\text{Ti}_{9.84}\text{O}_{2.25}\text{Nb}_{0.16}$ ($420\text{ }^\circ\text{C}$), (a) I_{149} (signal-to-axis $139\text{ cm}^{-1} - 159\text{ cm}^{-1}$), (b) I_{270} (signal-to-axis $260\text{ cm}^{-1} - 280\text{ cm}^{-1}$), (c) focus track value ($-0.11\text{ }\mu\text{m}$ to $6.14\text{ }\mu\text{m}$), (d) ratio map I_{149}/I_{270} ((a) vs. (b)).	61
Fig. 31: Phonon maps of maps of a Nb-doped TiO_2 thin film coated onto B270 glass by plasma emission controlled rf-magnetron sputtering with a 68% oxidized Ti target: (a) Eg(1) (red), (b) AB1g (blue), (c) B1g (green), (d) combined phonon map.	62
Fig. 32: Phonon maps of a TiO_2 thin film coated onto fused silica by reactive e-beam evaporation post-heated at $750\text{ }^\circ\text{C}$: (a) Eg(1) (red), (b) AB1g (blue), (c) B1g (green), (d) combined phonon map.	63
Fig. 33: TiO_2 phase maps of a TiO_2 thin film coated onto fused silica by reactive e-beam evaporation post-heated at $750\text{ }^\circ\text{C}$: (a) anatase, (b) brookite, (c) rutile, (d) combined TiO_2 phase map.	64
Fig. 34: Measured LaB_6 660 a diffractogram (black), fit to the measured signal (dashed red), instrument background signals (light blue), LaB_6 660 a literature intensities and peak positions ¹¹¹ (vertical green lines), and the residual signal between the fit and the measured signal (gray).	66
Fig. 35: Details view on ranges of the diffractograms shown in Fig. 34 around the (100) (left), (110) (mid), and (320) reflexes. Colors are as in Fig. 34: measured LaB_6 660 a diffractogram (black), a fit to the measured signal (dashed red), an instrument background signals (light blue), LaB_6 660 a literature peak positions ¹¹¹ (vertical green lines), and the residual signal between the fit and the measured signal (gray).	67
Fig. 36: Left: half-width at half maximum on the left side of the peak center (h.w.h.m.l) (gray squares), half-width at half maximum on the right side of the peak center (h.w.h.m.r) (black circles), and the shift of the peak positions; right: relative peak height (black triangles) and relative peak intensity (gray triangles) as compared to standard values. Trendlines are added as third-degree polynomials.	67
Fig. 37: Measured Raman spectrum (black) of a TiO_2 thin film on a B270 glass substrate and its decomposition into B270 glass substrate (light blue) and thin film (dark red). The thin film is furthermore split into an amorphous phase (dark gray) and a crystalline anatase content (green). The measured spectrum, fit (red dotted line), and substrate spectra are shifted by 300 units on the intensity axis. The excluded range is light red and the low priority range is light brown.	73
Fig. 38: Raman spectra of amorphous TiO_2 (black), $\text{Ti}_{0.92}\text{O}_2\text{Nb}_{0.08}$ (dark gray), and $\text{Ti}_{0.84}\text{O}_2\text{Nb}_{0.16}$ (light gray), normalized to 100 000 counts after the subtraction of the substrate spectra from the measured spectra.	75
Fig. 39: Asymmetric Lorentzian function and its four fitting factors: position x_0 , height A, half-width at half maximum on the left-side Δx_l and on the right-side Δx_r .	77
Fig. 40: Decomposition of a raw brookite TiO_2 Raman spectrum taken with a 780 nm laser (dark red) into the 'processed' spectrum (red), both available at RRUFF database, ¹²⁵ and their smoothed difference spectrum (light red), which we interpret as the phase background spectrum of brookite.	79
Fig. 41: (I) Decomposition of a reference monocrystalline bulk anatase raw spectrum ¹²⁶ into first-order Lorentzian peaks and the residual spectrum (dashed black line), which we interpret as the anatase background spectrum. The Eg peak at 143 cm^{-1} has an intensity of 50 000 units; (II) pseudo-Voigt peaks, grouped to three bands (a), (b), and (c) as models for the anatase background spectrum (for 780 nm laser excitation). The black dashed line (anatase background) is the residual spectrum in Fig. 41 (I); (III) TiO_2 anatase spectrum derived by subtraction of the substrate and amorphous spectrum from a measured spectrum, decomposed into modeled anatase first-order and background spectra. The Eg peak at 145 cm^{-1} has an intensity of 3 200 units. The excluded range is light red and the low priority range is light brown.	80
Fig. 42: (I) Spectra of five individual Si wafers and a variation of the laser focus on wafer 5; (II) measured Raman spectrum of a sixth Si substrate (black), modeled by seven reference spectra of five reference substrates with varying laser focus. The excluded range is light red and the low priority range is light brown.	83
Fig. 43: (I) Variation of the Si peak around 520 cm^{-1} of the spectra shown in Fig. 42; (II) measured and modeled ('fit') Si peak around 520.7 cm^{-1} , which was excluded from the fit, of the spectrum shown in Fig. 42 (II) – the error of the modeled peak is more than one third of the measured intensity.	85

Fig. 44: (I) Decomposition of measured B270 glass substrate spectra into luminescence and Raman active modes. (II) Measured (black) and modeled (red) Raman spectra of a B270 glass substrate composed by luminescence (light blue) and Raman bands (blue). The vertical dotted lines mark the base points of the luminescence spectrum, where the Raman spectrum is zero, and they separate the spectral ranges to be fitted individually. The excluded range is light red and the low priority range is light brown. _____	87
Fig. 45: (I) Decomposition of measured fused silica substrate spectra (gray) into luminescence (blue) and Raman bands (green); the measured and luminescence spectra are shifted by 100 units on the intensity axis. (II) Measured (black) and modeled (red) Raman spectra of fused silica substrate composed by luminescence (light blue) and Raman bands (blue). The vertical dotted lines mark the base points of the luminescence spectrum, where the Raman spectrum is zero, and they separate the spectral ranges to be fitted individually. The measured, fit, and luminescence spectra are shifted by 60 units on the intensity axis. _____	89
Fig. 46: Overview of the thin film Raman fitting model. _____	92
Fig. 47: Flowchart of the crystalline phases model. _____	94
Fig. 48: Literature raw anatase Raman spectra (RRUFF-ID R070582) ¹²⁶ produced with a 532 nm (light green line) and a 780 nm (light red line) laser and the corresponding phase backgrounds in dark green and dark red. The phase backgrounds are obtained in our work from the remaining spectra after fitting first-order Raman peaks to the reference spectra. _____	101
Fig. 49: Literature raw brookite Raman spectra (RRUFF-ID R050591) ¹²⁵ produced with a 532 nm (light green line) and a 780 nm (light red line) laser, the corresponding literature ‘processed’ spectra ¹²⁵ in medium green and red as well as the corresponding smoothed phase backgrounds in dark green and dark red (raw and processed spectra are shifted by 800 on the intensity axis). The phase background signals are obtained in our work from the remaining spectra after fitting first-order Raman peaks to the reference spectra. _____	103
Fig. 50: Rutile reference spectrum (light blue) ¹³⁷ , rutile phase background (dark blue), both shifted by 100 on the intensity axis; and rutile first-order Raman spectrum (blue). The phase background is obtained in our work from the remaining spectrum after fitting first-order Raman peaks to the reference spectrum. _____	104
Fig. 51: Raman spectra (produced in this work) of TiO ₂ thin films that were simultaneously coated on Si, B270 crown glass, and fused silica in the master’s thesis of M.Sc. Jingyi Shi. _____	105
Fig. 52: Overview of the thin film XRD fitting model. The X-ray diffractogram is decomposed into a thin film and a background. The thin film is divided into diffractograms of crystalline phases and an amorphous phase, and the background is divided into diffractograms of the substrate and an instrument background (plus a substrate holder when measured in ϑ - ϑ geometry). _____	108
Fig. 53: Example of a measured X-ray diffractogram of an anatase TiO ₂ thin film on a B270 glass substrate prepared by e-beam evaporation in the optical workshop at the University of Duisburg-Essen: (black), the fit (dashed red), the diffractograms of the substrate (light blue), of the instrument background (dashed blue), and the residual diffractogram (gray). The anatase diffractogram that contributes to the fit is not shown. _____	108
Fig. 54: Reference diffractograms of amorphous TiO ₂ samples prepared by e-beam evaporation in the optical workshop at the University of Duisburg-Essen and additional bands modeled by the XRD model of amorphous TiO ₂ . _____	109
Fig. 55: Brookite diffractograms: examples of a broad (dark green) and a narrow (medium green) modeled diffractogram (shifted by 1000 on the intensity axis), a literature diffractogram (black) ¹²⁵ and a modification (done in the current work) of the literature diffractogram normalized to 1000 intensity units. _____	113
Fig. 56: X-ray diffractograms of a B270 glass substrate in grazing incidence ϑ -2 ϑ geometry (dark blue) and in ϑ - ϑ geometry (light blue), of a fused silica substrate in grazing incidence ϑ -2 ϑ geometry (dark green) and in ϑ - ϑ geometry (light green), a self-made low-background holder in ϑ - ϑ geometry (black), and the instrument background (gray). _____	114
Fig. 57: Decomposition of a measured X-ray diffractogram of a rf-sputter coated TiO ₂ thin film on a B270 crown glass substrate deposited at 310 °C (black) into a background (light blue) and the thin film (dark red). The background is split into the B270 substrate (medium blue) and an instrument background (dashed dark blue). The film is further decomposed into anatase (green), brookite (orange), rutile (blue), and amorphous TiO ₂ (medium gray). The residual diffractogram is light gray and the fit of the modeled diffractogram to the measured one is the dashed red line. Peak positions of standard powder are added as light and the modeled peak positions are added as vertical lines. The graphs are shifted on the intensity axis (indicated by dotted baselines) as described in the text. _____	118
Fig. 58: Decomposition of a TiO ₂ film 633 nm Raman spectrum (on B270 deposited at 310 °C) into anatase, rutile, brookite, amorphous TiO ₂ , substrate, and instrument background (intensity shift: see text). _____	121

- Fig. 59: Decomposition of a TiO₂ film 532 nm Raman spectrum (on B270 deposited at 310 °C) into anatase, rutile, brookite, amorphous TiO₂, substrate, and instrument background (intensity shift: see text). _____ 122
- Fig. 60: Measured (black) and modeled (dashed red) Raman spectrum of an rf-diode sputtered mixed-phase TiO₂ thin film on a Si substrate decomposed into substrate (light blue) and thin film (dark red). The thin film is decomposed into anatase (green), brookite (orange), rutile (blue), and amorphous TiO₂ (dark gray) spectra. The residual spectrum is medium gray. The crystalline spectra are divided into first-order scattering (black dashed lines) and phase background (light gray lines). The heights of the Si peak and the residual spectrum at 520.7 cm⁻¹ are 21 000 and 10 000 Raman intensity units. The excluded ranges are light red and the low priority range is light brown. Intensity shifts are indicated by dotted lines. _____ 124
- Fig. 61: Measured (black) and modeled (dashed red) Raman spectrum of an rf-diode sputtered mixed-phase TiO₂ thin film on B270 glass decomposed into substrate (light blue) and thin film (dark red). The substrate spectrum is split into luminescence (mid blue) and Raman bands (dashed dark blue) and the thin film is decomposed into anatase (green), brookite (orange), rutile (blue), and amorphous TiO₂ (dark gray) spectra. The residual spectrum is medium gray. The crystalline spectra are divided into first-order scattering (black dashed lines) and phase background (light gray lines). The excluded range is light red and the low priority range is light brown. Intensity shifts are indicated by dotted lines. _____ 125
- Fig. 62: Measured (black) and modeled (dashed red) Raman spectrum of an rf-diode sputtered mixed-phase TiO₂ thin film on fused silica decomposed into substrate (light blue) and thin film (dark red). The substrate spectrum is split into luminescence (mid blue) and Raman bands (dashed dark blue) and the thin film is decomposed into anatase (green), brookite (orange), rutile (blue), and amorphous TiO₂ (dark gray) spectra. The residual spectrum is medium gray. The crystalline spectra are divided into first-order scattering (black dashed lines) and phase background (light gray lines). The excluded range is light red and the low priority range is light brown. The spectra are shifted on the intensity axis as indicated by dotted lines. _____ 126
- Fig. 63: Measured (black) and modeled (dashed red) X-ray diffractogram of a titanium oxide thin film with 8 at.% Nb – e-beam evaporated onto a B270 crown glass substrate and post-heated at 375 °C – decomposed into a background (light blue) and a thin film (dark red). The background is split into the B270 substrate (medium blue) and an instrument background (dashed dark blue). The film is decomposed into anatase (green), brookite (orange), rutile (blue), and amorphous TiO₂ (dark gray). The residual diffractogram is medium gray. The diffractograms are shifted on the intensity axis as indicated by dotted lines. _____ 130
- Fig. 64: Measured (black) and modeled (dashed red) X-ray diffractogram of an undoped TiO₂ thin film – e-beam evaporated onto a B270 crown glass substrate and post-heated at 420 °C – decomposed into a background (light blue) and a thin film (dark red). The background is split into the B270 substrate (medium blue) and an instrument background (dashed dark blue). The film is decomposed into anatase (green), brookite (orange), rutile (blue), and amorphous TiO₂ (dark gray). The residual diffractogram is medium gray. The diffractograms are shifted on the intensity axis as indicated by dotted lines. _____ 131
- Fig. 65: Measured (black) and modeled (dashed red) X-ray diffractogram of an undoped TiO₂ thin film – e-beam evaporated onto a B270 crown glass substrate and post-heated at 640 °C – decomposed into a background (light blue) and a thin film (dark red). The background is split into the B270 substrate (medium blue) and an instrument background (dashed dark blue). The film is decomposed into anatase (green), brookite (orange), rutile (blue), and amorphous TiO₂ (dark gray). The residual diffractogram is medium gray. The diffractograms are shifted on the intensity axis as indicated by dotted lines. _____ 132
- Fig. 66: Measured (black) and modeled (dashed red) X-ray diffractogram of a titanium oxide thin film with 8 at.% Nb – e-beam evaporated onto a B270 crown glass substrate and post-heated at 640 °C – decomposed into a background (light blue) and a thin film (dark red). The background is split into the B270 substrate (medium blue) and an instrument background (dashed dark blue). The film is decomposed into anatase (green), brookite (orange), rutile (blue), and amorphous TiO₂ (dark gray). The residual diffractogram is medium gray. The diffractograms are shifted on the intensity axis as indicated by dotted lines. _____ 133
- Fig. 67: Measured (black) and modeled (dashed red) X-ray diffractogram of a titanium oxide thin film with 16 at.% Nb – e-beam evaporated onto a B270 crown glass substrate and post-heated at 640 °C – decomposed into a background (light blue) and a thin film (dark red). The background is split into the B270 substrate (medium blue) and an instrument background (dashed dark blue). The film is decomposed into anatase (green), brookite (orange), rutile (blue), and amorphous TiO₂ (dark gray). The residual diffractogram is medium gray. The diffractograms are shifted on the intensity axis as indicated by dotted lines. _____ 134
- Fig. 68: Measured (black) and modeled (dashed red) Raman spectrum of an e-beam coated titanium oxide thin film doped with 8 at.% Nb on B270 glass post-heated at 375 °C – decomposed into substrate (light blue) and thin film (dark red). The substrate spectrum is split into luminescence (mid blue) and Raman bands (dashed dark

blue) and the thin film is decomposed into anatase (green), brookite (orange), rutile (blue), and amorphous TiO₂ (dark gray) spectra. The crystalline spectra are divided into first-order scattering (black dashed lines) and phase background (light gray lines). The excluded range is light red and the low priority range is light brown. Same sample as in Fig. 63. The spectra are shifted on the intensity axis as indicated by dotted lines. _____ 136

Fig. 69: Measured (black) and modeled (dashed red) Raman spectrum of an e-beam coated undoped TiO₂ thin film on B270 glass post-heated at 420 °C – decomposed into substrate (light blue) and thin film (dark red). The substrate spectrum is split into luminescence (mid blue) and Raman bands (dashed dark blue) and the thin film is decomposed into anatase (green), brookite (orange), rutile (blue), and amorphous TiO₂ (dark gray) spectra. The crystalline spectra are divided into first-order scattering (black dashed lines) and phase background (light gray lines). The excluded range is light red and the low priority range is light brown. Same sample as in Fig. 64. The spectra are shifted on the intensity axis as indicated by dotted lines. _____ 137

Fig. 70: Measured (black) and modeled (dashed red) Raman spectrum of an e-beam coated undoped TiO₂ thin film on B270 glass post-heated at 640 °C – decomposed into substrate (light blue) and thin film (dark red). The substrate spectrum is split into luminescence (mid blue) and Raman bands (dashed dark blue) and the thin film is decomposed into anatase (green), brookite (orange), rutile (blue), and amorphous TiO₂ (dark gray) spectra. The crystalline spectra are divided into first-order scattering (black dashed lines) and phase background (light gray lines). The excluded range is light red and the low priority range is light brown. Same sample as in Fig. 65. The spectra are shifted on the intensity axis as indicated by dotted lines. _____ 138

Fig. 71: Measured (black) and modeled (dashed red) Raman spectrum of an e-beam coated titania film doped with 8 at.% Nb on B270 glass post-heated at 640 °C – decomposed into substrate (light blue) and film (dark red). The substrate spectrum is split into luminescence (mid blue) and Raman bands (dashed dark blue) and the film is decomposed into anatase (green), brookite (orange), rutile (blue), and amorphous TiO₂ (dark gray). The crystalline spectra are divided into first-order scattering (black dashed lines) and phase background (light gray lines). The excluded range is light red and the low priority range is light brown. Same sample as in Fig. 66. Intensity shifts of the spectra are indicated by dotted lines. _____ 139

Fig. 72: Measured (black) and modeled (dashed red) Raman spectrum of an e-beam coated titania film doped with 8 at.% Nb on B270 glass post-heated at 640 °C – decomposed into substrate (light blue) and film (dark red). The substrate spectrum is split into luminescence (mid blue) and Raman bands (dashed dark blue) and the film is decomposed into anatase (green), brookite (orange), rutile (blue), and amorphous TiO₂ (dark gray). The crystalline spectra are divided into first-order scattering (black dashed lines) and phase background (light gray lines). The excluded range is light red and the low priority range is light brown. Same sample as in Fig. 67. Intensity shifts of the spectra are indicated by dotted lines. _____ 140

Fig. 73: Left column: Contributions (in thousand counts per second) of anatase, brookite, rutile, and amorphous TiO₂ to XRD diffractograms and (633 nm and 532 nm) Raman spectra of TiO₂ thin films diode-sputtered at temperatures of 155 °C – 415 °C. Right column: Apparent relative phase contents (relative number of X-ray or Raman photon counts) in the XRD diffractograms and (633 nm and 532 nm) Raman spectra. The lines are added to guide the eye. _____ 146

Fig. 74: left side: Raman intensity of anatase, brookite, rutile, and amorphous TiO₂ in multi-phase thin films as derived from Raman spectra measured with a 532 nm laser versus a 633 nm laser; right side: same data plotted as relative intensities (relative apparent phase contents). _____ 148

Fig. 75: Intensities (number of counts) of the TiO₂ phases, anatase, brookite, rutile, and amorphous TiO₂ in the 633 nm and 532 nm spectra Raman spectra vs. in the X-ray diffractograms in one thousand counts per second (kcps). _____ 150

Fig. 76: Top: a simulated rutile Raman spectrum (blue) with its phase background (light blue) compared to a simulated Raman spectrum of amorphous TiO₂ (gray), bottom: simulated brookite Raman spectrum (orange) with its phase background (light orange) compared to a simulated Raman spectrum of amorphous TiO₂ (gray). _____ 153

Fig. 77: Apparent phase contents of the TiO₂ phases, anatase, brookite, rutile, and amorphous TiO₂ in the Raman spectra (including 633 nm and 532 nm spectra) vs. in the X-ray diffractograms. _____ 155

Fig. 78: Quantification of 633 nm Raman spectra of TiO₂ phases in thin films that were diode-sputtered onto B270, fused silica, and Si substrates at various substrate temperatures of 155 °C – 415 °C. The values of anatase are marked as green squares, brookite as orange rhombuses, rutile as blue triangles, and amorphous TiO₂ as gray circles. The left side shows contributions (in thousand counts per second) of anatase, brookite, rutile, and amorphous TiO₂ to the Raman. The right side depicts the same values as relative contents. _____ 161

Fig. 79: Left side: contributions (in thousand counts per second) of anatase, brookite, rutile, and amorphous TiO₂ to XRD diffractograms and (633 nm) Raman spectra of e-beam evaporated TiO₂ thin films post-heated at

temperatures of 250 °C – 750 °C. For each phase, the Raman intensities refer to the left axis and the X-ray intensities refer to the right axis. Right side: apparent phase content (= relative amount of counts) of the TiO ₂ phases in the XRD diffractograms and (633 nm) Raman spectra. _____	165
Fig. 80: Raman Intensities (633 nm) of the TiO ₂ phases, anatase, brookite, rutile, and amorphous TiO ₂ vs. in the X-ray diffractograms e-beam of e-beam evaporated TiO ₂ thin films post-heated at temperatures of 250 °C – 750 °C in one thousand counts per second (kcps). _____	168
Fig. 81: Apparent phase contents of the TiO ₂ phases, anatase, brookite, rutile, and amorphous TiO ₂ in the Raman spectra (633 nm) vs. in the X-ray diffractograms of e-beam evaporated films. _____	169
Fig. 82: Raman intensity vs. XRD intensity of anatase, brookite, rutile, and amorphous TiO ₂ of rf-diode sputtered (DS) films as open symbols and e-beam evaporated (EB) films as closed symbols. The values of the e-beam coated film with crystalline islands are indicated by light colors. _____	172
Fig. 83: Diffractograms of multi-phase TiO ₂ thin films diode sputtered at temperatures between 155 °C and 415 °C after subtracting the B270 glass substrate diffractograms and the instrument backgrounds from the measured diffractograms. Left: whole range, mid: anatase (101) peak around 25.0° and rutile (110) peak around 27.2°, including the range around the brookite (211) peak position in literature at 30.8°. Right: range around the brookite (421) peak position in literature at 55.2°. ¹²⁵ _____	178
Fig. 84: Diffractogram of a diode sputtered multi-phase TiO ₂ thin film deposited at 310 °C (black), the simulated 'fit' TiO ₂ diffractogram (dashed red), the anatase (105) and (211) peaks (green), the rutile (211) and (220) peaks (dashed blue), and the brookite diffractogram (orange). _____	179
Fig. 85: Left side: lattice parameters a and c of anatase and rutile in rf-diode sputtered TiO ₂ films on B270 glass, right side: unit cell volume of anatase, rutile, and brookite. _____	179
Fig. 86: Raman spectra (633 nm) of multi-phase TiO ₂ thin films rf-diode sputtered at temperatures between 155 °C and 415 °C after subtracting the B270 glass substrate spectra from the measured spectra. Left: whole range, mid: anatase Eg peak, right: detailed view in the range of 100 cm ⁻¹ – 700 cm ⁻¹ . All spectra are shifted upwards on the intensity axis in steps of 10 cm ⁻¹ . Vertical lines indicate standard peak positions of each anatase (green) and the most intense brookite (narrowly dashed orange) and rutile (dashed blue) peaks. _____	181
Fig. 87: Raman peak shifts (in relation to standard values) vs. (full) widths of various anatase, brookite, and rutile peaks in Raman spectra of diode-sputtered multi-phase TiO ₂ thin films measured with a 633 nm laser. Increasing deposition temperature from 155 °C – 415 °C is indicated by arrows. _____	182
Fig. 88: Anatase Eg(1) Raman peak positions and widths of diode sputtered TiO ₂ thin films on B270 glass (green) compared to literature values (black), a straight trendline of Kelly et al. ¹⁵³ (gray) and the QVRM used in this work (red) with A ₁ = 28.8, A ₂ = 10.2, and γ ₂ = 0.63 · γ ₁ . The position (143 cm ⁻¹) and width (7 cm ⁻¹) of bulk material at room temperature are marked by dashed black lines. Parts of a figure of Swamy et al. ¹⁶³ are copied into the figure _____	187
Fig. 89: (A) & (B): Anatase Eg(1) peak width vs. crystallite size (from XRD), (C): anatase Eg(1) peak position vs. crystallite size (from XRD). The crystallite sizes are as determined by XRD the peak position are fitted by the Raman fit models for multi-phase TiO ₂ . Values of this study are represented by open green squares. Trendlines as predicted by equations (89) and (90) with α = 30 (light blue), α = 56 (red) are added. (A) is a comparison with a figure of Iida et al. ¹⁵¹ , their trendlines are black. Horizontal and vertical dashed lines are added at 5.4 nm, 7.5 nm, and 10 nm. (B) & (C) are comparisons to figures of Swamy et al. ⁸⁶ Values of Swamy et al. are marked by letters A-E. The QVRM trendlines of Kelly et al. ¹⁵³ in (B) and (C) are dark blue. _____	189
Fig. 90: Crystallite sizes of anatase (left-side) and rutile (right-side) as determined by XRD using the Scherrer formula (marked by crosses connected with dashed lines) and by Raman using models for phonon confinement: anatase estimated from Eg(1) peak width using equation (91) (light green squares) and Eg(1) peak position (92) (medium green squares), rutile estimated by PCM of Mazza et al. ⁴⁸ _____	190
Fig. 91: Grazing-incidence (7°) diffractograms of TiO ₂ , Ti _{0.92} O _{2.25} Nb _{0.08} , and Ti _{0.84} O _{2.25} Nb _{0.16} (shifted on the intensity axis in steps of 1.5 kcps). _____	197
Fig. 92: Grazing-incidence diffractograms (low intensity-range) of e-beam evaporated TiO ₂ films as-deposited and post heated at various temperatures (not shifted). The powder standard positions of the anatase (101), rutile (110), and brookite (211) are marked by vertical dashed lines. _____	197
Fig. 93: Grazing-incidence diffractograms (low intensity-range) of e-beam evaporated Ti _{0.92} O _{2.25} Nb _{0.08} films as-deposited and post heated at various temperatures (not shifted). The powder standard positions of the anatase (101), rutile (110), and brookite (211) are marked by vertical dashed lines. _____	198

Fig. 94: Grazing-incidence diffractograms (low intensity-range) of e-beam evaporated $Ti_{0.84}O_{2.25}Nb_{0.16}$ films as-deposited and post heated at various temperatures (not shifted). The powder standard positions of the anatase (101), rutile (110), and brookite (211) are marked by vertical dashed lines.	198
Fig. 95: Lattice parameters a and c , and unit cell volume V vs. annealing temperature	199
Fig. 96: Intensity ratio of the (105) and the (101) peak $I_{(105)}/I_{(101)}$ in the X-ray diffractograms in relation to the $I_{(105)}/I_{(101)}$ ratio in standard powder diffractograms vs. the annealing temperature.	201
Fig. 97: Average crystallite size of Nb0, Nb1, and Nb2 films according to Williamson-Hall plots vs. annealing temperature.	202
Fig. 98: Strain of Nb0, Nb1, and Nb2 films as obtained from Williamson-Hall vs. annealing temperature.	203
Fig. 99: Strain of ϑ - ϑ XRD (101), (105), and (200) reflections of Nb0, Nb1, and Nb2 films.	203
Fig. 100: Raman spectra of Nb0 films on B270 glass (not shifted).	204
Fig. 101: Raman spectra Nb1 and Nb2 films on B270 glass (not shifted).	205
Fig. 102: Thin film Raman spectra (633 nm) of Nb0, Nb1, and Nb2 films; full range (left), Eg(1) peak (middle), detailed view on lower intensity ranges (right); each spectrum is shifted in steps of 4 units on the intensity axis (left and middle column) or 2 units (right column).	206
Fig. 103: Thin film Raman spectra (633 nm) of Nb0 (top), Nb1 (mid), and Nb2 (bottom) films – range of main brookite and rutile peak positions. The spectra are not shifted on the intensity axis. Colors of the spectra are the same than in Fig. 102. Brookite standard positions are marked by narrowly dotted orange, and rutile by widely dotted blue vertical lines.	208
Fig. 104: Anatase Raman peak areas of e-beam evaporated Nb0, Nb1, and Nb2 films on B270 glass (and fused silica, 750 °C) vs. annealing temperature. The spectra of the Nb0 film annealed at 750 °C was taken with a newly installed laser.	209
Fig. 105: Raman Eg(3)/Eg(1) (pink), B1g/Eg(1) (green), and (A1g/B1g doublet)/Eg(1) peak intensity ratios of Nb0, Nb1, and Nb2 films. B1g/Eg(1) (gray crosses with solid line) and (A1g/B1g doublet)/Eg(1) (black stars with dashed line) intensity ratios of anatase nano particles by Yan et al. ¹⁷⁰ are added to the graph of the undoped TiO_2 films.	210
Fig. 106: Relative peak intensity ratios of Nb0, Nb1, and Nb2 films: ϑ - ϑ XRD (105)/(002) intensity ratio (left), Raman (B1g & A1g/B1g doublet)/Eg(3) (right) vs. the annealing temperature. The ratios are in relation to standard (XRD) and to Raman Sigma-Aldrich anatase powder. ^{147,169}	210
Fig. 107: Raman peak intensity ratios of (A&B)/Eg(3) (black), (A&B)/Eg(1) (medium gray), and Eg(3)/Eg(1) (light gray) vs. the Nb content (at.% in relation to the Ti content). “A&B” is the average intensity of the B1g peak at 399 cm^{-1} and the A1g/B1g-doublet at 517 cm^{-1} . The values are averaged over all temperatures.	212
Fig. 108: Positions vs. widths of the Eg(1), Eg(3), and B1(g) Raman peaks. Linear trend lines with arrows indicate the variation with the temperature.	213
Fig. 109: Raman peak asymmetries of e-beam evaporated Nb0 (left), Nb1 (mid), and Nb2 (right) films on B270 glass (and fused silica, 750 °C) vs. annealing temperature.	216
Fig. 110: Raman spectra of varying polarization (unpolarized (black), circularly polarized (red), orthogonally polarized (green)) on various positions on a $Ti_{0.84}O_{2.25}Nb_{0.16}$ film that was annealed at 640 °C, sorted by the Eg(1) peak position of the unpolarized spectra. Left: Eg(1) peak with average peak position of the whole sample at 150.2 cm^{-1} (dashed vertical line). The spectra of each position are shifted by 140 units on the intensity axis. Right: detailed view on the whole range of measurement (same spectra), shifted by 50 units for each position.	218
Fig. 111: Same spectra as in Fig. 110, sorted by the Eg(1) peak position of the spectra taken with circular polarization. Left: Eg(1) peak with average peak position of the whole sample at 150.2 cm^{-1} (dashed vertical line). The spectra of each position are shifted by 140 units on the intensity axis. Right: detailed view on the whole range of measurement (same spectra), shifted by 50 units for each position.	219
Fig. 112: Same spectra as in Fig. 110, sorted by the Eg(1) peak position of the spectra taken with orthogonal polarization. Left: Eg(1) peak with average peak position of the whole sample at 150.2 cm^{-1} (dashed vertical line). The spectra of each position are shifted by 140 units on the intensity axis. Right: detailed view on the whole range of measurement (same spectra), shifted by 50 units for each position.	220
Fig. 113: Reflectance (R), transmittance (T), and the resulting absorbance spectra (1-R-T) of reactive e-beam evaporated Nb0 (green), Nb1 (blue), and Nb2 (red) thin films on B270 glass (dashed black). Amorphous spectra of as deposited films (250 °C) are gray and crystalline spectra are colored. Increasing annealing temperatures is indicated by darker colors. Vertical lines mark the wavenumbers at which the light source was switched.	221

Fig. 114: Average transmittance of e-beam evaporated NbO (green squares), Nb1 (blue triangles), Nb2 (red circles) thin films on B270 glass (black dashed line) in the visible range (380 nm – 780 nm) versus the annealing temperature. _____	222
Fig. 115: Tauc plots of e-beam evaporated NbO (green), Nb1 (blue), and Nb2 (red) films on B270 substrates, amorphous as deposited (gray), and post-heated at 420 °C (light colors), 530 °C (medium colors), and 640 °C (dark colors). Top: Full range displaying several states at lower energies than the main band gaps; bottom: detailed view of the main band edges. _____	224
Fig. 116: Band gaps vs. annealing temperature of e-beam evaporated NbO (green), Nb1 (blue), and Nb2 (red) films on B270 substrates as determined by Tauc plots (see Fig. 115), compared to anatase (3.2 eV) and rutile (3.0 eV) standard values. ¹⁷³ _____	224
Fig. 117: Measured and modeled reflectance and transmittance spectra. The colors of the spectra are the same as in Fig. 113. The modeled spectra using SCOUT are shown as dashed lines. Spectra are shifted by 1 upwards each. 270 glass spectra are added without shift. _____	225
Fig. 118: refractive index n compared to Mergel et al. ⁵³ _____	226
Fig. 119: Left: Electrical resistivity of NbO (green), Nb1 (red), Nb2 (blue) thin films versus the annealing temperature as determined using a four-point-probe (solid lines). Three additional samples were prepared with stoichiometric oxygen content (open symbols). Values as determined by modeling optical transmittance and reflectance spectra to measured spectra using SCOUT (dashed lines) are added for the spectra of crystalline samples with the most precise fit (see Fig. 117). A dashed black line marks a critical resistivity that discriminates between samples with potential and linear current-voltage characteristics. Right: values compared to previously published work in Mukherjee et al. ¹⁰⁴ _____	227
Fig. 120: Electrical conductivity vs. unit cell volume (a^2c), compared to monocrystalline films of Furubayashi et al. ⁵⁶ _____	228
Fig. 121: Nb content (left) and O content (right) in PEM controlled rf-sputter coated Nb-doped TiO ₂ thin films on B270 glass. The samples are placed (a) 12.5 mm, (b) 42.5 mm, and (c) 72.5 mm horizontally from the Nb wire, and the Ti target surface is oxidized by 65%, 68%, 71%, or 78%. Oxygen values for 78%-ox.t (a) and 78%-ox.t (c) were not measured and are extrapolated. _____	233
Fig. 122: 2D representation of unit cell volume (left) and conductivity (right) vs. the oxidation state of the Ti target surface and the position of the sample horizontally from the Nb wires. _____	233
Fig. 123: Conductivities of the films that coated at the positions (a) 12.5 mm (red), (b) 42.5 mm (green), and (c) 72.5 mm (blue) horizontally from the Nb wires, with Ti target surface is oxidation states of 65%, 68%, 71%, or 78%. _____	235
Fig. 124: Raman spectra (633 nm) of PEM controlled rf-sputter coated Nb-doped TiO ₂ thin films (after subtraction of the substrate spectra from the measured spectra). The samples were placed (a) 12.5 mm, (b) 42.5 mm, and (c) 72.5 mm horizontally from the Nb wire, and the Ti target surface was oxidized by 65%, 68%, 71%, or 78%. The standard positions of anatase are marked green and of the strongest brookite peak is marked by a dotted orange line. _____	236
Fig. 125: Detailed view on the spectra of Fig. 124 in the range of the main brookite and rutile peak positions above 200 cm ⁻¹ . Brookite standard positions are marked by narrowly dotted orange, and rutile by widely dotted blue vertical lines. _____	238
Fig. 126: Anatase B1g position vs. B1g width (left) and Raman phonon domain size vs. the B1g position of the PEM films. _____	239
Fig. 127: Film thicknesses of PEM controlled rf-sputter coated Nb-doped TiO ₂ thin films on B270 glass, with 71% oxidation of the Ti target surface. The samples are placed (a) 12.5 mm, (b) 42.5 mm, and (c) 72.5 mm horizontally from the Nb wires are deposited for 10, 20, 40, or 60 minutes. _____	240
Fig. 128: Mass densities of PEM controlled rf-sputter coated Nb-doped TiO ₂ thin films on B270 glass, with 71% oxidation of the Ti target surface. The samples are placed (a) 12.5 mm, (b) 42.5 mm, and (c) 72.5 mm horizontally from the Nb wires are deposited for 10, 20, 40, or 60 minutes. _____	240
Fig. 129: Anatase phase backgrounds of e-beam evaporated undoped TiO ₂ films. Peak positions of supposed second-order Raman peaks (or other coupled vibrations) are indicated by dashed lines. _____	244
Fig. 130: Top: A nominal 'amorphous' phase background compared to anatase phase backgrounds of e-beam evaporated undoped TiO ₂ films (already shown in Fig. 129) with a supposed position of a disorder band; bottom: difference spectra of the phase backgrounds of the TiO ₂ films that were annealed 420 °C and 640 °C (light green) as well as of 530 °C and 640 °C. Gaussian bands which we consider as disorder-induced scattering are added by eye centered at 850 cm ⁻¹ . _____	245

Fig. 131: Anatase phase backgrounds of e-beam evaporated Nb-doped TiO ₂ films. _____	246
Fig. 132: Raman spectral comparison between crystalline and amorphous KPO ₃ (taken from Exarhos et al.). ¹⁸² _____	249
Fig. 133: Measured Raman spectrum of an amorphous TiO ₂ thin film decomposed into spectra of nominal anatase, brookite, and rutile structures. The corresponding nominal first-order spectra are black dashed and the nominal phase backgrounds are gray lines. _____	252
Fig. 134: Measured Raman spectrum of an amorphous TiO ₂ film decomposed into nominal crystalline phases (with individual band heights in the anatase phase background model). _____	255
Fig. 135: Raman maps of rf-diode sputtered TiO ₂ films on a B270 glass substrate deposited at 155 °C with ratio maps in the ranges of the following peaks: anatase Eg (I ₁₅₀ /I ₂₇₀ , green), brookite A1g (I ₂₄₄ /I ₂₇₀ , orange), and rutile Eg (I ₄₄₀ /I ₂₇₀ , blue). _____	258
Fig. 136: Anatase Raman maps of rf-diode sputtered TiO ₂ films on a B270 glass substrate deposited at temperatures of 200 °C – 415 °C. _____	259
Fig. 137: SEM image of a diode sputtered thin film coated at 310 °C. _____	259
Fig. 138: SEM image of a polycrystalline rf-diode sputtered 70 nm thick TiO ₂ thin film deposited at 200 °C in 200 k magnification. _____	260
Fig. 139: TiO ₂ phase maps (anatase (red), amorphous TiO ₂ or brookite (green), rutile (blue)) of e-beam evaporated undoped TiO ₂ films on B270 glass (deposited at 250 °C, annealed at 420 °C, 530 °C, 640 °C) or on fused silica (annealed at 750 °C). _____	262
Fig. 140: Combined TiO ₂ phase maps (overlay of anatase (red) and amorphous (green)) of a reactive e-beam coated TiO ₂ thin film annealed at 420 °C. This map appears already in Fig. 139. Positions 1 – 4 mark the measurement points of the corresponding spectra in Fig. 141. _____	263
Fig. 141: Locally resolved Raman spectra taken at the four positions that are marked in Fig. 140 and average spectrum of NbO annealed at 420 °C. Literature positions are marked by vertical transparent lines for anatase (red solid), brookite (orange narrowly dashed), and rutile (blue widely dashed). _____	263
Fig. 142: Combined TiO ₂ phase maps (overlay of anatase (red), amorphous or brookite (green), rutile (blue)) of a reactive e-beam coated TiO ₂ thin film annealed at 750 °C. This map appears already in Fig. 139. Positions 1 – 3 mark the measurement points of the corresponding spectra in Fig. 143. _____	264
Fig. 143: Locally resolved Raman spectra taken at the three positions that are marked in Fig. 142 and average spectrum of NbO annealed at 750 °C. Literature positions are marked by vertical transparent lines for anatase (red solid), brookite (orange narrowly dashed), and rutile (blue widely dashed). _____	264
Fig. 144: Combined phonon maps of anatase (Eg(1) (red), B1g (green), A1g/B1g-doublet (blue)) of e-beam evaporated Nb0 (left), Nb1 (mid), and Nb2 (right) films on B270 glass (deposited at 250 °C, annealed at 420 °C, 530 °C, 640 °C) or on fused silica (annealed at 750 °C). _____	266
Fig. 145: Micro Raman spectra of various positions on the anatase Nb2 640 °C map. The spectra are sorted by the Eg(1) height, shifted on the intensity axis by 80 each, and the Eg(1) peak is multiplied by a factor of 0.25 with an offset of +60, normalized to the intensity at 1000 cm ⁻¹ . (Temperature set point of 500 °C resulted in an annealing temperature of 640 °C ± 20 °C. _____	268
Fig. 146: SEM images (200 000 x) of (a) TiO ₂ , (b) Ti _{0.92} O _{2.25} Nb _{0.08} , and (c) Ti _{0.84} O _{2.25} Nb _{0.16} films annealed at 640 °C, (d) micro-grain boundaries in the Ti _{0.84} O _{2.25} Nb _{0.16} film. _____	269
Fig. 147: EDX linescan across a domain boundary of as Ti _{0.84} O _{2.25} Nb _{0.16} film annealed at 640 °C, and normalized intensities (average = 1) of Ti, O, Nb and Si. _____	270
Fig. 148: SEM images of a Ti _{0.84} O _{2.25} Nb _{0.16} film annealed at 640 °C in (a) 10 000 x and (b) 100 000 x magnification, providing a detailed view on the micro-domains. _____	271
Fig. 149: SEM images (4000 x) of (a) TiO ₂ , (b) Ti _{0.92} O _{2.25} Nb _{0.08} , (c) Ti _{0.84} O _{2.25} Nb _{0.16} films annealed at 640 °C using the standard SEI (secondary electron imaging) detector, (d) the area of (c) scanned with a LABE (low angle backscatter electron) detector. _____	272
Fig. 150: SEM images (50 000 x) of film edges of e-beam coated films on Si substrates annealed at 640 °C: (a) TiO ₂ , (b) Ti _{0.92} O _{2.25} Nb _{0.08} , and (c) Ti _{0.84} O _{2.25} Nb _{0.16} . (d) shows another part of the edge shown in (c) with an intact domain that was broken off the edge. _____	274
Fig. 151: SEM images (200.000 x) of film edges of (a) TiO ₂ annealed at 420 °C, (b) TiO ₂ annealed at 640 °C (c) Ti _{0.92} O _{2.25} Nb _{0.08} annealed at 640 °C, and (d) Ti _{0.84} O _{2.25} Nb _{0.16} annealed at 640 °C. _____	275
Fig. 152: anatase Raman phonon maps of Ti _{0.92} O _{2.25} Nb _{0.08} films annealed at 350 °C, 375 °C, 400 °C, and 450 °C. _____	276

Fig. 153: Anatase phonon maps of a $Ti_{0.92}O_{2.25}Nb_{0.08}$ film annealed at 375 °C: (a) Eg(1) (red), (b) AB1g (blue), (c) B1g (green), and (d) combined phonon map.	277
Fig. 154: Various crystalline anatase and amorphous TiO_2 spectra that correspond to randomly chosen coordinates of the map in Fig. 153 (sorted by the intensity of the Eg(1) peak). The spectra are shifted by 60 units on the Raman intensity axis, the range between 100 cm^{-1} and 200 cm^{-1} is divided by 4 and then shifted upwards by 90 units.	278
Fig. 155: SEM image of $Ti_{0.92}O_{2.25}Nb_{0.08}$ film annealed at 375 °C (same resolution as in Fig. 153).	278
Fig. 156: Raman anatase phonon map of an e-beam coated $Ti_{0.92}O_2Nb_{0.08}$ (right) film on B270 glass after annealing at 350 °C.	279
Fig. 157: Combined anatase phonon maps of PEM controlled rf-sputter coated Nb-doped TiO_2 thin films on B270 glass. The samples are placed (a) 12.5 mm, (b) 42.5 mm, and (c) 72.5 mm horizontally from the Nb wire, and the Ti target surface is oxidized by 65%, 68%, 71%, or 78%.	282
Fig. 158: Phonon domain sizes in the combined anatase phonon maps of PEM controlled rf-sputter coated Nb-doped TiO_2 thin films on B270 glass. The samples are placed (a) 12.5 mm, (b) 42.5 mm, and (c) 72.5 mm horizontally from the Nb wire, and the Ti target surface is oxidized by 65%, 68%, 71%, or 78%.	283
Fig. 159: Conductivity vs. phonon domain of PEM controlled rf-sputter coated Nb-doped TiO_2 thin films on B270 glass. The samples are placed (a) 12.5 mm, (b) 42.5 mm, and (c) 72.5 mm horizontally from the Nb wire, and the Ti target surface is oxidized by 65%, 68%, 71%, or 78%.	284
Fig. 160: 2D representation of the conductivity of the films annealed at 475 °C vs. the oxidation state of the Ti target surface and the position of the sample horizontally from the Nb wires.	284
Fig. 161: 2D representations of the average conductivity of both annealing temperatures (530 °C and at 475 °C) (top), and the Raman domain size (bottom) vs. the oxidation state of the Ti target surface and the position of the sample horizontally from the Nb wires.	285
Fig. 162: 2D representations of Raman anatase peak parameters of the Eg(1) peak (left) and the B1g peak (right) vs. the ox.t. and the sample position. The figures show the peak widths (top), positions (middle), and intensities (bottom).	286
Fig. 163: Combined anatase phonon maps of PEM controlled rf-sputter coated Nb-doped TiO_2 thin films on B270 glass, with 71% oxidation of the Ti target surface. The samples are placed (a) 12.5 mm, (b) 42.5 mm, and (c) 72.5 mm horizontally from the Nb wires are deposited for 10, 20, 40, and 60 minutes.	287
Fig. 164: S1-S4: Phonon domain size vs. film thickness, in the Raman maps of the samples coated at positions (a) 12.5 mm, (b) 42.5 mm, and (c) 72.5 mm horizontally from the Nb wires.	288
Fig. 165: Darkfield spectrum measured inside of a Renishaw InVia μ Raman spectrometer (without incident laser beam).	292
Fig. 166: Screenshot of the Renishaw noise filter program. The top left window shows the correlation function, the top right figure is the map and the amount of signal (low = green, high = red) that is affected by the PCA component (here, component 100 is shown). The lower window shows the residual signal that remains when all higher components are deleted.	292
Fig. 167: Example of an auto-correlation function that becomes stationary above 100 components.	293
Fig. 168: Measured (black) and modeled (dashed red) X-ray diffractogram of a $Ti_{0.84}O_{2.25}Nb_{0.16}$ film on B270 glass (light blue) measured in ϑ - ϑ geometry. The films was e-beam evaporated and post-heated at 640 °C. The residual spectrum contains strong signals arising from the substrate holder.	293
Fig. 169: Decomposition of a 633 nm Raman spectrum of an rf-magnetron sputtered Nb-doped TiO_2 thin film on a B270 crown glass substrate (deposited 12.5 mm horizontally from the Nb wire with an estimated target surface oxidation of 68%) into anatase, rutile, brookite, amorphous TiO_2 , substrate, and the substrate. The main phase, anatase, has a strong phase background. The anatase phase background is so intense that it can hardly be separated from the extremely weak anatase B1g peak or from possible small rutile or amorphous TiO_2 contents. The Raman spectra are shifted on the intensity axis in (1, 2, 3, 4, 5, and 7) steps of 50 units as indicated by dotted lines.	294
Fig. 170: Decomposition of an X-ray diffractogram of an rf-diode-sputtered TiO_2 thin film on a B270 crown glass substrate deposited at 155 °C into anatase, rutile, brookite, amorphous TiO_2 , substrate, and instrument background. The diffractograms are shifted on the intensity axis in steps of 25 000 counts as indicated by dotted lines.	295
Fig. 171: Decomposition of an X-ray diffractogram of an rf-diode-sputtered TiO_2 thin film on a B270 crown glass substrate deposited at 200 °C into anatase, rutile, brookite, amorphous TiO_2 , substrate, and instrument	

<i>background. The diffractograms are shifted on the intensity axis in steps of 25 000 counts as indicated by dotted lines.</i>	296
<i>Fig. 172: Decomposition of an X-ray diffractogram of an rf-diode-sputtered TiO₂ thin film on a B270 crown glass substrate deposited at 275 °C into anatase, rutile, brookite, amorphous TiO₂, substrate, and instrument background. The diffractograms are shifted on the intensity axis in steps of 25 000 counts as indicated by dotted lines.</i>	297
<i>Fig. 173: Decomposition of an X-ray diffractogram of an rf-diode-sputtered TiO₂ thin film on a B270 crown glass substrate deposited at 415 °C into anatase, rutile, brookite, amorphous TiO₂, substrate, and instrument background. The diffractograms are shifted on the intensity axis in steps of 25 000 counts as indicated by dotted lines.</i>	298
<i>Fig. 174: Decomposition of a 633 nm Raman spectrum of an rf-diode-sputtered TiO₂ thin film on a B270 crown glass substrate deposited at 155 °C into anatase, rutile, brookite, amorphous TiO₂, and the substrate. The Raman spectra are shifted on the intensity axis in (1, 2, 3, 4, 5, and 7) steps of 25 units as indicated by dotted lines.</i>	299
<i>Fig. 175: Decomposition of a 633 nm Raman spectrum of an rf-diode-sputtered TiO₂ thin film on a B270 crown glass substrate deposited at 200 °C into anatase, rutile, brookite, amorphous TiO₂, and the substrate. The Raman spectra are shifted on the intensity axis in (1, 2, 3, 4, 5, and 7) steps of 30 units as indicated by dotted lines.</i>	300
<i>Fig. 176: Decomposition of a 633 nm Raman spectrum of an rf-diode-sputtered TiO₂ thin film on a B270 crown glass substrate deposited at 275 °C into anatase, rutile, brookite, amorphous TiO₂, and the substrate. The Raman spectra are shifted on the intensity axis in (1, 2, 3, 4, 5, and 7) steps of 30 units as indicated by dotted lines.</i>	301
<i>Fig. 177: Decomposition of a 633 nm Raman spectrum of an rf-diode-sputtered TiO₂ thin film on a B270 crown glass substrate deposited at 415 °C into anatase, rutile, brookite, amorphous TiO₂, and the substrate. The Raman spectra are shifted on the intensity axis in (1, 2, 3, 4, 5, and 7) steps of 50 units as indicated by dotted lines.</i>	302
<i>Fig. 178: Decomposition of a 532 nm Raman spectrum of an rf-diode-sputtered TiO₂ thin film on a B270 crown glass substrate deposited at 155 °C into anatase, rutile, brookite, amorphous TiO₂, and the substrate. The Raman spectra are shifted on the intensity axis in (1, 2, 3, 4, 5, and 7) steps of 5 units as indicated by dotted lines.</i>	303
<i>Fig. 179: Decomposition of a 532 nm Raman spectrum of a TiO₂ thin film on an rf-diode-sputtered B270 crown glass substrate deposited at 200 °C into anatase, rutile, brookite, amorphous TiO₂, and the substrate. The Raman spectra are shifted on the intensity axis in (1, 2, 3, 4, 5, and 7) steps of 10 units as indicated by dotted lines.</i>	304
<i>Fig. 180: Decomposition of a 532 nm Raman spectrum of an rf-diode-sputtered TiO₂ thin film on a B270 crown glass substrate deposited at 275 °C into anatase, rutile, brookite, amorphous TiO₂, and the substrate. The Raman spectra are shifted on the intensity axis in (1, 2, 3, 4, 5, and 7) steps of 10 units as indicated by dotted lines.</i>	305
<i>Fig. 181: Decomposition of a 532 nm Raman spectrum of a TiO₂ thin film on an rf-diode-sputtered B270 crown glass substrate deposited at 415 °C into anatase, rutile, brookite, amorphous TiO₂, and the substrate. The Raman spectra are shifted on the intensity axis in (1, 2, 3, 4, 5, and 7) steps of 15 units as indicated by dotted lines.</i>	306
<i>Fig. 182: Measured (black) and modeled (dashed red) X-ray diffractogram of a titanium oxide thin film with 8 at.% Nb – e-beam evaporated onto a fused silica substrate and post-heated at 750 °C – decomposed into a background (light blue) and a thin film (dark red). The background is split into the fused silica substrate (medium blue) and an instrument background (dashed dark blue). The film is decomposed into anatase (green), brookite (orange), rutile (blue), and amorphous TiO₂ (dark gray). The residual diffractogram is medium gray. The diffractograms are shifted on the intensity axis in steps of 10 kcps as indicated by dotted lines.</i>	307
<i>Fig. 183: Measured (black) and modeled (dashed red) spectrum of an e-beam coated titanium oxide thin film doped with 8 at.% Nb on fused silica post-heated at 750 °C – decomposed into substrate (light blue) and thin film (dark red). The substrate spectrum is split into luminescence (mid blue) and Raman bands (dashed dark blue) and the thin film is decomposed into anatase (green), brookite (orange), rutile (blue), and amorphous TiO₂ (dark gray) spectra. The crystalline spectra are divided into first-order scattering (black dashed lines) and phase background (light gray lines). The excluded range is light red and the low priority range is light brown. The Raman spectra are shifted on the intensity axis in (1, 2, 3, 4, 5, and 7) steps of 200 units as indicated by dotted lines.</i>	308

Fig. 184: Decomposition of measured B270 glass substrate Raman spectra (532 nm) into luminescence and Raman active modes. _____	309
Fig. 185: AFM images of an uncoated B270 glass substrate (left) and a substrate that was coated with TiO ₂ for 2 minutes by rf-diode sputtering (right). The images have areas of 1 μm × 1 μm and were taken using a height sensor (top) as well as an adhesion sensor (bottom). _____	309
Fig. 186: XPS spectrum of a TiO ₂ thin film rf-diode sputtered for 2 minutes onto a B270 glass substrate. ____	310
Fig. 187: Relationship between the Raman peak width and the crystallite size (as estimated by XRD with the Scherrer method) of two sets of nano powders differently synthesized from hydrolysis of alkoxide. Figure taken from Iida et al. ¹⁵¹ _____	310
Fig. 188: Rutile Raman peak positions vs. widths of diode sputtered mixed-phase TiO ₂ thin films on B270 glass (Eg: left side, A1g: right side) marked as blue triangles. The arrows indicate increasing deposition temperature (155 °C – 415 °C). The figure contains literature values of Swamy et al. (open symbols) and of Mazza et al. (closed symbols) as well as the values calculated with a phonon confinement model by Mazza et al. Parts of a figure of Swamy et al. is added to this figure. ^{48,163} _____	311
Fig. 189: Measured (black) and modeled (“fit”, dashed red) XRD diffractograms of an undoped TiO ₂ film on B270 glass annealed at 640 °C (black), fitted peak positions (blue), and peak positions (dotted red) modeled by lattice parameters a and c. The fitted and the modeled positions are less than 0.01° apart. _____	311
Fig. 190: XRD (101) peak width of e-beam evaporated Nb0, Nb1, and Nb2 thin films in theta-theta geometry vs. annealing temperature. _____	312
Fig. 191: Crystallite size of (101)-oriented grains according to Scherrer in e-beam evaporated Nb0, Nb1, and Nb2 films vs. annealing temperature. _____	312
Fig. 192: Raman spectra of varying polarizations (unpolarized (black), circularly polarized (red), orthogonally polarized (green)) on various positions on a Ti _{0.84} O _{2.25} Nb _{0.16} film that was annealed at 640 °C, sorted by the height of the Eg(1) peak in the unpolarized spectra. Left: Eg(1) peak. The spectra of each position are shifted on the intensity axis. Right: detailed view on the whole range of measurement (same spectra), shifted by 50 units on the intensity axis for each position. _____	313
Fig. 193: Lorentz-Lorentz plots of the refractive indices of Nb0, Nb1, Nb2 with two trendlines each, of which one goes through zero. _____	314
Fig. 194: Comparison of the Nb0 trendlines from Fig. 193 with literature values. Parts of Fig. 12 of Mergel et al. were copied into this figure. ⁵³ _____	314
Fig. 195: Potential current-voltage characteristics of e-beam coated crystalline Nb0, Nb1, and Nb thin films on B270 glass. All displayed films show a power of 1.3 (±0.1) relationship. _____	315
Fig. 196: Linear current-voltage characteristics of e-beam coated Nb0, Nb1, and Nb thin films, and of the B270 glass substrate. The films are amorphous and not post-heated, except of the crystalline undoped films post-heated at 420 °C and 530 °C (light and medium green lines). _____	315
Fig. 197: Oxygen content of PEM controlled rf-sputter coated Nb-doped TiO ₂ thin films on B270 glass as determined by RBS at the surface (RBS.s), at the interface (RBS.i) and by EDX vs. the average of both RBS values. _____	316
Fig. 198: Comparison of Raman peak parameters and conductivities of PEM controlled rf-sputter coated Nb-doped TiO ₂ thin films on B270 glass. The Ti target surface is oxidized by 65%, 68%, 71%, or 78%. The samples are placed 12.5 mm, 42.5 mm, and 72.5 mm horizontally from the Nb wires and the film thickness decreases with the distance from the wire. _____	316
Fig. 199: SEM image (100 000 x) of a TiO ₂ film annealed at 640 °C. _____	317
Fig. 200: SEM image (200 000 x) of a TiO ₂ film annealed at 640 °C. _____	317
Fig. 201: SEM image (1 000 000 x) of a TiO ₂ film annealed at 640 °C. _____	318
Fig. 202: SEM image (100 000 x) of a Ti _{0.92} O _{2.25} Nb _{0.08} film annealed at 640 °C. _____	318
Fig. 203: SEM image (200 000 x) of a Ti _{0.92} O _{2.25} Nb _{0.08} film annealed at 640 °C. _____	319
Fig. 204: EDX spectra of Nb2 (640 °C) with acceleration voltages of 5 kV (red), 10 kV (blue), and 15 kV (green). _____	319
Fig. 205: EDX maps (4 μm × 4 μm) of Ti _{0.84} O _{2.25} Nb _{0.16} film annealed at 640 °C of (a) Ti, (b) O, (c) Nb, and (d) Si. _____	320
Fig. 206: 2D representations of Raman anatase peak parameters of the Eg(1) peak (left) and the B1g peak (right) vs. the ox.t. and the sample position. The figures show the peak widths (top), positions (middle), and intensities (bottom). _____	320

List of Tables

<i>Table 1: Structural properties of TiO₂ allomorphs</i>	23
<i>Table 2: Influence of material properties on Raman peak shape and band gap</i>	40
<i>Table 3: Deposition parameters of rf-diode sputtered films</i>	48
<i>Table 4: Interpretation of colors in the combined phonon maps or TiO₂ phase maps</i>	62
<i>Table 5: Fit parameters of the amorphous phase model</i>	93
<i>Table 6: Fit parameters of the first-order scattering model of anatase</i>	95
<i>Table 7: Linked parameters of the first-order scattering model of anatase</i>	95
<i>Table 8: Fit parameters of the first-order scattering model of rutile</i>	96
<i>Table 9: Linked parameters of the first-order scattering model of rutile</i>	96
<i>Table 10: Fixed parameters of the first-order scattering model of rutile</i>	96
<i>Table 11: Fit parameters of the first-order scattering model of brookite</i>	97
<i>Table 12: Fixed parameters of the first-order scattering model of brookite</i>	97
<i>Table 13: Linked parameters of the phase background spectra</i>	99
<i>Table 14: Fit parameters of the anatase phase background model</i>	100
<i>Table 15: Linked parameters of the anatase phase background model</i>	101
<i>Table 16: Fit parameters of the anatase phase background model</i>	105
<i>Table 17: Fit parameters of the B270 glass model</i>	106
<i>Table 18: Fit parameters of the amorphous TiO₂ phase XRD model</i>	110
<i>Table 19: Fit parameters for each individual peak of the single-phase anatase XRD model</i>	111
<i>Table 20: Fit parameters of the multi-phase anatase and rutile XRD models</i>	112
<i>Table 21: Fit parameters of the minor-phase brookite XRD model</i>	113
<i>Table 22: Fit parameters for the substrate and background XRD models</i>	115
<i>Table 23: Fit results of the decomposition of amorphous TiO₂ into nominal crystalline phases</i>	253

Acknowledgements

My university work was a journey. In this journey I had the luck and pleasure to cooperate with people of various fields. Considering its interdisciplinary nature and variety of fields (physical experiments, engineering, project management, networking, computer simulations, and supervision of students), I am deeply grateful to many people. Their academic, organizational, and personal support made my work possible.

After my state exam in the Technical Physics group of Prof. Dr. Dr. h.c. Volker Buck and Prof. Dieter Mergel, a new fund of the Mercator Research Center Ruhr allowed me to network, find project partners, and to write an application for a project, which was then funded by the Bundesministerium für Bildung und Forschung (BMBF) and supervised by Prof. Dr. Dr. h.c. Buck. In that project we invented a coating technology that allows to coat metal alloys using the anodic vacuum arc. My originally intended dissertation topic was connected to the work of that project. The project has finally resulted in a patent application.

I have therefore changed the topic of my dissertation to TiO₂ thin films, which I had been working on during my cooperation with Prof. Dieter Mergel and his post-doc, Dr. Sanat Kumar-Mukherjee, and during the supervision of students.

Thanks to Prof. Dr. Dr. h.c. Buck's and Dr. Nicolas Wöhrle's connection to the Center for Nanointegration Duisburg-Essen (CENIDE), our lab and offices could move into the NanoEnergieTechnikZentrum (NETZ), which gave me the opportunity to extensively use a new state-of-the-art Raman spectrometer in the Interdisciplinary Center for Analytics on the Nanoscale (ICAN). This then allowed me to focus my research on Raman spectra of TiO₂ thin films.

I am very grateful and would like to express my acknowledgements to:

Prof. Dr. Dieter Mergel, my supervisor, for giving me the opportunity to do this work, his dedicated supervision of my work, his valuable and patient guidance, and the interesting and friendly conversations about physics and life. I am deeply thankful for all of his support.

Prof. Dr. Dr. h.c. Volker Buck for welcoming me to the Thin Film group, his support, his supervision during my state examination and during the work on my former PhD topic, which brought forth a patent application, his trust in my project work/management, connecting me to CENIDE, wise advice, and for creating a workgroup spirit in which the members take responsibility for each other like in a family.

Prof. Dr. Friederike Deuerler for her support and supervision of my work at the chair of Materials Technology at the University of Wuppertal.

Dr. Bärbel Maullu and Dietrich Tönnies for their supervision of my teaching at the University of Duisburg-Essen, the interesting and friendly conversations, their support and trust in my work.

Prof. Dr. Dietrich Wolf for excellent lectures as well as interesting and friendly conversations.

The Science Support Center of the University of Duisburg Essen for their organizational and financial support.

All above mentioned as well as the Zentrales Innovationsprogramm Mittelstand (ZIM), the Mercator Research Center Ruhr (MERCUR), and the BMBF for funding my work. Special thanks go to the BMBF for their trust in me and for including me as a civil representative into the Beraterkreis Energietechnologien für die Zukunft in 2011.

Prof. Dr. Matthias Wuttig for his willingness to be my second examiner.

Dr. Christian Notthoff for encouraging me to work in the Thin Film group of the University of Duisburg-Essen as well as to write my doctoral thesis, interesting discussions on good scientific work, his lectures and seminars when I was a student, his assistance and trust in my work with the scanning electron microscope, arranging X-ray absorption fine structure and small-angle X-ray scattering measurements, having the experience to control an airplane, the good time at university and during climbing, and our friendship.

Dr. Nicolas Wöhrl for his scientific as well as personal advice, guidance during my work in the NETZ, arranging my stay in China, cooperation in many ways, good conversations, the respectful and friendly atmosphere, and for the good time at conferences, in China, and during climbing.

Dr. Oleksiy Filipov for introducing me to working at the lab, patiently teaching me experimental skills, discussions on physics and life, and our friendship.

Dipl.-Phys.Ing. Martin Jerman for the evaporation of e-beam films, the transmittance and reflectance measurements, discussions on physics and life, and our friendship.

Gérald Kämmerer for cooperation in many ways, support with quantum mechanics, discussing details of my work, interesting conversations, good times, and our friendship.

Prof. Dr. Axel Lorke for the excellent lecture on solid state physics, his support, and his trust in my abilities.

Prof. Dr. Gerhard Wurm for backing my work with staunchly fairness.

Prof. Dr. Stefan Thomae for providing me opportunities to grow, and for not succeeding in stopping me.

Prof. Dr. Norbert Treitz (R.I.P.) for inspiration, new perspectives on physics, sharpening my mind, as well as endless exciting and good conversations about physics, ethics, art, and life.

Dr. Yang Yang He and Bao Sheng Cao for inviting me to a talk at the Dalian Nationalities University (大连民族学院), Optoelectronic Institute of Technology, Dalian, China, and our friendship.

Monika Timpner for her support in many ways, measurements of Raman maps, good times, and our friendship.

Konstantin Thronberens for the cooperation in our work with the anodic vacuum arc, processing of Raman spectra, good times, and our friendship.

Dr. Sanat Kumar Mukherjee for the cooperation in our work, the preparation of plasma-emission controlled rf-magnetron sputtered Nb-doped TiO₂ films, good conversations, and our friendship.

Jingy Shi for the preparation of rf-diode-sputtered TiO₂ films, lending me her mobile phone during my stay in China, and our friendship.

Shixun Cui for the preparation of plasma-emission controlled rf-magnetron sputtered Nb-doped TiO₂ films with varying film thickness, his help and connections for my stay in China, and our friendship.

The members of the Thin Film group, especially Patricia Pop-Ghe, Regina Berendakova, Tatiana-Fedosenko Becker, Michael Becker, Markus Neubert, and Viktoria Khlopyanova for our cooperation, their support, interesting discussions on physics and about life, good times inside and outside the university as well as on conferences, and for our friendship.

Dr. Alexei Poukhovoi for our cooperation, good conversations, and ceremonial handover of the joy and burden of a certain desk.

Hayat Zayani, Reinhard Remfort, André Giese, Paul Sela, Sebastian Tigges, Sven Daamen, Marc Michalewski, Azadeh Soleimani Esfahani, Mohammed Abass, and Berrin Küzün for our cooperation, their support, and the good times at the university.

Dr. Luís Rino and Joana Mendes for interesting conversations and a good time in China.

Dipl.-Phys.Ing. Klaus Pärschke for his technical help, good advice, and interesting conversations.

Heidi Pärschke for her kind help with bureaucracy and friendly conversations.

Dipl.-Phys.Ing. Ingo Erdmann for his support as well as our cooperation in so many ways, good times, and our friendship.

Henry Pusch for life lessons.

Brigitte Fricke for her support with bureaucracy.

The members of the chair of Materials Technology at the University of Wuppertal for preparing me for working in the economy.

The CENIDE team – especially the director Dr. Tobias Teckentrup, the PR and science manager Steffi Nickol, the coordinator Marion Franke, the coordination assistant Melanie Daamen, the technicians Dr.-Ing. Ralf Starke and Sebastian Rosendahl – for their support in so many ways, for hosting my work in the NETZ, cooperation, friendly conversations, and for creating the open-minded spirit of interdisciplinary working.

The ICAN team for their support in so many ways and for giving me access to a high variety of analysis equipment. I am especially grateful to Dr. Ulrich Hagemann for his support, his trust in my work with the Raman spectrometer, and for X-ray photoelectron spectroscopy measurements, Marcel Wienand for his patient help with bureaucracy and organization as well as for friendly conversations, Dr.-Ing. Steffen Franzka for measurements with the atomic force microscope, and Dr. Markus Heidelmann for transmission electron microscopy experiments, and interesting discussions on physics.

The employees that have been working in the NETZ building for creating an atmosphere that makes you look forward to go to work, and for living the interdisciplinary CENIDE spirit.

Dr. Gregor Fornalczyk for our great cooperation in many ways, and the good times at meetings and conferences.

Prof. Dr. Claudia Staudt, Benedikt Crone and BASF SE for the great cooperation.

Claus Irsa for the spirit of our cooperation, interesting and friendly conversations, and the good times.

Bernd Oberschachtsiek and the Zentrum für BrennstoffzellenTechnik (ZBT) GmbH for great cooperation in many ways, and to Sebastian Stypka for the brainstorming which eventually resulted in my project on anodic arc evaporation, for the good times and our friendship.

Frank Mumme and the Kunststoff-Institut für die mittelständische Wirtschaft NRW GmbH (Kunststoffinstitut Lüdenscheid), Weißer + Gießhaber GmbH, Bauser GmbH, Braunform GmbH, and Kisico Kirchner, Simon & Co. GmbH for the good cooperation.

Christian Kloos and the Schulz-Electronic GmbH for the helpful cooperation and the customized power supplies.

Dietrich Sekels, Stefan Hiebel, Denis Filistovich for interesting cooperations, their support in many ways, and good conversations.

Prof. Dr. Winterer for giving me access to the X-ray diffractometer and the scanning electron microscope of the Nanoparticle Process Technology group at the University of Duisburg-Essen.

The members of the Nanoparticle Process Technology group, especially Alexander Kompch, Thomas Winter, Viktor Mackert, Dr. Stevan Ognjanovic, Samer Suleiman, Lukas Helmbrecht, and Ulf Spengler, for introducing me to operating the X-ray diffractometer, cooperation, support, good conversations, and for the good time at the University or during climbing.

Dr. Hans-Werner Becker for the Rutherford backscattering spectrometry (RBS) measurements in the Rubion group at the Ruhr University Bochum and for introducing me to the evaluation of the RBS spectra.

Smail Boukercha for experiments with the scanning electron microscope and energy dispersive X-ray spectroscopy.

Prof. Dr. Burak Atakan for giving me access to the X-ray diffractometer of the Fachgebiet Thermodynamik, Institut für Verbrennung und Gasdynamik, Abteilung Maschinenbau und Verfahrenstechnik, Fakultät für Ingenieurwissenschaften, Universität Duisburg-Essen.

Dr. Daniel Stenders, Dipl.-Ing. Andreas Görnt, Dr. Christian Pflitsch for their support with the X-ray diffractometer.

Prof. Dr. Marika Schleberger for her support, friendly cooperation, and for giving me access to the atomic force microscope of the 2D Material Science group at the University of Duisburg-Essen.

Lara Bröckers for introducing me to using the atomic force microscope.

Prof. Dr. Roland Schmechel for giving me access to the four-point-probe of the Fachgebiet Nanostrukturtechnik, Fakultät für Ingenieurwissenschaften, University of Duisburg-Essen.

Dr. Matthias Caninenberg and Martin Dehnen for introducing me to using the four-point-probe and their support.

Dr. Thorsten Peters and Dr. Christian Zillich for the cooperation and support during my state examination and during my early steps of applying for project fundings.

Dr. Jan Wieneke for the cooperation and support during my state examination, for networking, and for the good conversations that I remembered well during my PhD studies, which helped me to keep going

Christian Gollwitzer for X-ray absorption fine structure and small-angle X-ray scattering measurements, and Patrick Kluth for discussion on the small-angle X-ray scattering

measurements. Too bad that we could not meet and continue our measurements due to external circumstances that are beyond our control.

Dr. Horst Ehrich, Brunhilde Hasse, Michael Mausbach, Hans-Peter Hinz, K.G. Müller, Dr. Hans-Michael Katsch and their colleagues for their innovative research on vacuum arcs.

Prof. Dr. Ulrich Schreiber of the Department of Geology at the University of Duisburg-Essen for interesting cooperation and fascinating conversations on the emergence of life.

Astrid Hilker, Doris Schwarzer, Linda Dorsch, Gabriela Binder, Britta Oppermann, Ulrike Dunkelberg, Gisela Dittmaier, and the other administrative staff members of the University of Duisburg-Essen for helpful and friendly support in so many ways.

Alexandra Esser, Astrid Lewalter, and the Projektträger Jülich for their helpful and friendly project administration.

Marcel Hentschel, Annerose Seidel, Betisa Schahabian, and the other administrative staff members at the University of Wuppertal that helped me with bureaucracy.

Dr. Isabel Aller and the patent department for the kind help with the patent application.

Dr. Matthias Voetz, my mentor of the Deutsche Physikalischen Gesellschaft (DPG), for the dedicated and passionate mentoring, giving me insight into different fields of work, as well as very helpful, interesting, and friendly conversations.

The organization team of the mentoring program of the DPG, Andreas Hofmann, Dr. Anja Metzelthin, Claudia Zoll, Dr. Daniel Fulger, Dr. Rolf Loschek, Eva Cauet, Marcel Wunram, Florian Weiser and Markus Tegeder for their passionate and elaborate organization of the DPG mentoring program, and for welcoming me as a member of the organization team.

Dr. Péter Krüger, Dr. Martin Letz, Dr. Uwe Möller, Dr. Jan Marien, Dr., Helmut Dumont, Dr. Michael Graefenstedt, Dr. Dagmar Thien, Dr. Clemens Wünsche, Achim Manze, Dr. Andreas Meschede, Dr. Markus Heinrich, Dr. Dirk Macke, and the DPG mentors which I did not mention by name, for the effort and passion they put into the mentoring program, and for interesting, inspiring, and helpful conversations.

All friends who are still befriended with me although I have not managed well to keep in touch during my PhD time, who inspired me to keep going, for our friendships and so many things, Kim Carson, Krischan Bülte and his family, Katrin, Babsi and Lotta, Laura Karsten and her family, Martin Schubert, Antigone Reiff, Tobias Häusler, Goerg Börner, Sanni and Stefan Belda, Amina and Christian Buck and their family, Prof. Dr. Stefan Jansen, Markus Köhl, Karin

and Dr. Tim Loppe, Dr. Frank Fasbender, Dr. Deniz Yilmas, and all of my friends, which I did not mention by name, from or in Krefeld, the Ruhr area, the Sauerland, Karlsruhe, Kassel, Saxony, Switzerland, and last but not least, André Hertel with the Grusi Homepage and die Annern in Upper Franconia.

My bands and the music scene, clubs, zines, non-profit-organizations, supporters, and organizers for the catharsis and entropy!

My horde, Dr. Oliver Kann, Christian Gemsa, Annette and Dr. Jürgen Habermaier, Jan Rummel and his family, Dirk Midderhoff, Veit Benning and his family, Irmi, Bernd, Joscha, and Dr. Ben Weinberg, and last but not least, Friedrich and Ulrike Sibierski for so many things.

I am deeply grateful to my parents Annette and Karl-Heinz Schipporeit, my brother Dennis Schipporeit, and all of my family members for their care and inspiration, and their support in so many ways throughout my whole life.

I am especially grateful to my girlfriend Nadja for our love and for her inspiring encouragement during my PhD time.

All the people I did not mention here, who are in my heart or contributed to my PhD directly or indirectly.

Publications and presentations related to this dissertation

Publications

- S. Schipporeit**, D. Mergel (2018). Backcover Image. *J. Raman Spectrosc.* 49.
- S. Schipporeit**, D. Mergel (2018). *Spectral decomposition of Raman spectra of mixed-phase TiO₂ thin films on Si and silicate substrates.* *J. Raman Spectrosc.* 49, 1217–1229.
- S. K. Mukherjee, A. Nebatti, F. Mohtascham, **S. Schipporeit**, C. Notthoff, D. Mergel (2014). *Influence of thickness on the structural properties of radio-frequency and direct-current magnetron sputtered TiO₂ anatase thin films.* *Thin Solid Films* 558, (2), 443–448.
- S. K. Mukherjee, H. W. Becker, A. P. Cadiz Bedini, A. Nebatti, C. Notthoff, D. Rogalla, **S. Schipporeit**, A. Soleimani-Esfahani, D. Mergel (2014). *Structural and electrical properties of Nb-doped TiO₂ films sputtered with plasma emission control.* *Thin Solid Films* 568, 94–101.

Poster(s)

- S. Schipporeit**, S. K. Mukherjee, A. Nebatti, F. Mohtascham, C. Notthoff, D. Mergel (2014). *Influence of film thickness on structural properties of TiO₂ films coated with RF and DC magnetron sputtering.* DPG Spring Meeting, Dresden.

Lecture(s)

- S. Schipporeit** (2014). Invited guest lecture: *Transparent conducting oxides*, Optoelectronic Institute of Technology, Dalian Nationalities University (大连民族学院), Dalian, China.

Talks (lecturer highlighted)

- S. Schipporeit**, D. Mergel, V. Buck (2017). *Quantitative Raman spectroscopy of doped and undoped multiphase TiO₂ thin films on complex substrates.* DPG Spring Meeting, Dresden.
- S. Schipporeit** (2017). Invited talk: *Thin film deposition and characterization techniques.* Working group Lorke, Faculty of Physics, Experimental Physics. University of Duisburg-Essen.
- J. Shi, **S. Schipporeit**, K. Pärschke, D. Mergel (2016), *Structural and optical properties of TiO₂-films with thicknesses from 2 to 200 nm deposited with RF-diode sputtering.* DPG Spring Meeting, Regensburg.
- S. Schipporeit** (2014). *Strukturelle und elektrische Eigenschaften von Nb-dotiertem TiO₂, gesputtert mit Plasma-Emissions-Regelung.* Invited talk. Workshop Sputter deposition of oxidic thin films. University of Duisburg-Essen/RWTH Aachen.
- S. Schipporeit** (2014), S. K. Mukherjee, H. W. Becker, A. P. Cadiz Bedini, C. Notthoff, A. Nebatti, D. Rogalla, A. Soleimani-Esfahani, D. Mergel. *Structural and electrical properties of Nb doped TiO₂ anatase films (2 – 17 at.%) sputtered with plasma emission control.* DPG Spring Meeting, Dresden.

Erklärung zur Dissertation

Ehrenwörtliche Erklärung zu meiner Dissertation

mit dem Titel:

Decomposition, quantitative and qualitative evaluation of TiO₂ thin film Raman spectra

Hiermit erkläre ich, dass

- ich die beigefügte Dissertation selbstständig verfasst habe,
- keine vorausgegangenen Promotionsverfahren in der Physik oder in einem anderen Fach endgültig gescheitert sind,
- ich bei der Abfassung der Dissertation nur die angegebenen Hilfsmittel benutzt und alle wörtlich oder inhaltlich übernommenen Stellen als solche gekennzeichnet habe,
- ich die Dissertation nur in diesem Promotionsverfahren eingereicht habe.

Essen, den 15.05.2020

Sebastian Schipporeit

DuEPublico

Duisburg-Essen Publications online

UNIVERSITÄT
DUISBURG
ESSEN

Offen im Denken

ub | universitäts
bibliothek

Diese Dissertation wird via DuEPublico, dem Dokumenten- und Publikationsserver der Universität Duisburg-Essen, zur Verfügung gestellt und liegt auch als Print-Version vor.

DOI: 10.17185/duepublico/74147

URN: urn:nbn:de:hbz:464-20210505-141447-3



Dieses Werk kann unter einer Creative Commons Namensnennung 4.0 Lizenz (CC BY 4.0) genutzt werden.